Technical Report Documentation Page

1. Report No. FHWA/TX-09/0-5134-2	2. Government Accession No.	3. Recipient's Catalog No.
4. Title and Subtitle CHARACTERIZATION OF SELF-CONSOLIDATING CONCRETE FOR DESIGN OF PRECAST, PRESTRESSED BRIDGE GIRDERS		5. Report Date Published: December 2008 6. Performing Organization Code
7. Author(s) David Trejo, Mary Beth Hueste, Young Hoon Kim, and Hakan Atahan		8. Performing Organization Report No. Report 0-5134-2
9. Performing Organization Name and Address Texas Transportation Institute The Texas A&M University System College Station, Texas 77843-3135		10. Work Unit No. (TRAIS) 11. Contract or Grant No. Project No. 0-5134
12. Sponsoring Agency Name and Address Texas Department of Transportation Research and Technology Implementation Office P. O. Box 5080 Austin, Texas 78763-5080		13. Type of Report and Period Covered Technical Report: September 2004 – December 2007 14. Sponsoring Agency Code

15. Supplementary Notes
Project performed in cooperation with the Texas Department of Transportation and the Federal Highway Administration.
Project Title: Self-Consolidating Concrete for Precast Structural Applications
URL: http://tti.tamu.edu/documents/0-5134-2.pdf

16. Abstract
This report documents the findings of a Texas Department of Transportation sponsored research project to study self-consolidating concrete (SCC) for precast concrete structural applications. Self-consolidating concrete is a new, innovative construction material that can be placed into forms without the need for mechanical vibration. The mixture proportions are critical for producing quality SCC and require an optimized combination of coarse and fine aggregates, cement, water, and chemical and mineral admixtures. The required mixture constituents and proportions may affect the mechanical properties, bond characteristics, and long-term behavior, and SCC may not provide the same in-service performance as conventional concrete (CC). Different SCC mixture constituents and proportions were evaluated for mechanical properties, shear characteristics, bond characteristics, creep, and durability. Variables evaluated included mixture type (CC or SCC), coarse aggregate type (river gravel or limestone), and coarse aggregate volume. To correlate these results with full-scale samples and investigate structural behavior related to strand bond properties, four girder-deck systems, 40 ft (12 m) long, with CC and SCC pretensioned girders were fabricated and tested. Results from the research indicate that the American Association of State Highway Transportation Officials Load and Resistance Factor Design (AASHTO LRFD) Specifications can be used to estimate the mechanical properties of SCC for a concrete compressive strength range of 5 to 10 ksi (34 to 70 MPa). In addition, the research team developed prediction equations for concrete compressive strength ranges from 5 to 16 ksi (34 to 110 MPa). With respect to shear characteristics, a more appropriate expression is proposed to estimate the concrete shear strength for CC and SCC girders with a compressive strength greater than 10 ksi (70 MPa). The researchers found that girder-deck systems with Type A SCC girders exhibit similar flexural performance as deck-systems with CC girders. The AASHTO LRFD (2006) equations for computing the cracking moment, nominal moment, transfer length, development length, and prestress losses may be used for SCC girder-deck systems similar to those tested in this study. For environments exhibiting freeze-thaw cycles, a minimum 16-hour release strength of 7 ksi (48 MPa) is recommended for SCC mixtures.

17. Key Words	18. Distribution Statement
Self-Consolidating Concrete, Prestressed Precast Concrete, Mechanical Properties, Shear Characteristics, Bond Characteristics, Creep, Freezing and Thawing, TxDOT Type A Girder, AASHTO LRFD Specifications	No restrictions. This document is available to the public through NTIS: National Technical Information Service 5285 Port Royal Road Springfield, Virginia 22161

19. Security Classif.(of this report)	20. Security Classif.(of this page)	21. No. of Pages	22. Price
Unclassified	Unclassified	384	

Form DOT F 1700.7 (8-72) **Reproduction of completed page authorized**

CHARACTERIZATION OF SELF-CONSOLIDATING CONCRETE FOR DESIGN OF PRECAST, PRESTRESSED BRIDGE GIRDERS

by

David Trejo, Ph.D., P.E.
Associate Research Engineer
Texas Transportation Institute

Mary Beth Hueste, Ph.D., P.E.
Associate Research Engineer
Texas Transportation Institute

Young Hoon Kim
Graduate Research Assistant
Texas Transportation Institute

and

Hakan Atahan, Ph.D.
Post-Doctoral Research Associate
Texas Transportation Institute

Report 0-5134-2
Project Number 0-5134
Research Project Title: Self-Consolidating Concrete for Precast Structural Applications

Performed in cooperation with the
Texas Department of Transportation
and the
Federal Highway Administration

Published: December 2008

TEXAS TRANSPORTATION INSTITUTE
The Texas A&M University System
College Station, Texas 77843-3135

DISCLAIMER

The contents of this report reflect the views of the authors, who are responsible for the facts and the accuracy of the data presented herein. The contents do not necessarily reflect the official view or policies of the Federal Highway Administration (FHWA) or the Texas Department of Transportation (TxDOT). This report does not constitute a standard, specifications, or regulation. The engineer in charge was David Trejo, Ph.D., P.E.

ACKNOWLEDGMENTS

This project was conducted at Texas A&M University (TAMU) and was supported by TxDOT and FHWA through the Texas Transportation Institute (TTI) as part of Project 0-5134, Self-Consolidating Concrete for Precast Structural Applications. This research was jointly performed with a Drs. David Fowler and Eric Koehler at the University of Texas at Austin, who focused on developing the mixture proportions and evaluating the fresh properties of SCC. Their work is presented in Report 0-5314-1, *Self-Consolidating Concrete for Precast Structural Applications: Mixture Proportioning, Workability, and Early-Age Hardened Properties*. The valuable input of J. Tucker (TxDOT, Research Project Director), J. J. Seiders (TxDOT, Program Coordinator), R. Browne (TxDOT, Project Advisor), J. Moore (TxDOT, Project Advisor), P. Almeida (TxDOT, Project Advisor), and P. Forsling (Federal Highway Administration, Project Advisor) are appreciated. The authors also wish to thank Dr. P. Keating, M. Potter, S. Smith, and J. Perry of the Civil Engineering High Bay Structural and Materials Laboratory (HBSML) at TAMU and all the students who assisted with the project. The creep parts of this report were prepared and data were collected by J. J. Kim. Include also are thanks to BASF Construction Chemicals LLC (Al Pinnelli, V. Bui, E. Attiogbe, and B. Rogers). Field testing and fabrication of the girders was done at the Texas Concrete Company, Victoria, Texas. The research team thanks B. Patton from Texas Concrete Company.

TABLE OF CONTENTS

LIST OF FIGURES

Page

LIST OF TABLES

Page

EXECUTIVE SUMMARY

Self-consolidating concrete (SCC) is defined as highly flowable and nonsegregating concrete that does not require mechanical vibration. Implementing this material in precast plants in Texas has the potential to increase production and safety and decrease costs for fabrication of concrete products. This research evaluated the potential for implementing SCC in precast plants specifically for the fabrication of pretensioned bridge girders. Fabrication with conventional concrete requires a relatively large crew to place, consolidate, and finish these girders. In addition to the crew requirements, the noise associated with the consolidation equipment is excessive – reducing this noise will result in a better and safer work environment.

Mixture proportions are critical for producing quality SCC and require an optimized combination of coarse and fine aggregates, cement, water, and chemical and mineral admixtures. To achieve the full benefits of SCC it is common to reduce the coarse aggregate content and increase the cement paste content of the SCC mixtures. The increased paste content results in good flowability. Concerns with increasing the paste content include the potential for increased creep, decreased shear capacity, nonstandard relationships between compressive strength and other mechanical properties, reduction in bond, different in-service performance as compared to conventional concrete (CC), and increased costs.

The research team performed significant research to evaluate if girders containing SCC can be designed using the American Association of State Highway and Transportation Officials (AASHTO) Load and Resistance Factor Design (LRFD) Specifications. Different SCC mixture constituents and proportions were evaluated for mechanical properties, shear characteristics, bond characteristics, creep, and durability. Variables evaluated included mixture type (CC or SCC), coarse aggregate type (river gravel or limestone), and coarse aggregate volume.

To correlate these results with full-scale samples and investigate structural behavior related to strand bond properties, four full-scale girder-deck systems, 40 ft (12 m) long, with CC and SCC pretensioned girders were fabricated and tested. It should be noted that comparisons were made based on similar 16-hour release strengths. Although the concrete mixtures had similar 16-hour compressive strength values, other characteristics could be different and longer-term strengths were significantly different. However, the practice in Texas is to proportion concrete mixtures to obtain the required 16-hour compressive strength and to provide a check of

later age strength requirements – basically the 16-hour compressive strength is the critical parameter for precast plants.

To assess the applicability of the current AASHTO LRFD Specifications to SCC girders, the research team evaluated whether CC design equations were appropriate for SCC. The research team assessed prediction equations for the modulus of rupture, modulus of elasticity, and splitting tensile strength – all of which are important for the design of prestressed concrete girders. The results indicate that these equations can be used to estimate the mechanical properties of SCC for concrete compressive strengths ranging from 5 to 10 ksi (34 to 70 MPa). In addition, the research team developed new equations for concrete compressive strength ranges from 5 to 16 ksi (34 to 110 MPa). In addition to assessing and developing new prediction equations, the team compared the shear capacity, bond, creep, and durability of SCC mixtures with conventional concrete mixtures.

The results indicate that the concrete shear strength of conventional concrete and SCC may be different and that the AASHTO and MCFT equations may overestimate the shear capacity for both SCC and conventional concrete when the compressive strength is greater than 10 ksi (70 MPa). The researchers developed a new equation for estimating the shear capacity of SCC and conventional concrete for these conditions. Because all mixtures exhibited higher compressive strengths, the team did not assess the shear capacity for compressive strengths less than 10 ksi (70 MPa).

Evaluations for the reduction in bond for top bars were also performed using pull-out tests. The results indicate that the reductions in bond for SCC were similar to that of CC and the AASHTO LRFD (2006) multiplier of 1.4 for computing the development length of top bars is appropriate. Although this was the case for the conditions in this research, deeper girders could exhibit a reduction in bond. Deeper girders were not tested in this project.

The results from the creep study indicated similar creep from the SCC and conventional concrete for concretes with comparable 16-hour strengths. The researchers recommend that the AASHTO LRFD (2006) prediction equation for estimating creep be used for SCC.

The durability of SCC mixtures seems to show similar performance with conventional concrete mixtures with the exception of the freeze-thaw performance of the 5 ksi (34 MPa) release strength mixture. Testing indicated that the SCC with a 5 ksi (34 MPa) release strength exhibited severe damage when evaluated using AASHTO T161 (ASTM C666), procedure A.

Until further testing can be performed, it is recommended that SCC be used in environments where the number of freeze-thaw cycles is low or if using SCC in freeze-thaw environments that a minimum 16-hour release strength of 7 ksi (48 MPa) be specified.

In addition to the smaller scale laboratory tests, full-scale TxDOT Type A girders with cast-in-place concrete decks were evaluated. The girder-deck systems with Type A SCC girders exhibit similar flexural performance as deck-systems with Type A CC girders. The researchers recommend that the AASHTO LRFD (2006) equations for computing the cracking moment, nominal moment, transfer length, development length, and prestress losses may be used for SCC girder-deck systems similar to those tested in this study.

The conclusions of the research findings indicate that SCC should be allowed for use in precast plants in Texas, specifically those plants producing precast, prestressed girders. However, the research found that SCC could be sensitive to environmental and transport conditions. Precast plants should have a good quality control program in place and careful monitoring of the aggregate moisture is necessary. Some segregation of the SCC was observed by the researchers when fabricating the full-scale girders – producers should be aware of this potential segregation issue. Lastly, as with most research, not all combinations of materials, mixtures, or girders were evaluated and reasonable care should be taken when extending the findings of this research to other applications.

CHAPTER 1
INTRODUCTION

1.1 GENERAL

American Concrete Institute (ACI) Committee 237 (2007) defines Self-consolidating concrete (SCC) as highly flowable and nonsegregating concrete that does not need mechanical vibration. To achieve the required fresh properties such as high workability and stability, SCC typically has higher paste volumes and lower coarse aggregate volumes than conventional concrete (CC). Optimized dosages of chemical admixtures (high-range water reduced admixtures [HRWRAs]) can provide both resistance to segregation and high workability. Several universities and transportation agencies have conducted research to develop SCC mixture proportions to evaluate the mechanical and durability characteristics and to evaluate full-scale specimens with SCC (Burgueño and Bendert 2005, Hamilton and Labonte 2005, Naito *et al.* 2006, Ozyildrim 2007, Schindler *et al.* 2007b, Zia *et al.* 2005). In general, when the fresh quality of SCC was satisfactory, the performance of SCC was comparable to that of CC. However, knowledge about the performance of SCC precast, prestressed concrete members is limited. In addition, there is a need to verify the applicability of design equations provided in the American Association of State Highway Transportation Officials Load and Resistance Factor Design (AASHTO LRFD) Specifications (AASHTO 2004, 2006), which is based on the measured properties and performance of CC.

Because there are several advantages of using SCC, the application of this material in precast, prestressed concrete structures could provide significant benefits to the precast industry. Practical benefits include (FHWA and NCBC 2005):

- better finish quality,
- less noise,
- decreased time for placement,
- lower maintenance cost for construction equipment,
- lower labor demands and costs, and
- better quality concrete.

Some state transportation agencies in the United States recently began the task of developing manuals and guidelines for the application of SCC to precast and/or prestressed concrete structural members. Limited research has been conducted to compare performance-based mixture proportions based on 16-hour release strength. Many challenges exist for the application of SCC in the precast, prestressed industry. Precast, prestressed structural members require higher quality control than conventional cast-in-place (CIP) concrete members due to the early strength requirements. In addition, the higher paste content and lower coarse aggregate content of SCC could affect the in-service and structural performance of SCC precast, prestressed girders.

Different mechanical properties can affect structural performance. Mechanical properties include compressive strength, modulus of elasticity (MOE), modulus of rupture (MOR), and splitting tensile strength (STS). These are fundamental properties required to design structural members and predict behavior. Higher paste volumes and lower coarse aggregate volumes can potentially reduce aggregate interlock, resulting in lower shear capacity. Also, highly flowable concrete mixtures such as SCC have the potential to reduce bond capacity due to bleeding. Longer-term properties, such as creep and shrinkage, also need to be investigated. Higher paste volumes in concrete increase creep and shrinkage. These characteristics of SCC can increase loss of prestress, resulting in reduction of capacity and serviceability. Also, the pore structure and air void system of SCC could differ from those of CC, resulting in different durability performance. To successfully implement use of SCC in precast, prestressed structural members, the overall structural and in-service performance, including camber, deflection, prestress loss, flexural capacity, and transfer and development length need to be characterized. Furthermore, appropriate design and prediction equations are necessary to design precast, prestressed structural members made with SCC. More comprehensive research including fresh properties and hardened properties and an assessment of the applicability of design equations are required to provide reliable high-performance precast, prestressed concrete members made with SCC.

1.2 OBJECTIVES AND SCOPE

The objective of this study is to investigate the hardened properties of SCC, including the mechanical properties, shear characteristics, bond characteristics, creep, durability, and structural performance for precast, prestressed concrete structural member applications. The first research

task is to investigate the hardened properties of SCC with various mixture proportions in the laboratory. Author compared the hardened properties of SCC with those of CC. Full-scale Type A girders were fabricated and tested to validate the structural behavior of SCC. These experimental results were used to determine if the standard design equations in the AASHTO LRFD Specifications are appropriate for SCC (AASHTO 2004, 2006). The 2006 AASHTO LRFD Specifications modified several prediction equations. Because implementation of the current AASHTO LRFD Specifications is being transitioned in by the design practices of state transportation agencies, both 2004 and 2006 versions were evaluated. When necessary, new prediction equations are proposed to design precast, prestressed girders containing SCC.

The proposed overall research program included eight tasks including the application of SCC in precast, prestressed bridge girders. The following tasks, described below, were performed.

1.2.1 Task 1: Fresh Characteristics

To achieve adequate flow and stability characteristics, SCC typically has higher paste and lower coarse aggregate volumes than CC. Mixture proportions, workability, and stability of SCC were studied at the University of Texas at Austin (Koehler and Fowler 2008). This report does not include the findings from this task and only focuses on the hardened properties of SCC, which were evaluated at Texas A&M University.

1.2.2 Task 2: Mechanical Characteristics

Fresh properties of SCC could potentially influence the mechanical properties of SCC. These mechanical properties are crucial to the design and performance of precast, prestressed bridge girders. MOE represents the stress-strain relationship in the elastic range and is used in the prediction of deflection and camber of precast, prestressed concrete members. MOR and STS are indirect measurements of the tensile strength of concrete and are used to predict and limit the allowable stresses in critical regions in precast, prestressed concrete members. These properties are used to predict the elastic behavior and flexural and shear capacity of structural members in design standards. Compressive strength is commonly used to predict the structural capacity and the other mechanical properties (MOE, MOR, and STS). Author used test results to evaluate the impact of SCC mixture proportions on mechanical properties and then compared these properties

with those of CC. The applicability of the AASHTO LRFD prediction equations was evaluated. Other available prediction equations were also assessed to determine if they can reasonably predict the mechanical properties of SCC. When necessary, new prediction equations are proposed for SCC in this study.

1.2.3 Task 3: Shear Characteristics

Because the coarse aggregate content directly affects aggregate interlock, SCC may not provide the same shear capacity as CC. Shear capacity is crucial to the shear design of precast, prestressed bridge girders. Push-off tests were performed to investigate the influence of SCC aggregate and paste volumes on shear capacity, and these results were compared with those obtained from similar CC samples. Energy absorption methods were used to quantitatively assess aggregate interlock. Crack slip, crack width, normal stress, and shear stress were measured to evaluate aggregate interlock of the SCC and CC. The relationships between these parameters were used to propose aggregate interlock models to modify the Modified Compression Field Theory (MCFT) adopted in the AASHTO LRFD Specifications. Finally, appropriate equations for shear were proposed for the shear design of precast, prestressed SCC members based on the findings of this study. Applicability of the proposed equations was assessed for the design of precast, prestressed concrete girders.

1.2.4 Task 4: Bond Characteristics

Highly flowable concrete mixtures such as SCC have a potential risk of segregation of aggregate and paste, resulting in reduced bond due to bleeding. Section R 12.2.4 (ACI Committee 318 2005) indicates the reduced bond capacity of horizontal reinforcement near the top surface resulting from bleeding as the top-bar effect. Pull-out tests were performed to evaluate the relative bond resistance for SCC and CC mixtures containing both top and bottom bars. This research determined whether the top bar factor in the AASHTO LRFD Specifications was applicable to the SCC mixtures evaluated in this study.

1.2.5 Task 5: Creep

High paste volumes, typical of SCC mixtures, may lead to increased creep, which increases concrete compressive strain in prestressed concrete structures. This leads to a reduction in the prestressing force for these members. The objective of this portion of the test program was

to measure and compare creep for SCC and CC mixtures. The applicability of the AASHTO LRFD prediction equations was evaluated. Other available prediction equations were also assessed to determine if they can reasonably predict creep in SCC.

1.2.6 Task 6: Durability

Fresh properties of SCC could potentially influence the durability of SCC. The dispersion mechanism and performance of HRWRAs could influence the air void system and the interfacial transition zone between the aggregate and cement paste. The pore structure and air void system are significant factors that can influence the durability of SCC. The objective of the experimental program was to evaluate the durability of the SCC mixtures. Permeability, diffusivity, and freezing and thawing resistance were assessed in this study.

1.2.7 Task 7: Full-Scale Testing and Validation

Based on test results of various mixtures evaluated in the laboratory, author selected one SCC and one CC mixture containing each aggregate type for full-scale testing. Full-scale precast, prestressed girders were cast at a precast plant. A deck was cast on each girder to represent actual composite bridges found in the field. The presence of the deck alters the section properties of the composite girders, resulting in a change in the overall behavior. The objective of the experimental program was to investigate the overall in-service and structural performance of full-scale, precast, prestressed girder-deck systems and to compare this performance with similar systems containing CC. Also, laboratory test results were correlated with full-scale testing. The following hardened properties and structural performance parameters were investigated:

- early age characteristics and plant observation,
- mechanical properties,
- flexural capacity,
- transfer length,
- development length,
- prestress losses, and
- camber and deflection.

Finally, the applicability of the AASHTO LRFD prediction equations for hardened properties was evaluated. Recommendations for the use of SCC in precast, prestressed concrete bridge girders are provided.

1.3 ORGANIZATION OF THIS REPORT

Chapter 2 of this report provides a review of previous SCC studies and background of design equations related to mechanical characteristics, bond characteristics, shear characteristics, creep, durability, and mixture proportions on the performance of precast, prestressed structural members. Chapter 3 presents materials, mixture proportions, and mechanical and chemical properties of materials used in this study. Chapter 4 describes the test matrix and test procedures of all experimental programs, both laboratory- and full-scale testing. Chapter 5 presents the test results and analyses of the mechanical testing program: compressive strength, MOE, MOR, and STS. Chapter 6 describes the results of the shear push-off tests and analyses of the aggregate interlock models applicable to the AASHTO LRFD Specifications. Chapter 7 presents the test results for bond, creep, and durability characteristics of the SCC mixtures. Chapter 8 presents the test results and analyses for the structural performance of full-scale Type A girders made with the SCC mixtures. Chapters 5 to 8 include the comparison of hardened properties between SCC and CC mixtures, the impact of mixture proportions on hardened properties, and the assessment of the applicability of the AASHTO LRFD Specifications along with other applicable prediction equations. Finally, the findings from this study and recommendations are summarized in Chapter 9. Additional information is provided in the Appendices.

CHAPTER 2
LITERATURE REVIEW

2.1 GENERAL

SCC was first developed and extensively used for bridges in the early 1990s in Japan (Okamura and Ozawa 1994). Several European countries organized an association in 1996 to develop SCC for field and precast applications. Recently the Self-Compacting Concrete European Project Group developed the "European Guidelines for Self Compacting Concrete" (EFNARC 2001, 2005). Because SCC is very sensitive to variations of mixture constituent types and quantities and environmental conditions, precasters having better quality control programs are more likely willing to use SCC to obtain competitive advantages (Daczko *et al.* 2003, Walraven 2005). The Precast/Prestressed Concrete Institute (PCI) recommended the "Interim Guidelines for the Use of Self-Consolidating Concrete in Precast/Prestressed Concrete Institute Member Plants (TR-6-03)" in 2003 (PCI 2003). ACI Committee 237 *Self-Consolidating Concrete* also recently reported the current knowledge and guidelines of SCC for the application of SCC in 2007 (ACI Committee 237 2007).

Experiences around the world indicate that SCC results in better consolidation, better finish quality, less manpower, less noise, decreased times for placement, and lower maintenance cost of equipment (FHWA and NCBC 2005). If the desired fresh characteristics of SCC are satisfied, the potential for adding value to the overall construction and in-service performance increases. However, current information is insufficient to better understand the hardened characteristics of SCC, with one specific need being precast, prestressed bridge girder applications where high early strengths are required. Furthermore, hardened properties of SCC are not fully understood for the design of precast, prestressed structural members.

Some state transportation agencies in the United States began the task of developing manuals and guidelines for the application of SCC for precast and/or prestressed concrete structural members. A National Cooperative Highway Research Program project (No. 18-12) is currently developing mixture proportions and proposing guidelines for the application of SCC to precast, prestressed concrete bridge members. Several state research agencies and universities have worked on research to identify the fresh and hardened properties for the application of SCC in precast, prestressed concrete members.

2.2 FRESH CHARACTERISTICS

There are three key characteristics of SCC in the fresh state: filling ability, passing ability, and resistance to segregation or stability. Filling ability is the ability of concrete to fill the form with its own weight. Passing ability is the ability of fresh concrete to flow through congested spaces between strands or reinforcement without segregation or blocking. Finally, resistance to segregation or stability is the ability to maintain a homogeneous composition without bleeding in the fresh state. There is no single method to evaluate all the fresh characteristics of SCC (EFNARC 2005, PCI 2003). Several test methods to evaluate the fresh properties of SCC are presented in the Precast/prestressed Concrete Institute Interim Guideline and the European Guidelines (EFNARC 2005, PCI 2003). Among these test methods, the slump flow test for evaluating filling ability and stability, the J-ring test for passing ability, and the column segregation test for stability were standardized by the American Society for Testing and Materials (ASTM) (ASTM C1610/C 2006, ASTM C1611 2005, ASTM C1621 2006).

To obtain high workability and stability in SCC mixtures, advanced mixture proportioning techniques, aggregate properties, and supplementary cementitous materials (SCMs) and HRWRAs are important issues. Mixture proportions, fly ash, and HRWRAs are briefly discussed in this section.

Based on rheological models and empirical results, numerous different mixture proportion methods and procedures have been developed since the emergence of SCC. The PCI and European SCC guidelines suggest the rational mix design method originally developed by Okamura and Ouchi (1999) and PCI (2003). Statistical design approaches based on extensive experimental results were also proposed by some researchers (Ghezal and Khayat 2002, Sonebi 2004). However, there is no standard method for SCC mixture proportioning (EFNARC 2005, PCI 2003). Mixture proportions of SCC typically have a lower total volume of coarse aggregate and a higher fine aggregate to coarse aggregate ratio than CC mixtures proportioned following the ACI mixture proportioning method (D'Ambrosia *et al.* 2005). According to European SCC guidelines, SCC typically has lower coarse aggregate volumes, higher paste volumes, low water-cementitous material ratios, high dosages of HRWRA, and occasional viscosity modifying admixtures (VMAs) (EFNARC 2005). Mineral fillers such as limestone powders have also been used with the replacement of cement (Ghezal and Khayat 2002).

Shape, texture, and gradation of aggregate influence fresh properties (Mehta and Monterio 2005). Generally, angular and round shaped gravel reduce particle friction, resulting in high workability in SCC. However, early applications of SCC widely used crushed aggregates, up to three times more than river gravel (Domone 2006). Even though the source of aggregate mostly depends on local availability, the maximum size and total volume of coarse aggregate are intentionally selected to achieve the proper passing ability and adequate flowability (Domone 2006). The maximum aggregate size also is limited in SCC applications, especially in congested areas. A maximum coarse aggregate size from 0.63 to 0.78 in. (16 to 20 mm) is mainly used. The key to proper mixture proportioning is to improve particle distribution to achieve good filling, passing, and stability (EFNARC 2005).

Fly ash provides several advantages for fresh and hardened properties of SCC. Fly ash has a spherical particle shape, and particle size varies from less than 1 μm to nearly 100 μm in diameter. According to ASTM C618, *Standard Specification for Coal Fly Ash and Raw or Calcined Natural Pozzolan for Use in Concrete* (2008), there are two types of fly ash: Class F fly ash and Class C fly ash. These ashes come from different sources of coal. Class F fly ash has lower CaO content than Class C fly ash. In general, Class C fly ash is more reactive than Class F fly ash, resulting in faster strength development. When fly ash is used, the hydration process has an additional reaction of SiO_2 with water and lime (CH) from the byproducts of the hydration of dicalcium silicate (C_2S) and tricalcium silicate (C_3S), as shown in the following formula.

$$2SiO_2 + 3CH + H \rightarrow \underset{\text{(C-S-H)}}{C_3S_2H_4} \qquad (2.1)$$

Fly ash can also reduce the heat of hydration and increase workability. Workability improves as a result of the reduction of internal friction between the particles. This reduction in internal friction is achieved because fly ash particles are spherical. Fly ash can be successfully used for high-strength and high-performance concrete. Therefore, SCC mixture proportions utilizing fly ash could offset the high cost of cement and the required amount of HRWR admixtures to reach desirable workability (Patel *et al.* 2004, Sonebi 2004). When the dispersion of particles improves, resulting in a more effective hydration process, workability and strength

gain and development also improve. However, high replacement of fly ash or slag significantly reduced the strength of SCC (Schindler *et al.* 2007b).

HRWRA is the essential component to achieve the required fresh and hardened characteristics in SCC. Polycarboxylate HRWRAs are a new generation of admixtures implemented for use in SCC in the 1990s. The mechanism of dispersing this new admixture is different from that for polynaphthalene sulfonate (PNS) and polymelamine sulfonate (PMS) based HRWRAs, which are regarded as old generation admixtures (Xu and Beaudoin 2000). The dispersing mechanism of polycarboxylate based HRWRAs is more effective than that of PNS and PMS HRWRAs, resulting in higher workability with smaller dosages and better workability retention (AASHTO 2006, CEB-FIP 1990, Shiba *et al.* 1998). The mechanisms of these two types of HRWRA are well described in a recently published text book (Mehta and Monterio 2005).

In general, SCC mixture proportions have high paste volume and low coarse aggregate volume. For this research project, mixture proportions and fresh characteristics were studied at the University of Texas at Austin (Koehler and Fowler 2008). Comprehensive studies are required to understand the impact of fresh characteristics on hardened properties, and this research is the subject of this report.

2.3 MECHANICAL CHARACTERISTICS

The typical mixture proportions of SCC are different from the typical mixture proportions of CC. A review of compressive strength, MOE, MOR, and STS associated with SCC in the literature is presented below.

2.3.1 Compressive Strength

Compressive strength is the representative value of mechanical properties. Because this value is highly correlated to elastic behavior, tensile strength, flexural strength, and bond strength, this value should be evaluated to predict the behavior of structural components. Compressive strength is dependent on the age of the concrete, the gradation of the aggregate, curing conditions, the type of admixtures, the water-cement ratio, curing and testing, temperature, and testing parameters such as size of equipment and loading conditions (Mehta and

Monterio 2005). The porosity of each component and the interfacial zone are crucial parameters to determine the strength of concrete (Mehta and Monterio 2005).

The mixture proportions associated with performance-based hardened properties are in high demand for application in precast, prestressed concrete members. For that, cement is a key component of concrete for developing early strength. The fineness of the cement and the chemical constituents influence the fresh and hardened characteristics. Workability and hydration can vary depending on the chemistry of the cement. For precast, prestressed concrete structures, Type III cement is used to achieve high early strength. High early strength is critical to ensure the bonding and transfer of the prestress force after release.

Some researchers have studied compressive strength related to mixture proportions. According to a comprehensive survey on SCC, the strength of SCC is controlled mainly by the composition of the powder (here the cement and SCMs)—this is generally the water-cementitious materials ratio (*w/cm*). Water-powder ratio typically includes limestone dust, etc.—rather than the water to powder ratios as is typical with conventional concrete (Domone 2006). The *w/cm* dominantly affects the compressive strength rather than the total paste volume (Pineaud *et al.* 2005). SCC has higher compressive strength than CC (D'Ambrosia *et al.* 2005, Hamilton and Labonte 2005, Issa *et al.* 2005, Naito *et al.* 2006), whereas coarse and fine aggregate ratio did not affect the early and later compressive strength in a range between 5470 (38 MPa) and 9530 psi (66 MPa). VMAs can also influence the rate of hydration of cement at low water-cement ratios because they limit the available water for hydration and also alter the air void system. Therefore, reduced compressive strength has been observed in SCC when using VMAs at low water-cement ratios (Girgis and Tuan 2004, Khayat 1996, Khayat 1998). However, over dosage of VMAs did not influence the hardened properties of SCC (MacDonanld and Lukkarila 2002).

In general, compressive strength development and the impact of mixture proportions on strength are not fully understood for application of the SCC mixtures in precast, prestressed structural members because the proportions and compositions are highly advanced. Furthermore, there was insufficient research about hardened properties of SCC mixtures considering the crucial design criterion of the plants, high concrete compressive strength at release. Compressive strength is directly used in predicting other mechanical properties (MOE, STS, and MOR), bond and shear characteristics, creep, and overall structural performance.

2.3.2 Modulus of Elasticity (MOE)

MOE represents the stress-strain relationship of concrete in the elastic range. This property is needed to predict the camber, deflection, and prestress losses of prestressed, precast girders. MOE depends on the stiffness of the cement paste and aggregate, porosity, the interfacial transition zone, size of samples, and mixture proportions. Many researchers identified aggregate characteristics as significantly important in predicting MOE (ACI Committee 363 1992, Aitcin and Mehta 1990, Al-Omaishi 2001, Baalbaki 1992, Carrasquillo *et al.* 1981, Cetin and Carrasquillo 1998). The stiffness of concrete depends on the stiffness of both the paste and the aggregate. The MOE of high-strength concrete depends primarily on the stiffness of the cement paste rather than the stiffness of the aggregate compared to normal strength concrete (Cetin and Carrasquillo 1998).

MOE and strength also depend on the aggregate characteristics. The CEB-FIP (1990) and AASHTO LRFD Bridge Design Specifications (2006) considered the source of aggregate as the important parameter in predicting MOE along with compressive strength. When the aggregate stiffness is significant, the volume of coarse aggregate could also influence the MOE of the concrete. The MOE of SCC is typically lower than that of CC with the same strength due to the lower volume of coarse aggregate in SCC mixtures (Bonen and Shah 2004). Several researchers found that the MOE of SCC was slightly lower than that of conventional concrete (Dehn *et al.* 2000, Felekoglu *et al.* 2006, Ma and Dietz 2002, Naito *et al.* 2006, Walraven 2005, Zia *et al.* 2005). Schindler *et al.* (2007b) reported that the coarse to fine aggregate ratio did not affect MOE. The total paste volume affects the MOE of SCC mixtures (Pineaud *et al.* 2005).

As expected, the MOE of SCC mixtures is lower than that of CC mixtures according to previous research. However, the impact of SCC mixture proportions on MOE have not been fully understood for the application of SCC mixtures in precast, prestressed structural members associated with prestress losses, camber, and deflection.

According to several existing equations, MOE is estimated using the concrete compressive strength and unit weight, indicating the porosity of aggregate. The AASHTO LRFD Bridge Design Specifications (2006) recommended the following equation for MOE (psi [MPa]):

$$E_c = 33\,K_1\,w_c^{1.5}\sqrt{f_c'}\ \text{(psi)}\quad\left[E_c = 0.043K_1\,w_c^{1.5}\sqrt{f_c'}\ \right]\text{(MPa)} \qquad (2.2)$$

where E_c is the MOE (psi [MPa]), f'_c is compressive strength at test day (psi [MPa]), w_c is the unit weight of concrete (lb/ft^3 [kg/m^3]), and K_1 is the correction factor for the aggregate. K_1 should be taken as 1.00 unless determined by physical testing. This equation is applicable when the unit weight of concrete is between 90 and 155 lb/ft^3 (1441 and 2483 kg/m^3) and the compressive strength is up to 15 ksi (103 MPa).

Finally, the applicability of AASHTO LRFD prediction equations must be investigated to appropriately design the precast, prestressed structural members made with SCC. Other available prediction equations will also be assessed to determine if they can reasonably predict the MOE of SCC.

2.3.3 Modulus of Rupture and Splitting Tensile Strength (MOR and STS)

The tensile strength of concrete is important to predicting the initiation of cracking of a concrete member when it is subjected to external loads. For design considerations, the shear, punching, anchorage, crack width control, and minimum reinforcement depend on the tensile strength (Walraven 2005). The degree of cracks in the members can reduce the moment of inertia, resulting in reduction of overall capacity and serviceability, such as excessive deflection. The allowable stresses of the extreme fibers at the critical sections due to flexure are used to design the structural members. When a concrete member is subjected to high shear stress, the maximum principal tensile stress reaches the tensile strength of concrete resulting in the initiation of diagonal shear cracks. To estimate the tensile strength of concrete, MOR and STS are generally determined by testing flexural prisms and splitting cylinders, respectively.

Several factors influence the tensile strength of concrete. The strength of paste and the bond between the aggregate and paste influence the tensile strength. Aggregate type also affects the tensile strength of high-strength concrete (Cetin and Carrasquillo 1998). Because SCC mixtures have typically different proportions compared to CC mixtures, SCC mixtures have potentially different MOR and STS resulting from the complexity of the strength of components and bonding between them. However, the impact of mixture proportions of SCC on MOR and STS is not fully understood for the application of the SCC mixtures in precast, prestressed structural members.

Typically, both MOR and STS are related to the square root of the compressive strength. The AASHTO LRFD Bridge Design Specifications (2006) provides allowable tensile stress

limits for flexure at release and service conditions as the function of the square root of the compressive strength. The AASHTO LRFD Specifications (2006) also recommends the upper and lower bounds as 11.7 and 7.6 times (0.97 and 0.63) the square root of the compressive strength (psi [MPa]) for estimating the MOR of concrete. The lower bound is generally used as the design value to prevent cracking of concrete in flexure in the service stage. The upper bound is used to calculate the cracking moment for use in the check for the required minimum reinforcement. The minimum reduced nominal moment capacity of flexural members is 20 percent higher than the corresponding cracking moment to avoid sudden failure after cracking. These equations are applicable for compressive strengths up to 15 ksi (103 MPa). The AASHTO LRFD Bridge Design Specifications (2006) also recommends a STS of 7.3 (0.59) times the square root of the compressive strength (psi [MPa]).

Finally, the applicability of the AASHTO LRFD prediction equations needs to be investigated to design precast, prestressed structural members made with SCC. Other available prediction equations will also be assessed to determine if they can reasonably predict the MOR and STS of SCC.

2.4 SHEAR CHARACTERISTICS

In general, shear strength is the sum of the contribution of the concrete and shear reinforcement. Aggregate interlock, or crack friction, is the significant contribution to shear capacity. Therefore, the coarse aggregate content directly affects aggregate interlock. SCC mixtures typically have low coarse aggregate volumes compared to CC mixtures.

Currently, there are few research results available to quantify the effect of coarse aggregate volume in high-strength CC and SCC on aggregate interlock. Burgueño and Bendert (2005) performed experimental tests to quantify the shear capacity of SCC to compare with CC mixtures in a limited number of samples. It is notable that their push-off samples have internal reinforcement crossing the crack plane, which is a fundamental test for interface shear transfer design in AASHTO LRFD Article 5.8.4.1 rather than general shear design in AASHTO LRFD Bridge Design Specifications (2004). SCC mixtures with low coarse aggregate volumes exhibited low shear stresses when interface shear reinforcement was used. In prestressed concrete beam tests some researchers found that the shear performance of SCC is similar to that of CC (Burgueño and Bendert 2007, Hamilton and Labonte 2005, Naito *et al.* 2006, Ozyildrim

2007). While some researchers indicated that the shear capacity of SCC generally was slightly lower than CC, researchers have found that the shear capacity of SCC beams still had sufficient safety margin compared with predicted capacity using existing design equations such as ACI 318-05, AASHTO Standard Specifications, AASHTO LRFD Bridge Design Specifications, Euro code, and truss model with crack friction (Burgueño and Bendert 2007, Choulli *et al.* 2005, Hamilton and Labonte 2005, Hegger *et al.* 2007, Ozyildrim 2007).

The impact of mixture SCC proportions on shear capacity is not fully understood for the application of the SCC mixtures in precast, prestressed structural members. Especially, an appropriate experimental program is needed to quantify aggregate interlock of SCC compared to CC to assess the applicability of the current AASHTO LRFD shear design. Based on the experimental results, the appropriate aggregate interlock model and design equations for SCC mixtures are necessary to estimate shear capacity of concrete and amount of shear reinforcement.

To evaluate the shear characteristics of SCC and to propose appropriate design equations, the background of shear design and theoretical aggregate interlock models have to be fully understood. The following subsections discuss these topics.

2.4.1 AASHTO LRFD Shear Design

An ASCE-ACI Committee 445 report (1998), identifies five principal mechanisms of shear transfer after cracking as follows:

1) Shear stresses in uncracked flexural compression zones, which have been traditionally considered as the contribution of concrete.
2) Aggregate interlock or crack friction, which is the significant contribution to shear capacity after crack with slippage.
3) Dowel action of the longitudinal bars, which is a significant contribution to shear capacity on transverse reinforcement.
4) Tensile stresses in the shear reinforcement.
5) Residual tensile stress across the crack, which is considered in the fracture mechanism approach.

In addition, arch action should be considered in deep beams; this can be modeled in a strut-tie model approach. It is difficult to quantify the resistance of each mechanism for a particular beam. Therefore, many theoretical and empirical approaches have been proposed by different researchers. Some practical and rational methods have been developed and adopted for design purposes.

Traditional empirical formulas are based on an extensive number of beam tests in shear. In the traditional design approach, including the ACI 318 *Building Code Requirements for Structural Concrete* (2005), the contribution of concrete is evaluated based on a 45-degree truss model. Shear reinforcement requirements are determined when the design concrete shear strength is not sufficient. With this approach, the concrete contribution and steel contribution to shear are estimated independently for simplicity and conservatism.

In the compression field theory, the tensile stress on the principal crack plane is assumed to be zero based on a variable-angle truss model. The MCFT used in the AASHTO LRFD Bridge Design Specifications was updated to include consideration of the contribution of tensile stresses on the crack planes (Collins and Mitchell 1991, Collins and Mitchell 1980). In the MCFT, the concrete contribution and the shear reinforcement contribution vary and are determined dependently using three basic concepts: geometric conditions, equilibrium conditions, and material stress-strain relationships. Even though solving the equations is more complex than using traditional approaches, the MCFT theory has been accepted as a more accurate and rational design approach for beam shear. The following three equations are used to determine the contribution of concrete and steel, respectively (Vecchio and Collins 1986) (psi, in. [MPa, mm]):

$$v = v_c + v_s = \beta \sqrt{f_c'} + \rho_z f_y \cot\theta \quad \text{(psi [MPa])} \tag{2.3}$$

where:

$$\beta = \frac{4 \cot\theta}{1 + \sqrt{500\,\varepsilon_1}} \quad \text{(psi)} \left[\beta = \frac{0.33 \cot\theta}{1 + \sqrt{500\,\varepsilon_1}} \right] \quad \text{(MPa)} \tag{2.4}$$

and

$$\beta \le \frac{v_{ci}}{\sqrt{f'_c}} = \frac{2.16}{0.31 + 24\dfrac{w}{(a_g + 0.63)}} \quad \text{(psi, in.)} \tag{2.5}$$

$$\left[\beta \le \frac{v_{ci}}{\sqrt{f'_c}} = \frac{0.18}{0.31 + 24\dfrac{w}{(a_g + 16)}}\right] \quad \text{(MPa, mm)}$$

and

$$\rho_z = \frac{A_v}{b_w s} \quad \text{(in. [mm])} \tag{2.6}$$

where v_c is the concrete contribution to shear (psi [MPa]), v_s is the stirrup contribution to shear (psi [MPa]), θ is the angle of the diagonal compressive stresses in the web (degree), β is the factor of tensile stress in the cracked concrete (psi/psi [MPa/MPa]), ρ_z is the ratio of the stirrup area to the web area, A_v is the nominal area of stirrups (in.^{2}/in.^{2} [mm^2/mm^2]), b_w is the web width (in. [mm]), s is the spacing of the stirrups (in. [mm]), f_y is the yield stress of the stirrups (psi [MPa]), ε_1 is the principal tensile strain in the concrete (in./in. [mm/mm]), w is the crack width (in. [mm]), a_g is the maximum aggregate size (in. [mm]), and v_{ci} is the limiting value of the maximum shear stress on the shear plane in the cracked concrete (psi [MPa]).

The use of a variable angle, θ, within the diagonal crack model is appropriate for the design of prestressed concrete members because the prestressing force can significantly reduce the longitudinal tensile strain in the web, ε_x, resulting in a lower angle, θ, and increasing both v_c and v_s (Bentz *et al.* 2006). In addition, a clamping force from the prestressing steel contributes to increased normal stress, resulting in a higher shear strength capacity. Combined with v_{ci}, the factor for tensile stress, β, is determined to evaluate the ability of the cracked concrete to resist shear. It should be noted that Equations 2.4 and 2.5 are derived from panel and push-off test results, respectively. After the first cracking of concrete and initiation of starting crack slip, the tensile stress on the crack plane can be expressed with the β value of Equation 2.4. Figure 2.1 illustrates the tensile stress on the crack plane before slip occurs. After the initiation of crack slip, the average stress on the crack plane can be expressed with the β value of Equation 2.5.

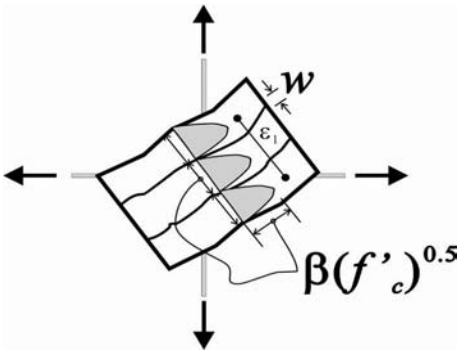

Figure 2.1. Illustration of Tensile Stress on the Crack Plane Prior to Slip Occurrence for Equation 2.4 (Vecchio and Collins 1986).

The limiting value of v_{ci} was derived from push-off tests with external restrained bars from the early study of Walraven and Reinhardt (1981), as discussed by Vecchio and Collins (1986). Walraven's test results confirmed his theoretical aggregate interlock model. The analytical model assumes the concrete consists of a rigid, perfectly plastic paste and rigid spherical aggregates of various sizes intruded into this paste. After the formation of a crack plane, for normal strength concrete the aggregate keeps its shape (for example, the crack plane follows a path around the aggregate particles). These spherical aggregates effectively provide aggregate interlock between aggregate and paste (see Figure 2.2). Protruded aggregates sliding against the paste generate normal and shear stresses. The volume and size distribution of the aggregate can be computed to determine the projected contact areas on the x and y directions (for example, crack slip and crack width directions), a_x and a_y, which are functions of crack slip and crack width between adjoining crack surfaces. For high-strength concrete it is thought that the aggregates fail due to the high-strength paste, thus reducing aggregate interlock. These theoretical and experimental findings were used to develop the MCFT theory and finally were adopted in the AASHTO LRFD Bridge Design Specifications in 1994 (AASHTO 1994).

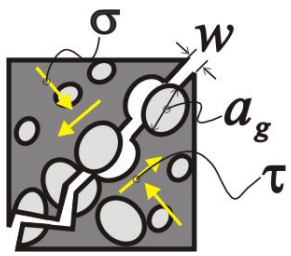

Figure 2.2. Schemetic for Aggregate Interlock (Vecchio and Collins 1986).

Because release strength is critical for plant productivity, precast industries use high early strength concrete. Therefore, it is necessary to review both Walraven's study and the MCFT with respect to high-strength concrete. Walraven focused on normal strength concrete containing river gravel (f'_c ranging from 3.6 to 10 ksi [25 to 70 MPa]), and his research was referenced in developing the MCFT. Later in his study, Walraven updated his analytical model for high-strength concrete (f'_c = 14.5 ksi [100 MPa]) by introducing the fracture reduction factor, c (Walraven and Stroband 1994). The analytical procedure discussed below presents the relevant equations. The MCFT minimizes the contribution of aggregate interlock to concrete having a 28-day f_c' higher than 10 ksi (70 MPa) by taking the maximum aggregate size, a_g, as zero (Bentz *et al.* 2006). Therefore, aggregate interlock is assumed to have a negligible contribution to shear strength of high-strength concrete. However, there are little data available to estimate the aggregate interlock of SCC mixtures. Furthermore, an appropriate prediction equation has not been developed for estimating the shear capacity of SCC mixtures.

2.4.2 Analytical Development of the AASHTO LRFD Specifications for Shear

Bazant and Gambarova (1980) proposed the rough crack model based on theoretical relationships between normal stress, σ, shear stress, τ, crack width, w, and crack slip, δ. This model is expressed in Equations 2.7 and 2.17, which are based on experimental data from push-off tests with constant crack width (Fenwick and Paulay 1968, Paulay and Loeber 1974).

$$\sigma = -\frac{c_1}{w}(c_2|\tau|)^p \quad \text{(psi [MPa])} \tag{2.7}$$

$$\tau = \tau_u r \frac{c_3 + c_4|r|^3}{1 + c_4 r^4} \quad \text{(psi [MPa])} \tag{2.8}$$

$$r = \frac{\delta}{w} \quad \text{(in. [mm])} \tag{2.9}$$

$$\tau_u = \tau_0 \frac{c_0}{c_0 + w^2} \quad \text{(psi, in. [MPa, mm])} \tag{2.10}$$

$$p = 1.30\left(1 - \frac{0.231}{1 + 4.6944\,w + 3632\,w^2}\right) \quad \text{(in.)} \tag{2.11}$$

$$\left[p = 1.30 \left(1 - \frac{0.231}{1 + 0.185\, w + 5.63\, w^2} \right) \right] \text{ (mm)}$$

$$c_0 = 0.01\, a_g^2 \quad (\text{in.}^2\ [\text{mm}^2]) \tag{2.12}$$

$$c_1 = 0.003049 \quad (\text{lb/in.}) \quad [c_1 = 0.000534] \quad (\text{N/mm}) \tag{2.13}$$

$$c_2 = 0.999776 \quad (\text{in.}^2/\text{lb}) \quad [c_2 = 145] \quad (\text{mm}^2/\text{N}) \tag{2.14}$$

$$c_3 = \frac{355}{\tau_0} \quad (\text{lb/in.}^2) \quad \left[c_3 = \frac{2.45}{\tau_0} \right] \quad (\text{N/mm}^2) \tag{2.15}$$

$$c_4 = 2.44 \left(1 - \frac{14735}{\tau_0} \right) \quad (\text{lb/in.}^2) \quad \left[c_4 = 2.44 \left(1 - \frac{4}{\tau_0} \right) \right] \quad (\text{N/mm}^2) \tag{2.16}$$

$$\tau_0 = 0.245\, f_c' \quad (\text{lb/in.}^2\ [\text{N/mm}^2]) \tag{2.17}$$

When crack slip, δ (in. [mm]), is larger than crack width, w (in. [mm]), the shear stress, τ, reaches the maximum shear stress, τ_u (psi [MPa]). The variable a_g is the maximum size of the aggregate (in.[mm]), and f'_c is the compressive strength of concrete at 28 days (psi [MPa]). From the best-fit curves of previous test results, the main variables are σ, τ, w, δ, and a_g. In addition, the ratio, $r = \delta/w$ is regarded as an important parameter to estimate the shear stress. However, this value was obtained from experimental work that maintained a constant crack width during push-off tests.

Walraven (1981) assessed the contribution of aggregate to shear in cracked concrete with a probabilistic and mathematical approach to estimate shear and normal stresses resulting from aggregate interlock. The frictional coefficient, μ, is a constant value of 0.4 based on a best-fit to the experimental data (Walraven 1981). According to a comparison between their experimental and analytical results, the friction coefficient was a significant factor, as shown in Figure 2.3, to quantify shear and normal stress due to aggregate interlock. Therefore, an appropriate μ value should be estimated to predict aggregate interlock.

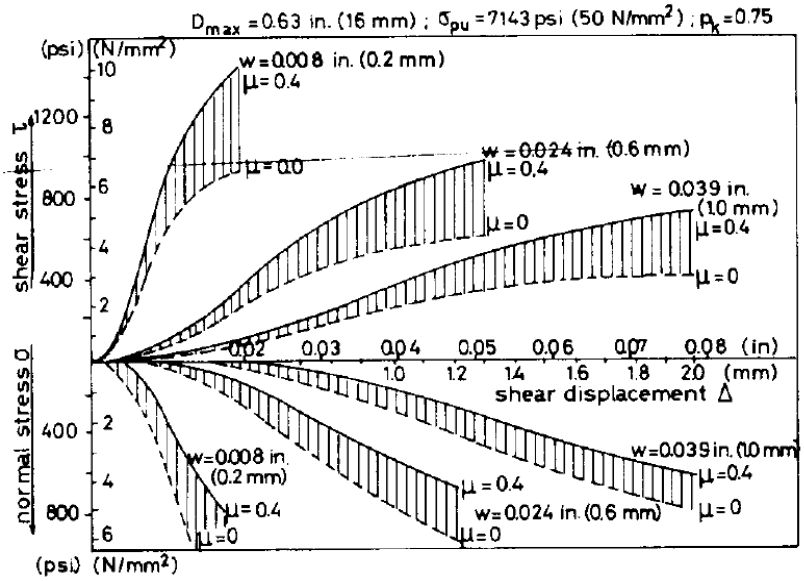

Figure 2.3. The Role of Friction Coefficient (Walraven 1981).

Yoshikawa *et al.* (1989) proposed an analytical model based on previous experimental and analytical work to estimate aggregate interlock in cracked concrete. The proposed equations are based on the experimental data of Fenwick and Paulay (1968), Houde and Mirza (1972), Paulay and Loeber (1974), Walraven and Reinhardt (1981), and Yoshikawa *et al.* (1989). The equation for maximum shear stress is obtained from the work by Bazant and Gambarova (1980). Yoshikawa *et al.* (1989) updated the coefficients for maximum shear stress equation. The form of Equation 2.18 (Bazant and Gambarova 1980) was adopted in the maximum shear stress, τ_{max}, of the MCFT (see Equation 2.22).

$$\tau_u = \tau_0 \frac{c_5}{\left[c_6 + \left(\frac{w}{a_g} \right)^{c_7} \right]} \quad \text{(psi, in. [MPa, mm])} \qquad (2.18)$$

According to Equation 2.18, both the empirical coefficients c_5 and c_6 are 0.01. The empirical coefficient c_7 is $\tau_0 = (0.2\text{-}0.3) \times f_c'$ (psi [MPa]).

Using the above parameters, the frictional coefficient, μ, is proposed as follows:

$$\mu = c_8 \mu_0 e^{(c_9 w)} \qquad (2.19)$$

where c_8 varies between 0.5 and 1.5, c_9 is 0.61, and μ_0 is 1.16. The friction coefficient increases as the crack width increases. Early studies focused on testing with constant crack width without measuring normal stresses. Therefore, during testing externally applied lateral forces kept a constant crack width. This is expected, as the small crack widths resulted in higher normal stresses and relatively lower shear stresses (Laible *et al.* 1977, Paulay and Loeber 1974, Yoshikawa *et al.* 1989).

According to Yoshikawa *et al.*'s analysis, the coefficient is not easily defined due to varied experimental data. The shear displacement, δ, with crack width, w, relationship, shown in Equation 2.20, was proposed by Yoshikawa based on the previous experimental work:

$$\delta = 1.42 \left(\frac{a_g}{0.63}\right)^{-1.20} w^{1.31} \text{ (in.)} \quad \left[\delta = 1.42 \left(\frac{a_g}{16}\right)^{-1.20} w^{1.31}\right] \text{ (mm)} \qquad (2.20)$$

where δ is the measured shear displacement (in. [mm]) at the maximum shear stiffness in the constant crack width (in. [mm]), w is crack width (in. [mm]), and a_g is maximum aggregate size (in. [mm]).

Walraven's theoretical and experimental findings (Walraven 1981) were mainly used to develop the MCFT theory and finally were adopted in the AASHTO LRFD Bridge Design Specifications since 1994. The MCFT theory constructed transmission of shear stress across a crack by aggregate interlock (Vecchio and Collins 1986). Equation 2.21 was derived by Vecchio and Collins (1986) from the Walraven's test data and theoretical equations (1981) as shown in Figure 2.4.

$$\frac{\tau}{\tau_{max}} = 0.18 + 1.64 \frac{\sigma}{\tau_{max}} - 0.82 \left(\frac{\sigma}{\tau_{max}}\right)^2 \text{ (psi [MPa])} \qquad (2.21)$$

where τ_{max} is the maximum shear stress (psi [MPa]), τ is shear stress (psi [MPa]), and σ is normal stress (psi [MPa]).

The maximum shear stress τ_{max} in Equation 2.21 can be defined as the following equation (psi [MPa]):

$$\tau_{max} = \frac{12\sqrt{f_c'}}{0.31 + 24\dfrac{w}{(a_g + 0.63)}} \text{ (psi, in.)} \quad \left[\tau_{max} = \frac{\sqrt{f_c'}}{0.31 + 24\dfrac{w}{(a_g + 16)}}\right] \text{ (MPa, mm)} \qquad (2.22)$$

where τ_{max} was defined earlier, a_g is the maximum size of the aggregate (in.[mm]), and f'_c is the compressive strength of concrete at 28 days (psi [MPa]).

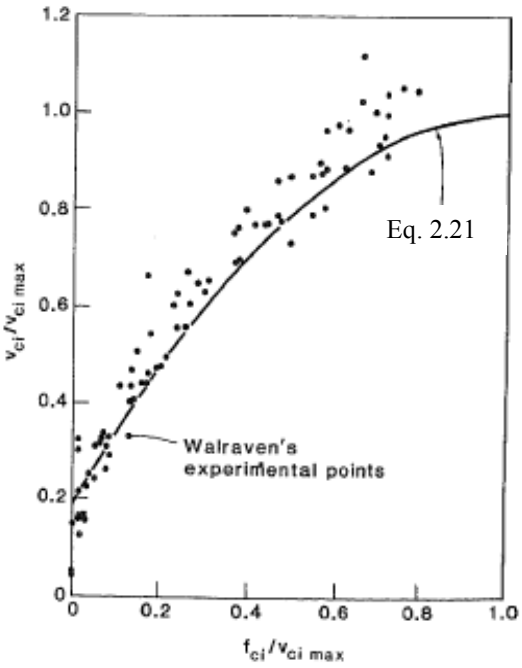

Figure 2.4. Walraven's Data and Equation 2.21 (Vecchio and Collins 1986).

The implemented equation in the AASHTO LRFD Bridge Design Specifications (AASHTO 2004, 2006) presents a simplified shear stress equation as follows (psi [MPa]):

$$v_{ci} = 0.18\,\tau_{max} \text{ (psi [MPa])} \qquad (2.23)$$

where v_{ci} is the limiting value of the maximum shear stress on the shear plane in the cracked concrete (psi [MPa]) and τ_{max} is the maximum shear stress (psi [MPa]).

The simplified equation neglects the beneficial normal stress effect because of practical application to design (Duthinh 1999). According to Duthinh (1999), the coefficient 0.18 is the shear friction factor, *SF*. This value is obtained from the intercept of the y-axis in Figure 2.4.

The general assumptions in the AASHTO LRFD Bridge Design Specifications, MCFT theory, and the simplified MCFT theory are as follows (AASHTO 2006, Bentz *et al.* 2006):

- The maximum size aggregate is assumed to be zero for high-strength concrete (f'_c > 10,000 psi [70 MPa]).
- Frictional coefficient, μ, is assumed to be 0.4 based on best-fitting (based on Walraven [1981]).
- The strength of paste, σ_{pu}, is obtained from push-off tests (based on Walraven [1981]).
- The aggregate is spherical aggregate (most likely river gravel aggregate) (based on Walraven [1981]).
- The maximum shear stress, τ_{max}, on the crack plane is a function of the crack width and the maximum coarse aggregate size.

Therefore, the above assumptions are theoretically and empirically obtained from the various tests on normal and conventional concrete. The effect of the fracture of coarse aggregate in high-strength concrete is not precisely considered in the shear design. Furthermore, the data from SCC are not sufficient to understand aggregate interlock for the SCC mixtures. All the experimental work and theoretical formulations are necessary to validate the current shear design equation and propose an appropriate equation for the design of precast, prestressed structural members containing SCC mixtures.

2.5 BOND CHARACTERISTICS

When uncombined mixing water separates from the cement paste and aggregate in a concrete mixture, rising water can accumulate beneath the reinforcement and on the top concrete surface resulting in a high water-cement ratio (*w/c*), lower strength, and lower bond. Therefore,

the accumulated water beneath the horizontal reinforcement near the concrete surface can reduce the bond capacity of reinforcement (Menzel 1952). High flowable concrete mixtures such as SCC have a potential risk of segregation of aggregate and paste, which can result in reduced bond due to bleeding. Reduced bond capacity of horizontal reinforcement near the top surface resulting from bleeding is defined as the top-bar effect (Jeanty *et al.* 1988). In Article 5.11.2.1.2 of the AASHTO LRFD Bridge Design Specifications (2004, 2006), the calculated development length increased by 40 percent when the horizontal reinforcement is located at a position higher than 12 in. (305 mm) from the bottom face of the member (AASHTO 2006). The top bar effect is also a potential issue for precast, prestressed members. When the strands have a harped or draped pattern, the strands at the end section are located near the top surface compared to the location of the strands in the midspan. Mild reinforcement on the top flange is also critical for controlling cracking in the end zone. Therefore, the bleeding water, which is free water isolated from the fresh concrete, is prone to accumulation underneath horizontal bars located near the surface. The air void and locally low strength of the interface between the concrete and steel can cause low friction and mechanical bond capacity. VMAs control bleeding, segregation, and surface settlement in SCC (Domone 2006, Khayat *et al.* 2007, Khayat and Guizani 1997). Therefore, the reduction in bond caused by the top bar effect can be reduced by using VMAs (Khayat 1998). However, VMAs can adversely affect the bond strength according to Girgis and Tuan (2004). Because the top bar effect is highly correlated to the stability of SCC mixtures, tests are needed to assess the impact of stability on the top bar effect.

ACI 318-05 (Section R12.2.4; 2005) and 2004 AASHTO LRFD Bridge Design Specifications (Article 5.11.2.1.2) require the use of a multiplier of 1.3 or 1.4, respectively, for top bars when computing the required development.

Generally, the stability of the SCC is evaluated in the fresh state. However, the impact of mixture proportions of the SCC on bond capacity and top bar effect is still not fully understood. Furthermore, the top bar in the AASHTO LRFD Specifications needs to be evaluated for applicability for SCC.

2.6 CREEP AND SHRINKAGE

Creep and shrinkage are representative time-dependent properties of concrete that influence prestress losses, camber, and deflection in prestressed members. Shrinkage and creep

are viscoelastic phenomena of hardened cement paste influenced by similar material characteristics and environmental conditions (Mehta and Monterio 2005). Because both creep and shrinkage of concrete are similarly affected by internal and external factors, this section discusses both properties. However, a more detailed shrinkage test program and results for this project are discussed by researchers at the University of Texas at Austin (Koehler and Fowler 2008).

Shrinkage depends on the characteristics of aggregate stiffness and texture, *w/c*, volume of paste, volume of coarse aggregate, cement type, admixture type and curing method, volume to surface area ratio of a structural member, environmental conditions (i.e., humidity and temperature), and duration of drying time. Shrinkage causes an asymmetrical volumetric change due to the drying and wetting of capillary pores. Creep depends on the same factors as shrinkage along with magnitude and age of loading and time (AASHTO 2006). Creep is a volumetric change due to external loads. In concrete, long-term creep deformations are generally larger than the initial elastic deformation due to the applied load. The creep shortening of concrete under permanent loading typically ranges from 0.5 to 4 times the initial elastic shortening. The magnitude mainly depends on concrete maturity at the time of loading (AASHTO 2006).

For interpretation of creep strain and comparison of test results, basic equations are presented below.

The creep coefficient is defined as follows:

$$\psi(t,t_i) = \frac{\varepsilon_C}{\varepsilon_{inst}} \tag{2.24}$$

where $\psi(t,t_i)$ is the creep coefficient, ε_{inst} is the initial strain due to applied load in compression, and ε_C is the creep strain.

Specific creep, ε_{sp}, is defined as follows:

$$\varepsilon_{sp} = \frac{\varepsilon_C}{\sigma} \tag{2.25}$$

where σ is the stress due to applied compressive load, which must be smaller than 50 percent of the compressive strength.

Because SCC has high paste volume (or high sand to aggregate ratio) to achieve high workability and high early strength, several researchers expected relatively large creep and shrinkage of SCC for precast, prestressed concrete, resulting in large prestress losses (Issa *et al.* 2005, Naito *et al.* 2006, Schindler *et al.* 2007b, Suksawang *et al.* 2006). D'Ambrosia *et al.* (2005) also claimed high autogenous shrinkage at early ages resulting in high early cracking of SCC with low *w/cm* and high paste volume. However, the fast early strength gain mitigated the risk of cracking. Even though mechanical properties of SCC are superior to those of CC, creep and shrinkage of SCC was significantly high (Issa *et al.* 2005).

Naito *et al.* (2006) also found that SCC exhibited higher shrinkage and creep than CC, which was attributed to high fine aggregate volume in the SCC. Naito *et al.* (2006) found that the ACI 209 prediction model (1992) overestimated the shrinkage of CC and SCC by 18 and 39 percent, respectively. The creep coefficient of SCC and CC was 40 and 6 percent higher than the ACI 209 prediction model (1992), respectively.

On the other hand, Schindler *et al.* (2007b) found that the shrinkage of SCC is similar or less than that of CC. At early ages AASHTO LRFD Specifications (2004) underestimated the shrinkage values (7 and 14 days), while it overestimated the shrinkage at later ages (56 and 112 days) for both CC and SCC. When the shrinkage of SCC was compared to that of CC at 112 days, the sand to aggregate ratio effect was not significant for the shrinkage of SCC. The creep coefficients of SCC mixtures were also smaller than those of CC at all loading ages. This was attributed to the low *w/c* (Schindler *et al.* 2007b). According to Sucksawang *et al.* (2006), fly ash (Class F) and silica fume and slag could reduce the capillary that causes high shrinkage. Finally, fly ash was excellent among other SCMs in reducing shrinkage.

In general, several research projects investigated creep and shrinkage of SCC mixtures. Because creep and shrinkage are sensitively affected by mixture proportions and environmental factors, the results vary and give different trends. Therefore, more data are necessary to understand the behavior of creep and shrinkage of SCC mixtures compared with CC mixtures. For this study, shrinkage of SCC mixtures was investigated by researchers at the University of Texas at Austin (Koehler and Fowler 2008) and creep of the SCC mixtures was investigated by researchers at Texas A&M University.

Prediction equations for creep and shrinkage of concrete account for internal and external factors. Mixture proportions are the internal factors, such as the ratio of fine aggregate and cement contents, admixtures, shape of coarse aggregate, and so on. Otherwise, environmental elements, such as relative humidity and temperature, are external factors. Each factor is not independent from the other factors. Because there are many internal and external factors affecting characteristics of creep and shrinkage, it is not easy to predict and determine creep and shrinkage accurately. That is why many prediction formulas have not been accepted widely as reasonable prediction models.

Table 2.1 shows a summary of the input parameters to estimate creep and shrinkage using various prediction models found in the literature. Prediction models can indirectly consider the aggregate type as the stiffness of concrete based on the MOE and compressive strength of concrete. Both creep and shrinkage increase initially after loading. Generally, the ACI Committee 209 model (1992), CEB-FIP model (CEB-FIP 1993), BP model (Bazant and Panula 1984), B3 model (Bazant and Baweja 2000), and GL2000 model (Gardner and Lockman 2001) consider various internal and external parameters. The applicable concrete compressive strength at 28 days for the ACI 209 model, CEB-FIP model, BP model, B3 model, and GL 2000 model vary from 3000 to 10,000 psi (20 to 70 MPa) according to ACI 209 Committee report (2008). More detailed equations are presented in Appendix A.

Table 2.1. Input Parameters for Predicting Creep and Shrinkage.

	Models	AASHTO 2004	AASHTO 2006	ACI 209	CEB-FIP	BP	B3	GL 2000
External Factors (Environment and Time)	Curing conditions	-	-	S, C	-	-	S, C	-
	Age of loading	C	C	C	C	C	C	C
	Relative humidity	S, C	S, C	S, C	S, C	S, C	S, C	S
External Factors (Physical Condition)	Specimen size	S, C	S, C	S, C	S, C	S, C	S	S, C
	Specimen shape	-	-	-	-	S, C	S	-
Internal Factors (Mechanical Properties)	f_c' at 28 days	C	-	C	S, C	S, C	S, C	S, C
	f_c' at age of loading	-	S, C	C	-	-	-	C
	MOE at 28 days	-	-	C	C	S, C	C	C
	MOE at age of loading (or drying for shrinkage)	-	-	C	C	S, C	-	C
Internal Factors (Composition)	Cement type	-	-	C	S, C	C	S, C	S
	Water-cement ratio (w/c)	-	-	-	-	S, C	C	-
	Aggregate-cement ratio	-	-	-	-	S, C	C	-
	Fine aggregate to all aggregate ratio	-	-	S, C	-	S, C	-	-
	Air	-	-	S, C	-	-	-	-

Note: S = Shrinkage, C = Creep, - = no data.

The AASHTO LRFD Bridge Design Specifications (2006) provide prediction for creep and shrinkage models while allowing the use of two alternative methods: the CEB-FIP model (1993) and the ACI 209 Committee model (1992). The AASHTO LRFD Bridge Design Specifications (2006) prediction model was based on the research of Hue *et al.* (2001), Al-Omaishi *et al.* (2001), Collins and Mitchell (1991), and Tadros *et al.* (2003). It is noted that these prediction models are applicable up to a compressive strength of 15 ksi (103 MPa) (AASHTO 2006). However, there are not sufficient data and information for estimating creep and shrinkage of SCC mixtures based internal factors.

Compressive strength at the age of loading is used in the AASHTO LRFD (2006) prediction equation for creep and shrinkage instead of the 28-day compressive strength used in the AASHTO LRFD (2004). Finally, the applicability of prediction equations has to be investigated for use in the design of precast, prestressed structural members made with SCC.

Other available prediction equations will be assessed to determine if they can reasonably predict the creep and shrinkage of SCC.

2.7 DURABILITY

Permeability and diffusivity depend on the soundness of pore structure: total numbers, size, and distribution of pores. Assie *et al.* (2005) observed that when SCC mixtures contain more limestone powder and a high dosage of HRWRA, they present lower permeability and similar diffusivity compared to CC . The permeability of SCC was greatly enhanced with the use of fly ash and silica fume especially at ages of 56 and 91 days (Suksawang *et al.* 2006). The proportion of HRWRA is greater in SCC than CC. Therefore, the air void system could be destabilized by the effects of HRWRA and affect the freeze and thawing resistance (Khayat and Assaad 2002). Freeze and thawing resistance of SCC with granite coarse aggregate and natural sand was acceptable because the HRWRA resulted in a poorly distributed and inadequate air void system (Ozyildrim 2007). With various types of HRWRAs and air-entraining admixtures (AEAs) and combinations of admixtures, the SCC mixtures had surface areas less than 0.94 $in.^2/in.^3$ (24 mm^2/mm^3) and spacing factors much larger than 0.008 in. (0.20 mm); these values indicate excellent durability compared with CC (Christensen and Ong 2005).

In general, the durability of SCC mixtures is sensitive to the mixture proportions and admixture types. Air void systems and pore structures of SCC mixtures differ from CC mixtures. Therefore, typical durability parameters including permeability, diffusion coefficient, and freezing and thawing resistance of the SCC mixtures are assessed in this study.

2.8 FLEXURAL CAPACITY

Flexural capacity is a fundamental structural performance for precast, prestressed structural members. Flexural behavior relates to MOE, MOR, and prestress losses and development length. In service load conditions, the tensile stress of the top and bottom fibers should be checked to determine whether this stress is within the allowable tensile limit, which generally is determined from the MOR. This allowable stress should be checked at the stage after transfer, along with the compressive concrete strength at release. After casting decks, the allowable stress should also be checked, considering different section properties and effective prestress after losses. The stresses are generally checked at the end zone, transfer length region,

and midsapn. In general, this step controls the selection of cross-section and number and locations of strands.

According to the AASHTO LRFD Specifications (2004, 2006), the tensile stress of a prestressed concrete member is 6 times (0.49) the square root of the compressive strength (psi [MPa]) for estimating allowable tensile stress at service.

The elastic and post-cracking behavior of SCC can be different due to different mechanical and bond mechanisms. MOE, prestress loss, and MOR can be useful to predicting elastic and cracking occurrence. However, post-cracking behavior is a more complicated response. Therefore, flexural testing is important to full-scale testing and validation. However, there were few full-scale flexural tests conducted on prestressed, precast girders made with SCC.

Flexural capacity can be estimated based on three basic assumptions: plane sections remain plane, the concrete and steel are perfectly bonded and have the same thermal coefficient, and the strain distribution is linear across the section. According to Naaman (2004), the AASHTO LRFD Specifications is superior in simplicity and generality to the ACI 318-02 code for the design of prestressed concrete members. This is because only the location of the neutral axis, c, is required to solve the equilibrium equation and the stress in the strands, f_{ps} at the nominal flexural moment resistance, M_n. To determine f_{ps} at the nominal flexural moment resistance, M_n, following the AASHTO LRFD Specifications (2006), the average stress in strands, f_{ps}, should be obtained from the following equation, where effective prestress after losses, f_{pe}, is not less than 0.5 f_{pu} (AASHTO LRFD 2006 Article 5.7.3.1.1-1):

$$f_{ps} = f_{pu}\left(1 - k\frac{c}{d_p}\right) \text{ (psi, in. [MPa, mm])} \qquad (2.26)$$

where f_{pu} is the ultimate strength of the prestressed strand (ksi [MPa]), c is the depth of neutral axis at ultimate (in. [mm]), d_p is the distance from the extreme compression fiber to the centroid of tensile force in strands (in. [mm]), and k is defined as the following equation (AASHTO LRFD 2006 Article 5.7.3.1.1-2) (psi/psi [MPa/MPa]):

$$k = 2\left(1.04 - \frac{f_{py}}{f_{pu}}\right) \text{ (ksi)} \quad \left[k = 2\left(1.04 - \frac{f_{py}}{f_{pu}}\right)\right] \text{ (MPa)} \qquad (2.27)$$

where f_{py} is the yield stress of the strands (ksi [MPa]). When the neutral axis falls in the top flange, the section is treated as a rectangular beam. When the neutral axis falls in the web, the section can be treated as a T-section beam. The neutral axis can then be calculated using the following equation:

$$c = \frac{A_{ps}\, f_{py} + A_s\, f_y - A_s'\, f_y'}{0.85\, f_c' \beta_1\, b_w + k\, A_{ps} \dfrac{f_{pu}}{d_p}} \quad \text{(ksi, in. [MPa, mm])} \qquad (2.28)$$

where A_{ps} is the area of strands (in.^{2} [mm^2]), f_{pu} is the tensile strength of prestressing steel (ksi [MPa]), f_{py} is the yield strength of prestressing steel (ksi [MPa]), A_s is the area of mild steel tension reinforcement (in.^{2} [mm^2]), A'_s is the area of compression tension reinforcement (in.^{2} [mm^2]), f_y is the yield strength of tension reinforcement steel (ksi [MPa]), f'_y is the yield strength of compression reinforcement steel (ksi [MPa]), h_f is the width of compression flange (in. [mm]), b_w is the width of web (in. [mm]), d_p is the distance from the extreme compression fiber to the centroid of tensile force in strands (in. [mm]), c is the distance between the neutral axis and the compressive face (in. [mm]), and β_1 is the stress block factor (see AASHTO LRFD 2006 Article 5.7.2.2).

The nominal moment capacity, M_n, can be calculated using the following equation (kip-ft [kN-m]):

$$M_n = A_{ps}\, f_{ps} \left(d_p - \frac{a}{2} \right) - A_s'\, f_y' \left(d_s' - \frac{a}{2} \right) + 0.85\, f_c' (b - b_w)\, \beta_1\, h_f \left(\frac{a}{2} - \frac{h_f}{2} \right) \qquad (2.29)$$

where d_s' is the depth of the compressive reinforcement (in. [mm]) and a is the depth of the equivalent stress block (in. [mm]).

As shown in the above equations, the nominal moment depends on many aspects of properties of concrete and bond characteristics. Therefore, full-scale testing is necessary to validate the design equations of the AASHTO LRFD. Moreover, the comparison of flexural capacity between SCC and CC girders is essential to validate overall structural performance of the precast, prestressed structural members made with SCC.

2.9 TRANSFER LENGTH AND DEVELOPMENT LENGTH

Bond mechanisms of prestressing strands are different from the bond mechanisms of mild steel reinforcement. This section explains the unique bond characteristics and the design of prestressed structural members. This section presents the definition of transfer and development length, bond mechanism, design equations, and recent findings related to SCC mixtures.

As shown in Figure 2.5, transfer length, l_t, is the transition distance from the free end of the prestressing strands to the fully bonded zone having an effective stress of the strands, f_{pe}, which is the stress of strands after prestress losses. Flexural bond length, l_f, is the additional bond length required for the strands to reach the stress, f_{ps}, corresponding to the stress in the strands at ultimate conditions, used to calculate the nominal moment capacity of the girder. As shown in Figure 2.5, the development length, l_d, is estimated as the sum of the transfer length, l_t, and the flexural bond length, l_f.

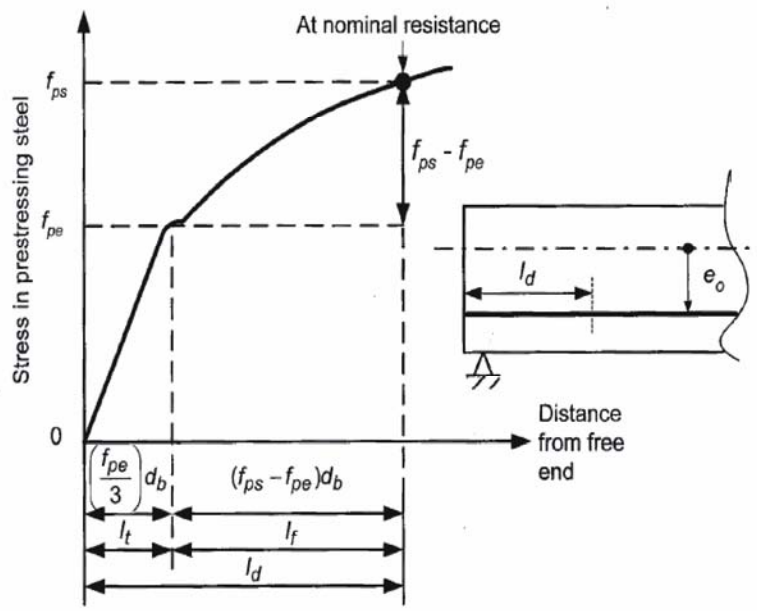

Figure 2.5. Definition of Development Length (Naaman 2004).

Transfer length and development length should be appropriately estimated to predict the flexural and shear design capacity along the entire span length.

Bond mechanisms consist of three major mechanisms: chemical and physical adhesion, friction, and mechanical resistance (Hanson and Kaar 1959). Adhesion is the weakest bond

between the concrete and strands. After slippage, adhesion makes no contribution to bond. The significant bond mechanisms of the strand are the frictional mechanism and mechanical resistance. The frictional mechanism is well known as the Hoyer effect or "lack of fit" mechanism (Hoyer and Friedrich 1939, Stoker and Sozen 1970). After releasing the strands, the diameter of the strand at the girder ends expands because of Poisson's effect. The expanded part produces a wedge action between the concrete and strands, resulting in friction between the surrounding concrete and the strands. The friction force is a function of the radial compressive stress on the strand. Therefore, the frictional bond depends on the compressive strength and time-dependent behavior of the concrete (creep and shrinkage). When the compressive strength increases, transfer length decreases (Catrodale *et al.* 1988, Kaar *et al.* 1963, Mitchell *et al.* 1993). Mechanical interlocking is also a distinguishable bond mechanism for strands. The interlocking stress is generated by the concrete bearing force against twisting wires of strands. However, time-dependent properties such as the development of concrete compressive strength and prestress loss could change the bond stress, resulting in the elongation of the transfer length.

Application of external loads increases the strand stress in addition to the effective stress, that is, the flexural bond stress induced by the external load. When cracking occurs, flexural bond stress increases significantly adjacent to cracks with stress concentrations and the loss of adhesion and frictional bond result in bond slip. The stresses are continuously redistributed from the initial crack to the adjacent end region. This region is referred to as the crack influence length or crack bond stress wave. When cracks propagate toward the beam end, the stand stress dramatically increases because of the frictional loss and the reduction of bearing stress (Hanson and Kaar 1959, Janney 1954).

The transfer and development length were proposed by many researchers to reasonably predict bond properties in prestressed concrete members (Buckner 1995, Lane 1998). Since 1998 the transfer length in the AASHTO LRFD Bridge Design Specifications (2004, 2006) has been changed to 60 strand diameters, d_b, from 50 d_b as required in the AASHTO LRFD (1996). High effective stress, f_{pe}, results in a longer transfer length (Hanson and Kaar 1959, Russell and Burns 1993). The ACI 318-05 recommended a transfer length of 50 d_b for shear design (Section 11.4.3) and $f_{pe}/3d_b$ for estimating development length (Section R12.9.1.1). The development length proposed by the AASHTO LRFD Bridge Design Specifications (2004) and the ACI 318-05 Code (2005) is based on extensive experimental data from research using CC mixtures (AASHTO

2006, ACI Committee 318 2005, Hanson and Kaar 1959, Janney 1954, Kaar *et al.* 1963). In October 1988, the Federal Highway Administration (FHWA) issued a memorandum requiring a 1.6 multiplier on the development length estimation (AASHTO 2004, 2006). The AASHTO LRFD Specifications (2004) also included the κ factor as 1.6 for all precast, prestressed beams regardless of the depth of beams. However, the κ factor was updated with the limit of depth of beams in the AASHTO LRFD (2006). The worst-case characteristics of strands shipped before 1997 and a lack of data made this conservative (AASHTO 2004, 2006, Lane 1990).

In the AASHTO LRFD Bridge Design Specifications (2006) Article 5.11.4.2 Equation 5.11.4.2-1, the 1.6 multiplier factor κ was used to avoid the bond failure resulting from inadequate development length in the structural member having the high shear effect in the beam with a depth greater than 24 in. (0.6 m), as shown in Equation 2.30. Otherwise, the 1.0 factor κ was recommended for prestressed members with a depth less than or equal to 24.0 in. (0.6 m), as shown in Equation 2.30. In 2001, the Florida Department of Transportation concluded that the adverse affect of shear stress on bond should be considered to estimate the development length of beams with a depth greater than 24 in. (0.6 m) (Shahawy 2001).

According to the AASHTO LRFD Specifications (2006), the gradual buildup of the strand force over the transfer and development lengths can be determined as follows:

$$l_d \geq \kappa \left(f_{ps} - \frac{2}{3} f_{pe} \right) d_b \text{ (ksi, in)} \quad \left[l_d \geq \frac{\kappa}{6.9} \left(f_{ps} - \frac{2}{3} f_{pe} \right) d_b \right] \text{ (MPa, mm)} \quad (2.30)$$

where d_b is the nominal strand diameter (in. [mm]), f_{ps} is the average stress in prestressing steel corresponding to the nominal flexural resistance of the member (ksi [MPa]), f_{pe} is the effective stress in the prestressing steel after losses (ksi [MPa]), and κ is 1.0 for pretensioned members with a depth less than or equal to 24 in. (610 mm) or 1.6 for pretenstioned members with a depth greater than 24 in. (610 mm).

In Equations 5.11.4.2-3 and 5.11.4.2-4 of the AASHTO LRFD (2006), bilinear equations are proposed to predict the stress of strand along the entire span length, and these are repeated here as Equations 2.31 and 2.32:

$$f_{px} = \frac{f_{pe} l_{px}}{60\, d_b} \quad \left[\text{for } l_{px} \le l_{tr}\,(60\, d_b)\right] \text{ (ksi, in. [MPa, mm])} \qquad (2.31)$$

$$f_{px} = f_{pe} + \frac{(l_{px} - 60\, d_b)}{(l_d - 60\, d_b)}\left(f_{ps} - f_{pe}\right) \quad \left[\text{for } l_{px} > l_{tr}\,(60\, d_b)\right] \text{ (ksi, in. [MPa, mm])} \qquad (2.32)$$

where l_{px} is the distance from the free end of the prestressed strand to the section of the member under consideration (in. [mm]) and f_{px} is the design stress in the prestressed strand at nominal flexural strength at the section of member under consideration (ksi [MPa]). Figure 2.6 illustrates the bilinear equations for estimating the stress in prestress strands at the nominal resistance of the member.

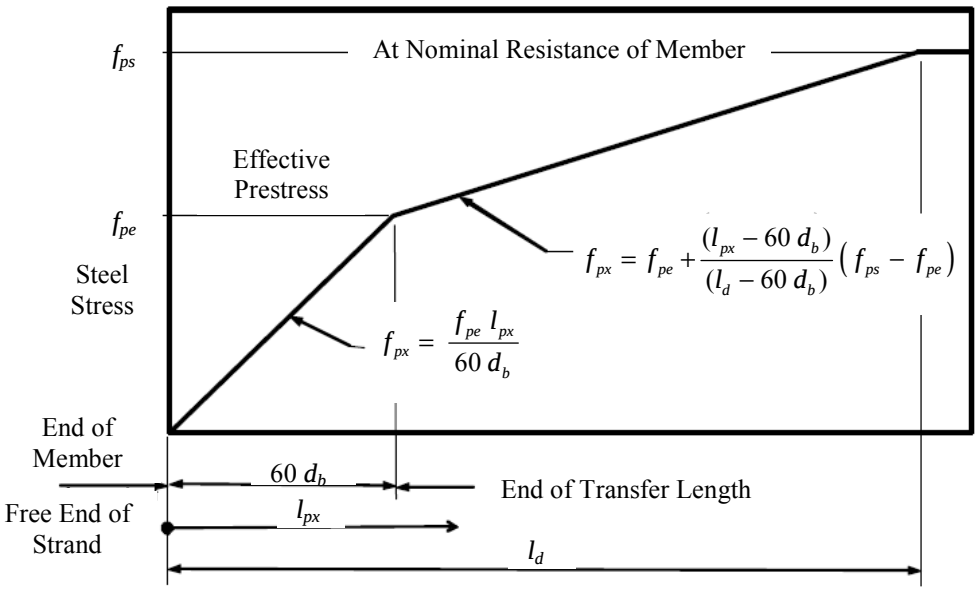

Figure 2.6. Idealized Relationship between Steel Stress and Distance from the Free End of Strand (AASHTO 2006).

The AASHTO LRFD Bridge Design Specifications (2004) all use the alternative equation for prestressed beams based on the studies of Lane (1990, 1998). The development length can be determined as follows (AASHTO LRFD 2004 Equation 5.11.4.2-2):

$$l_d \geq \frac{4\, f_{pbt}\, d_b}{f_c'} + \frac{6.4\,(f_{ps} - f_{pe})\, d_b}{f_c'} + 10 \quad \text{(ksi, in.)} \tag{2.33}$$

$$\left[l_d \geq \frac{4\, f_{pbt}\, d_b}{f_c'} + \frac{6.4\,(f_{ps} - f_{pe})\, d_b}{f_c'} + 254 \right] \quad \text{(MPa, mm)}$$

where d_b is the nominal strand diameter (in. [mm]), f_{pbt} is the stress in prestressing steel immediately prior to transfer (ksi [MPa]) which is 0.75 f_{pu} (ksi [MPa]) for the low relaxation strands, f_{ps} is the average stress in prestressing steel corresponding to the nominal flexural resistance of the member (ksi [MPa]), f_{pe} is the effective stress in the prestressing steel after losses (ksi [MPa]), and f'_c is the specified compressive strength of concrete at 28 days (ksi [MPa]).

These bond mechanisms highly depend on the physical and chemical properties of concrete. SCC mixtures have potentially different bond performance than CC mixtures. According to previous research, the transfer lengths of SCC beams were longer than those of CC beams (Burgueño and Haq 2007, Erkmen *et al.* 2007). According to Girgis and Tuan (2004), transfer length of some SCC mixtures is 50 percent longer than that of CC mixtures. The transfer length of SCC with limestone was generally similar to that of CC. However, the bond strength of SCC with fly ash was lower than CC, indicating longer transfer length (Hegger *et al.* 2007). According to Maekawa *et al.* (2003), the SCC has low *w/c* and less porosity resulting in high bond strength based on finite element analytical approaches and test results. According to Larson *et al.* (2005), the top strand has about 50 percent longer transfer length compared to the bottom strands. They also found that, in general, the transfer length of top strands is satisfactory estimated by ACI 318-05. It is noted that a single strand with 8 in. × 24 in. (0.2 m × 0.6 m) depth beams was tested to evaluate transfer and development length in their study.

Trent (2007) tested 24 beams with 14 in. (0.35 m) depth and single strands. The development length of SCC beams was 20 percent shorter than the value estimated using ACI 318-05 and the AASHTO LRFD Bridge Design Specifications (2006) with a κ factor of 1.0. He concluded that, in general, the transfer and development length of strands in SCC beams are satisfactorily estimated, with conservatism, using the AASHTO LRFD Bridge Design Specifications (2004 and 2006) regardless of the κ factor.

According to the basic theory of prestressed concrete from an early study by Guyon (1953), bond performance depends on the quality of the concrete. The high paste volume and the stability of SCC mixtures potentially influence the bond mechanisms resulting in the change of prestressing stresses of strands. Furthermore, case studies are limited to understanding the impact of the SCC mixtures on the design equations to reasonably estimate the transfer and development length.

Finally, the applicability of the AASHTO LRFD Specifications for estimating transfer and development length has to be investigated for implementation of SCC mixtures. In this study, equations of the AASHTO LRFD (2004, 2006) are examined.

2.10 PRESTRESS LOSSES

Prestress losses occur due to several factors including environmental conditions, material properties, and construction practices. The estimation of prestress losses needs to be accurate to predict time-dependent behavior, such as long-term deflection and service stresses of prestressed concrete members. Transfer and development length and flexural and shear capacities of the members also require accurate estimation of prestressing forces after losses.

Figure 2.7 shows prestress losses of strands as a function of construction and load sequence. Before transfer (release of strands) the initial jacking stress of strands has components of several losses such as the anchorage seating, the initial relaxation of strands, and temperature effect. At transfer, immediate losses occur due to elastic shortening of the concrete. Creep, shrinkage, and relaxation also produce additional losses before casting deck. Deck weight and superimposed dead and live loads produce elastic gain in the strands for the composite member. After casting the deck, the shrinkage and creep of the girder and the deck and relaxation of strands occurs over time, resulting in long-term prestress losses (Tadros *et al.* 2003).

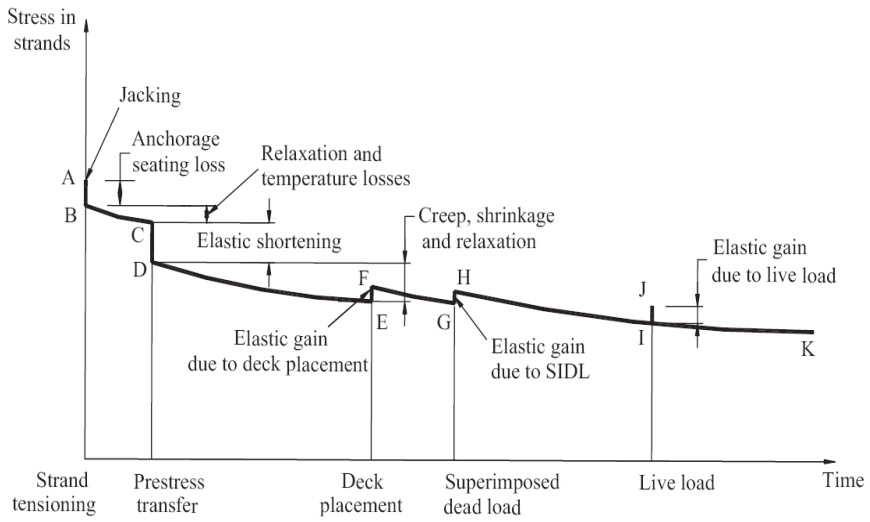

Figure 2.7. Stress versus Time of Prestressed Strands (Tadros *et al.* 2003).

Generally, there are refined methods and lump-sum methods for estimation losses in prestressed, precast members. This section explains these refined methods. All components of prestress losses typically consist of elastic shortening, creep, shrinkage, and relaxation. Based on Tadros (2003) and Al-Omaishi (2001), the AASHTO LRFD refined method (2004) was calibrated with modern high-strength materials and considering the interaction between the girder and deck in terms of creep and shrinkage of the deck. The AASHTO LRFD Bridge Design Specifications (2006) provides a step-by-step prestress loss estimation method.

When the prestressed, precast members are subjected to normal loading and environmental conditions as defined in AASHTO LRFD (2006), elastic shortening of the member is estimated by AASHTO LRFD Equation 5.9.5.2.3a-1 (2006) as:

$$\Delta f_{pES} = \frac{E_p}{E_{ct}} f_{cgp} \quad \text{(ksi [MPa])} \tag{2.34}$$

where Δf_{pES} is the elastic shortening from prestress losses (ksi [MPa]), E_p is the MOE of strands (ksi [MPa]), E_{ct} is the MOE of concrete at transfer (ksi [MPa]), and f_{cgp} is the concrete stress at the center of gravity of the strands due to the prestressing force immediately after transfer and the self-weight of the member at the section of maximum moment (ksi [MPa]).

The elastic shortening can be also calculated using the transformed section properties. This equation is based on the assumption that the strand and concrete are equally strained in compression and tension (AASHTO 2006). This alternative equation is used for the prediction of elastic losses in this study:

$$\Delta f_{pES} = \frac{A_{ps} f_{pbt} (I_g + e_m^2 A_g) - e_m M_g A_g}{A_{ps} (I_g + e_m^2 A_g) + \frac{A_g I_g E_{ci}}{E_p}} \text{ (ksi [MPa])} \quad (2.35)$$

where A_{ps} is the area of strands (in.^{2} [mm^2]), A_g is the gross area of section (in.^{2} [mm^2]), E_{ci} is the MOE of concrete at transfer (ksi [MPa]), E_p is the modulus of elasticity of strands (ksi [MPa]), e_m is the average eccentricity of the strands at midspan (in. [mm]), f_{pbt} is the stress in the strand immediately prior to transfer (ksi [MPa]), I_g is the moment of inertia of the gross section (in.^{4} [mm^4]), and M_g is the midspan moment due to member self-weight (kip-in. [kN-mm]).

Equation 5.9.5.4.1-1 is the general equation to predict approximate time-dependent prestress losses with three components which are creep, shrinkage, and relaxation. A more detailed method is the refined estimate of time-dependent loss in AASHTO LRFD Article 5.9.5.4 (2006). In general, the time-dependent loss, Δf_{pLT}, can be determined as follows (2006 AASHTO LRFD Equation 5.9.5.4.1-1):

$$\Delta f_{pLT} = (\Delta f_{pSR} + \Delta f_{pCR} + \Delta f_{pR1})_{id} + (\Delta f_{pSD} + \Delta f_{pCD} + \Delta f_{pR2} - \Delta f_{pSS})_{df} \text{ (ksi [MPa])} \quad (2.36)$$

where Δf_{pSR} is the prestress loss due to shrinkage of the girder between transfer and deck placement (ksi [MPa]), Δf_{pCR} is the prestress loss due to creep of the girder between transfer and deck placement (ksi [MPa]), Δf_{pR1} is the prestress loss due to relaxation of prestressing strands between transfer and deck placement (ksi [MPa]), Δf_{pR2} is the prestress loss due to relaxation of prestressing strands in composite section between time of deck placement and final time (ksi [MPa]), Δf_{pSD} is the prestress loss due to shrinkage of the girder between time of deck placement and final time (ksi [MPa]), Δf_{pCD} is the prestress loss due to creep of the girder between time of deck placement and final time (ksi [MPa]), Δf_{pSS} is the prestress loss due to shrinkage of the deck

composite section (ksi [MPa]), $(\Delta f_{pSR} + \Delta f_{pCR} + \Delta f_{pR1})_{id}$ is the sum of time-dependent prestress losses between transfer and deck (ksi [MPa]), and $(\Delta f_{pSD} + \Delta f_{pCD} + \Delta f_{pR2} - \Delta f_{pSS})_{df}$ is the sum of time-dependent prestress losses after deck placement (ksi [MPa]).

The AASHTO LRFD Bridge Design Specifications (2004) presented the prestress losses as follows (2004 AASHTO LRFD Equation 5.9.5.1-1):

$$\Delta f_{pT} = \Delta f_{pES} + \Delta f_{pR1} + \Delta f_{pSR} + \Delta f_{pCR} + \Delta f_{pR2} \quad \text{(ksi [MPa])} \tag{2.37}$$

where Δf_{pT} is the total prestress loss (ksi [MPa]), Δf_{pES} is the prestress loss due to elastic shortening (ksi [MPa]), Δf_{pR1} is the prestress loss due to steel relaxation at transfer (ksi [MPa]), Δf_{pSR} is the prestress loss due to concrete shrinkage (ksi [MPa]), , Δf_{pCR} is the prestress loss due to concrete creep (ksi [MPa]), and , Δf_{pR2} is the prestress loss due to steel relaxation after transfer (ksi [MPa]).

Several research studies have estimated the prestress losses of SCC mixtures. According to Ruiz *et al.* (2007), the prestress loss of SCC is comparable to that of CC in 6.5 in. × 12 in. (165 mm × 305 mm) by 18 ft (5.5 m) long beams. When the measured values were compared to the equation proposed by Tadros *et al.* (2003), this equation overpredicted the prestress losses of SCC and CC by about 35 and 20 percent, respectively. Erkmen *et al.* (2007) also found that SCC and CC have similar elastic shortening and long-term losses. They also found that the AASHTO LRFD method (2004), PCI Design Handbook (PCI 2004), and PCI general method (PCI 1975) predicted conservatively total prestress loss in 38 ft (11.5 m) long Mn/DOT 36M-I girders. Some researchers found that SCC girders have less prestress losses than CC girders, indicating less creep and shrinkage (Naito *et al.* 2006, Trent 2007). Contrary to their expectations and concerns, high paste volume and low aggregate volume did not cause larger amounts of prestress losses. The prediction equations generally conservatively predicted prestress losses. These results could be attributed to the short duration of monitoring the prestress losses, which was less than 1 year (Erkmen *et al.* 2007). One study performed field monitoring of full-scale beams and found that the prestress loss of SCC seems to be similar to that of CC (Burgueño and Bendert 2007).

The high paste volume and stability of SCC mixtures potentially influence the bond mechanisms resulting in the large prestress losses of strands. According to previous research, the prestress losses of SCC mixtures were not significantly different from those of CC mixtures.

However, more comprehensive research is required to better estimate prestress losses. To date, the case studies to understand the applicability of the design equations to estimate accurate prestress losses to SCC girders are limited.

Finally, the applicability of the AASHTO LRFD Specifications (2004, 2006) for estimating the prestress losses in SCC girders needs to be assessed.

2.11 CAMBER AND DEFLECTION

Camber and deflection are in-service performance measures of precast, prestressed structural members. Creep, shrinkage, MOE, development of compressive strength, bond, and prestress losses are related to the behaviors of camber and deflection. Camber growth caused by the creep effect due to the axial prestressing force is typically larger than the downward deflection caused by the creep effect due to the self-weight of the girder.

Some researchers have monitored camber and deflection of SCC precast, prestressed structural members. According to Gross *et al.* (2007) and Erkmen *et al.* (2007), the overall behavior between SCC and CC members is similar. However, initial camber was significantly higher in SCC girders due to low MOE and higher creep and shrinkage of the SCC compared with CC laboratory results (Gross *et al.* 2007).

There is limited knowledge of the impact of the SCC on camber and deflection. To predict camber and deflection, it is necessary to have a good understanding of mechanical and time-dependent material along with an accurate estimation of prestress losses. Because the SCC members might have different mechanical and time-dependent properties, camber and deflection can be different from CC members. For accurate prediction and estimation of camber and deflection, more data and comprehensive studies are necessary with comprehensive understanding of mechanical, bond, and time-dependent properties.

2.12 SUMMARY

According to several research studies and recommendations, SCC mixtures typically have a high paste volume and low coarse aggregate to minimize the friction of particles and maximize stability. Therefore, many researchers are concerned that SCC mixture proportions could affect adversely hardened properties such as less aggregate interlock resulting in low shear capacity and high shrinkage and creep resulting in high prestress losses. Low elastic modulus

could also increase the gap between actual and predicted behaviors (i.e., deflection, camber). Several universities and transportation agencies have conducted research to develop SCC mixture proportions, evaluate mechanical and time-dependent properties, and validate with full-scale tests. Many researchers have noted several advantages of SCC such as ease of placement, reduction of casting time, and better finishing when used in precast, prestressed concrete structural members. However, some researchers had difficulties in field application due to a lack of robustness of SCC resulting in some segregation, poor workability, poor surface quality, and/or low mechanical or bond strength (Burgueño and Haq 2007, Erkmen *et al.* 2007, Ozyildrim 2007). Full-scale tests were also performed to evaluate field application, structural behavior, prestress losses, camber, and deflection. In general, when the fresh quality of SCC was satisfactory, the overall performance of SCC was comparable to that of CC. However, information to characterize the hardened properties of SCC for precast, prestressed concrete members is still limited. The applicability of the AASHTO LRFD Specifications, which is based on CC, has not been fully evaluated for use in designing SCC members. The study described in this report is valuable because comprehensive test results will be provided and the applicability of the AASHTO LRFD Specifications will also be discussed.

CHAPTER 3
MATERIALS

3.1 LABORATORY PROGRAM

Constituent materials used to make SCC can have a significant influence on the fresh and hardened characteristics of the SCC. The following sections discuss constituent materials used for manufacturing SCC in the laboratory program. Information on the chemical and physical characteristics of the constitutive materials and the mixture proportions are also presented.

3.1.1 Cement

A Type III cement (Alamo Cement Company, San Antonio, Texas) was used in the laboratory testing phase. Table 3.1 shows the chemical composition of the cement used in the laboratory testing. Table 3.2 shows the physical properties of cement used in the laboratory testing.

Table 3.1. Chemical Characteristics of Type III Cement Used in Laboratory Testing.

Chemical Composition	Proportions (%)
SiO_2	20.6
Al_2O_3	4.9
Fe_2O_3	3.4
CaO	64.1
MgO	0.8
SO_3	3.5
Na_2O	-
K_2O	-
Total Alkalies	0.5
Free Lime	1.5
C_3S	56.6
C_2S	16.3
C_3A	7.2
C_4AF	10.3

Table 3.2. Physical Characteristics of Type III Cement Used in Laboratory Testing.

Physical Characteristics	Type III Cement
Blaine Fineness, ft^2/lb (m^2/kg)	2630 (539)
Setting Time	
Initial, min	110
Final, min	210
Compressive Strength	
1 day, ksi (MPa)	3.5 (24.1)
3 day, ksi (MPa)	4.7 (32.6)
7 day, ksi (MPa)	5.7 (39.1)
28 day, ksi (MPa)	6.8 (46.8)
Specific Gravity	3.15
Loss on Ignition, %	2.1

3.1.2 Fly Ash

Untreated Class F fly ash (Boral Material Technologies, Rockdale, Texas) was used in the SCC mixtures. Table 3.3 shows the chemical characteristics of the fly ash used in the laboratory testing. Table 3.4 shows the physical characteristics of the fly ash used in the laboratory testing.

Table 3.3. Chemical Characteristics Class F Fly Ash.

Chemical Composition	Proportions (%)
SiO_2	52.5
Al_2O_3	21.8
Fe_2O_3	4.90
CaO	13.9
MgO	2.00
SO_3	0.79
Na_2O	0.32
K_2O	0.74
Total Alkalies	0.81

Table 3.4. Physical Characteristics of Fly Ash.

Physical Properties	Class F Fly Ash
Specific Gravity	2.33
Strength Activity Index with Portland Cement at Specific Day, % of Control	
7 day	73.6
28 day	82.0
Loss on Ignition, %	1.05

3.1.3 Aggregate

The properties of the aggregate used in the laboratory test program are presented in the following sections.

3.1.3.1 Coarse Aggregate

River gravel and limestone aggregates were used in this study. The same type and source were used for both SCC and CC mixtures. Fordyce Murphy Quarry in Victoria, Texas, provided the river gravel, and Hanson Aggregate in New Braunfels, Texas, provided the limestone. Table 3.5 shows the characteristics of the coarse aggregate used for the SCC and CC mixtures. The nominal maximum size aggregate was 0.75 in. (19 mm). Figure 3.1 shows the gradation of the coarse aggregates. These gradations meet the requirement of ASTM C33, *Standard Specification for Concrete Aggregates* (2007).

Table 3.5. Properties of Coarse Aggregate.

Physical Properties	Aggregate Type	
	Fordyce Murphy River Gravel	Hanson Aggregate Limestone
Specific Gravity	2.59	2.59
Absorption Capacity, %	0.78	1.43

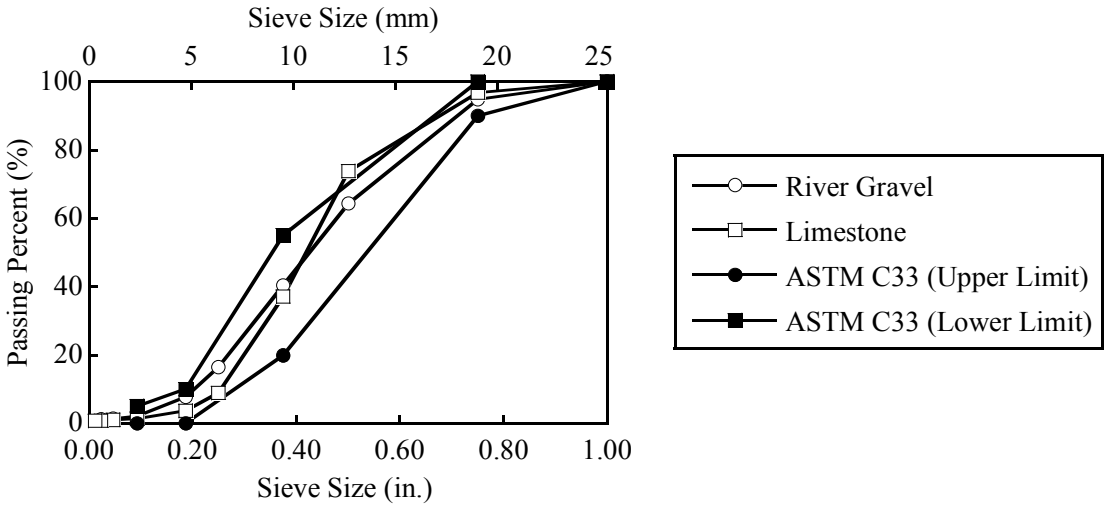

Figure 3.1. Gradation of Coarse Aggregates Used in Laboratory Testing.

3.1.3.2 Fine Aggregate

Table 3.6 shows the characteristics of the fine aggregate used in this study for the SCC and CC mixtures. Figure 3.2 shows the gradation of the fine aggregates. These gradations meet the requirement of ASTM C33.

Table 3.6. Properties of Fine Aggregate.

Physical Properties	Aggregate Type	
	Fordyce Murphy Natural Sand (I)	TXI (Austin) Natural Sand (II)
Specific Gravity	2.58	2.60
Absorption Capacity, %	0.54	0.56
Fineness Modulus	2.72	2.89

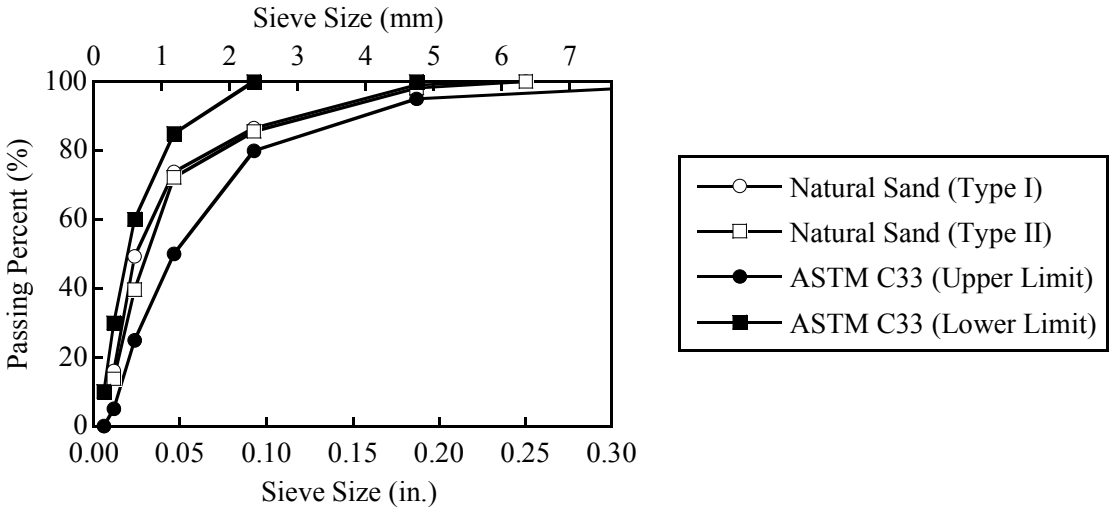

Figure 3.2. Gradation of Fine Aggregates Used in Laboratory Testing.

3.1.4 Chemical Admixtures

To achieve 16-hour target strengths and high workability, chemical admixtures were used. BASF Construction Chemicals LLC provided all admixtures. Polycarboxylate based HRWRAs were used for both CC and SCC mixtures. All of the chemical admixtures, including HRWRAs used in this study, are given in Table 3.7. Retarder, VMA, and accelerators were also provided by BASF. Section 3.1.6 explains the purpose for each admixture type along with mixture proportions.

Table 3.7. Chemical Admixture Types.

Admixture Type	SCC	CC
HRWRA	Glenium 3400NV	PS 1466
Retarder	Delvo Stabilizer	-
Experimental Admixture	PT1482	-
VMA	VMA 362	-

Note: - indicates no addition.

3.1.5 Mild Steel Reinforcement

Grade 60 reinforcement meeting ASTM A615, *Standard Specification for Deformed and Plain Carbon-Steel Bars for Concrete Reinforcement* (2008), (#5 [M16]) was used for the pull-out and push-off samples, with a yield strength, f_y, between 62 and 68 ksi (427 and 469 MPa) according to mill certificates and laboratory tests at High Bay Structural and Materials Laboratory (HBSML). The tensile strength, f_u, is between 103 and 110 ksi (710 and 758 MPa). The chemical composition and mechanical properties of the mild steel reinforcement is presented in Table 3.8. Tensile elongation (TE) is the maximum elongation of reinforcements at ultimate failure.

Table 3.8. Chemical and Mechanical Properties of #5 (M16) Steel Reinforcement.

Reinforcement (#5 [M16])	Mill Certificate Information		HBSML Test Information	
Properties	1st Set	2nd Set	1st Set	2nd Set
f_y, ksi (MPa)	68 (468)	62 (428)	64 (441)	66 (455)
f_u, ksi (MPa)	104 (717)	103 (710)	109 (752)	110 (758)
Tensile Elongation (%)	16	12	16	15
Composition	Proportions (Wt. %)			
C	0.3700	0.4200		
Mn	1.1200	0.8500		
P	0.0180	0.0160		
S	0.0380	0.0290		
Si	0.2700	0.1900		
Cu	0.3000	0.3500		
Cr	0.1900	0.2000		
Ni	0.1000	0.1400		
Mo	0.0340	0.0370		
Cb	0.0020	0.0020		
V	0.0010	0.0010		
Sn	0.0120	0.0130		
B	0.0004	0.0004		
Ti	0.0020	0.0010		

3.1.6 Mixture Proportions

To quantify the hardened properties of SCC, researchers evaluated 12 SCC mixture proportions with three main variables: 16-hour release strengths (5 and 7 ksi [34 and 48 MPa]), two aggregate types (river gravel and limestone), and three different volumes of coarse aggregate. For river gravel, two additional mixture proportions were used for 5 ksi [34 MPa] target strength. The ratio of the coarse aggregate volume to total aggregate volume was varied to optimize the SCC mixture proportions. Changing these ratios results in changes to paste volume.

Four CC mixture proportions served as control mixtures and consisted of two release strengths (5 and 7 ksi [34 and 48 MPa]) and the two coarse aggregate types.

Figure 3.3 explains the mixture proportion identification. For the SCC mixtures, the coarse aggregate volumes were varied from 32 to 38 percent.

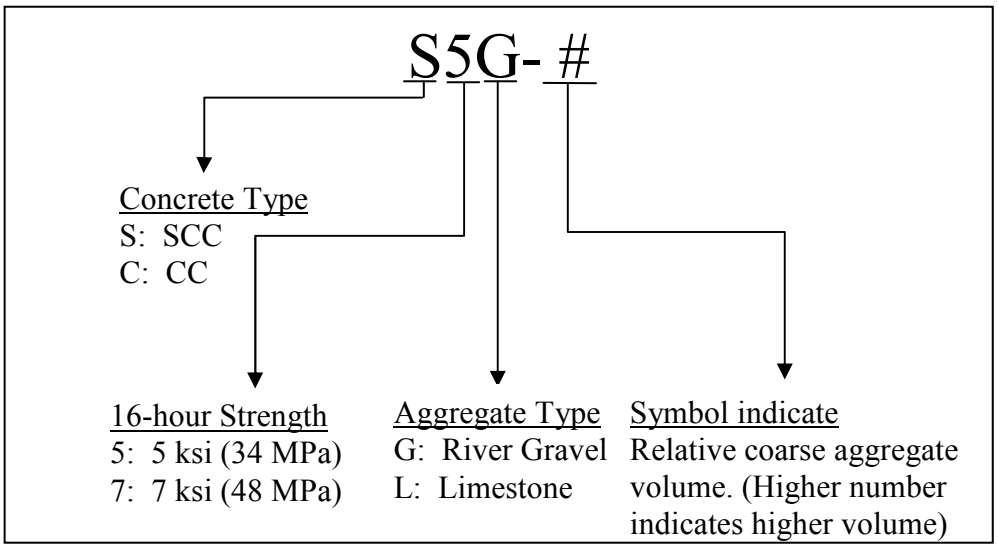

Figure 3.3. Mixture Identification.

Different types of HRWRA were used to achieve the target workability. For the 7 ksi (48 MPa) SCC mixtures, an experimental admixture was used to achieve the target strength at 16 hours and extend workability retention. A retarder was also used for the 5 ksi (34 MPa) SCC mixtures to extend workability retention. VMA was used to achieve target workability and stability for the S7L-6 mixtures. AEAs were not used in this study.

The mixture proportions of CC mixtures were based on typical mixture proportions of precasters in Texas (Hueste *et al.* 2004). Note that the objective of this research is to compare the

performance of SCC mixtures with CC mixtures based on their targeted 16-hour release strengths. In general, these early strengths are the critical factor for fabricating girders in Texas. The total volume of cementitious material was limited to 700 lb/yd^3 (415 kg/m^3) in accordance with TxDOT Standard, *Standard Specifications for Construction and Maintenance of Highways, Streets, and Bridges* (TxDOT 2004). The total volume of coarse aggregate was 40 percent for the 5 and 7 ksi (34 and 48 MPa) limestone mixture proportions and 44 percent for the 5 and 7 ksi (34 and 48 MPa) river gravel mixture proportions. Tables 3.9 to 3.12 present all CC and SCC mixture proportions.

Table 3.9. Mixture Proportions of River Gravel SCC.

Coarse Aggregate Type	River gravel							
16-hour Target Strength	5000 psi (34 MPa)					7000 psi (48 MPa)		
Mixture ID	S5G -1	S5G -2	S5G -3a	S5G -3b	S5G -3c	S7G -4	S7G -5	S7G -6
Cement, lb/yd^3 (kg/m^3)	624 (370)	646 (383)	633 (376)			720 (427)		
Fly Ash, lb/yd^3 (kg/m^3)	156 (93)	239 (142)	298 (177)			180 (107)		
Water, lb/yd^3 (kg/m^3)	252 (150)	260 (154)	255 (152)			208 (123)		
Coarse Agg., lb/yd^3 (kg/m^3)	1461 (867)	1535 (911)	1374 (815)	1511 (897)	1649 (978)	1414 (839)	1527 (906)	1641 (973)
Fine Agg., lb/yd^3 (kg/m^3)	1456 (864)	1251 (742)	1368 (812)	1232 (731)	1095 (650)	1408 (836)	1296 (769)	1184 (702)
HRWRA, oz/yd^3 (L/m^3)	74 (2.9)	81 (3.1)	92 (3.6)	80 (3.1)	82 (3.2)	140 (5.4)	117 (4.5)	108 (4.2)
Retarder, oz/yd^3 (L/m^3)	27 (1.0)	27 (1.0)	25 (1.0)	25 (1.0)	25 (1.0)	-	-	-
Exp. Admix., oz/yd^3 (L/m^3)	-	-	-	-	-	578 (22.4)		
VMA, oz/yd^3 (L/m^3)	-	-	-	-	-	-	-	-
Proportion Characteristics								
w/cm(*)	0.33	0.30	0.28			0.23		
w/c	0.4	0.4	0.4			0.29		
Coarse Agg. Vol., %	33.5	35.1	31.5	34.6	37.8	32.3	35.0	37.6

Table 3.10. Mixture Proportions of River Gravel CC.

Coarse Aggregate Type	River Gravel	
16-hour Targeted Strength	5000 psi (34 MPa)	7000 psi (48 MPa)
Mixture ID	C5G	C7G
Cement, lb/yd^3 (kg/m^3)	625 (371)	700 (415)
Water, lb/yd^3 (kg/m^3)	225 (134)	200 (119)
Coarse Agg., lb/yd^3(kg/m^3)	1935 (1148)	1935 (1148)
Fine Agg., lb/yd^3 (kg/m^3)	1232 (731)	1232 (731)
HRWRA, oz/yd^3 (L/m^3)	56 (2.2)	91 (3.5)
Proportion Characteristics		
w/c	0.36	0.285
Coarse Agg. Vol., %	44.3	44.3

Table 3.11. Mixture Proportions of Limestone SCC.

Coarse Aggregate Type	Limestone					
16-hour Target Strength	5000 psi (34 MPa)			7000 psi (48 MPa)		
Mixture ID	S5L -3a	S5L -3b	S5L -3c	S7L -4	S7L -5	S7L -6
Cement, lb/yd^3 (kg/m^3)	640 (380)			720 (427)		
Fly Ash, lb/yd^3(kg/m^3)	426 (253)			180 (107)		
Water, lb/yd^3(kg/m^3)	288 (171)			225 (133)		
Coarse Agg., lb/yd^3 (kg/m^3)	1259 (747)	1385 (822)	1511 (896)	1394 (827)	1505 (893)	1617 (959)
Fine Agg., lb/yd^3 (kg/m^3)	1264 (750)	1138 (675)	1011 (600)	1399 (830)	1287 (764)	1175 (697)
HRWR, oz/yd^3 (L/m^3)	60 (2.3)	58 (2.2)	58 (2.2)	108 (4.2)	117 (4.5)	108 (4.2)
Retarder, oz/yd^3 (L/m^3)	26 (1.0)	26 (1.0)	26 (1.0)	-	-	-
Exp. Admix., oz/yd^3 (L/m^3)	-	-	-	578 (22.4)		
VMA, oz/yd^3 (L/m^3)	-	-	-	-	-	4 (0.2)
Proportion Characteristics						
w/cm$^{(*)}$	0.270			0.285		
w/c	0.45			0.31		
Coarse Agg. Vol., %	29.0	31.9	34.8	31.9	34.5	37.0

Table 3.12. Mixture Proportions of Limestone CC.

Coarse Aggregate Type	Limestone	
16-hour Target Strength	5000 psi (34 MPa)	7000 psi (48 MPa)
Mixture ID	C5L	C7L
Cement, lb/yd^3 (kg/m^3)	600 (356)	680 (403)
Water, lb/yd^3 (kg/m^3)	252 (149)	224 (133)
Coarse Agg., lb/yd^3 (kg/m^3)	1750 (1039)	1752 (1039)
Fine Agg., lb/yd^3 (kg/m^3)	1380 (820)	1382 (820)
HRWRA, oz/yd^3 (L/m^3)	37 (1.4)	68 (2.6)
Proportion Characteristics		
w/c	0.42	0.33
Coarse Agg. Vol., %	40.1	40.1

3.2 FULL-SCALE TEST PROGRAM

The following sections discuss constituent materials used for manufacturing SCC in the full-scale test program. R and L represent river gravel and limestone in the mixture proportions, respectively. The CC-R and SCC-R girders were fabricated on March 26, 2007. A second set of girders, CC-L and SCC-L, were fabricated on July 12, 2007. Cement, fly ash, and aggregates were obtained from the same source. Information on the chemical and physical characteristics of the constitutive materials and the mixture proportions are presented next.

3.2.1 Cement

Full-scale testing used a Type III cement (Alamo Cement Company, San Antonio, Texas). The chemical and physical properties of cement are shown in Tables 3.13 and 3.14.

3.2.2 Fly Ash

The Class F fly ash, from the same source used in the laboratory testing phase, was used in the fabrication of the field samples. The girders contained untreated Class F fly ash (Boral Material Technologies, Rockdale, Texas). The chemical characteristics and physical properties can be referred to Section 3.1.2.

3.2.3 Aggregate

The same aggregate source used in laboratory test program was used for the full-scale test program. The information can be found in Section 3.1.3. For limestone mixtures, natural sand was provided from Fordyce Murphy Quarry in Victoria, Texas.

Table 3.13. Chemical Characteristics of Type III Cement Used in Full-scale Testing.

Chemical Composition	Proportions (%)	
	Girder ID	
	CC-R, SCC-R	CC-L, SCC-L
SiO_2	20.6	20.5
Al_2O_3	4.5	4.6
Fe_2O_3	3.6	3.5
CaO	64.6	64.5
MgO	0.7	0.7
SO_3	3.7	3.7
Loss of Ignition	1.9	1.7
Total Alkalies (NaO_{2eq})	0.50	0.55
Insoluble	0.13	0.11
C_2S	16.3	16.3
C_3S	56.5	60
C_3A	5.8	6.5
C_4AF	11.0	10

Table 3.14. Physical Characteristics of Type III Cement Used in Full-scale Testing.

Physical Properties	Girder ID	
	CC-R, SCC-R	CC-L, SCC-L
Blaine Fineness, ft^2/lb (m^2/kg)	2640 (541)	2586 (530)
Specific Gravity	3.15	3.15
Compressive Strength		
1-day strength, psi (MPa)	3840 (26)	3880 (27)
3-day strength, psi (MPa)	5300 (37)	5360 (37)
7-day strength, psi (MPa)	6280 (43)	6240 (43)
28-day strength, psi (MPa)	6810 (47)	7460 (51)

3.2.4 Chemical Admixtures

Admixtures for mixture proportions were provided by BASF Construction Chemicals LLC. Information on these admixtures can be found in Section 3.1.4.

3.2.5 Mild Steel Reinforcement for Girder and Deck

Grade 60 reinforcement meeting ASTM A615 (#4 [M13]) was used in the girders and decks. The yield strength, f_y, of the reinforcement was 62 and 65 ksi (427 and 448 MPa) for the decks and between 66 and 69 ksi (452 and 477 MPa) for the girders according to mill certificates and laboratory tests performed at HBSML. The elastic modulus of the reinforcement was assumed to be 29,000 ksi (200 GPa). The chemical compositions and mechanical properties of

mild steel reinforcements are presented in Table 3.15. The reinforcement (#5 [M16]) used for the deck is the same as that described in the laboratory test program.

Table 3.15. Chemical and Mechanical Properties of #4 (M13) Steel Reinforcement.

Reinforcement (#4 [M13])	Mill Certificate Information			HBSML Test Information	
Applications	Girders		All Decks	Girders	Deck
f_y, ksi (MPa)	69 (477)	66 (452)	62 (427)	65 (448)	65 (448)
f_f, ksi (MPa)	104 (720)	103 (709)	99.5 (686)	104 (717)	104 (717)
Tensile Elongation (%)	13	16	12	-	11
Composition	Proportions (Wt. %)				
C	0.3700	0.3800	0.3900		
Mn	1.1200	0.8900	0.8700		
P	0.0180	0.0110	0.0110		
S	0.0380	0.0290	0.0310		
Si	0.2700	0.1700	0.1900		
Cu	0.3000	0.3000	0.3900		
Cr	0.1900	0.1400	0.1400		
Ni	0.1000	0.1800	0.2000		
Mo	0.0340	0.0480	0.0520		
Cb	0.0020	0.0020	0.0040		
V	0.0010	0.0010	0.0010		
Sn	0.0120	0.0120	0.0160		
B	0.0004	0.0003	0.0030		
Ti	0.0020	0.0010	0.0010		

3.2.6 Prestressing Steel

The prestressing steel for the girders was 0.5 in. (12.7 mm) diameter, Grade 270, low-relaxation, seven-wire strand manufactured by American Spring Wire Corp. in Houston, Texas. The strand met the requirement of ASTM A416, *Standard Specification for Steel Strand, Uncoated Seven-Wire for Prestressed Concrete*. Properties of the strand are presented in Table 3.16. The yield stress is estimated based on 1 percent elongation of strands according to ASTM A416. The strands were slightly weathered.

Table 3.16. Characteristics of Strands (Reported by Manufacturer).

Materials	0.5 in. (12.7 mm) diameter 270 ksi (1862 MPa) low-relaxation strands	
Girder ID	CC-R and SCC-R	CC-L and SCC-L
A_s, in.^{2} (mm^2)	0.15281 (98.6)	0.15281 (98.6)
P_y, kip (kN)	38.54 (171.4)	39.67 (176.5)
P_u, kip (kN)	44.19 (196.6)	44.43 (197.6)
Tensile Elongation, %	8.81% ≥ 4%	7.77% ≥ 4%
E_p, ksi (MPa)	28,000 (193,120)	28,000 (193,080)

Note: A_s = area of strands, P_y = yield strength, and P_u = tensile strength.

The stress-strain relationship was constructed with the modified Ramberg-Osgood function (Mattock 1979) as follows:

$$f_p = E_p \varepsilon_p \left\{ A + \frac{(1-A)}{\left[1 + \left(B \varepsilon_p\right)^C\right]^{1/C}} \right\} \tag{3.1}$$

where f_p is the strand stress, E_p is the MOE, and ε_p is the strand strain. Based on reported properties, the coefficients, (A, B, and C) were determined as shown in Figure 3.4.

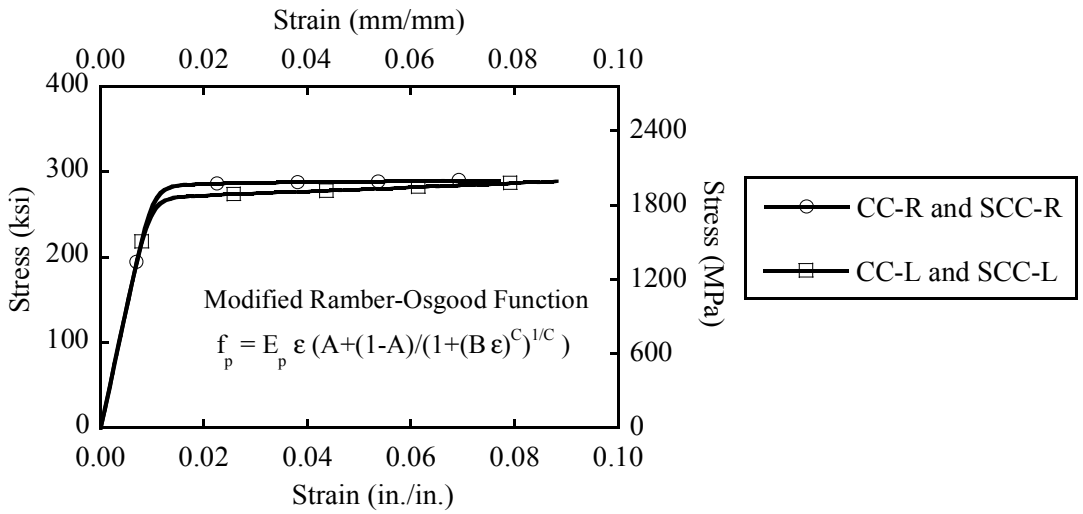

Variables	CC-R and SCC-R	CC-L and SCC-L
A	0.008590	0.002549
B	103.580	97.920
C	8	8

Figure 3.4. Stress-Strain Relationship of Prestressing Steel.

3.2.7 Mixture Proportions

This section presents mixture proportions used for full-scale girders and decks.

3.2.7.1 Girder

Among the 14 SCC mixture proportions studied in this laboratory program, proportions with the highest volume of coarse aggregate for each aggregate type were used in the full-scale precast/prestressed TxDOT Type A girders. This was done because plants will want to maximize the coarse aggregate to make the mixtures more cost effective. Among the four CC mixture proportions, one mixture proportion with each aggregate type was used to construct the companion (i.e., control) girder. Girders and their representative mixtures are shown in Table 3.17.

Table 3.17. Girder ID and Corresponding Mixture ID.

Girder ID	CC-R	SCC-R	CC-L	SCC-L
Mixture ID	C5G	S5G-3c	C5L	S5L-3c

3.2.7.2 Cast-in-Place (CIP) Deck

In accordance with the TxDOT Design Manual, TxDOT Class S concrete was used for the deck. This concrete was provided by a local ready mix concrete plant, TransitMix in Bryan, Texas. Class S concrete is normally proportioned for a minimum compressive strength of 4000 psi (28 MPa) at 28 days. The strength range for this concrete was between 5 and 8 ksi (34 and 55 MPa). The CIP deck on the SCC-R girder exhibited the highest strength compared with the other deck concretes as shown in Table 3.18.

Table 3.18. 28-Day Compressive Strength of CIP Concrete on Girders.

Girder ID	CC-R	SCC-R	CC-L	SCC-L
Average, psi (MPa)	6481 (45)	7921 (54)	5762 (40)	5386 (37)
Std. Dev., psi (MPa)	395 (2.7)	177 (1.2)	269 (1.8)	209 (1.4)

CHAPTER 4
EXPERIMENTAL PROGRAM

4.1 EARLY-AGE CHARACTERISTICS

All laboratory mixtures included the same test methods to evaluate the early-age characteristics. SCC mixtures were evaluated for filling ability, passing ability, stability, unit weight, and air content, and CC mixtures were evaluated for slump, unit weight, and air content.

To evaluate filling ability, passing ability, and stability of the early age characteristics of SCC, slump flow, T_{50}, and visual stability index (VSI) were measured in accordance with ASTM C1611, *Test Method for Slump Flow of Self-Consolidating Concrete* (2005). The target slump flow was between 27 and 29 in. (686 and 737 mm). Slump flow is the measured maximum diameter of flow after lifting an inverted slump cone. The average diameter of the slump flow is the average value of two perpendicular measurements. The T_{50} value represents the time in seconds when the flow patty of SCC reaches a diameter of 20 in. (508 mm). VSI is a visual examination used to rank the stability of SCC on a scale of 0 to 3 in 0.5 unit increments. A VSI of 0 is highly stable without segregation and represents an ideal condition, while a VSI of 3 is highly unstable with significant segregation. According to ACI 237 Committee report (2007), VSI from 2 to 3 indicates segregation potential and typically results in a large mortar halo or/and aggregate pile in the center of the slump spread. Unit weights were measured according to AASHTO T121, *Standard Method of Test for Mass per Cubic Meter* (*Cubic Foot*)*, Yield, and Air Content* (*Gravimetric*) *of Concrete* (2004). A pressure type air meter measured the air content in accordance with AASHTO T152, *Standard Method of Test for Air Content of Freshly Mixed Concrete by the Pressure Meter* (2004). It should be noted that there was no vibration or tamping to consolidate the fresh SCC concrete.

To evaluate the fresh characteristics of CC, slump was measured in accordance with ASTM C143, *Standard Test Method for Slump of Hydraulic Cement Concrete* (2005). Air content and unit weight were also measured in accordance with AASHTO T152 and AASHTO T121, respectively.

A 4 ft^3 (0.11 m^3) capacity drum mixer mixed the concrete. Tamping rods and a vibration table consolidated the CC mixture. After casting, the samples were covered with wet burlap and plastic sheets.

4.2 MECHANICAL PROPERTIES

4.2.1 Test Matrix

Because SCC typically has higher paste volumes and lower coarse aggregate volumes than CC, the mechanical properties of SCC could be different from those of CC. Fourteen SCC mixture proportions were evaluated. Four CC mixture proportions were used as control mixtures. Table 4.1 shows the test matrix for determining the mechanical properties. For all tests, at least three samples were evaluated for mechanical properties at certain ages. In accordance with the AASHTO Standards, mechanical properties (compressive strength, MOE, MOR, and STS) were tested at designated ages. Table 4.2 summarizes test matrix and the test times of each mechanical characteristic.

Table 4.1. Test Matrix (Mechanical Properties).

Concrete Type	16-hour Target Compressive Strength	Aggregate Type	Mixture ID	Number of Sample	Tests	Age of Samples
SCC	5 ksi (34 MPa)	River Gravel	S5G-1	At least 3 samples at test date	f_c' MOE MOR STS	See Table 4.2
			S5G-2			
			S5G-3a			
			S5G-3b			
			S5G-3c			
		Limestone	S5L-3a			
			S5L-3b			
			S5L-3c			
CC		River Gravel	C5R			
		Limestone	C5L			
SCC	7 ksi (48 MPa)	River Gravel	S7G-4			
			S7G-5			
			S7G-6			
		Limestone	S7L-4			
			S7L-5			
			S7L-6			
CC		River Gravel	C7R			
		Limestone	C7L			

Table 4.2. Test Times of Mechnical Characteristiscs of All Mixtures.

Age of Samples	Mechanical Tests			
	Compressive Strength	MOE	MOR	STS
16 hours	√	√	√	√
3 days	√	-	-	-
7 days	√	√	√	√
28 days	√	√	√	√
56 days	√	√	√	√
91 days	√	√	-	-

Note: √ indicates at least triplicate samples were tested.

4.2.2 Test Procedures

4.2.2.1 Compressive Strength

Laboratory samples were cast in accordance with AASHTO T126, *Standard Method of Test for Making and Curing Concrete Test Specimens in the Lab* (2004). Sample sizes were 4 in. × 8 in. (100 mm × 200 mm) cylinders. After 15.5 hours, the molds were removed and the samples were transported to the environmental room (73 ^{o}F [23 ^{o}C] and greater than 97 percent relative humidity [RH]) in accordance with AASHTO T126 (2004).

In accordance with AASHTO T22, *Standard Method of Test for Compressive Strength of Cylindrical Concrete Specimens* (2004), compressive strength was determined at 16 hours and 3, 7, 28, 56, and 91 days. The load rate was 2100 psi (14.5 MPa) per minute until failure. A 500 kip (2220 kN) capacity materials testing system (MTS) machine was used to test all mechanical characteristics of the CC and SCC mixtures except for MOR.

4.2.2.2 Modulus of Elasticity

Laboratory samples were cast in accordance with AASHTO T126. For MOE, the sample size was 4 in. × 8 in. (100 mm × 200 mm) cylinders. The curing regime was the same as the compressive strength test.

In accordance with ASTM C469, *Standard Test Method for Static MOE and Poisson's Ratio of Concrete in Compression* (2005), MOE was evaluated at 16 hours and 7, 28, 56, and 91 days. Two linear variable differential transducers (LVDTs) measured the strain of concrete in the compression up to 40 percent of compressive strength at the age of testing.

4.2.2.3 Modulus of Rupture

Laboratory samples were cast in accordance with AASHTO T126 and AASHTO T23, *Standard Method of Test for Making and Curing Concrete Test Specimens in the Field* (2004). For MOR tests, 4 in. × 4 in. × 16 in. (100 mm × 100 mm × 400 mm) and 6 in. × 6 in. × 20 in. (150 mm × 150 mm × 500 mm) prism samples were cast. According to AASHTO T23, flexural strength test specimens made in the field shall not have a width or depth of less than 6 in. (150 mm). Prisms meeting the AASHTO T23 requirement and small prisms were cast to evaluate size effect on MOR. After 15.5 hours, the molds were removed and the samples were transported to the environmental room (73°F [23°C] and greater than 97 percent RH) in accordance with AASHTO T23 (2004) and T126 (2004).

In accordance with AASHTO T97, *Standard Method of Test for Flexural Strength of Concrete Using Simple Beam with Third-Point Loading* (2004), 4 in. × 4 in. × 16 in. (100 mm × 100 mm × 400 mm) prisms were tested at 16 hours and 7, 28, and 56 days. Three 6 in. × 6 in. × 20 in. (150 mm × 150 mm × 500 mm) prisms were tested at 28 days to evaluate the effect of size on the test results. A 20 kip (90 kN) capacity MTS machine was used to evaluate MOR.

4.2.2.4 Splitting Tensile Strength

Laboratory samples were cast in accordance with AASHTO T126**.** For STS, the sample size was 4 in. × 8 in. (100 mm × 200 mm) cylinders. Curing regime is the same as that for the compressive strength test.

In accordance with AASHTO T198, *Standard Method of Test for STS of Cylindrical Concrete Specimens* (2004), STS was tested at 16 hours and 7, 28, and 56 days.

4.3 SHEAR CHARACTERISTICS

4.3.1 Test Matrix

A total of 48 push-off samples (36 SCC and 12 CC samples) were fabricated and assessed for shear characteristics. A test matrix was designed to investigate the effect of coarse aggregate volume on aggregate interlock. CC mixtures typically have higher coarse aggregate volumes than SCC mixtures. Changes in coarse aggregate volume could affect the shear capacity of the concrete mixtures. Twelve SCC mixture proportions were evaluated with three main variables: two 16-hour release strengths (5 and 7 ksi [34 and 48 MPa]), two aggregate

types (river gravel and limestone), and three different volumes of coarse aggregate. Four CC mixture proportions were used as control mixtures and consisted of two 16-hour specified release strengths (5 and 7 ksi [34 and 48 MPa]) and two coarse aggregate types (river gravel and limestone). Table 4.3 shows the test matrix for the shear characteristics test program. To identify the coarse aggregate volumes used in the mixtures, the sample ID identifies the test matrix. For example, SR5/31.5 represents a SCC [S] mixture with river gravel [R] and 5 ksi [5] release strength with 31.5 percent coarse aggregate by volume, V_{CA}.

Table 4.3. Test Matrix (Shear Characteristics).

Concrete Type	16-hour Target Compressive Strength	Aggregate Type	Mixture ID	V_{CA}, %*	Sample ID	Number of Sample	Age of Samples (Days)
SCC	5 ksi (34 MPa)	River Gravel	S5G-3a	31.5	SR5/31.5	3	28 ± 1
			S5G-3b	34.6	SR5/34.6		
			S5G-3c	37.8	SR5/37.8		
		Limestone	S5L-3a	28.0	SL5/28.0		
			S5L-3b	31.9	SL5/31.9		
			S5L-3c	34.8	SL5/34.8		
CC		River Gravel	C5R	44.3	CR5/44.3		
		Limestone	C5L	40.1	CL5/40.1		
SCC	7 ksi [7] (48 MPa)	River Gravel	S7G-4	32.3	SR7/32.3		
			S7G-5	35.0	SR7/35.0		
			S7G-6	37.6	SR7/37.6		
		Limestone	S7L-4	31.9	SL7/31.9		
			S7L-5	34.5	SL7/34.5		
			S7L-6	37.0	SL7/37.0		
CC		River Gravel	C7R	44.3	CR7/44.3		
		Limestone	C7L	40.1	CL7/40.1		

Note: *V_{CA} represents the coarse aggregate volume.

4.3.2 Sample Design

The dimensions of the samples, similar to those used by Walraven (1981), were 6 in. × 15.75 in. (125 mm × 400 mm) in cross-section and 26 in. (660 mm) long (see Figure 4.1). The shear plane is 59.3 in.^{2} (1510 mm^2) [4.96 in. × 12 in. (126 mm × 305 mm)]. All push-off samples contained steel reinforcement to prevent premature failure of the specimen ends during application of the load. This reinforcement was placed only in the ends and did not cross the shear plane and, as such, had no affect on aggregate interlock. Because no reinforcement passed through the shear plane, a stiff frame system externally restrained this plane.

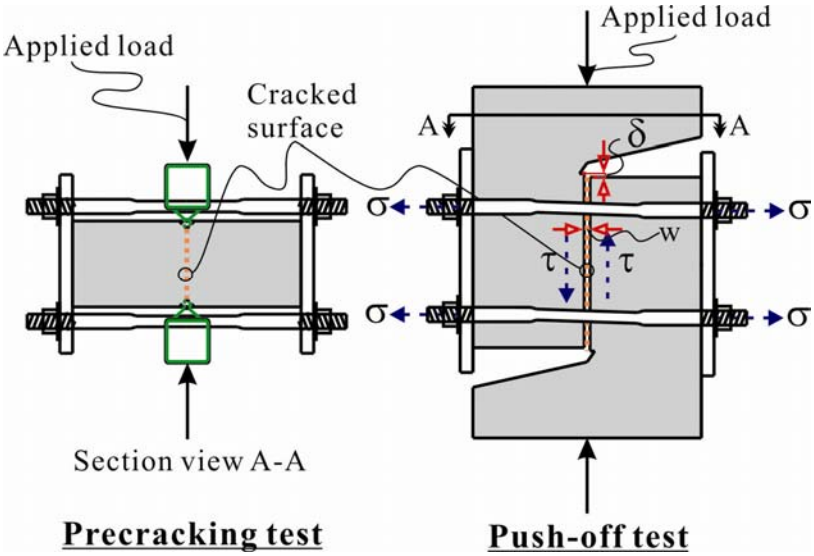

Figure 4.1. Test Specimen for Evaluating Aggregate Interlock.

The system consists of two steel plates [12.375 in. × 15.5 in. × 0.875 in. (314 mm × 394 mm × 22 mm)] and four steel rods with tightening nuts. The four steel rods provided confinement between the two steel plates and measured axial strains. The middle sections of the 1.25 in. (32 mm) diameter steel rods were turned down to a diameter of 0.875 in. (22.2 mm) within the strain measuring regions and were designed to sustain the expected ultimate stresses (i.e., axial force and shear and biaxial bending). The strain gage patterns were selected to measure the axial strain while compensating for the strain from biaxial bending. Because the rod length [15.75 in. (400 mm)] is five times longer than the diameter [0.875 in. (22 mm)] the shear strains are negligible compared to the axial strains (Boresi and Schmidt 2002). Four strain gages were attached on the center of each steel rod in the axial direction. Based on uniaxial tension tests of the steel rod material, an appropriate stress-strain relationship was constructed.

4.3.3 Test Procedures

Concrete used for fabrication of the shear samples was evaluated for compressive strength and splitting tensile strength (see Section 4.2.1.1). At 7 days, the compressive strength of each batch was compared to ensure that the batches had statistically similar strengths. At 28 ± 1 days, the compressive and splitting tensile strength tests were performed along with the push-off test program.

4.3.3.1 Precracking Test

At 28 ±1 days after casting, precracking and push-off tests were performed at HBSML to determine the contribution of aggregate interlock to the overall shear capacity of members containing SCC and CC. Three push-off samples were used for each mixture proportion. Two consecutive batches of each concrete mixture were cast on the same date. Each batch had a volume of 3.75 ft^3 (0.106 m^3) to produce two push-off test samples and 22 cylinders [4 in. by 8 in. (102 mm by 203 mm)]. All samples were covered with wet burlap and plastic sheets and exposed to a 73 ^oF (23 ^oC) environment for approximately 16 hours. After the forms were released, the samples were moved into a curing room and cured for 28 days at 73 ^oF (23 ^oC) and greater than 97 percent relative humidity.

Prior to the push-off test, a precracking test was conducted to form a crack on the shear plane of each specimen (see Figure 4.2). This test simulates 45-degree initial diagonal cracks in a concrete structural elements subjected to pure shear (see Figure 4.3). This cracking is a critical part of the test because the intentionally cracked shear plane becomes the initial condition for aggregate interlock.

A precrack was formed by a line load applied by the MTS machine through two steel rods placed along the lower and upper surfaces of the shear plane of each sample. Detached digital gages attached on the lower and upper surfaces measured initial crack width. The MTS applied loads from 0 to 25 kip (0 to 111 kN) within 1 minute at a loading rate of 0.012 kip/s (0.053 kN/s) until formation of the precrack. The initial crack widths were less than 0.02 in. (0.5 mm) in all samples.

Figure 4.2. Precracking Test.

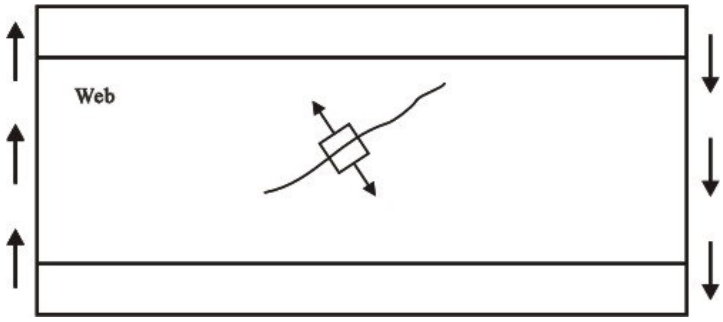

Figure 4.3. Initiation of Web-Shear Cracking in Full-scale Test (Collins and Mitchell 1980).

4.3.3.2 Push-off Test

Figure 4.4 shows the push-off test and Figure 4.5 shows the aggregate interlock after slip in a full-scale beam under shear stress after slip. The initial crack width is critical because the contact area is a function of crack width. So, the restrained frame is essential to controlling the initial crack width.

During the push-off tests the precracked specimens were subjected to a shear force with no bending effect. Before initiating the push-off tests, demountable digital gages measured

crack widths. After detaching these gages, the crack slip and crack widths were measured with two x-y strain gages and four LVDTs at 0.5 second intervals. One x-y strain gage and a combination of two LVDTs measured crack slip and crack width of the separating surfaces perpendicular to the shear plane. Initial normal stresses on the shear plane were less than 0.04 ksi (0.3 MPa) and were controlled by adjusting the torque on the nuts of the four steel rods. Applied loads and axial strains of the steel rods were measured at 0.5 second intervals, and the loading rate was 0.012 kip/s (0.053 kN/s). When the average crack slip reached 0.24 in. (6 mm), the test was terminated. Previous research reported three typical loading patterns. These patterns include (1) monotonic loading with constant crack width, (2) cyclic loading with constant crack width, and (3) loading with variable crack width. Because many existing aggregate interlock models relate shear stress and crack slip to a constant crack width, monotonic and cyclic loading with constant crack width are regarded as ideal theoretical conditions. However, these rarely occur in reinforced or prestressed concrete members. Monotonic loading with varied crack width actually occurs in concrete members (Maekawa *et al.* 2003, Paulay and Loeber 1974). As already noted, it is also likely that clamping forces of the stiff frame system used in this research represent the prestressing forces provided by prestressed tendons in a prestressed concrete member.

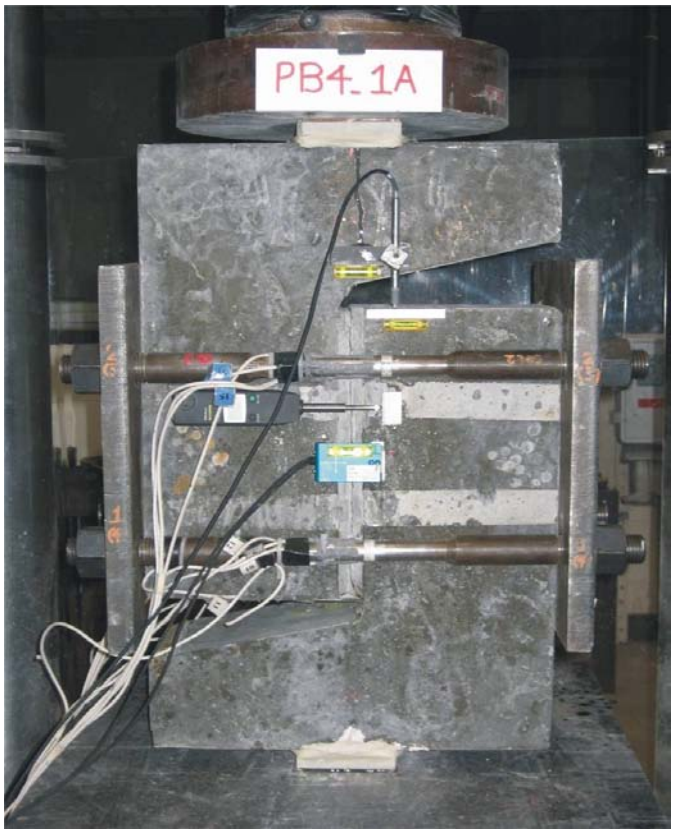

Figure 4.4. Push-off Test.

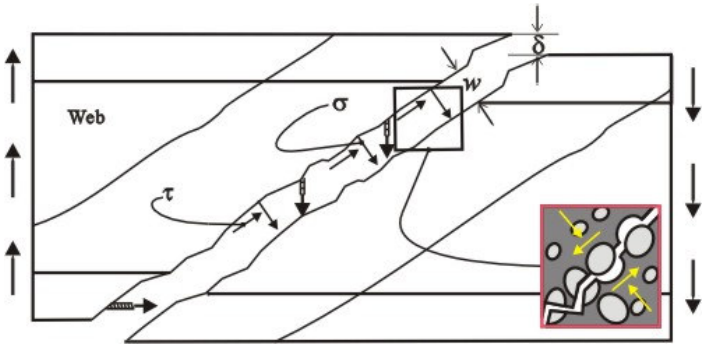

Figure 4.5. Aggregate Interlock after Slip in Full-scale Test (Collins and Mitchell 1980).

4.4 BOND CHARACTRISTICS

4.4.1 Test Matrix

A total of 40 pull-out samples (20 SCC and 20 CC samples) were fabricated to evaluate the relative bond performance of SCC. A test plan was designed to evaluate bond performance with respect to different concrete mixtures as well as bar locations within the section height. This test program investigated the influence of concrete type (SCC versus CC) and bar placement on measured bond strength. The major bond mechanisms at the reinforcement and concrete interface are chemical adhesion between the bar and concrete, frictional force due to the roughness of the interface, and mechanical anchorage or bearing of the deformed bar ribs. According to the ACI 408 Committee report (2003), the mechanical properties of concrete, the volume of the concrete around bars (concrete cover), the confinement of transverse reinforcement, the surface condition, and the geometry of the bars are possible parameters influencing bond performance.

Two SCC mixture proportions were evaluated with two aggregate types (river gravel and limestone) and one release strength (5 ksi [34 MPa]). Two CC mixture proportions were used as control mixtures and consisted of one release strength (5 ksi [34 MPa]) and two coarse aggregate types (river gravel and limestone). Table 4.4 summarizes the test matrix of bond characteristics. Figure 4.6 provides an identification scheme for each sample.

Table 4.4. Test Matrix (Bond Characteristics).

Concrete Type	16-hour Target Compressive Strength	Aggregate Type	Mixture ID	Bar Location	Number of Samples	Age of Samples (Days)
SCC	5 ksi (34 MPa)	River Gravel	S5G-3c	Top	5	35
				Bottom	5	
		Limestone	S5L-3c	Top	5	
				Bottom	5	
CC		River Gravel	C5G	Top	5	
				Bottom	5	
		Limestone	C5L	Top	5	
				Bottom	5	

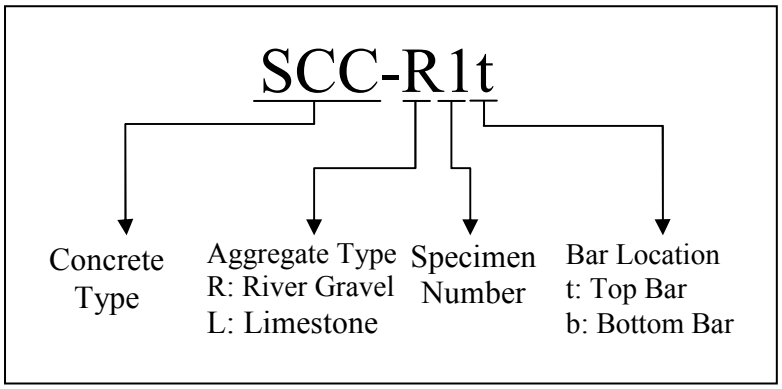

Figure 4.6. Sample ID.

4.4.2 Sample Design

As shown in Figure 4.7, the pull-out specimens were 9 in. × 16 in. × 20 in. (229 mm × 406 mm × 508 mm) rectangular samples containing two #5 (M16) horizontal bars with one in the top and one in the bottom location. The concrete clear cover for both bars was 3 in. (76 mm). The embedded length for all reinforcement was 5 in. (127 mm).

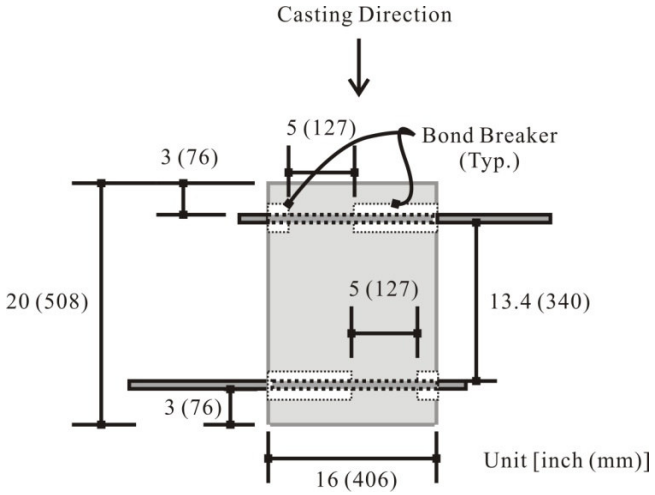

Figure 4.7. Pull-out Specimen Layout.

4.4.3 Test Procedures

Sample preparation and test methods were the same as described earlier. At 35 days, the compressive strength test was performed along with pull-out test program.

4.4.3.1 Pull-out Test

Five consecutive batches of each concrete mixture were cast on the same date. Each batch had a volume of 3.75 ft^3 (0.106 m^3) to produce one pull-out test sample and seven cylinders of 4 in. × 8 in. (100 mm × 200 mm). All samples were covered with wet burlap and plastic sheets and exposed to a 73 ^oF (23 ^oC) environment for approximately 16 hours. After the forms were removed, the samples were moved into a curing room and cured for 35 days at 73 ^oF (23 ^oC) and greater than 97 percent relative humidity.

Pull-out tests were performed at 35 days after casting. Figure 4.8 shows the setup for the pull-out tests. After placing the pull-out specimen in the reaction frame, the reinforcement was wedged into a grip at the actuator end and a small load was placed on the bar to set the specimen. After setting, the MTS applied a load of 0.08 kip/s (0.36 kN/s) until either the bar yielded or the concrete to reinforcement interface failed. The load and bar slip were documented. To avoid the confining effect of the reaction frame on the bond zone, bond breakers were used and the 5 in. (127 mm) embedment length was located about 10 in. (254 mm) from the reaction frame. The applied load and displacement of the LVDTs, used to measure bar slip, were taken at 0.20 second intervals.

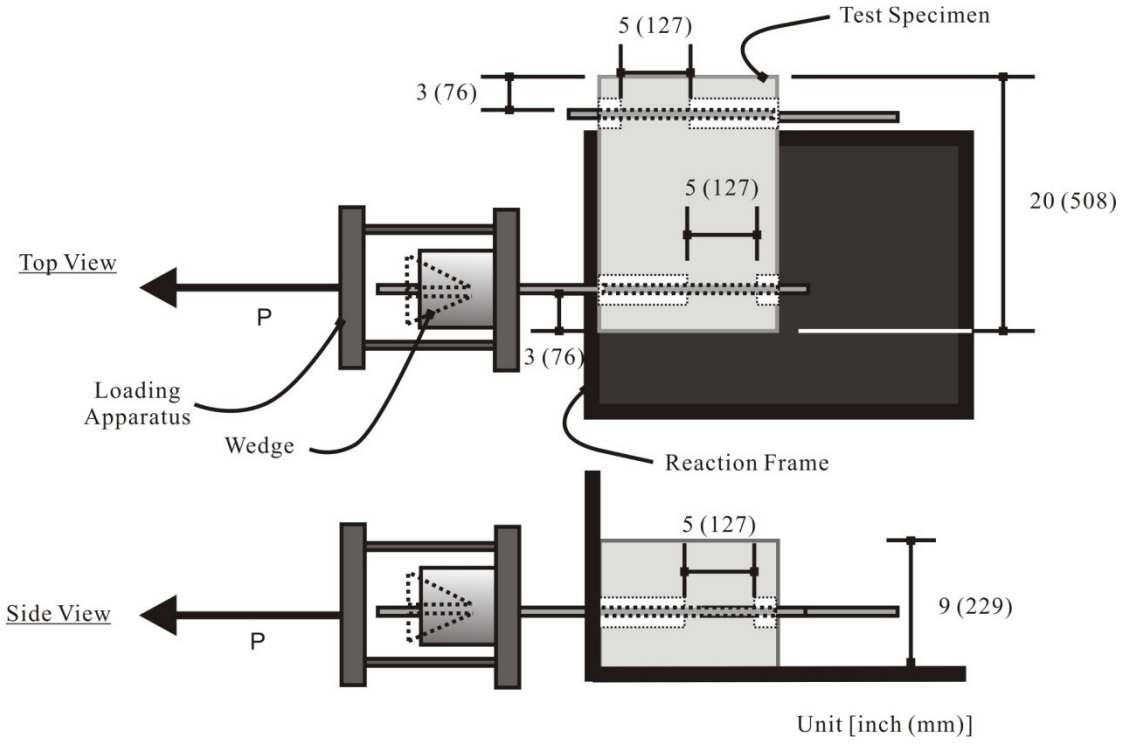

Figure 4.8. Test Setup for Pull-out Test.

The average bond stress was estimated using the surface area of the reinforcement and the maximum applied load necessary to pull out the embedded reinforcement based on basic bond mechanisms, as follows:

$$u_b = \frac{P_{\max}}{\pi d_b L_d} \tag{4.2}$$

where u_b is the average bond stress (ksi [MPa]), $P_{\max}$ is the maximum actuator load (kip [kN]), d_b is diameter of the reinforcement (in. [mm]), and L_d is the embedment length (in. [mm]). In this research bond failure before yielding the reinforcement is desirable to estimate the bond stress as a function of concrete type and bar placement.

According to the Section 12.1 of ACI 318-05 (ACI Committee 318 2005), the development length of reinforcement for sufficient anchorage is inversely proportional to the square root of the compressive strength. This indicates that the average bond stress proportionally increases with an increase in the square root of compressive strength. Because the strength of concrete can vary between concrete mixtures and bar locations, the compressive strength of concrete should be considered when evaluating bond stress.

Bond can be assessed using a normalized parameter (bond ratio) based on the average bond stress of a bottom bar to the compression top bar as shown below:

$$Bond\ Ratio = \frac{u_{b\ (Bottom\ bar)}}{u_{b\ (Top\ bar)}} \tag{4.3}$$

where $u_{b(Bottom\ bar)}$ and $u_{b(Top\ bar)}$ are the average bond stress values (psi [MPa]) of the bottom and top bars, respectively. When this value is greater than 1.0, the "top bar effect" is present, indicating that either the concrete properties or construction practices are reducing the bond of the top bar relative to the corresponding bottom bar. Values equal to or less than 1.0 indicate no influence on the bond due to top bar effects.

4.5 CREEP

4.5.1 Test Matrix

To evaluate the creep properties of SCC and CC, both concrete types were cast with different mixture proportions. Two types of aggregate were used (river gravel and limestone) and the 16-hour compressive strength was targeted as 5 and 7 ksi (34 and 48 MPa) for each type of concrete. Mixture proportions, type of aggregate, and compressive strength were all factors considered for the test matrix, which is shown in Table 4.5.

Table 4.5. Test Matrix (Creep).

Concrete Type	Aggregate Type	16-hour Target Compressive Strength	Mixture ID	Age of Initial Load (Days)
SCC	River gravel	5 ksi (34 MPa)	S5G-3c	7
		7 ksi (48 MPa)	S7G-6	
	Limestone	5 ksi (34 MPa)	S5L-3c	
		7 ksi (48 MPa)	S7L-6	
CC	River gravel	5 ksi (34 MPa)	C5G	
		7 ksi (48 MPa)	C7G	
	Limestone	5 ksi (34 MPa)	C5L	
		7 ksi (48 MPa)	C7L	

4.5.2 Sample Design

Creep was tested using creep frames similar to those shown in Figure 4.9. The frame was composed of three plates, two springs, and four threaded rods. Between the two base plates, two springs were aligned to the center of the plate. Between the steel plates and cylinders, half-cylinders distributed the load and reduced the direct impact of loading on the samples. Eight frames were required for the test with one frame per mixture containing two cylinders from each of the two batches for that mixture. All samples were stored in a shrinkage room at 50 ± 1 percent relative humidity and a temperature at 73 ^{o}F (23 ^{o}C).

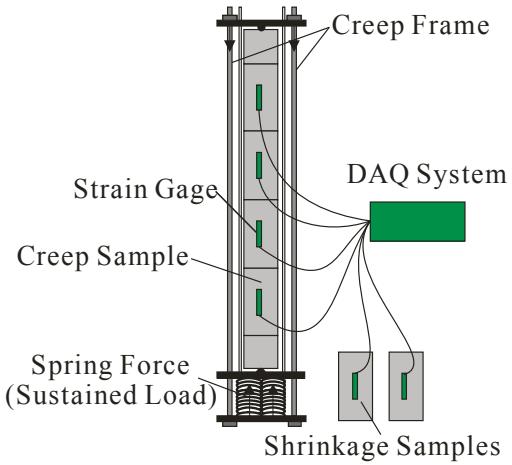

Figure 4.9. Schematic Diagram of Creep Test Setup.

4.5.3 Test Procedures

The compressive strength of each batch was compared to ensure that the batches had statistically similar strengths. At 7 days, the compressive strength test, as described earlier, was performed along with initial loading of the creep specimens.

4.5.3.1 Creep Test

4.5.3.2.1 Preparation. According to ASTM C512, *Standard Test Method for Creep of Concrete in Compression*, 4 in. × 8 in. (100 mm × 200 mm) concrete samples were cast to evaluate the compressive strength and creep. Two batches were used for each mixture proportion. Twelve specimens per batch were made for each test condition: two were tested for compressive strength at 16 hours after casting, two were loaded for creep monitoring, two were monitored for shrinkage and other effects, and two were tested for 7-day compressive strength with four extra samples. Before removal from the molds, specimens were stored at 73 ^{o}F (23 ^{o}C) and covered with burlap or plastic sheets to prevent moisture loss as required by ASTM C512 (2002). After 16 hours, select specimens were removed from the mold to be used for the first compressive strength test.

To consider the external factors, such as humidity and temperature, the condition of the curing room before and after loading provide conditions (50 ± 1 percent RH with a temperature at 73 ^{o}F [23 ^{o}C]) in the shrinkage room. In addition, the top and bottom of the specimens were

sulfur capped to ensure specimens are aligned when they were loaded in the frames. Prior to the loading, the specimens were stored in a curing room.

4.5.3.2.2 Instrumentation and Data Acquisition. After removal of the molds, strain gages were attached to the creep and shrinkage (control) cylinders along the longitudinal axis. Strain gages were connected in a Wheatstone bridge circuit to increase the sensitivity of the measurements and to reduce the number of channels required to record the data. In addition, strain gages were attached to a steel block to compensate for the temperature strains. In case temperature in the shrinkage room varied, the temperature and relative humidity were held constant throughout the test. Two strain gages, 180 degrees apart, were attached to each specimen along the longitudinal axis of the cylinder.

After loading the creep frames in a MTS machine, it was necessary to disconnect the wires to move the frame into the shrinkage room. Wires were reconnected as soon as possible.

4.5.3.2.3 Load Application. A 500 kip (2220 kN) MTS machine was used to load the creep frame, as shown in Figure 4.10. This machine is a servo-controlled closed-loop hydraulically operated machine that can be programmed to run in displacement and load controlled mode. Before the load was applied to the creep frame, the initial strain was recorded. Then, after loading, four nuts over the top plate were tightened, and a second reading was recorded. Finally, the load was released, and a third reading was recorded.

According to the ASTM C512, the load applied to the creep frame should not be higher than 40 percent of concrete compressive strength to ensure elastic behavior. If the loading exceeds more than 40 percent of the compressive strength, microscopic cracks in the samples may occur, resulting in an increase in creep.

Figure 4.10. Loading with 500 kip (2220 kN) MTS Machine.

4.6 DURABILITY

4.6.1 Test Matrix

Table 4.6 summarizes the test matrix for durability tests. Durability tests include freezing and thawing resistance, the rapid chloride penetration test (RCPT), and diffusivity test.

Table 4.6. Test Matrix (Durability Properties).

Concrete Type	16-hour Target Compressive Strength	Aggregate Type	Mixture ID	Number of Sample	Age of Samples at Beginning of Test		
					Freezing and Thawing	RCPT	Diffusivity
SCC	5 ksi (34 MPa)	River Gravel	S5G-3a	At least 3 samples for each test	14	7, 28, and 91	140
			S5G-3b				
			S5G-3c				
		Limestone	S5L-3a				Not Tested
			S5L-3b				
			S5L-3c				
CC		River Gravel	C5R				
		Limestone	C5L				
SCC	7 ksi (48 MPa)	River Gravel	S7G-4				140
			S7G-5				
			S7G-6				
		Limestone	S7L-4				Not Tested
			S7L-5				
			S7L-6				
CC		River Gravel	C7R				
		Limestone	C7L				

4.6.2 Test Procedures

4.6.2.1 Freezing and Thawing Resistance

To evaluate the durability of SCC and CC, two types of aggregate were used (river gravel and limestone) and the 16-hour compressive strength was targeted as 5 and 7 ksi (34 and 48 MPa) for each type of concrete. Mixture proportions, type of aggregate, and compressive strength were all factors considered for the test matrix, which is shown in Tables 4.7 and 4.8.

According to AASHTO T161, *Standard Method of Test for Resistance of Concrete to Rapid Freezing and Thawing* (2004), the relative dynamic elastic modulus of concrete was measured to assess the durability. Three samples of 4 in. × 3 in. × 16 in. (100 mm × 75 mm × 400 mm) prisms per each mixture were prepared and cured following AASHTO T126.

Table 4.7. Characteristics of River Gravel SCC and CC Mixtures.

Mixture ID	S5G-3a	S5G-3b	S5G-3c	S7G-4	S7G-5	S7G-6	C5G	C7G
Mixture Type	SCC						CC	
16-hour Compressive Strength, ksi (MPa)	5 (34)			7 (48)			5 (34)	7 (48)
Air Content, %	1.4	1.6	1.4	1.1	0.8	0.8	1.2	1.1
V_{paste}, %	37.1			35.3			27.4	27.4
V_{FA}, % Mass	32.0			22.5			0	0
HRWRA Type	Type I			Type I			Type II	
Experimental Admixtures	-			Yes			-	
Retarder	Yes			-			-	

Note: - indicates no admixture was added.

Table 4.8. Characteristics of Limestone SCC and CC Mixtures.

Mixture ID	S5L-3a	S5L-3b	S5L-3c	S7L-4	S7L-5	S7L-6	C5L	C7L
Mixture type	SCC						CC	
16-hour Compressive Strength, ksi (MPa)	5 (34)			7 (48)			5 (34)	7 (48)
Air Content %	1.1	1.0	0.9	1.3	1.2	1.1	1.3	1.5
V_{paste}, %	42.5			36.2			28.4	28.4
V_{FA}, % Mass	40			20			0	0
VMA	-					Yes	-	
HRWRA Type	Type I			Type I			Type II	
Experimental Admixtures	-			Yes			-	
Retarder	Yes			-			-	

Note: - indicates that there is no addition.

Rapid freezing and thawing cycles were cycled according to procedure A in AASHTO T161, which is defined as rapid freezing and thawing in water. The samples were subjected to 300 cycles of freezing and thawing. If the sample has a relative dynamic MOE of 60 percent or less of the initial value, the test is stopped. The relative dynamic MOE of the samples was calculated as follows:

$$P_c = \frac{n_1^2}{n^2} \times 100 \qquad (4.4)$$

where P_c is the relative dynamic MOE after c cycles of freezing and thawing (%), n is the fundamental transverse frequency at 0 cycles of freezing and thawing, and n_1 is the fundamental transverse frequency at c cycles of freezing and thawing. The durability factor (DF) can then be calculated as follows:

$$DF = \frac{P \times N}{M} \tag{4.5}$$

where P is the relative dynamic MOE at N cycles (%), N is the number of cycles at which P reaches the specified minimum value for discontinuing the test or the specified number of cycles at which the exposure is to be terminated, whichever is less, and M is the specified number of cycles at which the exposure is to be terminated which is equal to 300 cycles.

4.6.2.2 Rapid Chloride Penetration Test

ASTM C1202, *Standard Test Method for Concrete's Ability to Resist Chloride Ion Penetration* (1997), tests were performed on samples with ages of 7, 28, and 91 days using 4 in. × 8 in. (100 mm × 200 mm) cylindrical test samples. The test matrix for this testing is the same as the freezing and thawing test program. Curing and sample perperation was performed following AASHTO T126.

This test method measures the electrical conductance of concrete samples to provide a rapid indication of its resistance to chloride ion penetration (ASTM C1202 1997). The method involves the application of a 60 V potential difference through a concrete sample embedded in test cells. One test cell contains sodium hydroxide (NaOH) and the other test cell contains sodium chloride (NaCl). The total charge passed through the sample during the 6-hour period provides a qualitative measure of chloride ion penetrability as shown in Table 4.9.

Table 4.9. Chloride Ion Penetrability Based on Charge Passed.

Charge Passed, Coulombs	Chloride Ion Penetrability
> 4000	High
2000-4000	Moderate
1000-2000	Low
100-1000	Very Low
< 100	Negligible

4.6.2.3 Diffusivity Test: Determination of Chloride Diffusion Coefficient

Only SCC mixtures containing river gravel were evaluated for diffusion coefficients. According to ASTM C1556, *Standard Test Method for Determining the Apparent Chloride Diffusion Coefficient of Cementitious Mixtures by Bulk Diffusion* (2003), 4 in. × 8 in. (100 mm × 200 mm) cylindrical test samples were cast. Specimens were cured for 28 days before ponding samples in the exposure solution of sodium chloride (NaCl). The finished surfaces of the specimen were exposed to the exposure liquid. The standard indicates that the specimens must remain in the exposure liquid at least 35 days. The standard also allows extending the exposure times for mixtures such as those that are more mature, were made with low *w/c*, or high performance mixtures containing SCMs. Because very low water to cementitious material ratios were used in the design of SCC mixtures, researchers extended the exposure time for the samples used in this project to 140 days.

The chloride ion contents of the powder samples ground from each layer were determined. In a saturated concrete where no pressure exists, the transportation of chloride ions is provided by concentration gradient. The diffusion of ions from high concentration regions to low concentration regions can be best described by Fick's second law, as shown in following equation:

$$C(x,t) = C_s - (C_s - C_i) \times erf\left(\frac{x}{\sqrt{4\,D_a\,t}}\right) \tag{4.6}$$

where $C(x,t)$ is chloride concentration measured at depth, x, and exposure time, t, by percent mass, C_s is the surface chloride concentration at the interface of the exposure liquid and test specimen and is determined by a regression analysis, C_i is the initial chloride concentration of the cementitious mixture prior to submersion in the exposure solution, x is the depth below the exposure surface to the middle of a layer, D_a is the apparent chloride diffusion coefficient, t is the time, and *erf* is the error function defined as:

$$erf(z) = 2 \,/\, \sqrt{\pi} \times \int_0^z e^{(-u^2)} du \tag{4.7}$$

To find the diffusion coefficient at 28 days, the following equation curve was used (Thomas and Bamforth 1999, Thomas and Bentz 2000):

$$D(t) = D_{ref} \times \left(\frac{t_{ref}}{t} \right)^{m} \tag{4.8}$$

$$m = 0.2 + 0.4\left(\%FA / 50\right) \tag{4.9}$$

where D_{ref} is diffusion coefficient at some reference time, t_{ref} (= 140 days in this study), $D(t)$ is the diffusion coefficient at time, t, m is the constant depending on mixture proportions, and FA is the replacement level of fly ash (%).

4.7 FULL-SCALE TESTING

The applicability of selected SCC mixture proportions was verified by fabricating and testing precast, prestressed TxDOT Type A girders. After production, in-service performance (i.e., camber, deflection, and prestress losses) was monitored and structural tests were performed to compare properties of the SCC girder systems. Girder systems containing CC were fabricated and tested as control specimens. Flexural capacity, transfer and development length, and shear performance were investigated in the full-scale tests along with mechanical properties. This section presents the test matrix and the design of the TxDOT Type A girder and deck. Fabrication of the girders and decks and test procedures will also be presented.

4.7.1 Test Matrix

The specimens tested in this study consisted of a total of four TxDOT Type A (AASHTO Type I) girders. The girders were fabricated at a precast plant in Texas and were designed to investigate the overall long-term behavior and structural performance of full-scale girders made with SCC. Table 4.10 shows the test matrix for full-scale test. Development length tests were performed at each end of each girder (i.e., two data points were obtained from each girder). Mechanical properties were tested for each mixture. Other tests (flexural capacity,

transfer length, prestress losses, and camber and deflection) were also assessed. More information is provided in the respective test procedure section.

Table 4.10. Test Matrix for Full-Scale Test.

Concrete Type	16-hour Target Compressive Strength	Aggregate Type	Number of Girder	Mixture ID	Girder ID	Test ID (Development Length)
CC	5 ksi (34 MPa)	River Gravel	1	C5G	CC-R	CC-R1
						CC-R2
SCC		River Gravel	1	S5G-3c	SCC-R	SCC-R1
						SCC-R2
CC		Limestone	1	C5L	CC-L	CC-L1
						CC-L2
SCC		Limestone	1	S5L-3c	SCC-L	SCC-L1
						SCC-L2

Note: concrete decks were constructed in these girders. Information on the deck will be presented in a later section.

4.7.2 Specimen Design

4.7.2.1 Girder Design

The dimensions of the Type A girder are shown in Figure 4.11. The layout of the strands satisfy the service limit state at the release concrete strength, 5 ksi (34 MPa), in accordance with the AASHTO LRFD Specifications (2004). According to the superstructure design recommendations in the TxDOT Bridge Design Manual (2001), an economical span limit is 40 ft (12 m) and the upper limit is 60 ft (18 m).

The Type A girder was designed in accordance with the AASHTO LRFD Bridge Design Specifications (2006) and TxDOT Bridge Design Manual (2001). The TxDOT Bridge Design Manual took precedence over the AASHTO LRFD Specifications when differences existed. TxDOT PSTR14 (v.4) is also used to check the designed precast, prestressed girders in accordance with current bridge design specifications (AASHTO 2006) for HL 39 loading condition. Based on the above considerations, the final design was checked for loading in a four-point bending configuration.

Ten straight strands in the bottom flange controlled the bottom and top fiber stresses at the end and midspan as shown in Figure 4.12. Two straight tendons were placed in the top

flange. Girders were also under-reinforced to satisfy the minimum elongation requirement of 3.5 percent in the bottom row of strands at ultimate flexural failure (Buckner 1995).

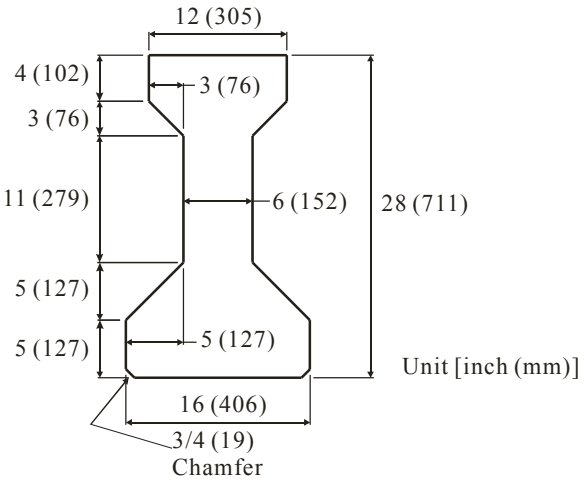

Figure 4.11. Dimension of Cross-Section of Type A Girder.

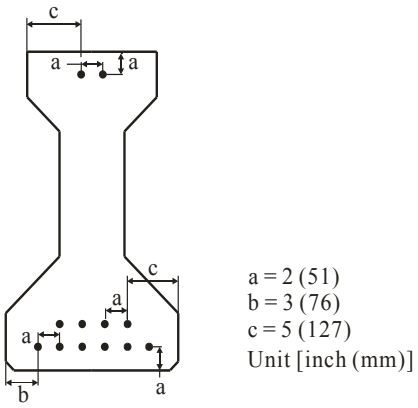

Figure 4.12. Layout of Strands for Tested Girders.

Mild steel reinforcement was placed in accordance with the AASHTO LRFD Bridge Design Specifications (2006) and TxDOT Bridge Design Manual (2001). Layouts of reinforcements and reinforcement details are shown in Figures 4.13 and 4.14.

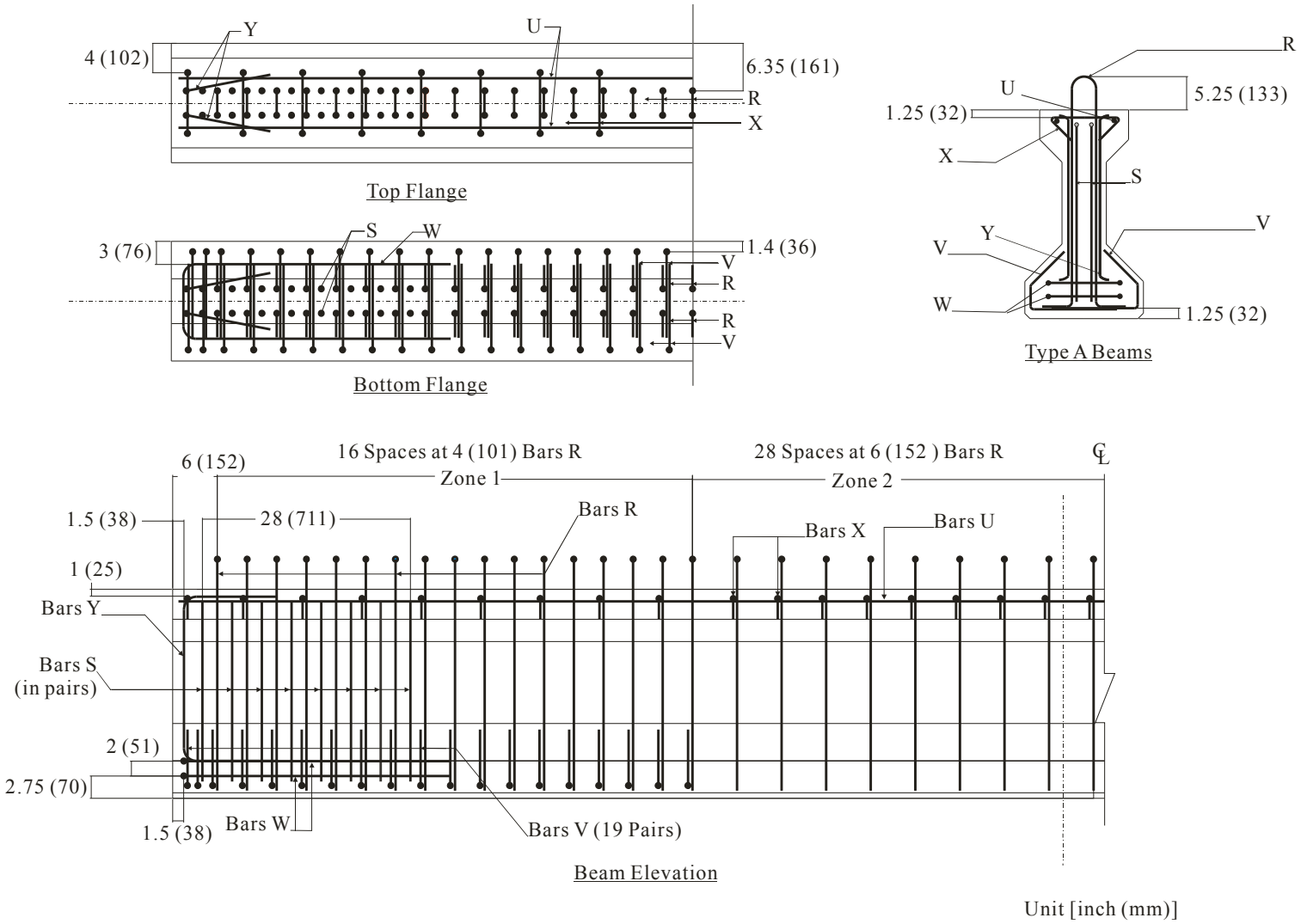

Figure 4.13. Layout of Reinforcement.

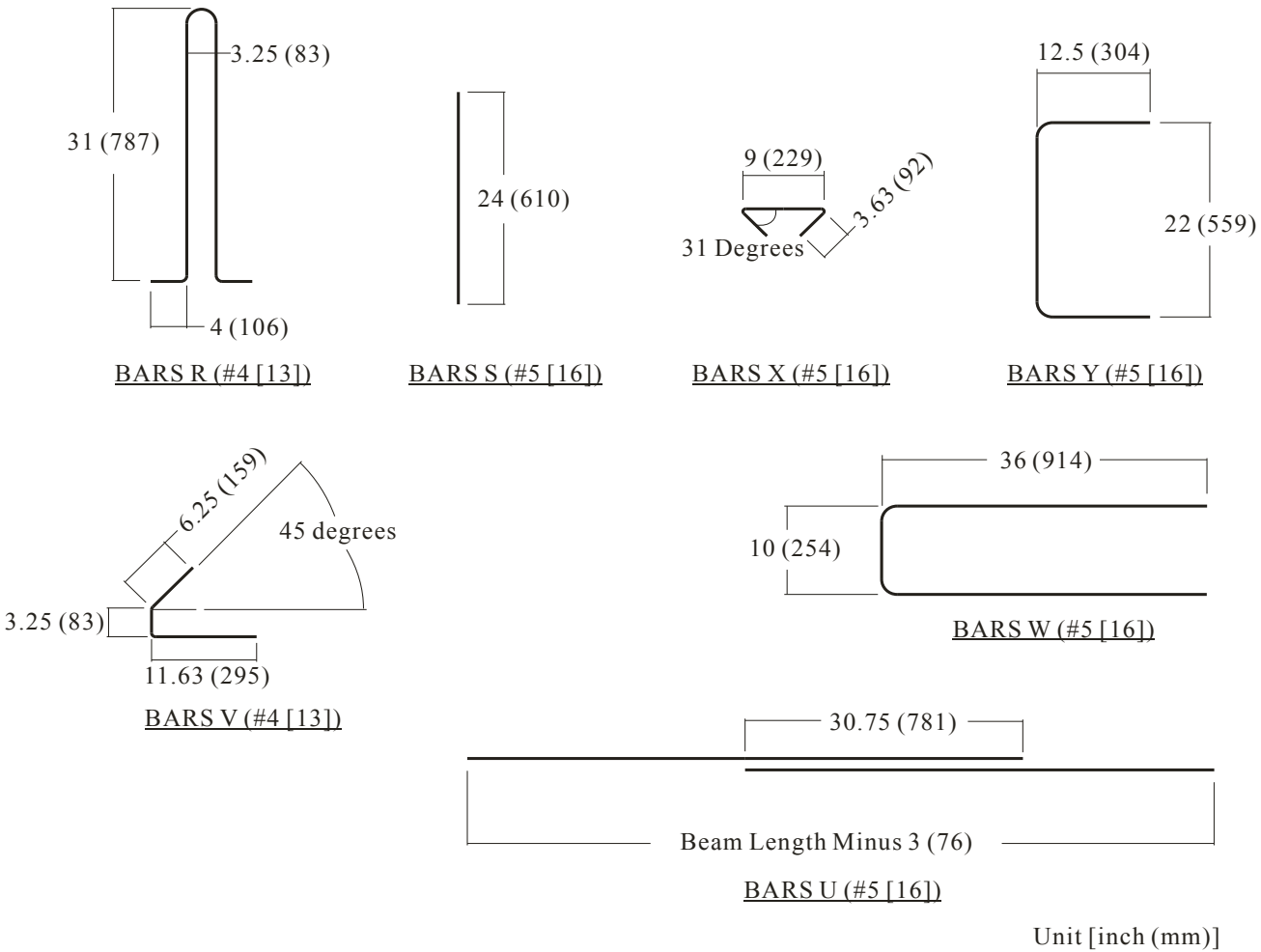

Figure 4.14. Detail of Reinforcements.

4.7.2.2 Deck Design

The CIP deck thickness and width represent actual field conditions and were included to investigate the longer-term behavior of the girders. The shrinkage of the deck and creep in the girder affect the strain profile of the composite girders, resulting in changes for estimating prestress losses.

Researchers determined that the deck should be 8 in. (0.2 m) thick and 64 in. (1.6 m) wide to meet standard TxDOT practice. According to TxDOT Standard CIP criteria, the maximum clear span from girder flange to girder flange is limited to 8.686 ft (2.6 m) with an 8 in. (0.2 m) thick slab.

The neutral axis at the ultimate flexural failure is located in the deck. Analyses indicated that the deck will contribute compressive stress and will develop large tensile strains in the lower level strands under flexural and development length tests.

Longitudinal and lateral reinforcement was placed in the deck to mimic actual deck construction practices in Texas and to control the temperature and shrinkage. The details of the deck are presented in Figure 4.15.

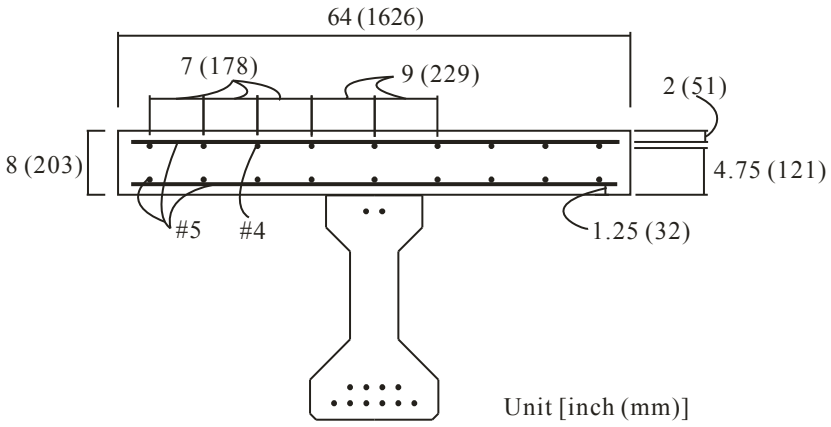

Figure 4.15. Details of Deck.

4.7.2.3 Fabrication of Type A Girders

All girders were fabricated with the same prestressing conditions and were monitored continuously after casting. The CC-R and SCC-R girders were fabricated on March 26, 2007.

The second set of girders, CC-L and SCC-L, were fabricated on July 12, 2007. The layout of the girders on the prestressing bed is shown in Figure 4.16.

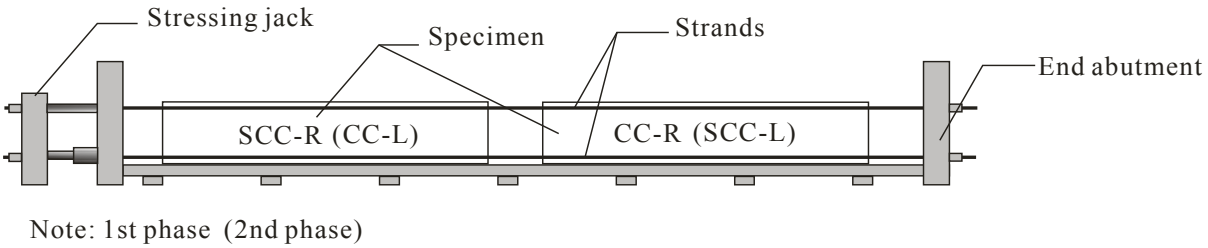

Figure 4.16. Layout of Girders.

A data acquisition system (DAQ system) was positioned next to the prestressing bed in a protected shelter. The computer and DAQ system had a capacity of 107 channels.

All strands were gradually stressed at the same time using the equipment shown in Figure 4.17. Before placing each strand, load cells monitored the stresses in the strands until release. The target load for each strand was 31 kip (137 kN), 0.75 of f_{pu} for the CC and SCC girders.

Figure 4.17. Prestressing Bed with Strands.

After stressing the strands, mild reinforcement was placed according to the design drawings. After placing the mild reinforcement, temperature probes and embedded concrete strain gages were installed at designated locations. All wires were connected to the DAQ system and measurements were recorded at 15 minute intervals.

4.7.2.4 Fabrication of Mechanical Samples

Test samples were fabricated in a building next to the casting bed (see Figure 4.18). Three 4 in. × 8 in. (102 mm × 203 mm) cylinders of each concrete type were cast to test

compressive strength at 16 hours using a sure-cure system, which the plant provided. The sure-cure system is designed to match the actual temperature of girder. To evaluate the mechanical and durability characteristics, 118 compressive cylinders, 30 MOR beams, 10 freeze-thaw beams, and 8 shrinkage samples were cast. The day after casting, the samples for mechanical testing were transported from the plant to environmental rooms (> 98 percent RH and 72 ± 2 ^{o}F [22 ± 1 ^{o}C]) at Texas A&M University. Compressive strengths of cylinders at 16 hours and release time were evaluated at the plant.

Figure 4.18. Preparation of Small Samples.

4.7.2.5 Fabrication of Composite Girders

Girders were transported from the prestressing bed to a storage area until transporting to HBSML. The first girder set (CC-R and SCC-R) was stored at the plant for 6 days after casting. The second girder set was stored in the plant for 5 days. The DAQ system monitored the temperature, concrete strain, and end slip of strands at 15 minute intervals. Girders were simply supported during storage.

All fabrication of the decks was performed at HBSML. Overhang brackets were installed at 3 ft (1.0 m) intervals to support the deck. After forming, reinforcing bars were placed and tied and the concrete was placed (see Figures 4.19 and 4.20). TxDOT Class S concrete was used for the deck. The forms were removed after approximately 3 days. The beams were monitored until structural tests were performed.

Figure 4.19. Placement of Reinforcement.

Figure 4.20. Placement of Deck Concrete.

4.7.3 Test Procedures

4.7.3.1 Early Age Characteristics and Plant Observation

Tests to evaluate workability and stability of the SCC were performed following the test standards presented in the laboratory test program (Section 4.1). The casting procedure and the instrumentation to measure the hydration of concrete are explained below.

4.7.3.1.1 CC-R and SCC-R Girders. Girders were fabricated and cast at Texas Concrete Company, Victoria, Texas. Each girder required two batches of concrete. The volume of each batch was between 2 and 3.25 ft^3 (0.06 and 0.09 m^3). Samples for mechanical properties were taken from the second batch. Weather conditions on March 26, 2007, were windy and the temperature was approximately 70 ^oF (21 ^oC). Before placing concrete in the girder forms the fresh characteristics were assessed. After it was determined that the concretes met the required characteristics (slump flow, stability, etc.) the concrete was placed in the forms. Slump flow and stability were assessed for both batches.

The cement, water, and aggregate were initially batched and mixed. A retarder was then added to the mixture and mixed. HRWRA was then added and mixed. After sufficient mixing the concrete was discharged into a bucket auger with an approximate drop height from the mixer to the bucket auger of 3 to 5 ft (0.9 m to 1.5 m). Each batch was then transported approximately 100 yards (91 m) from the mixer and placed into the form. The CC mixture concrete was continuously discharged into the forms while moving along the forms. Mechanical vibration consolidated the CC. For the SCC mixture, the majority of the concrete was placed in the form from one end. As the form was filled the forklift with the bucket auger moved along the form to complete the placement. No consolidation was used for the girders containing SCC. After placement, beams were covered with a tarpaulin.

4.7.3.1.2 CC-L and SCC-L Girders. The girders containing limestone aggregate were cast using the same procedures as the girders containing the river gravel. To evaluate the temperature history of the girder, a sure-cure system was used for the early age compressive specimens. The weather conditions on the day of casting (7/12/07) consisted of a light wind and a temperature of approximately 100 ^oF (38 ^oC). After placement, the girders were covered with wet burlap.

Temperature probes monitored the hydration of the concrete in all the girders. The temperature probes were located at the mid-height, bottom flange, and top flange at the beam as shown in Figure 4.21. The temperature readings were used to calculate the heat-induced strain in the beams. The temperature of the girders was continuously monitored after placement of the concrete.

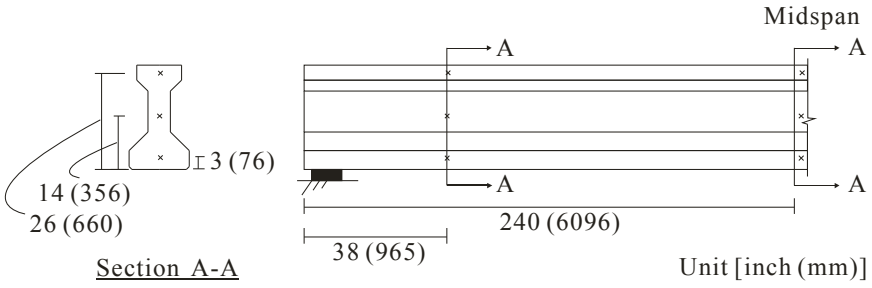

Figure 4.21. Locations of Temperature Probes.

4.7.3.2 Mechanical Properties

Mechanical properties (compressive strength, MOE, MOR, STS) of each mixture were evaluated following the regime described in the laboratory test program. For compressive strength, additional samples for 16-hour and release strength were cast and cured using the sure-cure system.

4.7.3.3 Flexural Test Procedure

After finishing monitoring the girder, the composite deck system was tested for flexural capacity. An overview of test setup is shown in Figure 4.22.

Destructive tests validated the flexural capacity of girders containing CC and SCC. Steel, H-shape frames were anchored with post-tensioned Dywidag threaded rods on the strong floor at HBSML. A 600 kip (2700 kN) actuator was used to load the specimen. Neoprene pads were placed under the load points (36 in. × 8 in. [914 mm × 203 mm]) to distribute the load evenly to the composite deck system.

Neoprene bearing pads (70 durometer) (8 in. × 8 in. × 3 in. [203 mm × 457 mm × 76 mm] thick) supported the girders. The center of the bearing pads was positioned 6 in. (152 mm) from the beam end, resulting in a span length of 39 ft (11.8 m).

The DAQ system recorded data at 5 second intervals to assess the following characteristics:

- moment - curvature relationship (load - displacement relationship),
- initial stiffness,
- bond performance prior to cracking,
- bond performance after cracking, and
- crack patterns.

To investigate the bond performance of the composite deck system, concrete gages, LVDTs, and strain gages were placed on the Type R bars. A load cell measured loads on the hydraulic ram. String pots measured displacement.

Figure 4.22. Overview of Test Setup.

The loading increment was estimated based on the time to first cracking and the strain of the top fiber on the deck at midspan. Before cracking, the loading increment was 20 kip (89 kN). After cracking, the loading increment was decreased to 10 kip (44 kN). After each incremental load, crack locations and widths were marked and recorded. When the moment capacity of the composite girder reached the ultimate state (3000 microstrain at the top fiber), the test was terminated. Figure 4.23 shows the schematic diagram of the strain gage locations for the flexural test. Figure 4.24 shows the schematic diagram of the string potentiometer locations for measuring deflections. The moment-curvature relationship, initial stiffness, and the bond behavior in the transfer length zone and the constant moment region were evaluated to compare the flexural behavior of CC and SCC composite deck systems.

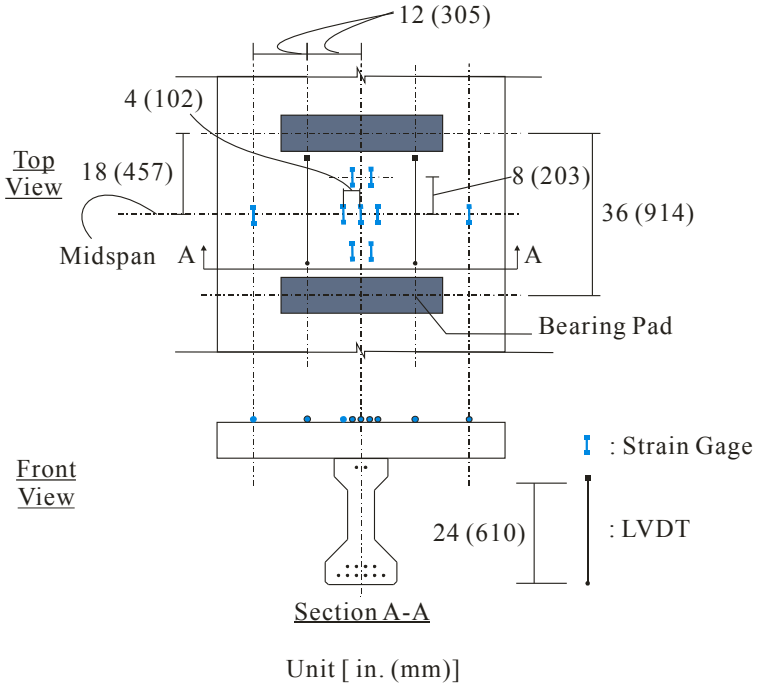

Figure 4.23. Diagram of Installation of Strain Gages and LVDTs for Measuring Strain of Top Fiber of Deck Concrete under Flexural Test.

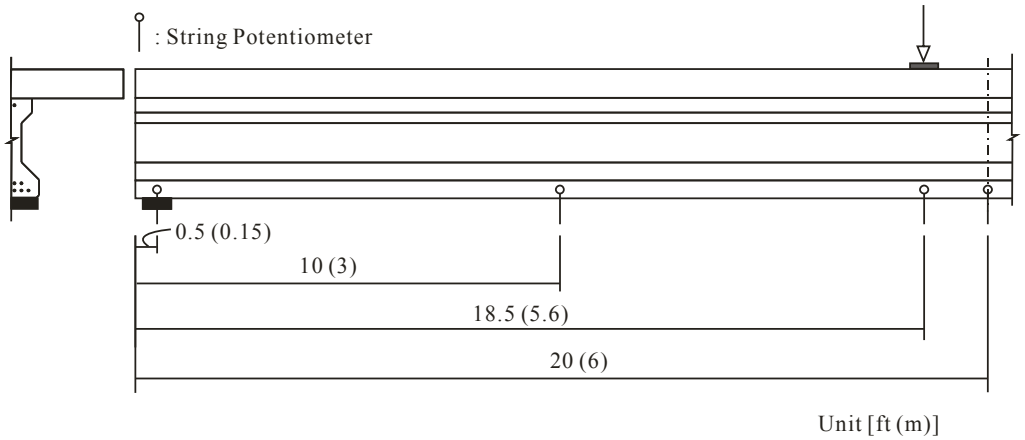

Figure 4.24. Diagram of Installation of String Potentiometers for the Flexural Test.

LVDTs were installed to investigate strain profiles and crack widths in the constant moment region. Figure 4.25 shows the LVDT installation locations to measure the strain of strands on the bottom flange.

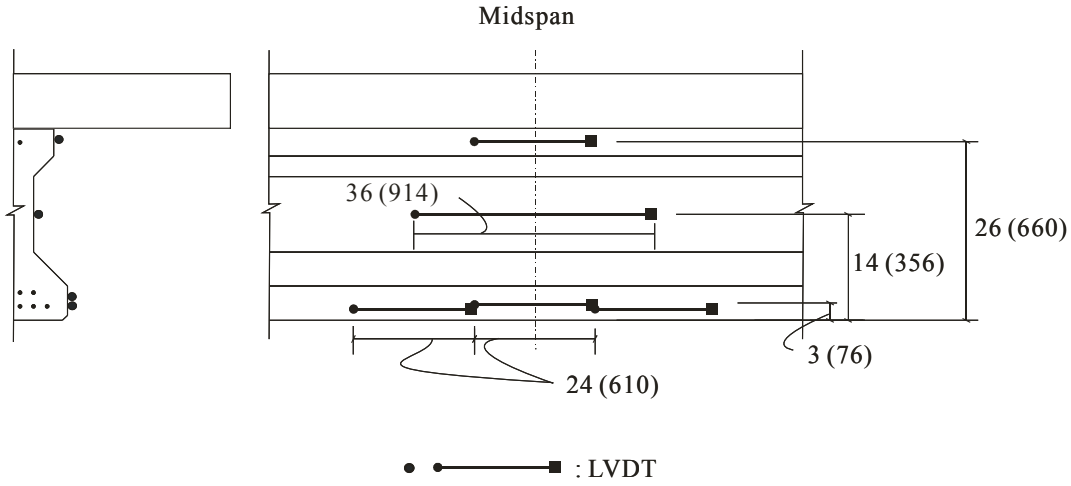

Figure 4.25. Average Strain of Stands of the Constant Moment Region.

4.7.3.4 Transfer Length

According to AASHTO LRFD Bridge Design Specifications (2006), the transfer length, l_{tr} , is the transition distance from the free end of the strands to the fully bonded zone with effective prestress. In this study, the transfer length, l_{tr} , was measured with two methods: concrete strain readings and end slip readings. The method used to measure transfer length

included the use of embedded concrete strain gages. Two types of concrete strain gages were used: Quarter-bridge 120 Ω strain gages and full-bridge 350 Ω strain gages. Instrumented locations of embedded concrete strain gages are shown in Figure 4.26. Both ends of the beam have the same pattern of instrumentation.

The transfer length was estimated with concrete strain gages from the vertical centroid of gravity of the strands. The strands were gradually released over a 4-minute period. During strand release, LVDTs measured the end slip of five strands of the bottom flange on both ends of each girder. After releasing, the strands were flame-cut.

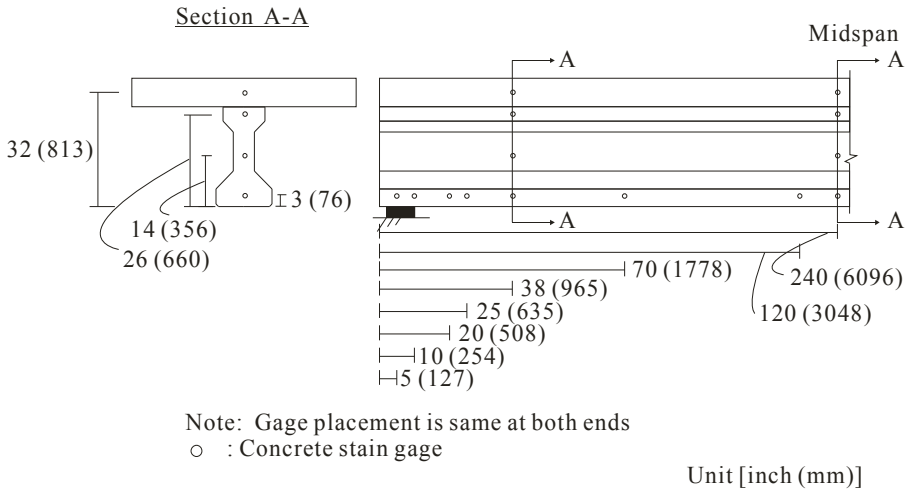

Figure 4.26. Locations of Strain Gages.

Buckner (1995) and Barnes (2000) found that shear lag effects occur when the surface concrete strain is measured. This results in recorded values lower than actual transfer length values in the middle of the beam section as shown in Figure 4.27 (Barnes 2000). Therefore, it was thought that concrete strain gages could provide better values of the actual transfer length.

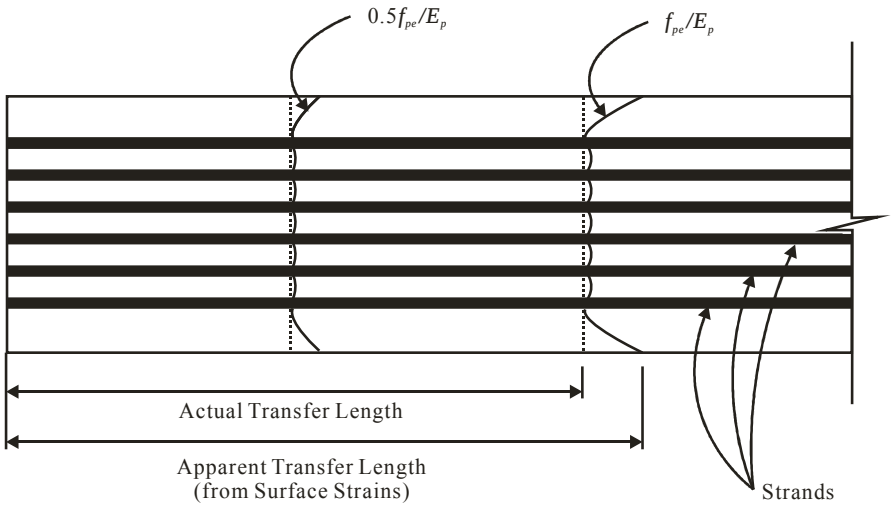

Figure 4.27. Shear Lag Effect on Transfer Length (Barnes 2000).

To determine a reasonable transfer length, the following methods were followed. The first step was using the following equation to correct the strain profile by considering the self-weight of the girder at transfer.

$$\varepsilon_w = \frac{M_w \, y_{gage}}{E_{ci} \, I_{tr}} \tag{4.10}$$

where ε_w is strain at the level of the embedded concrete strain gages (in./in. [mm/mm]), M_w is the moment due to the self-weight of the girder (kip-ft [kN-m]), E_{ci} is the elastic modulus of concrete at transfer (ksi [MPa]), I_{tr} is the moment of inertia of the transformed section (in^4 [mm^4]), and y_{gage} is the vertical distance from the centroid of the transformed section to the location of concrete strain gages (in. [mm]).

As shown in Figure 4.28, the second step was to best fit a function through data using the first step. The third step was to find the likely domain of the 100 percent strain plateau by visually inspecting the data as shown in Figure 4.28. In the final step, the 95 percent average maximum strain (AMS) was calculated as the mean values of these maximum stains. The first intersection of the line and strain profile indicates the transfer length, l_{tr}.

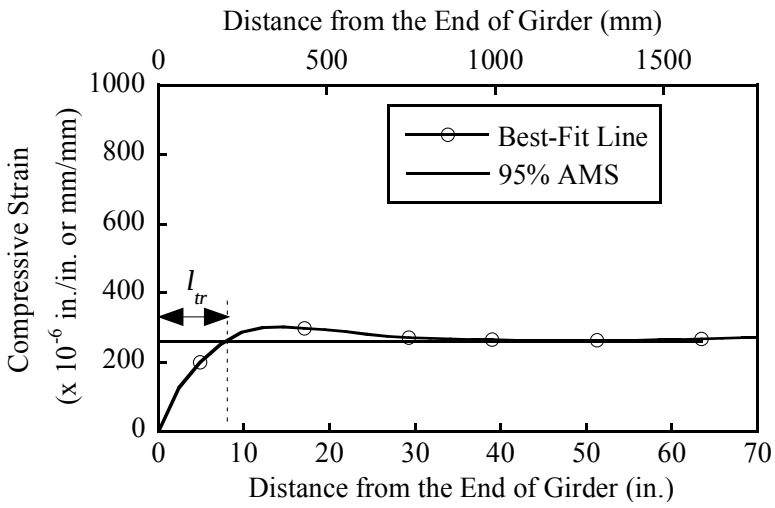

Figure 4.28. Determining Transfer Length Using the 95% AMS Method.

As shown in Figure 4.29, the transfer length increases with time as a result of prestress losses, concrete creep, shrinkage, and strand relaxation. Slab weight, MOE, and the transformed section are used to evaluate the long-term transfer length.

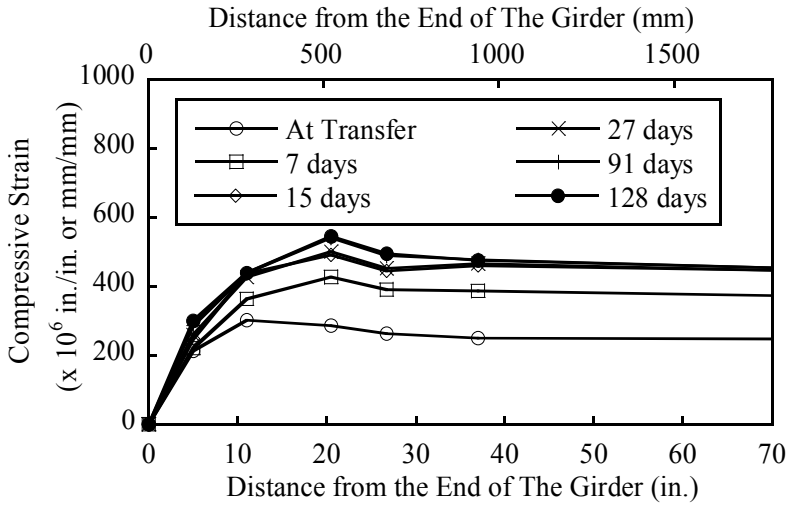

Figure 4.29. Long-Term Raw Strain Profile of North span of Girder CC-R.

The second method used to assess the transfer length included measuring end slip (draw-in end slip) with LVDTs. The layout for the LVDT's used in this study are shown in Figure 4.30.

Upon release, the elastic shortening of the strand was measured to determine the end slip of the strands. The amount of end slip is correlated with transfer length, stress of strands at transfer, and the MOE of the strands.

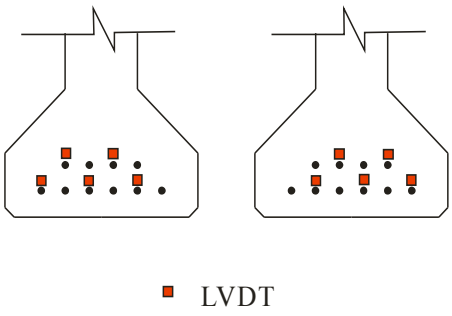

Figure 4.30. Locations of LVDTs for Draw-In End Slip.

When considering the bond mechanism of transfer length, two principal mechanisms, friction and mechanical resistance, actively resist the slippage of strands immediately after transfer. To determine the end slip of strands, five LVDTs were installed on the strands prior to release at each end of the girder. The equation for obtaining the actual end slip, $\Delta_{End\ slip}$, is expressed as follows:

$$\Delta_{End\ slip} = \Delta_B - \Delta_{ES} \tag{4.11}$$

where Δ_B is the measured displacement of end-slip through the LVDT (in. [mm]), Δ_{ES} is the elastic shortening of strands between the end of section and the location of the LVDT ($P_J\Delta_A/E_pA_p$) (in. [mm]), Δ_A is the measure distance from the surface of the section to attached point of LVDT on strands (in. [mm]), P_J is the measured prestressing forces immediately before transfer (kip [kN]), E_p is the elastic modulus of the strands (ksi [GPa]), and A_p is the area of strands (in.^{2} [mm^2]).

Based on Mast's strand slip theory (Logan 1997), the end slip of the strands is used to determine the initial transfer length. The relationship between end slip, $\Delta_{End\ slip}$, and initial transfer length, $l_{tr\Delta}$, is as follows:

$$\Delta_{End\ slip} = avg\ f_{pi}(0, l_{tri}) \frac{l_{tr\Delta}}{E_p} \tag{4.12}$$

$$f_{pi} = f_{pj} - \Delta f_{pR}(t_0, t_{tr}) - \Delta f_{pES} \tag{4.13}$$

where E_p is the elastic modulus of strand (ksi [MPa]), $avg\ f_{pi}(0, l_{tri})$ is the average initial stress of strands between the ends of the section and transfer length (ksi [MPa]), Δf_{pES} is the prestress losses due to elastic shortening at transfer (ksi [MPa]), f_{pj} is the initial jacking stress of strands (ksi [MPa]), $\Delta f_{pR}(t_0, t_{tr})$ is the estimated relaxation of strands between t_0 and t_{tr} (ksi [MPa]), t_0 is the time at jacking (hour), and t_{tr} is the time at transfer (hour).

4.7.3.5 Development Length Test

Flexural testing of the girder-deck system was performed first, followed by testing at both ends to determine the development length of the girders. The embedment length, l_e, is the length of the embedded strands from the girder end to the loading point for the development length test (see Figure 4.31). To determine the transition point from flexural to bond failure, the embedment length and test span length can be varied from test to test. Embedment lengths longer than the required development length will result in a flexural failure. Embedment lengths shorter than the development length should result in a bond/shear failure or bond/flexural failure.

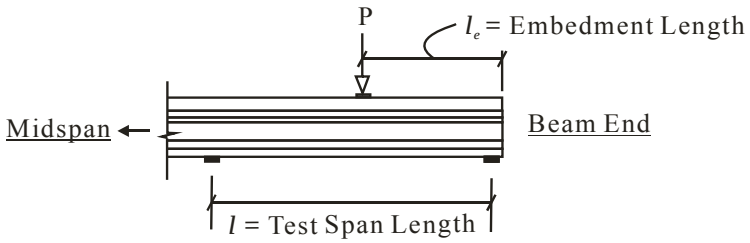

Figure 4.31. Definition of Embedment Length and Test Span Length.

A DAQ system recorded data at 5-second intervals to assess the following characteristics:

- moment - curvature relationship,
- bond characteristics of the development length region,
- shear performance, and

- crack patterns.

4.7.3.5.1 Test Configuration. After completing the flexural tests, each end of the composite girder was tested to evaluate development length. Based on Equation 5.11.4.2-2 in the AASHTO LRFD Specifications (2004), the theoretical development length was larger than about 80 in. (2.0 m). The test span length was 13.5 ft (4.1 m) for the first trial. The interior support was shifted inward for the composite deck system to have a 13.5 ft (4.1 m) span length as shown in Figure 4.32 (a). The loading increments and measured parameters were the same as in the procedure of the flexural tests. After testing the first trial, the second trial testing was performed with a 12.5 ft (3.8 m) span length and 70 in. (1.8 m) embedment lengths as shown in Figure 4.32 (b).

Table 4.11 summarizes the test identifications, embedment length, and span length for the development length tests. The overhead crane was used to reduce the negative moment.

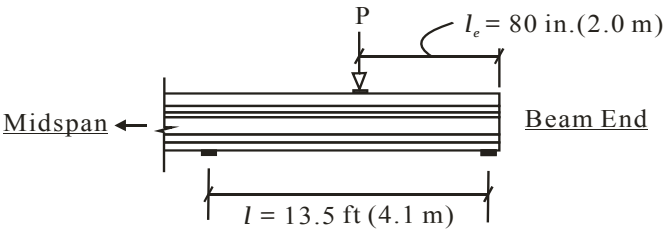

(a) First Trial

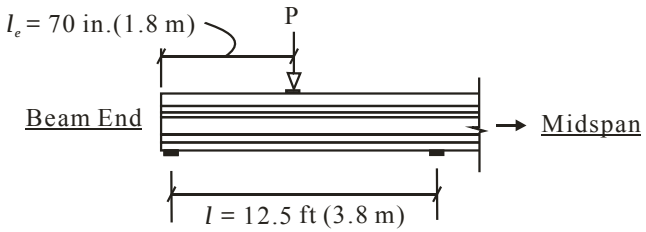

(b) Second Trial

Figure 4.32. Test Setup for Development Length Test.

Table 4.11. Configuration for Development Length.

Girder ID	CC-R		SCC-R		CC-L		SCC-L	
Test ID	CC-R1	CC-R2	SCC-R1	SCC-R2	CC-L1	CC-L2	SCC-L1	SCC-L2
l_e , in. (m)	80 (2.0)	70 (1.8)	80 (2.0)	80 (2.0)	80 (2.0)	70 (1.8)	80 (2.0)	70 (1.8)
l , ft (m)	13.5 (4.1)	12.5 (3.8)	13.5 (4.1)	13.5 (4.1)	13.5 (4.1)	12.5 (3.8)	13.5 (4.1)	12.5 (3.8)
Overhead Crane Application	No				Yes			

4.7.3.5.2 Instrumentations. Figure 4.33 shows the location of the strain gages for measuring the strains in the top fiber of the deck to determine the ultimate strain.

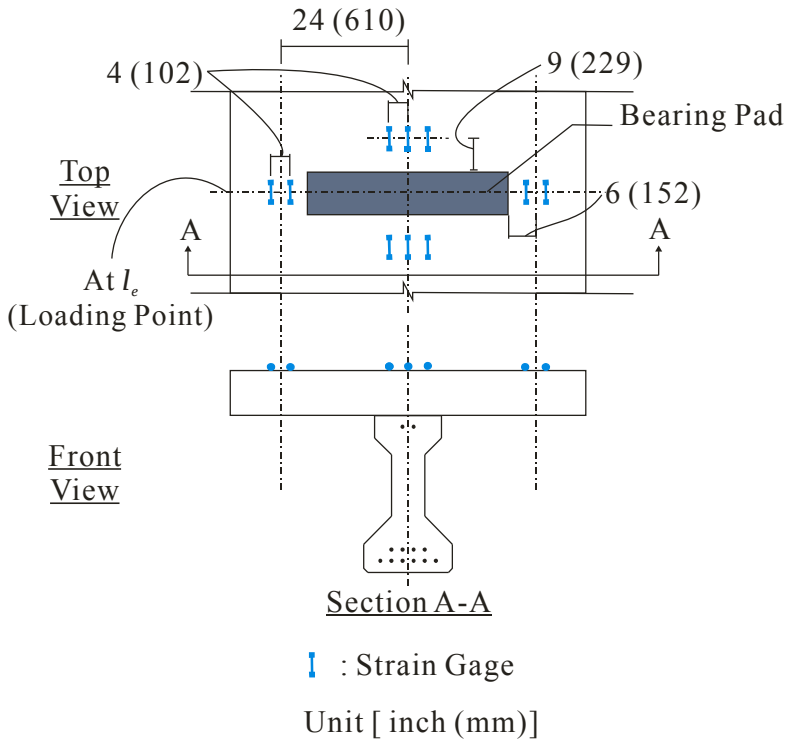

Figure 4.33. Diagram of Locations of Strain Gages or Deck Concrete for Development Length Tests.

Strain gages were attached to the bottom flange of the girder, located at the centroid of gravity of the strands as shown in Figure 4.34. Concrete strain gages also detected failure of strands and concrete cracks.

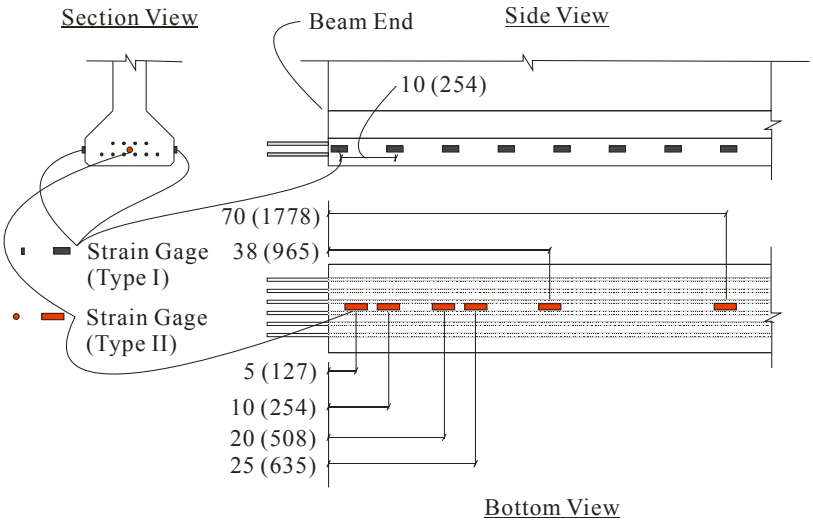

Figure 4.34. Diagram of Concrete Surface Strain Gage Layout (Type I) and Embedded Concrete Strain Gage Layout (Type II).

In addition to the 10 LVDTS attached on the end of the 10 strands, LVDTs measured the diagonal tensile strains and stresses on the critical section from the support as shown in Figure 4.35. Shear strain was measured with the LVDTs installed at the critical section for shear, 3 ft (910 mm) from the end and with strain gages on the Type R reinforcement. Strain gages were attached on steel reinforcement corresponding to the mid-height of the web of the girder.

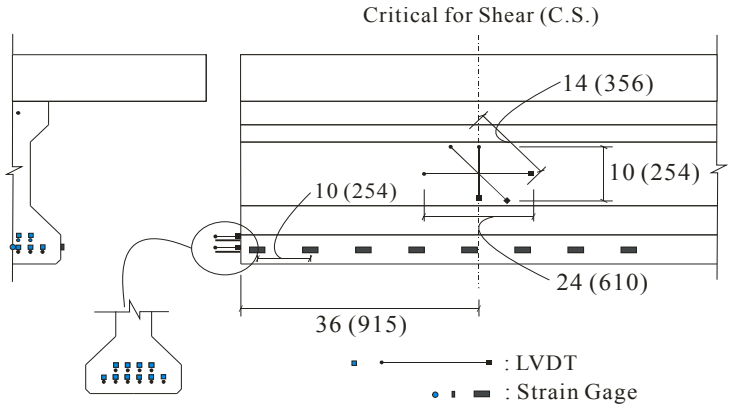

Figure 4.35. Locations of LVDTs and Strain Gages for Shear and Development Length.

Figure 4.36 shows the principal strains at the critical web concrete section. Positive values represent the average principal tensile strain, ε_1, that crosses cracks, and negative values represent the average principal compressive strain, ε_2, on the cracked web concrete member.

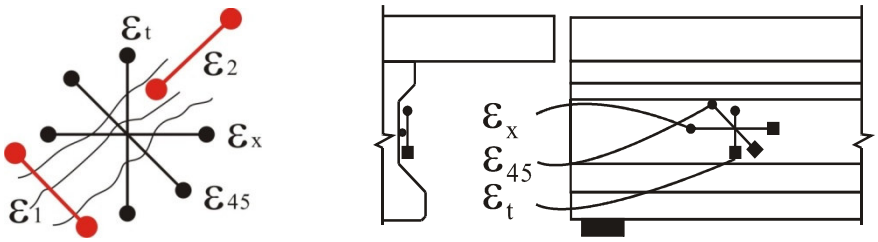

Figure 4.36. Strains on Web at Critical Section for Shear.

The prestressed strain due to longitudinal compressive stress was included for the calculation. Shear strain, γ_{xy}, due to the applied load was estimated as follows:

$$\gamma_{xy} = 2\,\varepsilon_{45} - \varepsilon_t - \varepsilon_x \tag{4.14}$$

where ε_x is the longitudinal strain of the member, ε_t is the perpendicular strain of the member, ε_{45} is the diagonal strain.

The principal strains, ε_1 and ε_2, can be calculated from these equations as follows:

$$\varepsilon_1 = \frac{\varepsilon_x + \varepsilon_t}{2} + \sqrt{\left(\frac{\varepsilon_x - \varepsilon_t}{2}\right)^2 + \left(\frac{\gamma_{xy}}{2}\right)^2} \tag{4.15}$$

$$\varepsilon_2 = \frac{\varepsilon_x + \varepsilon_t}{2} - \sqrt{\left(\frac{\varepsilon_x - \varepsilon_t}{2}\right)^2 + \left(\frac{\gamma_{xy}}{2}\right)^2} \tag{4.16}$$

where ε_x and ε_t were defined earlier, ε_1 is principal tensile strains, and ε_2 is principal compressive strains.

4.7.3.6 Prestress Losses

Load cells measured the jacking stresses, f_{pj}, and the initial stress, f_{pi} on the girders. Load cells were fabricated at HBSML and consisted of a strain gage with a Wheatstone bridge circuit to measure axial stresses. The load cells compensate for the induced moments, torsional

moments, and temperature effects. One load cell for each strand was installed between a spring loaded anchor and the dead abutment as shown in Figure 4.37.

Figure 4.37. Load Cells between Spring Loaded Anchor and Dead Abutment.

Concrete strain gages measured prestress losses. Elastic shortening, losses due to creep and shrinkage of the girder, and elastic gain were calculated from the embedded concrete strain gages. Test results were used to validate AASHTO LRFD equations (2004, 2006). The applicability of the AASHTO LRFD equations can be assessed. Here, the AASHTO LRFD (2006) equations are presented to estimate elastic shortening. This gives an idea about the complexity of prestress losses associated with properties of concrete and bond properties. Other time-dependent losses associated with environmental conditions are more complicated.

4.7.3.7 Camber and Deflection

Camber and deflection were measured with string potentiometers and stringlines (see Figures 4.38 and 4.39). When the deflection stabilized, the deflection monitoring was terminated.

(a) (b)

Figure 4.38. Initial Camber Reading (a) and Stringlines (b).

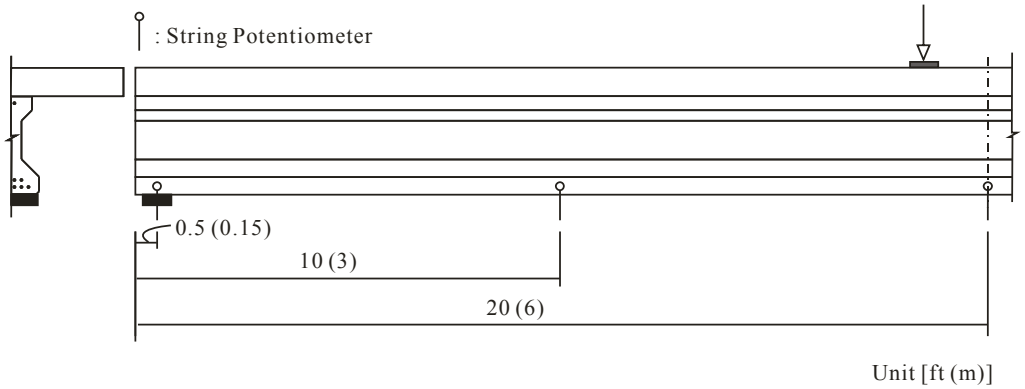

Figure 4.39. Location of String Potentiometer for the Camber and Deflection.

The instantaneous deflection was estimated using the following equations. The downward deflection of the self-weight of the girder, Δ_{Girder}, can be estimated from the following equation:

$$\Delta_{Girder} = \frac{5\,w\,L^4}{384\,E_{ci}\,I}\downarrow \tag{4.17}$$

and the initial camber, Δ_{fps}, due to the initial prestressing force was estimated as follows:

$$\Delta_{fps} = \frac{P_i\,e_c\,L^2}{8\,E_{ci}\,I}\uparrow \tag{4.18}$$

where w is the self-weight of the girder (klf. [kN/m]), P_i is the measured initial prestress force (kip [kN]), e_c is the eccentricity of prestressing strands (in. [mm]), L is the measured span length (ft [m]), E_{ci} is the MOE at transfer (ksi [GPa]), I is the moment of inertia of the girder (in.^{4} [mm^4]), ↓ indicates the downward deflection, and ↑ indicates the upward deflection.

The net camber, $\Delta_{i(net)}$, can be calculated as the difference between the two equations: the camber due to initial prestressing force, Δ_{fpi}, and the downward deflection due to the self-weight of the girder, Δ_{Girder} as:

$$\Delta_{i(net)} = \Delta_{fpi} - \Delta_{Girder} \tag{4.19}$$

An incremental time-step method procedure estimated curvature increments at 1 week intervals when the girders were stored at the plant. The incremental curvature can be determined as follows:

$$\Delta\phi_{T7} = \phi_7 - \phi_i \tag{4.20}$$

where $\Delta\phi_{T7}$ is the curvature increment between 7 days and time at transfer (rad/in. [rad/m]), ϕ_7 is the measured curvature at 7 days (rad/in. [rad/mm]), and ϕ_i is the measured curvature at transfer (rad/in. [rad/mm]).

Based on basic mechanics, the camber growth can be calculated with the following equation:

$$\Delta_{T7} = \Delta\phi_{T7} \frac{L^2}{8} \tag{4.21}$$

where Δ_{T7} is the growth of camber at 7 days after the transfer (in. [mm]), and L is the measured span length (ft [m]).

The camber after 7 days can be calculated as follows:

$$\Delta_7 = \Delta_{im} + \Delta_{T7} \tag{4.22}$$

where Δ_7 is the final camber at 7 days (in. [mm]) and Δ_{im} is the initial camber (in. [mm]).

CHAPTER 5
RESULTS AND ANALYSIS OF LABORATORY STUDY: MECHANICAL PROPERTIES

5.1 EARLY-AGE CHARACTERISTICS

Tables 5.1 and 5.2 present the early age characteristics of the SCC mixtures. Measured slump flow was between 27.5 and 29.5 in. (699 and 749 mm). The air contents of the SCC mixtures ranged between 0.8 and 1.6 percent. The T_{50} ranged from 1.0 to 7.0 seconds. The 7 ksi (48 MPa) SCC mixtures exhibited higher viscosities than the 5 ksi (34 MPa) mixtures. The stability of all SCC mixtures was between 0.5 and 1.0, indicating high stability of the SCC mixture proportions. Temperature was measured with thermocouples embedded in a separate cylinder until 16 hours after casting.

Tables 5.3 and 5.4 show the early-age characteristics of CC mixtures.

Table 5.1. Early-Age Characteristics of River Gravel SCC Mixture.

	Mixture ID							
Test	S5G -1	S5G -2	S5G -3a	S5G -3b	S5G -3c	S7G -4	S7G -5	S7G -6
Slump Flow, in. (mm)	27.5 (700)	27.5 (700)	27.5 (700)	28.5 (725)	28.0 (710)	28.0 (710)	28.0 (710)	28.0 (710)
Air, %	1.4	1.5	1.4	1.6	1.4	1.1	0.8	0.8
Unit Weight, lbs/ft^3 (kg/m^3)	148.6 (2377)	148.3 (2373)	148.2 (2371)	148.1 (2371)	148.1 (2371)	151.0 (2415)	151.6 (2425)	151.6 (2425)
T_{50}, sec.	2.3	2.4	2.7	2.3	2.0	7.1	7.0	6.9
VSI	0.5	0.5	0.5	1.0	1.0	0.5	0.5	0.5
Max. Temp., ^{o}F (^{o}C)	-	93 (33.9)	97 (36.1)	89 (31.7)	101 (38.3)	100 (37.8)	101 (38.3)	107 (41.7)

Table 5.2. Early-Age Characteristics of Limestone SCC Mixture.

Test	Mixture ID					
	S5L -3a	S5L -3b	S5L -3c	S7L -4	S7L -5	S7L -6
Slump Flow, in. (mm)	29.0 (735)	28.5 (725)	28.5 (725)	29.0 (735)	29.5 (750)	29.0 (735)
Air, %	1.1	1.0	0.9	1.3	1.2	1.1
Unit Weight, lbs/ft^3 (kg/m^3)	146.7 (2345)	146.7 (2347)	147.0 (2351)	149.6 (2395)	150.0 (2400)	150.0 (2400)
T_{50}, sec.	2.7	2.9	3.2	4.8	4.5	6.9
VSI	1.0	0.5	1.0	1.0	1.0	1.0
Max. Temp., ^{o}F (^{o}C)	101 (38.3)	99 (37.2)	108 (42.2)	106 (41.1)	116 (46.7)	106 (41.1)

Table 5.3. Early-Age Characteristics of River Gravel CC Mixture.

	Mixture ID	
Test	C5G	C7G
Slump, in. (mm)	7.5 (190)	6.5 (165)
Air, %	1.2	1.1
Unit weight, lbs/ft^3 (kg/m^3)	152 (2430)	154 (2465)
Max. concrete temp., ^{o}F (^{o}C)	107 (41.7)	112 (44.4)

Table 5.4. Early-Age Characteristics of Limestone CC Mixture.

	Mixture ID	
Test	C5L	C7L
Slump, in. (mm)	8.0 (200)	8.0 (200)
Air, %	1.3	1.5
Unit weight, lbs/ft^3 (kg/m^3)	150 (2400)	152 (2430)
Max. concrete temp., ^{o}F (^{o}C)	106 (41.1)	116 (46.7)

5.2 DEVELOPMENT OF COMPRESSIVE STRENGTH

This section presents characteristics of compressive strength.

5.2.1 16-hour Release Strength

Figure 5.1 shows the compressive strength of the river gravel and limestone mixtures at 16 hours. With the exception of mix S5G-1, each mixture achieved its target strength of 5 ksi (34 MPa) and 7 ksi (48 MPa). Nine samples of each mixture were tested to evaluate 16-hour strength. The box plots show the mean, the 1st (25 percent) and 3rd (75 percent) quartiles, and the outliers. The SCC and CC mixtures have similar compressive strength at 16 hours with each aggregate type and strength level. In the case of the limestone mixtures, the 16-hour strength was approximately 30 and 28 percent higher than the 5 ksi (34 MPa) and 7 ksi (48 MPa) target strengths, respectively.

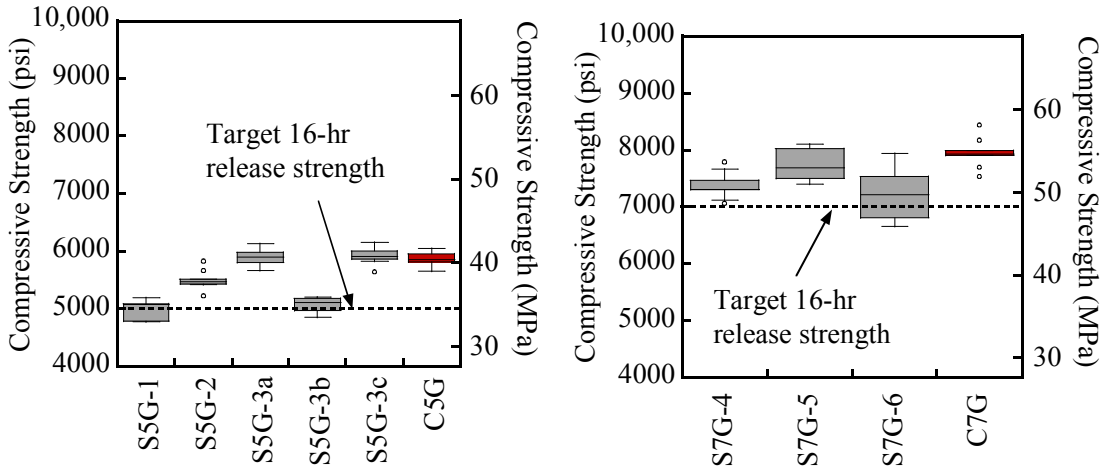

(a) 5 ksi (34 MPa) River Gravel (b) 7 ksi (48 MPa) River Gravel

Figure 5.1. Compressive Strength at 16 hours.

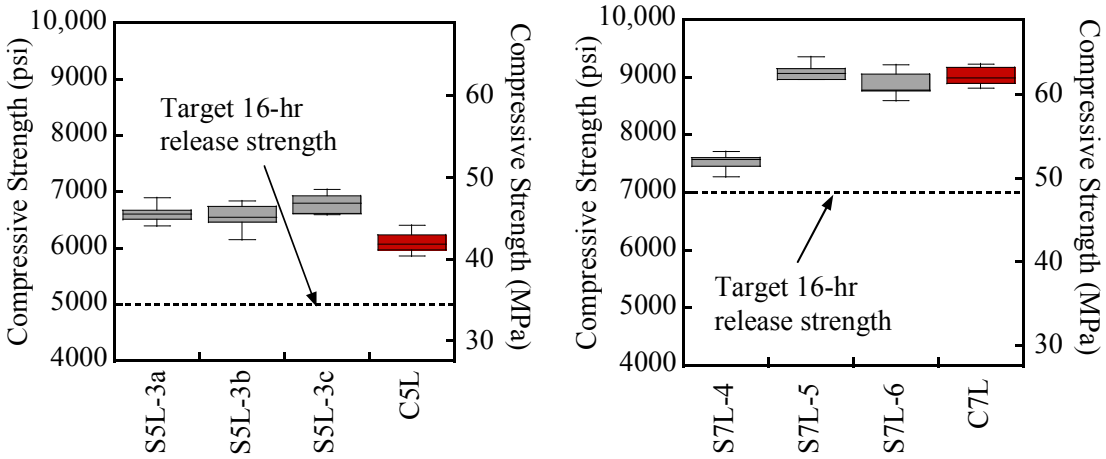

(c) 5 ksi (34 MPa) Limestone (d) 7 ksi (48 MPa) Limestone

Figure 5.1. Compressive Strength at 16 hours (cont.).

5.2.2 Development of Compressive Strength

Figure 5.2 shows the development of compressive strength of the SCC mixture from 16 hours to 91 days. The 5 ksi (34 MPa) river gravel SCC mixtures achieved an ultimate strength at 91 days of 13.5 ksi (93 MPa). The 7 ksi (48 MPa) river gravel SCC mixtures achieved an ultimate strength at 91 days of 17 ksi (117 MPa). For the limestone SCC mixtures, the ultimate strength developed was 15 and 17 ksi (105 and 117 MPa) for the 5 and 7 ksi (34 MPa and 48 MPa) 16-hour target strengths, respectively.

At 28 days the compressive strengths of the river gravel SCC mixtures were about 28 percent and 24 percent higher than those of river gravel CC mixtures for the 5 and 7 ksi (34 and 48 MPa) mixtures, respectively. The compressive strengths of the limestone SCC mixtures were about 30 percent and 17 percent higher than those of the limestone CC mixtures for 5 and 7 ksi (34 and 48 MPa), respectively. There are two reasons for these higher compressive strengths. The CC mixtures had 3 to 5 percent lower *w/c* compared to the SCC mixtures except for the 7 ksi (48 MPa) limestone mixture. However, the volume of cement was higher in the SCC mixtures than the CC mixtures. The SCC mixtures contain a high volume of fly ash to obtain high workability. Although the strength of SCC mixtures at release (at 16 hours) is similar to that of the CC mixtures, the contribution of fly ash toward the compressive strength at later ages is significant. The polycarboxylate HRWRA likely improved the dispersion of cement and fly ash

particles resulting in better hydration of these particles. The filler effect of the fly ash also likely improved the development of strength of SCC mixtures.

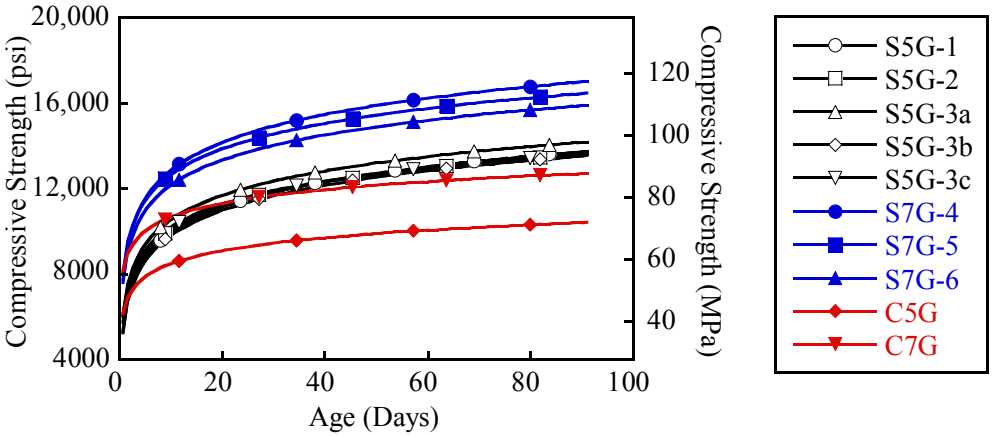

(a) River Gravel

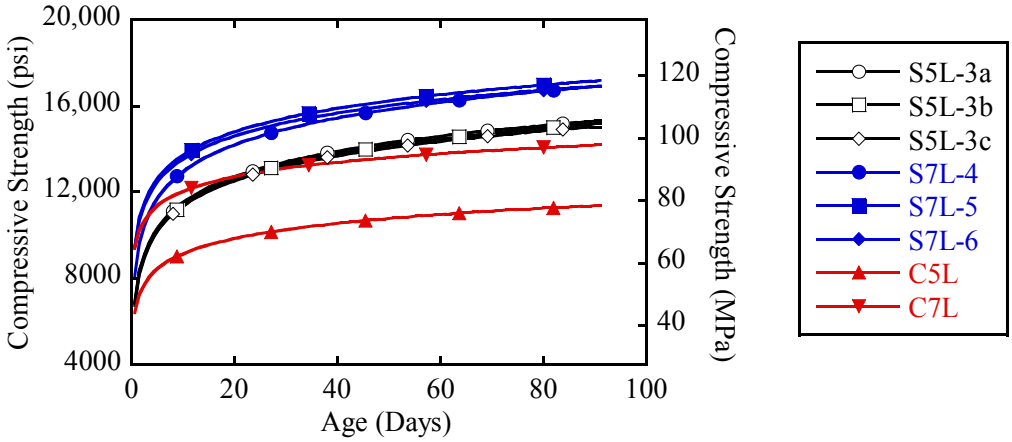

(b) Limestone

Figure 5.2. Development of Compressive Strength.

Figure 5.3 shows the ratio of the average compressive strength to 28 days for all mixtures. Overall trends for all mixtures are similar. The ultimate strength is approximately 10 to 20 percent higher than the 28-day strengths.

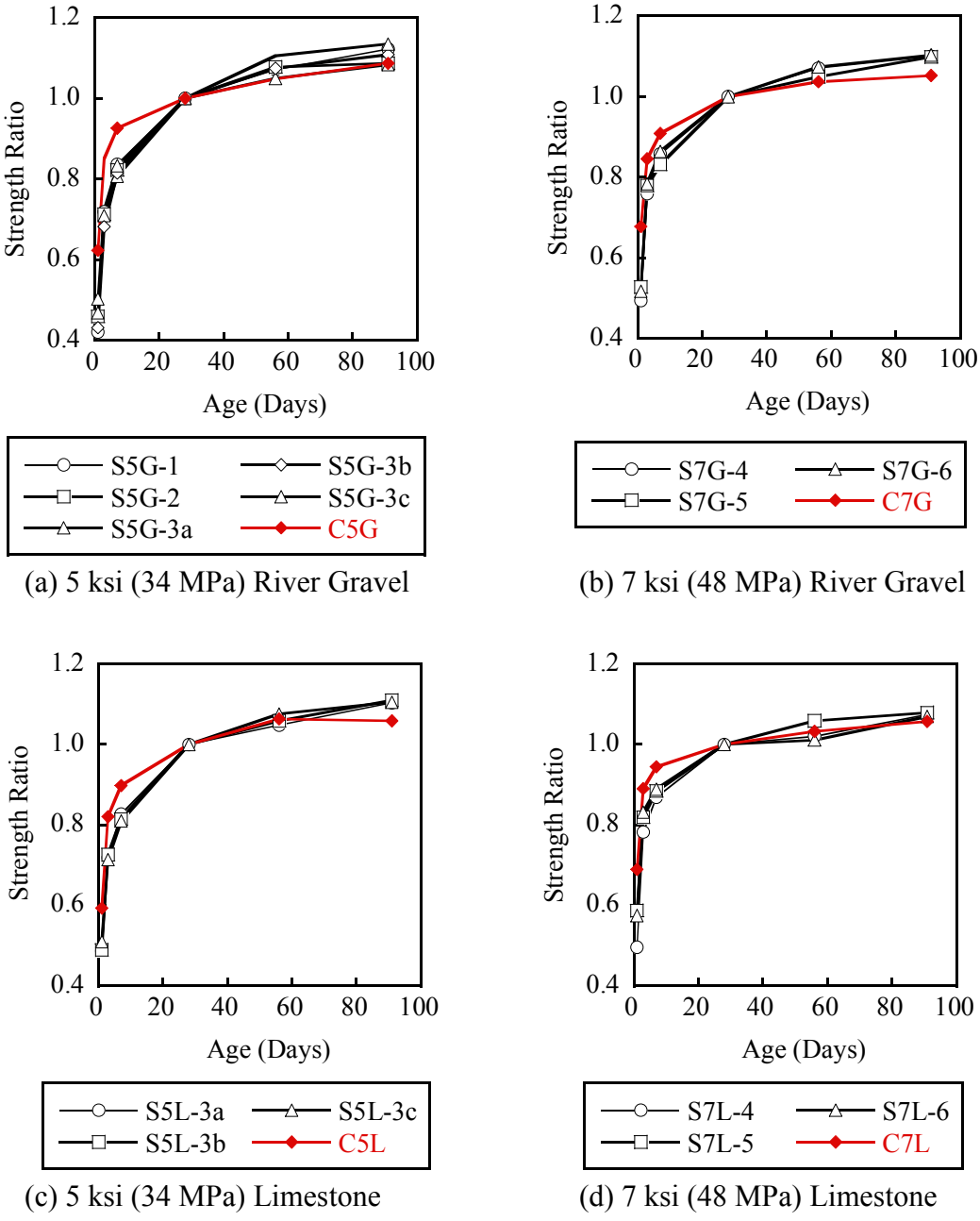

(a) 5 ksi (34 MPa) River Gravel

(b) 7 ksi (48 MPa) River Gravel

(c) 5 ksi (34 MPa) Limestone

(d) 7 ksi (48 MPa) Limestone

Figure 5.3. Compressive Strength Ratio as a Function of Time.

5.2.3 The Effect of Coarse Aggregate Volume on Compressive Strength

A statistical analysis was performed to assess whether the coarse aggregate volume significantly influences compressive strength. Researchers varied the ratio of coarse aggregate to total volume to investigate the effect of coarse aggregate volume on mechanical properties.

Linear regression analysis models were used to evaluate the effect of the coarse aggregate volume. Two significant variables predict compressive strength: coarse aggregate volume (V_{CA}) and age of testing. When this model was developed, 16-hour strength was excluded because of the high variation of values resulting from the high sensitivity to the environmental conditions during mixing. Because the relationship between the compressive strength and age is not linear, the age was transformed to a logarithmic variable to stabilize the variable.

For all the mixtures, the statistical models for the compressive strength of the SCC mixtures were determined as follows.

For 5 ksi (34 MPa) river gravel mixture:

$$f_c' = 3339 \log(\text{Age}) - 50.9\, V_{CA} + 8765 \quad \text{(psi, days, \%)} \tag{5.1}$$

where f'_c is the compressive strength (psi), Age is the age of samples after casting (days), and V_{CA} is the volume of coarse aggregate (%). The adjusted R^2 was 96 percent and *p*-value of coefficient of V_{CA} was 0.025 with a standard error of 18.

For 7 ksi (48 MPa) river gravel mixture:

$$f_c' = 3282 \log(\text{Age}) - 170.3\, V_{CA} + 15{,}600 \quad \text{(psi, days, \%)} \tag{5.2}$$

where f'_c is the compressive strength (psi), Age is the age of samples after casting (days), and V_{CA} is the volume of the coarse aggregate (%). The adjusted R^2 was 94 percent and *p*-value of coefficient of V_{CA} was less than 0.0001 with a standard error of 27.

For 5 ksi (34 MPa) limestone mixture:

$$f_c' = 3555 \log(\text{Age}) - 51.2\, V_{CA} + 9624 \quad \text{(psi, days, \%)} \tag{5.3}$$

where f'_c is the compressive strength (psi), Age is the age of samples after casting (days), and V_{CA} is the volume of coarse aggregate (%). The adjusted R^2 was 97 percent and *p*-value of coefficient of V_{CA} was less than 0.006 with a standard error of 18.

For 7 ksi (48 MPa) limestone mixture:

$$f'_c = 2670 \log(\text{Age}) + 65.8\, V_{CA} + 8972 \quad \text{(psi, days, \%)} \tag{5.4}$$

where f'_c is the compressive strength (psi), Age is the age of samples after casting (days), and V_{CA} is the volume of coarse aggregate (%). The adjusted R^2 was 93 percent and *p*-value of coefficient of V_{CA} was less than 0.005 with a standard error of 23.

The coarse aggregate volume is statistically significant at the 95 percent confidence level (*p*-value of 0.05). *p*-values larger than 0.05 indicate that the predictor is not a significant contributor to predict the response at the 95 percent confidence level. The river gravel SCC mixture exhibited negative multipliers for the coarse aggregate volume, indicating that increasing the volume of the coarse aggregate results in decreasing compressive strengths. This was also the case for the 5 ksi (34 MPa) limestone SCC mixture.

Several researchers studied the effect of coarse aggregate on the mechanical properties of concrete (Aitcin and Mehta 1990, Neville 1995). Low *w/c* can densify the interfacial transition zone (ITZ) between the coarse aggregate and cement paste, resulting in higher strength. The surface texture, shape, size, strength, and mineralogical characteristics of the coarse aggregate affect the mechanical properties of concrete.

The results indicate that increasing the aggregate content for the river gravel mixtures results in decreasing strengths. The smooth surface of the river gravel and resulting weak ITZ likely contributes to this negative correlation for both the 5 and 7 ksi (35 and 48 MPa) river gravel mixtures. This negative correlation, although small, was also observed in the 5 ksi (34 MPa) limestone mixture. The increase in aggregate likely resulted in larger amounts of weak or susceptible ITZs, resulting in lower strengths at higher limestone values. The 7 ksi (48 MPa) limestone mixture exhibited a positive correlation between strength and increasing aggregate volume. In this case the ITZ was likely not the weakest link, resulting in increasing strength with increasing aggregate volumes. It should be noted that the correlation between aggregate volume

and strength had a minimal influence from an engineering perspective on the compressive strengths.

Furthermore, the elastic properties of limestone and mortar paste were likely more similar compared to river gravel (Aulia and Deutschmann 1999, Sengul *et al.* 2002). Therefore, the stress concentrations on the contact surface were likely reduced, resulting in higher strengths than river gravel SCC mixtures.

5.3 MODULUS OF ELASTICITY (MOE)

A total of 111 samples (river gravel mixtures) and 89 samples (limestone mixtures) were tested to evaluate the MOE of SCC.

5.3.1 Relations for MOE of SCC Mixtures

Figure 5.4 shows the relationship between compressive strength and MOE of SCC. The types of coarse aggregate significantly influenced MOE.

Compressive strength and unit weight of SCC mixtures were analyzed for the river gravel and limestone mixtures, and theses values were correlated with MOE of the mixtures. Common equations for predicting MOE from compressive strength for the CC mixtures are presented in Table 5.5. Test results from this research were compared to the equation for the CC mixture. When the K_1 value is 1.0, the MOE of AASHTO (2006) is identical to that of AASHTO (2004).

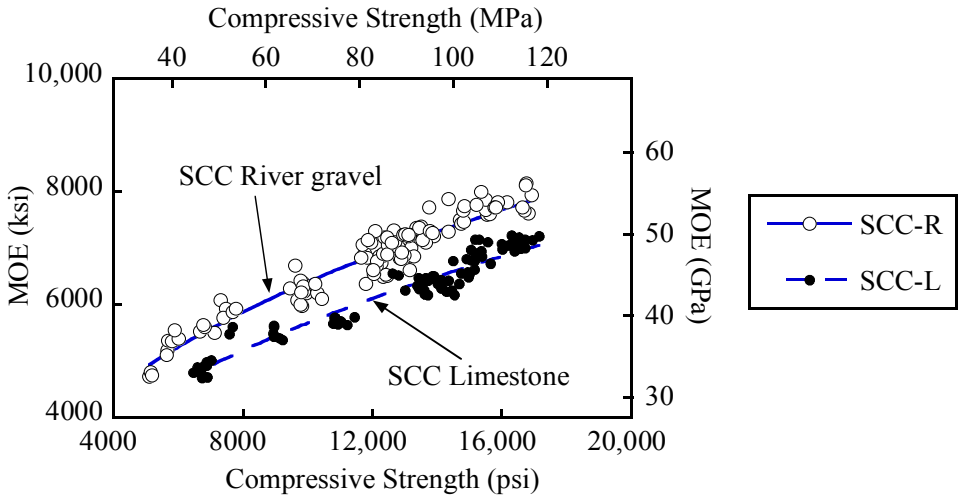

Figure 5.4. MOE of SCC.

Table 5.5. Existing Prediction Equations MOE of CC Mixtures.

Equation Source	Prediction Model	
	(psi)	(MPa)
AASHTO (2006)	$33K_1 w_c^{1.5}\sqrt{f_c'}$ (i)	$0.043K_1 w_c^{1.5}\sqrt{f_c'}$
ACI 318 (2005)	$33 w_c^{1.5}\sqrt{f_c'}$	$0.043 w_c^{1.5}\sqrt{f_c'}$
ACI 363 (1992)	$(40,000\sqrt{f_c'}+10^6)\,(w_c/145)^{1.5}$	$(3320\sqrt{f_c'}+6900)\,(w_c/2320)^{1.5}$
CEB-FIP (1990)	$593,400\,\alpha\,(f_c'/10)^{1/3}$ (ii)	$21,500\,\alpha\,(f_c'/10)^{1/3}$
NS 3473 (1992)	$309,500\,(f_c')^{0.3}$	$9500\,(f_c')^{0.3}$
Ahmad and Shah (1985)	$w^{2.5}\,(f_c')^{0.325}$	$3.385\times10^{-5}\,w^{2.5}\,(f_c')^{0.325}$

Notes: (i) K_1: Correction factor for source of aggregate. No specific value is recommended, and should be taken as 1.00 unless determined by physical test.
(ii) α = 1.2 for basalt, dense limestone aggregates; 1.0 for quartzite aggregates; 0.9 for limestone aggregates; 0.7 for sandstone aggregates.

5.3.1.1 MOE of SCC Mixtures Containing River Gravel

MOE is the function of compressive strength and unit weight of concrete. Compressive strength and unit weight of concrete are proportionally correlated to MOE. The basic prediction equation is designed as follows:

$$\text{MOE} = A\,(f_c')^n \left(\frac{w_c}{150}\right)^m \quad \text{(ksi, lb/ft}^3\text{)} \tag{5.5}$$

$$\left[\text{MOE} = A'\,(f_c')^n \left(\frac{w_c}{2400}\right)^m\right] \quad \text{(MPa, kg/m}^3\text{)}$$

where f'_c is the compressive strength (psi [MPa]) and w_c is the unit weight of the concrete (lb/ft^3 [kg/m^3]). The value of A [A'], n, and m are best-fit coefficients.

The correlation coefficient was 93 percent with A = 198,500, A' = 8981, m = 1, and n = 0.378.

$$\text{MOE} = 198,500\,(f_c')^{0.378}\left(\frac{w_c}{150}\right)^{1.0} \quad \text{(psi, lb/ft}^3\text{)} \tag{5.6}$$

$$\left[\text{MOE} = 8981 \left(f_c' \right)^{0.378} \left(\frac{w_c}{2400} \right)^{1.0} \right] \quad \text{(MPa, kg/m}^3\text{)}$$

A power regression equation was used to determine these coefficients. Note that this prediction equation is valid in the strength range of 5 to 17 ksi (35 to 117 MPa). Figure 5.5 shows the experimental data along with the 95 percent prediction intervals for this model. When estimating the prediction intervals, the unit weight of SCC mixtures was assumed to be 150 lb/ft^3 (2400 kg/m^3), which is approximately the mean unit weight of concretes containing river gravel. The unit weight of concrete is also assumed to be 150 lb/ft^3 (2400 kg/m^3) for other prediction equations.

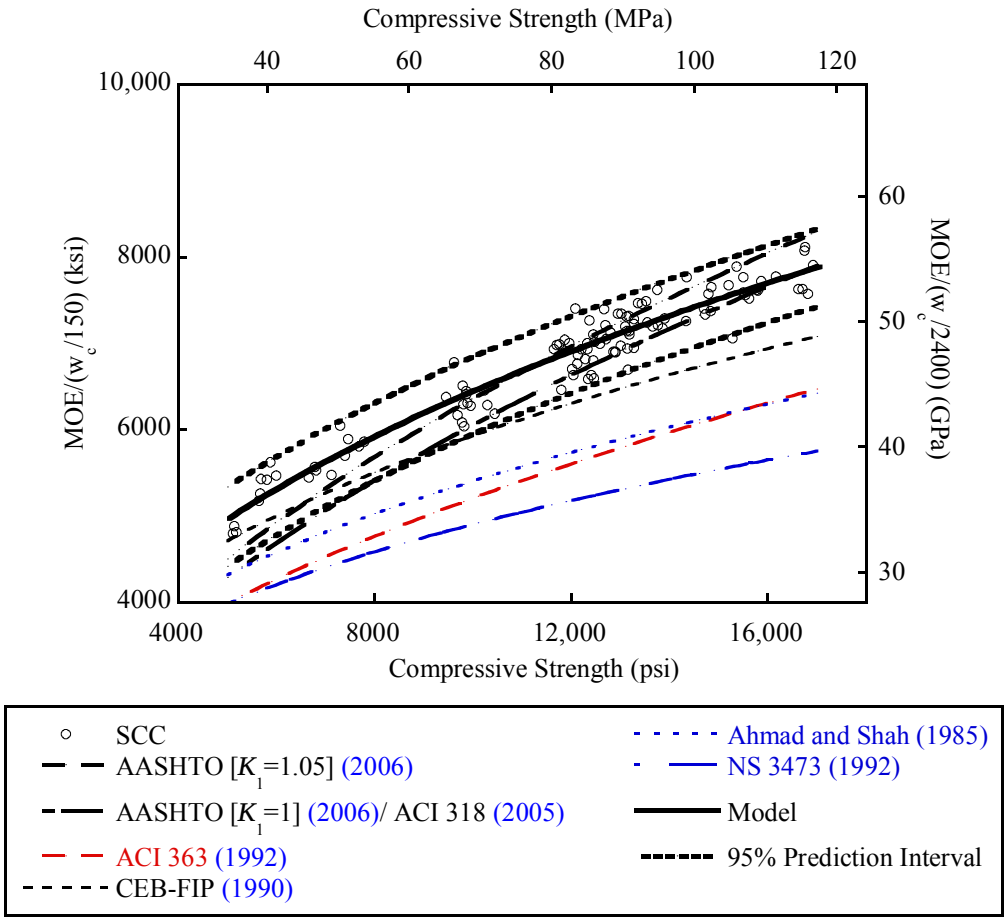

Figure 5.5. Prediction Equations for MOE for River Gravel SCC Mixture.

As shown in Figure 5.5, prediction equations of Ahmad and Shah, NS 3473, and ACI 363 underestimated the MOE of the river gravel SCC mixture (ACI Committee 363 1992, Ahmad and Shah 1985, NS 3473 1992), while the CEB-FIP prediction equation predicted the MOE of the river gravel SCC mixture within the 95 percent prediction confidence limits up to a compressive strength of 8 ksi (55 MPa) (CEB-FIP 1990). Above compressive strengths of 8 ksi (55 MPa), the CEB-FIP prediction equation predicted MOE more conservatively.

The AASHTO LRFD (K_1 = 1) and ACI 318 prediction equations estimated MOE between 9 and 17 ksi (60 and 120 MPa) fairly well. Below a compressive strength of 9 ksi (60 MPa), the prediction equations underestimated the MOE of the river gravel SCC mixtures. The best fit equation for the river gravel SCC mixture resulted when the value of K_1 and the unit weight of concrete were 1.05 and 150 lb/ft^3 (2400 kg/m^3), respectively. The calibrated AASHTO LRFD equation was within the 95 percent prediction interval.

Because the unit weight of the CC (153 lb/ft^3 [2450 kg/m^3]) and SCC (150 lb/ft^3 [2400 kg/m^3]) mixtures are different, the assumption that the unit weight is 150 lb/ft^3 (2400 kg/m^3) may not be appropriate for comparing MOEs of the CC and SCC.

Because the model includes a term w_c/150, showing the CC data on Figure 5.5 may not be appropriate for comparing the SCC and CC mixtures. As a consequence, this relation should be shown separately using a new model excluding unit weight. For this purpose, the following relation was used. It should be noted that this model depends on the compressive strength and is normally distributed. There were no outliers or influential data points. To compare MOEs of the SCC and CC mixtures, the following equation is proposed.

$$\text{MOE} = 181,710\,(f_c')^{0.39} + 61,500 \ \text{(psi)} \left[\text{MOE} = 8727\,(f_c')^{0.39} + 424\right] \ \text{(MPa)} \qquad (5.7)$$

Figure 5.6 shows the prediction equation with 95 percent prediction intervals for the CC and SCC mixtures. The MOE for the CC mixtures exhibits significantly larger values than those of the SCC mixtures. Because the river gravel is believed to be stiffer than cement paste, CC mixtures containing 44.3 percent volume of river gravel can be inferred to be higher MOE than SCC mixtures containing 31.5 to 37.8 percent volume of river gravel.

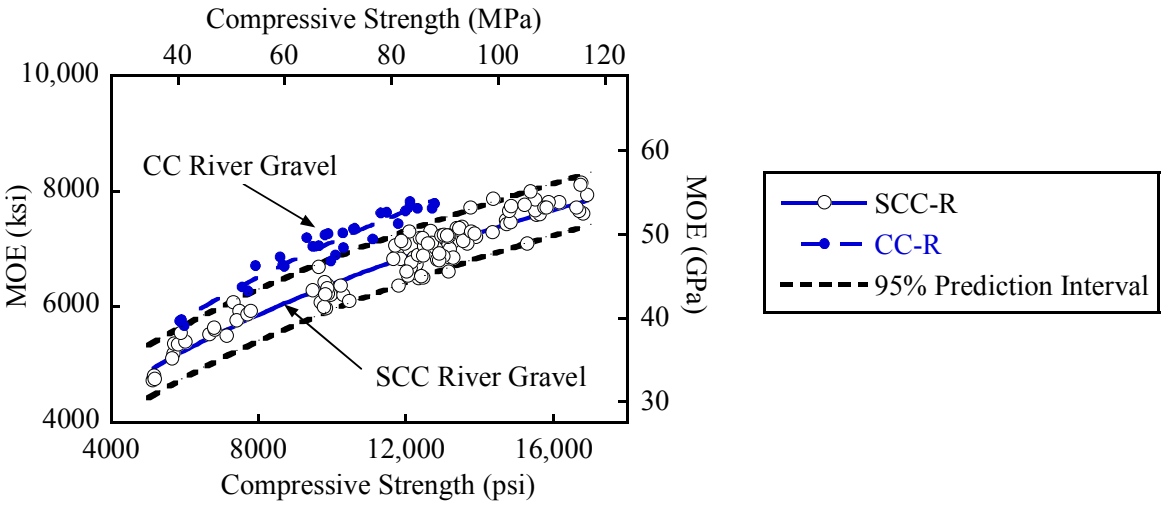

Figure 5.6. Comparison of SCC and CC Mixture Using Eq. 5.7.

5.3.1.2 MOE of SCC Mixtures Containing Limestone

For limestone SCC mixture, MOE was predicted as follows:

$$\text{MOE} = 173{,}960\,(f_c')^{0.383}\left(\frac{w_c}{150}\right)^{2.3} \quad \text{(psi, lb/ft}^3\text{)} \tag{5.8}$$

$$\left[\text{MOE} = 9420\,(f_c')^{0.383}\left(\frac{w_c}{2400}\right)^{2.3}\right] \quad \text{(MPa, kg/m}^3\text{)}$$

where f'_c is the compressive strength (psi [MPa]) and w_c is the unit weight of concrete (lb/ft^3 [kg/m^3]). The mean measured unit weight of 148 lb/ft^3 (2371 kg/m^3) was used to predict MOE values.

As shown in Figure 5.7, prediction equations from Ahmad and Shah, ACI 363, and NS 3473 underestimate MOE of limestone SCC mixtures. When α is assumed to be 1.0, the CEB-FIP model predicted MOE fairly well.

The AASHTO (K_1 = 1) and ACI 318 prediction equations estimated the mean MOE for the SCC mixtures containing limestone between 5 and 12 ksi (35 and 83 MPa) fairly well. For best fitting of the limestone SCC mixtures, the value of K_1 and the unit weight were assumed to be 0.95 and 148 lb/ft^3 (2370 kg/m^3), respectively. As shown in Figure 5.7, the AASHTO equation was within the 95 percent prediction interval.

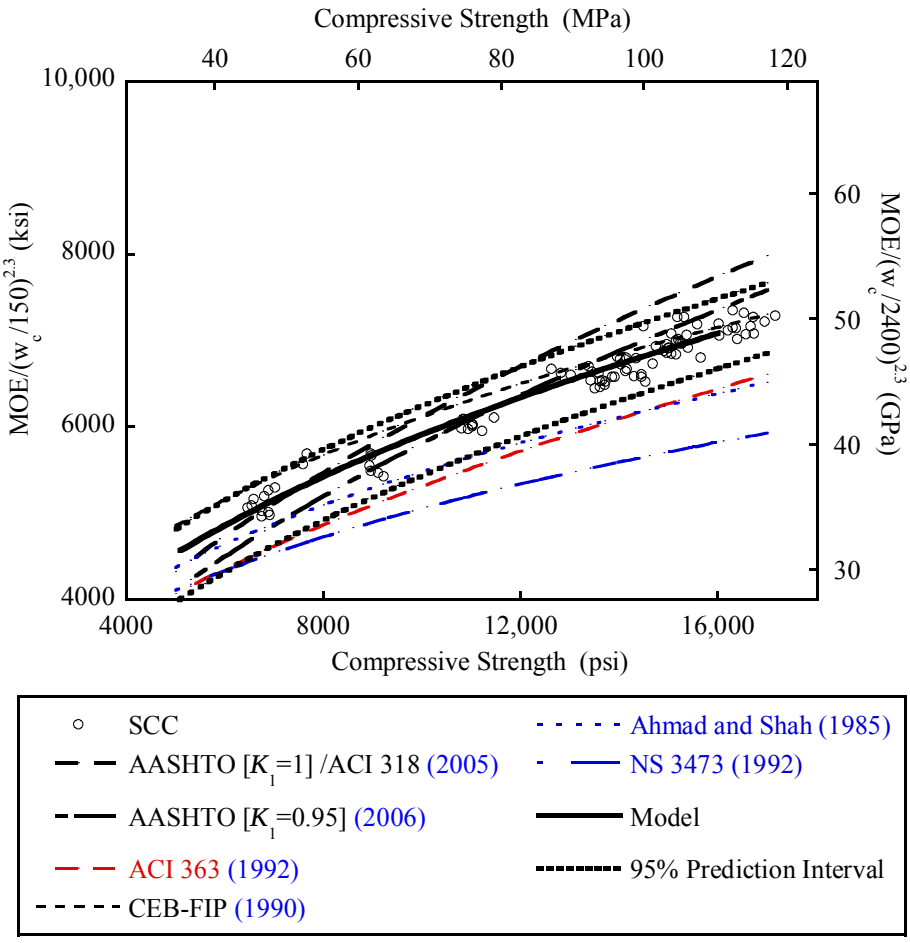

Figure 5.7. Prediction Equations for MOE for Limestone SCC.

Because the unit weight of concrete is different for the CC and SCC mixtures with limestone, the previous plots based on the assumption of 148 lb/ft^3 (2371 kg/m^3) may be appropriate for comparing the MOE of the CC and SCC mixtures. To compare the MOE (psi [MPa]) between SCC and CC containing limestone coarse aggregate, the following equation is proposed:

$$\text{MOE} = 141,050\,(f_c')^{0.40} + 90,000 \ \text{(psi)} \ \left[\text{MOE} = 7120\,(f_c')^{0.40} + 621\right] \ \text{(MPa)} \qquad (5.9)$$

Figure 5.8 shows the MOE of SCC and CC mixtures containing limestone. The MOE of the limestone SCC mixture is lower than that of the CC mixture, falling slightly below the upper bound of prediction interval.

Because limestone aggregate has higher absorption capacity (1.43 percent), this aggregate may have higher porosity and lower stiffness than the river gravel. The limestone aggregate likely has similar stiffness to that of cement paste, which results in minimal changes in MOE with increasing aggregate volume.

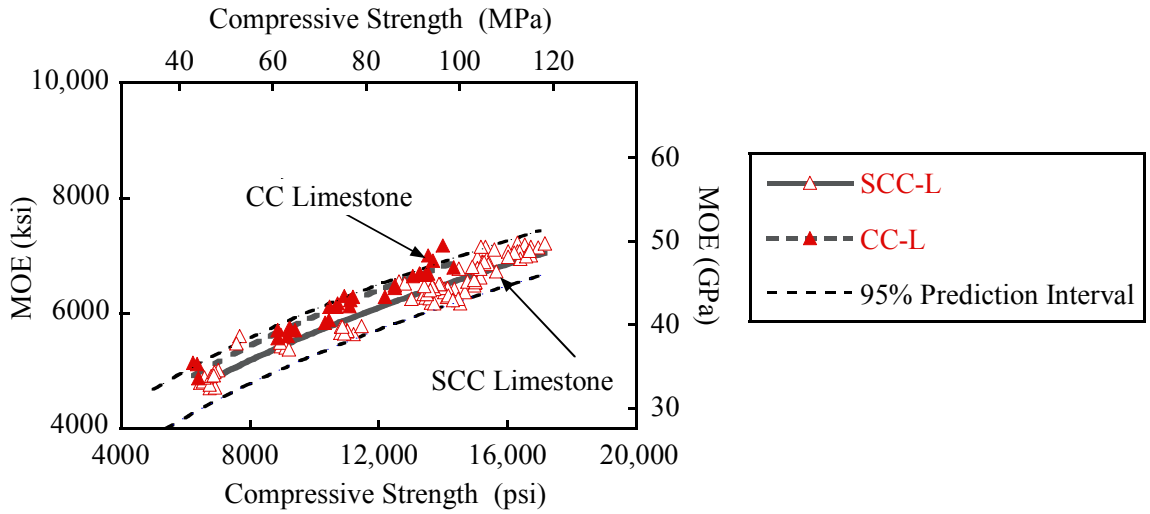

Figure 5.8. Comparison of SCC and CC Mixtures Using Eq. 5.9.

5.3.1.3 Determination of MOE of SCC Mixtures - Combined Data

For the unified design equations, the following equation is proposed for SCC mixtures. The equation variable includes the SCC unit weight and compressive strength as follows:

$$\text{MOE} = 267{,}100\,(f_c')^{0.343}\left(\frac{w_c}{150}\right)^{3.3} \quad \text{(psi, lb/ft}^3\text{)} \qquad (5.10)$$

$$\left[\text{MOE} = 10{,}153\,(f_c')^{0.343}\left(\frac{w_c}{2400}\right)^{3.3}\right] \quad \text{(MPa, kg/m}^3\text{)}$$

where f'_c is the compressive strength (psi [MPa]) and w_c is the unit weight of concrete (lb/ft^3 [kg/m^3]). The correlation coefficient is 84 percent with A = 267,100, A' = 10,153, m = 3.3, and n = 0.343. This equation provides a good fit for SCC mixtures. The measured unit weight of 149 lb/ft^3 (2385 kg/m^3) was used to predict this fit. As shown in Figure 5.9, the AASHTO LRFD (K_1 = 1) and ACI 318 prediction equations estimated the average MOE value within the 95 percent prediction interval.

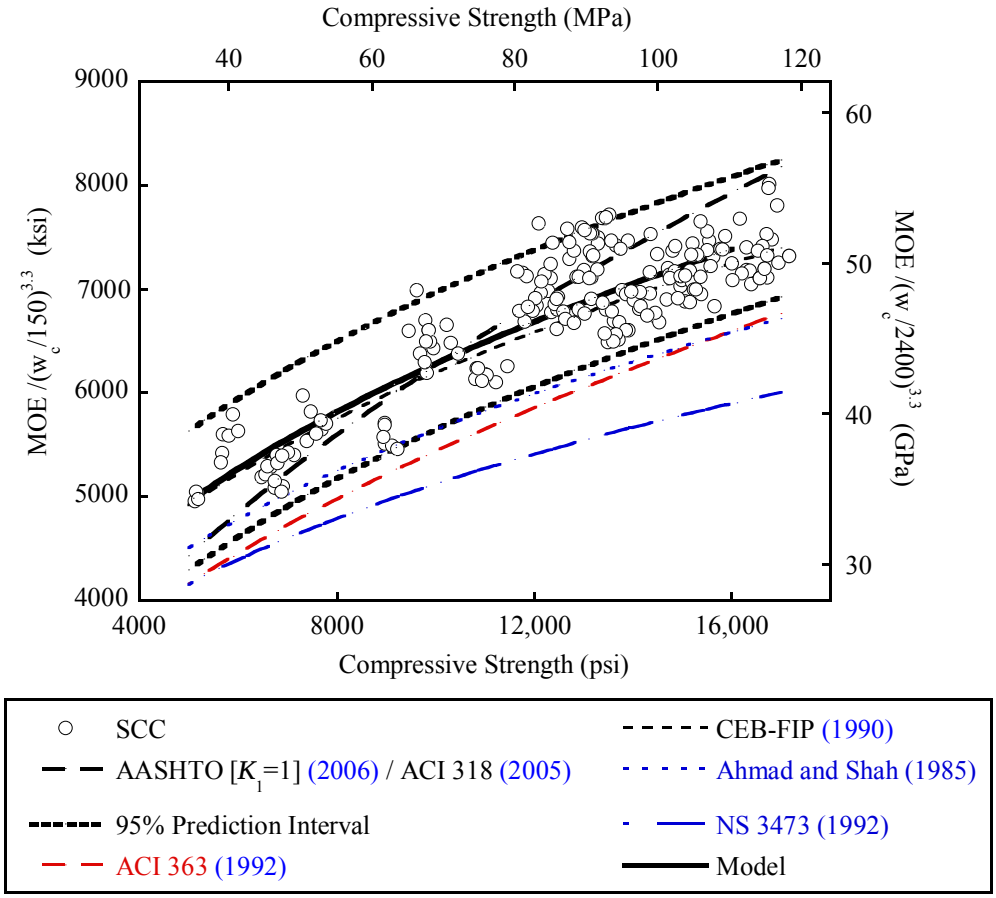

Figure 5.9. Unified MOE for SCC Mixtures.

The CEB-FIP prediction equation also provides a fairly good MOE prediction with an α factor of 1.0 (quartzite aggregates). When the CEB-FIP prediction equation with an α factor of 0.9 is used for the limestone mixture, this equation is similar to the prediction equation of Ahmad and Shah. The Ahmad and Shah, ACI-363, and NS 3473 prediction equations predicted the MOE of SCC very conservatively.

5.3.2 The Effect of Coarse Aggregate Volume on MOE of SCC Mixtures

For all the SCC mixtures, the statistical models for the MOE of SCC mixtures were determined as follows.

For 5 ksi (34 MPa) river gravel mixture:

$$\text{MOE} = 221,790\, f_c'^{0.364} + 14,550\, V_{CA} - 522,850 \quad \text{(psi, \%)} \tag{5.11}$$

where f'_c is the compressive strength (psi) and V_{CA} is the volume of coarse aggregate (%). The adjusted R^2 was 94 percent and *p*-value of coefficient of V_{CA} was 0.26 with a standard error of 12,949.

For 7 ksi (48 MPa) river gravel mixture:

$$\text{MOE} = 205,750\, f_c'^{0.376} + 32,650\, V_{CA} - 1,187,300 \quad \text{(psi, \%)} \tag{5.12}$$

where f'_c is the compressive strength (psi) and V_{CA} is the volume of coarse aggregate (%). The adjusted R^2 was 95 percent and *p*-value of coefficient of V_{CA} was less than 0.0001 with a standard error of 12,779.

For 5 ksi (34 MPa) limestone mixture:

$$\text{MOE} = 184,770\, f_c'^{0.371} + 13,350\, V_{CA} - 469,150 \quad \text{(psi, \%)} \tag{5.13}$$

where f'_c is the compressive strength (psi) and V_{CA} is the volume of coarse aggregate (%). The adjusted R^2 was 97 percent and *p*-value of coefficient of V_{CA} was 0.09 with a standard error of 7669.

For 7 ksi (48 MPa) river gravel mixture:

$$MOE = 157,010\ f_c'^{0.395} - 41,530\ V_{CA} + 1,380,820 \quad \text{(psi, \%)} \qquad (5.14)$$

where f'_c is the compressive strength (psi) and V_{CA} is the volume of coarse aggregate (%). The adjusted R^2 was 96 percent and *p*-value of coefficient of V_{CA} was less than 0.0001 with a standard error of 8557.

For the 5 ksi (34 MPa) mixtures, the volume of coarse aggregate was not statistically significant at the 95 percent confidence level. For the 7 ksi (48 MPa) river gravel SCC mixtures, the volume of the coarse aggregate was statistically significant, showing increasing MOE with increasing aggregate volume.

As noted previously, higher paste volumes and the use of fly ash can enhance the compressive strength of concrete, resulting in higher MOE values for the SCC mixtures. The MOE of the limestone aggregate could be less than that of mortar paste for the 7 ksi (48 MPa) limestone mixtures. Because of this the MOE of 7 ksi (48 MPa) mixtures could decrease as the volume of limestone aggregate increases. For the 5 ksi (34 MPa) limestone SCC mixtures, the strength of paste is likely lower than that of the 7 ksi (48 MPa) limestone SCC mixtures. As a result, the volume of limestone aggregate is not a statistically significant variable for the 5 ksi (34 MPa) limestone SCC mixtures.

5.4 MODULUS OF RUPTURE (MOR)

5.4.1 Relations for MOR of SCC Mixtures

Figure 5.10 shows the relationship between compressive strength and MOR for SCC mixtures with river gravel and limestone. River gravel SCC mixtures have slightly higher MOR values than the limestone SCC mixtures.

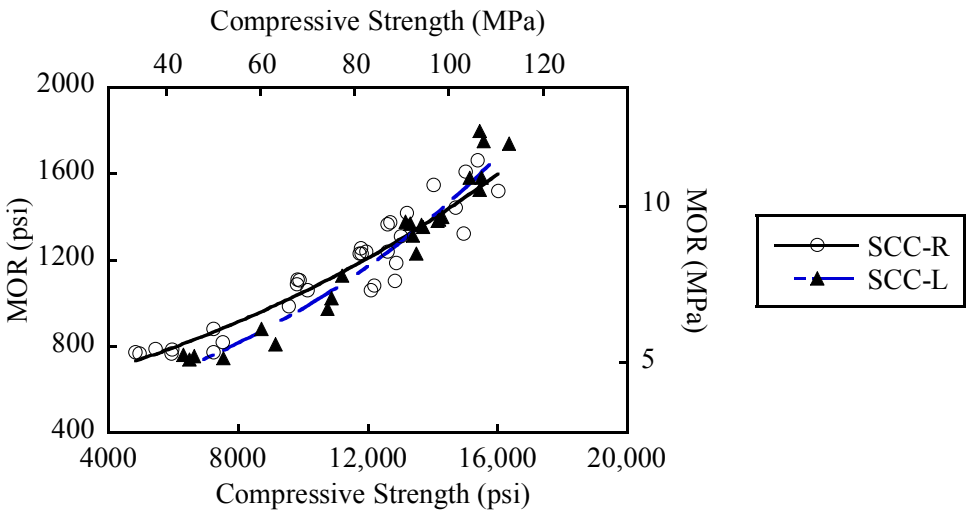

Figure 5.10. MOR for SCC Mixtures.

The average strength ratio of 6 in. × 6 in. to 4 in. × 4 in. (150 mm × 150 mm to 100 mm × 100 mm) prisms was 0.88 ± 0.02 (95 percent prediction interval) indicating that the true mean will have a 95 percent probability of being between 0.86 and 0.90.

The relationship between the 6 in. × 6 in. and 4 in. × 4 in. (150 mm × 150 mm to 100 mm × 100 mm) prisms is shown in Figure 5.11. There is linear relationship with a correlation of determination of 82 percent. This relationship is only valid when the compressive strength is between 9.5 ksi (66 MPa) and 15.5 ksi (107 MPa). These results show that the specimen test size has a significant influence on the MOR value.

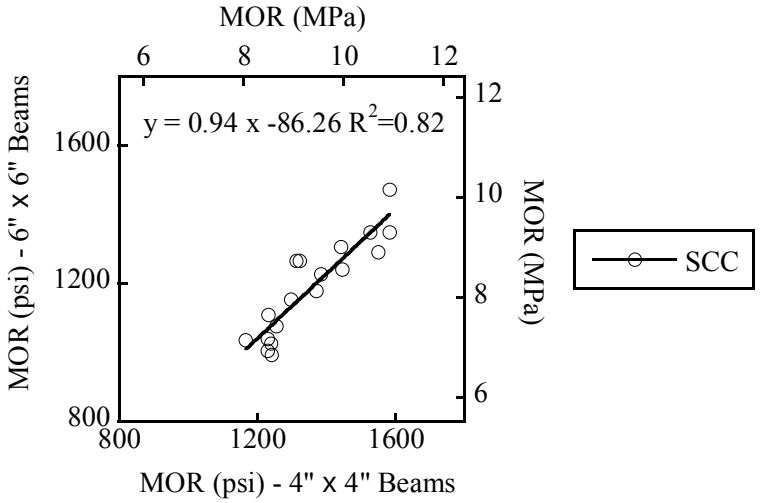

Figure 5.11. Size Effect of MOR.

According to Bazant and Li (1995), the modulus of rupture is inversely proportional to the beam depth when the same concrete was used. Because size effect exists in beams, the MOR results of the 4 in. × 4 in. (100 mm × 100 mm) prisms were converted into MOR results for 6 in. × 6 in. (150 mm × 150 mm) prisms.

Table 5.6 shows prediction equations for MOR for CC mixtures. According to the AASHTO LRFD Specifications (2004), only the lower bound of the AASHTO (2006) equation is used to design structural members.

Table 5.6. Prediction Equations for MOR.

	MOR	
	(psi)	(MPa)
AASHTO (2006)	$7.6\ (f_c')^{0.5}$ (Lower Bound)	$0.63\ (f_c')^{0.5}$
	$11.7\ (f_c')^{0.5}$ (Upper Bound)	$0.97\ (f_c')^{0.5}$
ACI 318 (2005)	$7.5\ (f_c')^{0.5}$	$0.62\ (f_c')^{0.5}$
ACI 363 (1992)	$11.7\ (f_c')^{0.5}$	$0.97\ (f_c')^{0.5}$
CEB-FIP (1990) (6 in. × 6 in. [150 mm × 150 mm])	$11.04\left[\frac{f_c'-1160}{10}\right]^{2/3}$	$2.10\left[\frac{f_c'-8}{10}\right]^{2/3}$
CEB-FIP (1990) (4 in. × 4 in. [100 mm × 100 mm])	$12.23\left[\frac{f_c'-1160}{10}\right]^{2/3}$	$2.33\left[\frac{f_c'-8}{10}\right]^{2/3}$
Ahmad and Shah (1985)	$2.3\ (f_c')^{2/3}$	$0.44\ (f_c')^{2/3}$

MOR for the SCC mixtures was predicted using compressive strength. Because the relationship between MOR and compressive strength is not linear, a logarithmic transformation was used to stabilize the variations. The transformed model was dependent on the compressive strength and was normally distributed without outliers or influential data.

The prediction equation for the MOR for SCC mixtures is as follows,

$$\text{MOR} = 375\times10^{3.68\times10^{-5} f_c'}\ \text{(psi)}\ \left[\text{MOR} = 2.59\times10^{5.34\times10^{-3} f_c'}\right]\ \text{(MPa)} \qquad (5.15)$$

where f'_c is the compressive strength (psi [MPa]) of the SCC mixtures. The coefficient of the correlation of the MOR is 92 percent. This equation is appropriate for compressive strengths between 5 and 16 ksi (35 and 110 MPa).

Figure 5.12 shows the existing and the new prediction equations calculating compressive strength and MOR for SCC mixtures. The AASHTO LRFD upper bound equation appropriately estimates the MOR of the SCC evaluated with f'_c < 13 ksi (90 MPa). The ACI 363 equation is based on MOR data for 4 in. × 4 in. (100 mm × 100 mm) prisms from Carrasquillo ***et al.*** (1981). The Ahmad and Shah prediction equation slightly overestimated MOR of the SCC mixtures for compressive strengths between 5 and 12 ksi (34 and 83 MPa). The AASHTO LRFD lower bound equation appropriately estimates the MOR of the SCC evaluated with f'_c from 5 to 10 ksi (34 to 69 MPa). For compressive strength values above 10 ksi (70 MPa), the equation underestimates MOR of the SCC mixtures.

From the results in this research, the CEB-FIP prediction equation is the most appropriate equation for predicting MOR for SCC mixtures with compressive strengths ranging from 5 to 17 ksi (34 to 117 MPa). The CEB-FIP prediction equation considers the size effect of the prism.

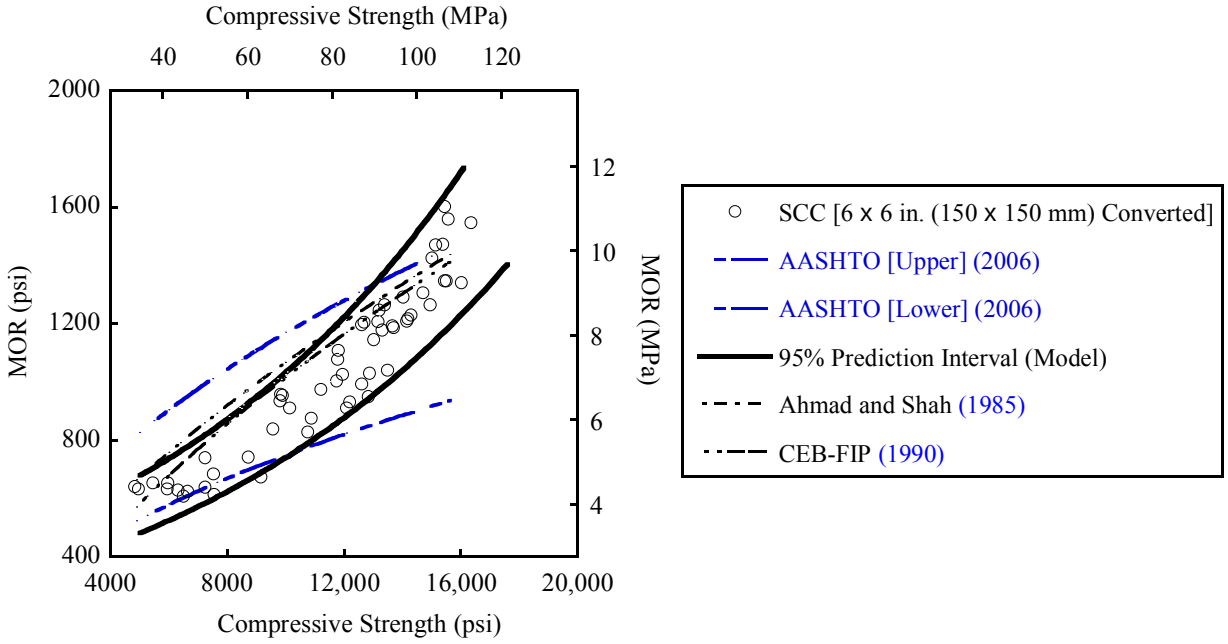

Figure 5.12. MOR Prediction Equations.

Because the lower bound of the AASHTO equation underestimated MOR for compressive strengths over 10 ksi (70 MPa), a modification of this equation can be developed to better predict MOR of SCC mixtures.

The prediction equations are presented in Table 5.7. Practical equations are also proposed with simplified equations. The equations are shown with actual data in Figure 5.13. The 95 percent prediction intervals of the mean prediction equation can be defined as the upper and lower bounds of prediction equation.

Table 5.7. Prediction Equations for MOR of SCC Mixtures.

	Lower Bound, psi (MPa)	Mean (Eq. 5.15), psi (MPa)	Upper Bound, psi (MPa)
Developed Model	$315\times10^{3.7\times10^{-5}\,f_c'}$ $(2.18\times10^{5.34\times10^{-3}\,f_c'})$	$375\times10^{3.7\times10^{-5}\,f_c'}$ $(2.59\times10^{5.34\times10^{-3}\,f_c'})$	$440\times10^{3.7\times10^{-5}\,f_c'}$ $(3.04\times10^{5.34\times10^{-3}\,f_c'})$
Simplified Model	$0.75\ f_c'^{(0.75)}$ $(0.22\ f_c'^{(0.75)})$	$0.95\ f_c'^{(0.75)}$ $(0.27\ f_c'^{(0.75)})$	$1.15\ f_c'^{(0.75)}$ $(0.33\ f_c'^{(0.75)})$

Note: equations in parentheses are for SI units.

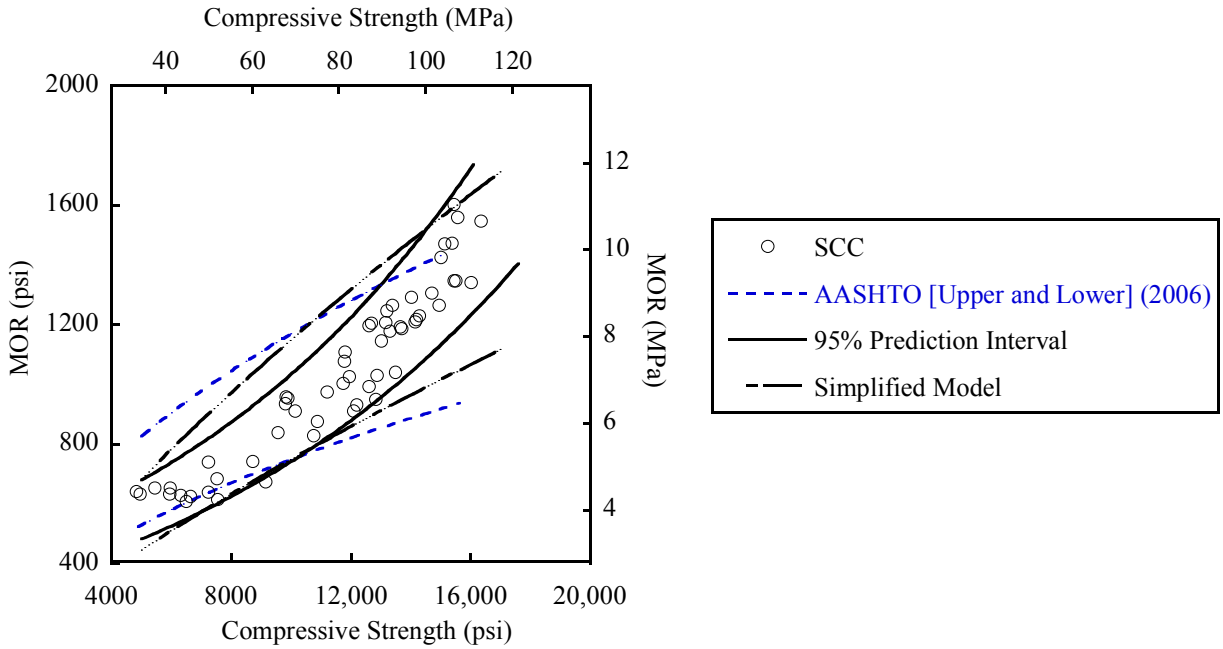

Figure 5.13. Proposed Upper and Lower Bounds of MOR for SCC Mixtures.

5.4.2 The Effect of Coarse Aggregate Volume on MOR of SCC Mixtures

For all the SCC mixtures, the statistical models for MOR of SCC mixtures were determined as follows.

For 5 ksi (34 MPa) river gravel mixture:

$$\log(\text{MOR}) = 3.49\times10^{-5}\ f_c' + 0.0022\ V_{CA} + 2.53\ \ (\text{psi}, \%) \qquad (5.16)$$

where f'_c is the compressive strength (psi) and V_{CA} is the volume of coarse aggregate (%). The adjusted R^2 was 94 percent and *p*-value of coefficient of V_{CA} was 0.4731 with a standard error of 0.00290.

For 7 ksi (48 MPa) river gravel mixture:

$$\log(\text{MOR}) = 3.79\times10^{-5}\ f_c' + \ 0.0027\ V_{CA} + 2.45\ \ (\text{psi}, \%) \qquad (5.17)$$

where f'_c is the compressive strength (psi) and V_{CA} is the volume of coarse aggregate (%). The adjusted R^2 was 91 percent and *p*-value of coefficient of V_{CA} was 0.6340 with a standard error of 0.00543.

For 5 ksi (34 MPa) limestone mixture:

$$\log(\text{MOR}) = 3.86\times10^{-5}\ f_c' + 0.0006\ V_{CA} + 2.52\ \ (\text{psi}, \%) \qquad (5.18)$$

where f'_c is the compressive strength (psi) and V_{CA} is the volume of coarse aggregate (%). The adjusted R^2 was 95 percent and *p*-value of coefficient of V_{CA} was 0.8587 with a standard error of 0.00340.

For 7 ksi (48 MPa) river gravel mixture:

$$\log(\text{MOR}) = 4.75\times10^{-5}\ f'_c - 0.0040\ V_{CA} + 2.57 \quad \text{(psi, \%)} \tag{5.19}$$

where f'_c is the compressive strength (psi) and V_{CA} is the volume of coarse aggregate (%). The adjusted R^2 was 96 percent and *p*-value of coefficient of V_{CA} was 0.34445 with a standard error of 0.00396.

Finally, the effect of coarse aggregate volume on the MOR is statistically insignificant at the 95 percent confidence level.

5.5 SPLITTING TENSILE STRENGTH (STS)

5.5.1 Relations for STS of SCC Mixtures

Figure 5.14 shows the relationship between the compressive strength and the STS of SCC mixtures with river gravel and limestone. River gravel SCC mixtures have significantly higher the STS than limestone SCC mixtures.

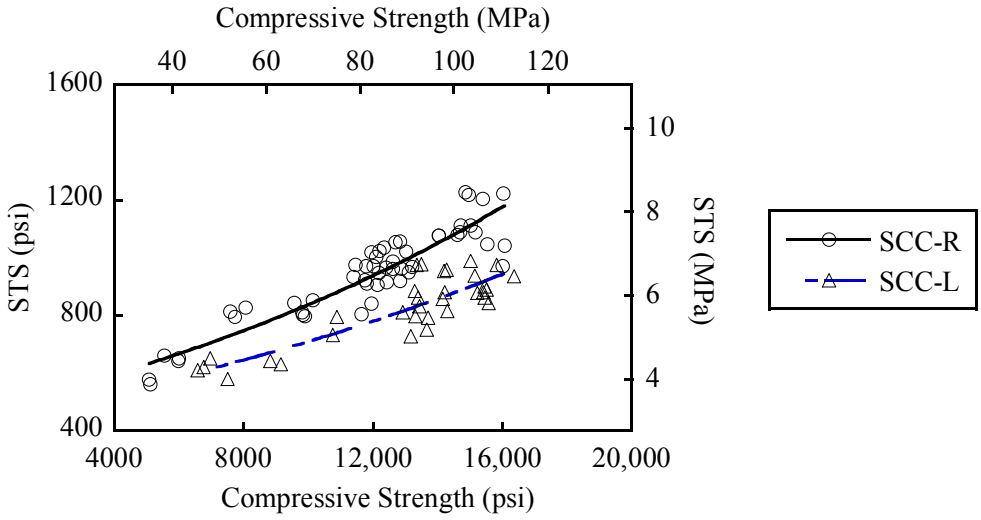

Figure 5.14. STS of SCC Mixtures.

The effect of coarse aggregate type is more significantly observed in the STS results than the MOR results. These results can be attributed to the bond between coarse aggregate and cement paste and the aggregate strength. Generally, the ITZ is weaker than the bulk cement paste strength and the aggregate strength (Mehta and Monterio 2005). When the cement paste and ITZ have relatively higher strengths than aggregate strength, the fracture of aggregate precedes the

fracture of the cement and the ITZ. If the cement paste has lower strength than the aggregate strength, the fracture occurs in either the ITZ or cement paste. Therefore, the low strength of limestone aggregate leads to lower STS values than mixtures containing river gravel. After performing the STS tests, the cracked surfaces of the limestone mixtures were smooth, with most of limestone fractured (see Figure 5.15 (a)). However, the river gravel mixture had some failures in the ITZ, resulting in a rougher profile of the cracked surface (see Figure 5.15 (b)). Therefore, in this research the limestone seems to exhibit the lowest strength of all other components, individually, the ITZ, cement paste, and river gravel.

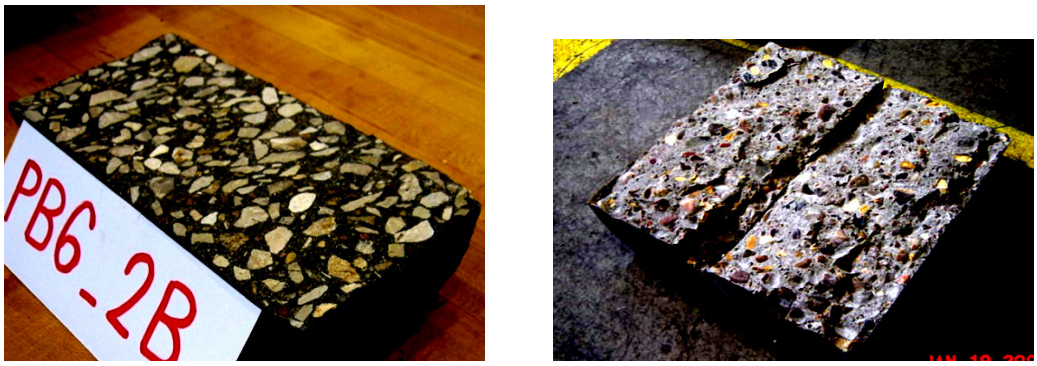

(a) River Gravel SCC (b) Limestone SCC

Figure 5.15. Fracture Surface in STS.

Simple linear regression analysis predicted STS of SCC mixtures as a function of compressive strength. Logarithmic transformation stabilized the variation and provided a better prediction. The transformed model was independent of the compressive strength and normally distributed without outliers and influential data.

The prediction equation of the STS for the SCC mixtures was determined to be:

$$\text{STS} = 490 \times 10^{2.1\times10^{-5} f_c'} \text{ (psi)} \quad \left[\text{STS} = 3.39 \times 10^{3.0\times10^{-3} f_c'}\right] \text{ (MPa)} \qquad (5.20)$$

where the f'_c is the compressive strength (psi [MPa]) of the SCC mixtures. The coefficient of correlation of the prediction equation is 92 percent. This equation is valid between the compressive strengths of 5 and 16 ksi (35 and 110 MPa). Table 5.8 shows commonly used

prediction equations for CC. The STS of AASHTO (2004) equation is identical to that of the AASHTO (2006) equation.

Table 5.8. Existing Prediction Equations for STS.

	STS	
	(psi)	(MPa)
AASHTO (2004, 2006)	$7.3\,(f_c')^{0.5}$	$0.59\,(f_c')^{0.5}$
ACI 318 (2005)	$6.7\,(f_c')^{0.5}$	$0.56\,(f_c')^{0.5}$
ACI 363 (1992)	$7.4\,(f_c')^{0.5}$	$0.59\,(f_c')^{0.5}$
CEB-FIP (1990)	$8.2\left[\frac{f_c'-1160}{10}\right]^{2/3}$	$1.56\left[\frac{f_c'-8}{10}\right]^{2/3}$
Ahmad and Shah (1985)	$4.34\,(f_c')^{0.55}$	$0.46\,(f_c')^{0.55}$

The relationship between compressive strength and STS for the SCC mixtures with prediction curves is shown in Figure 5.16. This figure shows new and existing prediction equations for the relationship between compressive strength and STS.

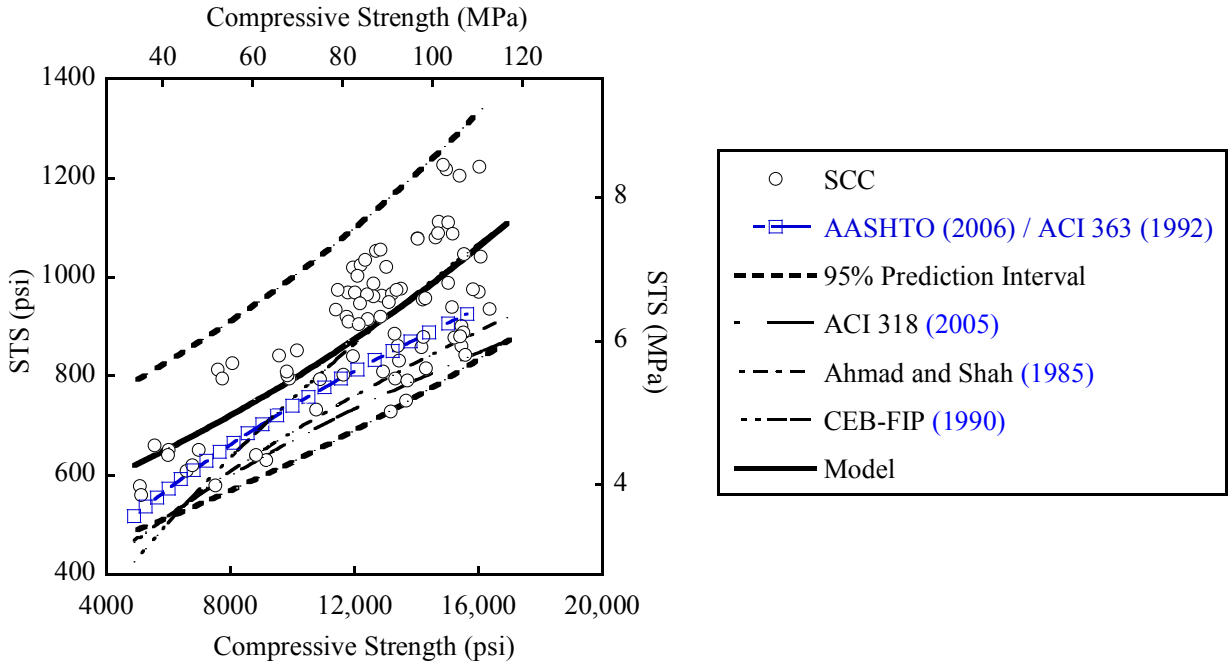

Figure 5.16. STS Prediction Equations.

Because the AASHTO and ACI 363 prediction equations are the same, one curve represents both equations. The CEB-FIP equation is the least conservative equation among the common prediction equations

Because upper and lower bound values are useful for predicting the STS range, the upper and lower prediction equations are proposed here for STS of SCC mixtures. The lower bound is appropriate for the design of concrete members when the STS value is needed.

Table 5.9 shows the prediction equations for STS of SCC mixtures. The upper and lower bounds (practical equations) were obtained from the 95 percent prediction interval.

Table 5.9. Prediction Equations for STS of SCC Mixtures.

	Lower Bound, psi (MPa)	Mean, (Eq. 5.20) psi (MPa)	Upper Bound, psi (MPa)
Developed Model	$385\times10^{2.1\times10^{-5}\,f_c'}$ $(2.67\times10^{3.0\times10^{-3}\,f_c'})$	$490\times10^{2.1\times10^{-5}\,f_c'}$ $(3.39\times10^{3.0\times10^{-3}\,f_c'})$	$610\times10^{2.1\times10^{-5}\,f_c'}$ $(4.23\times10^{3.0\times10^{-3}\,f_c'})$
Simplified Model	$6.3\sqrt{f_c'}$ $(0.52\sqrt{f_c'})$	$8.2\sqrt{f_c'}$ $(0.68\sqrt{f_c'})$	$10.2\sqrt{f_c'}$ $(0.85\sqrt{f_c'})$

Note: equations in parentheses are for SI units.

To visualize the equations shown in Table 5.9, the prediction equations are plotted for the SCC mixtures in Figure 5.17.

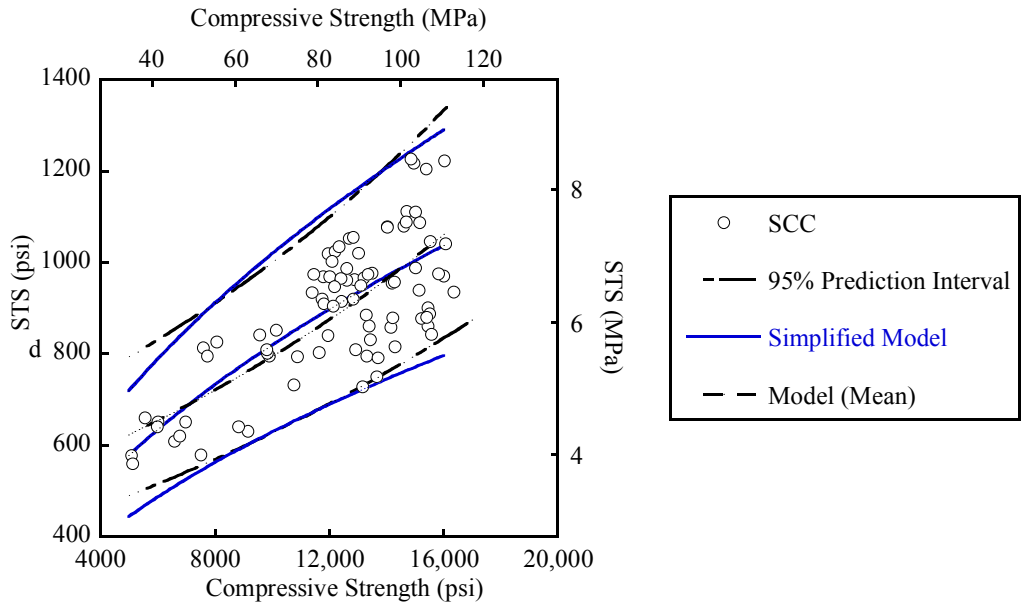

Figure 5.17. Proposed Upper and Lower Bounds of STS for SCC Mixtures.

5.5.2 The Effect of Coarse Aggregate Volume on STS of SCC Mixtures

For all the SCC mixtures, the statistical models for the STS of SCC mixtures were determined as follows.

For 5 ksi (34 MPa) river gravel mixture:

$$\log(\text{STS}) = 2.74 \times 10^{-5}\ f_c' + 0.0023\ V_{CA} - 2.58\ \ (\text{psi}, \%) \tag{5.21}$$

where f'_c is the compressive strength (psi) and V_{CA} is the volume of coarse aggregate (%). The adjusted R^2 was 88 percent and *p*-value of coefficient of V_{CA} was 0.2849 with a standard error of 0.0019.

For 7 ksi (48 MPa) river gravel mixture:

$$\log(\text{STS}) = 1.71 \times 10^{-5}\ f_c' - 0.0071\ V_{CA} + 3.03\ \ (\text{psi}, \%) \tag{5.22}$$

where f'_c is the compressive strength (psi) and V_{CA} is the volume of coarse aggregate (%). The adjusted R^2 was 79 percent and *p*-value of coefficient of V_{CA} was 0.0174 with a standard error of 0.0027.

For 5 ksi (34 MPa) limestone mixture:

$$\log(\text{STS}) = 2.09 \times 10^{-5}\ f_c' - 0.0057\ V_{CA} - 2.84\ \ (\text{psi}, \%) \tag{5.23}$$

where f'_c is the compressive strength (psi) and V_{CA} is the volume of coarse aggregate (%). The adjusted R^2 was 85 percent and *p*-value of coefficient of V_{CA} was 0.0579 with a standard error of 0.0027.

For 7 ksi (48 MPa) river gravel mixture:

$$\log(\text{STS}) = 2.43 \times 10^{-5} \; f_c' - 0.0037 \; V_{CA} + 2.71 \;\; (\text{psi}, \%) \qquad (5.24)$$

where f'_c is the compressive strength (psi) and V_{CA} is the volume of coarse aggregate (%). The adjusted R^2 was 89 percent and *p*-value of coefficient of V_{CA} was 0.2114 with a standard error of 0.0029.

The effect of the coarse aggregate volume on STS is statistically insignificant at the 95 percent confidence level except for the 7 ksi (48 MPa) river gravel SCC mixture.

In the prediction equations for the 7 ksi (48 MPa) river gravel SCC mixtures, STS and volume of coarse aggregate are negatively correlated indicating that STS decreases as the volume of coarse aggregate increases. The smooth surface of the river gravel probably decreases the bond and reduces the STS of SCC mixtures.

5.6 COMPARISON OF SCC AND CC

The SCC mixtures were compared with the CC mixtures along with the AASHTO LRFD equations and the models.

5.6.1 Modulus of Elasticity

As shown in Figure 5.18, the MOE of the CC mixtures is slightly higher than the SCC mixtures. The 2006 AASHTO LRFD equation provides a reasonable prediction of the MOE for the SCC mixtures with f'_c value ranging from approximately 6 to 12 ksi (41 to 83 MPa). The developed equations can be used for estimating the MOE of the SCC with f'_c values ranging from 5 to 17 ksi (34 to 120 MPa).

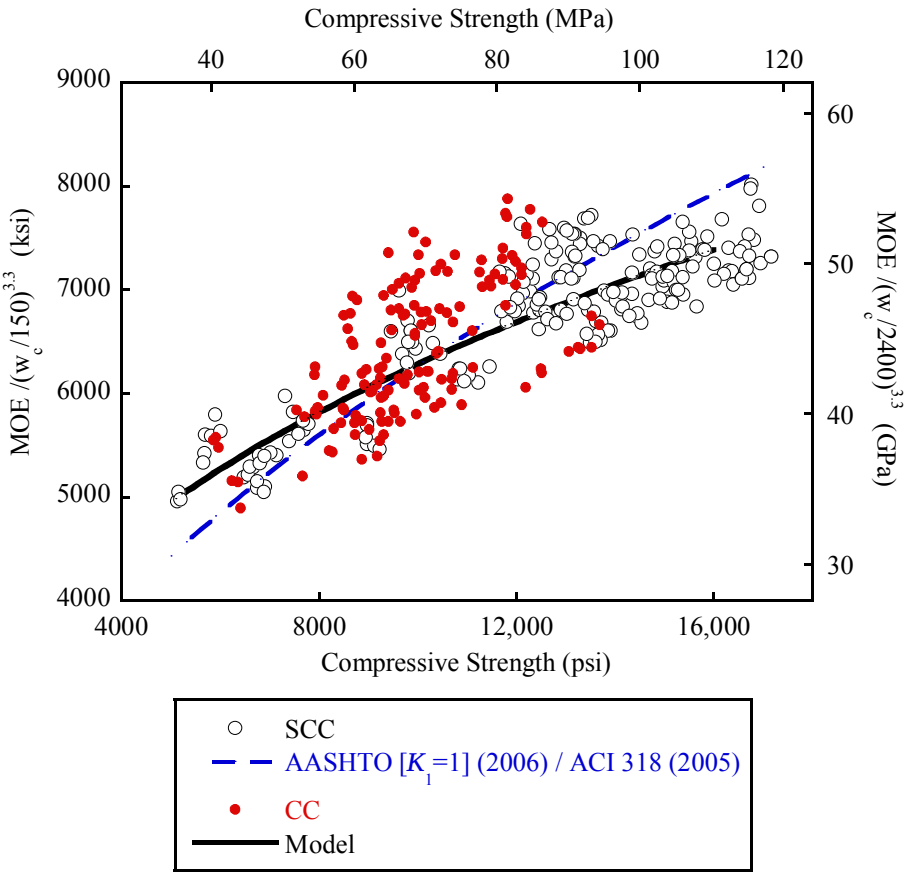

Figure 5.18. Comparison between CC and SCC Mixtures (MOE).

5.6.2 Modulus of Rupture

As shown in Figure 5.19, MOR of the SCC mixtures is lower than the CC mixtures. Most of the data from the CC mixtures fell within the upper and lower bounds of the AASHTO LRFD equations (2006). As mentioned previously, the applicability of the AASHTO LRFD (2006) for the SCC mixtures should be considered along with the range of compressive strength. The 2006 AASHTO LRFD lower bound equation is appropriate for estimating the MOR of the SCC evaluated in this study with f'_c values ranging from 5 to 10 ksi (34 to 69 MPa). The 2006 AASHTO LRFD upper bound equation is appropriate for estimating the MOR of the SCC evaluated with f'_c values less than 13 ksi (90 MPa). The developed equations can be used for estimating the MOR of the SCC with f'_c values ranging from 5 to 16 ksi (34 to 110 MPa).

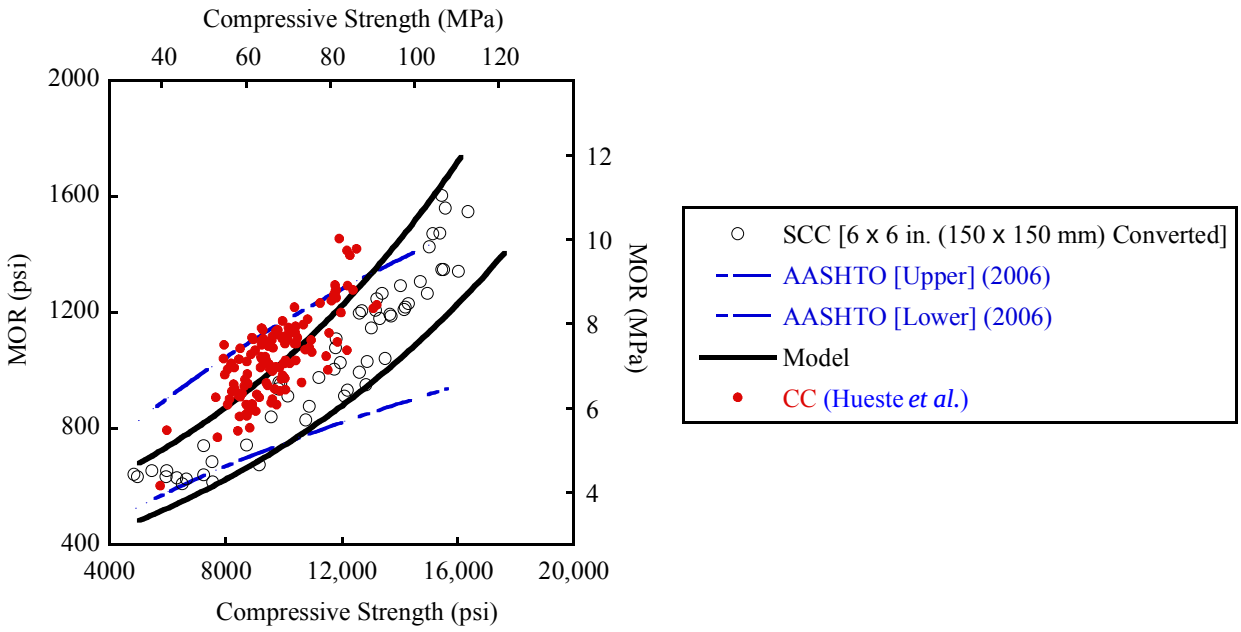

Figure 5.19. Comparison between CC and SCC Mixtures (MOR).

5.6.3 Splitting Tensile Strength

As shown in Figure 5.20, STS of the SCC mixtures are higher than those of the CC mixtures. This result is contradictory from that for MOR results. This discrepancy could be attributed to the difference of stress and strain distribution and the different location of the initiation of fracture. The initial cracking in MOR occurs in the extreme tension fiber. In STS the fracture occurs in the inner core due to largely homogeneous and uniform transverse tensile stresses along diametrically opposite line loads. The extreme fibers in STS are subjected to compression loads. However, the condition of extreme fiber is critical in MOR. This can be explained by noting that high paste volumes in the SCC mixtures have weaker surfaces than the CC mixtures. The inner core strength depends on the overall properties of the aggregate, paste, and ITZ, while the surface strength depends on paste strength rather than the aggregate strength.

The difference between STS in the CC and SCC mixtures can be explained by the higher tensile strength of the inner core. This can be explained by the role of HRWRA. HRWRA can improve the microstrucutral characteristics of the SCC mixture. Therefore, the effect of this refinement increased the strength of the paste and the bond characteristics between the coarse

aggregate and paste. Similar results were reported in other studies (Naito *et al.* 2006, Walraven 2005).

The 2006 AASHTO LRFD equation is appropriate for estimating the STS of the SCC evaluated in this study with f'_c values ranging from 5 to 16 ksi (34 to 110 MPa).

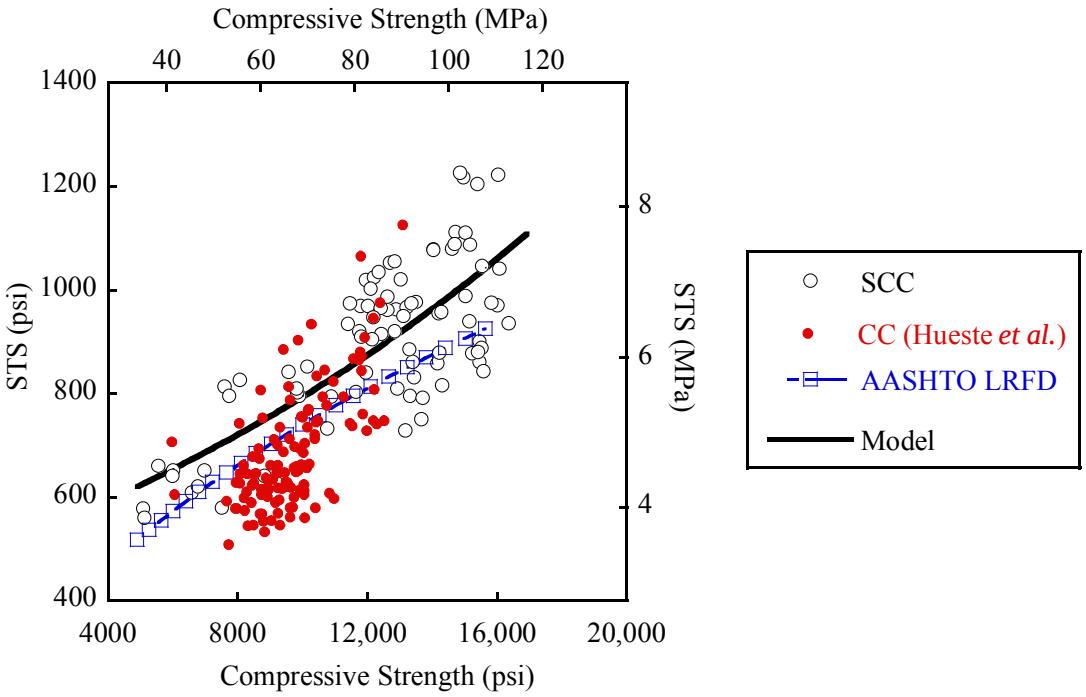

Figure 5.20. Comparison between CC and SCC Mixtures (STS).

5.7 SUMMARY

Based on the experimental results, the following conclusions of compressive strength, MOE, MOR, and STS were drawn.

1) The SCC exhibited higher early strengths, workability, and later age strengths.
2) The volume of coarse aggregate was found to be negatively correlated to the compressive strength in the 5 and 7 ksi (34 and 48 MPa) 16-hour release strength river gravel and limestone mixtures. The 7 ksi (48 MPa) 16-hour release strength limestone mixtures exhibited a positive correlation. This may be attributed to the

weaker limestone aggregate strength. The aggregate volume had a minimal influence, from an engineering perspective, on the compressive strengths.

3) The high stiffness of the river gravel resulted in significantly higher values of elastic modulus in these mixtures compared to the limestone mixtures. The CC tends to have higher elastic modulus values than the SCC. The effect of the volume of the coarse aggregate is more pronounced for the 7 ksi (48 MPa) 16-hour release strength mixtures with both aggregate types.
4) The 2006 AASHTO equation (2006 AASHTO LRFD Equation 5.4.2.4-1) was appropriate to predict the MOE of the SCC when assuming K_1 is 1.0 and the unit weight was 149 lb/ft^3 (2385 kg/m^3). For the river gravel mixtures, K_1 and the unit weight were 1.05 and 150 lb/ft^3 (2400 kg/m^3), respectively. For the limestone mixtures, K_1 and unit weight were 0.95 and 148 lb/ft^3 (2370 kg/m^3), respectively. The 2006 AASHTO LRFD equation provides a reasonable prediction of the MOE for the river gravel and limestone SCC mixtures with ranges of f'_c from approximately 6 to 12 ksi (41 to 83 MPa). The equations developed in this research were appropriate for estimating the MOE of the river gravel and limestone SCC mixtures with f'_c values ranging from 5 to 17 ksi (34 to 120 MPa).
5) The MOR of SCC mixtures containing river gravel was higher than that of the limestone SCC mixtures. The SCC mixtures exhibit lower MOR values when compared with the CC mixtures.
6) The 2006 AASHTO LRFD lower bound equation for MOR (2006 AASHTO LRFD Article 5.4.2.6) is appropriate for estimating the MOR of the SCC mixtures evaluated in this study with f'_c values ranging from 5 to 10 ksi (34 to 69 MPa). The 2006 AASHTO LRFD upper bound equation for MOR (2006 AASHTO LRFD Article 5.4.2.6) is appropriate for estimating the MOR of the SCC mixtures evaluated in this study with f'_c values less than 13 ksi (90 MPa).
7) The STS of the SCC mixtures containing river gravel is significantly higher than that of the SCC limestone mixtures. The low strength of limestone aggregate likely leads to lower STS values.
8) Contrary to the MOR results, the SCC mixtures tended to have higher STS values than the CC mixtures.

9) The 2006 AASHTO LRFD Equation for predicting STS (2006 AASHTO LRFD Article 5.4.2.7) estimated the STS of the SCC mixtures evaluated in this study with f'_c from 5 to 16 ksi (34 to 110 MPa) fairly well.
10) Models for the MOE, MOR, and STS have been developed for estimating the mechanical properties of the SCC evaluated in this study.
11) The volume of the coarse aggregate was not a statistically significant variable for predicting MOR and STS of the CC and SCC mixtures.

CHAPTER 6
RESULTS AND ANALYSIS OF LABORATORY STUDY: SHEAR CHARACTERISTICS

6.1 MECHANICAL PROPERTIES AND PRECRACKING RESULTS

The test matrix, sample design and test procedures for the shear characterization tests are described in Section 4.3. Three push-off samples were used for each mixture proportion and two batches of each mixture were cast on the same day. At 7 days, the compressive strength of each batch was compared to ensure that the batches had statistically similar strengths with a coefficient of variance (COV) of approximately 3.3 percent between average values of two batches each. Compressive strength and STS were measured using three cylinders for each test. Compressive strength, STS, and precracking load results are presented in Tables 6.1 and 6.2.

Table 6.1. Mechanical Properties and Precracking Load of River Gravel SCC and CC.

		SR5 /31.5	SR5 /34.6	SR5 /37.8	SR7 /32.3	SR7 /35.0	SR7 /37.6	CR5 /44.3	CR7 /44.3
Compressive Strength	Avg., psi (MPa)	12,320 (85)	12,140 (84)	11,950 (82)	14,750 (102)	15,290 (105)	16,030 (111)	10,390 (72)	12,150 (84)
	Std. Dev., psi (MPa)	164 (1.13)	440 (3.03)	418 (2.88)	98 (0.68)	214 (1.48)	37 (0.26)	55 (0.38)	697 (4.81)
STS	Avg., psi (MPa)	911 (6.28)	859 (5.92)	945 (6.52)	1071 (7.38)	981 (6.76)	941 (6.49)	938 (6.47)	797 (5.50)
	Std. Dev., psi (MPa)	187 (1.29)	149 (1.03)	109 (0.75)	110 (0.76)	130 (0.90)	144 (0.99)	80 (0.55)	364 (2.51)
Precracking Load	Avg., kip (kN)	42 (187)	35 (156)	41 (182)	44 (196)	41 (182)	42 (187)	42 (187)	51 (227)
	Std. Dev., kip (kN)	3.4 (15)	7.1 (32)	3.9 (17)	1.3 (5.8)	3.5 (16)	4.7 (21)	2.4 (10.7)	4.7 (21)

Table 6.2. Mechanical Properties and Precracking Load of Limestone SCC and CC.

		SL5 /29.0	SL5 /31.9	SL5 /34.8	SL7 /31.9	SL7 /34.5	SL7 /37.0	CL5 /40.1	CL7 /40.1
Compressive Strength	Avg., psi (MPa)	14,250 (98)	13,410 (92)	13,170 (91)	15,480 (107)	15,980 (110)	15,280 (105)	9,590 (66)	13,400 (92)
	Std. Dev., psi (MPa)	38 (0.26)	55 (0.38)	224 (1.54)	403 (2.78)	285 (1.97)	110 (0.76)	1254 (8.65)	95 (0.66)
STS	Avg., psi (MPa)	897 (6.18)	944 (6.51)	862 (5.94)	952 (6.56)	1024 (7.06)	898 (6.19)	867 (5.98)	947 (6.53)
	Std. Dev., psi (MPa)	124 (0.85)	138 (0.95)	161 (1.11)	108 (0.74)	156 (1.08)	95 (0.66)	71 (0.49)	109 (0.75)
Precracking Load	Avg., kip (kN)	30 (133)	33 (147)	33 (147)	34 (151)	35 (156)	35 (156)	32 (142)	34 (151)
	Std. Dev., kip (kN)	2.3 (10)	1.3 (5.8)	1.3 (5.8)	4.5 (20)	2.9 (13)	1.1 (4.9)	1.6 (7.1)	4.7 (21)

6.2 DEVELOPMENT OF EVALUATION METHODS

6.2.1 Normalized Shear Stress versus Crack Width

Figure 6.1 shows typical plots of shear stress versus crack slip, normal stress versus crack width, and crack slip versus crack width. As the crack width increases, the crack slip increases along with high normal and shear stresses. Therefore, these variables are highly correlated with nonlinear relationships. Many previous researchers provided similar individual plots showing values of two or three variables. For example, the theoretical crack slip model is an example of a three-variable plot developed by Walraven and Reinhardt (1981) shown in Figure 6.2. However, conventional plots neglect the effect of the normal stress on the shear stress. An increase in normal stress σ results in increased shear stress τ. As such, a direct comparison between absolute shear stresses cannot fully explain aggregate interlock in the samples with varying normal stresses.

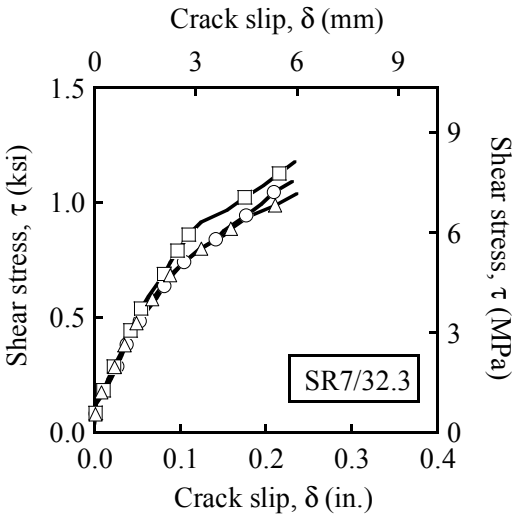

(a) Typical plots of τ versus δ

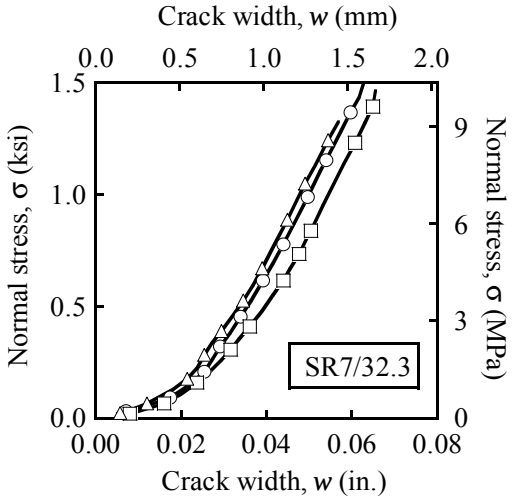

(b) Typical plot of σ versus *w*

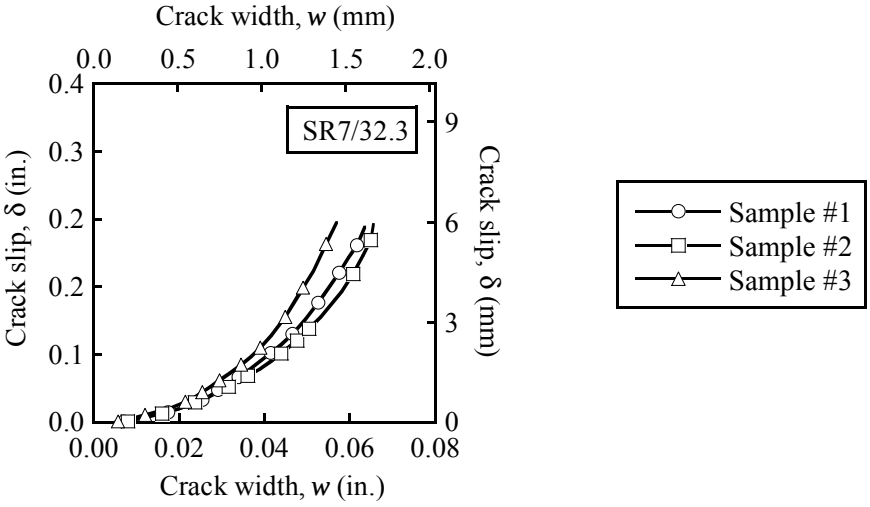

(c) Typical plot of *w* versus δ

Figure 6.1. Typical Plots of Measured Parameters.

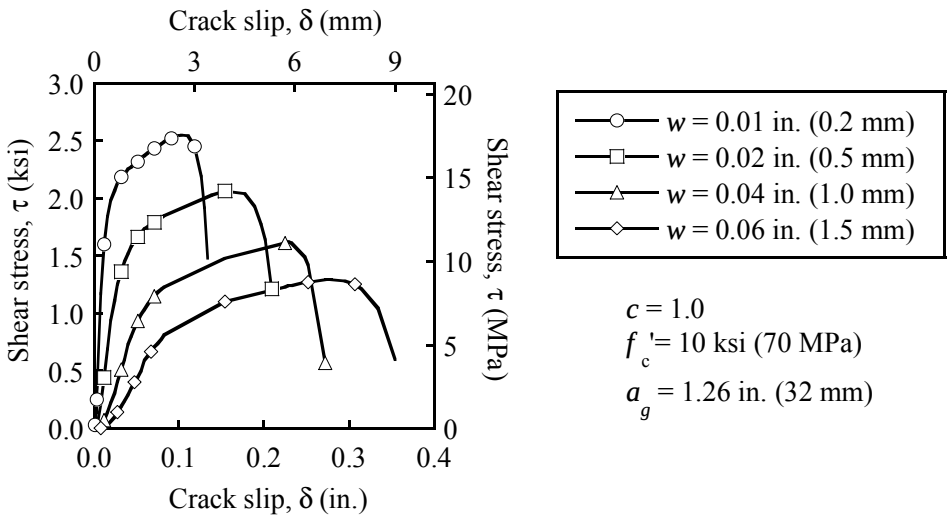

Figure 6.2. Crack Slip Model Based on Walraven's Test Results (Adapted from Data of Walraven and Reinhardt 1981).

Figure 6.3 shows various parameters to estimate normal and shear stresses with geometric contact areas between facing crack surfaces. These normal stresses and shear stresses can be theoretically expressed as follows (Walraven and Reinhardt 1981, Walraven and Stroband 1994):

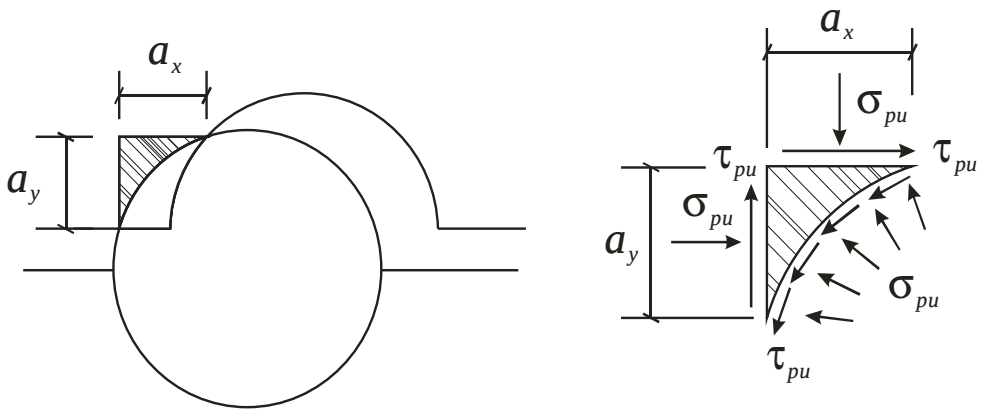

Figure 6.3. Schematic of Aggregate Interlock from Walraven's Theory (Walraven and Reinhardt 1981).

$$\sigma = c\,\sigma_{pu}\,(A_x - \mu\,A_y) \tag{6.1}$$

$$\tau = c\,\sigma_{pu}\,(A_y + \mu\,A_x) \tag{6.2}$$

where σ_{pu} is the strength of the paste, μ is the coefficient of friction, c is the fracture reduction factor, and A_x and A_y are contact areas of integration for a_x and a_y, respectively (see Figure 6.3). The detail equations to estimate A_x and A_y are presented in Appendix B. Contact areas are a function of crack width, crack slip, and coarse aggregate configurations (for example, distribution of size of aggregate, volume of aggregate p_k, and maximum size of aggregate a_g). The ratio of shear stress to normal stress, τ/σ, can be normalized as follows:

$$\frac{\tau}{\sigma} = \frac{(A_y + \mu\,A_x)}{(A_x - \mu\,A_y)} \tag{6.3}$$

Therefore, plots of τ/σ versus w provide an assessment of the aggregate interlock excluding the effect of σ_{pu} and c. Figure 6.4 shows the typical plot of τ/σ versus w of the SR/32.3 mixture. The parameters σ_{pu} and c describe the initial conditions of aggregate interlock before the initiation of slippage, where c is determined by the fracture of aggregate during precracking and σ_{pu} is the paste strength, which is a function of compressive strength. In other words, these plots show that aggregate interlock changes as crack width increases. However, there is no information for crack slip, δ, in the plot of τ/σ versus w. Therefore, an energy absorption concept is proposed below to provide a more comprehensive approach for evaluating aggregate interlock.

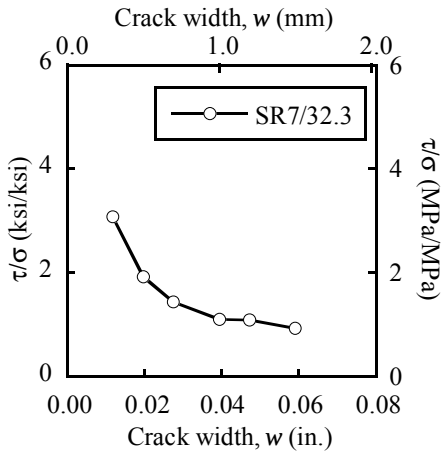

Figure 6.4. Typical Plot of τ/σ versus *w*.

6.2.2 Indication of Energy Absorption due to Aggregate Interlock

The equivalent shear strength divided by the equivalent normal strength provides a quantifiable comparative assessment of the amount of normalized absorbed energy due to aggregate interlock up to a certain limit of slip, δ'. Barragan *et al.* (2006) introduced the concept of equivalent shear strength in the push-off test in a recent study on steel fiber-reinforced concrete. A simple approach to evaluate aggregate interlock is to determine equivalent shear strength (V_{eq}), defined as the area under the $\tau-\delta$ curve divided by the slip limit as shown in Figure 6.5 and Equation 6.4.

$$V_{eq}(\delta') = \frac{\int_0^{\delta'} \tau(\delta)\, d\delta}{\delta'} \tag{6.4}$$

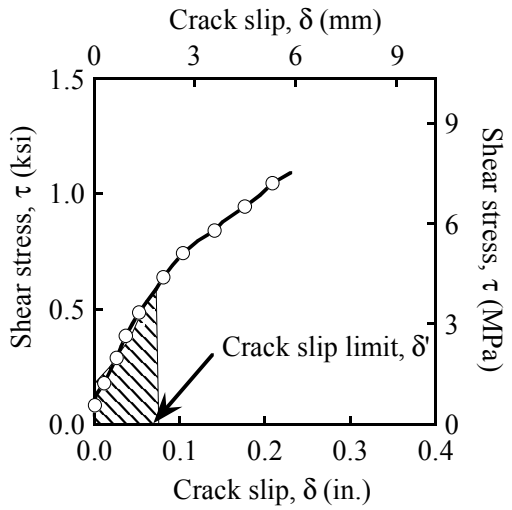

Figure 6.5. Definition of Equivalent Shear Strength.

To normalize these values, the equivalent shear strength (V_{eq}) can be divided by the equivalent normal strength (N_{eq}), defined as the area under the σ–δ curve, divided by the slip limit, as expressed in Equation 6.5.

$$N_{eq}(\delta') = \frac{\int_0^{\delta'} \sigma(\delta)\, d\delta}{\delta'} \tag{6.5}$$

The result is $E(\delta')$ determined in Equation 6.6, which provides an indication of the energy absorption due to aggregate interlock.

$$E(\delta') = \frac{V_{eq}(\delta')}{N_{eq}(\delta')} \tag{6.6}$$

Higher values of $E(\delta')$ indicate higher contributions of aggregate interlock. Mean E-values determined for the push-off test specimens are presented in the following section.

6.3 EVALUATION OF AGGREGATE INTERLOCK

6.3.1 Shear-to-Normal Stress Ratio versus Crack Width

Figure 6.6 shows results from CC and SCC tests for different release strengths and aggregate types and for crack widths of 0.01 to 0.06 in. (0.3 to 1.5 mm). Higher stress ratios represent higher aggregate interlock at a given crack width.

Tables 6.3 to 6.6 also provide the values of shear stress, normal stress, and the shear-to-normal stress ratio for each sample. In general, the CC samples exhibit higher mean τ/σ values compared to SCC samples for all mixtures. For all mixtures, as the crack width increased the stress ratio decreased. For the river gravel mixtures, when the crack width reached about 0.06 in. (1.5 mm), the values of the stress ratio converged at approximately 1.0, indicating that there is no distinction between aggregate interlock for the river gravel mixtures. Therefore, a crack width value of 0.06 in. (1.5 mm) is reasonable to evaluate aggregate interlock for different river gravel mixture proportions. However, limestone mixture proportions reached the experimentally defined maximum crack slip, δ, of 0.24 in. (6 mm) before reaching a crack width larger than 0.04 in. (1 mm).

For both SCC and CC, the aggregate type has a significant influence on absolute values and decay of the slopes. River gravel exhibits higher values of τ/σ compared to limestone aggregate. As the crack width increases, the fracture of river gravel clearly progresses, resulting in decreasing τ/σ values. However, most limestone aggregates contributing to aggregate interlock fracture before reaching a crack width of 0.04 in. (1.0 mm). After reaching a crack width of 0.04 in. (1.0 mm), the progression of the limestone aggregate fracture is nearly nondistinguishable, indicating that the precracking likely fractured the large majority of the coarse limestone aggregate.

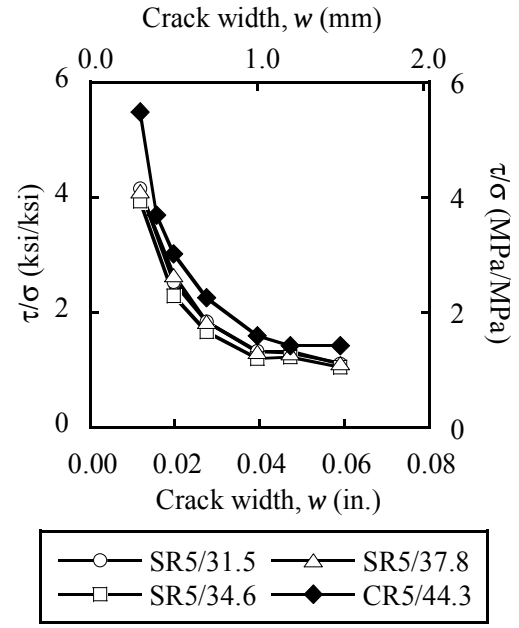

(a) 5 ksi (34 MPa) River Gravel

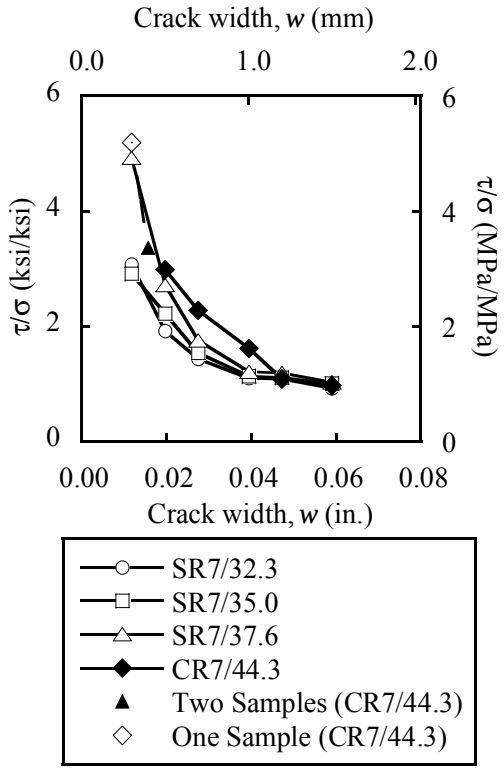

(b) 7 ksi (48 MPa) River Gravel

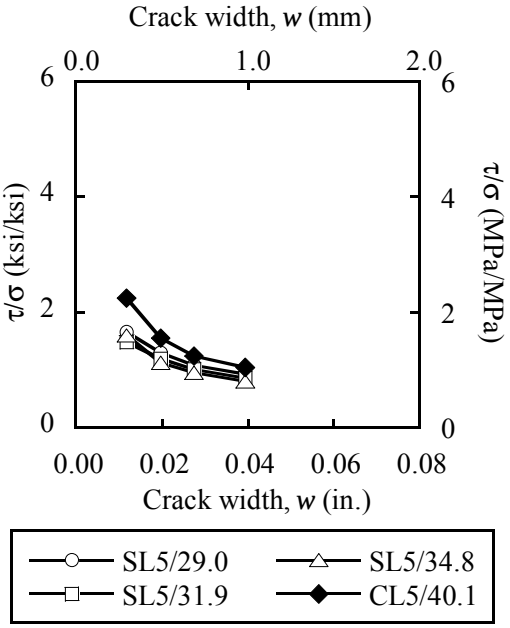

(c) 5 ksi (34 MPa) Limestone

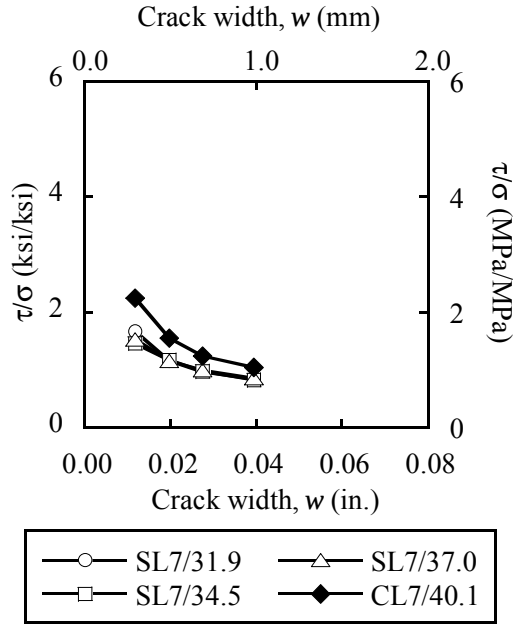

(d) 7 ksi (48 MPa) Limestone

Note: Data are evaluated with the mean value of three samples, except as noted.

Figure 6.6. Plot of Mean Shear-to-Normal Stress Ratio versus Crack Width.

Table 6.3. Summary of Test Results (5 ksi [34 MPa] SCC and CC River Gravel).

Description	w, in. (mm)	Sample #1			Sample #2			Sample #3			Mean	Std.Dev.
		σ, MPa (ksi)	τ, MPa (ksi)	τ/σ, ksi/ksi (MPa/MPa)	σ, MPa (ksi)	τ, MPa (ksi)	τ/σ, ksi/ksi (MPa/MPa)	σ, MPa (ksi)	τ, MPa (ksi)	τ/σ, ksi/ksi (MPa/MPa)	τ/σ, ksi/ksi (MPa/MPa)	τ/σ, ksi/ ksi (MPa/MPa)
SR5/31.5	0.01 (0.30)	0.30 (0.04)	1.50 (0.22)	5.08	0.17 (0.02)	0.62 (0.09)	3.63	0.54 (0.08)	2.05 (0.30)	3.77	4.16	0.80
	0.02 (0.50)	0.71 (0.10)	2.06 (0.30)	2.90	0.42 (0.06)	1.06 (0.15)	2.50	1.11 (0.16)	2.43 (0.35)	2.19	2.53	0.36
	0.03 (0.70)	1.32 (0.19)	2.64 (0.38)	2.01	0.76 (0.11)	1.44 (0.21)	1.89	1.96 (0.28)	3.13 (0.45)	1.60	1.83	0.21
	0.04 (1.00)	2.93 (0.42)	4.15 (0.60)	1.41	1.68 (0.24)	2.37 (0.34)	1.41	3.95 (0.57)	4.60 (0.67)	1.16	1.33	0.14
	0.05 (1.20)	2.92 (0.42)	4.21 (0.61)	1.44	2.29 (0.33)	3.09 (0.45)	1.35	4.95 (0.72)	6.00 (0.87)	1.21	1.33	0.12
	0.06 (1.50)	5.67 (0.82)	6.70 (0.97)	1.18	3.92 (0.57)	4.34 (0.63)	1.11	7.54 (1.09)	7.82 (1.13)	1.04	1.11	0.07
SR5/34.6	0.01 (0.30)	0.86 (0.12)	3.80 (0.55)	4.42	0.46 (0.07)	1.59 (0.23)	3.44	0.48 (0.07)	1.87 (0.27)	3.93	3.93	0.49
	0.02 (0.50)	2.22 (0.32)	5.06 (0.73)	2.28	0.92 (0.13)	2.06 (0.30)	2.23	1.09 (0.16)	2.56 (0.37)	2.36	2.29	0.07
	0.03 (0.70)	4.05 (0.59)	6.35 (0.92)	1.57	1.76 (0.26)	3.10 (0.45)	1.77	2.12 (0.31)	3.51 (0.51)	1.66	1.66	0.10
	0.04 (1.00)	7.13 (1.03)	8.36 (1.21)	1.17	4.62 (0.67)	5.57 (0.81)	1.21	4.32 (0.63)	5.30 (0.77)	1.23	1.20	0.03
	0.05 (1.20)	8.04 (1.17)	9.58 (1.39)	1.19	5.81 (0.84)	7.27 (1.05)	1.25	5.37 (0.78)	6.52 (0.95)	1.21	1.22	0.03
	0.06 (1.50)	10.53 (1.53)	11.66 (1.69)	1.11	8.62 (1.25)	9.16 (1.33)	1.06	8.02 (1.16)	7.94 (1.15)	0.99	1.05	0.06
SR5/37.8	0.01 (0.30)	0.42 (0.06)	1.95 (0.28)	4.60	0.18 (0.03)	0.55 (0.08)	3.06	0.52 (0.08)	2.40 (0.35)	4.64	4.10	0.90
	0.02 (0.50)	0.91 (0.13)	2.48 (0.36)	2.72	0.45 (0.07)	1.19 (0.17)	2.63	1.17 (0.17)	3.00 (0.44)	2.57	2.64	0.07
	0.03 (0.70)	2.29 (0.33)	3.85 (0.56)	1.68	0.85 (0.12)	1.66 (0.24)	1.96	2.03 (0.29)	3.79 (0.55)	1.86	1.83	0.14
	0.04 (1.00)	4.77 (0.69)	6.21 (0.90)	1.30	2.03 (0.29)	2.75 (0.40)	1.35	4.26 (0.62)	5.56 (0.81)	1.30	1.32	0.03
	0.05 (1.20)	5.88 (0.85)	7.54 (1.09)	1.28	2.75 (0.40)	3.58 (0.52)	1.30	5.15 (0.75)	6.67 (0.97)	1.29	1.29	0.01
	0.06 (1.50)	8.45 (1.23)	9.41 (1.36)	1.11	4.57 (0.66)	5.05 (0.73)	1.10	7.36 (1.07)	8.45 (1.23)	1.15	1.12	0.02
CR5/44.3	0.01 (0.30)	0.33 (0.05)	1.23 (0.18)	3.76	0.46 (0.07)	0.27 (0.04)	0.59	0.27 (0.04)	1.92 (0.28)	7.22	5.49	3.31
	0.02 (0.50)	0.47 (0.07)	1.60 (0.23)	3.43	0.57 (0.08)	1.11 (0.16)	1.95	0.38 (0.06)	2.14 (0.31)	5.68	3.68	1.88
	0.03 (0.70)	0.65 (0.09)	1.76 (0.26)	2.71	0.73 (0.11)	1.48 (0.21)	2.03	0.54 (0.08)	2.36 (0.34)	4.33	3.02	1.18
	0.04 (1.00)	1.06 (0.15)	2.18 (0.32)	2.05	1.18 (0.17)	2.17 (0.31)	1.84	0.98 (0.14)	2.81 (0.41)	2.88	2.26	0.55
	0.05 (1.20)	2.07 (0.30)	3.09 (0.45)	1.50	2.22 (0.32)	3.44 (0.50)	1.55	2.34 (0.34)	4.06 (0.59)	1.73	1.59	0.13
	0.06 (1.50)	2.80 (0.41)	3.90 (0.57)	1.39	2.87 (0.42)	4.03 (0.58)	1.40	3.37 (0.49)	4.87 (0.71)	1.45	1.42	0.03
	0.01 (0.30)	5.26 (0.76)	5.44 (0.79)	1.03	4.39 (0.64)	4.82 (0.70)	1.10	5.69 (0.83)	6.96 (1.01)	1.22	1.12	0.10

Table 6.4. Summary of Test Results (7 ksi [48 MPa] SCC and CC River Gravel).

Description	*w*, in. (mm)	Sample #1			Sample #2			Sample #3			Average	Std. Dev.
		σ, MPa (ksi)	τ, MPa (ksi)	τ/σ, ksi/ksi (MPa/MPa)	σ, MPa (ksi)	τ, MPa (ksi)	τ/σ, ksi/ksi (MPa/MPa)	σ, MPa (ksi)	τ, MPa (ksi)	τ/σ, ksi/ksi (MPa/MPa)	τ/σ, ksi/ksi (MPa/MPa)	τ/σ, ksi/ ksi (MPa/MPa)
SR7/32.3	0.01 (0.30)	0.35 (0.05)	1.02 (0.15)	2.96	0.29 (0.04)	1.07 (0.16)	3.74	0.48 (0.07)	1.21 (0.18)	2.53	3.07	0.61
	0.02 (0.50)	0.75 (0.11)	1.43 (0.21)	1.91	0.74 (0.11)	1.60 (0.23)	2.15	1.05 (0.15)	1.78 (0.26)	1.70	1.92	0.23
	0.03 (0.70)	1.68 (0.24)	2.36 (0.34)	1.41	1.53 (0.22)	2.46 (0.36)	1.60	2.35 (0.34)	3.00 (0.44)	1.27	1.43	0.16
	0.04 (1.00)	3.85 (0.56)	4.09 (0.59)	1.06	3.40 (0.49)	4.15 (0.60)	1.22	4.73 (0.69)	4.76 (0.69)	1.00	1.10	0.11
	0.05 (1.20)	4.87 (0.71)	5.19 (0.75)	1.06	4.39 (0.64)	5.40 (0.78)	1.23	5.93 (0.86)	5.84 (0.85)	0.99	1.09	0.12
	0.06 (1.50)	7.28 (1.06)	6.76 (0.98)	0.93	7.09 (1.03)	6.82 (0.99)	0.96	8.49 (1.23)	7.43 (1.08)	0.88	0.92	0.04
SR7/35.0	0.01 (0.30)	0.37 (0.05)	1.02 (0.15)	2.77	0.09 (0.01)	0.25 (0.44)	2.83	0.39 (0.06)	1.23 (0.18)	3.13	2.91	0.19
	0.02 (0.50)	1.05 (0.15)	1.94 (0.28)	1.84	0.33 (0.05)	0.94 (0.14)	2.88	1.14 (0.17)	2.18 (0.32)	1.92	2.21	0.58
	0.03 (0.70)	2.16 (0.31)	2.95 (0.43)	1.36	0.80 (0.12)	1.55 (0.22)	1.94	2.46 (0.36)	3.23 (0.47)	1.31	1.54	0.35
	0.04 (1.00)	4.37 (0.63)	4.85 (0.70)	1.11	2.20 (0.32)	2.81 (0.41)	1.28	5.21 (0.76)	5.18 (0.75)	0.99	1.13	0.14
	0.05 (1.20)	5.17 (0.75)	5.80 (0.84)	1.12	3.22 (0.47)	3.91 (0.57)	1.21	6.42 (0.93)	6.42 (0.93)	1.00	1.11	0.11
	0.06 (1.50)	7.17 (1.04)	7.33 (1.06)	1.02	5.52 (0.80)	5.58 (0.81)	1.01	9.28 (1.35)	8.90 (1.29)	0.96	1.00	0.03
SR7/37.6	0.01 (0.30)	0.18 (0.03)	1.61 (0.23)	9.11	0.18 (0.03)	0.58 (0.08)	3.20	0.14 (0.02)	0.34 (0.05)	2.46	4.92	3.65
	0.02 (0.50)	0.63 (0.09)	2.37 (0.34)	3.73	0.46 (0.07)	1.08 (0.16)	2.36	0.42 (0.06)	0.85 (0.12)	2.06	2.71	0.89
	0.03 (0.70)	1.70 (0.25)	3.01 (0.44)	1.78	0.84 (0.12)	1.59 (0.23)	1.89	0.88 (0.13)	1.42 (0.21)	1.61	1.76	0.14
	0.04 (1.00)	3.80 (0.55)	4.39 (0.64)	1.15	2.09 (0.30)	2.90 (0.42)	1.39	3.10 (0.45)	3.34 (0.48)	1.08	1.20	0.16
	0.05 (1.20)	4.99 (0.72)	5.58 (0.81)	1.12	2.95 (0.43)	4.00 (0.58)	1.36	4.85 (0.70)	5.33 (0.77)	1.10	1.19	0.14
	0.06 (1.50)	7.75 (1.12)	7.63 (0.11)	0.98	4.98 (0.72)	5.54 (0.80)	1.11	7.89 (1.14)	7.57 (1.10)	0.96	1.02	0.08
CR7/44.3	0.01 (0.30)	-	-	-	0.20 (0.03)	1.05 (0.15)	5.20	-	-	-	5.20	2.15
	0.02 (0.50)	0.18 (0.03)	0.58 (0.08)	3.32	0.37 (0.05)	1.25 (0.18)	3.40	-	-	-	3.36	0.06
	0.03 (0.70)	0.23 (0.03)	0.93 (0.13)	3.97	0.55 (0.08)	1.51 (0.22)	2.73	0.33 (0.05)	0.74 (0.11)	2.25	2.98	0.88
	0.04 (1.00)	0.45 (0.07)	1.20 (0.17)	2.70	0.97 (0.14)	1.95 (0.28)	2.01	0.62 (0.09)	1.33 (0.19)	2.13	2.28	0.37
	0.05 (1.20)	0.90 (0.13)	1.65 (0.24)	1.84	2.01 (0.29)	3.05 (0.44)	1.52	1.28 (0.19)	1.92 (0.28)	1.50	1.62	0.19
	0.06 (1.50)	1.06 (0.15)	2.00 (0.29)	1.89	2.70 (0.39)	3.88 (0.56)	1.44	1.64 (0.24)	2.41 (0.35)	1.15	1.09	0.37
	0.01 (0.30)	1.76 (0.26)	2.58 (0.37)	1.46	4.42 (0.64)	5.19 (0.75)	1.18	2.74 (0.40)	3.42 (0.50)	1.01	0.97	0.23

Table 6.5. Summary of Test Results (5 ksi [34 MPa] SCC and CC Limestone).

Description	*w*, in. (mm)	Sample #1			Sample #2			Sample #3			Average	Std. Dev.
		σ, MPa (ksi)	τ, MPa (ksi)	τ/σ, ksi/ksi (MPa/ MPa)	σ, MPa (ksi)	τ, MPa (ksi)	τ/σ, ksi/ksi (MPa/ MPa)	σ, MPa (ksi)	τ, MPa (ksi)	τ/σ, ksi/ksi (MPa/ MPa)	τ/σ, ksi/ksi (MPa/MPa)	τ/σ, ksi/ ksi (MPa/MPa)
SL5/29.0	0.01 (0.30)	0.25 (0.04)	0.43 (0.06)	1.68	0.67 (0.10)	0.94 (0.14)	1.40	0.51 (0.07)	0.96 (0.14)	1.88	1.66	0.24
	0.02 (0.50)	0.69 (0.10)	0.93 (0.13)	1.35	1.48 (0.21)	1.65 (0.24)	1.11	1.63 (0.24)	2.32 (0.34)	1.43	1.29	0.17
	0.03 (0.70)	1.38 (0.20)	1.50 (0.22)	1.09	2.75 (0.40)	2.59 (0.38)	0.94	3.22 (0.47)	3.85 (0.56)	1.20	1.08	0.13
	0.04 (1.00)	3.09 (0.45)	2.81 (0.41)	0.91	5.24 (0.76)	4.43 (0.64)	0.84	5.96 (0.86)	6.12 (0.89)	1.03	0.93	0.09
	0.05 (1.20)	4.01 (0.58)	3.73 (0.54)	0.93	5.99 (0.87)	5.81 (0.84)	0.97	6.90 (1.00)	7.66 (1.11)	1.11	1.00	0.09
	0.06 (1.50)	-	-	-	-	-	-	-	-	-	-	-
SL5/31.9	0.01 (0.30)	0.29 (0.04)	0.35 (0.05)	1.20	0.57 (0.08)	0.88 (0.13)	1.53	0.41 (0.06)	0.69 (0.10)	1.70	1.48	0.25
	0.02 (0.50)	0.84 (0.12)	1.02 (0.15)	1.22	1.45 (0.21)	1.62 (0.23)	1.12	1.16 (0.17)	1.42 (0.21)	1.23	1.19	0.06
	0.03 (0.70)	1.75 (0.25)	1.75 (0.25)	1.00 (1.00)	2.94 (0.43)	2.86 (0.41)	0.97	2.13 (0.31)	2.21 (0.32)	1.04	1.00	0.03
	0.04 (1.00)	3.69 (0.54)	3.19 (0.46)	0.86 (0.86)	5.68 (0.82)	4.65 (0.67)	0.82	3.93 (0.57)	3.48 (0.50)	0.89	0.86	0.03
	0.05 (1.20)	4.53 (0.66)	4.11 (0.60)	0.91 (0.91)	6.50 (0.94)	5.80 (0.84)	0.89	4.73 (0.69)	4.65 (0.67)	0.98	0.93	0.05
	0.06 (1.50)	-	-	-	-	-	-	-	-	-	-	-
SL5/34.8	0.01 (0.30)	0.50 (0.07)	0.73 (0.11)	1.47 (0.47)	0.72 (0.10)	1.14 (0.17)	1.58	0.76 (0.11)	1.33 (0.19)	1.75	1.60	0.14
	0.02 (0.50)	0.95 (0.14)	1.03 (0.15)	1.09 (1.09)	1.76 (0.26)	1.92 (0.28)	1.09	2.13 (0.31)	2.53 (0.37)	1.19	1.12	0.06
	0.03 (0.70)	1.81 (0.26)	1.68 (0.24)	0.93 (0.93)	3.13 (0.45)	2.84 (0.41)	0.91	3.92 (0.57)	3.90 (0.57)	0.99	0.94	0.05
	0.04 (1.00)	3.65 (0.53)	2.90 (0.42)	0.79 (0.79)	5.48 (0.79)	4.14 (0.60)	0.76	6.85 (0.99)	5.76 (0.84)	0.84	0.80	0.04
	0.05 (1.20)	4.24 (0.61)	3.69 (0.54)	0.87 (0.87)	6.15 (0.89)	4.96 (0.72)	0.81	7.64 (1.11)	7.00 (1.02)	0.92	0.86	0.06
	0.06 (1.50)	-	-	-	-	-	-	-	-	-	-	-
CL5/40.1	0.01 (0.30)	0.41 (0.06)	0.99 (0.14)	2.40 (2.40)	0.31 (0.04)	0.65 (0.09)	2.07	0.34 (0.05)	0.98 (0.14)	2.90	2.24	0.42
	0.02 (0.50)	0.85 (0.12)	1.31 (0.19)	1.53 (1.53)	0.62 (0.09)	0.97 (0.14)	1.56	0.69 (0.10)	1.26 (0.18)	1.83	1.54	0.17
	0.03 (0.70)	1.39 (0.20)	1.68 (0.24)	1.21 (1.21)	1.07 (0.16)	1.35 (0.20)	1.26	1.37 (0.20)	1.86 (0.27)	1.36	1.23	0.08
	0.04 (1.00)	2.80 (0.41)	2.77 (0.40)	0.99 (0.99)	2.28 (0.33)	2.47 (0.36)	1.08	2.71 (0.39)	2.94 (0.43)	1.09	1.04	0.05
	0.05 (1.20)	3.66 (0.53)	3.72 (0.54)	1.02 (1.02)	3.11 (0.45)	3.43 (0.50)	1.10	3.17 (0.46)	3.64 (0.53)	1.15	1.06	0.07
	0.06 (1.50)	5.94 (0.86)	5.59 (0.81)	0.94 (0.94)	4.88 (0.71)	4.65 (0.67)	0.95	4.49 (0.65)	4.54 (0.66)	1.01	0.95	0.04

Table 6.6. Summary of Test Results (7 ksi [48 MPa] SCC and CC Limestone).

Description	*w*, in. (mm)	Sample #1			Sample #2			Sample #3			Average	Std. Dev.
		σ, MPa (ksi)	τ, MPa (ksi)	τ/σ, ksi/ksi (MPa/MPa)	σ, MPa (ksi)	τ, MPa (ksi)	τ/σ, ksi/ksi (MPa/MPa)	σ, MPa (ksi)	τ, MPa (ksi)	τ/σ, ksi/ksi (MPa/MPa)	τ/σ, ksi/ksi (MPa/MPa)	τ/σ, ksi/ ksi (MPa/MPa)
SL7/31.9	0.01 (0.30)	0.28 (0.04)	0.49 (0.07)	1.75	0.48 (0.07)	0.76 (0.11)	1.57	0.58 (0.08)	0.96 (0.14)	1.66	1.66	0.09
	0.02 (0.50)	0.77 (0.11)	0.95 (0.14)	1.23	1.05 (0.15)	1.19 (0.17)	1.14	1.31 (0.19)	1.41 (0.20)	1.08	1.15	0.08
	0.03 (0.70)	1.60 (0.23)	1.60 (0.23)	1.00	1.91 (0.28)	1.90 (0.28)	0.99	2.96 (0.43)	2.58 (0.37)	0.87	0.96	0.07
	0.04 (1.00)	3.58 (0.52)	3.00 (0.44)	0.84	3.66 (0.53)	3.24 (0.47)	0.88	5.69 (0.83)	4.46 (0.65)	0.78	0.84	0.05
	0.05 (1.20)	4.52 (0.66)	4.02 (0.58)	0.89	4.51 (0.65)	4.33 (0.63)	0.96	6.53 (0.95)	5.68 (0.82)	0.87	0.91	0.05
	0.06 (1.50)	-	-	-	-	-	-	-	-	-	-	-
SL7/34.5	0.01 (0.30)	0.34 (0.05)	0.49 (0.07)	1.43	0.58 (0.08)	0.77 (0.11)	1.32	0.62 (0.09)	1.02 (0.15)	1.63	1.46	0.16
	0.02 (0.50)	0.71 (0.10)	0.88 (0.13)	1.25	1.31 (0.19)	1.40 (0.20)	1.06	1.45 (0.21)	1.71 (0.25)	1.18	1.16	0.09
	0.03 (0.70)	1.51 (0.22)	1.52 (0.22)	1.01	2.44 (0.35)	2.28 (0.33)	0.93	2.65 (0.38)	2.59 (0.38)	0.98	0.97	0.04
	0.04 (1.00)	3.46 (0.50)	2.81 (0.41)	0.81	4.73 (0.69)	3.77 (0.55)	0.80	5.08 (0.74)	4.23 (0.61)	0.83	0.81	0.02
	0.05 (1.20)	4.61 (0.67)	3.94 (0.57)	0.85	5.60 (0.81)	4.84 (0.70)	0.87	5.96 (0.86)	5.44 (0.79)	0.91	0.88	0.03
	0.06 (1.50)	-	-	-	-	-	-	-	-	-	-	-
SL7/37.0	0.01 (0.30)	0.70 (0.10)	1.01 (0.15)	1.45	0.56 (0.08)	0.82 (0.12)	1.47	0.49 (0.07)	0.82 (0.12)	1.65	1.53	0.11
	0.02 (0.50)	1.35 (0.20)	1.52 (0.22)	1.13	1.07 (0.16)	1.19 (0.17)	1.11	0.99 (0.14)	1.22 (0.18)	1.24	1.16	0.07
	0.03 (0.70)	2.31 (0.34)	2.29 (0.33)	0.99	1.97 (0.29)	1.85 (0.27)	0.94	1.88 (0.27)	1.98 (0.29)	1.05	1.00	0.06
	0.04 (1.00)	4.41 (0.64)	3.66 (0.53)	0.83	4.30 (0.62)	3.54 (0.51)	0.82	3.57 (0.52)	3.24 (0.47)	0.91	0.85	0.05
	0.05 (1.20)	5.13 (0.74)	4.61 (0.67)	0.90	5.22 (0.76)	4.67 (0.68)	0.90	4.23 (0.61)	4.18 (0.61)	0.99	0.93	0.05
	0.06 (1.50)	-	-	-	-	-	-	-	-	-	-	-
CL7/40.1	0.01 (0.30)	0.41 (0.06)	0.99 (0.14)	2.40	0.31 (0.04)	0.65 (0.09)	2.07	0.34 (0.14)	0.98 (0.14)	2.90	2.24	0.42
	0.02 (0.50)	0.85 (0.12)	1.31 (0.19)	1.53	0.62 (0.09)	0.97 (0.14)	1.56	0.69 (0.18)	1.26 (0.18)	1.83	1.54	0.17
	0.03 (0.70)	1.39 (0.20)	1.68 (0.24)	1.21	1.07 (0.16)	1.35 (0.20)	1.26	1.37 (0.27)	1.86 (0.27)	1.36	1.23	0.08
	0.04 (1.00)	2.80 (0.41)	2.77 (0.40)	0.99	2.28 (0.33)	2.47 (0.36)	1.08	2.71 (0.43)	2.94 (0.43)	1.09	1.04	0.05
	0.05 (1.20)	3.66 (0.53)	3.72 (0.54)	1.02	3.11 (0.45)	3.43 (0.50)	1.10	3.17 (0.53)	3.64 (0.53)	1.15	1.06	0.07
	0.06 (1.50)	5.94 (0.86)	5.59 (0.81)	0.94	4.88 (0.71)	4.65 (0.67)	0.95	4.49 (0.66)	4.54 (0.66)	1.01	0.95	0.04

6.3.2 Energy Absorption (*E* –Value) versus Crack Slip

The *E*-values of all mixtures are presented in Appendix C. Figure 6.7 shows *E*-values for all mixtures corresponding to a crack slip of 0.02 in. (0.5 mm). Each bar of the chart shows the mean *E*-value and standard deviation from three samples. The CC mixtures, with a higher volume of coarse aggregate, tend to have a higher *E*-value relative to the SCC mixtures with the same 16-hr target strength and aggregate type. The exception is for the 7 ksi (48 MPa) release strength mixtures containing river gravel. The 5 ksi (34 MPa) release strength mixtures containing river gravel have higher mean *E*-values compared with other mixtures. The aggregate type also significantly affects the mean *E*-value at the specified crack slip of 0.02 in. (0.5 mm). Figure 6.8 shows *E*-value results from the push-off tests for the different release strengths and aggregate types as a function of the crack slip limit, δ'. Figure 6.8 indicates that for lower crack slip values, CC has higher mean *E*-values compared. The exception is the 7 ksi (48 MPa) release strength mixture containing river gravel where the values are similar. The lower *E*-value for the 7 ksi (48 MPa) release strength CC mixture containing river gravel is likely a result of the higher precracking load and the corresponding larger initial precrack width [> 0.01 in. (0.3 mm)]. For both SCC and CC mixtures, the aggregate type has a significant influence on shear capacity. River gravel increases the contribution to shear compared with limestone aggregate. However, the effect of the volume of aggregate on the aggregate interlock is not clear. Therefore, statistical methods are used to evaluate the effect of the volume of coarse aggregate on the aggregate interlock. These results are discussed in Section 6.3.3.

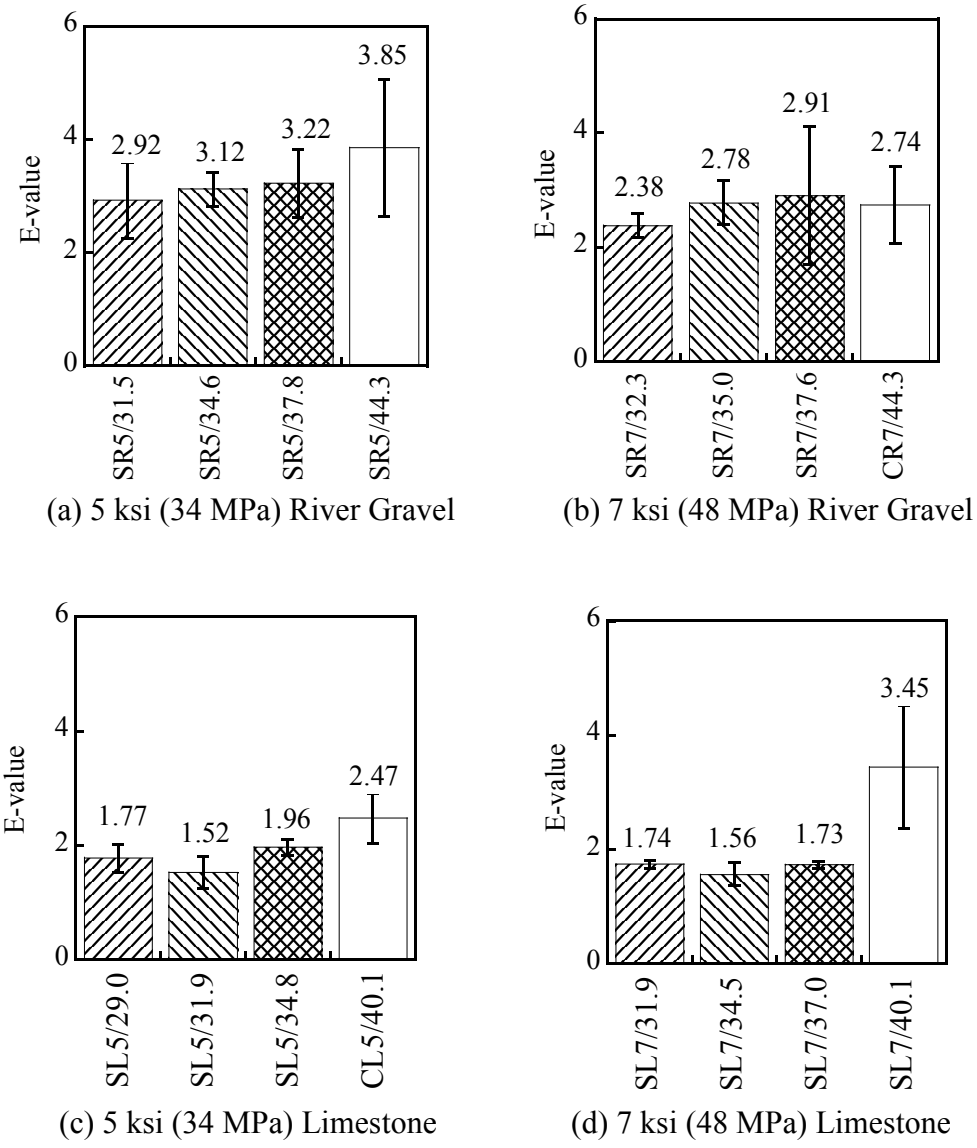

(a) 5 ksi (34 MPa) River Gravel

(b) 7 ksi (48 MPa) River Gravel

(c) 5 ksi (34 MPa) Limestone

(d) 7 ksi (48 MPa) Limestone

Figure 6.7. Plot of Mean *E*-value by Mixture Type (δ' = 0.02 in. [0.5 mm]).

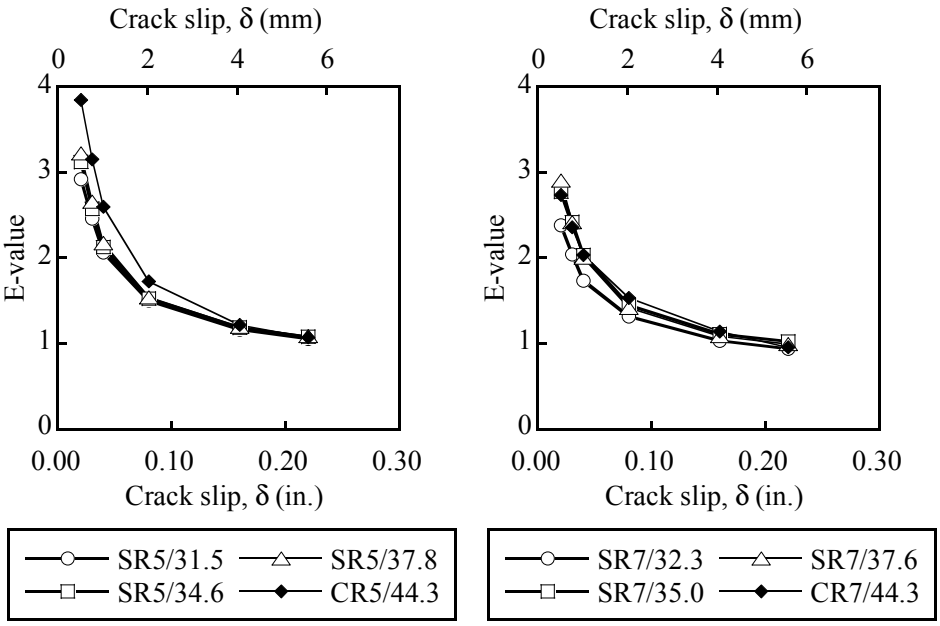

(a) 5 ksi (34 MPa) River Gravel (b) 7 ksi (48 MPa) River Gravel

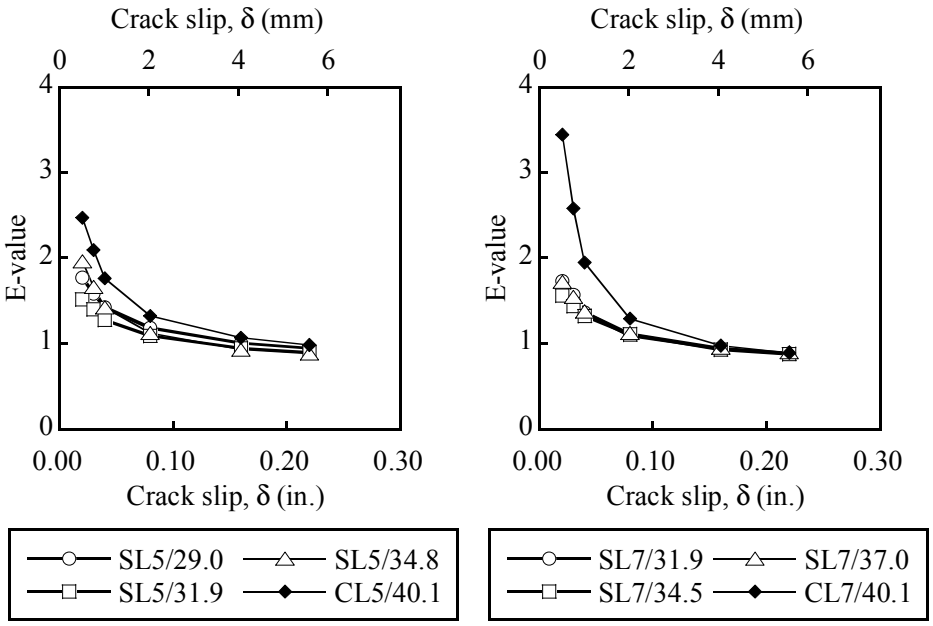

(c) 5 ksi (34 MPa) Limestone (d) 7 ksi (48 MPa) Limestone

Figure 6.8. Plot of Mean *E*-value versus Crack Slip.

Figure 6.9 shows a comparison of the crack plane for river gravel and limestone mixtures after the push-off tests. As discussed for the STS results (Section 5.5.1), the river gravel mixtures have rougher crack planes. The crack plane after the precracking test resembles that of the STS samples in terms of roughness of the crack plane surface. The profiles of the crack planes after the push-off tests changed because of the fracture of protruded aggregates and paste along the sliding planes. Similarly, the river gravel mixtures have higher profiles of roughness than limestone mixtures. Because it is difficult to quantify the roughness of the shear planes, the relationship between crack width and slip can be used to infer the initial condition of roughness of the shear plane. The roughness of the crack plane associated with the degree of aggregate fracture is presented in Section 6.4.1. During the push-off tests, the rate of increasing slip also indicates the reduction of the roughness.

(a) River Gravel (CR5/44.3) (b) Limestone (SL7/37.0)

Figure 6.9. Observation of Shear Planes.

6.3.3 Statistical Assessment

6.3.3.1 General

Statistical analysis was performed to evaluate the effect of coarse aggregate concrete strength on the *E*-value, which provides a measure of aggregate interlock.

6.3.3.2 Effect of Coarse Aggregate

For the statistical analysis, three samples are needed for each concrete mixture. Because two samples were obtained from one batch and the third sample was obtained from the second batch. The mixed procedure is a standard linear model that can consider the random effect and fixed effect (here, the batch that depends on the mix is the random effect) using the SAS Program (v. 9.1.3) (SAS Institute 2006). The code is presented in Appendix D. The analysis was performed with repeated measured *E*-values at slips of 0.02, 0.03, 0.04, and 0.08 in. (0.5, 0.7, 1, and 2 mm). The dependency on the volume (i.e., slope) can be estimated in this analysis. Linear contrast is the slope estimate in the regression analysis. The contrast is defined as a linear combination of two or more factor level means.

The basic formula can be expressed as follows:

$$\hat{L}_V = \sum_{i=1}^{k} c_i \overline{E(\delta')_i} \tag{6.7}$$

where $\hat{L}_v$ is the contrast for the effect of volume of coarse aggregate or type of coarse aggregate on the *E*-value, the contrast is orthogonal, which indicates the sum of the products of corresponding coefficients are zero, and $\overline{E(\delta')_i}$ is the mean value of the *E*-value of the *i*th mixture at a certain slip limit, δ'.

When the dependency of the volume of coarse aggregate is considered, the coefficient corresponding to volume of coarse aggregate can be calculated as follows:

$$c_i = \frac{\left(V_i - \left(\frac{\sum_{i=1}^{j} V_i}{j}\right)\right)}{\sum_{i=1}^{j}\left(V_i - \left(\frac{\sum_{i=1}^{j} V_i}{j}\right)\right)^2} \quad \text{where } \sum_{i=1}^{j} c_i = 0 \tag{6.8}$$

where c_i is the coefficient indicating ith level of coarse aggregate volume ($0 \le c_i \le 1$), j is the total number of coarse aggregate volume levels, and V_i is the volume of coarse aggregate of the ith level (%). Standard error is calculated as follows:

$$SE\left(\hat{L}\right) = \sigma\sqrt{\sum_{i=1}^{k}\frac{c_i}{n_i}} \tag{6.9}$$

where n_i is the sample size of the ith mixture and σ is the weighted average of the sample standard deviation. For the 95 percent confidence level, the p-value (which has favored the research hypothesis, H_1, is 0.05. In other words, the maximum risk of incorrectly rejecting the null hypothesis, H_0, is 0.05. The null hypothesis, H_0, and research hypothesis, H_1, are expressed as follows:

$$H_0: L_m = 0 \text{ versus } H_1: L_m \neq 0 \tag{6.10}$$

where m is the group of mixture proportions (i.e., river gravel CC and SCC mixtures).

The contrast for the interaction between aggregate type and the volume of aggregate intends to compare the volume effect of river gravel aggregate to the volume effect of limestone aggregate.

The effect of type of coarse aggregate is checked with the following contrast:

$$\hat{L}_{G-L} = \left(\sum_{i=1}^{k} \frac{1}{k} \overline{E(\delta')} \right)_G - \left(\sum_{j=1}^{k} \frac{1}{k} \overline{E(\delta')} \right)_L \tag{6.11}$$

where $\hat{L}_{G-L}$ is the contrast for the effect of type of coarse aggregate on the E-value. $\left(\sum_{i=1}^{k} \frac{1}{k} \overline{E(\delta')} \right)_G$ is the effect of river gravel aggregate on the E-value, and $\left(\sum_{j=1}^{k} \frac{1}{k} \overline{E(\delta')} \right)_L$ is the effect of limestone aggregate on the E-value.

The contrast, $\hat{L}_{VG-VL}$, for the interaction between aggregate type and volume of aggregate intends to compare the volume effect of river gravel aggregate to the volume effect of limestone aggregate.

$$\hat{L}_{VG-VL} = \hat{L}_{VG} - \hat{L}_{VL} \tag{6.12}$$

where $\hat{L}_{VG}$ is the contrast for the effect of volume of river gravel aggregate on the E-value, $\hat{L}_{VL}$ is the contrast for the effect of volume of limestone aggregate on the E-value.

Table 6.7 shows a summary of the mixed procedure for specific slip values. Table 6.8 shows the summary of the mixed procedure with the repeated measure across the slips.

As shown in Table 6.7, the effect of type of coarse aggregate on E-value seems to be significant at all slip ranges from 0.02 to 0.22 in. (0.5 to 5.5 mm). On the other hand, the volume effect seems to be a significant effect for both river gravel and limestone at the smaller slip range of 0.02 to 0.08 in. (0.5 to 2.0 mm) based on the p-value of 0.05 except for river gravel at the slip of 0.02 in. (0.5 mm). However, an increase in slip to more than 0.16 in. (4.0 mm) significantly reduces the effect of volume of coarse aggregate for river gravel and limestone mixtures.

As shown in Table 6.8, the effect of type of coarse aggregate can be significant at the p-value of 0.05 in the overall comparison from the slip range from 0.02 to 0.22 in. (0.5 to 5.5 mm). The volume effect of coarse aggregate is a significant effect at the p-value of 0.05. According to the p-value of $\hat{L}_{VG-VL}$, the difference between volume effect at river gravel aggregate and the volume effect at limestone aggregate cannot be clearly found at the p-value of 0.05.

Table 6.7. Summary of Results of Contrast at Individual Slip Values.

Contrast	Purpose	Slip, δ' , in.(mm)	Estimates	Standard Error	*p*-value
$\hat{L}_{G-L}$	Effect of Type of Coarse Aggregate	0.02 (0.5)	1.0998	0.1768	<0.0001
		0.03 (0.7)	0.8811	0.1087	<0.001
		0.04 (1.0)	0.6903	0.0675	<0.001
		0.08 (2.0)	0.3770	0.0334	<0.001
		0.16 (4.0)	0.1929	0.0201	<0.001
		0.22 (5.5)	0.1340	0.0188	<0.001
$\hat{L}_{VG}$	Volume Effect of River Gravel Mixtures	0.02 (0.5)	0.0532	0.0271	0.0678
		0.03 (0.7)	0.0413	0.0167	0.0249
		0.04 (1.0)	0.0345	0.0104	0.0042
		0.08 (2.0)	0.0185	0.0051	0.0024
		0.16 (4.0)	0.0058	0.0031	0.0782
		0.22 (5.5)	-0.0001	0.0029	0.9653
$\hat{L}_{VL}$	Volume Effect of Limestone Mixtures	0.02 (0.5)	0.1346	0.0335	0.0010
		0.03 (0.7)	0.0857	0.0206	0.0007
		0.04 (1.0)	0.0512	0.0128	0.0010
		0.08 (2.0)	0.0177	0.0063	0.0130
		0.16 (4.0)	0.0054	0.0038	0.1738
		0.22 (5.5)	0.0018	0.0036	0.6253
$\hat{L}_{VG-VL}$	Interaction between Volume and Type of Aggregate	0.02 (0.5)	-0.0814	0.0431	0.0773
		0.03 (0.7)	-0.0444	0.0265	0.1136
		0.04 (1.0)	-0.0167	0.0165	0.3253
		0.08 (2.0)	0.0008	0.0082	0.9232
		0.16 (4.0)	0.0004	0.0049	0.9375
		0.22 (5.5)	-0.0019	0.0046	0.6840

Table 6.8. Summary of Results of Contrast of Repeated Measures across the Slip Range.

Contrast	Purpose	Estimates	Standard Error	*p*-value
$\hat{L}_{G-L}$	Effect of Type of Coarse Aggregate	0.5598	0.0687	<0.0001
$\hat{L}_{V}$	Volume Effect of River Gravel Mixtures	0.0258	0.0106	0.0266
	Volume Effect of Limestone Mixtures	0.0496	0.0130	0.0015
$\hat{L}_{VG-VL}$	Interaction between Volume and Type of Aggregate	-0.0238	0.0168	0.1744

6.3.3.3 Effect of Concrete Strength

The effect of concrete strength on the *E*-values is also of interest. The expected *E*-value was estimated for a certain concrete strength regardless of river gravel and limestone. The expected *E*-value was calculated using the mixed procedure with a least-squares fit using the general linear model in SAS Program (v. 9.1.3) (SAS Institute 2006). The model considers concrete compressive strength and crack slip and interaction between compressive strength and crack slip as predictors.

As shown in Figure 6.10 and Table 6.9, relatively low compressive strengths and low slip values correspond to high *E*-values. As the slip increases, the effect of concrete strength decreases. When the strength of concrete is relatively low, the *E*-value tends to be large, indicating a higher contribution of aggregate interlock. When the strength of concrete is relatively high, the *E*-value tends to be small, indicating a lower contribution of aggregate interlock. The strength of concrete is inversely proportional to the *E*-value. From this trend, the following results can be inferred. The lower strength of concrete corresponds to a lower amount of fracture of coarse aggregate resulting in more aggregate interlock leading to greater energy absorption. Therefore, the strength of concrete is highly related to the amount of fracture of aggregate interlock at small crack slip values.

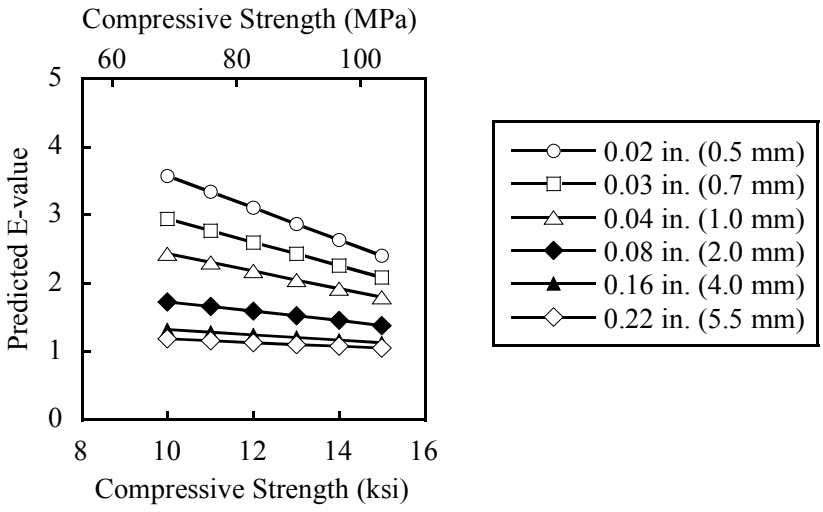

Figure 6.10. Predicted *E*-value of the Function of Strength and Slip.

Table 6.9. Summary of Predicted *E*-value for Different Compressive Strengths and Slip Values.

Slip, in (mm)	Compressive Strength, ksi (MPa)	Estimates	Standard Error	*p*-value
0.02 (0.5)	10 (69)	3.574	0.296	<0.001
	11 (76)	3.340	0.228	
	12 (83)	3.106	0.172	
	13 (90)	2.872	0.145	
	14 (97)	2.638	0.162	
	15 (103)	2.405	0.212	
0.03 (0.7)	10 (69)	2.944	0.208	
	11 (76)	2.773	0.160	
	12 (83)	2.602	0.121	
	13 (90)	2.431	0.102	
	14 (97)	2.260	0.114	
	15 (103)	2.089	0.149	
0.04 (1.0)	10 (69)	2.433	0.147	
	11 (76)	2.306	0.114	
	12 (83)	2.178	0.086	
	13 (90)	2.051	0.073	
	14 (97)	1.924	0.081	
	15 (103)	1.796	0.106	
0.08 (2.0)	10 (69)	1.734	0.073	
	11 (76)	1.665	0.056	
	12 (83)	1.596	0.042	
	13 (90)	1.527	0.036	
	14 (97)	1.458	0.040	
	15 (103)	1.389	0.052	
0.16 (4.0)	10 (69)	1.322	0.038	
	11 (76)	1.284	0.029	
	12 (83)	1.246	0.022	
	13 (90)	1.208	0.019	
	14 (97)	1.170	0.021	
	15 (103)	1.132	0.027	
0.22 (5.5)	10 (69)	1.187	0.030	
	11 (76)	1.161	0.023	
	12 (83)	1.134	0.018	
	13 (90)	1.107	0.015	
	14 (97)	1.081	0.017	
	15 (103)	1.054	0.022	

6.4 MODEL OF AGGREGATE INTERLOCK

Based on the experimental results, equations for aggregate interlock are proposed in this section.

6.4.1 Crack Width and Crack Slip Relationship

Based on the test results, the aggregate type significantly affects the crack slip and crack width relationship. The CC mixtures with river gravel (CC-R) exhibit a similar tendency compared to regression plots developed by Yoshikawa *et al.* (1989). Therefore, a new relationship for the river gravel SCC mixtures (SCC-R), limestone SCC mixtures (SCC-L), and limestone CC mixtures (CC-L) can be proposed with different regression coefficients. The expression proposed by Yoshikawa *et al.* (1989) is presented in Equation 2.20. In this equation, as the width increases, the crack slip exponentially increases. The following equation is proposed, based on the form of Yoshikawa's equation, but considering the resistance to progress of aggregate fracture from this study:

$$\delta = \left(\frac{(f)\,a_g}{1.26}\right)^{-1.20} w^{2.21} \quad \left[\delta = \left(\frac{(f)\,a_g}{32}\right)^{-1.20} w^{2.21}\right] \tag{6.13}$$

where δ is the crack slip (in. [mm]), f represents the degree of aggregate fracture from this study, a_g is the maximum size of coarse aggregate (in. [mm]), and w is the crack width (in. [mm]). The value of f is determined to best fit the experimental data by the method of least squares.

Table 6.10 shows the summary of coefficient, f, and standard error. All plots with the proposed equations are presented in Figure 6.11. A higher value of f represents a higher resistance to progress of the aggregate fracture. Therefore, the CC mixture with river gravel and a higher volume of aggregate has higher resistance. The range of the f value determined for hits study varies from 0.53 to 1.59. If the value of f is equal to 1.77, the relationship is close to the normal strength CC with river gravel, and is almost identical to Yoshikawa *et al.*'s equation. The CC-R mixtures exhibit less aggregate fracture. The SCC-L mixtures have greatest degree of aggregate fracture.

Table 6.10. *f*-values to Estimate Degree of Aggregate Fracture.

	f	Standard Error	R^2
CC-R	1.590	0.00440	0.99
SCC-R	1.030	0.00164	0.99
CC-L	0.566	0.00119	0.99
SCC-L	0.526	0.00042	0.99

Note: Higher value indicates less fracture of coarse aggregate.

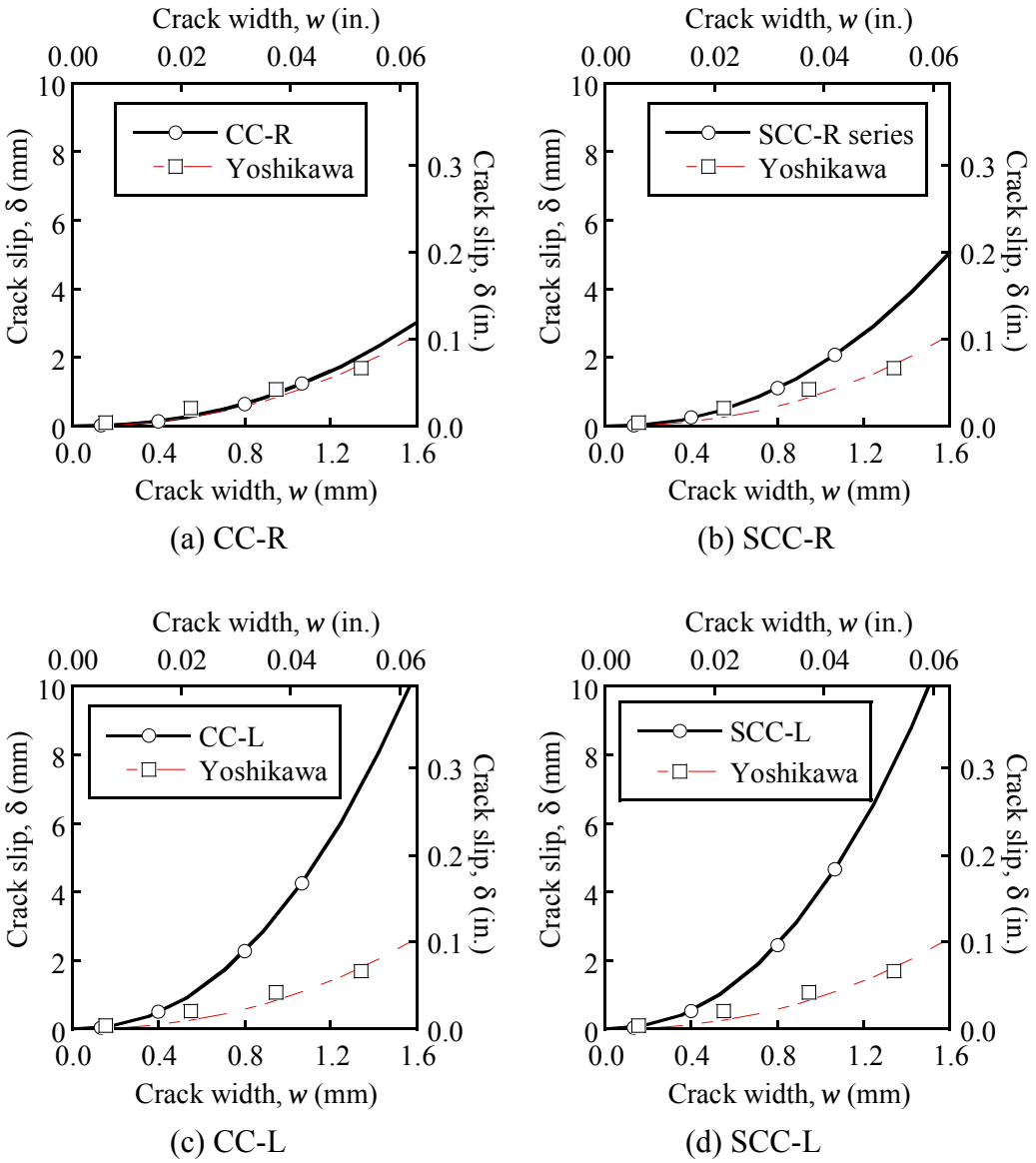

Figure 6.11. Comparison of Proposed Estimates of Crack Slip and Crack Width Relationship versus Yoshikawa *et al.* (1989).

These predicted equations are used to estimate A_x and A_y values from Equations 6.1 and 6.2. The A_x and A_y values are also functions of the crack width and crack slip. From these values, the degree of aggregate fracture also indicates the roughness of the shear plane. As the crack width increases, the crack slip also increases. The lower the profile of the crack plane becomes, the higher the rate of increasing slip. At a given crack width, the higher rate of slip indicates that a large amount of aggregate fracture is occurring. The SCC-L mixtures have the largest amount of aggregate fracture indicating a low roughness profile.

The rate of slip at a given crack width can be obtained from the change of crack slip with respect to the change of the crack width using Equation 6.13. For example, the rate of the crack slip can represent the initial state of roughness at the initial crack width (about 0.01 in. [0.3 mm]). As the crack slip increases, the profile of roughness decreases with the fracture of aggregate. Table 6.11 ranks the roughness based on the value of differentiated crack slip with respect to crack width when the crack width is very small. The CC-R mixtures have a high roughness profile resulting in a reduction of the rate of crack slip. Table 6.12 shows that the CC-R mixtures still have a rougher surface compared with other mixtures at larger crack widths.

Table 6.11. Roughness Ranking at Crack Width of 0.01 in. (0.3 mm).

	$d\delta/dw$	Roughness Ranking
CC-R	0.55	1
SCC-R	0.93	2
CC-L	1.91	3
SCC-L	2.08	4

Table 6.12. Roughness Ranking at Crack Width of 0.06 in. (1.5 mm).

	$d\delta/dw$	Roughness Ranking
CC-R	3.87	1
SCC-R	6.51	2
CC-L	13.35	3
SCC-L	14.58	4

6.4.2 Determination of Fracture Reduction Factor and Friction Coefficient

Equations 6.1 and 6.2 can be rearranged to find the values of the fracture reduction factor, *c*, and the friction coefficient, μ, as follows:

$$c\,\sigma_{pu} = \frac{\sigma A_x + \tau A_y}{A_x^2 + A_y^2} \tag{6.14}$$

$$c\,\mu\,\sigma_{pu} = \frac{\tau A_x - \sigma A_y}{A_x^2 + A_y^2} \tag{6.15}$$

The paste strength, σ_{pu}, can be obtained from optimal fitting of the data because of the difficulty of estimating the paste strength. Walraven (1981) proposed the paste strength as a function of the compressive strength, with the paste strength defined as follows:

$$\sigma_{pu} = 56.7\ f_c'^{0.56}\ \text{(psi)}\ \ [\sigma_{pu} = 6.4\ f_c'^{0.56}]\ \text{(MPa)}. \tag{6.16}$$

Both constants were determined when the sample is near the ultimate state and the value of the shear-to-normal stress ratio is near 1.0. This mixed procedure was also used to determine the coefficients for this study. Table 6.13 show the fracture reduction factor and friction coefficient, respectively. The standard error for fracture reduction factor and friction coefficient and the *p*-value to estimate fracture reduction factor and friction coefficient are also provided. The *p*-value and standard error provide the significance of all the information provided.

The fracture reduction factors, *c*, are 0.43 and 0.62 for the SCC and CC, respectively. The SCC samples have lower fracture reduction factor values than CC, indicating that SCC may have more aggregate fracture. When the river gravel and limestone were compared, the limestone mixtures have a significantly lower fracture reduction factor than limestone mixtures indicating the limestone mixture has more aggregate fracture. $\hat{L}_{G-L}$ also confirms the difference at *p*-value of 0.05. The overall fracture factor of all mixtures is 0.48 in this study.

The friction coefficients, μ, are 0.32 and 0.30 for the SCC and CC, respectively. The value of limestone mixtures (0.23) is slightly lower than river gravel mixture (0.40) for the

friction coefficient at p-value of 0.05. $\hat{L}_{G-L}$ indicates that river gravel mixtures have slightly higher friction coefficient at *p*-value of 0.05. The overall friction coefficient of all mixtures is 0.31 in this study.

Table 6.13. Fracture Reduction Factor (*c*) and Friction Coefficient (μ).

		Fracture Reduction Factor (*c*)			Friction Coefficient (μ)		
Average or Contrasts		Estimates	Standard Error	*p*-value	Estimates	Standard Error	*p*-value
SCC		0.4294	0.02002	<0.0001	0.3167	0.02716	<0.0001
CC		0.6200	0.03878	<0.0001	0.3012	0.05260	<0.0001
River Gravel		0.6238	0.02601	<0.0001	0.3990	0.03528	<0.0001
Limestone		0.3304	0.02452	<0.0001	0.2267	0.03326	<0.0001
$\hat{L}_{G-L}$		0.2933	0.03575	<0.0001	0.1723	0.04849	0.0026
SCC	River Gravel	0.5650	0.02832	0.4061	0.03841	<0.0001	<0.0001
	Limestone	0.2939	0.02832	0.2272	0.03841	<0.0001	<0.0001
CC	River Gravel	0.8000	0.06007	0.3775	0.08148	0.0003	<0.0001
	Limestone	0.4400	0.04905	0.2250	0.06653	0.0038	<0.0001
All Mixtures		0.4771	0.01787	<0.0001	0.3128	0.02425	<0.0001

6.4.3 Maximum Shear Stress

The maximum shear stress, $\tau_{max,}$ can be obtained from Equation 6.2 using values of *c* and μ from Table 6.13. Maximum shear stress, τ_{max}, at the given crack width is theoretically obtained from the relationship between crack slip and shear stress (Equation 6.2). Using maximum average shear stress for all samples of a mixture at the given crack widths (0.004, 0.01, 0.02, and 0.04 in. [0.1, 0.3, 0.5, and 1.0 mm]), the best-fit curve (straight linear regression curve with least squares) is predicted to evaluate aggregate interlock of SCC with the same form of equation in the MCFT (Equation 2.22). The MCFT considers higher concrete strength by stating that when the compressive strength, f'_c, is higher than 70 MPa (10,000 psi), the maximum aggregate size, a_g, should be assumed to be zero in the MCFT (Bentz *et al.* 2006). This assumption highly underestimates the aggregate interlock for shear when the paste strength is high compared to the aggregate strength.

The reciprocal form of Equation 2.22 in the MCFT and AASHTO LRFD Specifications is used to determine coefficients m_1 and m_2:

$$\frac{\sqrt{f_c'}}{\tau_{max}} = m_1 + m_2 \frac{w}{(a_g + 0.63)} \text{ (psi, in.)} \quad \left[\frac{\sqrt{f_c'}}{\tau_{max}} = m_1 + m_2 \frac{w}{(a_g + 16)} \right] \text{ (MPa, mm)} \quad (6.17)$$

The coefficients m_1 and m_2 are determined from the straight linear regression with least squares and are summarized in Table 6.14. All the *p*-values are smaller than 0.05 indicating coefficients provides the goodness of fit to data within 95% confidence interval. Figure 6.12 shows the best-fit curves of CC and SCC, along with the curves corresponding to the MCFT and AASHTO LRFD Specifications.

Table 6.14. Coefficients m_1 and m_2 in Equation 6.17 Based on τ_{max} in CC and SCC Push-Off Tests.

	m_1		m_2		a_g, in. (mm)	Note
	Estimate	Standard Error	Estimate	Standard Error		
AASHTO (upper limit, $\tau_{max(u)}$)	0.31	-	24	-	0.75 (19)	Full Aggregate Interlock
MCFT (lower limit, $\tau_{max(l)}$)	0.31	-	24	-	0*	No Aggregate Interlock
CC-R	0.4008	0.0032	22.050	0.1903	0.75 (19)	*p*-value < 0.05 (m_1 and m_2)
CC-L	0.8768	0.0159	48.841	0.9608		
SCC-R	0.5555	0.0050	29.804	0.3033		
SCC-L	0.9425	0.1835	81.784	11.093		
CC	0.6426	0.2020	35.445	12.189		
SCC	0.7490	0.2910	55.794	17.556		
All	0.6958	0.1841	45.619	11.108		

Note: * The value of a_g is equal to zero for high-strength concrete (f'_c > 10,000 psi [70 MPa]).

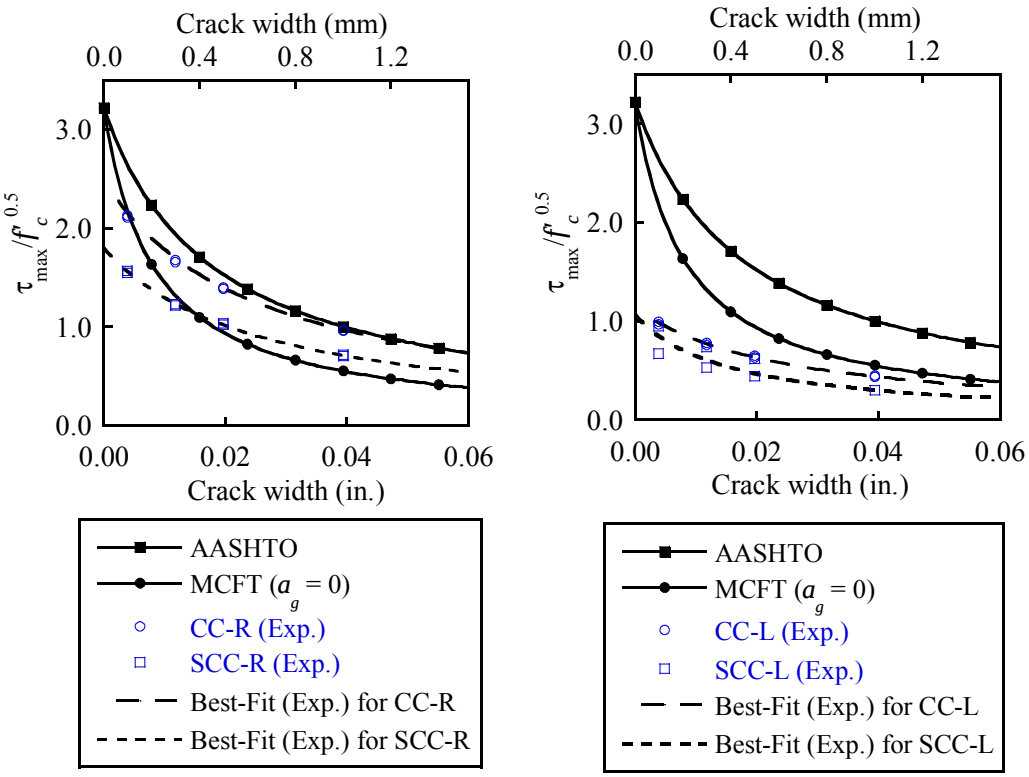

(a) CC-R and SCC-R

(b) CC-L and SCC-L

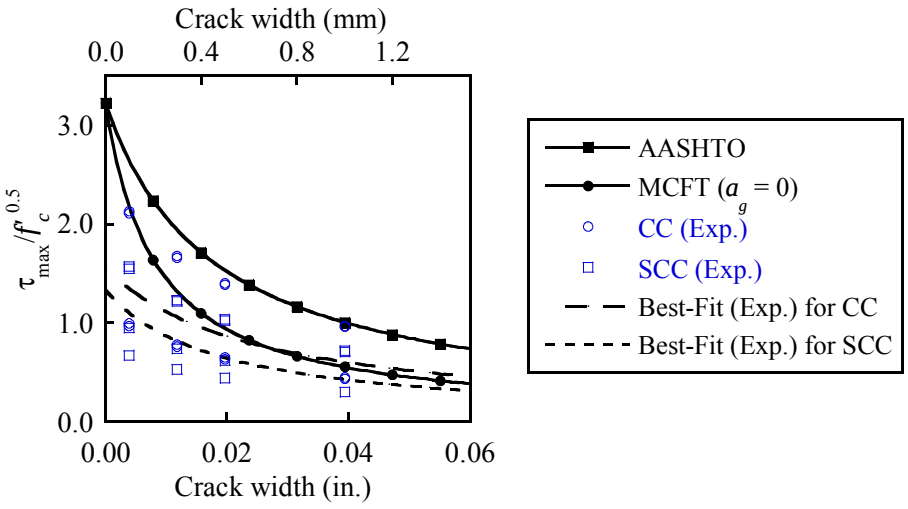

(c) CC and SCC

Figure 6.12. Best-Fit Curves for $\tau_{max}/\sqrt{f'_c}$ vesus Crack Width Compared to AASHTO and MCFT.

The maximum shear stress based on the AASHTO LRFD Specifications represents the upper limit of the contribution of aggregate interlock for shear because there is no consideration of aggregate fracture for high-strength concrete. The maximum stress found the MCFT using recommendation to set the maximum size of coarse aggregate to zero represents a lower limit of the contribution of aggregate interlock for shear. It is notable that these upper and lower limits are based on Walraven's test specimens. The difference of maximum shear stress between river gravel and limestone is shown in Figure 6.12 (a) and (b). The CC mixtures containing river gravel have the highest value of normalized maximum shear stress among the mixtures. As the crack width increases, the CC mixtures containing river gravel follow the AASHTO equation. The SCC mixture containing river gravel follows the MCFT equation (a_g = 0). The CC and SCC mixtures containing limestone tend to be the lower bound of all the prediction curves. All curves underestimate the aggregate interlock at low crack width values.

For the CC mixture, all best-fit curves generally show lower normalized maximum shear stress values as compared with the MCFT equation for crack widths ranging from 0 to 0.02 in. (0.51 mm) (see Figure 6.12 (c)). The SCC mixtures have slightly lower normalized maximum shear stresses than the CC mixtures. As the crack width increases, both CC and SCC mixtures follow the MCFT equation (a_g = 0). The coefficients from the best-fit curves are used to determine the shear friction factor.

6.4.4 Evaluation of Shear Friction Factor

The MCFT theory proposed a relationship between τ/τ_{max} and σ/τ_{max} for conventional normal strength concrete. Using a similar approach, an appropriate equation for the CC and SCC mixtures considered in this study can be proposed. As mentioned previously in Section 2.4, the latter version of the MCFT additionally neglected the beneficial contribution of normal stresses on the crack plane.

The MCFT equation for the relationship between τ/τ_{max} and σ/τ_{max} is recalled as following equation (Vecchio and Collins 1986):

$$\frac{\tau}{\tau_{max}} = 0.18 + 1.64\frac{\sigma}{\tau_{max}} - 0.82\left(\frac{\sigma}{\tau_{max}}\right)^2 \qquad (6.18)$$

where

$$\frac{\tau_{max}}{\sqrt{f_c'}} = \frac{12}{0.31 + 24\dfrac{w}{(a_g + 0.63)}} \text{ (psi, in.)} \qquad (6.19)$$

$$\left[\frac{\tau_{max}}{\sqrt{f_c'}} = \frac{1}{0.31 + 24\dfrac{w}{(a_g + 16)}}\right] \text{(MPa, mm)}$$

τ_{max} is the maximum shear stress (psi [MPa]), σ is the normal stress across cracks (psi [MPa]), τ is the shear stress (psi [MPa]), f'_c is the concrete compressive strength (psi [MPa]), w is the crack width (in. [mm]), and a_g is the maximum aggregate size (in. [mm]).

The general regression method procedure available in the SAS program (SAS Institute 2006) was used to determine the coefficients for the data from this study. The analysis of variance (AOV) tables for the CC mixture, SCC mixtures and combined data are provided in Tables 6.15, 6.16, and 6.17, respectively. When the model utility tests were performed in the *F*-test, both the quadratic model (Equation 6.20) and straight line regression (SLR) model (Equation 6.21) are clearly useful because the *p*-values are less than 0.0001.

$$\frac{\tau}{\tau_{max}} = n_1 + n_2\frac{\sigma}{\tau_{max}} - n_3\left(\frac{\sigma}{\tau_{max}}\right)^2 \qquad (6.20)$$

$$\frac{\tau}{\tau_{max}} = n_1 + n_2\frac{\sigma}{\tau_{max}} \qquad (6.21)$$

Table 6.18 shows the estimated coefficients for best-fit curve for CC and SCC mixtures with the equation formats for the relationship of τ/τ_{max} and σ/τ_{max}:

Table 6.15. AOV Table for CC Mixtures.

	CC (SLR model)				
Source	Degrees of Freedom	Sum of Squares	Mean Square	F Value	Pr >F
Model	1	1.50192075	1.51920752	174.98	<0.0001
Error	46	0.39937286	0.00868202	-	-
Corrected Total	47	1.91858038	-	-	-
	CC (Quadratic model)				
Source	Degrees of Freedom	Sum of Squares	Mean Square	F Value	Pr >F
Model	2	1.58936797	0.79468399	108.63	<0.0001
Error	45	0.32921240	0.00731583	-	-
Corrected Total	47	1.91858038	-	-	-

Table 6.16. AOV Table for SCC Mixtures.

	SCC (SLR model)				
Source	Degrees of Freedom	Sum of Squares	Mean Square	F Value	Pr >F
Model	1	18.07959710	18.07959710	975.74	<0.0001
Error	142	2.63112210	0.01852903	-	-
Corrected Total	143	20.71071921	-	-	-
	SCC (Quadratic model)				
Source	Degrees of Freedom	Sum of Squares	Mean Square	F Value	Pr >F
Model	2	18.08878290	9.04439145	486.38	<0.0001
Error	141	2.62193631	0.01859529	-	-
Corrected Total	143	20.71071921	-	-	-

Table 6.17. AOV Table for All Mixtures.

	CC and SCC (SLR model)				
Source	Degrees of Freedom	Sum of Squares	Mean Square	F Value	Pr >F
Model	1	16.52002527	16.52002527	1210.93	<0.0001
Error	190	2.59205745	0.01364241	-	-
Corrected Total	191	19.11208272	-	-	-
	CC and SCC (Quadratic model)				
Source	Degrees of Freedom	Sum of Squares	Mean Square	F Value	Pr >F
Model	2	16.54615673	8.27307836	609.38	<0.0001
Error	189	2.56592599	0.01357633	-	-
Corrected Total	191	19.11208272	-	-	-

Note: '-' indicates no availability.

Table 6.18. Coefficients n_1, n_2, and n_3 for Equations 6.20 and 6.21 in CC and SCC.

		n_1		n_2		n_3	
		Estimate	Standard Error	Estimate	Standard Error	Estimate	Standard Error
Quadratic Model (Eq. 6.20)	CC	0.0464	0.0238	1.7206	0.2243	–1.1214	0.3621
	SCC	0.1103	0.0204	0.9999	0.1028	0.06243	0.0888
	All	0.0913	0.0151	1.1468	0.0890	–0.1218	0.0878
SLR Model (Eq. 6.21)	CC	0.0952	0.0194	1.0647	0.0805	-	-
	SCC	0.1015	0.0160	1.0681	0.0342	-	-
	All	0.1045	0.0118	1.0304	0.0296	-	-

Note: '-' indicates no availability.

The lack of fit *F*-test was performed to determine whether the SLR model is adequate or not. For the lack of fit *F*-test, the null hypothesis, H_0, and research hypothesis, H_1, are expressed as follows:

$$H_0: n_3 = 0 \text{ versus } H_1: n_3 \neq 0 \tag{6.22}$$

Table 6.19 summarized the lack of fit *F*-tests. When the *p*-value is larger than 0.05 for CC, SCC, and all mixtures, the null hypothesis cannot be rejected at the *p*-value of 0.05. Therefore, this *F*-statistic concludes that the SLR model is adequate and the quadratic model is not required to explain the relationship of τ/τ_{max} and σ/τ_{max}.

Table 6.19. Summary of Lack of Fit *F*-test.

	F_{Lack}	df_{Lack}	df_{Error}	$F\ (df_{Lack}, df_{Error})$ at *p*-value = 0.05	*p*-value of F_{Lack}	Note
CC	0.11004	1	45	4.06	> 0.05	H_0 cannot be rejected.
SCC	0.01156	1	141	3.91	> 0.05	
All	0.03288	1	189	3.89	> 0.05	

The push-off data for all the CC mixtures were used to evaluate the relationship of τ/τ_{max} and σ/τ_{max} as in the following equation:

$$\frac{\tau}{\tau_{max}} = 0.0952 + 1.0647\frac{\sigma}{\tau_{max}} \tag{6.23}$$

where

$$\frac{\tau_{max}}{\sqrt{f_c'}} = \frac{12}{0.6426 + 35.445\,\dfrac{w}{\left(a_g + 0.63\right)}} \quad \text{(psi, in)}$$

$$\left[\frac{\tau_{max}}{\sqrt{f_c'}} = \frac{1}{0.6426 + 35.445\,\dfrac{w}{\left(a_g + 16\right)}}\right] \quad \text{(MPa, mm)}$$

The push-off test data for all the SCC mixtures were used to evaluate the relationship of τ/τ_{max} and σ/τ_{max} as in the following equation:

$$\frac{\tau}{\tau_{max}} = 0.1015 + 1.0681\,\frac{\sigma}{\tau_{max}} \tag{6.24}$$

where

$$\frac{\tau_{max}}{\sqrt{f_c'}} = \frac{12}{0.7490 + 55.794\,\dfrac{w}{\left(a_g + 0.63\right)}} \quad \text{(psi, in)}$$

$$\left[\frac{\tau_{max}}{\sqrt{f_c'}} = \frac{1}{0.7490 + 55.794\,\dfrac{w}{\left(a_g + 16\right)}}\right] \quad \text{(MPa, mm)}$$

Finally, the push-off test data for all the CC and SCC mixtures were used to evaluate the relationship of τ/τ_{max} and σ/τ_{max} as in the following equation:

$$\frac{\tau}{\tau_{max}} = 0.1045 + 1.0304\,\frac{\sigma}{\tau_{max}} \tag{6.25}$$

where

$$\frac{\tau_{max}}{\sqrt{f_c'}} = \frac{12}{0.6958 + 45.619\,\dfrac{w}{\left(a_g + 0.63\right)}} \quad \text{(psi, in)}$$

$$\left[\frac{\tau_{max}}{\sqrt{f_c'}} = \frac{1}{0.6958 + 45.619\,\dfrac{w}{(a_g + 16)}}\right] \text{ (MPa, mm)}$$

Figure 6.13 shows the developed relationships of τ/τ_{max} - σ/τ_{max} for the CC and SCC mixtures, given in Equations 6.24 and 6.25, as compared to the experimental data. Figure 6.14 shows the relationship of τ/τ_{max} - σ/τ_{max} of combined CC and SCC mixtures based on Equation 6.25. The MCFT and AASHTO relationships are shown for comparison.

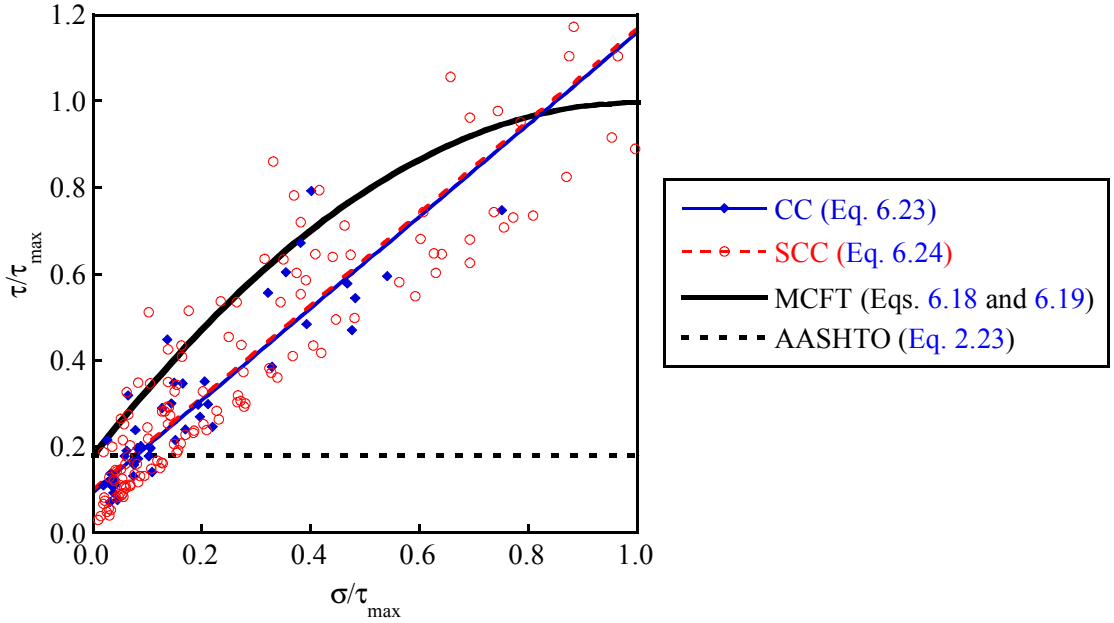

Figure 6.13. τ/τ_{max} versus σ/τ_{max} for CC and SCC.

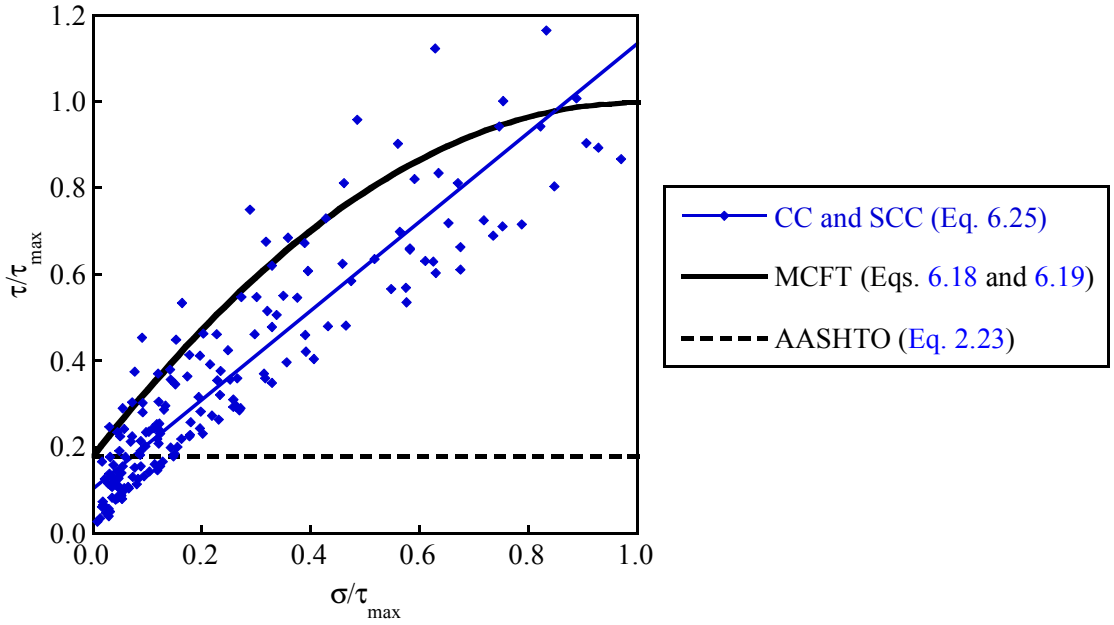

Figure 6.14. τ/τ_{max} versus σ/τ_{max} for Combined CC and SCC.

According to Duthinh (1999), the intercept of the y-axis for the relationship shown in Figure 6.12 is the shear friction factor, *SF,* in the MCFT. Therefore, *SF* values can be obtained from the relationships of τ/τ_{max} - σ/τ_{max} provided in Figure 6.13 and Figure 6.14. This study contains more data in the small crack width and small crack slip range, these data lead the intercept of the y-axis to be close to the origin. The data near the origin are more important to determining the shear friction factor. It should be noted that the contribution of normal stress on the crack plane was neglected for estimating the shear friction factor.

The *SF* value is the equal to the coefficient, n_1 in Equations 6.20 and 6.21:

$$\frac{v_{ci}}{\tau_{max}} = SF \tag{6.26}$$

As shown in Table 6.20, the *SF* for the SCC and of CC mixtures were within 7 percent of one another. However, the MCFT *SF* is approximately 75 percent higher than the *SF* values based on the test data. Therefore, the current *SF* in the MCFT does not seem to be appropriate for

the CC and SCC mixtures in this study. One explanation is that the compressive strength for the tested mixtures is higher than the normal strength samples used to develop the current factor.

Table 6.20. Shear Friction Factor (*SF*).

	CC	SCC	Combined CC and SCC	MCFT
SF	0.0952	0.1015	0.1045	0.18
Standard Error	0.0194	0.0160	0.0118	-

When the normal stress is neglected, as in the latter version of the MCFT (Collins and Mitchell 1991), only the *SF* value is used in the prediction equations. The value of β is the factor of tensile stress in the cracked concrete, which used to determine the limiting value of the concrete contribution to shear, v_{ci}. The following equations are proposed based on the data from this study:

For the CC mixtures (psi, in. [MPa, mm]):

$$\beta \le \frac{v_{ci}}{\sqrt{f_c'}} = \frac{1.1424}{0.6426 + 35.445\dfrac{w}{(a_g + 0.63)}} \quad \text{(psi, in.)} \tag{6.27}$$

$$\left[\beta \le \frac{v_{ci}}{\sqrt{f_c'}} = \frac{0.0952}{0.6426 + 35.445\dfrac{w}{(a_g + 16)}}\right] \quad \text{(MPa, mm)}$$

For the SCC mixtures (psi, in. [MPa, mm]):

$$\beta \le \frac{v_{ci}}{\sqrt{f_c'}} = \frac{1.2180}{0.7490 + 55.794\dfrac{w}{(a_g + 0.63)}} \quad \text{(psi, in.)} \tag{6.28}$$

$$\left[\beta \le \frac{v_{ci}}{\sqrt{f'_c}} = \frac{0.1015}{0.7490 + 55.794\dfrac{w}{(a_g + 16)}}\right] \quad \text{(MPa, mm)}$$

For the combined CC and SCC mixtures (psi, in. [MPa, mm]):

$$\beta \le \frac{v_{ci}}{\sqrt{f'_c}} = \frac{1.254}{0.6958 + 45.619\dfrac{w}{(a_g + 0.63)}} \quad \text{(psi, in.)} \qquad (6.29)$$

$$\left[\beta \le \frac{v_{ci}}{\sqrt{f'_c}} = \frac{0.1045}{0.6958 + 45.619\dfrac{w}{(a_g + 16)}}\right] \quad \text{(MPa, mm)}$$

6.4.5 Impact on Shear Design

The impact of the proposed equations for β based on this study (Equation 6.27, 6.28, and 6.29) were evaluated for cases with and without shear reinforcement.

6.4.5.1 No Shear Reinforcement

The following two equations for b from MCFT were presented in Section 2.4.1:

$$\beta = \frac{4\cot\theta}{1 + \sqrt{500\,\varepsilon_1}} \quad \text{(psi)} \qquad \left[\beta = \frac{0.33\cot\theta}{1 + \sqrt{500\,\varepsilon_1}}\right] \quad \text{(MPa)} \qquad (6.30)$$

and

$$\beta \le \frac{v_{ci}}{\sqrt{f'_c}} = \frac{2.16}{0.31 + 24\dfrac{w}{(a_g + 0.63)}} \quad \text{(psi, in.)} \qquad (6.31)$$

$$\left[\beta \le \frac{v_{ci}}{\sqrt{f_c'}} = \frac{0.18}{0.31 + 24\dfrac{w}{(a_g + 16)}}\right] \text{ (MPa, mm)}$$

Equation 6.32 is used to limit the β value for both MCFT and the newly proposed Equations 6.27 to 6.29.

The crack width, *w*, can be evaluated using the principal tensile strain, ε_1, and the average spacing of the diagonal cracks, $s_{m\theta}$, as in the following equation from the MCFT:

$$w = \varepsilon_1 s_{m\theta} \tag{6.32}$$

$$\text{where } s_{m\theta} = \frac{1}{\left(\dfrac{\sin\theta}{s_x} + \dfrac{\cos\theta}{s_v}\right)}$$

where $s_{m\theta}$ is the crack spacing in the direction of principal strain and ε_1, s_x, and s_v are the crack spacing parameters of longitudinal and shear reinforcement, respectively. The crack spacing depends on the reinforcement spacing. According to the AASHTO recommendations and the MCFT, s_x is the lesser of either the effective shear depth, d_v, or the maximum distance between layers of longitudinal reinforcement. The parameter θ is the angle of the diagonal compressive stresses in the web. Because shear reinforcement is not used for this first case, s_v is equal to zero.

After the crack width in Equation 6.31 is replaced by Equation 6.32, the equation can be rearranged as follows:

$$\beta \le \frac{2.17}{0.31 + \dfrac{0.686\,\varepsilon_1\, s_{xe}}{\sin\theta}} \text{ (psi, in.)} \quad \left[\beta \le \frac{0.18}{0.31 + \dfrac{0.686\,\varepsilon_1\, s_{xe}}{\sin\theta}}\right] \text{ (MPa, mm)} \tag{6.33}$$

$$\text{where } s_{xe} = \frac{1.38\, s_x}{a_g + 0.63} \text{ (in.)} \quad \left[s_{xe} = \frac{35\, s_x}{a_g + 16}\right] \text{ (mm)}$$

For the members without shear reinforcement, the maximum post-cracking shear capacity can be calculated when Equations 6.31 and 6.33 present the same β value (Bentz *et al.* 2006). In this study, the same conditions were used to compare the β value from the MCFT with Equations 6.27 to 6.29. Therefore, the equation is expressed as follows:

$$\tan\theta = \frac{0.568 + \dfrac{1.258\, s_{xe}\, \varepsilon_1}{\sin\theta}}{1 + \sqrt{500\, \varepsilon_1}} \tag{6.34}$$

From the MCFT and the simplified MCFT (Bentz *et al.* 2006), the longitudinal strain, ε_x, and principal tensile strain, ε_1, can be found as in following equation:

$$\varepsilon_1 = \varepsilon_x(1+\cot^2\theta) + \frac{\cot^4\theta}{15{,}000\left(1+\sqrt{500\,\varepsilon_1}\right)} \tag{6.35}$$

Based on this study, equations are proposed as follows.

For CC mixtures (psi, in. [MPa, mm]):

$$\beta \le \frac{1.1424}{0.6426 + \dfrac{1.0127\,\varepsilon_1\, s_{xe}}{\sin\theta}} \text{ (psi, in.)} \quad \left[\beta \le \frac{0.0952}{0.6426 + \dfrac{1.0127\,\varepsilon_1\, s_{xe}}{\sin\theta}}\right] \text{ (MPa, mm)} \tag{6.36}$$

$$\text{where } s_{xe} = \frac{1.38\, s_x}{a_g + 0.63} \text{ (in.)} \left[s_{xe} = \frac{35\, s_x}{a_g + 16}\right] \text{ (mm)}$$

For SCC mixtures (psi, in. [MPa, mm]):

$$\beta \le \frac{1.2180}{0.7490 + \frac{1.5941\,\varepsilon_1\,s_{xe}}{\sin\theta}} \text{ (psi, in.)} \quad \left[\beta \le \frac{0.1015}{0.7490 + \frac{1.5941\,\varepsilon_1\,s_{xe}}{\sin\theta}}\right] \text{ (MPa, mm)} \quad (6.37)$$

$$\text{where } s_{xe} = \frac{1.38\,s_x}{a_g + 0.63} \text{ (in.)} \left[s_{xe} = \frac{35\,s_x}{a_g + 16}\right] \text{ (mm)}$$

For combined CC and SCC mixtures (psi, in. [MPa, mm]):

$$\beta \le \frac{1.254}{0.6958 + \frac{1.3034\,\varepsilon_1\,s_{xe}}{\sin\theta}} \text{ (psi, in.)} \quad \left[\beta \le \frac{0.1045}{0.6958 + \frac{1.3034\,\varepsilon_1\,s_{xe}}{\sin\theta}}\right] \text{ (MPa, mm)} \quad (6.38)$$

$$\text{where } s_{xe} = \frac{1.38\,s_x}{a_g + 0.63} \text{ (in.)} \left[s_{xe} = \frac{35\,s_x}{a_g + 16}\right] \text{ (mm)}$$

To estimate the β value for each equation, selected design parameters are shown in Table 6.21. It should be noted that the strength of concrete is assumed to be higher than 10,000 psi (70 MPa).

The estimated β and θ values for each mixture are presented in Table 6.22. The MCFT overestimates β values by a factor of approximately two over equations developed for the CC and SCC mixtures in this study. The β value of SCC is slightly lower than that of CC. The shear capacity of concrete can be estimated by the product of β and the square root of concrete compressive strength. If the strength of concrete between the CC and SCC is assumed to be identical, the CC has approximately 7 percent higher capacity than the SCC mixtures in this study. Similar θ values were determined for the SCC and CC mixtures from this study. These θ values are larger than those estimated from the MCFT and AASHTO expressions.

Table 6.21. Selected Design Parameters.

	Maximum Size of Coarse Aggregate a_g, in. (mm)	Longitudinal Strain $\varepsilon_x \times 10^{-3}$, in./in. (mm/mm)	Crack Spacing Parameter s_x, in. (mm)
AASHTO	0.75 (19)	1.000	10 (250)
MCFT ($a_g = 0$)	0		
CC	0.75 (19)		
SCC			
Combined CC and SCC			

Table 6.22. Estimated Beta and Theta Values.

	Principal Tensile Strain $\varepsilon_x \times 10^{-3}$, in./in. (mm/mm)	θ Degree	β
AASHTO	1.168	34.56	0.272
MCFT ($a_g = 0$)	1.049	43.24	0.203
CC (Eq. 6.34)	1.003	62.08	0.102
SCC (Eq. 6.35)	1.002	63.90	0.095
Combined CC and SCC (Eq. 6.36)	1.003	63.01	0.098

6.4.5.2 Shear Reinforcement

According to the MCFT, the tension is transmitted on the shear crack surface by the increase of shear reinforcement stresses at low shear stresses. As the applied shear force increases, the shear reinforcement at the cracks reaches the yield stress. The local shear stress on the crack cannot exceed the maximum allowable shear stress, v_{ci}, to prevent the occurrence of slip.

Based on the equilibrium conditions between concrete and steel stresses on the crack, the principal concrete tensile stress is limited by the following equation:

$$f_1 = \beta\sqrt{f'_c} < v_{ci}\tan\theta + \frac{A_v}{s_v b_w}\left(f_{vy} - f_v\right) \tag{6.39}$$

where f_1 is the principal concrete tensile stress, β is the tensile stress factor in the cracked concrete (Equation 6.30), f'_c is the concrete compressive strength, θ is the angle of the diagonal

compressive stresses in the web, v_{ci} is the limiting value of the maximum shear stress on the shear plane in the cracked concrete, A_v is the area of shear reinforcement, s_v is the spacing of shear reinforcement, b_w is the thickness of web, f_v is the stress of shear reinforcement, and f_{vy} is the yield stress of shear reinforcement.

To compare the impact of equation on the shear design, two cases were considered.

- Case 1: Before shear failure (prior to yielding of shear reinforcement) and
- Case 2: Shear failure (at yielding of shear reinforcement).

The typical details for Type A girders (which are the same as in the full-scale testing) are used to evaluate the impact of the proposed equations (see Table 6.23). Compressive strength of concrete and elastic modulus of steel are assumed to be 13,000 psi (90 MPa) and 29,000 ksi (200 GPa), respectively. The value of θ is assumed to be 35 degrees, as observed in the full-scale test program.

Table 6.23. Assumptions of Design Parameters.

	Maximum Size of Coarse Aggregate a_g in. (mm)	s_x in. (mm)	s_v in. (mm)	A_v in.^{2} (mm^2)	f_{vy} ksi (MPa)	θ Degree
AASHTO	0.75 (19)	22.3 (565)	4 (102)	0.40 (25)	65 (450)	35
MCFT (a_g = 0)	0					
CC	0.75 (19)					
SCC						
Combined CC and SCC						

Table 6.24 shows the estimated concrete and steel stress before shear failure using the different models. Table 6.25 shows the estimated concrete and steel stress at shear failure indicating the yielding of shear reinforcements. Because of the steel contribution, the concrete stress is smaller than the limiting values provided by Equation 6.39. Therefore, all models predict the same stress values for the concrete and steel. Even though yielding of shear

reinforcement occurs, the contribution of concrete and steel are still the same because the stress of concrete did not exceed the limiting values. In other words, the concrete stress does not reach the limiting value of shear stress before initiation of shear reinforcement yielding.

Table 6.24. Estimated Concrete and Steel Stress for Type A Girder (Case 1 Before Shear Failure).

	f_1, ksi (MPa)	f_v, ksi (MPa)	Crack Width w, in. (mm)
AASHTO	0.39 (2.7)	19 (130)	0.004 (0.1)
MCFT ($a_g = 0$)	0.39 (2.7)	19 (130)	0.004 (0.1)
CC	0.39 (2.7)	19 (130)	0.004 (0.1)
SCC	0.39 (2.7)	19 (130)	0.004 (0.1)
Combined CC and SCC	0.39 (2.7)	19 (130)	0.004 (0.1)

Note: f_1 is the principal tensile stress of concrete, and f_v is the steel stress of shear reinforcement.

Table 6.25. Estimated Concrete and Steel Stress for Type A Girder (Case 2 at Shear Failure).

	f_1, ksi (MPa)	f_v, ksi (MPa)	Crack Width w, in. (mm)
AASHTO	0.29 (2.0)	65 (450)	0.014 (0.37)
MCFT ($a_g = 0$)	0.29 (2.0)	65 (450)	0.014 (0.37)
CC	0.29 (2.0)	65 (450)	0.014 (0.37)
SCC	0.29 (2.0)	65 (450)	0.014 (0.37)
Combined CC and SCC	0.290 (2.0)	65 (450)	0.014 (0.37)

Note: f_1 is the principal tensile stress of concrete, and f_v is the steel stress of shear reinforcement.

An extreme case is checked using a typical design of a deep beam. Type VI girders have a section depth of 72 in. (1.8 m). Deep section members are typical more vulnerable to shear stress. According to TxDOT design practice, the spacing of the R type shear reinforcement typically varies from 4 to 8 in. (102 to 203 mm).

According to a NCHRP Project 12-61 report, θ typically ranges from 18.1 to 43.9 degrees (Hawkins *et al.* 2005). Based on Canadian Standards Association (CAN3 A23.3-M04), θ is limited to 29 degrees minimum in design practice (CSA 1994). The high value of the angle typically requires a large amount of shear reinforcement. Based on these typical ranges, the shear stresses of concrete and steel were estimated with MCFT containing different limiting values for maximum shear stress from AASHTO, MCFT ($a_g = 0$), and the combined CC and SCC equation.

Table 6.26 compares shear capacities of concrete and steel with an angle θ of 18.1 degrees. This table considers two extreme cases of crack widths (small crack width and large crack width resulting in the yielding of steel) and two different spacings of shear reinforcement (4 and 8 in. [101 and 203 mm]). At a 8 in. (203 mm) shear reinforcement spacing, the shear capacity of concrete based on MCFT (a_g = 0) is approximately 7 to 10 percent smaller than AASHTO. The shear capacity of concrete based on the proposed equation is approximately 20 to 35 percent smaller than AASHTO. The compressive strength considered for Type VI girders is 13,000 psi (90 MPa).

Table 6.26. Estimated Concrete and Steel Stress for Type VI Girder (θ = 18.1 Degrees).

	s_v, in. (mm)	w, in. (mm)	θ, Degree	V_c, kip (kN)	V_s, kip (kN)	V, kip (kN)	Note
AASHTO	8 (203)	0.004 (0.1)	18.1	257 (1140)	85.0 (378)	342 (1520)	Slip
MCFT (a_g=0)				241 (1070)	85.0 (378)	326 (1450)	
Combined CC and SCC				191 (850)	85.0 (378)	276 (1230)	
AASHTO		0.021 (0.53)*		218 (970)	518 (2300)	736 (3270)	
MCFT (a_g=0)				199 (885)	518 (2300)	717 (3190)	
Combined CC and SCC				182 (810)	518 (2300)	700 (3110)	
AASHTO	4 (101)	0.004 (0.1)		342 (1520)	365 (1620)	707 (3150)	No Slip
MCFT (a_g=0)							
Combined CC and SCC							
AASHTO		0.021 (0.53)*		271 (1210)	1040 (4610)	1310 (5820)	
MCFT (a_g=0)							
Combined CC and SCC							

Note: * Large crack width causes the yielding of shear reinforcement.

Table 6.27 compares shear capacities of concrete and steel with an angle θ of 43.9 degrees. This table also considers two extreme cases of crack widths and two different spacings of shear reinforcement. When the angle θ is large, as in this case, the concrete capacities for shear estimated by the three different equations for a given crack width and shear reinforcement spacing are the same. This indicates the shear stress of concrete did not reach the maximum allowable stress and no slip is predicted.

Table 6.27. Estimated Concrete and Steel Stress for Type VI Girder (θ = 43.9 Degrees).

	s_v, in. (mm)	w, in. (mm)	θ, Degree	V_c, kip (kN)	V_s, kip (kN)	V, kip (kN)	Note
AASHTO	8 (203)	0.004 (0.1)	43.9	136 (605)	15 (67)	151 (672)	No Slip
MCFT (a_g=0)							
Combined CC and SCC							
AASHTO		0.044 (1.11)*		79 (351)	176 (783)	255 (1134)	
MCFT (a_g=0)							
Combined CC and SCC							
AASHTO	4 (101)	0.004 (0.1)		121 (538)	59 (262)	180 (800)	
MCFT (a_g=0)							
Combined CC and SCC							
AASHTO		0.023 (0.58)*		79 (351)	350 (1557)	429 (1908)	
MCFT (a_g=0)							
Combined CC and SCC							

Note: * Large crack width causes the yielding of shear reinforcement.

Table 6.28 compares shear capacities of concrete and steel with an angle θ of 29 degrees. When the angle is a typical value for a prestressed girder along with an 8 in. (203 mm) shear reinforcement spacing and 0.004 in. (0.1 mm) crack width, the AASHTO and MCFT (a_g = 0) equations overestimate the shear capacity compared to the proposed equation. For 4 in. (101 mm) spacing of shear reinforcement, the AASHTO, MCFT, and proposed equation estimate the same capacities for shear. Based on these comparisons, proposed equation is necessary to safely estimate the shear capacities of high-strength CC and SCC girders.

Table 6.28. Estimated Concrete and Steel Stress for Type VI Girder (θ = 29 Degrees).

	s_v, in. (mm)	w, in. (mm)	θ, Degree	V_c, kip (kN)	V_s, kip (kN)	V, kip (kN)	Note
AASHTO	8 (203)	0.004 (0.1)	29	231 (1030)	43 (190)	274 (1220)	No Slip
MCFT (a_g=0)				231 (1030)	43 (190)	274 (1220)	
Combined CC and SCC				208 (925)	43 (190)	252 (1120)	Slip
AASHTO		0.026 (0.65)		154 (685)	304 (1350)	458 (2040)	No Slip
MCFT (a_g=0)							
Combined CC and SCC							
AASHTO	4 (101)	0.004 (0.1)		204 (907)	176 (783)	381 (1700)	
MCFT (a_g=0)							
Combined CC and SCC							
AASHTO		0.013 (0.33)		154 (685)	600 (2670)	754 (3350)	
MCFT (a_g=0)							
Combined CC and SCC							

Note: * Large crack width causes the yielding of shear reinforcement.

Only two cases indicate the slip of shear plane. When the spacing of shear reinforcement is large along with small angle of the diagonal compressive stress (θ), the shear capacity of concrete reaches the limiting value of the maximum shear stress. This case shows a 2 to 24 percent reduction of total shear capacity when the new equations are used. Therefore, this study indicates that the MCFT and the AASHTO equations overestimate shear capacity when slip occurs in extreme cases such as for low shear reinforcement ratio and small angle of diagonal cracks compared with the new equations.

The applicability of the proposed equations is discussed with respect to the full-scale test program in Section 8.5.4.

6.5 SUMMARY

Based on the experimental results, the following conclusions were made.

1) The plot of τ/σ versus w provides a quantifiable comparative assessment of the aggregate interlock for the CC and SCC mixtures having different paste strengths and

a different level of initial fracture of the aggregate. As the crack width increases, the decreasing value of the normalized shear stress indicates a decrease in aggregate interlock.

2) The *E*-value, a measure of the absorbed energy of the aggregate interlock, provides a quantifiable comparative assessment up to a selected crack slip limit. The 5 ksi (34 MPa) river gravel SCC and CC specimens exhibited higher *E*-values than the other mixtures [7 ksi (48 MPa) river gravel CC and SCC, 5 and 7 ksi (34 and 48 MPa) limestone CC and SCC specimens]. This indicates that high-strength concrete [28-day compressive strength greater than 10 ksi (70 MPa)] can still exhibit aggregate interlock. In addition, the SCC mixture containing river gravel exhibits a higher potential to increase the contribution of aggregate interlock to shear.
3) The effects of coarse aggregate type and volume on the *E*-value were determined with statistical assessment (mixed procedure). The batch of concrete is regarded as the random effect in the mixed procedure statistical approach. The contrast was used to assess the effect of type and volume of coarse aggregate on the aggregate interlock.
4) Aggregate type is a critical factor influencing aggregate interlock. For both the SCC and CC specimens, concrete mixtures containing river gravel exhibited more aggregate interlock compared to those containing limestone aggregate. Statistically, the effect of aggregate type is clearly identified at all slip ranges.
5) The volume of aggregate influences the contribution of aggregate interlock to the shear capacity for the SCC and CC mixtures tested. The effect of volume is observed on both river gravel and limestone mixtures based on statistical analysis (the contrasts) with a *p*-value of 0.05.
6) Lower strength concrete tends to have less coarse aggregate fractures resulting in more aggregate interlock, leading to a large amount of energy absorption. Therefore, the strength of concrete is highly related to the amount of fracture of aggregate interlock at small crack widths when crack slip initiates.
7) The friction coefficients and fracture reduction factors were determined based on the statistical analysis (mixed procedure). The fracture reduction factors, *c*, were 0.43 and 0.62 for the SCC and CC mixtures tested, respectively. The friction coefficients, μ, were 0.32 and 0.30 for the SCC and CC mixtures tested, respectively.

8) The SCC exhibited lower maximum shear stresses compared with the CC.
9) An upper limit of the β value is proposed for both CC and SCC and combined CC and SCC data based on this study. The shear friction factor in this study, (approximately 0.10) is lower than the previously proposed value of 0.18 reported in the MCFT.
10) When the SCC and CC mixtures have the same concrete strength and this strength is higher than 10 ksi (70 MPa), the CC mixtures exhibit a higher concrete shear strength than the SCC mixtures when both are evaluated without shear reinforcement.
11) Finally, the proposed equation for β to compute the concrete shear strength using the MCFT approach (Equation 6.38) is necessary to estimate the appropriate shear capacity of high-strength CC and SCC girders, rather than with the AASHTO and MCFT (a_g = 0) expressions. The AASHTO and the MCFT expressions overestimate the shear capacity when low shear reinforcement ratios and small shear crack angles are assumed.

CHAPTER 7
RESULTS AND ANALYSIS OF LABORATORY STUDY: BOND, CREEP, AND DURABILITY

7.1 BOND CHARACTERISTICS

The experimental results and analysis for top bar effects on relative bond strength are presented below.

7.1.1 Bond Stresses

Two types of failure were observed during the pull-out tests. Most bars failed by creating a cone shaped failure surface through the concrete surrounding the reinforcing bar. The load-displacement curve is shown in Figure 7.1 (a). All reinforcing bars had stresses that exceeded the yield strength of the reinforcement, which corresponds to an applied load of 19 to 21 kip (85 to 93 kN). The second type of failure mode observed was failure of the reinforcement in tension. The load-displacement is shown in Figure 7.1 (b). In this case, yielding of the reinforcing bar was followed by strain hardening and a reduction in the bar diameter.

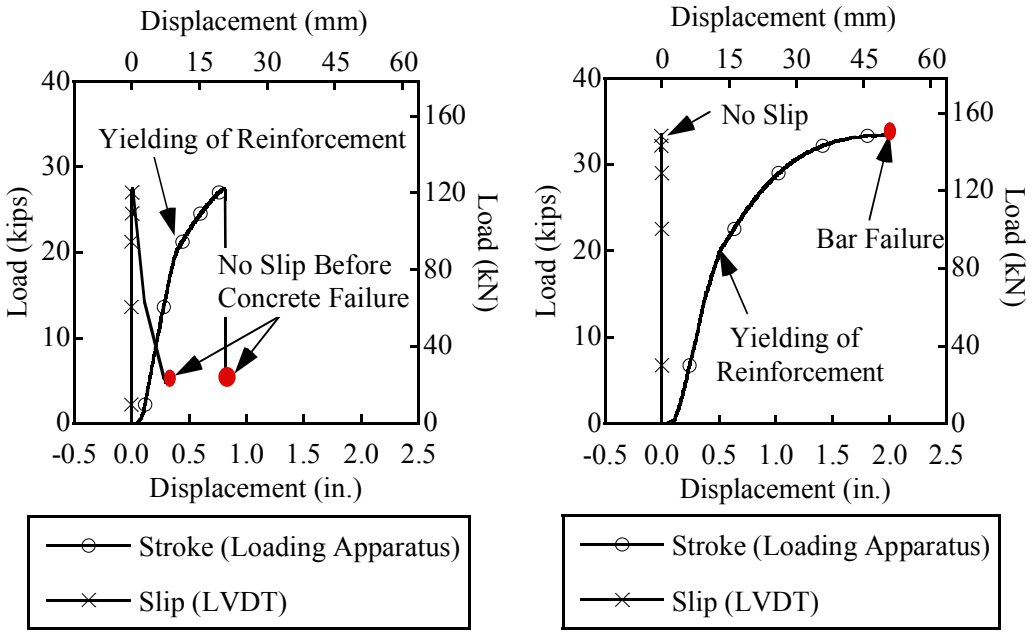

(a) Concrete Failure (b) Bar Failure

Figure 7.1. Typical Failure Modes.

Tables 7.1 to 7.4 and Figures 7.2 and 7.3 show the test results of the individual pull-out tests. Each test was conducted 35 days after casting the specimen. Each figure shows the difference between the measured bond stress for the top and bottom bars of each mixture. A total of 40 samples were tested to measure the relative bond stress for both the top and bottom bars. The average bond stress ranged from 2.29 to 3.40 ksi (16 to 23 MPa) for all samples. The range of concrete compressive strength was between 8345 and 13,358 psi (58 and 92 MPa).

Four samples of the 5 ksi (34 MPa) SCC-R mixture experienced bar failure indicating good bond. Five bottom bars failed by bar failure. Two top bars failed by bar failure.

Three bottom bars of 5 ksi (34 MPa) SCC-R mixture experienced strain hardening without bond slip, indicating sufficient bond between the reinforcing bar and concrete to reach stresses beyond the yield strength, as desired for ultimate strength design. Overall the average of bond stress of SCC-R mixture (3.04 ksi [21 MPa]) was higher than that of the CC-R mixtures (2.37 ksi [16 MPa]). The high bond strength of SCC mixture could be attributed to higher concrete strength.

Even though the strength of SCC-L was about 31 percent higher than that of CC-L, SCC-L does not seem to provide significant benefits for the bond of bars. The average computed bond stress for the CC-L mixtures (2.73 ksi [19 MPa]) was slightly higher than the average bond stress of the SCC-L mixture (2.66 ksi [18 MPa]).

Table 7.1. Test Results of CC-R Samples.

Sample ID	Compressive Strength, psi (MPa)	Std. Dev., psi (MPa)	Slump, in. (mm)	Pull-out Force, kip (kN)	Average Bond Stress, ksi (MPa)	Failure Mode
CC-R1t	8345 (58)	148 (1.0)	3.5 (89)	27.4 (122)	2.79 (19)	C
CC-R1b				33.3 (148)	3.40 (23)	B
CC-R2t	8809 (61)	592 (4.1)	5.0 (127)	33.5 (149)	3.40 (23)	B
CC-R2b				27.6 (123)	2.81 (19)	C
CC-R3t	8565 (59)	542 (3.7)	7.0 (177)	26.4 (117)	2.69 (19)	C
CC-R3b				29.8 (133)	3.04 (21)	C
CC-R4t	8671 (60)	356 (2.5)	5.25 (133)	25.0 (111)	2.55 (18)	C
CC-R4b				29.3 (130)	2.98 (21)	C
CC-R5t	9732 (67)	259 (1.8)	8.0 (202)	24.4 (109)	2.49 (17)	C
CC-R5b				33.5 (149)	3.40 (23)	C
Avg.	8824 (61)	380 (2.6)	5.75 (145)	29.0(129)	2.37 (16)	

Note: C: Concrete Failure, B: Bar Failure.

Table 7.2. Test Results of SCC-R Samples.

Sample ID	Compressive Strength, psi (MPa)	Std. Dev., psi (MPa)	Slump Flow, in. (mm)	T_{50}, sec	VSI	Pull-out Force, kip (kN)	Average Bond Stress, ksi (MPa)	Failure Mode
SCC-R1t	11,616 (80)	655 (4.5)	31.75 (803)	3.28	0.5~1	28.4 (126)	2.89 (20)	C
SCC-R1b						32.9 (146)	3.40 (23)	B
SCC-R2t	11,438 (79)	481 (3.3)	28.00 (708)	4.81	0.5~1	33.0 (147)	3.40 (23)	B
SCC-R2b						33.0 (147)	3.40 (23)	B
SCC-R3t	13,358 (92)	68 (0.5)	27.00 (683)	3.94	0.5~1	31.8 (141)	3.24 (22)	C
SCC-R3b						30.4 (135)	3.09 (21)	C
SCC-R4t	11,931 (82)	264 (1.8)	27.50 (696)	4.40	0.5~1	29.5 (131)	3.00 (21)	C
SCC-R4b						33.1 (147)	3.40 (23)	B
SCC-R5t	11,480 (79)	447 (3.1)	27.00 (683)	4.59	0.5~1	29.1 (129)	2.96 (20)	C
SCC-R5b						30.6 (136)	3.12 (22)	C
Avg.	11,965 (82)	383 (2.6)	28.00 (708)	4.2	0.5~1	31.2 (139)	3.04(21)	

Note: C: Concrete Failure, B: Bar Failure.

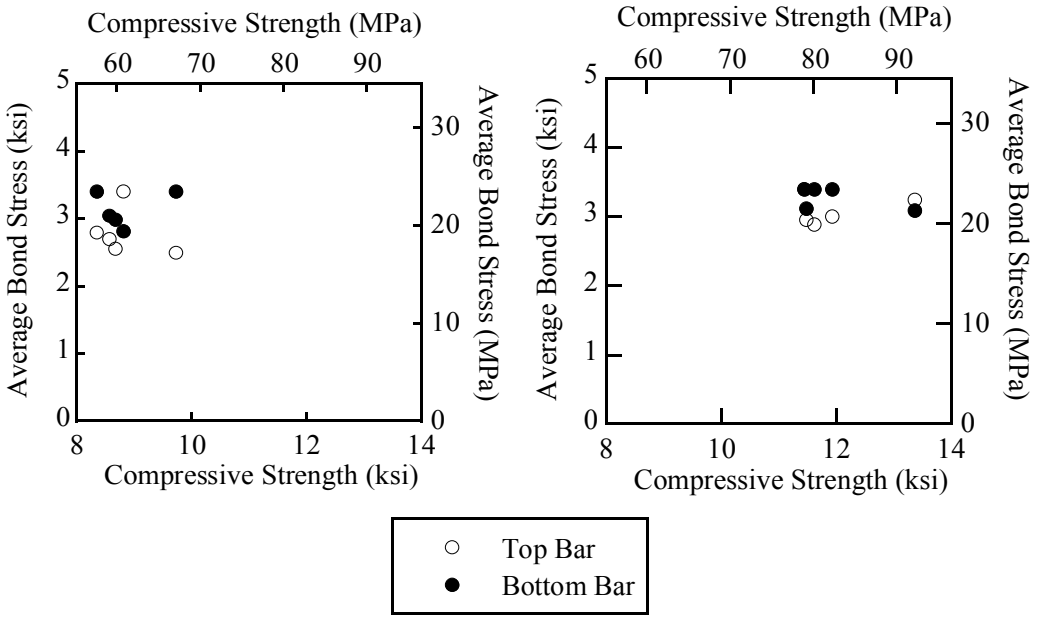

Figure 7.2. Average Bond Stress of Top and Bottom Bars (CC-R and SCC-R).

Table 7.3. Test Results of CC-L Samples.

Sample ID	Compressive Strength, psi (MPa)	Std. Dev., psi (MPa)	Slump, in. (mm)	Pull-out Force, kip (kN)	Average Bond Stress, ksi (MPa)	Failure Mode
CC-L1t	9613 (66)	157 (1.1)	8 (203)	24.6 (109)	2.51(17)	C
CC-L1b				28.8 (128)	2.93 (20)	C
CC-L2t	8830 (61)	413 (2.8)	8.5(216)	-	-	-
CC-L2b				28.0 (125)	2.85 (20)	C
CC-L3t	9517 (66)	161 (1.1)	7 (178)	26.6 (118)	2.69 (19)	C
CC-L3b				28.4 (126)	2.89 (20)	C
CC-L4t	9679 (67)	696 (4.8)	3 (76)	25.0 (111)	2.55 (18)	C
CC-L4b				28.6 (127)	2.91 (20)	C
CC-L5t	9756 (67)	73 (0.5)	7 (178)	25.3 (113)	2.58 (18)	C
CC-L5b				33.4 (149)	3.4* (23)	B
Avg.	9479 (65)	300 (2.1)	6.7 (178)	27.9 (124)	2.73(19)	

Note: C: Concrete Failure, B: Bar Failure, - indicates not tested.

Table 7.4. Test Results of SCC-L Samples.

Sample ID	Compressive Strength, psi (MPa)	Std. Dev., psi (MPa)	Slump Flow, in. (mm)	T_{50}, sec	VSI	Pull-out Force, kip (kN)	Average Bond Stress, ksi (MPa)	Failure Mode
SCC-L1t	12,072 (83)	57 (0.4)	26.0 (660)	4.19	0.5~1	23.0 (102)	2.34 (16.1)	C
SCC-L1b						28.6 (127)	2.91 (20.1)	C
SCC-L2t	12,560 (87)	209 (1.4)	31.0 (787)	2.85	0.5~1	23.9 (106)	2.43 (16.8)	C
SCC-L2b						33.4 (149)	3.40 (23.4)	B
SCC-L3t	12,117 (84)	314 (2.2)	26.0 (660)	6.57	0.5~1	29.4 (131)	2.99 (20.6)	C
SCC-L3b						24.7 (110)	2.52 (17.4)	C
SCC-L4t	12,754 (88)	409 (2.8)	25.0 (635)	5.56	0.5~1	22.5 (100)	2.29 (15.8)	C
SCC-L4b						25.5 (113)	2.74 (18.9)	C
SCC-L5t	12,703 (88)	259 (1.8)	27.5 (699)	2.97	0.5~1	26.9 (120)	2.33 (16.1)	C
SCC-L5b						26.4 (117)	2.69 (18.5)	C
Avg.	12,441 (86)	250 (1.7)	27.0 (686)	2.21	0.5~1	25.4 (113)	2.59 (17.9)	

Note: C: Concrete Failure, B: Bar Failure.

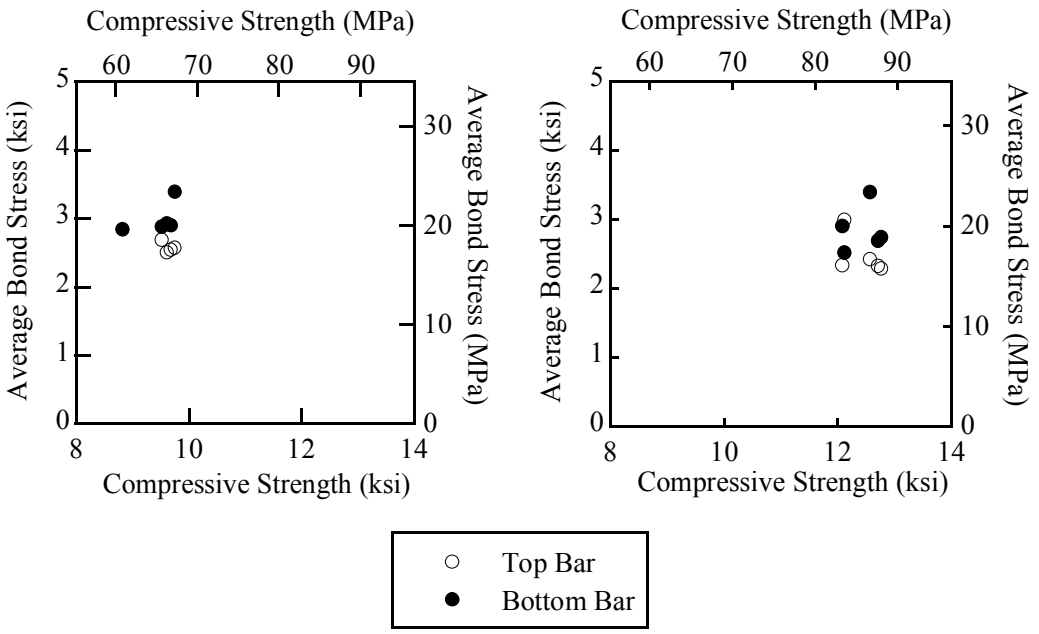

Figure 7.3. Average Bond Stress of Top and Bottom Bars (CC-L and SCC-L).

In general, the SCC mixture proportions have a higher compressive strength compared to CC mixture proportions at 35 days. As shown in Figure 7.4, at a given concrete compressive strength, most top bars exhibited less bond strength than the bottom bars for both the SCC and CC mixtures.

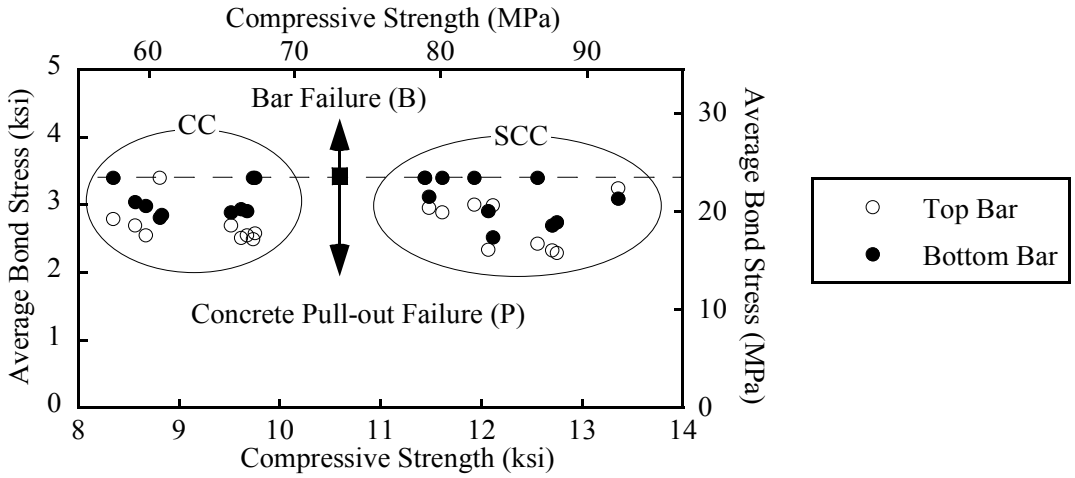

Figure 7.4. Average Bond Stress.

Figure 7.5 shows the relationship between compressive strength and average bond stresses. There is no observable correlation between compressive strength and bond stresses for the top and bottom bars.

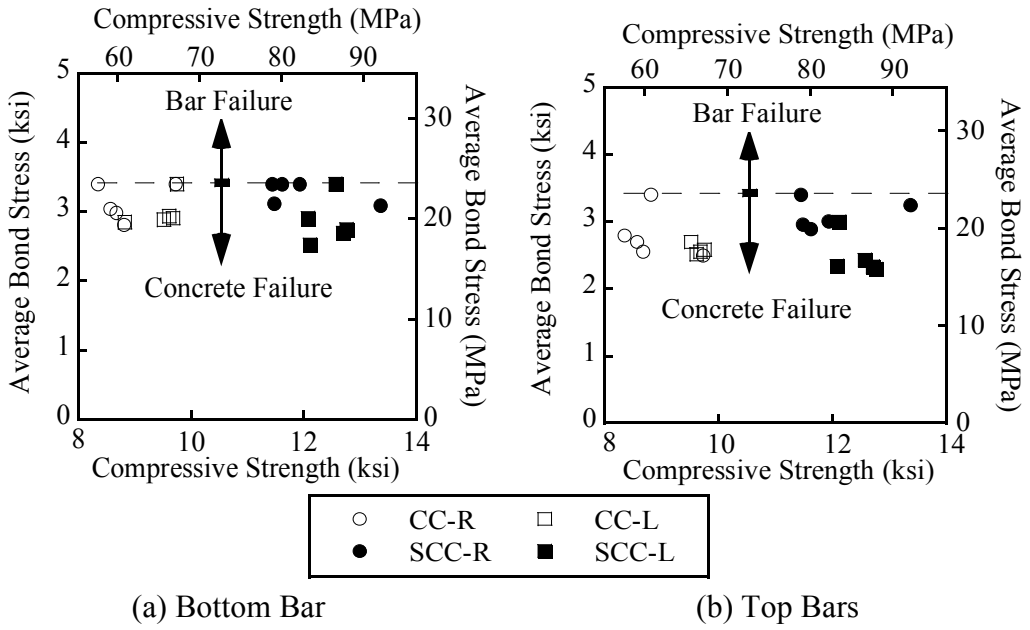

Figure 7.5. Compressive Strength versus Average Bond Stresses.

7.1.2 Assessment of Top Bar Effect

The impact of the top bar position on the bond stress between the reinforcement and concrete can be evaluated using the bond ratio. Figure 7.6 shows that the mean bond ratio of all specimens is higher than 1.0, indicating a reduction in the bond stress for the top bar relative to the bottom bar for a given pull-out sample. Therefore, water is likely collecting below the bar, increasing the *w/c* in this area, and thus decreasing the concrete strength and bond. The average bond ratio for the SCC with limestone aggregate was the highest among the different mixture proportions evaluated. The bond ratio for the SCC with river gravel aggregate indicates that the top bar effect is relatively small for this mixture. Furthermore, the SCC with river gravel has a lower bond ratio than the CC containing river gravel. An analysis was conducted to determine whether these differences are significant and is discussed in Section 7.1.4. The top bar multiplier of the AASHTO LRFD Specifications (2004, 2006) is approximately 20 percent higher than the observed bond ratio.

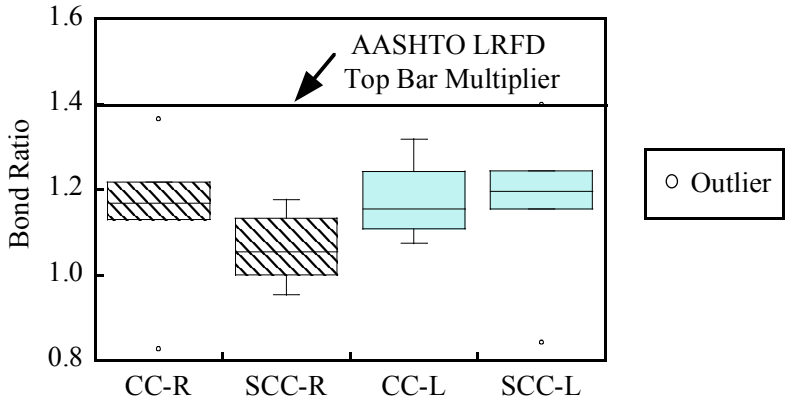

Figure 7.6. Bond Ratio Values to Evaluate Top Bar Effect.

7.1.3 Impact of Fresh Properties on Top Bar Effect

Researchers also assessed the impact of the fresh properties of the concrete mixtures on the bond ratio. The fresh properties of the CC mixtures can be evaluated using the slump measurements. As shown in Figure 7.7, no meaningful trends are observed when comparing the bond ratio to the slump. Because the vibrator practice has a greater influence on the bleeding potential of each sample, the slump does not give a good indication of the existence of reduced bond stress for top bars.

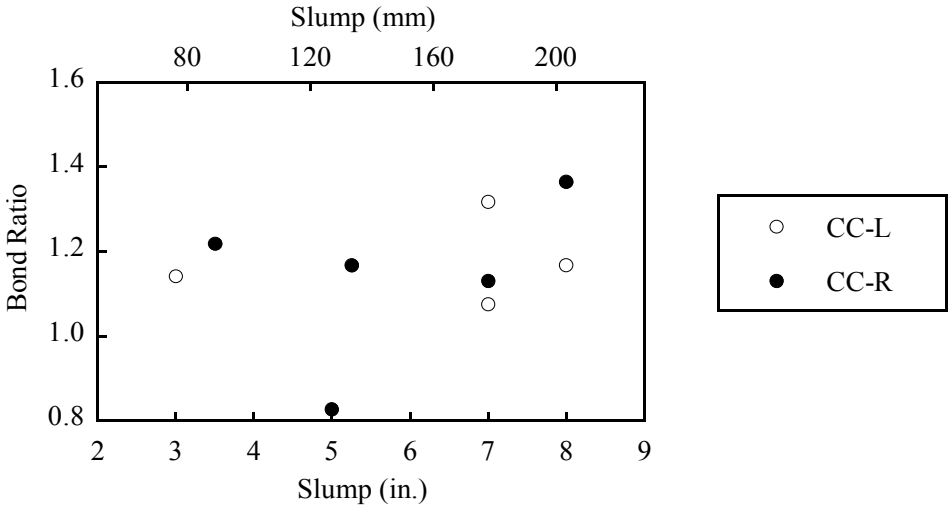

Figure 7.7. Bond Ratio versus Slump for CC Mixtures.

The fresh properties of SCC were evaluated by measuring the slump flow and T_{50}. Because the VSI value is a more subjective evaluation and because the SCC mixtures consistently were found to have VSI values between 0.5 and 1.0, the influence of the VSI value on the bond ratio was not assessed.

High slump flow and low T_{50} measurements indicate high workability. However, these measurements do not directly quantify the stability of a mixture, which can affect bleeding. As shown in Figure 7.8, slump flow or T_{50} does not directly influence the bond ratios for the SCC mixtures.

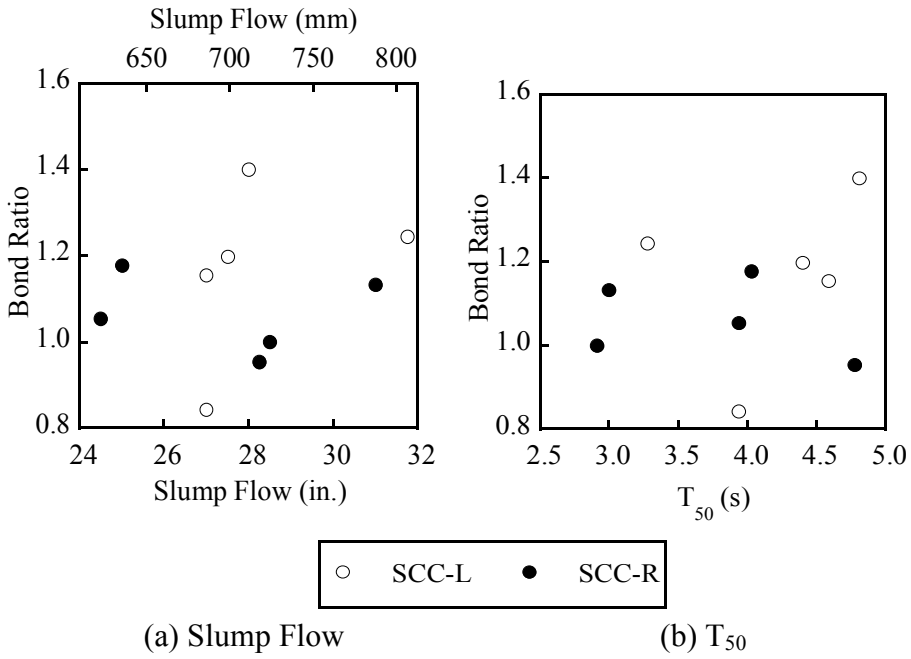

Figure 7.8. Bond Ratio versus Slump Flow for SCC Mixtures.

7.1.4 Statistical Assessment

A statistical analysis was performed to evaluate the significance of the mixture proportions and aggregate type on the bond ratio. For this analysis, the distribution is assumed to be normal for the residuals. As shown in Figure 7.9, the quantile plot is reasonably linear indicating that the assumption of a normal distribution for the statistical analysis is valid.

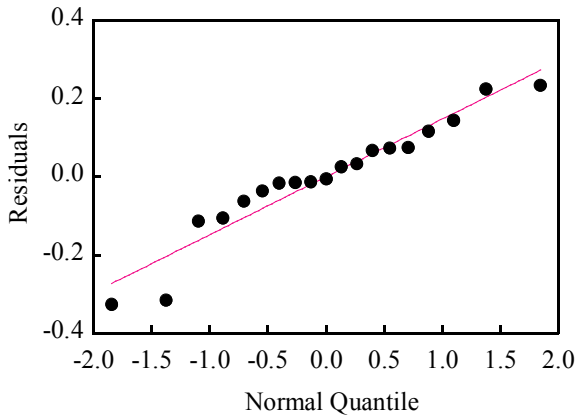

Figure 7.9. Quantile Plots for Bond Ratio.

According to previous observations for the test results, the fresh properties and compressive strength do not seem to influence the bond ratio, which is a measure of the top bar effect. Because each mixture proportion has a high variance for the bond ratio and similar mean bond ratios, the mean bond ratio for each mixture proportion was evaluated with statistical assessments to determine whether the mixture types significantly influence the bond stress ratio.

Table 7.5 provides the analysis of variance (ANOVA) table, obtained from the SAS Program (v. 9.1.3) (SAS Institute 2006). The ANOVA indicates that the type of concrete (SCC or CC) and the type of aggregate (limestone or river gravel) are not significant factors affecting the variance of the bond ratios. Because the *p*-value was larger than 0.05, the aggregate type, the concrete type, and combinations of aggregate type and mixture type are not significant factors affecting the bond ratio. The mean value of the bond ratio, indicating a top bar effect for all mixture proportions, is not significantly different. The interaction of mixture type (SCC or CC) with aggregate type is also not a significant factor. Therefore, the stable SCC mixtures considered in this study, having high paste volume, did not exhibit a significant top bar effect compared with the CC mixtures.

Table 7.5. ANOVA Table of Bond Ratio Value.

Source	Degree of Freedom	Type III Sum of Square	Mean Square	*p*-value
Agg	1	0.021144	0.02144	0.3797
Mix	1	0.009742	0.00974	0.5509
Agg x Mix	1	0.006294	0.00626	0.6316

Note: Agg: Two types of aggregate (Limestone and River Gravel).
Mix: Two types of mixtures (CC or SCC).

7.1.5 Summary

Based on the analysis and test results for assessing the relative bond for select SCC and CC mixtures, the following conclusions are drawn:

1) All 39 pull-out samples for evaluating the top bar effect for mild steel reinforcement had maximum stresses that exceeded the yield strength.
2) Most reinforcing bars failed by creating a splitting cone shaped failure surface initiated by concrete cone failure.
3) Most top bars exhibited lower bond strengths than the bottom bars for both the SCC and CC mixtures, indicating the existence of the top bar effect.
4) The relatively high bond strength of the SCC-R mixture may be attributed to the higher concrete compressive strength. However, the higher concrete compressive strength for the SCC-L mixture does not provide the same benefit of increased pull-out strength. The SCC-L mixture had slightly lower bond stress values than the CC-L mixtures.
5) The bond can be assessed using a bond ratio based on the ratio of the average bond stress of the bottom bar to the average bond stress of the companion top bar. The SCC-R mixture had the lowest bond ratio indicating the least top bar effect. The SCC-L mixture has highest bond ratio indicating the higher reduction of bond due to the top bar effect.
6) The measured fresh properties of the SCC and CC are not correlated with the bond ratio indicating the top bar effect in this study.
7) Based on a statistical analysis, the mixture type, aggregate type, and combination of aggregate and mixture types are not significant factors influencing the bond ratio.
8) All bond ratios are less than the top bar multiplier factor, 1.4, recommended in the AASHTO LRFD Specifications (2004 and 2006) for determining the tension development length of mild reinforcement. Therefore, the current AASHTO top bar factor of 1.4 is appropriate for the CC and SCC mixtures evaluated in this study.

7.2 CREEP

7.2.1 Compressive Strength and Creep Loading

A 16-hour compressive strength test was conducted using two cylinders from each batch. In the 16-hour test, the second batch of conventional concrete cast with limestone for 5 ksi (34 MPa) strength (CC5-L) had a significantly lower measured compressive strength than cylinders from the first batch. The reason for this lower 16-hour strength is unknown. However, after 7 days the strength was similar between the two batches. Because the loading was determined based on the compressive strength at 7 days, the samples from mixture CC5-L were used in the test program.

Table 7.6 shows the initial loading, loss of loading, and final loading. The loss of loading occurred when tightening the nuts for the four threaded rods.

Table 7.6. 7-Day Compressive Strength Cylinder Test and Creep Loading.

Concrete Type	Mixture ID	Average 7-day f'_c, ksi (MPa)	Initial Load, kip (kN)	Load Loss, kip (kN)	Creep Load, kip (kN)	Creep Load (% of f'_c)
SCC	S5G-3c	9.3 (63)	40 (178)	5 (22)	35 (156)	30
	S7G-6	11.6 (79)	47 (209)	9 (40)	38 (169)	26
	S5L-3c	9.4 (65)	43 (191)	7 (31)	36 (160)	30
	S7L-6	12.8 (88)	48 (214)	9 (40)	39 (173)	25
CC	C5G	9.4 (65)	39 (173)	3 (13)	36 (160)	31
	C7G	10.6 (73)	43 (191)	4 (18)	39 (173)	30
	C5L	8.5 (59)	35 (156)	2 (9)	33 (147)	31
	C7L	10.4 (72)	40 (178)	4 (18)	36 (160)	27

7.2.2 Overall Comparison of Creep

An overall comparison of the SCC and CC creep samples is shown in Figure 7.10. The measured creep curves were obtained from the average of two batches of each mixture. Each frame was equipped with four cylinders that were cast with the same mixture proportions from two different batches. The strain measurements for cylinders within each frame varied by as much as 15 percent. Appendix E provides data of each channel. The amount of cement paste and the stiffness of aggregate in mixtures can affect the creep. The impact of key variables on the creep is reviewed in the following subsections. Based on the ASTM C512, the strain readings of the control sample (i.e., shrinkage) are subtracted from the strain readings from the samples in

the creep frame. The S7L-6 mixtures have only readings from the creep frame due to the failure of strain gages in the control samples.

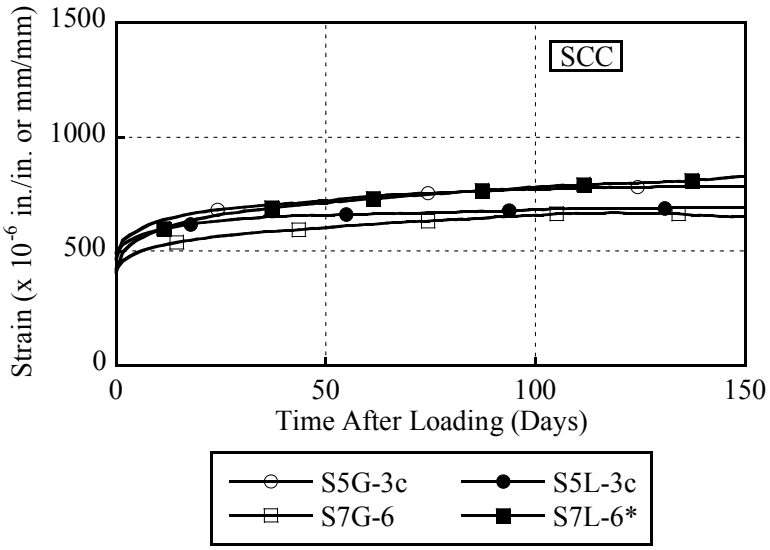

Note: * indicates no correction for creep strain.

(a) SCC

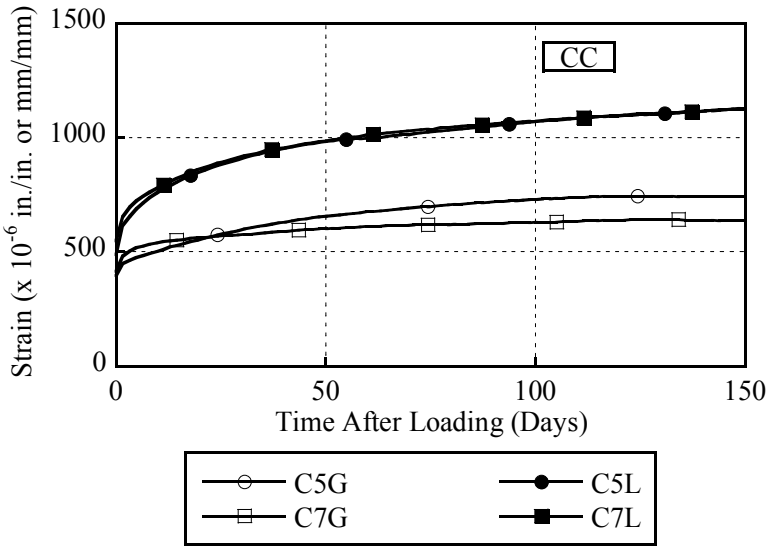

(b) CC

Figure 7.10. Creep of SCC and CC Mixtures.

7.2.2.1 Effect of Target 16-Hour Compressive Strength

In the experimental matrix, samples were cast with two levels of 16-hour target compressive strength, 5 and 7 ksi (35 and 48 MPa). For the SCC and CC mixtures the strength does not seem to be an important factor influencing creep. This is shown in Figure 7.11. The plot shows the average, maximum, and minimum values of creep. The average of the 5 and 7 ksi (35 and 48 MPa) mixtures was not significantly different. However, the variance of the overall creep was relatively large, with more variation observed for the 7 ksi (48 MPa) target release strength mixtures.

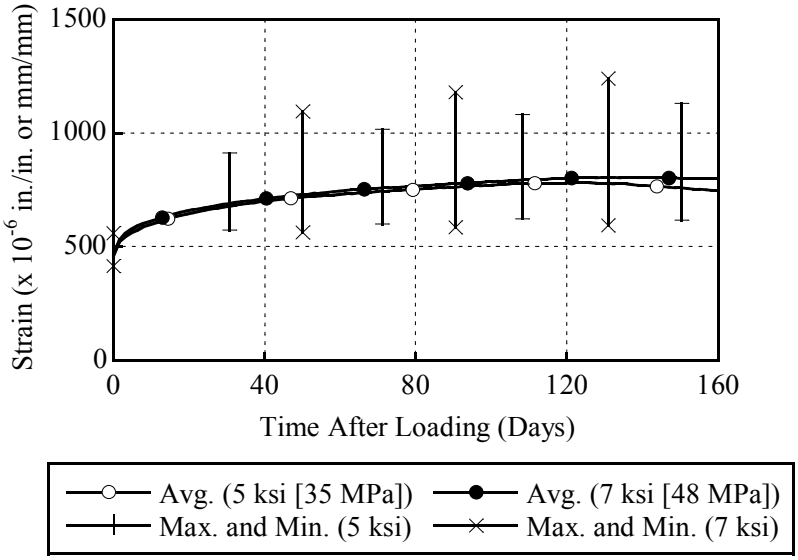

Figure 7.11. Effect of 16-hour Compressive Strength on Creep.

7.2.2.2 Effect of Aggregate Type

Both river gravel and limestone were used for the CC and SCC mixtures. These are representative coarse aggregates that are used widely in Texas. The type of aggregate is one of the most important factors that can determine not only compressive strength, but also creep. Because the stiffness of river gravel is higher than that of the limestone, it assumed that the concrete with river gravel will exhibit lower creep than the concrete with limestone. During the test program, the MOE of concrete with limestone aggregate was lower than that of the concrete with river gravel (see Section 5.3). Both the CEB-FIP (1993) and the 2006 AASHTO LRFD

prediction equations assume that the creep of limestone concrete mixture will be higher than that of river gravel concrete mixtures. As shown in Figure 7.12, the limestone mixtures have higher average and variance in measured creep relative to the river gravel mixtures.

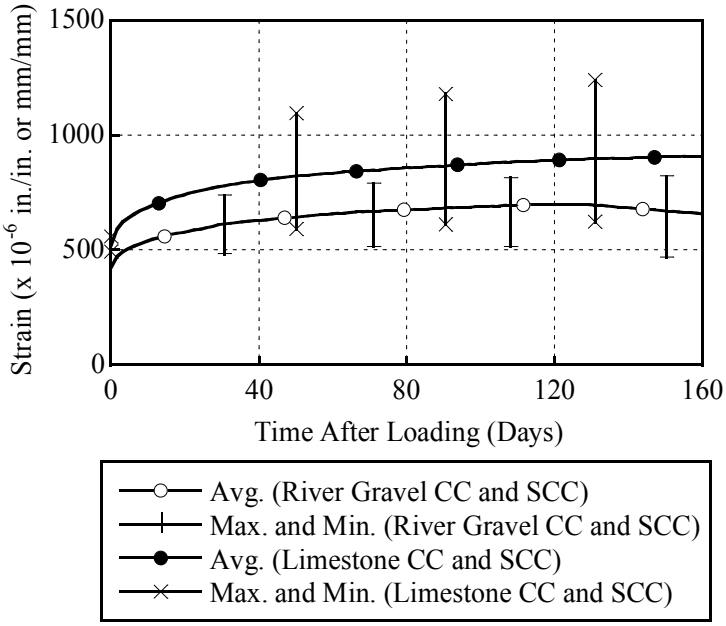

Figure 7.12. Creep of Type of Coarse Aggregate.

7.2.2.3 Comparison of SCC and CC

Figure 7.13 compares the average creep and overall range of creep measurements for the CC and SCC mixtures. Creep of the SCC mixtures is lower than that of the CC mixtures. The SCC mixtures contain greater cement contents, whereas the CC mixtures contain higher aggregate volumes. Maximum creep for CC is 18 percent higher than that of SCC. This might be attributed to the limestone CC mixture.

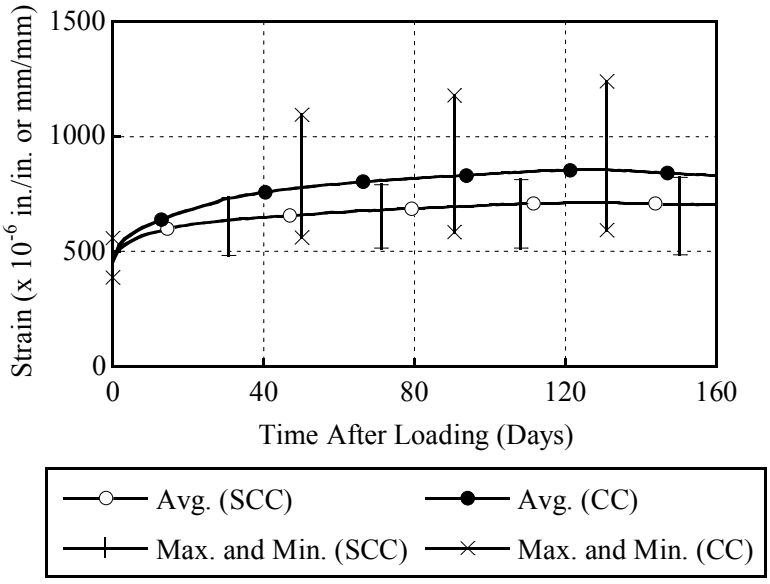

Figure 7.13. Creep of CC and SCC Mixtures.

For a more detailed comparison, considering strength level and type of coarse aggregate, Figure 7.14 shows the creep of each individual concrete mixture with solid circles corresponding to CC and open circles corresponding to SCC. The creep of the limestone CC mixture is obviously higher than that of the limestone SCC mixture for both the 5 and 7 ksi (34 and 48 MPa) mixtures. For the river gravel mixtures, SCC had similar creep compared with the CC mixture having the same target strength at 16 hours. This could be attributed to the high volume of the limestone aggregate along with the relatively low paste strength of the CC. However, the strength gain at later ages is significant for the SCC mixtures, mitigating further increases in creep. Because limestone SCC mixtures exhibited failure of the strain gages in the control samples, Figure 7.14 (d) shows the creep strain of 7 ksi (48 MPa) limestone mixtures for both the CC and SCC mixtures. Appendix F provides the comparisons between two mixtures to compare the effect of key parameters.

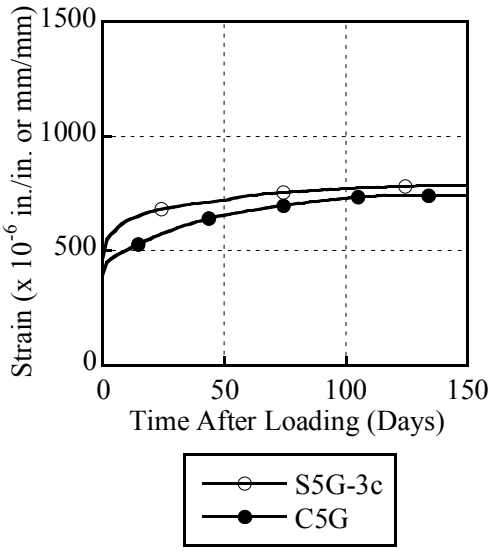

(a) 5 ksi (34 MPa) River Gravel

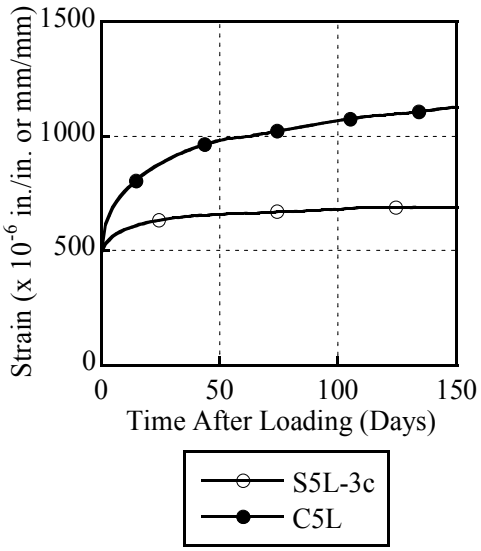

(b) 5 ksi (34 MPa) Limestone

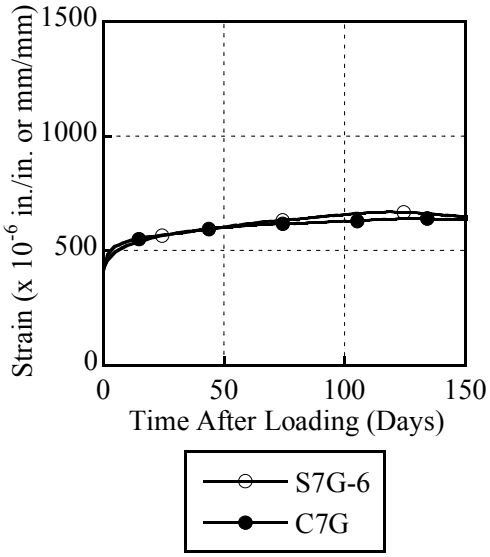

(c) 7 ksi (48 MPa) River Gravel

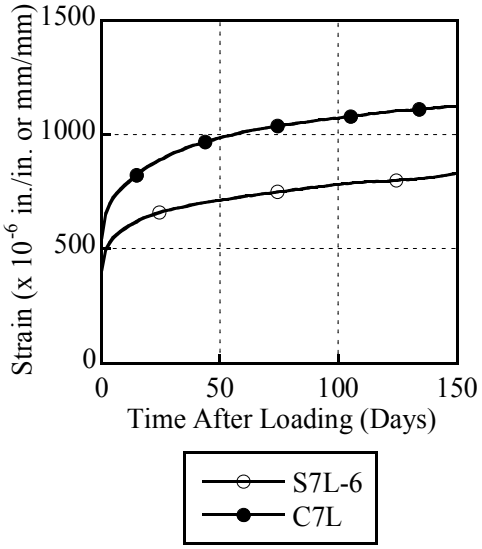

(d) 7 ksi (48 MPa) Limestone

Figure 7.14. Creep of All Mixtures.

7.2.3 Prediction Models for SCC and CC

Table 7.7 provides a summary of creep prediction equations evaluated in this study. The models are described in more detail in Appendix A. Because all the models, except for the BP and B3 models, proposed an expression for the creep coefficient, the compliance function of the BP and B3 models was converted to provide the creep coefficient. The creep coefficient

expressions can be multiplied by the elastic strain due to the applied load to determine the corresponding creep strain.

Table 7.7. Equations for Predicting Creep Coefficients as a Function of Time.

Models	Creep Coefficients
AASHTO LRFD (2004)	$3.5\ k_c k_f \left(1.58 - \frac{H}{120}\right) t_j^{-0.118} \frac{(t-t_i)^{0.6}}{10.0+(t-t_i)^{0.6}}$
AASHTO LRFD (2006)	$1.9 k_{vs} k_{hc} k_f k_{td} t_i^{-0.118}$
ACI Committee 209 (1992)	$\frac{t^{0.60}}{10+t^{0.60}} v_u$
CEB-FIP (1993)	$\phi_0 \beta_c (t-t_0)$
BP model (Bazant and Panula 1984)	$E(t')J(t,t')-1 = E(t')\left(\frac{1}{E_0}+C_0(t,t')+C_d(t,t',t_0)-C_P(t,t',t_0)\right)-1$
B3 model (Bazant and Baweja 2000)	$E(t')J(t,t')-1 = E(t')\left(\frac{1}{E_0}+C_0(t,t')+C_d(t,t',t_0)\right)-1$
GL 2000 model (Gardner and Lockman 2001)	$\phi(t_c)\left[2\left(\frac{(t-t_0)^{0.3}}{(t-t_0)^{0.3}+14}\right)+\left(\frac{7}{t_0}\right)^{0.5}\left(\frac{t-t_0}{t-t_0+7}\right)^{0.5} +2.5\left(1-1.086h^2\right)\left(\frac{t-t_0}{t-t_0+0.15\cdot(V/S)^2}\right)^{0.5}\right]$

All of the concrete mixture data were input into each of the prediction models. The creep strains were plotted along with the prediction equations and are presented in Appendix G. Figures 7.15 and 7.16 show prediction curves and the measured creep of the river gravel 5 ksi (34 MPa) SCC and CC mixtures. When applying these prediction formulas to the SCC and CC mixtures, it was observed that some predicted measurements of creep and shrinkage were similar for a given 16-hour strength and aggregate type. For example, the B3 and BP models and GL 2000 predict similar magnitudes of creep strain. The ACI 209 (the slump is assumed to be zero) and the 2004 AASHTO equations have similar magnitudes of creep strain. The AASHTO LRFD 2006 model predicts the creep strain of the S5G concrete well.

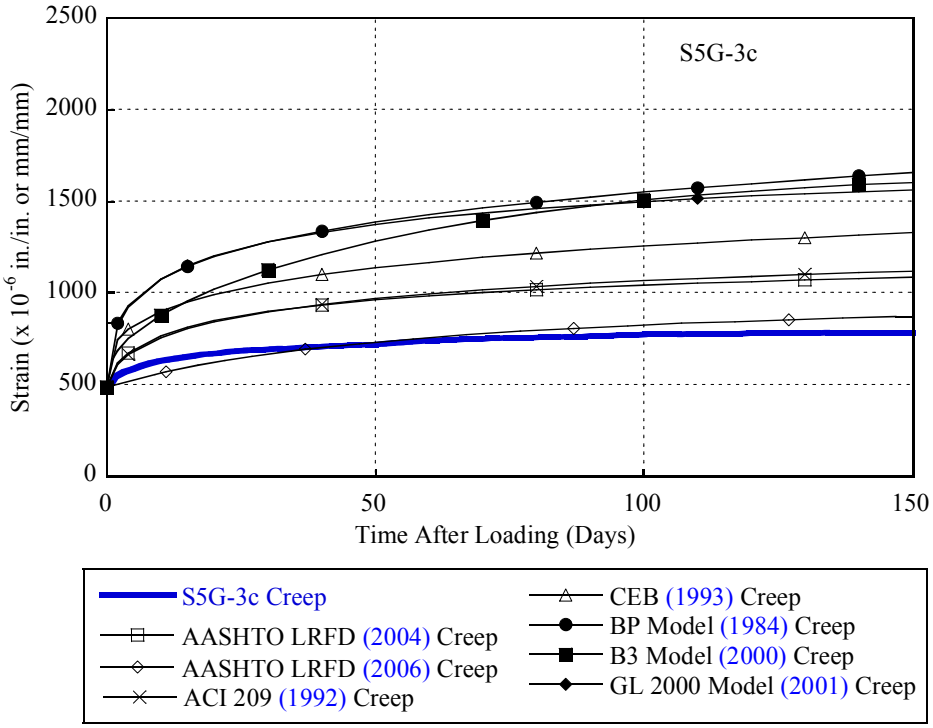

Figure 7.15. Creep versus Predictions for S5G-3c.

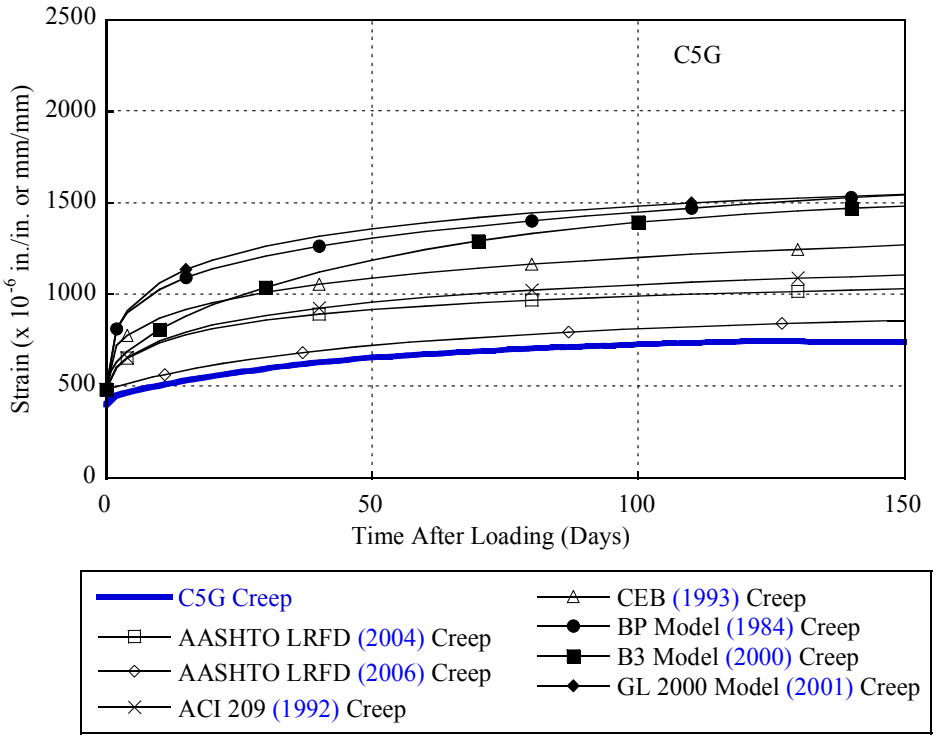

Figure 7.16. Creep versus Predictions for C5G.

Figures 7.17 and 7.18 show prediction curves and the measured creep for the river gravel 7 ksi (48 MPa) SCC and CC mixtures. The B3, BP, and GL 2000 models predict similar magnitudes of creep, but much higher than the creep for the C5G specimens. The AASHTO LRFD (2006) model best estimates the creep for the C5G concrete.

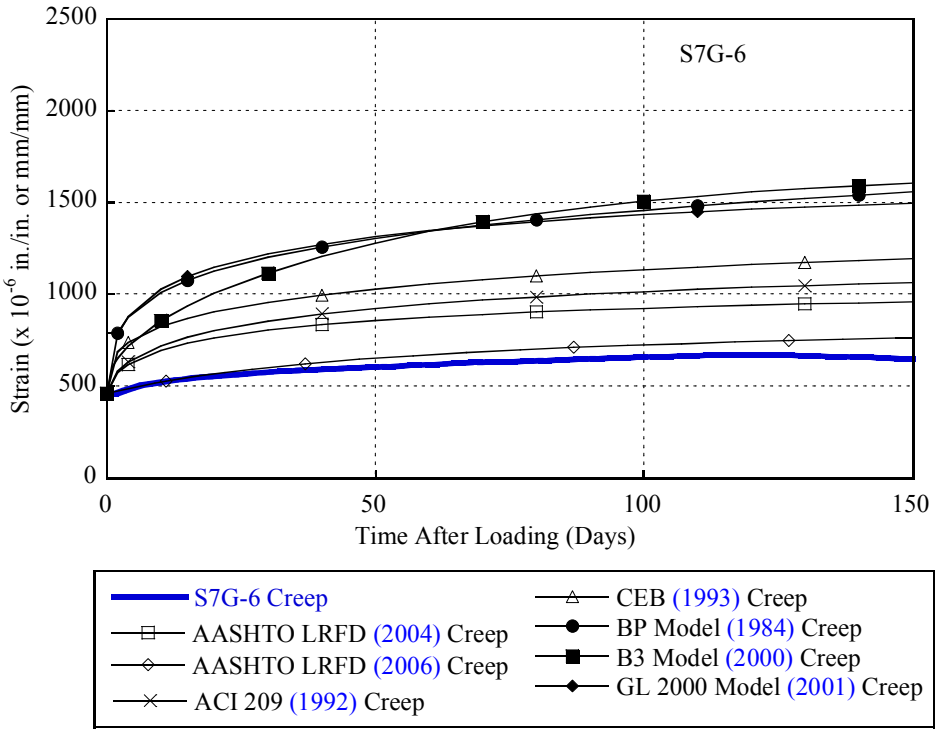

Figure 7.17. Creep versus Predictions for S7G.

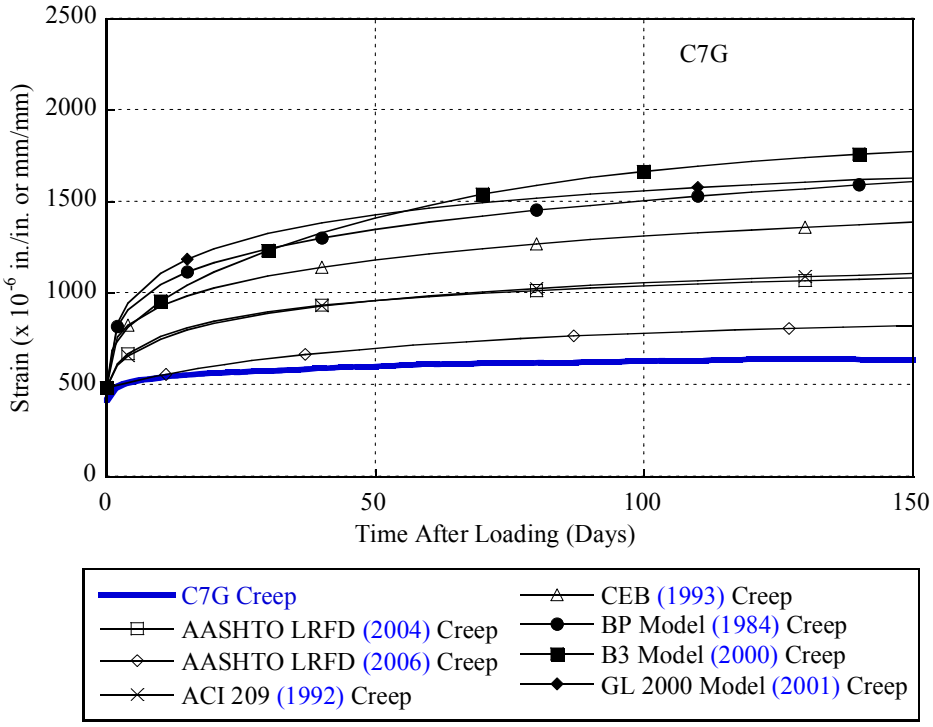

Figure 7.18. Creep versus Predictions for C7G.

Figure 7.19 shows that all prediction curves stabilized at approximately 500 days after loading.

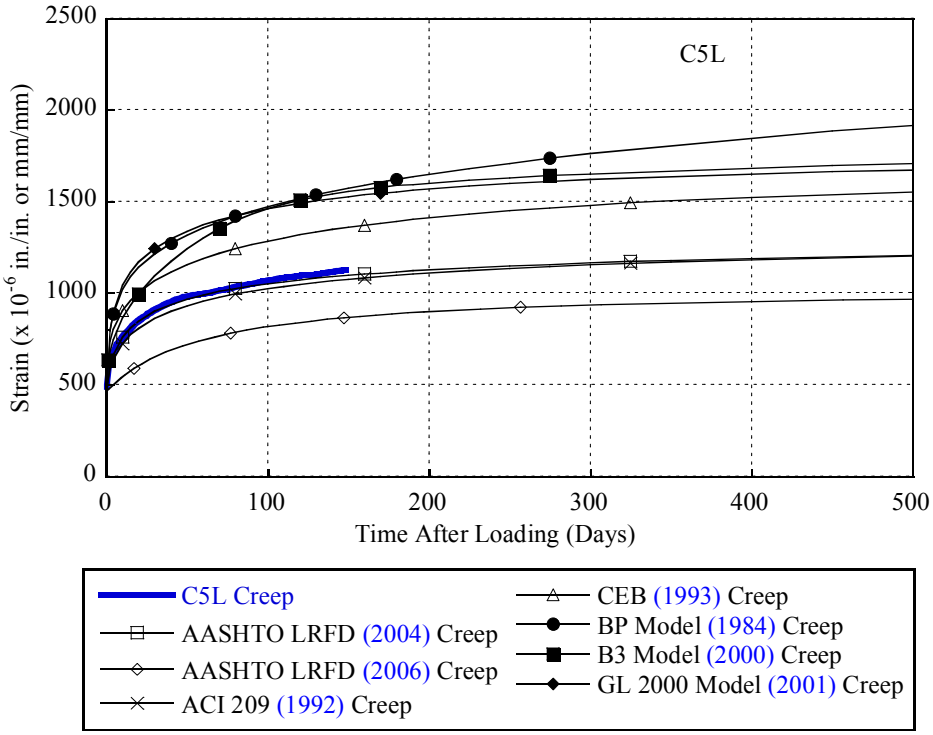

Figure 7.19. Creep versus Predictions for C5L for Later Ages.

7.2.4 Predicted Values versus Experimental Values

Creep coefficients and creep compliances for the CC and SCC mixtures were compared.

7.2.4.1 Creep Coefficients

Creep coefficients are used to predict the prestress losses in the AASHTO LRFD Bridge Design Specifications. Figure 7.20 shows the measured creep of the mixtures converted to the corresponding creep coefficient. The creep coefficients of limestone CC mixtures are larger than those of the other mixtures. Table 7.8 summarizes the creep coefficients calculated from prediction equations at 150 days and ultimate (75 years). Generally, the creep coefficients from AASHTO LRFD 2006 are the smallest among all the coefficients at 150 days and ultimate. The creep coefficients from AASHTO LRFD 2006 for all the mixtures are smallest and predict fairly well the measured creep coefficients at 150 days.

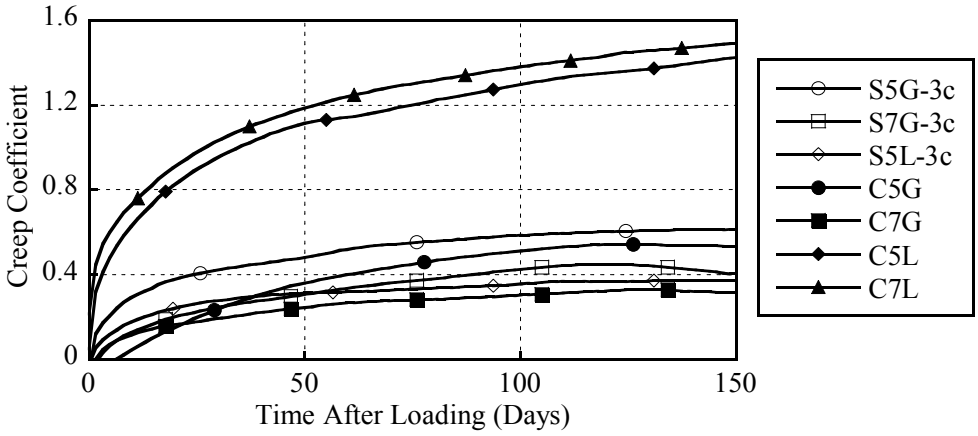

Figure 7.20. Comparison of Creep Coefficients from Different SCC and CC Mixtures.

Table 7.8. Summary of 150-day and Ultimate Creep Coefficients.

	Mixture ID							
Creep Coefficients	S5G-3c	S7G-6	S5L-3c	S7L-6	C5G	C7G	C5L	C7L
ASTM C512 (Creep Test Results)								
Test Results	0.61	0.40	0.37	-	0.54	0.32	1.43	1.50
Predicted Creep Coefficients (150 Days)								
AASHTO 2004	0.78	0.68	0.72	0.72	0.72	0.79	0.86	0.73
AASHTO 2006	0.65	0.53	0.64	0.48	0.64	0.58	0.70	0.59
ACI 209	0.96	0.96	0.96	0.96	0.96	0.96	0.97	0.94
BP	2.20	2.19	2.25	2.20	2.00	2.15	2.18	2.19
B3	1.57	1.74	1.50	2.02	1.38	1.79	1.54	1.59
CEB-FIP	1.96	1.78	1.85	1.85	1.85	1.98	2.12	1.88
GL 2000	2.07	2.07	2.07	2.07	2.07	2.07	2.07	2.07
Predicted Creep Coefficients (Ultimate)								
AASHTO 2004	1.31	1.15	1.22	1.22	1.22	1.33	1.45	1.24
AASHTO 2006	0.90	0.74	0.89	0.67	0.89	0.80	0.97	0.81
ACI 209	1.40	1.41	1.40	1.41	1.40	1.40	1.42	1.37
BP	2.76	2.51	2.61	2.61	2.61	2.79	2.98	2.64
B3	6.97	6.96	7.12	6.98	6.07	6.76	6.87	6.97
CEB-FIP	3.67	4.12	3.59	4.58	3.33	4.13	3.54	3.75
GL 2000	3.83	3.83	3.83	3.83	3.83	3.83	3.83	3.83

Note: - indicates no estimation.

7.2.4.2 Creep Compliance

According to ACI Committee 209 at its November 1999 committee meeting (Gardner and Lockman 2001) and RILEM Technical Committee 107 (1995), because the instantaneous MOE at loading time depends on the loading rate, the compliance or specific creep is considered as a more appropriate value for the creep comparisons. Creep values should be compared based on the compliance value, $J(t, t')$ or specific creep function (Mattock 1979).

The compliance function or value (creep function or value) can be obtained from the following equation:

$$J(t,t') = \frac{\phi(t,t')+1}{E(t')} = \frac{1}{E(t')} + \frac{\varepsilon_c}{\sigma} \qquad (7.1)$$

where $\phi(t, t')$ is the creep coefficient at time t, and $E(t')$ is the MOE at time, t', ε_c is the creep strain, σ is the constant stress, and ε_c/σ is the specific creep function. The compliance values for different concrete mixtures are compared in this study.

The errors of the prediction model can be estimated based on charts of measured versus predicted values. Figure 7.21 shows measured and predicted creep compliance to evaluate the accuracy of each model for estimating creep. In general, the prediction formulas overestimate measured creep. The 2004 AASHTO LRFD slightly overestimated measured creep except for the limestone CC mixtures. The 2004 and 2006 AASHTO LRFD equations are purposely developed to provide simple equations for the engineers. It should be noted that the AASHTO equations predict creep without consideration of the characteristics of mixture proportions. When the SCC mixture proportions are considered, the 2006 AASHTO LRFD prediction equation is appropriate for the estimation of creep of the SCC and CC mixtures. The predicted creep values are within ±50 percent error, which indicates that the accuracy of the model is acceptable according to the AASHTO LRFD Specifications (2006). The AASHTO LRFD Specifications also recommends the CEB-FIP and ACI 209 models. These models and the 2004 AASHTO LRFD also predict creep within ±50 percent error.

The BP, B3, and ACI 209 models consider the various aspects of mechanical properties and characteristics of mixture proportions impact on the creep. The mixture proportions are different between the CC and SCC, resulting in a different level for accuracy of each prediction model. The specific model sensitively considers the internal factors, such as mixture proportions and mechanical properties, resulting in either high level of accuracy or wide range of error magnitudes. Among these models, except for the 2004 and 2006 AASHTO LRFD, the BP model overestimates creep with a high degree of scatter, which indicates the high sensitiveness of internal parameters. In general, these models still overestimate creep for SCC when the mixture proportions are considered. Therefore, including information about the high paste volume and low coarse aggregate volume of SCC does not increase accuracy when using these creep prediction expressions.

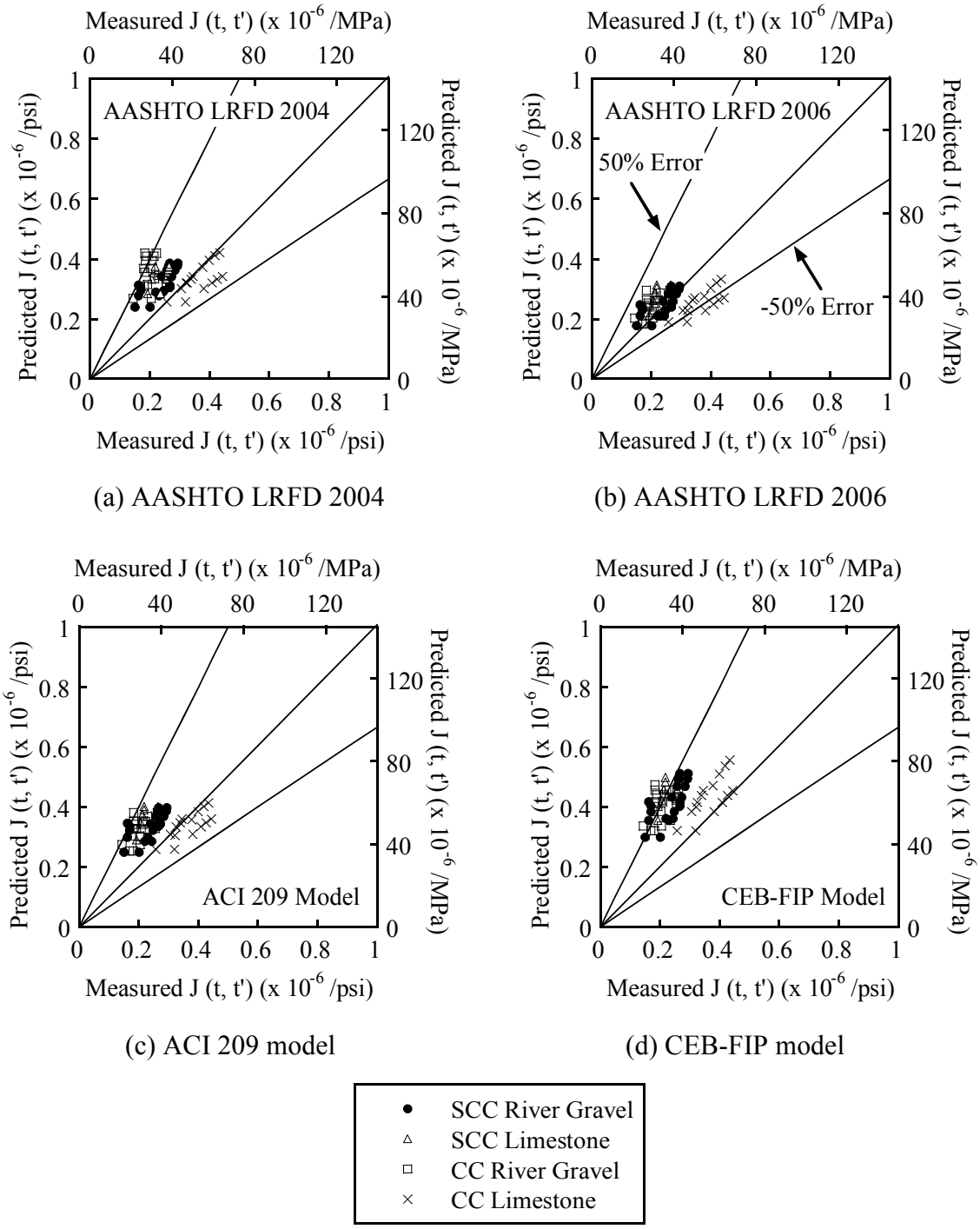

Figure 7.21. Predicted *J*(*t, t'*) and Measured *J*(*t, t'*).

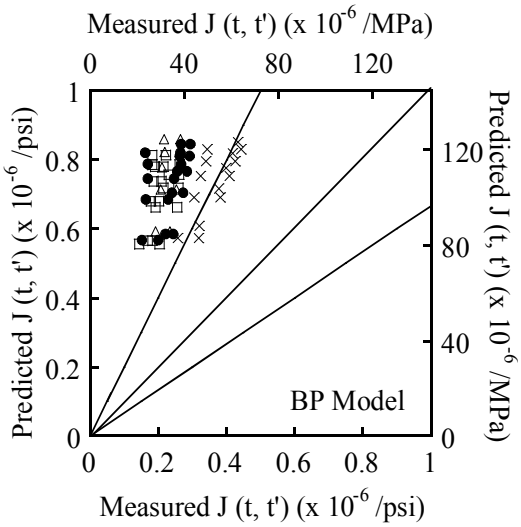

(e) BP model

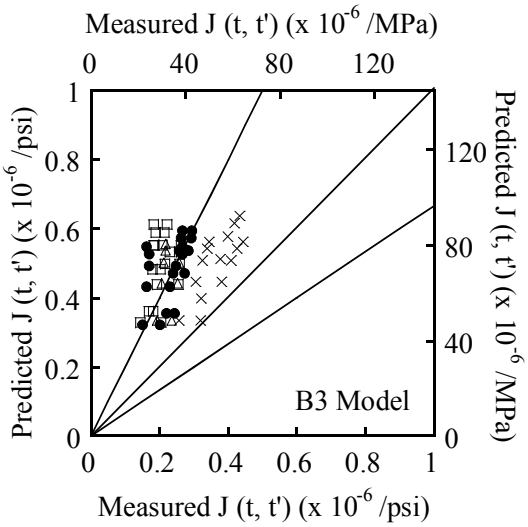

(f) B3 model

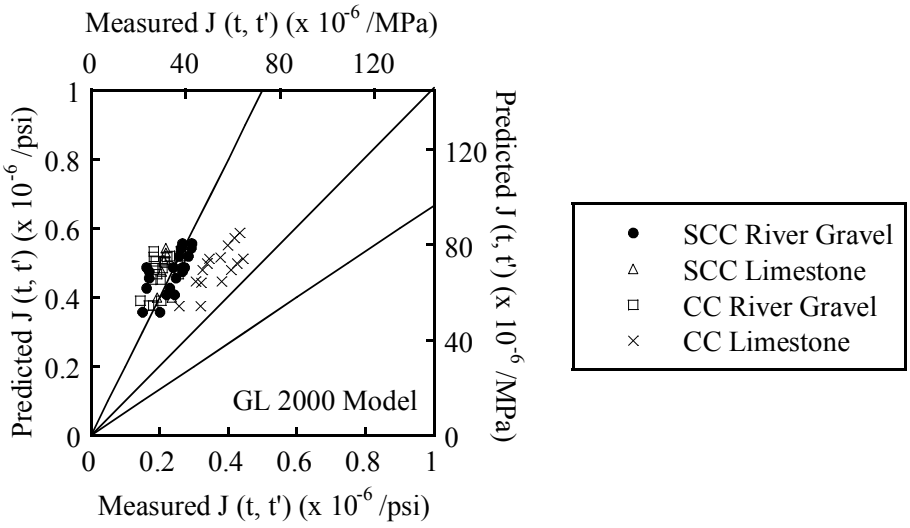

(g) GL 2000 model

Figure 7.21. Predicted *J*(*t, t'*) and Measured *J*(*t, t'*) (cont.).

The equations recommended by CEB-FIP, ACI 209, and 2004 AASHTO LRFD gave conservative prediction estimates of the measured creep strains. For the limestone CC mixtures, the ACI 209, CEB-FIP, and 2004 AASHTO LRFD models seem to be appropriate compared with the other models. The BP, B3, and GL 2000 models were conservative in estimating creep strains for all mixtures. Because these prediction equations were developed based on normal strength CC mixtures, these prediction equations likely need to be calibrated for the higher strength the SCC mixtures.

7.2.5 Summary

By analysis and comparison of test results and prediction models for SCC and CC mixtures, this research investigated whether existing prediction models for creep of CC are applicable to SCC mixtures. For SCC and CC, many factors can affect creep. Because the external factors were consistent during this test, the difference in creep is a result of constituent material type and proportions in the mixtures. The amount of cement paste, the stiffness of aggregate, and early gain of compressive strength from each mixture of SCC and CC were mainly investigated as affecting factors on creep. Based on the above test results, conclusions are drawn as following,

1) The river gravel SCC mixtures show similar creep to the river gravel CC mixtures with the same 16-hour target compressive strengths. Although the 16-hour compressive strengths of the SCC and CC mixtures were almost the same, the creep of the limestone CC was higher than that of the limestone SCC. In addition, CC samples with lower compressive strengths exhibited higher creep. The effect of the 16-hour compressive strength was found to not be a significant factor affecting creep.
2) Because the stiffness of the river gravel is higher than that of limestone, river gravel mixtures had lower creep compared to the limestone mixtures, as expected. The MOE provides an indication of the stiffness of aggregate. According to the mechanical property testing, the MOE of concrete with the limestone coarse aggregate is lower than the MOE for concrete with the river gravel. The effect of coarse aggregate type was clearly observed in the CC mixtures. However, the effect of the coarse aggregate types was not significant for the SCC mixtures.
3) The perceived impact of high paste volume and low coarse aggregate volume on the creep of SCC seems to be unfounded for the mixtures evaluated in this research. However, the SCC mixtures exhibited higher strengths than the CC mixtures, which could account for the similar or lower creep values.
4) The 2006 AASHTO LRFD Specifications allows prediction models to have ±50 percent error in creep prediction. The 2004 and 2006 AASHTO LRFD models, the ACI 209 model, and the CEB-FIP model provide fairly good predictions for the creep of both CC and SCC mixtures. Because the 2006 AASHTO LRFD model was

calibrated for high-strength concrete with low *w/c*, the prediction model seems to better predict CC and SCC mixtures evaluated in this study.

5) Prediction models are available that consider the compressive strength, MOE of aggregate, and mixture proportions. The BP, B3, and GL 2000 prediction models are based on data from normal strength CC and overestimated the creep for the SCC and CC mixtures evaluated in this research by more than 50 percent.

7.3 DURABILITY

Test results of permeability, diffusivity, and freezing and thawing resistance of the SCC are discussed in following sections.

7.3.1 Freezing and Thawing Resistance

This section will present the results of freezing and thawing resistances of the SCC and CC mixtures. Relative dynamic modulus can represent the damage due to freezing and thawing.

Figure 7.22 shows relative dynamic modulus versus number of cycles for the 5 ksi (34 MPa) SCC mixtures, 7 ksi (48 MPa) SCC mixtures, and CC mixtures. For the 5 ksi (34 MPa) SCC mixtures, relative dynamic modulus was significantly reduced to about 40 percent before approximately 150 cycles, indicating the air void size and distribution are not sufficient to resist the freezing and thawing damage. For the CC mixtures, the 5 ksi (34 MPa) CC mixtures have relatively low resistance to freezing and thawing compared to the 7 ksi (48 MPa) CC mixtures. Because the mixtures have similar air contents (approximately 1.2 percent with a standard deviation of 0.23 percent), the total volume of air content does not seem to be significant factor.

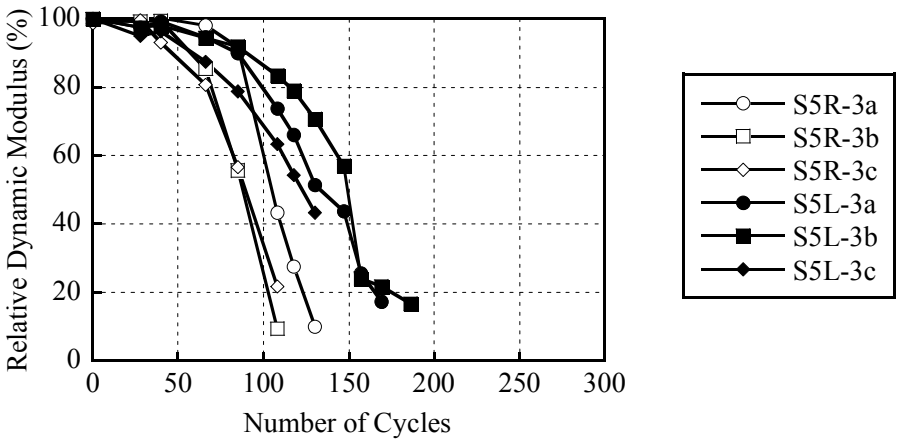

(a) 5 ksi (34 MPa) SCC Mixtures

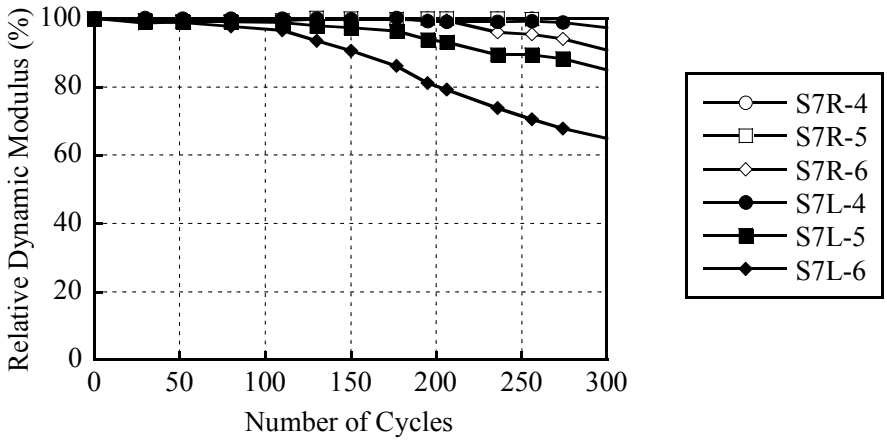

(b) 7 ksi (48 MPa) SCC Mixtures

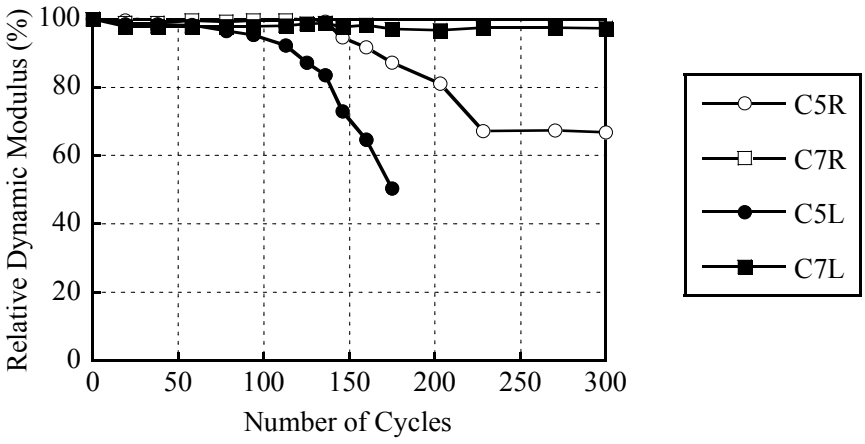

(c) CC Mixtures

Figure 7.22. Relative Dynamic Modulus versus Number of Cycles.

Tables 7.9 through 7.11 show the summary of test results for all the mixtures. The test results show the durability factor (DF) of each sample.

The durability factor DF can then be recalled as follows:

$$DF = \frac{P \times N}{M} \tag{7.2}$$

where P is the relative dynamic MOE at N cycles (%), N is the number of cycles at which P reaches the specified minimum value for discontinuing the test or the specified number of cycles at which the exposure is to be terminated, whichever is less, and M is the specified number of cycles at which the exposure is to be terminated, which is equal to 300 cycles.

Table 7.9. DF of 5 ksi (34 MPa) SCC Mixtures.

Mixture ID	S5G-3a			S5G-3b			S5G-3c			S5L-3a			S5L-3b			S5L-3c		
N (cycles)	121	101	96	85	82	82	110	85	101	130	165	100	133	133	175	114	115	114
P (%)	60	60	60	60	60	60	60	60	60	60	60	60	60	60	60	60	60	60
M (cycles)	300	300	300	300	300	300	300	300	300	300	300	300	300	300	300	300	300	300
DF	24.2	20.2	19.2	17.0	16.4	16.4	22.0	17.0	20.2	26.0	33.0	20.0	26.6	26.6	35.0	22.8	23.0	22.8
Average DF	21			17			20			26			29			23		
Standard Deviation	2.6			0.4			2.5			6.5			4.9			0.1		

Table 7.10. DF of 7 ksi (48 MPa) SCC Mixtures.

Mixture ID	S7G-4			S7G-5			S7G-6			S7L-4			S7L-5			S7L-6		
N (cycles)	300	300	300	-	300	300	300	300	300	300	300	300	300	300	300	300	300	256
P (%)	100	100	100	-	100	100	78	97	97	98	100	93	85	83	86	67	70	60
M (cycles)	300	300	300	-	300	300	300	300	300	300	300	300	300	300	300	300	300	300
DF	100	100	100	-	100	100	78	97	97	98	100	93	85	83	86	67	70	51
Average DF	100			100			91			97			85			63		
Standard Deviation	0			0			11			3.6			1.5			10.1		

Note: - indicates that there is no test result.

Table 7.11. DF of CC Mixtures.

Mixture ID	C5G			C7G			C5L			C7L		
N (cycles)	300	175	300	300	300	300	153	175	165	300	300	300
P (%)	100	60	100	100	100	100	60	60	60	60	100	100
M (cycles)	300	300	300	300	300	300	300	300	300	300	300	300
DF	100	35	100	100	100	100	31	35	33	60	100	100
Average	78			100			32.9			87		
Standard Deviation	38			0			2.2			23.09		

Test results show that the 5 ksi (34 MPa) SCC mixtures exhibit low DF after approximately 110 cycles. There is no significant effect of aggregate type on DF for the 5 ksi (34 MPa) mixtures. For the 7 ksi (48MPa) mixtures, the river gravel mixtures have higher DF than the limestone mixtures. For the CC mixtures, the 5 ksi (34 MPa) limestone CC mixture shows the lowest DF values. For the CC mixtures, the 7 ksi (48 MPa) mixture has excellent freezing and thawing resistance.

According to Thomas (2007), the high volume replacement of fly ash in cementitious material content can reduce the resistance to freezing and thawing. The 5 ksi (34 MPa) SCC mixtures have more than 32 percent by volume fly ash replacement. Higher *w/cm* also affects the low resistance along with poor distribution of voids. However, the 7 ksi (48 MPa) SCC mixtures containing approximately 20 percent replacement did not exhibit high degradation from freezing and thawing. This could be attributed to low *w/cm*.

7.3.2 Rapid Chloride Penetration Test

Figure 7.23 shows the rapid chloride resistance results for different CC and SCC mixtures. In general, the SCC mixtures have higher chloride permeability at early ages (7 days) compared to the CC mixtures. However, at later ages the SCC mixtures have lower permeability compared to the 5 ksi (34 MPa) CC mixtures for both aggregate types. For the 7 ksi (48 MPa) mixtures, SCC and CC have similar chloride ion permeability values at later ages (approximately 28 days).

Tables 7.12 through 7.14 show the classification from ASTM C1202 for the permeability of each sample at the day of testing. When the classification is considered, the SCC mixtures have moderate permeability and the CC mixtures have low or moderate permeability values. At 56 days the SCC mixtures have very low permeability and the CC mixtures have low permeability.

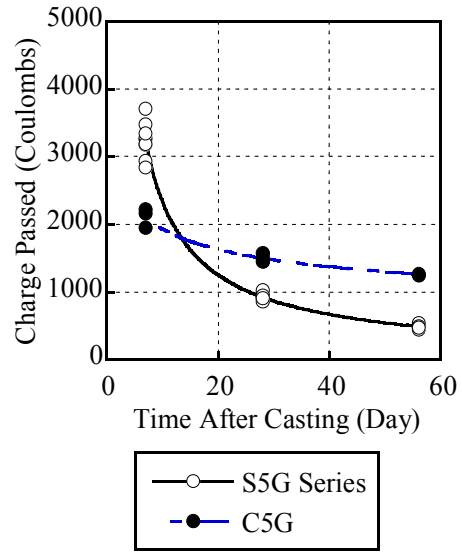

(a) 5 ksi (34 MPa) River Gravel

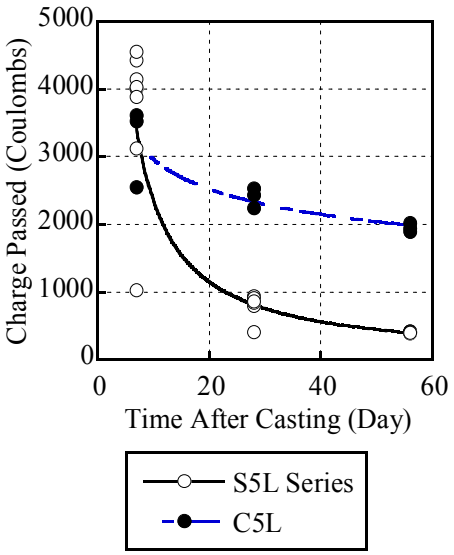

(b) 5 ksi (34 MPa) Limestone

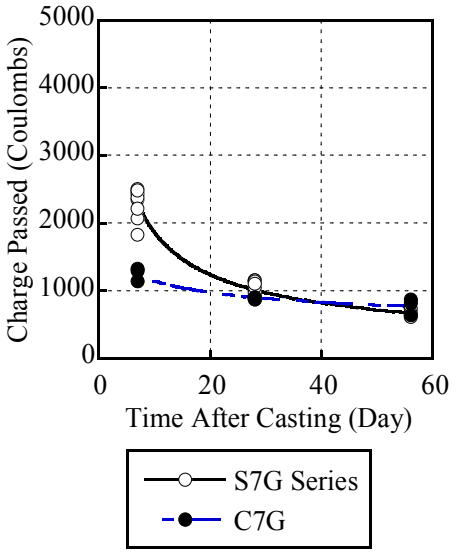

(c) 5 ksi (34 MPa) River Gravel

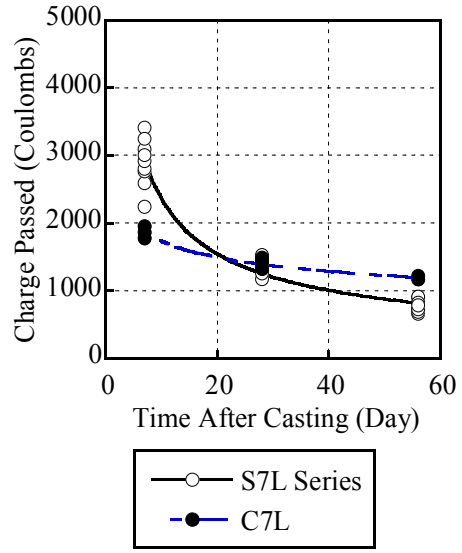

(d) 5 ksi (34 MPa) Limestone

Figure 7.23. Charge Passed versus Time.

Table 7.12. Permeability Class of River Gravel SCC Mixtures.

Age of Test	Mixture ID																	
	S5G-3a			S5G-3b			S5G-3c			S7G-4			S7G-5			S7G-6		
7 days	M	M	M	M	M	M	M	M	M	M	M	M	M	M	M	M	M	M
28 days	VL	VL	VL	VL	VL	VL	VL	L	VL	VL	L	L	L	VL	VL	L	L	L
56 days	VL	VL	VL	VL	VL	VL	VL	VL	VL	VL	VL	VL	VL	VL	VL	VL	VL	VL

Note: H = High, M = Moderate, VL = Very Low, L = Low.

Table 7.13. Permeability Class of Limestone SCC Mixtures.

Age of Test	Mixture ID																	
	S5L-3a			S5L-3b			S5L-3c			S7L-4			S7L-5			S7L-6		
7 days	M	H	M	H	H	M	H	H	-	M	M	M	M	M	M	M	M	M
28 days	VL	VL	VL	L	VL	VL	L	L	L	L	L	L	L	L	L	L	L	L
56 days	VL	VL	VL	VL	VL	VL	VL	VL	VL	VL	VL	VL	VL	VL	VL	VL	VL	VL

Note: H = High, M = Moderate, VL = Very Low, L = Low, - indicates there is no test.

Table 7.14. Permeability Class of CC Mixtures.

Age of Test	Mixture ID											
	C5G			C7G			C5L			C7L		
7 days	M	L	M	L	L	L	M	M	M	L	L	L
28 days	L	L	L	VL	VL	VL	M	M	M	L	L	L
56 days	L	L	L	VL	VL	VL	L	M	L	L	L	L

Note: H = High, M = Moderate, VL = Very Low, L = Low.

7.3.3 Diffusion Coefficient

The diffusion coefficient is determined by measuring the chloride concentration at different depth layers. The diffusion coefficients at 140 days were 1.21×10^{-9} and 2.39×10^{-9} in.^{2}/s (0.78×10^{-12} and 1.54×10^{-12} m^2/s) for 5 and 7 ksi (34 and 48 MPa) river gravel SCC mixtures, respectively. The diffusion coefficients at 28 days were estimated to be 2.53×10^{-9} and 4.40×10^{-9} in.^{2}/s (1.63×10^{-12} and 2.84×10^{-12} m^2/s) for 5 and 7 ksi (34 and 48 MPa) river gravel SCC mixtures, respectively. These values are typical of CC with similar *w/c*. Tables 7.15 and 7.16 show the diffusion coefficients for all mixtures. Figure 7.24 shows the plot of the predicted value by estimated average diffusion coefficients versus and measured values. The estimated diffusion coefficients of river gravel SCC mixtures seem to be significantly low indicating the fine capillary porosity and homogeneity. Generally, the fly ash also reduced diffusion coefficients. Similarly, SCC mixture had significantly low coefficient of chloride

migration, which seems to depend on the type of powder. The fly ash reduced significantly coefficient of chloride migration (Zhu and Bartos 2003).

Table 7.15. Diffusion Coefficient of 5 ksi (34 MPa) River Gravel Mixtures.

Day	Diffusion Coefficients $\times 10^{-9}$ in^2/s ($\times 10^{-12}$ m^2/s)	Mixture ID								
		S5G-3a			S5G-3b			S5G-3c		
140 days (Tested)	Values	0.92 (0.59)	0.68 (0.44)	17.1* (11)	0.67 (0.43)	1.55 (1.00)	0.98 (0.62)	1.50 (0.97)	0.33 (0.21)	3.07 (1.98)
	Average	0.81 (0.52)			1.05 (0.68)			1.63 (1.05)		
	Standard Deviation	0.17 (0.11)			0.45 (0.29)			1.38 (0.89)		
28 days (Predicted)	Values	1.91 (1.23)	1.43 (0.92)	35.7* (23)	1.40 (0.90)	3.23 (2.08)	2.0 (1.29)	3.13 (2.02)	0.68 (0.44)	6.39 (4.12)
	Average	1.68 (1.08)			2.20 (1.42)			3.40 (2.19)		
	Standard Deviation	0.34 (0.22)			0.93 (0.60)			2.87 (1.85)		

Note: * is the outlier.

Table 7.16. Diffusion Coefficient of 7 ksi (48 MPa) River Gravel Mixtures.

Day	Diffusion Coefficients, $\times 10^{-9}$ in.^{2}/s ($\times 10^{-12}$ m^2/s)	Mixture ID								
		S7G-4			S7G-5			S7G-6		
140 days (Tested)	Values	1.38 (0.89)	1.40 (0.90)	6.65 (4.29)	1.58 (1.02)	3.32 (2.14)	3.12 (2.01)	1.81 (1.17)	1.49 (0.96)	0.76 (0.49)
	Average	3.15 (2.03)			2.67 (1.72)			1.35 (0.87)		
	Standard Deviation	3.04 (1.96)			0.95 (0.61)			0.54 (0.35)		
28 days (Predicted)	Values	2.54 (1.64)	2.59 (1.67)	12.28 (7.92)	2.92 (1.88)	6.11 (3.94)	5.75 (3.71)	3.35 (2.16)	2.73 (1.76)	1.41 (0.91)
	Average	5.80 (3.74)			4.94 (3.18)			2.50 (1.61)		
	Standard Deviation	5.61 (3.62)			1.75 (1.13)			0.99 (0.64)		

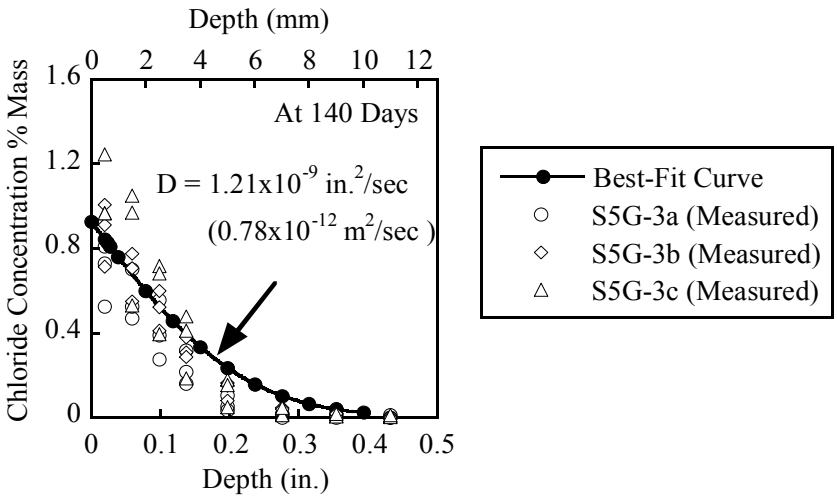

(a) 5 ksi (34 MPa) River Gravel SCC Mixture

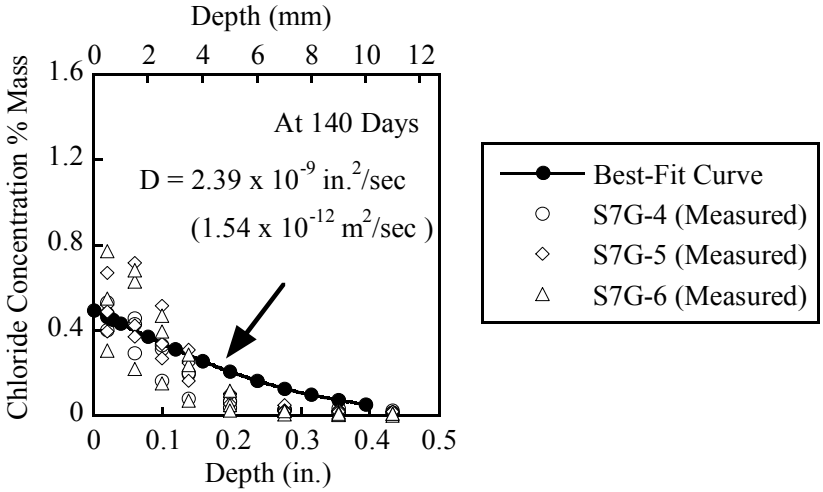

(a) 7 ksi (48 MPa) River Gravel SCC Mixture

Figure 7.24. Predicted Chloride Concentration (Percent Mass) versus Measured Values (140 Days).

7.3.4 Summary

Based on the experimental tests on the SCC and CC mixtures, the following conclusions can be drawn:

1) The 5 ksi (34 MPa) 16-hour release strength SCC mixtures exhibit low resistance to freezing and thawing. This could be a result of high paste volume, higher *w/cm*, or poor void distribution.
2) The 7 ksi (48 MPa) 16-hour release strength SCC mixtures exhibited good freezing and thawing resistance.
3) All SCC mixtures exhibited very low permeability compared to the CC mixtures at later ages indicating a potential for high resistance to chloride ion penetration.
4) After 140 days of ponding, the 5 ksi (34 MPa) and 7 ksi (48 MPa) 16-hour release strength SCC mixtures have low diffusion coefficients. These values are typical of CC mixtures with similar *w/c*.

CHAPTER 8
RESULTS AND ANALYSIS OF FULL-SCALE TESTING AND VALIDATION: FULL-SCALE SCC GIRDER-DECK SYSTEM

8.1 EARLY-AGE PROPERTIES AND FIELD OBSERVATION

For the first set of field tests, the fresh properties were assessed by researchers from the University of Texas at Austin (Koehler and Fowler 2008). The University of Texas group focused on assessing the workability and stability of the SCC mixture for the precast girder. This section presents follow-up testing and a description of the early-age characteristics of the SCC mixture for the precast girders. The full-scale girder test program is described in Section 4.7 of this report.

Generally, the passing ability of the SCC mixtures was excellent. When the auger bucket containing the SCC mixture arrived at the placement bed, some segregation of the aggregate was observed. This was due to the transportation of the SCC from the mixer to the placement bed and resulted in a small area (1 ft × 0.5 ft [0.3 m × 0.1 m]) of honeycombing, as shown Figure 8.1.

Figure 8.2 shows the overall surface condition of the girders containing the SCC mixtures. The surface conditions were considered to be very good. Table 8.1 provides a summary of the early-age characteristics of the mixtures used in the precast girders.

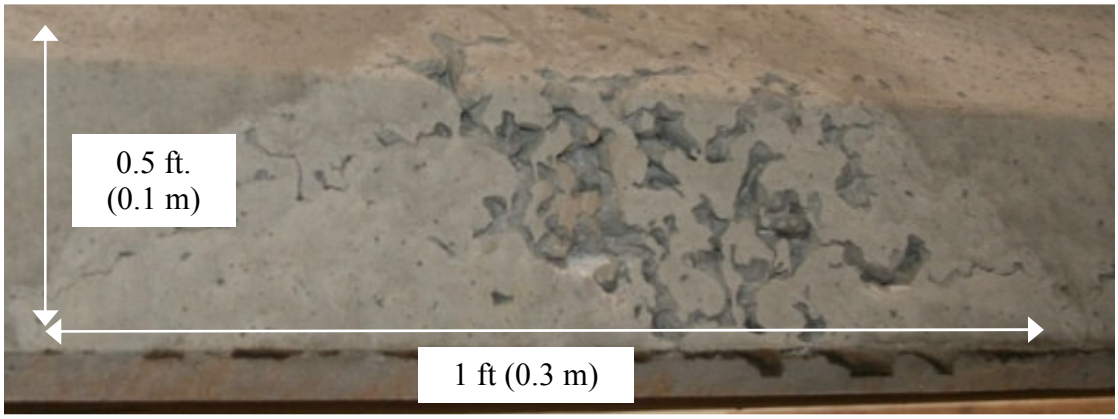

Figure 8.1. Localized Honeycombs on Surface of the SCC-R Mixture.

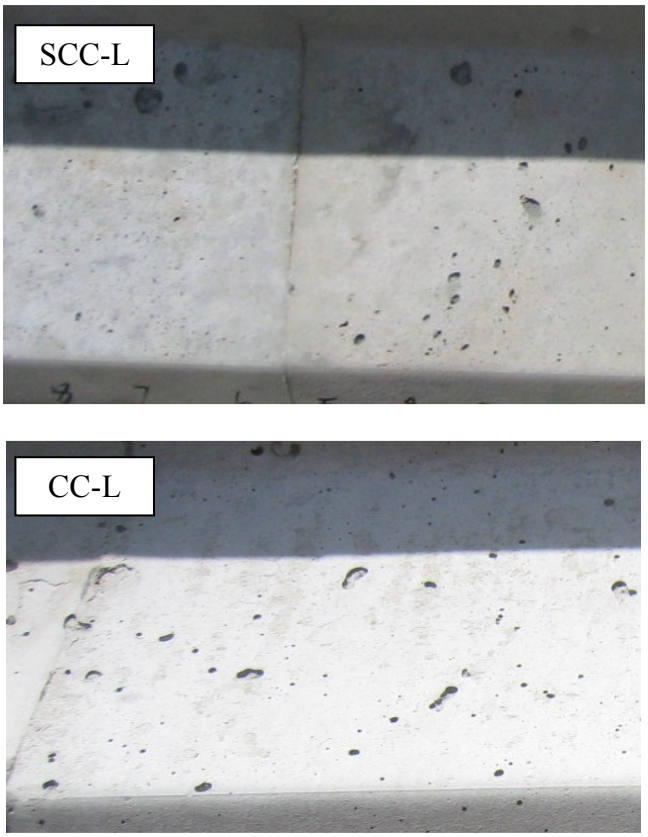

Figure 8.2. Representative Photos of Quality of Surface of Bottom Flange of SCC-L (Top) and CC-L (Bottom).

Table 8.1. Early-Age Chracteristics of Tested Girders.

Girder ID	CC-R		SCC-R		CC-L		SCC-L	
Cast Date	03/26/07		03/26/07		07/12/07		07/12/07	
Batch Number	1	2	1	2	1	2	1	2
Ambient Temp. ,°F (°C)	72 (22)				102 (39)			
Relative Humidity, %	-		-		39.5			
Slump, in. (cm)	8 (20)	-	-	-	8.25 (21)	6.50 (16.5)	-	-
Slump Flow, in.	-	-	27.0 (69)	28.5 (72)	-	-	26.0 (66)	22.0* (56)
T_{50}, sec	-	-	3.3	3.6	-	-	3.39	5.13*
VSI	-	-	1.0	1.5	-	-	1.0	1.0*
Concrete Temp. at Placement, °F (°C)	81 (27)	-	80 (27)	81 (27)	88 (31)	86 (30)	84 (29)	-
Air Cont., %	1.8	-	0.9	-	2.1	-	2.5	-

Note: * tests were performed after the placement of concrete into the form.
- indicates data not recorded.

The temperature of the girders was monitored in the field after casting. Figure 8.3 shows the history of average temperature values for all probes evaluated in the girder. The allowable hydration temperature of the TxDOT Specifications is limited to 150 °F (66 °C) for mixtures containing SCMs (TxDOT 2006). All concrete met this temperature requirement. The temperature of the SCC was higher than that of the CC for the mixtures containing river gravel. The SCC-L had a similar temperature profile as the CC-L mixture. It should be noted that the steel forms were heated for the limestone mixtures before the placement of concrete due to weather.

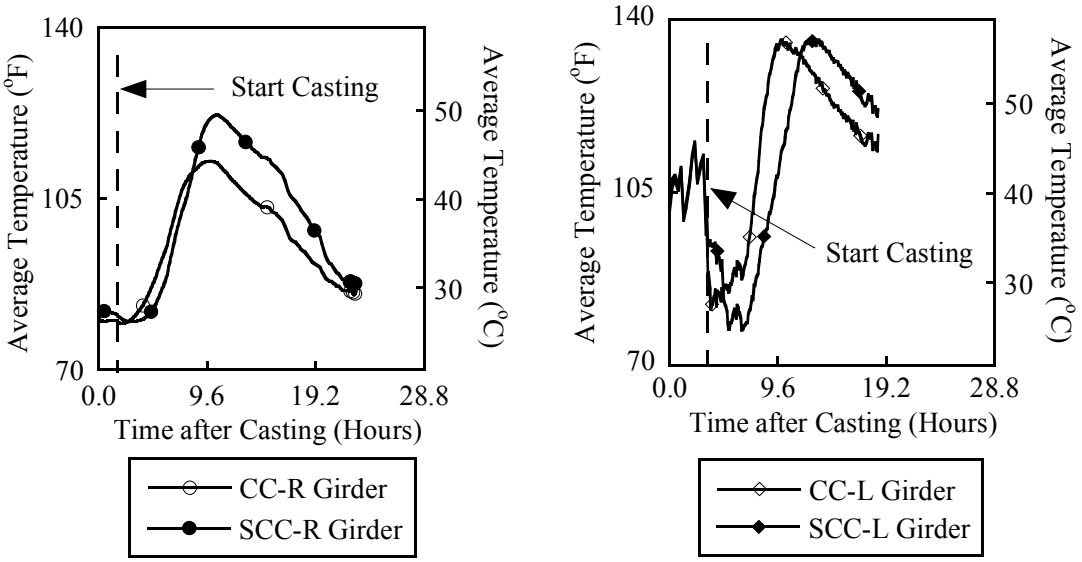

Figure 8.3. History of Average Hydration Temperature.

Figure 8.4 shows the distribution of concrete temperature at the girder ends and midspan when the average of temperature reached the maximum value at corresponding girder section. The distribution of the concrete temperature was similar, with the exception of the SCC-R girder, indicating the maturity values of the concretes are similar. The north span of the SCC-R girder showed high temperatures over the cross-section, indicating that the strength development could be higher than other regions. Transfer length data at this area were shorter than the other ends. These results will be presented and discussed in the following sections.

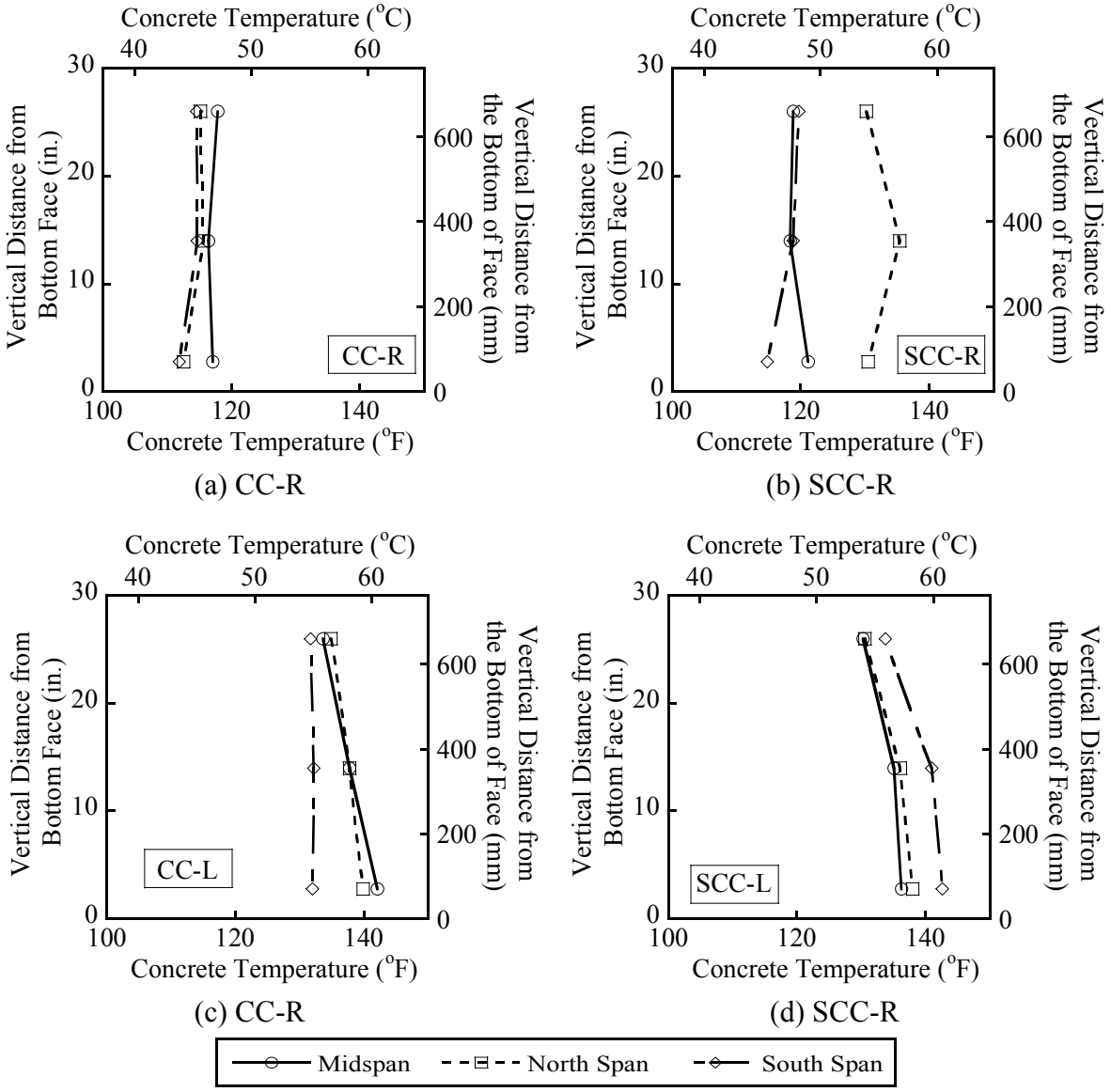

Figure 8.4. Distribution of Temperature at the Girder End and Midspan Sections.

8.2 MATERIAL MECHANICAL PROPERTIES

Samples were cast to assess the mechanical properties of the concrete used for the girders. Cylinders (4 in. × 8 in. [102 mm × 203 mm]) were used to assess compressive strength, MOE, and STS of the CC and SCC mixtures. MOR was determined using 6 in. × 6 in. × 20 in. (152 mm × 152 mm × 508 mm) prism specimens. For the 16-hour tests, a sure-cure system was used to match the conditions of the actual beams. Additional cylinders were also cast and placed

adjacent to the girders for testing. Except for the 16-hour tests, all mechanical tests were performed at HBSML.

8.2.1 Compressive Strength Development

After 16 hours, all the samples were stored in a constant temperature and humidity room (>98 percent RH and 72 ± 2 ^{o}F [22 ± 1 ^{o}C]). To investigate strength development, compressive strength was measured at 16 hours and 7, 28, 56, and 91 days. Table 8.2 shows the test results of the average compressive strength of all mixtures at 16 hours and at approximately the time of release. The target compressive strength was 5 ksi (34 MPa) at 16 hours. All the sure-cure samples exceeded the 16-hour target strength. Several of the samples placed next to the girders (i.e., the samples not matching the temperature profile of the girder) did not meet the target 16-hour strength. However, the sure-cure samples better represent the actual strength of the girder concrete. As such, the strands were released when the sure-cure samples indicated sufficient strength.

Table 8.2. Average Compressive Strength at 16 hours and Release of Girders.

Curing Method	Next to Girder		Sure-Cure		Next to Girder		Sure-Cure	
Girder ID	CC-R	SCC-R	CC-L	SCC-L	CC-L	SCC-L	CC-R	SCC-R
f'_c @16 hour, psi (MPa)	4933 (34)	4771 (33)	4813 (33)	6056 (42)	5310 (37)	6603 (46)	5080 (35)	5714 (39)
f'_c @ Release, psi (MPa)	-	-	5738 (39)	6712 (46)	5614 (37)	7200 (50)	6360 (44)	6510 (45)

Results from the tests are shown in Figure 8.5. The strength development of the SCC mixture was significantly different than the CC mixture at later ages. The compressive strength development of SCC-R and SCC-L is fairly similar. The compressive strength development of CC-R and CC-L is also similar. However, at 91 days, the compressive strength of SCC-R and SCC-L was approximately 30 percent higher than that of CC-R and CC-L mixtures. Even though the CC mixtures have slightly lower *w/c* than SCC mixtures, the strength gain of CC and SCC mixtures are significantly different at later ages. This can be attributed to the contribution of fly ash and high paste volume.

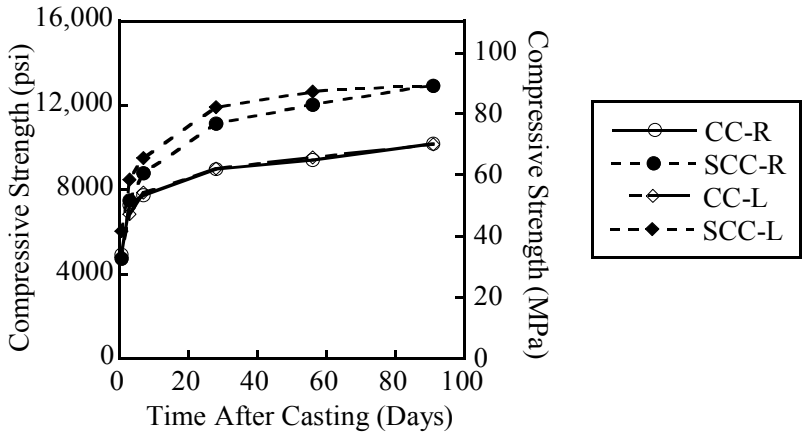

Figure 8.5. Compressive Strength Development of Girder.

8.2.2 Modulus of Elasticity

MOE was measured at 7, 28, 56, and 91 days. Figure 8.6 shows the MOE of all girders with respect to compressive strength. Based on the assumptions K_1 = 1.0 and w_c = 149 lb/ft^3 (2387 kg/m^3), the current AASHTO (2006) prediction curve (Equation 2.2) follows the general trend of the MOE of the CC-L mixtures shown in Figure 8.6. As shown in Figure 8.7, most data from the CC-R and SCC-R mixtures fall within the 20 percent error range. The data of both CC-L and SCC-L mixtures fall within the 20 percent error range.

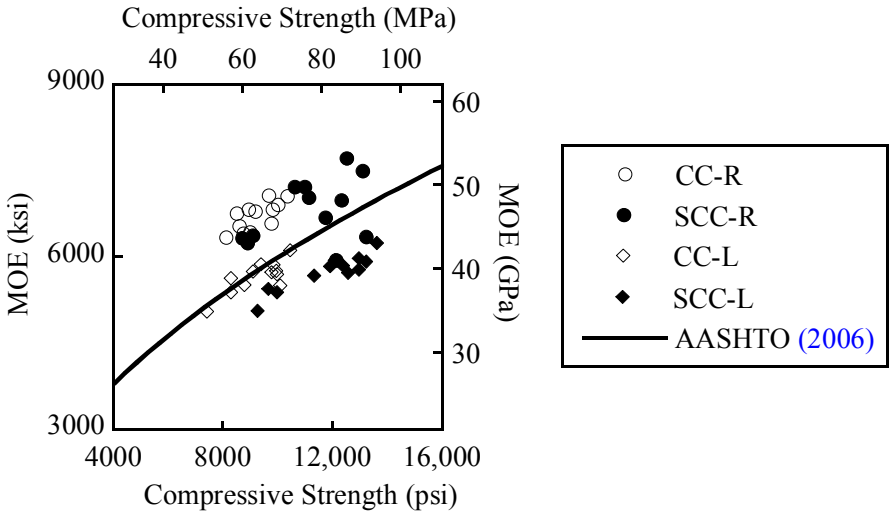

Figure 8.6. MOE of Girders.

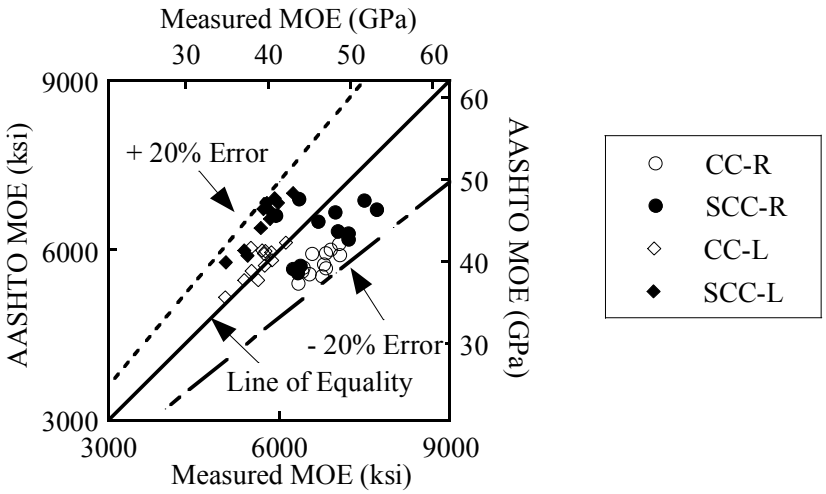

Figure 8.7. Measured MOE versus Estimated MOE Using AASHTO (2006).

8.2.3 Modulus of Rupture

MOR was measured at 7, 28, and 56 days. The current AASHTO LRFD Specifications (2006) seems to be appropriate for both CC and SCC mixtures, as shown in Figure 8.8. All measured data fall within the upper and lower bounds of the AASHTO predictions. Coefficients of the square root of the compressive strength were estimated based on the measured values, as shown in Table 8.3. The coefficient of the CC-R mixture is slightly higher than that of the SCC-R mixture, indicating lower MOR of the SCC-R mixture. The CC-L and SCC-L mixtures have similar coefficients for MOR.

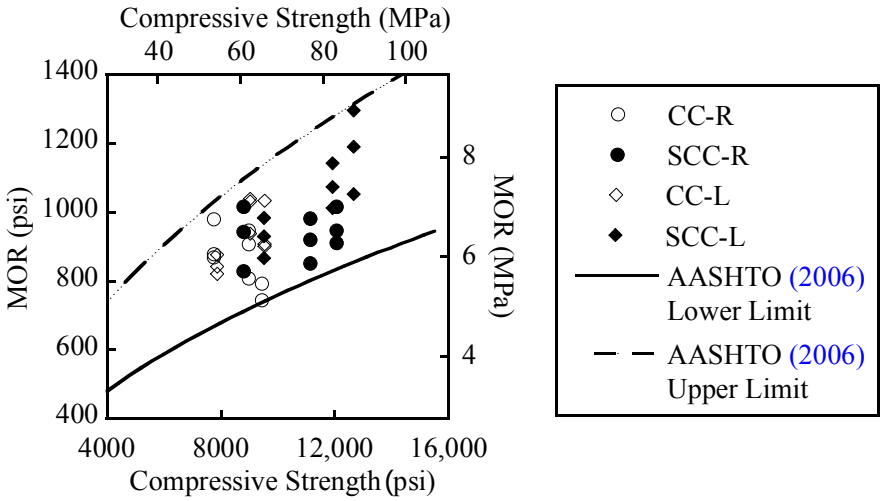

Figure 8.8. MOR of the Girders.

Table 8.3. Coefficients of MOR.

Measured Value / $\sqrt{f_c'}$ (psi)	CC-R	SCC-R	CC-L	SCC-L
Mean Value	9.4	9.1	10.0	10.0
Standard Deviation	1.1	0.9	0.7	0.8
Upper Bound (AASHTO)	11.7			
Lower Bound (AASHTO)	7.6			

8.2.4 Splitting Tensile Strength

STS was measured at 7, 28, and 56 days. The current AASHTO (2006) prediction equation for STS underestimates the experimental results for both the CC and SCC mixtures used in the girders as shown in Figure 8.9. The SCC-R and SCC-L mixtures have higher strengths resulting in higher STS. As shown in Figure 8.10, STS estimated by the AASHTO (2006) equation is generally lower than the measured STS of SCC mixtures: the majority of SCC data fall within the 30 percent error range. As such, the AASHTO (2006) gives a reasonable lower bound estimate of the STS for the SCC mixtures.

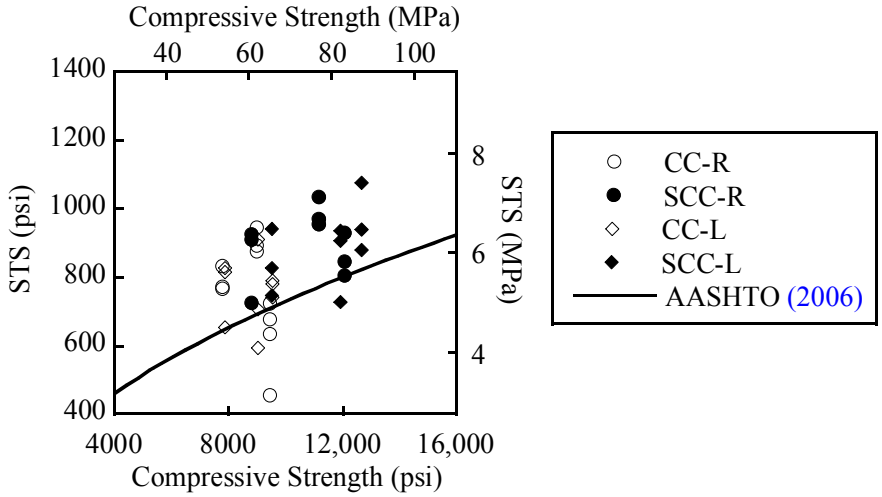

Figure 8.9. STS for Girders.

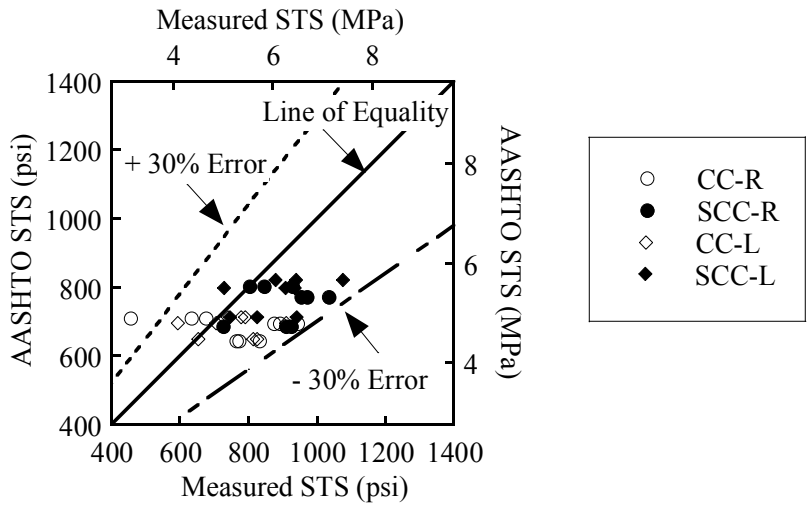

Figure 8.10. Measured STS versus Estimated STS Using AASHTO (2006).

8.3 FLEXURAL TESTS

The structural behavior of the CC and SCC girders during flexural testing are compared in this section. As the flexural crack propagates from the bottom flange to the web, cracked section properties become different from the gross section properties. This cracking reduces the effective moment of inertia as the neutral axis shifts upward. Because the contribution of the deck concrete for compression becomes dominant, the bonds in the bottom flange and uncracked sections of the girder contribute to tension. The local bond performance should be evaluated to compare CC and SCC girder performance.

8.3.1 Observations

8.3.1.1 Cracking Development

Generally, the progression of flexural cracking and maximum crack widths is similar for all the tests. The cracking load and measured crack widths are summarized in Table 8.4. The maximum crack width was measured at the extreme tension fiber of the bottom flange.

For all the girders, all the first cracking occurred at approximately 70 kip (311 kN) along with approximately the maximum crack width of 0.01 in. (0.3 mm). The flexural cracks propagating into the deck were observed at approximately 110 kip (490 kN). Observed maximum crack width at the nominal condition was approximately 0.06 in. (1.5 mm) for all the girders.

Table 8.4. Cracking Loads and Crack Widths.

	First Cracking		Flexural Cracking on Top Flange		Flexural Cracking into Deck		Final Reading	
Location	Web	Bottom Flange	Top Flange	Bottom Flange	Deck	Bottom Flange	Final	Bottom Flange
Values	Load, kip (kN)	Crack Width, in.(mm)	Load, kip (kN)	Crack Width, in.(mm)	Load, kip (kN)	Crack Width, in.(mm)	Load, kip (kN)	Crack Width, in.(mm)
CC-R	60-80 (270-360)	0.01 (0.3)	100 (445)	0.02 (0.6)	110 (490)	0.05 (1.25)	127 (565)	0.05 (1.25)
SCC-R	70 (311)	0.004 (0.1)	100 (445)	0.01 (0.3)	110 (489)	0.04 (1.0)	126 (560)	0.06 (1.5)
CC-L	70 (311)	0.01 (0.3)	90 (400)	0.03 (0.8)	100 (445)	0.02 (0.5)	125 (556)	0.06 (1.5)
SCC-L	70 (311)	0.01 (0.2)	90 (400)	0.2 (0.4)	110 (489)	0.05 (1.25)	125 (556)	0.06 (1.5)

Note: CC-R girder had the first cracking during the load increments from 70 to 80 kip (270 to 360 kN).

8.3.1.2 Cracks on Midspan

While the overall structural performance of the girders was similar, some differences were observed. The SCC-L girder showed slightly more cracks than the CC-L girder. However, overall behavior was almost identical. The flexural cracks at nominal conditions are shown in Figure 8.11. Typical flexural cracks propagating through the deck were observed.

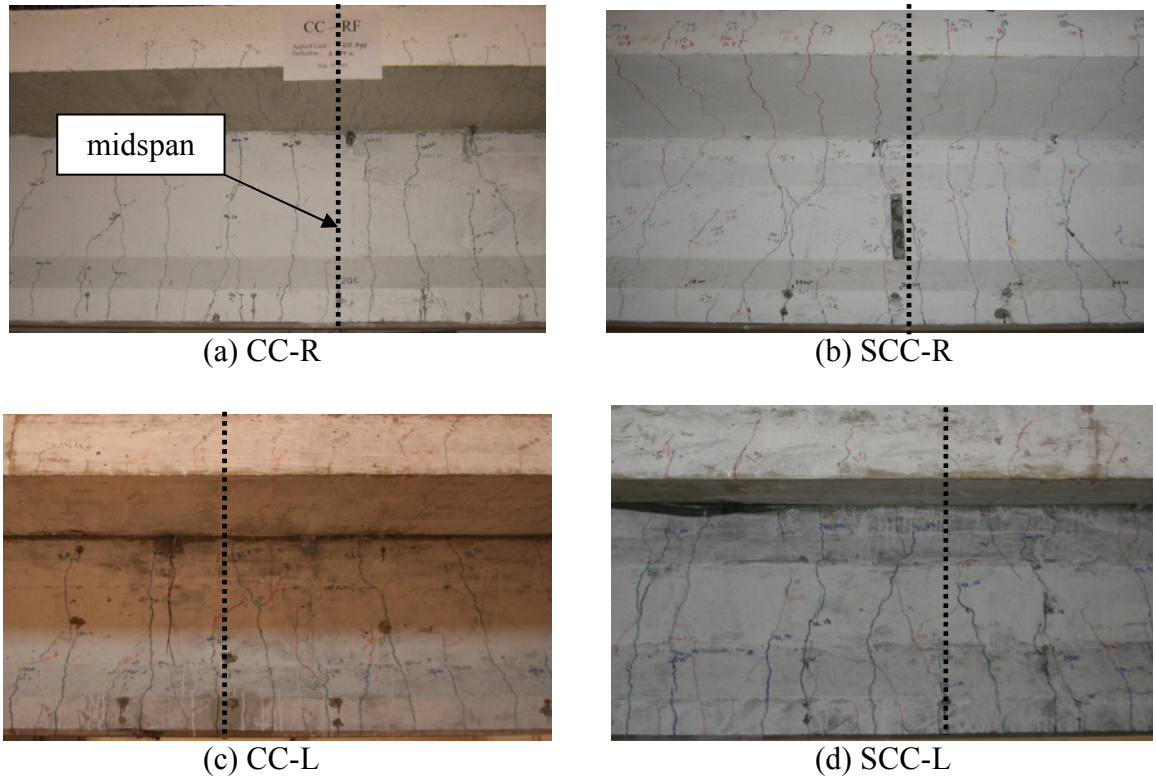

(a) CC-R (b) SCC-R

(c) CC-L (d) SCC-L

Figure 8.11. Crack Patterns of the Girders.

The final crack diagrams for all flexural tests are shown in Figure 8.12. Only the cracked regions of the midspans are shown. In general, the SCC girders exhibited more cracks than the CC girders. In the SCC-R and SCC-L girders more cracks were distributed along the span compared with the CC-R and CC-L girders. More small cracks with small crack widths were observed in the SCC-R and SCC-L girders.

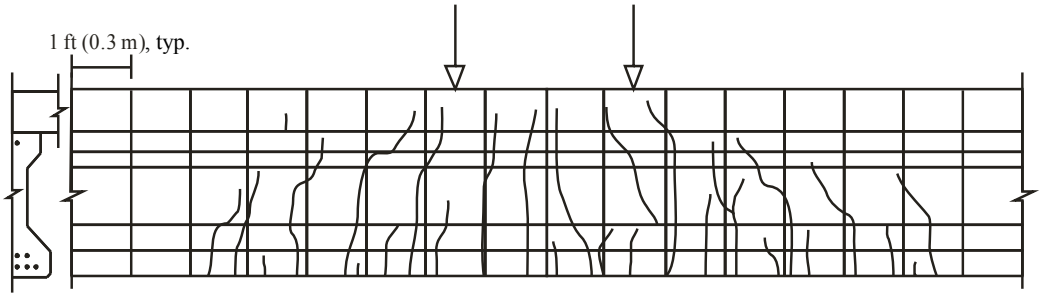

(a) CC-R

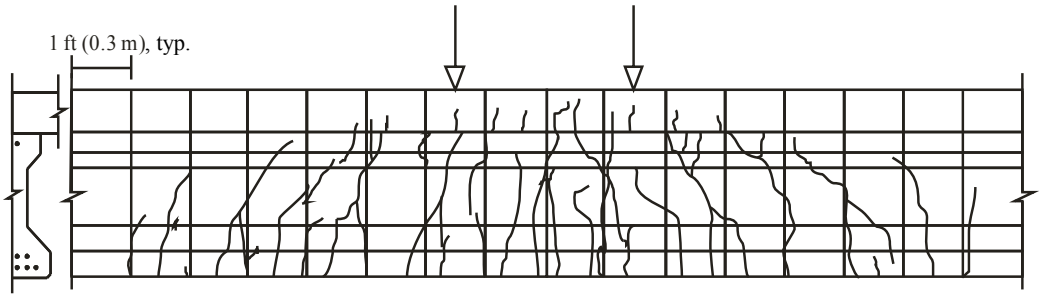

(b) SCC-R

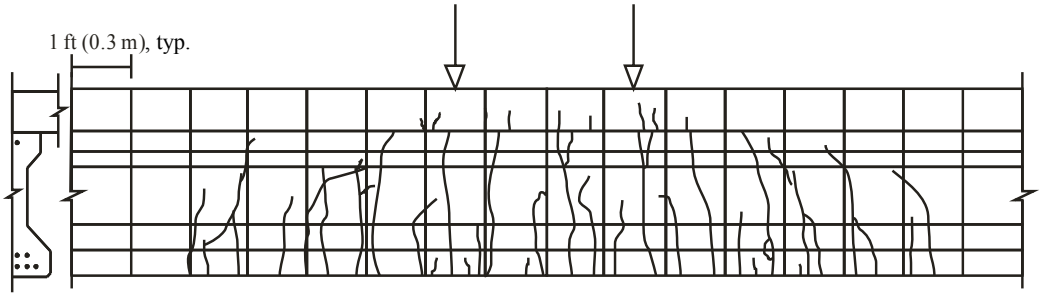

(c) CC-L

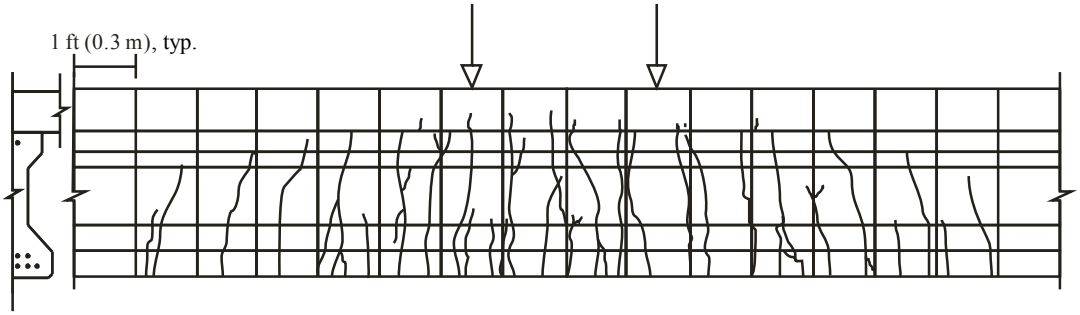

(d) SCC-L

Figure 8.12. Crack Diagram at the Ultimate State.

8.3.2 Moment-Curvature (Load-Deflection)

Table 8.5 shows the measured material properties of the concrete for the deck and girder. The table also shows the measured effective stresses of the strands after losses, f_{pe}, on the structural test date.

Table 8.5. Measured Properties of Materials.

Materials	f'_c, psi (MPa)	CC-R	SCC-R	CC-L	SCC-L
Girder	Average, psi (MPa)	9620 (66.3)	12,800 (88.3)	10,100 (69.6)	13,700 (94.5)
	Std. Dev., psi (MPa)	251 (1.73)	256 (1.77)	665 (4.59)	422 (2.91)
Cast-In-Place Concrete (Deck)	Average, psi (MPa)	6170 (42.5)	7530 (51.9)	5450 (37.2)	5280 (36.4)
	Std. Dev., psi (MPa)	227 (1.57)	143 (0.99)	563 (3.88)	393 (2.71)
Strands	f_{pe}, ksi (MPa)	201 (1390)	200 (1380)	201 (1450)	204 (1410)

The CC and SCC girders exhibited a similar response in terms of moment-curvature. Figure 8.13 shows the measured and the predicted moment-curvature of each girder. Measured properties of concrete and strands with effective stress of strands after losses were also used to compute the predicted moment-curvature relationship using the Response 2000 program, which is a sectional analysis tool implementing the Modified Compression Field Theory (Bentz 2000). The CC-R and SCC-R girders had similar predicted and measured responses in terms of moment-curvature, as shown in Figure 8.13 (a). The CC-L and SCC-L girders also had similar predicted and measured responses in terms of moment-curvature, as shown in Figure 8.13 (b).

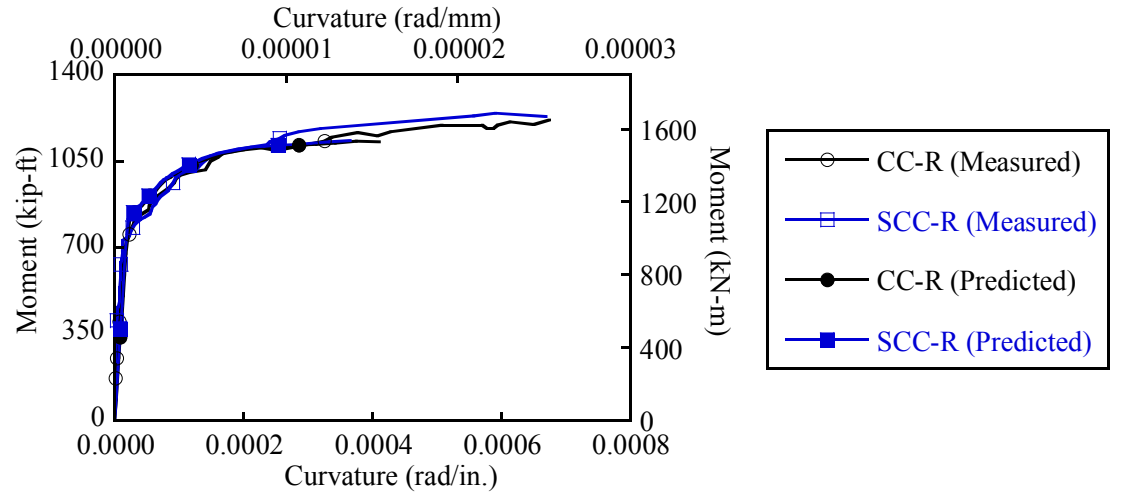

(a) CC-R and SCC-R

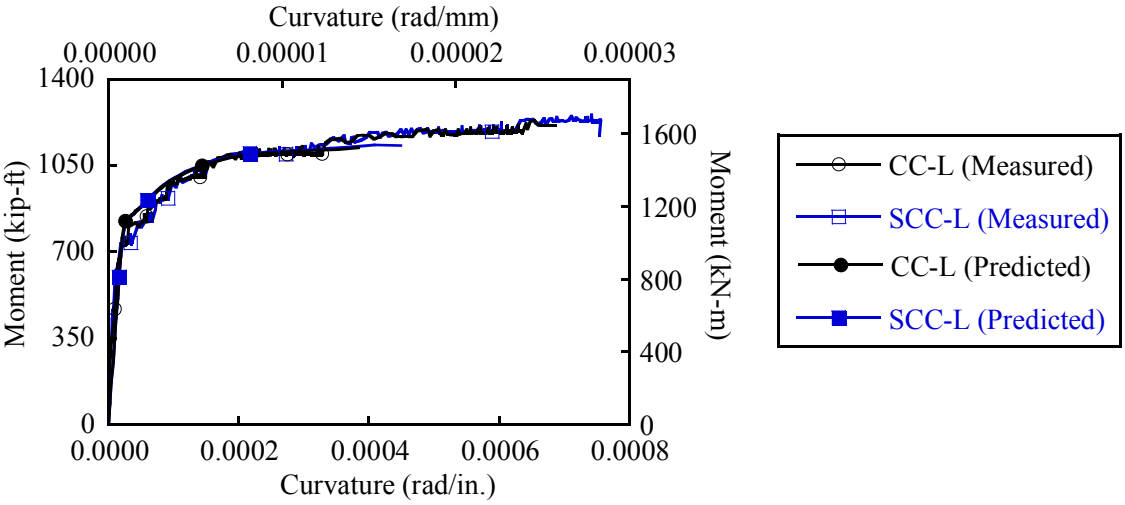

(b) CC-L and SCC-L

Figure 8.13. Moment versus Curvature Relationship.

Figure 8.14 shows the load-deflection for the girders loaded at the center. The girders had almost identical profiles. The CC-L and SCC-L girders had more deflection than the CC-R and SCC-R girders. This can be attributed to increased cracking (which is described in Section 8.3.1) of the limestone SCC girders resulting in a reduction of stiffness (I_{cr}).

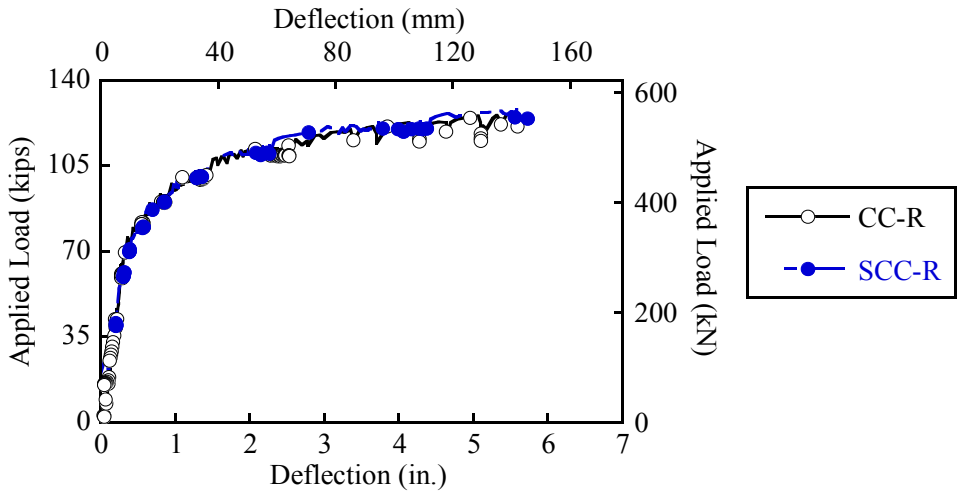

(a) CC-R and SCC-R

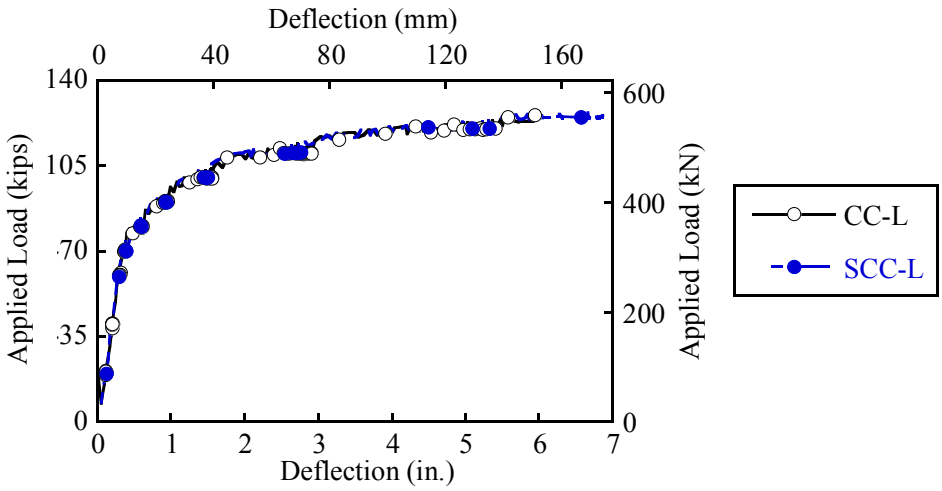

(b) CC-L and SCC-L

Figure 8.14. Load-Displacement.

As shown in Figure 8.15, the strain in the bottom fiber abruptly changes indicating the occurrence of flexural cracking. The locations indicated are used to estimate the cracking moment.

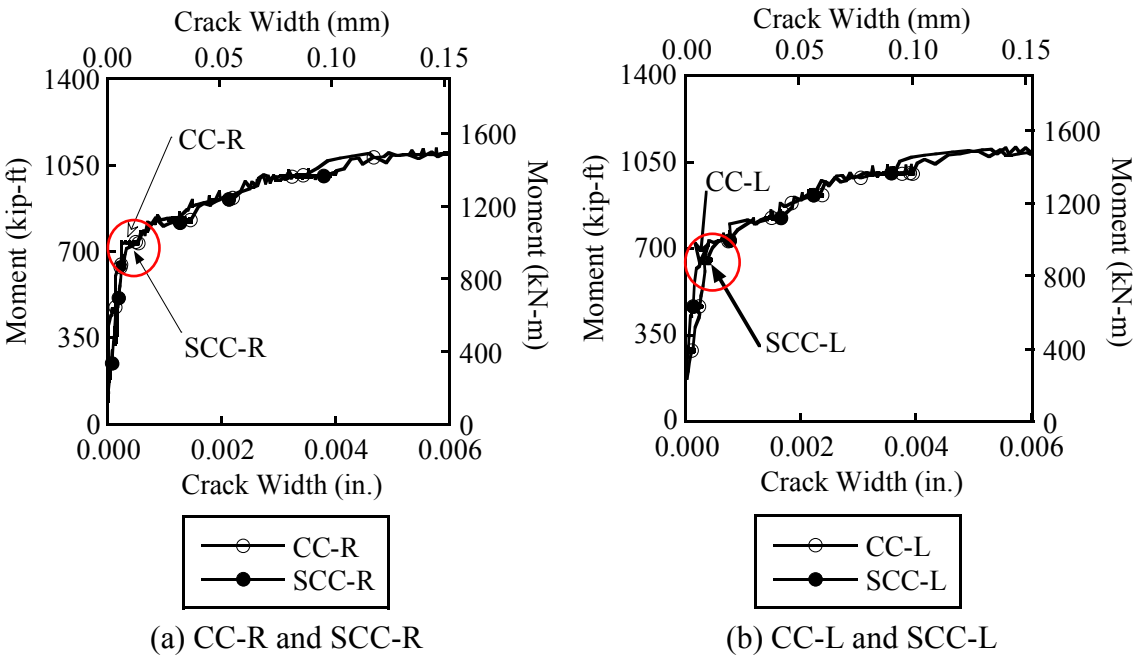

(a) CC-R and SCC-R (b) CC-L and SCC-L

Figure 8.15. Cracking Occurrence of the Bottom Fiber of Girder.

Table 8.6 summarizes the flexural test results. The first cracking of the CC-R girder exhibited a moment corresponding to a MOR of $13\sqrt{f_c'}$ psi ($1.08\sqrt{f_c'}$ MPa), which is 11 percent higher than upper bound prediction of AASHTO (2006). The SCC-R girder exhibited a moment corresponding to $10.6\sqrt{f_c'}$ psi ($0.88\sqrt{f_c'}$ MPa). The CC-L girder had a first cracking moment corresponding to $9.56\sqrt{f_c'}$ psi ($0.79\sqrt{f_c'}$ MPa). The SCC-L girder had the lowest first cracking moment corresponding to $7.33\sqrt{f_c'}$ psi ($0.61\sqrt{f_c'}$ MPa), which is 4 percent lower than the lower limit of AASHTO (2006). The measured nominal moment of all the girders was an average of 1245 kip-ft (1688 kN-m). The nominal moment values are predicted within +15 percent error. The cracking moments of CC-R and SCC-R girders were slightly underestimated, while the cracking moments of CC-L and SCC-L girders were slightly overestimated. This can be attributed to the low MOR of limestone mixtures. Reduced cracking moments were also observed in SCC girders. This result was also shown in the MOR tests described in Chapter 5. Table 8.6 shows that the SCC-L girder had approximately 15 percent higher maximum displacement than the CC-L girder.

Table 8.6. Summary of Flexural Test Results.

Girder ID	CC-R	SCC-R	CC-L	SCC-L
Measured Nominal Moment, kip-ft (kN-m)	1239 (1680)	1258 (1706)	1230 (1668)	1254 (1700)
Predicted Nominal Moment, kip-ft (kN-m)	1129 (1531)	1135 (1539)	1130 (1532)	1122 (1521)
Measured Cracking Moment, kip-ft (kN-m)	750 (1017)	720 (976)	650 (881)	625 (847)
Predicted Cracking Moment, kip-ft (kN-m)	635 (861)	667 (904)	663 (899)	721 (977)
Coefficient, α of the MOR at Cracking ($\alpha\sqrt{f_c'}$), psi (MPa)	13.0 (1.08)	10.6 (0.88)	9.56 (0.79)	7.33 (0.61)
Max. Displacement at Nominal Moment, in. (mm)	5.59 (142)	5.72 (145)	5.95 (151)	6.87 (175)

At nominal conditions, the overall behavior at the girders was governed by the capacity of the CIP concrete deck. As shown in Figure 8.16, the strains at the top fiber in the constant moment region for all composite deck systems reached nominal conditions, in excess of 3000 microstrain at the top fiber. As shown in Figure 8.16, at least three strain gages indicated the nominal conditions of over 3000 microstrain. This figure also shows that specific strain gage exceeded 3000 microstrain along with the schematic location of strain gages on the top fiber. Detailed locations of individual strain gages are described in Figure 4.23. Some strain gages adjacent to loading points indicated lower values than 3000 microstrain. This might be attributed to the disturbed strains due to the stress concentration of the loading points.

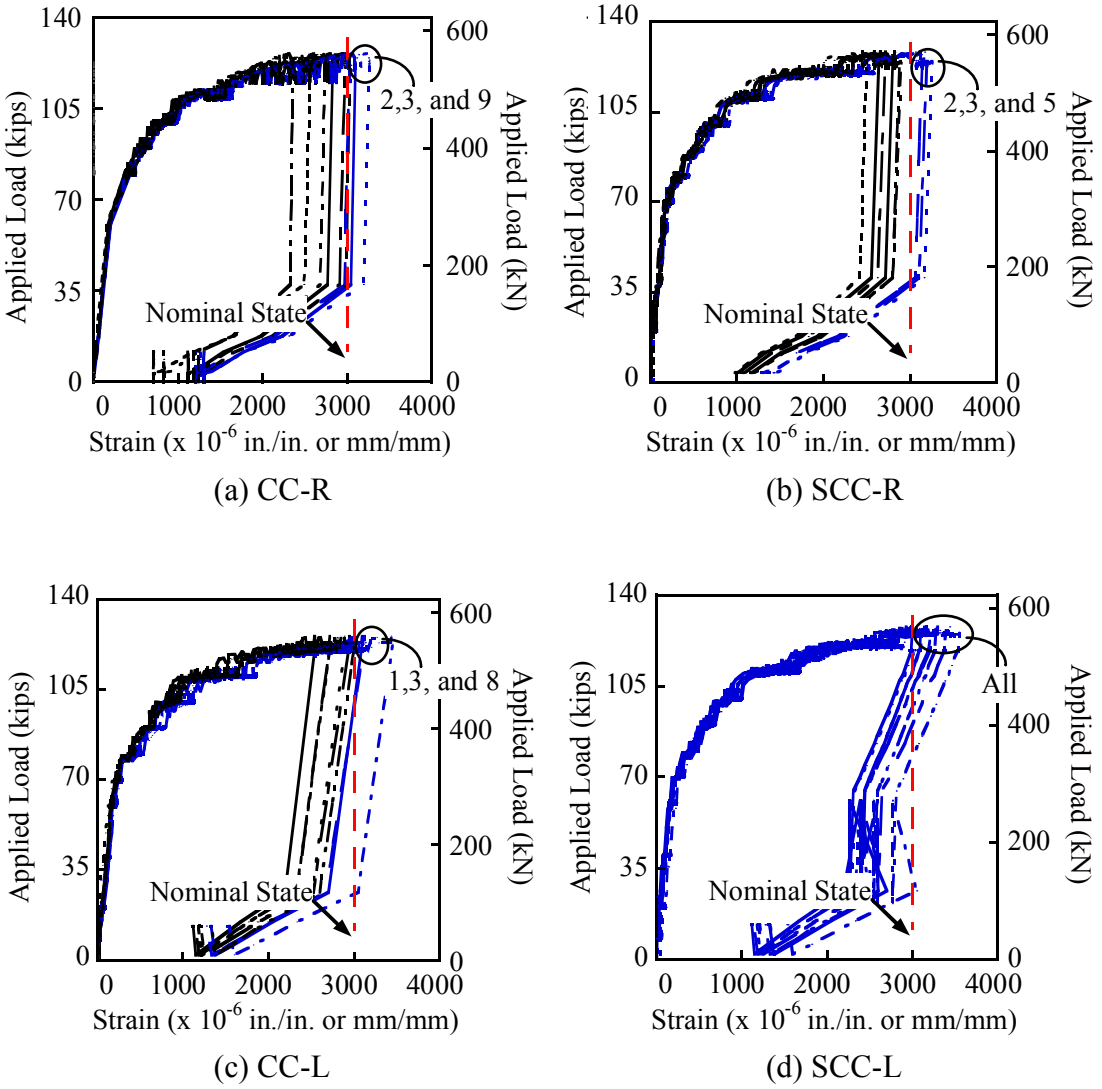

Note: Individual curve indicates the strains at top fiber

and figure below identifies the schematic drawing of the location of strain gages.

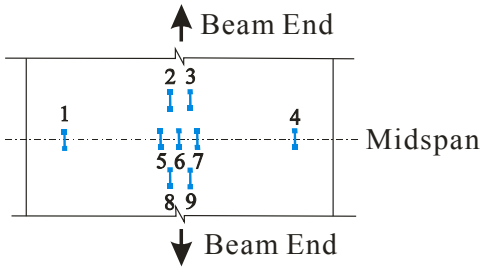

Figure 8.16. Strains at Top Fiber in Constant Moment Region.

8.3.3 Initial Stiffness

The elastic response between the CC and SCC girders is compared in Figure 8.17 to investigate the impact of the mechanical properties of the girder on the structural behavior. The initial stiffness at the midspan of the CC-R girder was slightly higher than that of SCC-R girder, while the initial stiffness of the CC-L girder was almost identical to that of the SCC-L girder. In summary, all girders had a similar overall stiffness in the elastic range, with no significant differences observed.

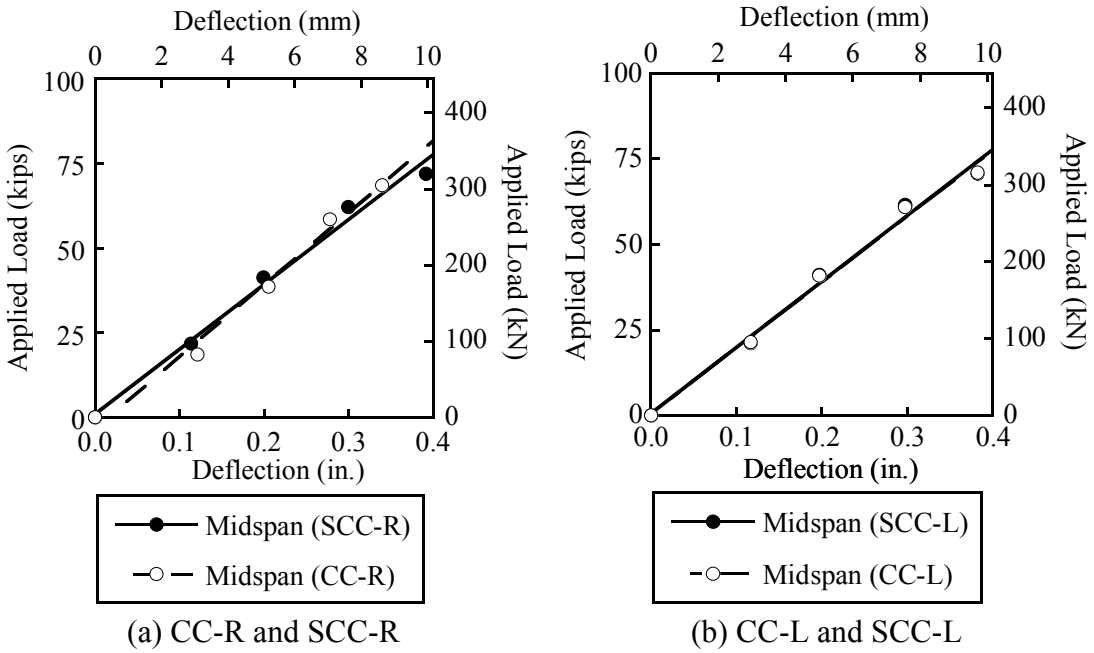

(a) CC-R and SCC-R (b) CC-L and SCC-L

Figure 8.17. Initial Load versus Midspan Deflection Relationship of the Girders.

8.3.4 Bond Performance Prior to Cracking (Transfer Length Region)

As described in Section 2.9, transfer length, l_t, is the transition distance from the free end of the prestressing strands to the fully bonded zone having an effective stress of the strands, f_{pe}. The 70 in. (1.8 m) distance girder ends were investigated. The distribution of strains at the centroid of gravity of strands (cgs) due to applied loads of approximately 60 kip (270 kN) are shown in Figure 8.18. The 60 kip (270 kN) applied load was the last loading step prior to initiating cracking of the girders.

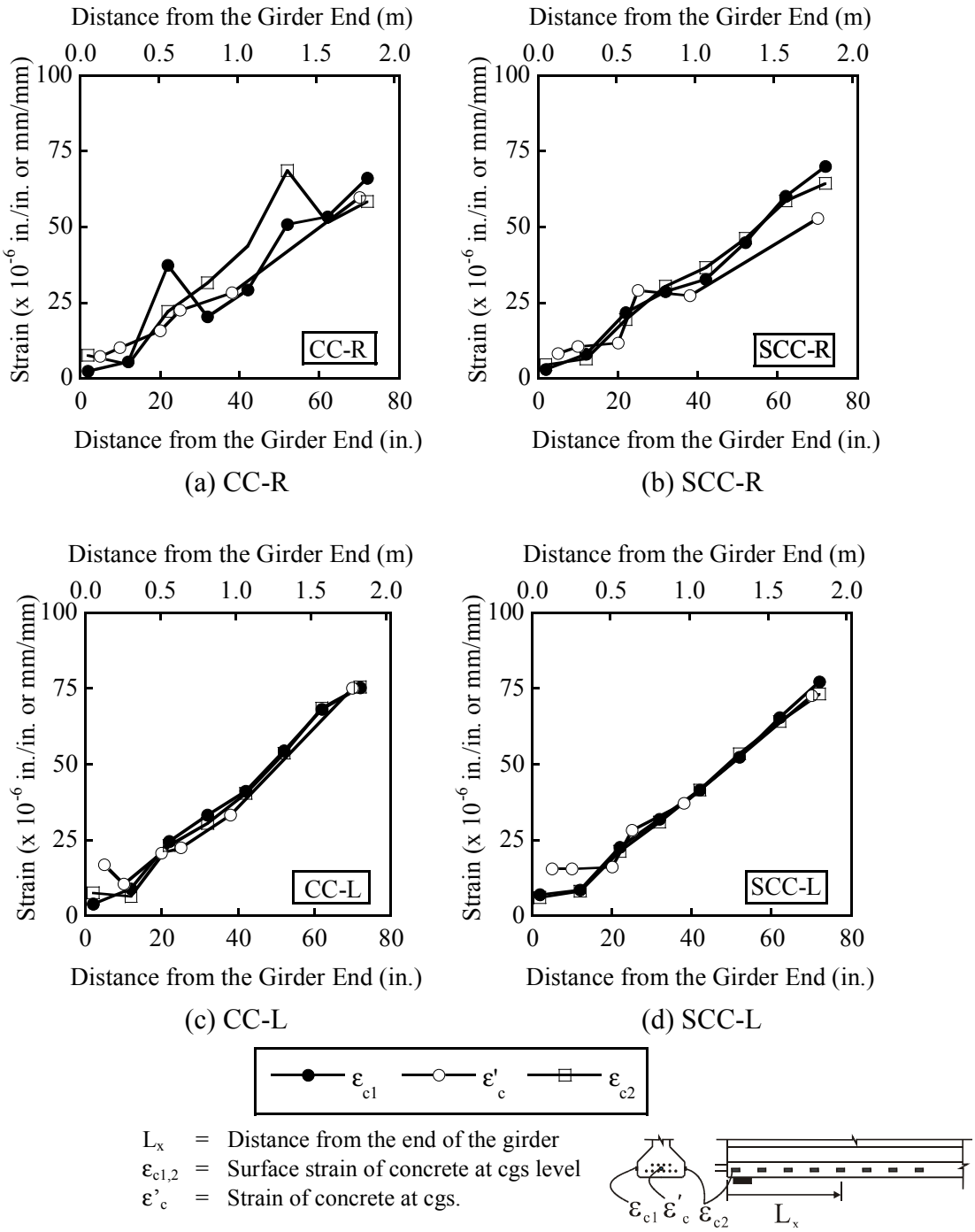

Figure 8.18. Distribution of Concrete Strains at cgs Level near Girder Ends [Applied Load = 60 kip (270 kN)].

There is no evidence to indicate bond failure or slip of the strands during the flexural test. The surface strain and concrete strain gage readings were very similar and included good bond between strands and concrete. When the strains of the CC and SCC girders are compared, the

strain values were very similar, indicating that local mechanical response was similar in the elastic range. For the CC-R girder, several strain gages seem to be affected by technical or temperature factors such as temperature effects or improper bonding between strain gages and the surface of concrete. There is slightly lower MOE of limestone mixtures resulting in the higher concrete strain in the transfer length region.

8.3.5 Bond Performance after Cracking (Transfer Length Region)

Overall post-cracking behavior is very similar between the CC and SCC girders. Figure 8.19 shows the distribution of strain for average values of both ends of each girder at nominal conditions. There was no evidence of bond failure or slip of strands. When the CC and SCC girders were subjected to a flexural load, the bond performance in the transfer length region of the CC and SCC girders exhibited similar behavior after cracking. At the ultimate state, the CC-L and SCC-L girders had about 50 percent higher strain values than the CC-R and SCC-R girders, indicating the build-up of high bond stress with the strands.

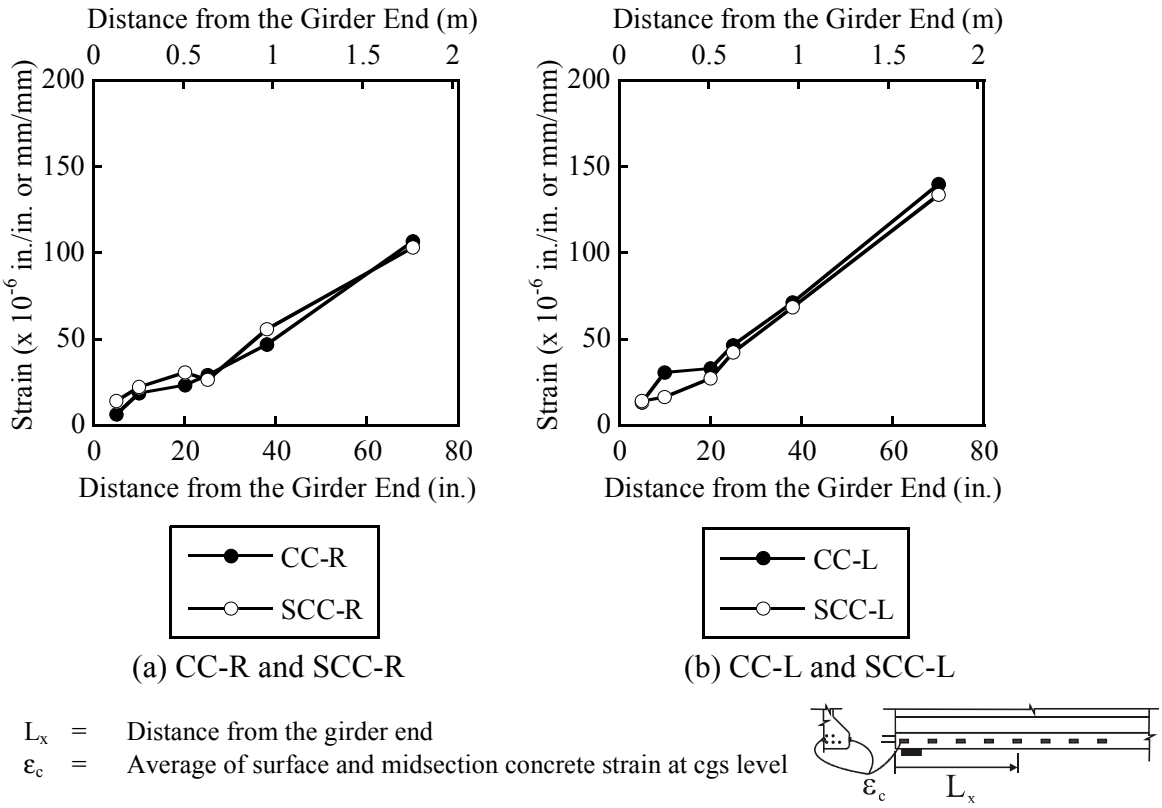

Figure 8.19. Distribution of Average Concrete Strain at Girder Ends: Strains at Nominal Load.

These results indicate that aggregate type may be a more significant factor in girder performance than concrete type (i.e., CC versus SCC). This can be attributed to the low MOE of limestone mixtures. Variation in the coarse aggregate volume did not observably impact girder stiffness.

8.3.6 Bond Performance (Constant Moment Region)

Figure 8.20 shows the average strain in the strands located in the top and bottom flange of the girder at the midspan section. As shown in Figure 8.20, the overall change of the strain in strands during flexural testing was similar in the CC-R and SCC-R girders. For the CC-L and SCC-L girders, the crack openings at the top and bottom flanges were similar. When the top fiber of the deck exceeded 3000 microstrain, corresponding to the last data points, the average strain of the strands in the bottom flange was determined to be approximately 0.02 in./in. (mm/mm).

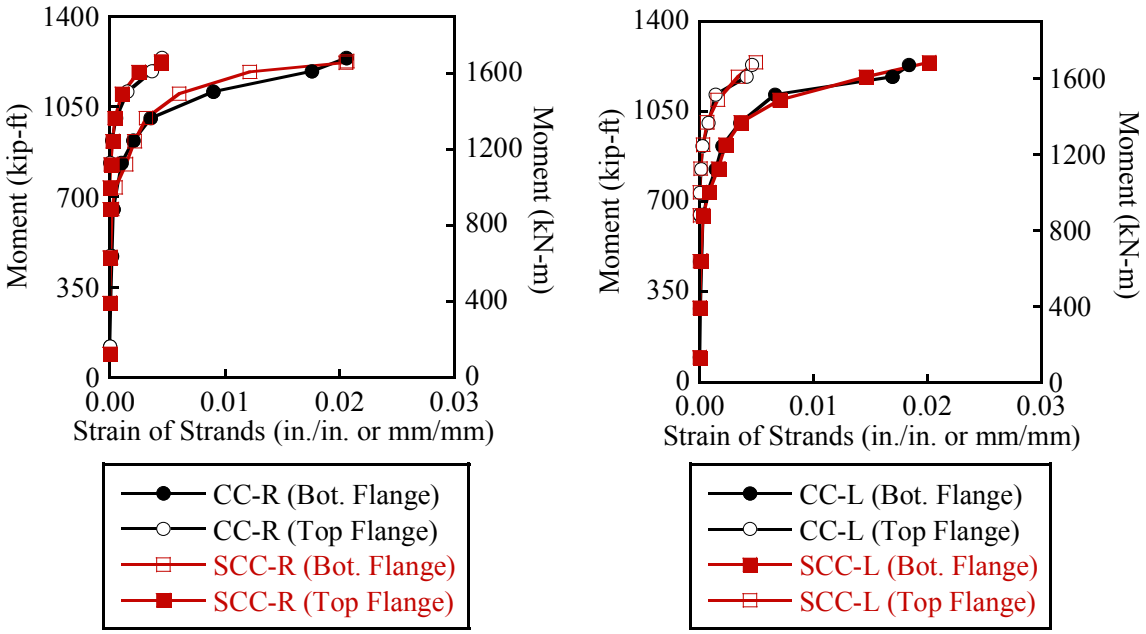

(a) CC-R and SCC-R (b) CC-L and SCC-L

Figure 8.20. Average Strain of Strands at the Top and Bottom Flanges at Midspan Section.

In summary, the flexural behavior of CC and SCC girders was almost identical for both the river gravel and limestone aggregate mixtures. The graphs of strand average strain also

indicate that the stress in strands at ultimate, f_{ps}, was also similar, indicating the bond performance is also similar.

8.4 TRANSFER LENGTH

8.4.1 Transfer Length as a Function of Time

The transfer length for each end of the girders was determined. The initial transfer length, l_{tr}, was measured immediately after release. The final transfer length, l_{tf}, was measured when the monitoring was terminated. Figure 8.21 shows that initial and long-term transfer lengths of all the girders were shorter than the transfer length of 60 bar diameter (60 d_b), which is specified by the AASHTO LRFD Specifications (2004, 2006). Each error bar in the graphs indicates the maximum and minimum transfer lengths for the corresponding girder. As shown in Figure 8.21, the SCC-R girders had similar or shorter initial and final transfer lengths compared to the CC-R girders. The final transfer length was approximately two times the initial transfer lengths for both the CC-R and SCC-R girders. The SCC-L girders had shorter initial and final transfer lengths compared to the CC-L girders. The final transfer length of the CC-L girder increased about 4 percent from the initial transfer length. The final transfer lengths of the SCC-L girder increased approximately 3 and 50 percent from the initial transfer lengths at each end. Generally, the CC-L girder had the longest transfer length among all girders.

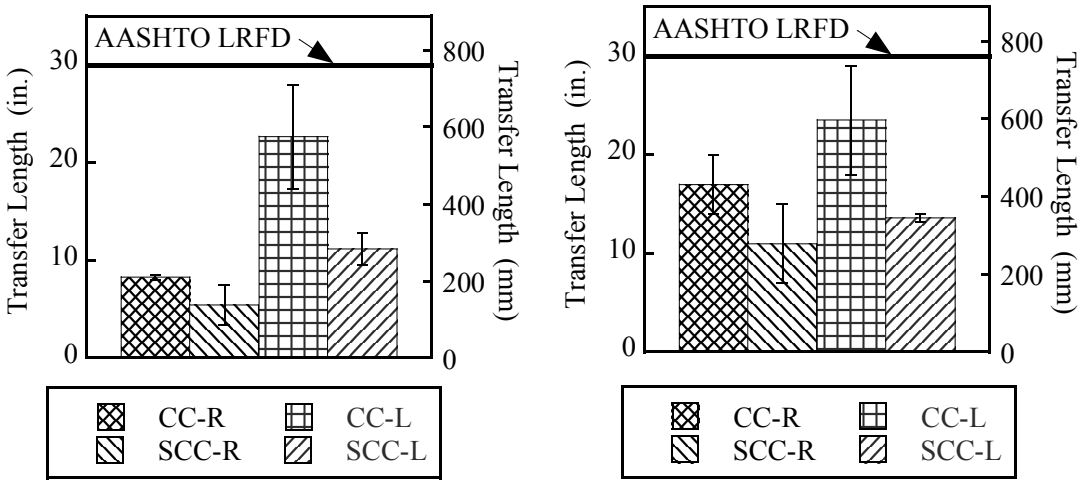

(a) Initial Transfer Length, l_{tr} (b) Final Transfer Length, l_{tf}

Figure 8.21. Girder Transfer Length.

Some researchers found that transfer length increases over time because the bond mechanism is influenced by time-dependent properties of concrete. Creep, shrinkage, and relaxation around the transfer region increase the transfer length (Barnes *et al.* 2003, Kaar *et al.* 1963, Lane 1998). Barnes *et al.* (2003) and Mitchell *et al.* (1993) found that the transfer length is inversely proportional to the square root of the concrete compressive strength and directly proportional to the strand diameter and the amount of prestress around the concrete. Therefore, both high concrete strength and a low effective prestress could lead to a shorter transfer length. Table 8.7 summarizes parameters that impact bond mechanisms resulting in the change in transfer lengths.

Table 8.7. Key Bond Parameters and Measured Transfer Length.

Girder ID	Location	f'_{ci}, ksi (MPa)	f'_c, ksi (MPa)	f_{pi}, ksi (MPa)	f_{pe}, ksi (MPa)	l_{tr}, in. (mm)	l_{tf}, in. (mm)	$\frac{l_{tf}}{l_{tr}}$
CC-R	North End	6.4 (44)	10 (70)	206 (1420)	200 (1380)	8.5 (220)	14 (360)	1.65
	South End			206 (1420)	200 (1380)	8.0 (203)	20 (510)	2.50
SCC-R	North End	6.5 (45)	13 (89.0)	203 (1400)	190 (1310)	3.3 (84)	7 (180)	2.12
	South End			205 (1410)	196 (1350)	7.5 (190)	15 (380)	2.00
CC-L	North End	5.6 (37)	10 (70)	208 (1430)	197 (1360)	28 (710)	29 (740)	1.04
	South End			211 (1460)	204 (1410)	17 (440)	18 (460)	1.04
SCC-L	North End	7.2 (50)	13 (90)	210 (1450)	197 (1360)	13 (330)	13 (340)	1.03
	South End			210 (1450)	200 (1380)	9.5 (240)	14 (360)	1.47

Note : f'_{ci} is the compressive strength of concrete at release with sure-cured samples, f'_c is compressive strength of concrete at service (in this case, 91 days), f_{pi} is the measured stress in strands immediately after transfer, f_{pe} is the measured effective stress in strands after all losses, l_{tr} is the initial transfer length, and l_{tf} is the final transfer length.

For the SCC-L girder, the high-strength at transfer girders significantly reduced compared to the CC-L girder. For the SCC girders, slightly lower effective prestress and higher concrete compressive strength were observed. Compressive concrete strength seems to be an important parameter to determine the initial transfer length. Figure 8.22 shows the initial and

long-term transfer lengths normalized with compressive strength. However, the normalized transfer lengths indicate that the compressive strength is not a key factor to lead to reduce transfer lengths in the SCC girders. The contribution of high concrete strength to the reduction of transfer lengths of the SCC girders was not shown in this study.

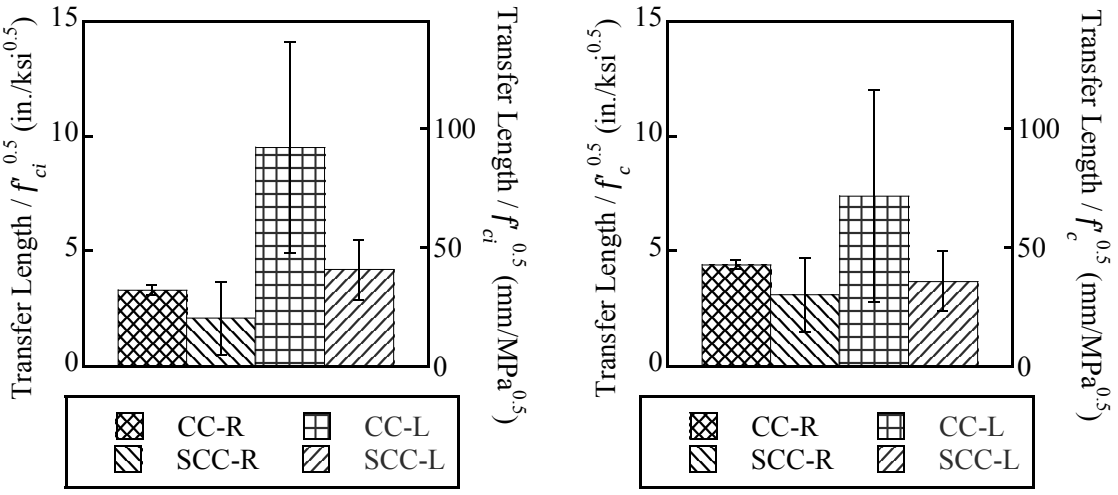

(a) Normalized Initial Transfer Length (b) Normalized Final Transfer Length

Figure 8.22. Girder Transfer Length Normalized with Compressive Strength.

8.4.2 Determination of Transfer Length from End Slip (Draw-In)

Table 8.8 shows a summary of the end slip (draw-in) measurements of strands after immediate release. According to Brooks *et al.* (1988), the initial end slip (draw-in) is a "direct indication of the bond quality of the concrete." Therefore, large end slip (draw-in) values indicate poor bond quality. The CC-L girders had the largest values of end slip among the girders. The SCC-R girders had the smallest values of end slip. Because the differences are very small, all the girders have excellent bond.

Table 8.8. Summary of End Slips.

Girder ID	CC-R	SCC-R	CC-L	SCC-L
Number of Observations*	8	8	10	9
Avg., in.(mm)	0.036 (0.91)	0.029 (0.74)	0.055 (1.40)	0.048 (1.22)
Std. Dev., in.(mm)	0.003 (0.08)	0.013 (0.33)	0.009 (0.23)	0.016 (0.41)

Note: *Number of LVDT measurements on strands.

The transfer lengths estimated from the concrete strain profile, l_{tr}^{*}, and the transfer length estimated from the end slips, $l_{tr\Delta}$, can be compared. Table 8.9 tabulates the transfer lengths estimated from two methods. Figure 8.23 shows that the two independent methods for estimating transfer lengths. Both the CC and SCC girders have one data point on the +30 percent error line and one data point showing more than 30 percent error for the comparison.

Table 8.9. Summary of Transfer Length Estimated from Two Methods.

Girder ID	Location	l_{tr}^{*}, in. (mm)	$l_{tr\Delta}$, in. (mm)	$\frac{l_{tr\Delta}}{l_{tr}^{*}}$
CC-R	North End	8.5 (220)	8.3 (211)	0.98
	South End	8.0 (203)	11 (280)	1.39
SCC-R	North End	3.3 (84)	6.9 (180)	2.09
	South End	7.5 (190)	8.7 (220)	1.16
CC-L	North End	28 (710)	14 (340)	2.07
	South End	17 (440)	17 (420)	1.05
SCC-L	North End	13 (330)	13 (340)	0.97
	South End	9.5 (240)	13 (320)	0.75

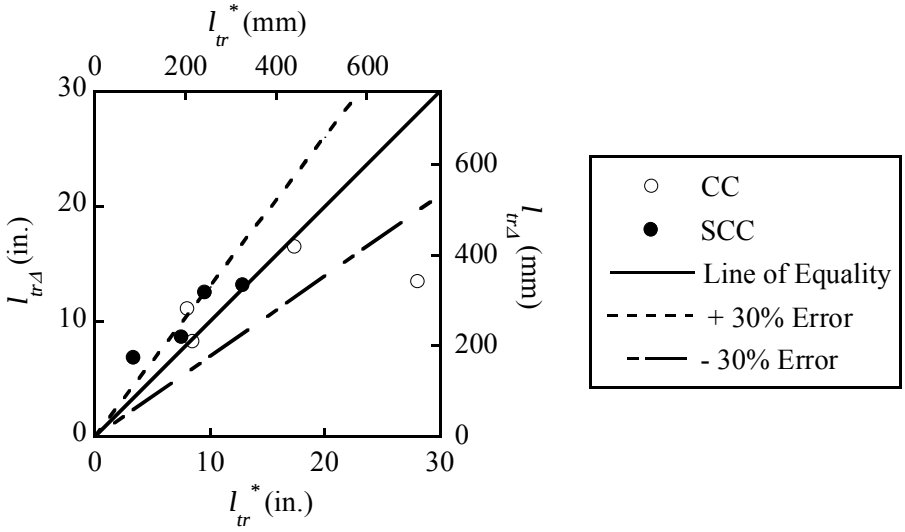

Figure 8.23. Comparison between Transfer Lengths Estimated from Concrete Strain Profile (l_{tr}^*) and Transfer Lengths Estimated from End Slips ($l_{tr\Delta}$).

All measured transfer lengths of the SCC girders were at least 50 percent shorter than the required 30 in. (762 mm) provided by the AASHTO LRFD Specifications. The transfer length of the CC girders is slightly longer than that of the SCC girders. Therefore, the AASHTO LRFD Specifications (2004, 2006) satisfactorily estimated all measured transfer lengths. The high concrete strength of the SCC girders leads to a short transfer length compared to the CC girders at release and later ages. For limestone mixtures, higher early strength of the SCC girder at release significantly reduced the transfer length compared with the CC girders. In this test program, two methods to estimate transfer length were used. The transfer lengths were determined from the measured concrete strain profile and Mast's theory using end slip measurement for both CC and SCC girders. Results indicate that the AASHTO LRFD equation for transfer length is conservative for the CC and SCC girders tested in this study.

8.5 DEVELOPMENT LENGTH TESTS

Development length tests were performed after each flexural test. The test setup is described in Section 4.7.3.5. In this study, 80 in. (2.0 m) embedment lengths were used for the initial trial. If this length was longer than the minimum development length, as indicated by reaching the nominal moment capacity, then a 70 in. (1.8 m) embedment length was used to test other girder end.

8.5.1 Flexural Behavior in Development Length Region

8.5.1.1 CC-R1 and CC-R2 Tests

The development length tests for the CC-R girder were performed by the test procedure in Section 4.7.3.5. At both ends, the girders were loaded to ultimate flexural conditions and the failure mode was in flexure. The strain in the top fiber of the deck exceeded 3000 microstrain indicating the ultimate state for flexure was achieved without any bond failure. The flexural failure with an embedment length of 80 in. (2.0 m) indicates that the minimum development length is likely less than 80 in. (2.0 m) for the CC-R1 test. However, the same strain level was achieved for the CC-R2 test, indicating the minimum development length is likely less than 70 in. (1.8 m). Figure 8.24 shows the moment-curvature of the girder for the development length tests for CC-R girder. Based on both tests, the minimum development length was less than 70 in. (1.8 m). This indicates that the build-up of stress of strands can increase up to the ultimate state without bond failure. Figure 8.25 shows the applied load versus measured strains for the development length tests at each end of girder CC-R.

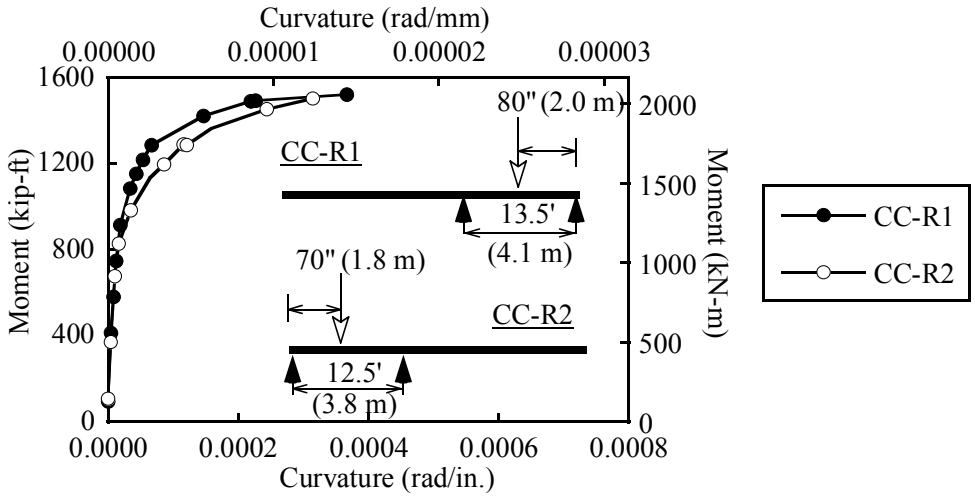

Figure 8.24. Moment-Curvature of the CC-R1 and CC-R2 Tests.

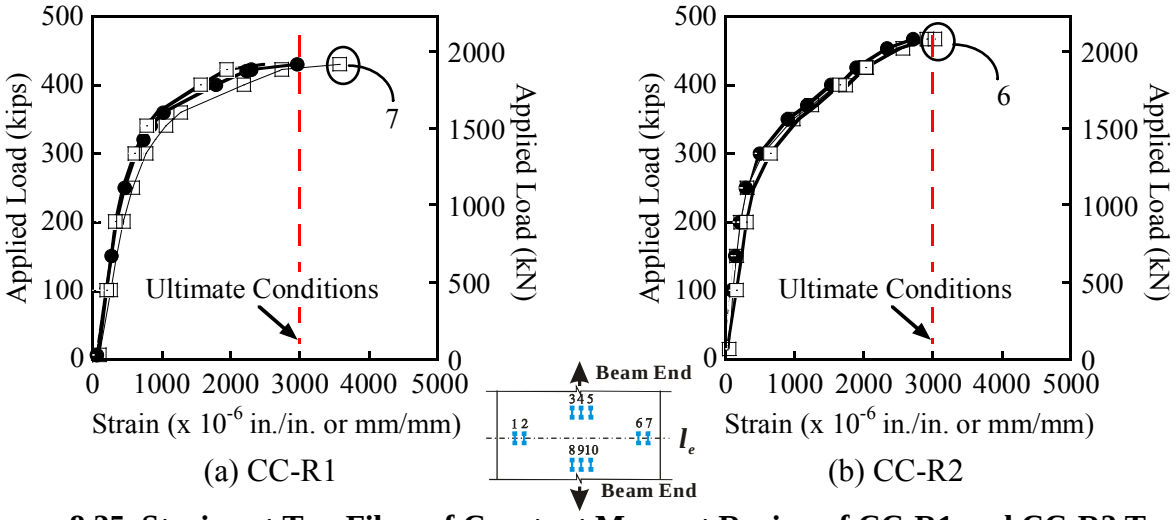

Figure 8.25. Strains at Top Fiber of Constant Moment Region of CC-R1 and CC-R2 Tests.

8.5.1.2 SCC-R1 and SCC-R2 Tests

For the SCC-R1 test, the span length was 13.5 ft (4.1 m) with the same loading locations as the CC-R1 test [80 in. (2.0 m)]. Figure 8.26 shows the primary cracks for the SCC-R1 test. Initially, there were diagonal shear cracks in the web 3.0 ft (1.0 m) from the girder end. This cracking occurred at 250 kip (1110 kN). For this first test, premature bond failure seemed to be caused by existing flexural cracks. As shown in Figure 8.26, the flexural cracks from the midspan flexural testing potentially shortened the free end of strands for the development length test. Thus, the 88 in. (2.2 m) length from the loading point to the inner support may have reduced the embedment length to approximately 76 in. (1.9 m). When the applied load reached 300 kip (1334 kN), extensive diagonal shear cracks on the web of the span adjacent to the inner support weakened this region (see Figure 8.27 (a)). At about 380 kip (1690 kN), the span finally failed by bond splitting failure accompanied by shear cracks passing through the damaged region at the interior support as shown in Figure 8.27 (b).

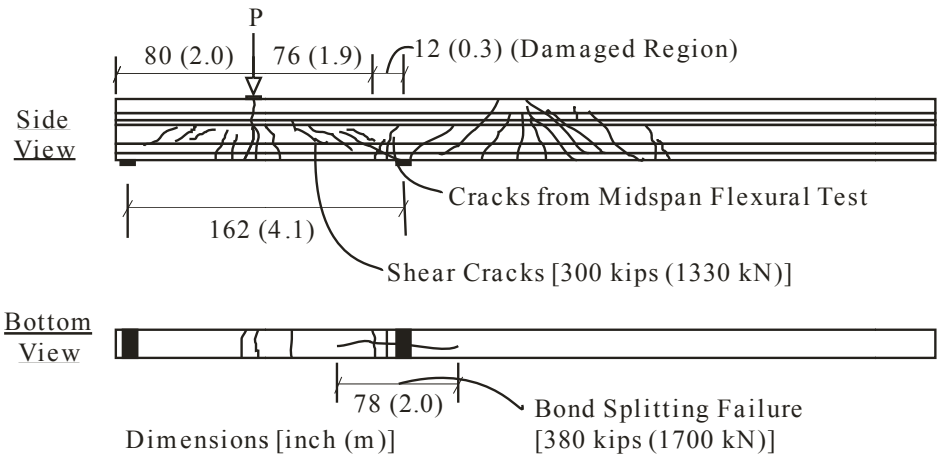

Figure 8.26. Primary Cracks of SCC-R1.

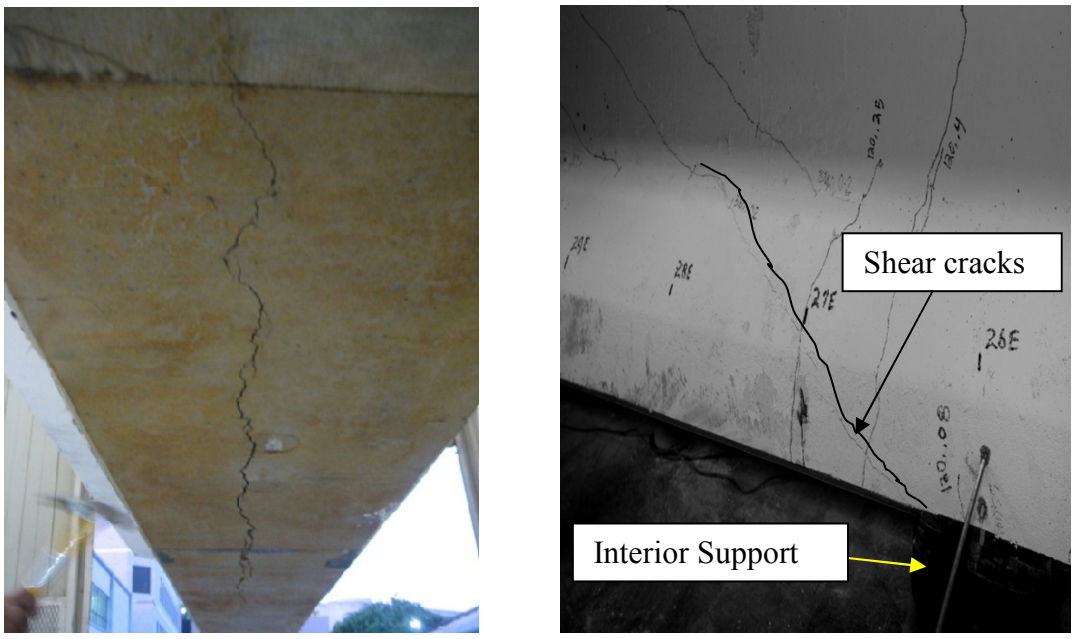

(a) Bond Splitting Failure (b) Shear Cracks

Figure 8.27. Bond Splitting Failure and Shear Cracks.

In addition to the presence of flexural cracks near the interior support, the self-weight of overhanging portion of the girder induced negative moments on the inner support resulting in compression stresses at the bottom fiber near the support. Therefore, the shear and moment capacities were reduced in this region. For this reason, the test setup for SCC-R2 was modified to

use the overhead crane. The overhead crane supported the weight of the overhang and reduced the negative moment.

Figure 8.28 shows the applied load versus measured strains for the development length tests at each end of girder SCC-R. The strain from the SCC-R1 is below the 3000 microstrain value desired to ensure that the strands are fully developed. This is due to the sudden bond and resulting shear failure near the inner support discussed earlier. The strain at top fiber of SCC-R2 exceeded 3000 microstrain, indicating that the girder achieved ultimate flexural conditions and the strands were fully developed. The four plots of strain data corresponding to the strain measurements on the top compression fiber along the midspan

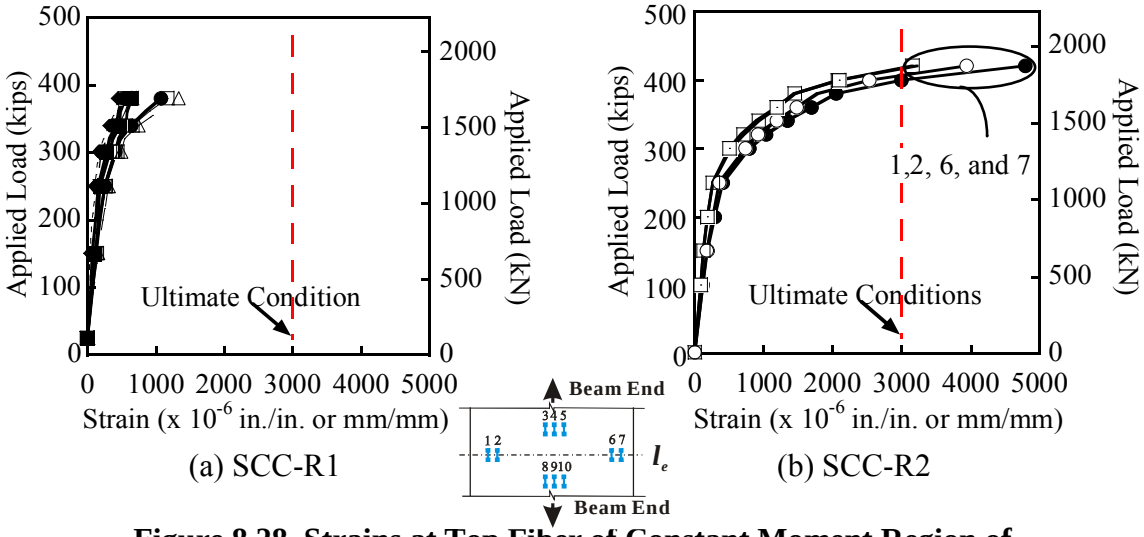

Figure 8.28. Strains at Top Fiber of Constant Moment Region of SCC-R1 and SCC-R2 Tests.

Figure 8.29 shows the moment-curvature plots for the SCC-R girder development length tests. The SCC-R1 results indicated that the girder resisted the applied load with brittle shear and bond failure rather than ductile flexural behavior. Therefore, the SCC-R1 had less curvature with respect to the same applied load than SCC-R2. The SCC-R2 test was loaded to ultimate flexural conditions with an 80 in. (2.0 m) embedment length. The results indicate that the strain of the strands could reach the ultimate state without bond failure and the development length is not greater than 80 in. (2.0 m).

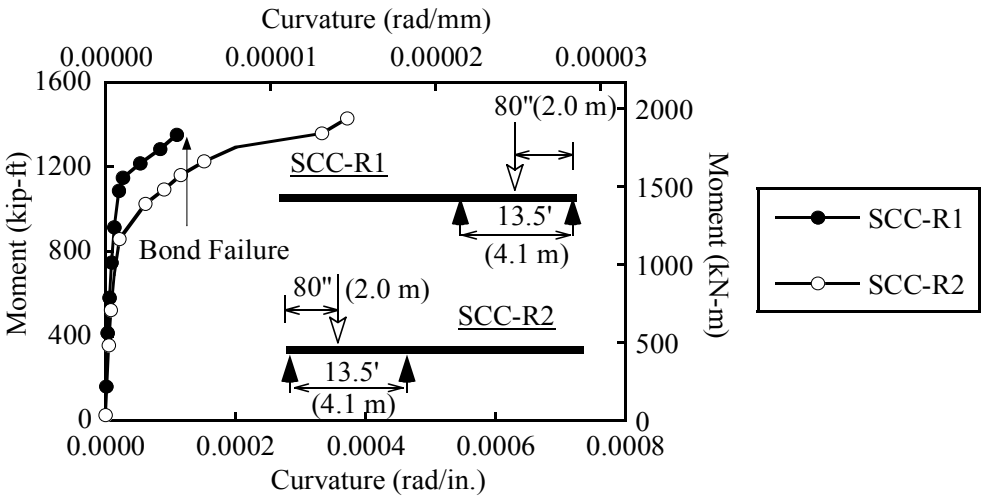

Figure 8.29. Moment-Curvature of SCC-R1 and SCC-R2 Tests.

8.5.1.3 CC-L1 and CC-L2 Tests

After the flexural test of the CC-L girder was performed, development length tests were performed (see Table 4.11). The development length test CC-L1 was performed and ultimate flexural conditions were achieved. The other end was tested to determine if the 70 in. (1.8 m) embedment length was longer than the minimum required development length. Again, the strain of the top fiber exceeded 3000 microstrain, indicating flexural failure.

Figure 8.30 shows the moment-curvatures data from the CC-L1 and CC-L2 tests. Figure 8.31 shows the applied load versus measured strains for the development length tests at each end of girder CC-L. The strain at top fiber of CC-L1 and CC-L2 exceeded 3000 microstrain, indicating that the girders achieved ultimate flexural conditions and the strands were fully developed. Therefore, the development length for the SCC-R girder is less than 70 in. (1.8 m).

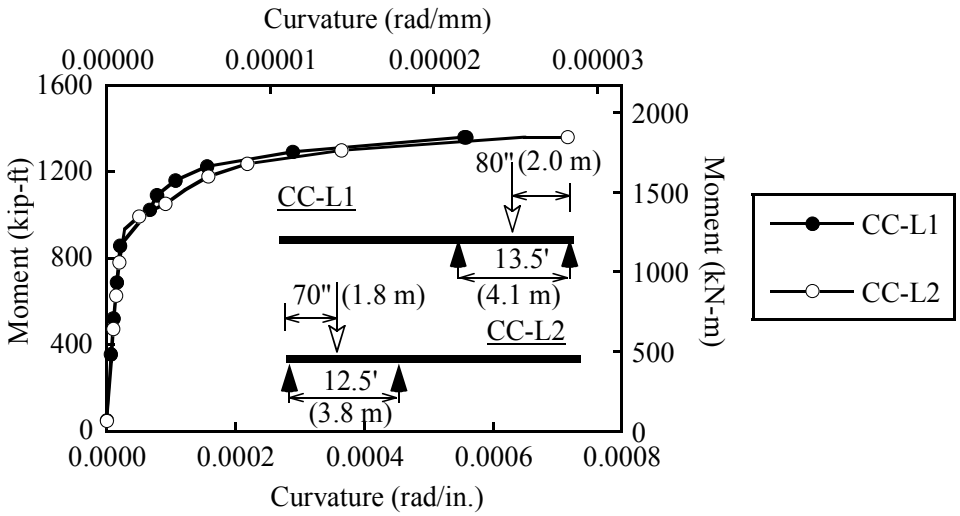

Figure 8.30. Moment-Curvature of CC-L1 and CC-L2 Tests.

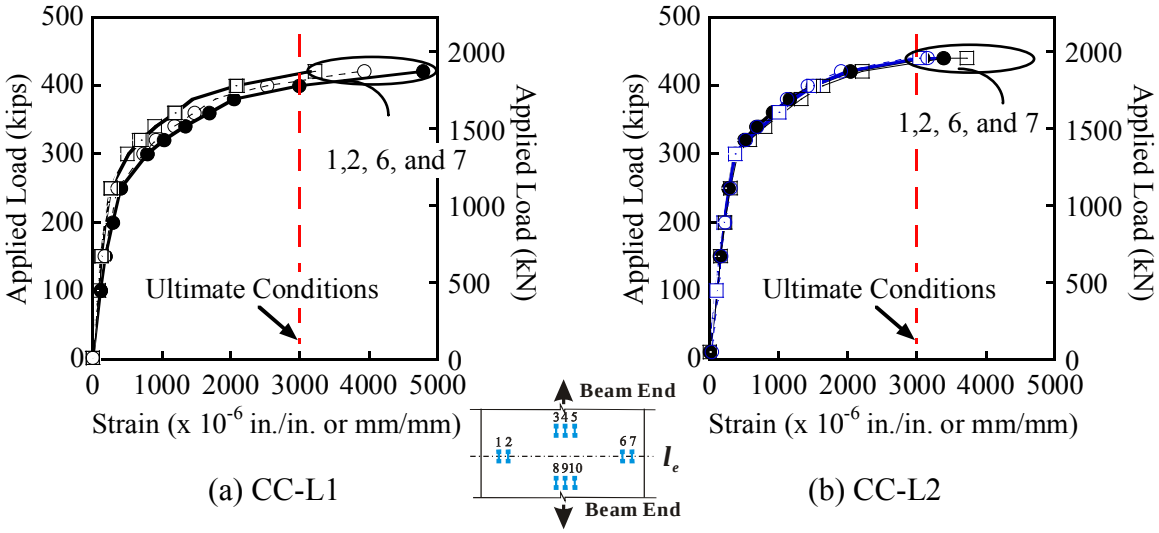

Figure 8.31. Strains at Top Fiber of Constant Moment Region of CC-L1 and CC-L2 Tests.

8.5.1.4 SCC-L1 and SCC-L2 Tests

After the SCC-L girder flexural test was performed, development length tests were performed (see Table 4.11). The SCC-L1 development length test was performed using an 80 in. (2.0 m) embedment length and ultimate flexural conditions were achieved. The other end was then tested to evaluate a 70 in. (1.8 m) development length.

Figure 8.32 shows the moment-curvature plots of the SCC-L1 and SCC-L2 tests. Both tests reached ultimate conditions with no premature bond or shear failure. Figure 8.33 shows the applied load versus measured strains for the development length tests at each end of girder SCC-L. The strain at top fiber of CC-L1 and CC-L2 exceeded 3000 microstrain, indicating that the girders achieved ultimate flexural conditions and the strands were fully developed. Therefore, the development length for the SCC-L girder was determined to be less than 70 in. (1.8 m).

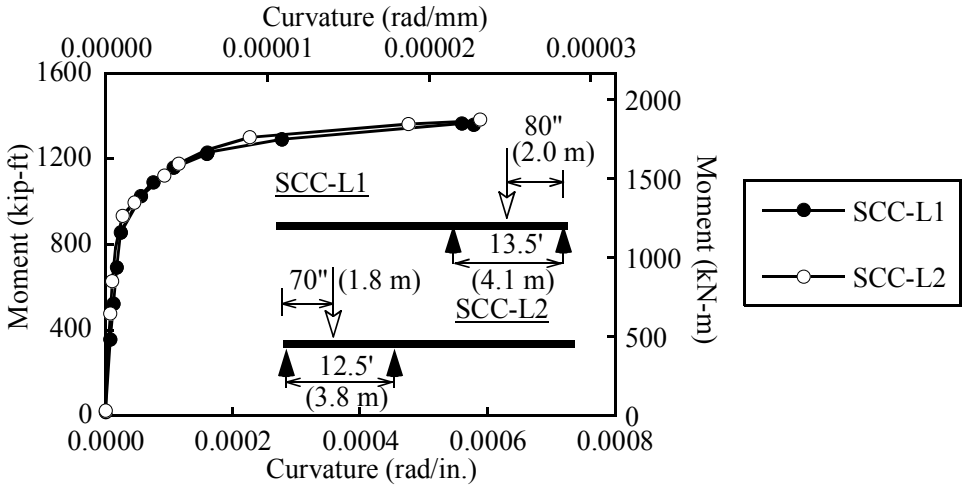

Figure 8.32. Moment-Curvature of SCC-L1 and SCC-L2 Tests.

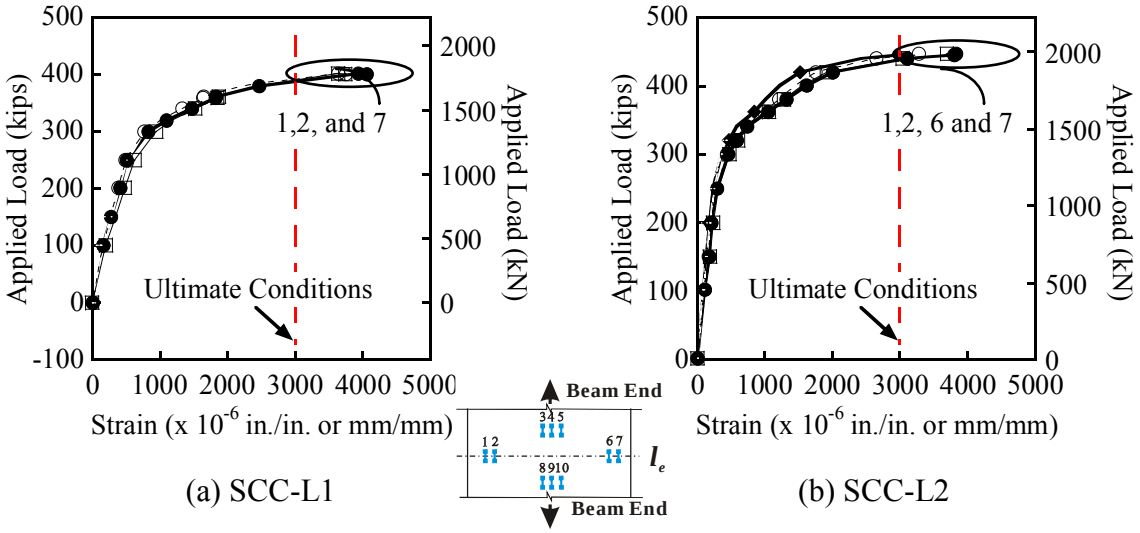

Figure 8.33. Strains at Top Fiber of Constant Moment Region of SCC-L1 and SCC-L2 Tests.

Based on the development length test results, girders CC-L and SCC-L exhibited similar bond performance for developing the stress of strands corresponding to ultimate flexural conditions.

8.5.2 Bond and Shear Characteristics in Development Length Region

According to the MCFT and the AASHTO LRFD Specifications (2004, 2006), the support region is subjected to high shear forces causing high tension in the longitudinal reinforcement. The shear force causes tensile stresses in the web reinforcement, prestressing strands and nonprestressing longitudinal reinforcement. To avoid yielding of the longitudinal reinforcement, the reinforcement and force in the tension zone should meet the following equation from AASHTO 2004 and 2006 (Article 5.8.3.5):

$$A_s f_y + A_{ps} f_{ps} \geq \frac{M_u}{\phi\, jd} + \left(\frac{V_u}{\phi} - 0.5V_s - V_p\right)\cot\theta \qquad (8.1)$$

where M_u is the factored moment (kip-in. [kN-m]), V_u is the factored shear force (kip [kN]), V_p is the component of the effective prestressing force in the direction of the applied shear (kip [kN]), V_s is the component of the stirrup in the direction of the applied shear (kip [kN]), A_{ps} is the area of the prestressing steel (in.^{2} [mm^2]), A_s is the area of nonprestressing steel (in.^{2} [mm^2]), f_{ps} is the stress in the strands for the nominal flexural moment (M_n) resistance (ksi [MPa]), f_y is the yield stress of reinforcement (ksi [MPa]), ϕ is the reduction factor for the nominal moment resistance, θ is the angle of inclination of the diagonal compressive stresses (degrees), jd is the effective shear depth and can be taken as the flexural lever arm, $d - a/2$, but should not be taken as less than 0.9 d nor 0.72 h, d is the distance from the top fiber to the center of gravity of prestressing strands, and h is the depth of section.

The second term $T = (V_u/\phi - 0.5\, V_s - V_p)\cot\theta$ is the tension force in resulting from the shear forces. This value is generally high in the support due to relatively high values of shear forces. Therefore, the tensile stresses and longitudinal reinforcement in the transfer length region should be investigated to profile the build-up of stress of strands.

Table 8.10 shows the strain values at 20 in. (0.5 m) from the girder end at the level of the cgs of the strands. Strain was measured with both surface and embedded concrete strain gages.

Except for the CC-R1 test, the surface and concrete strains are similar, indicating no cracks crossing the gages. The high tensile stress could indicate the high demand of longitudinal and shear reinforcements to avoid shear and bond failure. Because the 70 in. (1.8 m) embedment length girders have higher shear force on the support, they reasonably have slightly higher tensile stains compared to 80 in. (2.0 m) embedment length. The SCC-R2 test shows slightly higher tensile strains than the CC-R2 due to the intensive shear stress in the transfer length region. The CC-L and SCC-L girders exhibited the similar tensile stresses. However, the CC and SCC-L have higher tensile strains at applied load of 340 kip (1520 kN) compared to the CC-R and SCC-R samples except for SCC-R2. This indicates that the contribution of shear of the limestone concrete is lower than that of the river gravel concrete resulting in a higher demand on the longitudinal reinforcement to avoid shear and bond failure.

Table 8.10. Strain at 20 in. (0.5 m) from the End.

Test ID	Prestrain ($\times 10^{-6}$ in./in. [mm/mm])	Strain due to Applied Load (Tensile strain)						Note
		At 340 kip (1520 kN) ($\times 10^{-6}$ in./in. [mm/mm])			At Ultimate ($\times 10^{-6}$ in./in. [mm/mm])			Embedment Length, in. (m)
	ε_{pi}	ε'_c	ε_c		ε'_c	ε_c		
CC-R1	– 544	105	192	103	145	168	684*	80 (2.0)
CC-R2	– 485	92	170	166	133	227	235	70 (1.8)
SCC-R1	– 667	100	125	113	133	227	235	80 (2.0)
SCC-R2	– 804	191	245	255	277	280	260	80 (2.0)
CC-L1	– 679	132	176	183	156	202	236	80 (2.0)
CC-L2	– 754	182	182	182	221	260	258	70 (1.8)
SCC-L1	– 960	161	140	143	201	167	167	80 (2.0)
SCC-L2	– 869	166	164	156	236	235	235	70 (1.8)

Note: * Crack occurrence in the transfer length region, ε_{pi} is prestrain due to effective prestressing force, ε_c is concrete strain due to applied load on surface type gage, and ε'_c is concrete strain due to applied load in embedded type gage.

Web-shear cracks propagated through layers of strands on the bottom flange near the support of CC-L2 and SCC-L2 girders. However, there were no bond or shear failures. Figures 8.34 and 8.35 show the measured strain at the cgs level from surface and embedded strain gages, along with the measured prestrain, as a function of the distance from the girder end. In addition, an elevation view of the girder end with the crack locations and widths is provided. Figure 8.34 shows test CC-L2 and Figure 8.35 shows test SCC-L2.

As shown in Figure 8.34, the crack did not significantly affect the loss of bond. However, the tensile strain at 70 in. (1780 mm) from the end exceeded the compressive prestrain, ε_{pi}, indicating losses of prestrain or gage failure due to cracks. Because tensile strains at 5 and 20 in. (130 and 510 mm) did not exceed the compressive prestrain, crack opening was prevented by the prestressing force and the anchorage of type W, V, and R bars. Even though the shear crack propagated through the transfer length region in the bottom flange, there was no bond failure. Figure 8.35 also shows that the crack did not affect the loss of bond

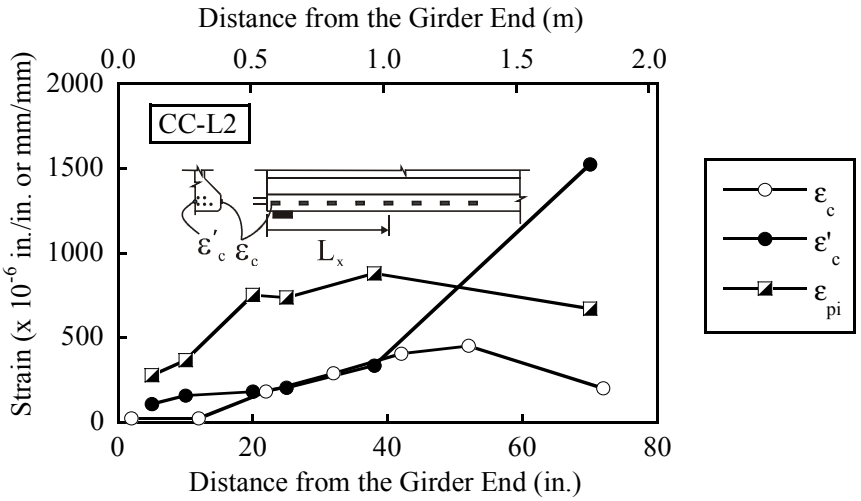

(a) Strain of cgs of strands

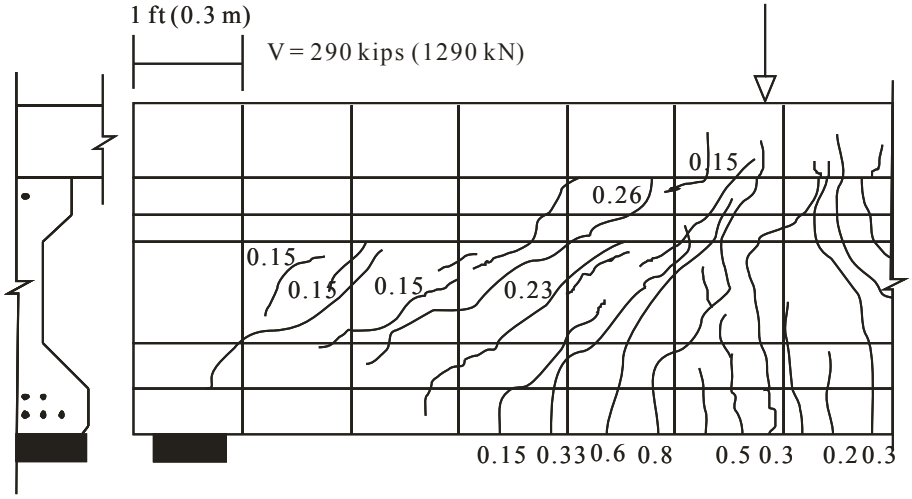

Crack width: mm (1 mm = 0.039 in.)

Note: crack width at the shear load of 310 kip (1380 kN)

ε_{pi} = measured prestrain due to effective prestressing force

ε_c = concrete strain due to applied load on surface type gage

ε_c' = concrete strain due to applied load in embedded type gage

L_x = distance from the girder end (in. [m])

(b) Crack Diagram

Figure 8.34. Strains at the Centroid of Gravity of Strands and Crack Diagram at Ultimate Loading (CC-L2).

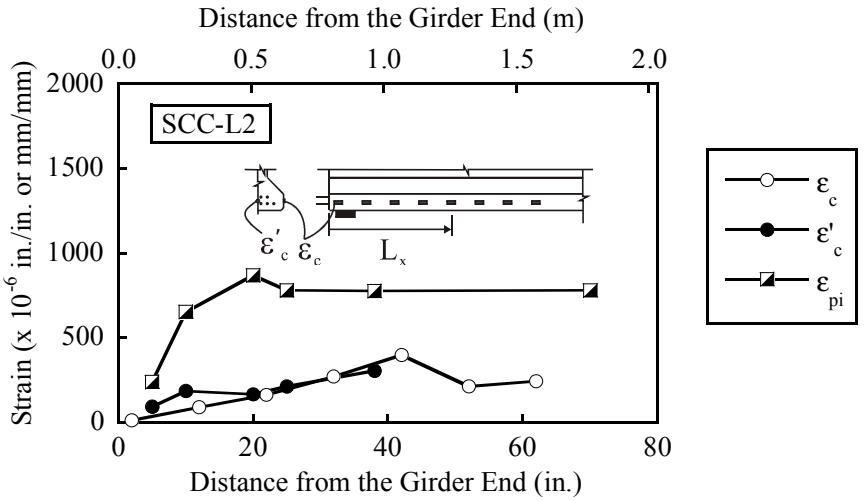

(a) Strain of cgs of strands

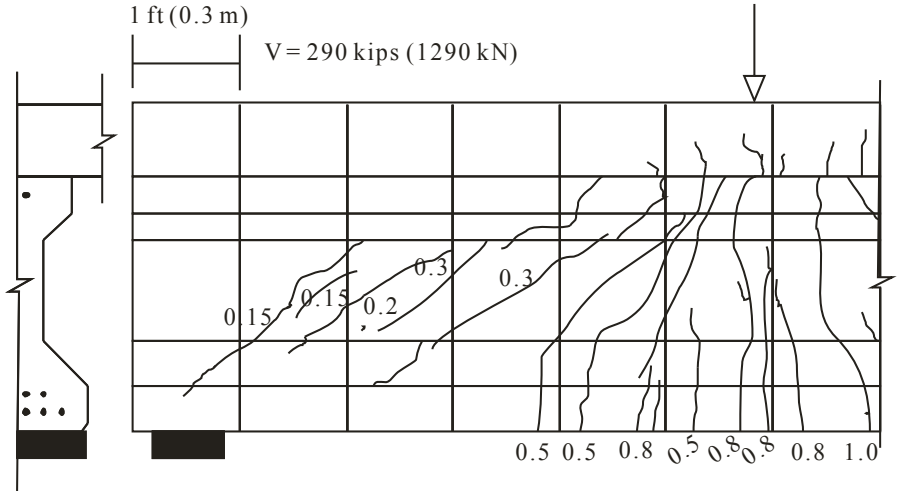

Crack width: mm (1 mm = 0.039 in.)

Note: crack width at the shear load of 310 kip (1380 kN)

ε_{pi} = measured prestrain due to effective prestressing force

ε_c = concrete strain due to applied load on surface type gage

ε'_c = concrete strain due to applied load in embedded type gage

L_x = distance from the girder end (in. [m])

(b) Crack Diagram

Figure 8.35. Strains at the Centroid of Gravity of Strands and Crack Diagram at Ultimate Loading (SCC-L2).

Figure 8.36 shows a typical plot of the end slips of strands during the development length tests. Each data point represents the slip measured in one strand at the corresponding applied load. As shown in these typical plots, the maximum measured slip was less than 0.01 in. (0.2 mm). There were no strand slips observed for all transfer zones at the girder ends.

It was recommended to avoid the propagation of cracks in the transfer zone to prevent the strand slip, finally resulting in bond failure (Russell and Burns 1993). In this study, the observed cracks in the transfer zone did not cause any measurable bond slip. There was also no strand slip observed at the girder end of the SCC-R1.

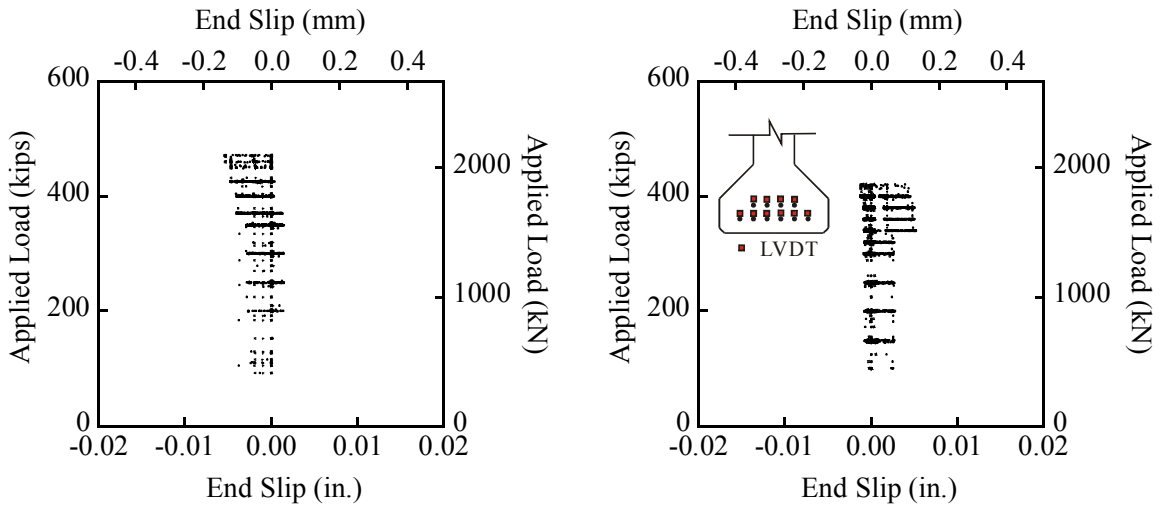

(a) CC-R2 (b) SCC-R2

Figure 8.36. Typical End Slip of Strands.

8.5.3 Comparisons between Experimental Results and AASHTO LRFD

8.5.3.1 Development Length

Bond failure did not occur during the development length tests, except for SCC-R1. After modifying the test setup, the 80 in. (2.0 m) development length was sufficient to cause flexural failure at the other end of the SCC-R girders. When monitoring the slip of strands at the end of the section, there was no larger slip than 0.01 in. (0.25 mm), indicating no bond failure for all tests. It should be noted that the premature bond failure was observed at SCC-R1 near the interior support. However, there was no end slip at the end of the section.

In summary, the development length is likely shorter than 70 in. (1.8 m) for the tested girders containing CC and SCC mixtures. Average stress in the strands at nominal flexural resistance, f_{ps}, was calculated based on Article 5.7.3.1.1-1 of the AASHTO LRFD Specifications (2004, 2006). The effective prestress, f_{pe}, was obtained from longer-term strain measurements. Table 8.11 shows the summary of development length values for all girders. The 2004 and 2006 AASHTO LRFD prediction equation provided a conservative estimation for both the CC and SCC girders. The 2004 AASHTO LRFD alternative prediction equation (Equation 2.33) provided a closer estimate of development length for both the CC and SCC girders.

Table 8.11. Summary of Development Length Test Results.

Test ID	l_d, in. (m)	Estimated l_d, in. (m)	2004 AASHTO, Alt. (Eq. 2.33) l_d, in. (m)	2004, 2006 AASHTO (Eq. 2.30) l_d, in. (m)	Failure Mode
CC-R1	< 80 (2.0)	< 70 (1.8)	> 87 (2.2)	> 120 (3.0)	Flexural
CC-R2	< 70 (1.8)				Flexural
SCC-R1	Bond Failure	< 80 (2.0)	> 73 (1.9)	> 120 (3.1)	Shear/Bond
SCC-R2	< 80 (2.0)				Flexural
CC-L1	< 80 (2.0)	< 70 (1.8)	> 90 (2.3)	> 120 (3.1)	Flexural
CC-L2	< 70 (1.8)				Flexural
SCC-L1	< 80 (2.0)	< 70 (1.8)	> 70 (1.8)	> 120 (3.0)	Flexural
SCC-L2	< 70 (1.8)				Flexural

8.5.3.2 Maximum Strain in Prestressing Strands

The measured strand strain, $\varepsilon_{max\text{-}exp}$, at the centroid of bottom rows of strands at nominal moment resistance of the beam is the summation of the strain from the LVDTs attached to the girder and the embedded strain gages. The embedded strain gages measure the prestrain, while the LVDTs measure the strain due to the applied load.

The CC and SCC girders had similar strain values when the same aggregate type was used. The CC-L and SCC-L girders have higher strand strains at the ultimate state compared to the CC-R and SCC-R girders. The strand strains were calculated at the ultimate in accordance with the AASHTO LRFD Specifications (2004, 2006). The calculated maximum strand strain values based on the AASHTO were generally lower than the measured values. The values are summarized in Table 8.12.

Table 8.12. Measured Maximum Ultimate Stand Strain.

Test ID	ε_{pe} in./in. or mm/mm	ε_{ps} in./in. or mm/mm	$\varepsilon_{max\text{-}exp}$ in./in. or mm/mm	$\varepsilon_{max\text{-}cal}$ in./in. or mm/mm	$\frac{\varepsilon_{max\text{-}exp}}{\varepsilon_{max\text{-}cal}}$
CC-R1	0.007	0.009	0.016	0.013	1.2
CC-R2	0.007	0.012	0.019	0.013	1.5
SCC-R1	0.007	0.003	0.010	0.012	0.8
SCC-R2	0.007	0.009	0.016	0.012	1.3
CC-L1	0.007	0.016	0.023	0.010	2.3
CC-L2	0.007	0.021	0.029	0.011	2.6
SCC-L1	0.007	0.016	0.023	0.009	2.6
SCC-L2	0.007	0.017	0.024	0.010	2.4

Note: ε_{pe} is the prestrain from measured concrete strain gage, ε_{ps} is the strain due to applied load at ultimate measured from LVDTs, $\varepsilon_{max\text{-}exp}$ is the measured ultimate strand strain, which is the sum of ε_{pe} and ε_{ps}, and $\varepsilon_{max\text{-}cal}$ is calculated ultimate strand strain based on AASHTO LRFD.

8.5.3.3 Nominal Moment

The AASHTO LRFD Specifications (2004, 2006) can reasonably estimate the shear-moment interaction resulting in the degradation of moment capacity associated with shear capacity. Development length tests were performed when flexural and shear stresses were present at the critical section. The longitudinal strain in the web can be estimated by the following equation (AASHTO LRFD Article 5.8.3.4.2-1):

$$\varepsilon_x = \frac{\frac{|M_u|}{d_v} + 0.5\,|V_u - V_p|\cot\theta - A_{ps}\,f_{po}}{2\left(E_s\,A_s + E_p\,A_{ps}\right)} \tag{8.2}$$

where M_u is the factored moment (kip-in. [kN-m]), V_u is the factored shear force (kip [kN]), V_p is the component in the direction of the applied shear of the effective prestressing force (kip [kN]), f_{po} is the stress in the prestressing steel (ksi [MPa]) and usually 0.7 f_{pu} in the AASHTO LRFD, A_{ps} is the area of the prestressing steel (in.^{2} [mm^2]), A_s is the area of nonprestressing steel (in.^{2} [mm^2]), E_s and E_p are the elastic modulus of nonprestressing steel and prestressing steel, respectively (ksi [MPa]), and θ is the angle of inclination of diagonal compressive stresses (degree). This value is always taken to be larger than 0 for conservatism in the design. As shown in Equation 8.2, a higher moment results in an increase of the longitudinal strain in the web.

Based on these concepts, the nominal moment capacity for each girder and during testing is estimated by the AASHTO LRFD Specifications (2004, 2006). The nominal moments were estimated by using the Equation 2.26 of the AASHTO LRFD Specifications.

Table 8.13 shows the calculated nominal moment capacity from the AASHTO LRFD Specifications (2004, 2006) and the measured maximum moment from each development length test. The measured ultimate moment of SCC-R1 was 3 percent higher than the calculated nominal moment resistance, $M_{n\text{-}AASHTO}$ based on the AASHTO LRFD Specifications (2004, 2006). The nominal moment resistance, $M_{n\text{-}exp}$ of all other tests was 7 to 31 percent higher than calculated nominal moment resistance, $M_{n\text{-}AASHTO}$.

Table 8.13. Measured Moment versus Calculated Moment Based on AASHTO (2004, 2006).

Test ID	$M_{n\text{-}AASHTO}$, kip-ft (kN-m)	$M_{n\text{-}exp}$, kip-ft (kN-m)	$\frac{M_{n-exp}}{M_{n-AASHTO}}$
CC-R1	1281 (1737)	1519 (2059)	1.19
CC-R2	1135 (1539)	1491 (2021)	1.31
SCC-R1	1279 (1734)	1323 (1794)	1.03
SCC-R2	1133 (1536)	1430 (1939)	1.26
CC-L1	1273 (1726)	1361 (1845)	1.07
CC-L2	1126 (1527)	1361 (1845)	1.21
SCC-L1	1271 (1723)	1366 (1852)	1.07
SCC-L2	1126 (1527)	1382 (1874)	1.23

8.5.4 Shear Performance

8.5.4.1 Shear Force Causing Web-Shear Cracking

There were concerns regarding the shear performance of the SCC mixtures, as they have lower amounts of aggregate compared to typical CC mixtures. This section will investigate the local shear behavior of the girders and will show how the local shear demand impact the overall failure mode.

Web-shear cracking occurs when the maximum principal tensile stress is equal to the tensile strength of concrete. When the element is subjected to prestress and shear stresses at the center of the web, the principal stresses can be calculated as follows (Collins and Mitchell 1991, Naaman 2004):

$$\sigma_1 = \sqrt{v^2 + \left(\frac{f_{pc}}{2}\right)^2} - \frac{f_{pc}}{2} \tag{8.3}$$

where σ_1 is the principal stress (psi [MPa]), v is the shear stress at the web (psi [MPa]), and f_{pc} is the compressive stress due to the effective prestressing force, taken as the positive value (psi [MPa]).

To solve the cracking shear stress in the web, v_{cw} (psi [MPa]), σ_1 becomes equal to the tensile strength, f_t :

$$v_{cw} = f_t \sqrt{1 + \frac{f_{pc}}{f_t}} \tag{8.4}$$

When f_t is approximately $4\sqrt{f_c'}$ psi ($0.33\sqrt{f_c'}$ MPa), based on direct tension test data, this equation becomes the basic web-shear cracking equation of ACI 318-05 and the AASHTO Standard Specifications (2002):

$$V_{cw-ACI} = \left(3.5\sqrt{f_c'} + 0.3\ f_{pc}\right) b_w\ d + V_p \quad \text{(kip, in.)} \tag{8.5}$$

$$[V_{cw-ACI} = \left(0.29\sqrt{f_c'} + 0.3\ f_{pc}\right) b_w d + V_p \quad \text{(kN, mm)}\ ]$$

where $V_{cw\text{-}ACI}$ is the shear force corresponding to web-shear cracking, f'_c is the compressive strength of concrete (psi [MPa]), b_w is the width of web (in. [mm]), d is the distance from the extreme compression fiber to the centroid of the tension strands (in. [mm]), V_p is the component in the direction of the applied shear of the effective prestressing force (kip [kN]), and f_{pe} is the longitudinal compressive stress at the centroid of the beam (psi [MPa]).

The MCFT theory also assumes the same value for f_t as the cracking stress of concrete for the diagonal tensile stresses. This value is used to estimate the β value from Equation 2.4.

For the MCFT, the shear forcem corresponding to web-shear cracking is estimated as follows,

$$V_{cw-MCFT} = \beta \sqrt{f_c'} b_w \, jd \tag{8.6}$$

where jd is the effective shear depth which can be taken as the flexural lever arm (in. [mm]), $d - a/2$, but should not be taken as less than 0.9 d nor 0.72 h; d is the distance from the top fiber to the centroid of gravity of strands (in. [mm]); and h is the depth of section (in. [mm]). The values of $V_{cw\text{-}MCFT}$ for the girders in this test program were obtained by using the RESPONSE 2000 Program (Bentz 2000).

Diagonal cracks occurred in the critical section where maximum shear force acted in all the tests. If the shear capacity of the girder is not sufficient to resist the applied shear force, a shear failure could increase the potential for bond slip or bond failure. Therefore, the shear capacity significantly affects bond performance.

Table 8.14 shows the comparison between predicted and measured web-shear cracking loads. Figure 8.37 shows the plots of the comparison between predicted and measured force corresponding to web-shear cracking. The web-shear cracking force based on Equation 8.5, $V_{cw\text{-}ACI}$, is slightly higher than the web-shear cracking based on the MCFT, $V_{cw\text{-}MCFT}$. All the web-shear cracking forces were estimated based on the measured concrete tensile strength. When the principal tensile strain, ε_1, exceeds $\varepsilon_{cr} = f_t/E_c$ (about 0.0001 in./in. [mm/mm]), the web-shear cracking load, $V_{cw\text{-}exp}$, is obtained from the LVDT measurements. This calculation was compared to the crack mapping to confirm the estimation.

In general, the measured web-shear cracking forces were similar to the predicted web-shear cracking force. The ACI 318-05 and AASHTO Standard Specifications approach underestimate the web-shear cracking values. The MCFT predicts the web-shear cracking for the SCC and CC girders within ±30 percent.

Table 8.14. Shear Force Causing Web-Shear Cracking (Predicted versus Measured Values).

Test ID	$V_{cw\text{-}ACI}$, kip (kN)	$V_{cw\text{-}MCFT}$, kip (kN)	$V_{cw\text{-}exp}$, kip (kN)	$\frac{V_{cw-exp}}{V_{cw-ACI}}$	$\frac{V_{cw-exp}}{V_{cw-MCFT}}$
CC-R1	90 (400)	137 (609)	174 (774)	1.9	1.3
CC-R2	90 (400)	162 (721)	163 (725)	1.8	1.0
SCC-R1	99 (442)	159 (707)	173 (770)	1.7	1.1
SCC-R2	99 (442)	150 (667)	136 (605)	1.4	0.9
CC-L1	92 (407)	149 (663)	163 (725)	1.8	1.1
CC-L2	92 (407)	179 (796)	164 (729)	1.8	0.9
SCC-L1	102 (454)	171 (761)	135 (600)	1.3	0.8
SCC-L2	102 (454)	188 (836)	195 (867)	1.9	1.0

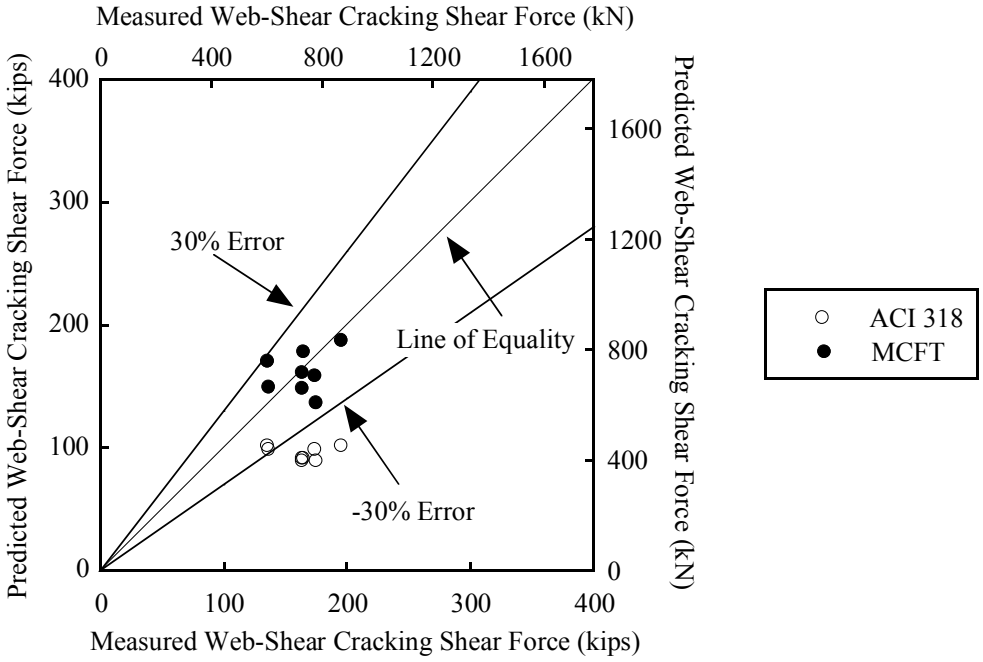

Figure 8.37. Measured versus Predicted Shear Force Causing Web-Shear Cracking.

8.5.4.2 Principal Strains at Critical Section for Shear

The cirtical section for shear shall be taken as the effective shear depth, d_v, from the internal face of the support. Figures 8.38 and 8.39 show the principal tensile and compressive strains of the concrete at the critical section for shear. The average tensile strain is related to the contribution to shear in the MCFT. Therefore, the higher value indicates a higher contribution to shear. Generally, the river gravel girders tend to have a higher contribution to shear than the limestone aggregate girders. The CC-R2 and the SCC-R2 tests exhibited slightly higher principal tensile strains compared to the limestone girder tests.

When evaluating the shear performance of girders containing river gravel, the CC-R girder exhibit slightly higher principal strains than the SCC-R girder. The SCC-R1 test showed dominant diagonal shear cracks on the span at the interior support rather than in the development length region. Therefore, the measured principal stresses on the cracked web member and the strains in the steel are lower in the development length region.

The CC-R2 test exhibited higher principal tensile strains in the cracked web and higher strain in the shear reinforcement, indicating degradation of the shear cracking load at early stages. However, the strain stabilized because flexural behavior governed in the final failure mode. The SCC-R2 test indicated that the web in the 80 in. (2.0 m) development length region was damaged due to reduced shear capacity. The first web-shear cracking occurred at slightly lower stress levels than for CC-R1 and CC-R2 tests. However, the final failure mode was flexural.

The large-scale tests showed very similar principle strains at the shear critical sections for both the SCC-L and CC-L tests, as shown in Figure 8.39.

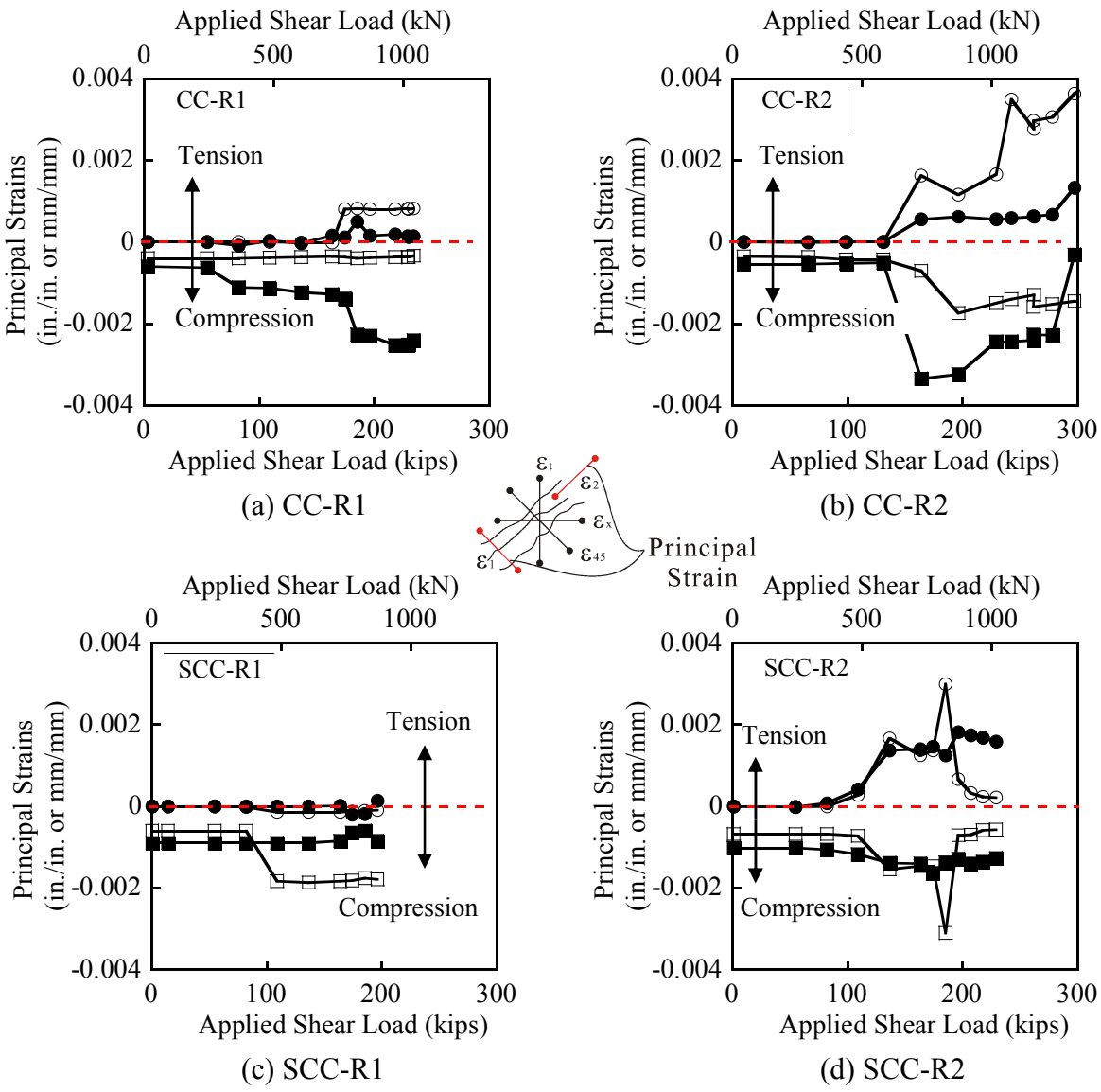

Figure 8.38. Principal Strains of Cracked Web Concrete in CC-R and SCC-R Girders.

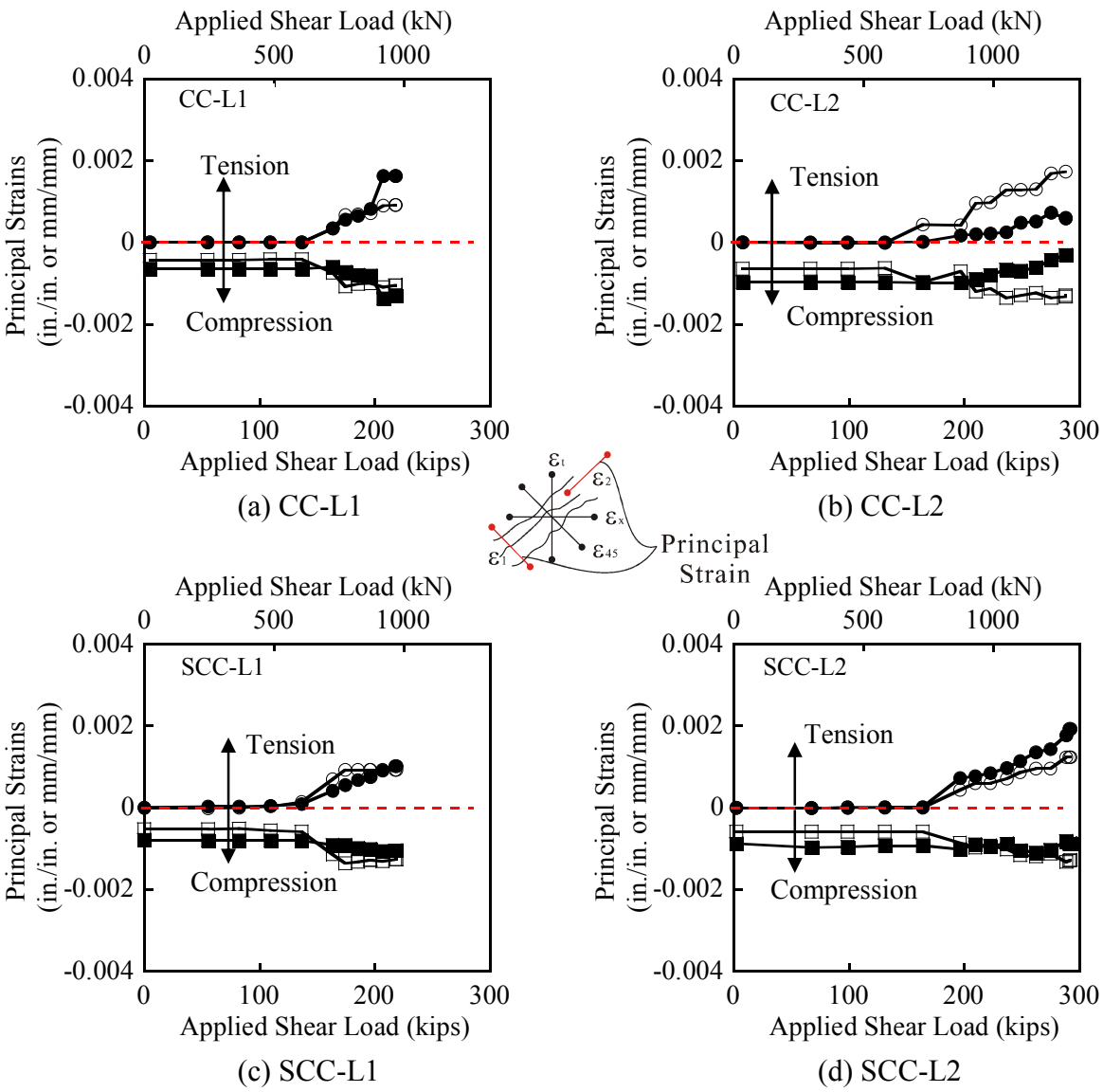

Figure 8.39. Principal Strains of Cracked Web Concrete in CC-L and SCC-L Girders.

8.5.4.3 Strain in Shear Reinforcement

Figures 8.40 and 8.41 show the measured strains in the web steel as a function of the applied shear load, which is the shear force acting on the critical section. Strains in the shear reinforcement did not reach the yield strain of 2000×10^{-6}. This indicates that the girders did not reach their ultimate shear capacity. According to the prediction from the MCFT, the first web-shear cracks preceded the flexural cracks and flexural-shear cracks. The curved shape indicates that the web steel contribution to shear strength stabilized as the load increased, with more

flexural cracks forming at the loading points. CC-R2, CC-L1, CC-L2, SCC-L1, and SCC-L2 tests show this behavior.

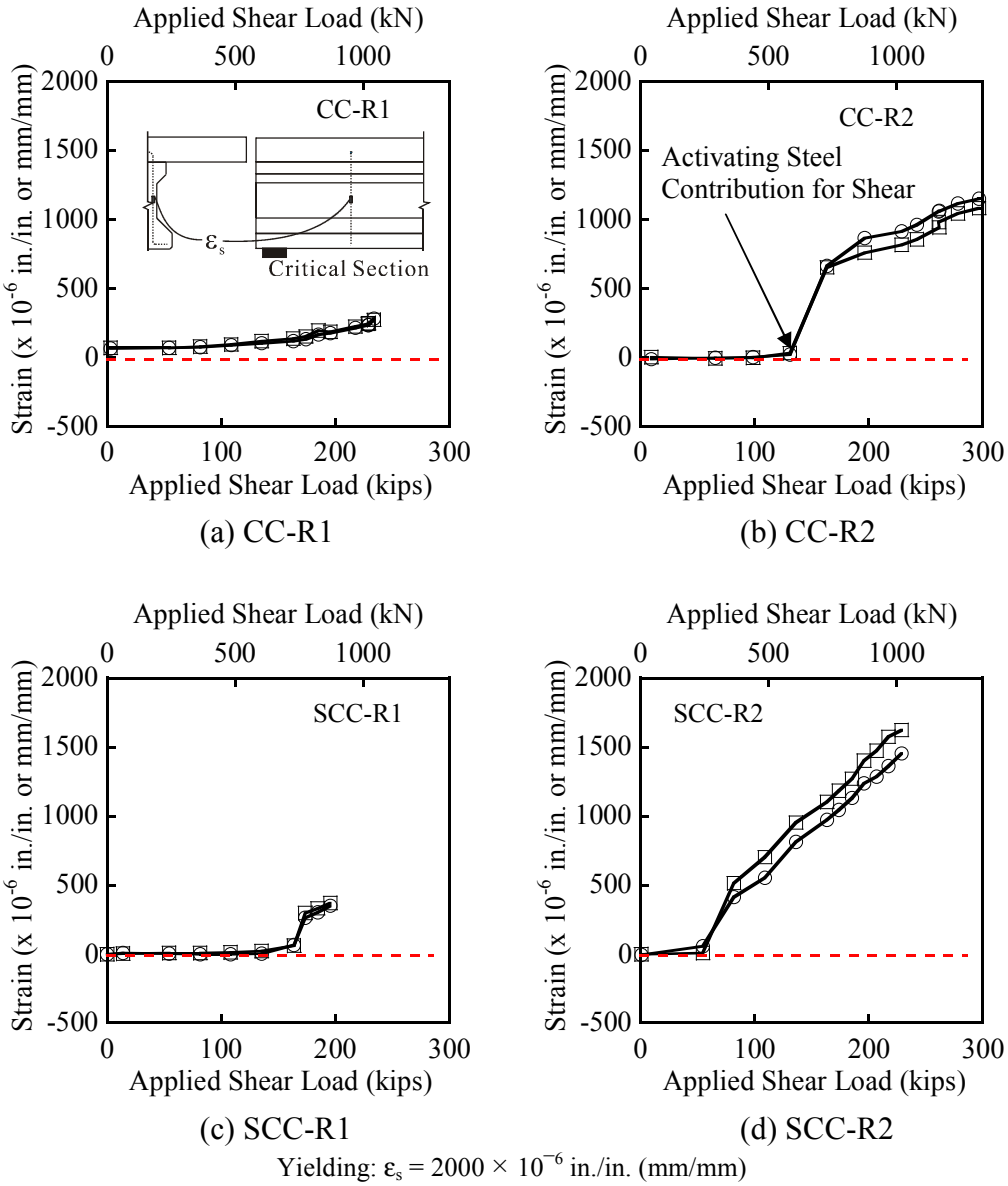

Figure 8.40. Web Steel Strains near Critical Section for Shear in CC-R and SCC-R Girders (36 in. [0.9 m]).

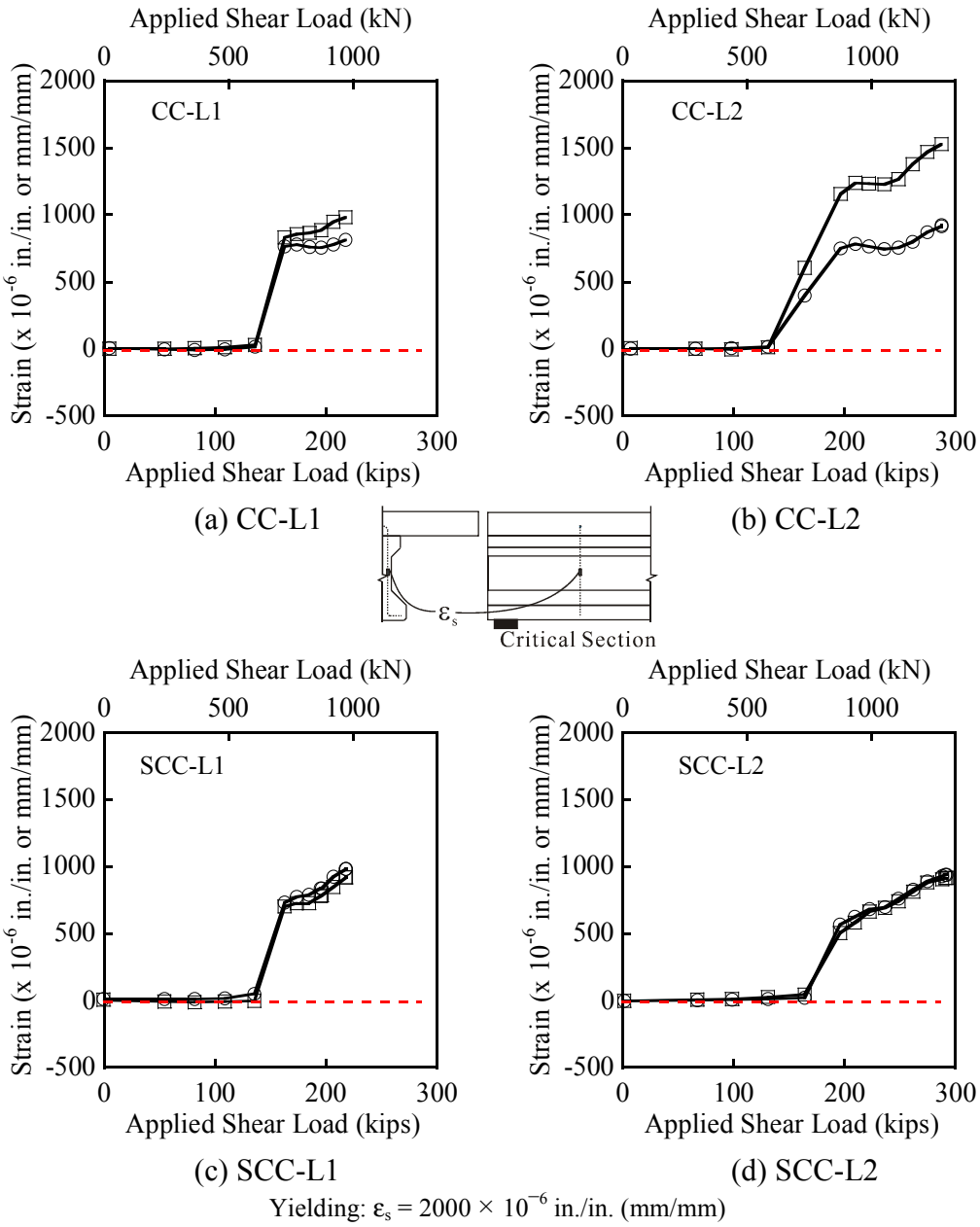

Figure 8.41. Web Steel Strains near Critical Section for Shear in CC-L and SCC-L Girders (36 in.[0.9 m]).

8.5.4.4 Comparison of Estimated Shear Capacity

The purpose of the tests at the girder ends was to evaluate the development length of the strands in the SCC girders compared to the CC girders and the AASHTO Specifications. Although shear failures did not occur, the test data are useful in estimating shear capacity. The measured crack width, w, and the angle of the diagonal compressive stresses in the web, θ, were used to predict the concrete and steel contribution to shear strength as shown in Figure 8.42. The shear capacity was calculated from the MCFT and proposed equations in Chapter 6 for the limiting value of the maximum shear stress on the shear plane in the cracked concrete, v_{ci}. The crack width, w, is equal to the product of ε_1 and the spacing of diagonal crack spacing, $s_{m\theta}$. When the values of θ, ε_1, and $s_{m\theta}$ are known, the shear forces in the steel and concrete are estimated by the iteration procedures in the MCFT. The detailed iteration procedures are presented in the textbook by Collins and Mitchell (1991). The experimental and estimated shear capacities are compared to validate the proposed equation (Equation 6.38) in Chapter 6 and the AASHTO LRFD Specifications.

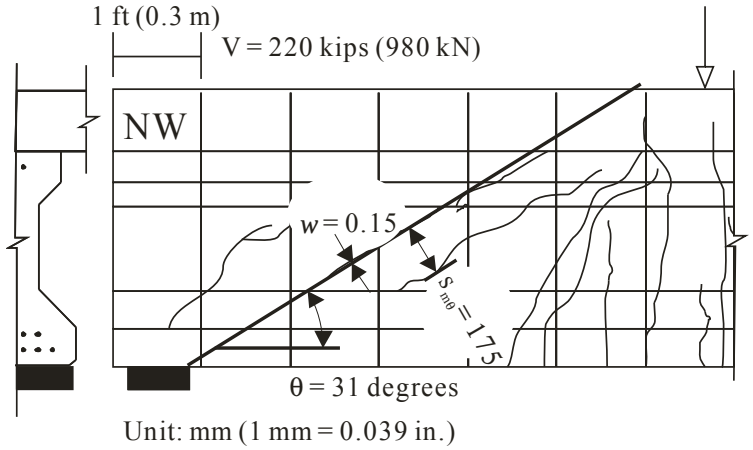

Figure 8.42. Measured Crack Width and Angle of Diagonal Crack (CC-L1).

Based on this procedure, the applied shear and predicted shear values are compared as shown in Table 8.15. As discussed in Chapter 6, the same shear capacity was estimated with all the different limiting values for the maximum shear stress on the shear plane. In this estimation, all the values estimated from AASHTO and the proposed equations are identical. As discussed in

Chapter 6, the angle and shear reinforcement ratios were not so small to activate the slip before the yielding of the shear reinforcement.

For each girder end, a unique crack pattern was observed with a different crack width, crack angle, and diagonal crack spacing. These values are summarized in Table 8.15, along with analytical and experimental estimates of the concrete and web steel contributions to the shear capacity at the critical section. Different contributions to the shear capacity were observed depending on the mixture type, aggregate type, and test series. The concrete strengths determined for the girders with limestone aggregate are lower than for girders with river gravel coarse aggregates. The limestone SCC mixtures have lowest concrete strength values among all the mixtures.

The ratio of analytical and measured shear forces indicates the accuracy of the prediction. When the ratio is larger than 1.0, the AASHTO shear design overestimates shear force based on the same ε_1 and θ and $s_{m\theta}$ values of both analytical and experimental estimations. When the ratio is smaller than 1.0, the AASHTO shear design underestimates shear force. Because the steel contribution is involved, the interpretation is complicated. In cases where the AASHTO is not conservative, proposed equation is necessary to estimate the reduced capacity of high-strength CC and SCC mixtures. In these tests, the AASHTO shear design underestimates concrete contribution to shear. Therefore, The AASHTO LRFD shear design overestimates steel contribution to shear. Overall average ratio of analytical and measured shear capacity is 0.97 for all the tests.

In summary, the AASHTO LRFD shear design reasonably estimates the shear capacity of the concrete and steel for the tested girders. There is no significant change for the shear design of the Type A girder with the SCC mixtures.

Table 8.15. Analytical versus Experimental Results for Shear Capacity at Critical Section.

	CC-R1	CC-R2	SCC-R1	SCC-R2	CC-L1	CC-L2	SCC-L1	SCC-L2	Avg.
w, in. (mm)	0.004 (0.1)	0.008 (0.2)	0.006 (0.15)	0.008 (0.2)	0.006 (0.15)	0.010 (0.26)	0.008 (0.20)	0.012 (0.30)	0.008 (0.20)
θ, degrees	24	25	26	25	31	30	37	36	29
$s_{m\theta}$, in. (mm)	3.95 (100)	5.92 (150)	6.90 (175)	3.95 (100)	6.90 (175)	4.11 (104)	5.09 (129)	5.09 (129)	5.24 (133)
Analytical Estimation (AASHTO and Proposed Equation)									
V_c, kip (kN)	88 (391)	79 (351)	96 (427)	83 (369)	69 (307)	56 (249)	56 (249)	53 (236)	73 (325)
V_s, kip (kN)	145 (645)	185 (823)	111 (494)	283 (1259)	82 (365)	262 (1165)	106 (471)	170 (756)	168 (747)
V=V_s+V_c, kip (kN)	233 (2869)	264 (3600)	207 (2196)	366 (5599)	151 (1622)	318 (5184)	162 (2097)	223 (3363)	241 (3324)
Experimental Estimation									
V_c= V-V_s, kip (kN)	142 (632)	106 (471)	125 (556)	0	84 (374)	71 (316)	93 (414)	184 (818)	115 (512)
V_s, kip (kN)	88 (391)	204 (907)	71 (316)	273 (1214)	136 (605)	219 (974)	127 (565)	106 (471)	153 (681)
V, kip (kN)	230 (1741)	310 (4036)	196 (1405)	230 (5401)	220 (2691)	290 (4333)	220 (2513)	290 (2097)	248 (3027)
Anal./Exp. Ratio									
Anal./Exp. for V_c	0.62	0.75	0.77	-	0.82	0.79	0.60	0.29	0.66
Anal./Exp. for V_s	1.65	0.91	1.56	1.04	0.60	1.20	0.83	1.60	1.17
Anal./Exp. for V	1.01	0.85	1.06	1.59	0.69	1.10	0.74	0.77	0.97

Note: V_c = concrete shear capacity, V_s = web steel shear capacity, V = total shear capacity = V_c+V_s.

8.5.5 Tests Observation

8.5.5.1 Crack Development

The cracking loads and measured crack widths are summarized in Table 8.16. The maximum crack width was measured at the extreme tension fiber of the bottom flange for flexural cracks, within the web depth for shear cracks. Generally, the progress of shear and flexural cracks and maximum crack widths are similar for all the tests.

Table 8.16. Cracking Loads and Crack Widths (Development Length Test).

	Web Cracking Load		Flexural Cracking Load		Flexural Cracking into Deck	Final Reading	
Location	Web	Web	Bottom Flange	Bottom Flange	Deck	Final	Bottom Flange
Values	Applied Load, kip (kN)	Crack Width, in. (mm)	Applied Load, kip (kN)	Crack Width, in. (mm)	Applied Load, kip (kN)	Applied Load, kip (kN)	Crack Width, in. (mm)
CC-R1	300 (1330)	0.003 (0.08)	300 (1330)	0.003 (0.08)	380 (1690)	400 (1890)	0.016 (0.4)
CC-R2	300 (1330)	0.004 (0.1)	300 (1330)	0.004 (0.1)	350 (1557)	425 (1890)	0.040 (1.0)
SCC-R1	300 (1330)	-	320 (1420)	0.006 (0.15)	340 (1510)	380 (1690)	0.035 (0.9)*
SCC-R2	200 (890)	-	300 (1330)	-	350 (1557)	400 (1780)	0.080 (2.0)
CC-L1	300 (1330)	0.006 (0.15)	300 (1330)	0.008 (0.2)	340 (1510)	400 (1780)	0.032 (0.8)
CC-L2	300 (1330)	0.006 (0.15)	300 (1330)	0.006 (0.15)	340 (1510)	420 (1870)	0.032 (0.8)
SCC-L1	300 (1330)	0.004 (0.15)	300 (1330)	0.004 (0.15)	340 (1510)	400 (1780)	0.049 (1.25)
SCC-L2	300 (1334)	0.006 (0.15)	300 (1334)	0.006 (0.15)	320 (1420)	446 (1980)	0.039 (1.0)

Note: *Maximum shear crack was remarkably 0.25 in. (6.4 mm) on the bottom flange.

8.5.5.2 Cracks on Tested Span

Figure 8.43 shows the crack diagrams in the development length region of CC-R1 and SCC-R1 girders at ultimate loading.

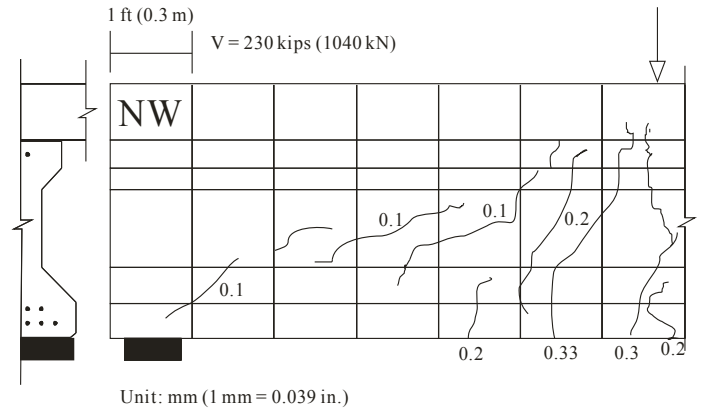

(a) CC-R1 (Shear @ 230 kip [1040kN])

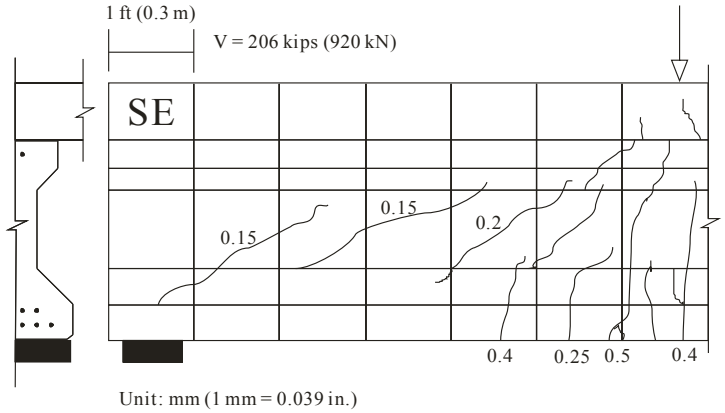

(b) SCC-R1 (Shear @ 206 kip [920kN])

Figure 8.43. Comparison of Crack Diagrams for CC-R1 versus SCC-R1 Tests.

Figure 8.44 shows the crack diagrams for the development length region of the CC-L2 and SCC-L2 girders at ultimate loading. When cracks are compared from all test specimens, the SCC girders have slightly wider flexural crack widths than the CC girders at ultimate (CC: 0.016 to 0.032 in. [0.04 to 0.8 mm] versus SCC: 0.035 to 0.040 in. [0.9 to 1.25 mm]). The girders containing limestone aggregate had more shear and flexural cracks compared to the girders containing river gravel aggregate.

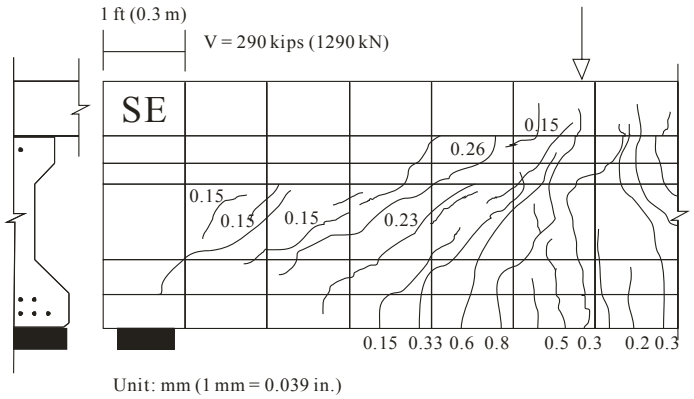

(a) CC-L2 (Shear @ 290 kip [1290 kN])

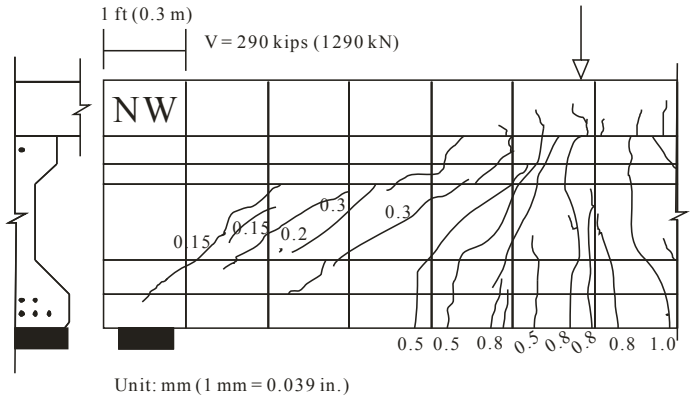

(b) SCC-L2 (Shear @ 290 kip [1290 kN])

Figure 8.44. Comparison of Crack Diagrams for CC-L2 versus SCC-L2 Girders.

8.6 PRESTRESS LOSSES

8.6.1 Initial Stresses of Strands

Load cells monitored the jacking stresses of strands and stresses immediately before transfer of strands. No significant loss of anchorage seating was observed at tensioning. Strand stresses between the time of casting and the time at transfer were continuously monitored at 5 second intervals. There was no significant relaxation of strands between casting and transfer. The relaxation of strands can be estimated after tensioning of strands.

The stresses on the strands are time-dependent values due to the relaxation of strands as follows:

$$f_{pbt} = f_{pj} - \Delta f_{pR}(t_0, t_{tr}) \quad (8.7)$$

where f_{pbt} is the stress immediately before transfer (ksi [MPa]), f_{pj} is the initial jacking stress (ksi [MPa]), $\Delta f_{pR}(t_0, t_{tr})$ is the relaxation of strands between t_0 and t_{tr} (ksi [MPa]), t_0 is the time at jacking (hour), and t_{tr} is the time at transfer (hour).

There were no apparent losses due to relaxation before transfer. The strand stresses in the bottom flange at each event are summarized in Table 8.17.

Table 8.17. Stresses of Strands in Bottom Flange.

Description	Time	CC-R, SCC-R		Time	CC-L, SCC-L	
		Avg.	Std. Dev.		Avg.	Std. Dev.
Initial Jacking Stress, f_{pj} at t_0, ksi (MPa)	3/22/07 4:30 PM	208.5 (1438)	3.93 (27)	7/10/07 9:00 AM	217.03 (1496)	7.73 (53)
Stress at Casting, f_{pj}, ksi (MPa)	3/26/07 4:42 PM	212.4 (1464)	4.57 (32)	7/12/07 4:00 PM	216.4 (1492)	5.27 (36)
Stress Immediately Before Transfer, f_{pbt} at t_{tr}, ksi (MPa)	3/27/07 3:20 PM	213.0 (1469)	4.72 (33)	7/13/07 2:20 PM	216.8 (1495)	5.77 (40)

Ambient and concrete temperature influences the strain of concrete and strands, and these result in changes in the prestress. Thermal linear strain can be determined with the following equation:

$$\varepsilon_t = \alpha_t \Delta T \quad (8.8)$$

where ε_t is the thermal strain, α_t is the coefficient of linear thermal expansion ($^oF^{-1}$ [$^oC^{-1}$]), and ΔT is the temperature change (^{o}F [^{o}C]).

Based on a thermal coefficient, α_t, of $6.0 \times 10^{-6}/^oF$ for steel, the thermal effect is not significant with the temperature observed during these cast dates. Table 8.18 shows the average stresses of jacking stress of all girders. Even though the temperature of strands was considered, the relaxation of strands between time at jacking and time at transfer apparently did not cause a significant loss of prestress. For CC-L and SCC-L girders, temperature effect was also minimal.

Table 8.18. Temperature Effect on Stresses of Strands of All Girders.

Girder ID	Time/ Measured	Avg. Temperature, °F (°C)	Avg. Stresses, f_{pj}, ksi (MPa)	Std. Dev., ksi (MPa)
CC-R and SCC-R	3/24/07 12:16 PM	79 (26)	208.3 (1434)	5.01 (35)
	3/26/07 9:16 AM	72 (22)	211.9 (1462)	4.56 (31)
CC-L and SCC-L	7/12/07 12:57 PM	100 (38)	217.4 (1499)	6.74 (47)
	7/12/07 1:42 AM	105 (41)	218 (1503)	6.92 (48)

8.6.2 Concrete Strain Profile

Concrete strain gages monitored the changes of strain in the strands resulting from short- and longer-term effects of concrete and strands. The basic assumption is that the concrete and strands is perfectly bonded and has the same thermal expansion coefficient. The history of concrete strain gage profiles at the midspan, south end, and north end are presented in Figure 8.45 for all girders. During girder casting, the strain gage readings did not represent the actual behavior of the hardened concrete. The viscoelastic state of plastic concrete, the fluctuation of temperature, and the shape of the gage likely affected the strain reading during hydration. To estimate the strain of the concrete, the reading immediately before transfer was taken as the base reading of strain.

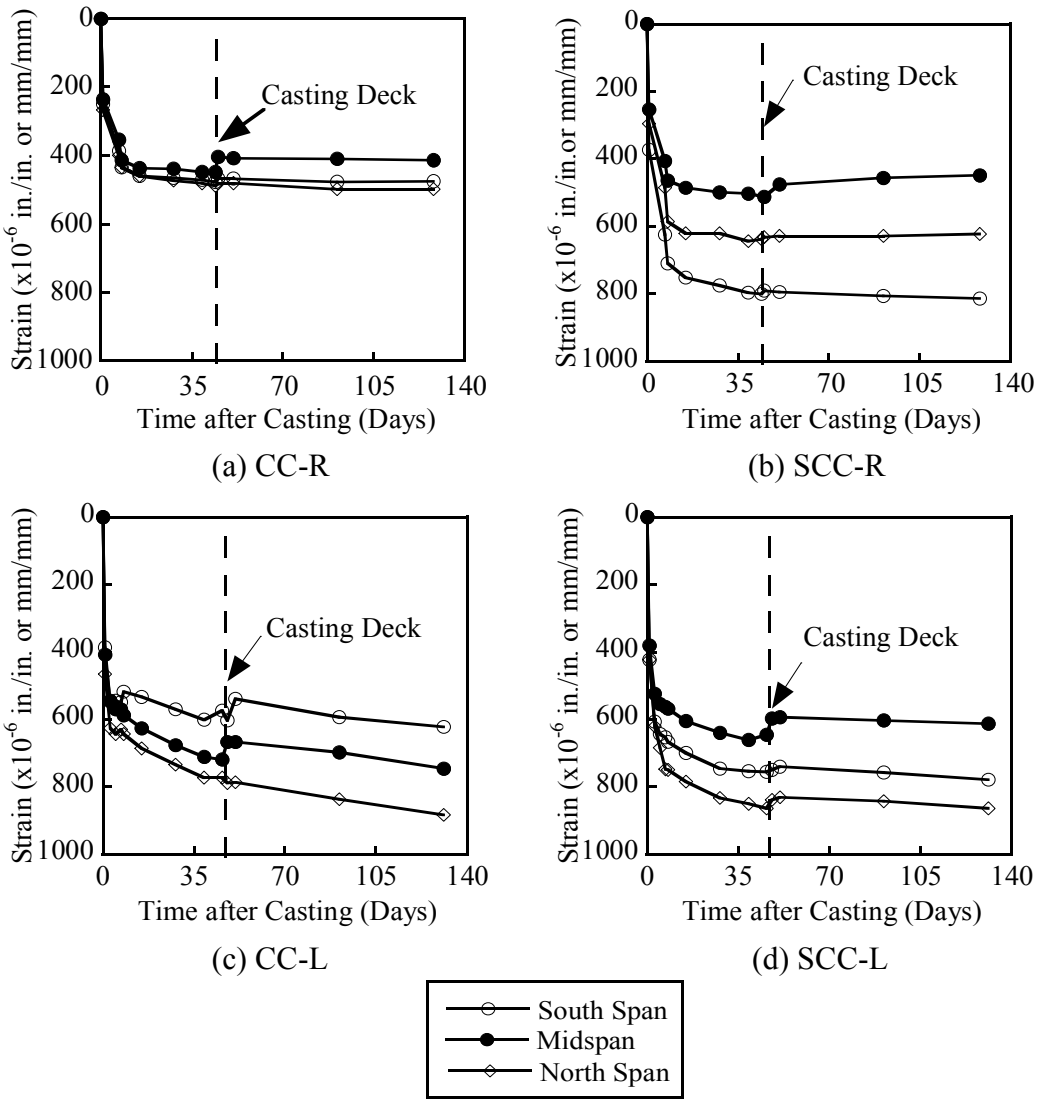

Figure 8.45. Embedded Concrete Strain Gage History.

The change in concrete strain reflects the elastic shortening, creep, and shrinkage of concrete, and relaxation of strains. When the CIP concrete deck was cast, immediate elastic gain at midspan was observed. After transfer, a dramatic increase in shrinkage and creep was observed, as expected, for all the girders. Before stabilization of strains, the high strains of end span were observed. It might be attributed to the creep of self-weight of girders mitigating increase of strain at the midspan at early ages.

According to manufacturer's the calibration data sheet for strain gages, the thermal output is less than 10 microstrain indicating self-compensating thermal output between 70 ^{o}F (21 ^{o}C) and 100 ^{o}F (38 ^{o}C). Therefore, the change of strain within the range represents not the

thermal change of the strain gages but the actual thermal change of concrete. Some strain gages showed high values prior to transfer, representing thermal expansion of the concrete.

8.6.3 Prestress Losses due to Elastic Shortening

Concrete strain readings at transfer are presented in Figure 8.46. The strain readings immediately before transfer were taken as the base values. To estimate elastic shortening, the elastic modulus of the concrete at transfer is also estimated from the strength of concrete at transfer based on the match-cured samples. The thermal change of the girder is not a significant factor in elastic shortening during transfer. Thermal changes of the strands were not significant prior to and after transfer and did not result in a change in the strand stress.

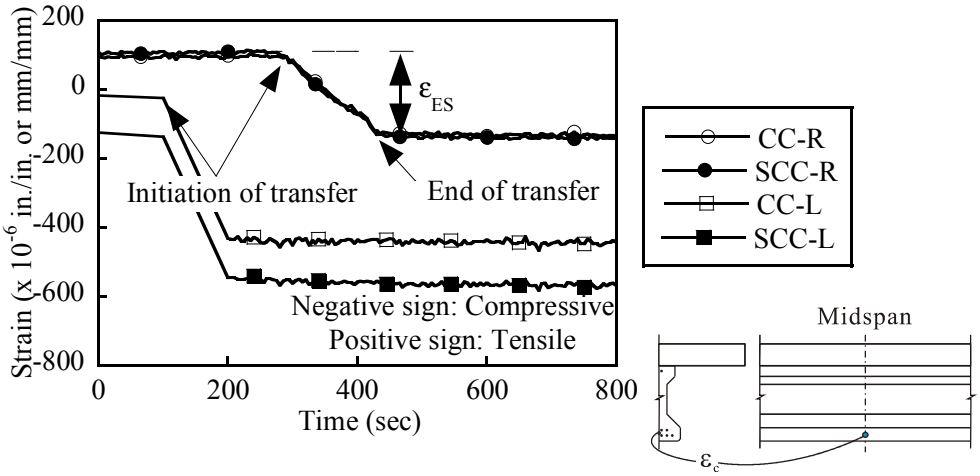

Figure 8.46. Estimation of Elastic Shortening of All Girders.

Table 8.19 shows the estimated prestress losses due to elastic shortening at girder midspan. There was no significant difference between the SCC and CC girders in the same prestressing bed. The SCC-R girder had approximately 7 percent higher losses due to elastic shortening than the CC-R girder, while the CC-L girder had approximately 4 percent higher losses due to elastic shortening than the SCC-L girder.

Table 8.19. Elastic Shortening at Transfer at Midspan.

Girder ID	Δ_{pES}, $\times 10^{-6}$ in./in. (mm/mm)	Concrete Temperature, °F (°C)	$\Delta\varepsilon_t$, ksi (MPa)	Δf_{ES}, ksi (MPa)
CC-R	236	85 (29)	0	6.7 (46)
SCC-R	253	85 (29)	0	7.0 (49)
CC-L	407	105* (41)	0	11.0 (76)
SCC-L	381	105* (41)	0	10.7 (74)

Note: * Ambient temperature,

Δ_{pES} is the measured strain of girder caused by elastic shortening, $\Delta\varepsilon_t$ is the thermal strain at transfer, and Δf_{ES} is the prestress loss due to elastic shortening.

8.6.4 Elastic Prestress Gain due to Weight of Deck Slab

When the weight of the deck was placed on the girder, the strands had an instant elastic prestress gain. Figure 8.47 shows the elastic prestress gains in the CC-L and SCC-L girders at midspan.

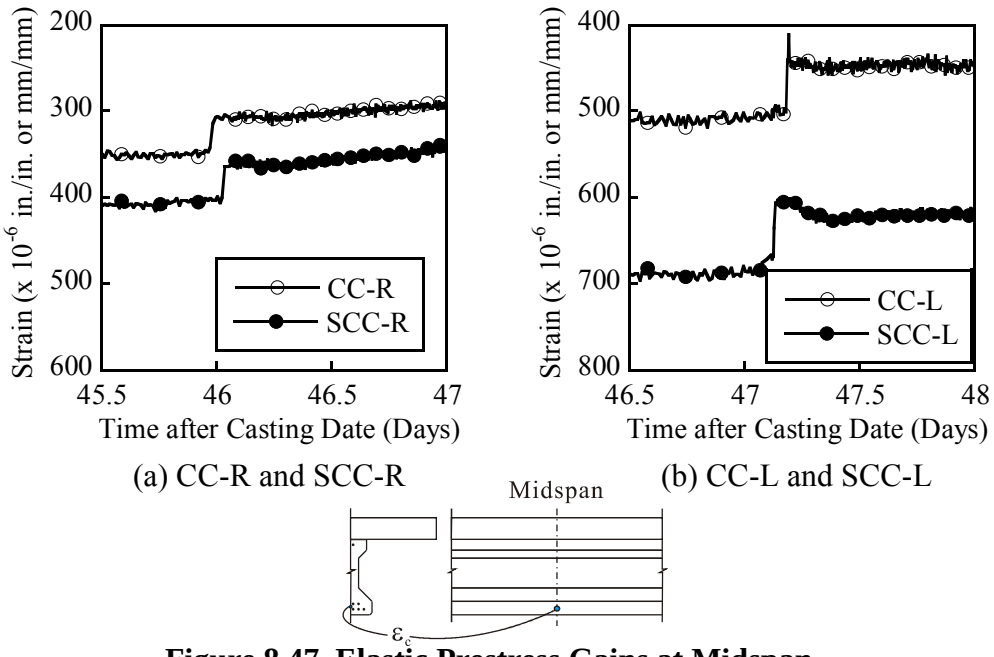

Figure 8.47. Elastic Prestress Gains at Midspan.

8.6.5 Prestress Losses due to Long-Term Effects

Long-term prestress losses prior to deck placement mainly occurred from concrete shrinkage, along with creep due to sustained loading from the axial prestressing force and girder self-weight. After casting the deck, the composite girder-deck system experienced prestress losses from creep, with the sustained load stress increasing due to the deck weight and from shrinkage of the girder and deck. Relaxation of the strands also contributed to the long-term prestress losses.

Measured prestress losses at the midspan, north end (3.2 ft [1 m] from girder end), and south end (3.2 ft [1 m] from girder end) are presented in Tables 8.20 thru 8.22. Positive values indicate prestress losses, while negative values indicate prestress gains. The data are summarized graphically in Figure 8.48.

Table 8.20. Summary of Measured Prestress Losses at Midspan of Girders.

Girder ID	Elastic Losses, ksi (MPa)	Elastic Gain due to Deck, ksi (MPa)	Long-Term Losses before Deck, ksi (MPa)	Long-Term Losses after Deck, ksi (MPa)	Sum of Long-Term Losses, ksi (MPa)	Total Prestress Losses, ksi (MPa)
CC-R	6.61 (45.6)	−1.05 (−7.24)	5.94 (41.0)	−1.00 (−6.90)	4.94 (34.2)	11.5 (79.3)
SCC-R	7.09 (48.9)	−1.12 (−7.72)	7.26 (50.1)	−1.80 (−12.4)	5.46 (37.7)	12.6 (86.9)
CC-L	11.4 (78.6)	−1.35 (−9.31)	8.47 (58.4)	0.98 (6.76)	9.45 (65.2)	20.9 (144)
SCC-L	10.7 (73.8)	−1.33 (−9.17)	7.84 (54.1)	−1.38 (−9.52)	6.46 (44.5)	17.1 (118)

Table 8.21. Summary of Measured Prestress Losses at North End of Girders.

Girder ID	Elastic Losses, ksi (MPa)	Elastic Gain due to Deck, ksi (MPa)	Long-Term Losses before Deck, ksi (MPa)	Long-Term Losses after Deck, ksi (MPa)	Sum of Long-Term Losses, ksi (MPa)	Total Prestress Losses, ksi (MPa)
CC-R	7.02 (48.4)	−0.13 (−0.90)	6.19 (42.7)	0.09 (0.62)	6.28 (43.3)	13.3 (91.7)
SCC-R	10.4 (71.8)	−0.21 (−1.45)	11.9 (81.8)	0.48 (3.31)	12.3 (84.8)	22.8 (157)
CC-L	13.1 (90.3)	−0.11 (−0.76)	8.56 (59.0)	3.07 (21.2)	11.6 (80.0)	24.7 (170)
SCC-L	11.9 (82.1)	0.33 (2.28)	11.9 (82.3)	0.35 (2.41)	12.3 (84.8)	24.1 (166)

Table 8.22. Summary of Measured Prestress Losses at South End of Girders.

Girder ID	Elastic Losses, ksi (MPa)	Elastic Gain due to Deck, ksi (MPa)	Long-Term Losses before Deck, ksi (MPa)	Long-Term Losses after Deck, ksi (MPa)	Sum of Long-Term Losses, ksi (MPa)	Total Prestress Losses, ksi (MPa)
CC-R	7.47 (51.5)	–0.06 (0.41)	5.97 (41.2)	0.52 (3.59)	6.49 (44.8)	14.0 (96.5)
SCC-R	8.30 (57.2)	–0.29 (–2.00)	9.68 (66.7)	–0.55 (–3.79)	9.13 (63.0)	17.4 (120)
CC-L	10.8 (74.5)	–0.72 (–4.96)	6.02 (41.5)	0.60 (4.14)	6.61 (45.6)	17.4 (120)
SCC-L	11.8 (81.4)	–0.62 (–4.27)	9.26 (63.9)	0.69 (4.76)	9.95 (68.6)	21.8 (150)

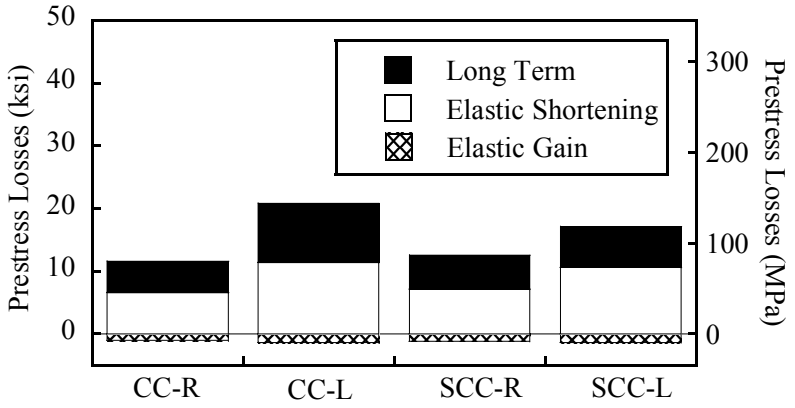

(a) Midspan

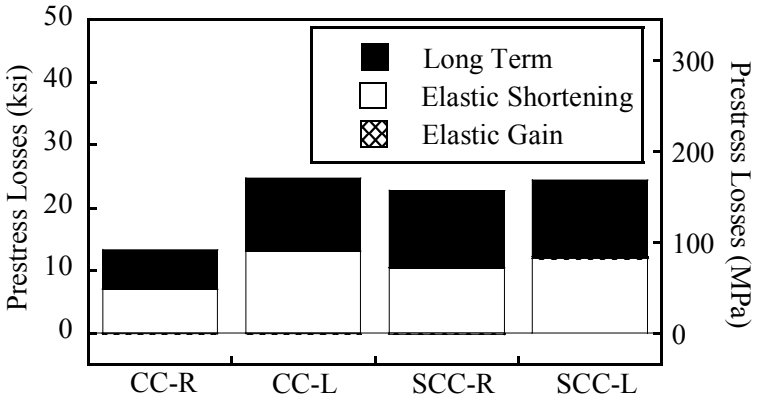

(b) North Span

Figure 8.48. Prestress Losses for All Girders.

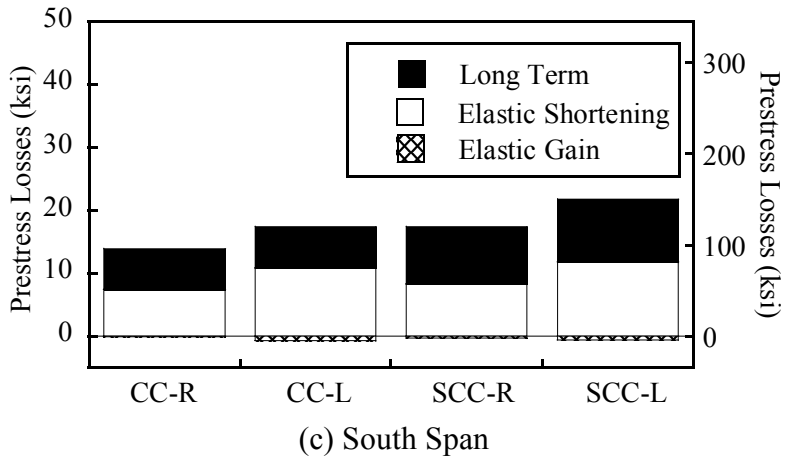

(c) South Span

Figure 8.48. Prestress Losses for All Girders (cont.).

Because the elastic gain due to the girder self-weight and superimposed deck self-weight, initial prestress losses were reasonably lower than the north span and south span. The creep effect of girder and deck weights reduced the prestress losses after the casting of decks. The shrinkage of deck increases the deflection downward resulting in the increase of strand stress resulting in the reduction of prestress loss. However, both ends have large amounts of long-term losses due to the minimal effect of creep from deck weight and shrinkage of the deck. Therefore, large amounts of longer-term losses at the south and north spans were observed compared to losses at the midsapn.

Until approximately 130 days, elastic loss was approximately 50 or more percent of all losses for all girders. Elastic losses of the CC-R girder are slightly lower than those of the SCC-R girders. The SCC-R mixture had higher paste volume and lower aggregate volume resulting in lower stiffness and higher deformation under the same axial prestressing loads. As shown in Figure 8.48, the overall comparison shows that the CC-R girder had the lowest total long-term and elastic losses compared to the other girders. The CC-L and SCC-L girders had slightly higher elastic losses due to lower MOE values compared to the CC-R and SCC-R girders.

8.6.6 AASHTO LRFD Specifications (2004)

The prestress losses at midspan of the girder were estimated at approximately 130 days using the 2004 AASHTO LRFD Specifications. The estimated AASHTO prestress losses were higher than the measured prestress losses given in Figure 8.49 for both the CC and SCC girders. This may be attributed to the relatively short duration of monitoring. The AASHTO LRFD Specifications assume the relative humidity to be 60 percent, as is common practice in Texas. Total long-term prestress losses are the sum of creep, shrinkage, and relaxation. In the AASHTO LRFD Specifications (2004), the losses or gains due to the deck placement and the shrinkage of the deck concrete are not included in the estimation.

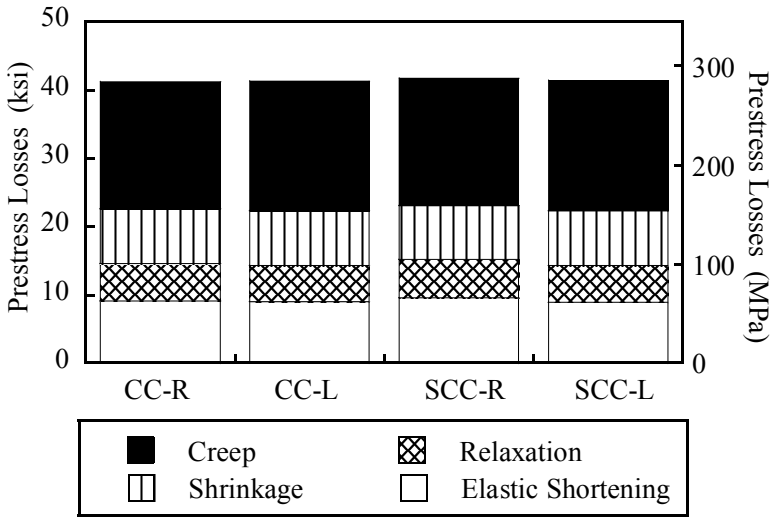

Figure 8.49. Prestress Losses at Midspan Estimated by 2004 AASHTO LRFD.

8.6.7 AASHTO LRFD Specifications (2006)

The AASHTO LRFD Specifications (2006) provide equations to estimate the prestress losses by considering construction sequence and creep and shrinkage of the composite girder-deck system. Positive values indicate prestress losses and negative values indicate prestress gains. Table 8.23 shows measured prestress losses at the midspan and the predicted prestress losses according to the AASHTO LRFD Specifications (2006). Table 8.24 shows the ratios of the measured prestress losses to the estimated values (140 days). However, AASHTO time-dependent losses were computed to correspond to the age of the girders. The AASHTO LRFD

expressions overestimated the measured values. For the elastic prestress losses and elastic gain, the AASHTO LRFD predicted within ±30 percent errors. For all cases, the long-term loss estimates did not correlate well with the measured values for this research. However, it should be noted that the girders were tested at a relatively short time after casting, and in design long-term estimates are typically considered at later ages.

Table 8.23. Prestress Losses Estimated by the AASHTO LRFD (2006).

Girder ID	Elastic Losses, ksi (MPa)	Elastic Gain due to Deck, ksi (MPa)	Long-Term Losses before Deck, ksi (MPa)	Long-Term Losses after Deck, ksi (MPa)	Total Long-Term Losses, ksi (MPa)	Total Prestress Losses, ksi (MPa)
CC-R	9.22 (63.6)	−1.34 (−9.24)	18.6 (128)	13.1 (90.3)	31.8 (219)	39.7 (274)
SCC-R	9.09 (62.7)	−1.36 (−9.38)	18.3 (126)	13.0 (89.6)	31.3 (216)	39.1 (269)
CC-L	9.95 (68.6)	−1.54 (−10.6)	20.5 (142)	13.9 (95.8)	34.4 (237)	42.9 (295)
SCC-L	9.18 (63.3)	−1.53 (−10.6)	17.7 (122)	12.0 (82.7)	29.8 (205)	37.4 (258)

Table 8.24. Ratios of Measured Prestress Losses to AASHTO LRFD (2006) Estimates.

Girder ID	Elastic Losses	Elastic Gain due to Deck Placement	Long-Term Losses before Deck Placement	Long-Term Losses after Deck Placement	Total Long-Term Losses	Total Prestress Losses
CC-R	0.72	0.78	0.32	–0.08	0.16	0.29
SCC-R	0.78	0.82	0.40	–0.14	0.17	0.32
CC-L	1.15	0.88	0.41	0.07	0.27	0.49
SCC-L	1.16	0.87	0.44	–0.11	0.22	0.46

8.7 CAMBER AND DEFLECTION HISTORY

The initial camber values at the quarter point and midspan of the girders was measured to a 0.1 in. (3 mm) accuracy. Table 8.25 shows the initial camber of each girder at the time of release. Initial cambers were similar between the CC-R and SCC-R girders. However, the initial camber of the SCC-L girder was less than that of the CC-L girder. This might be attributed to the

strength of concrete at transfer. The SCC-L girder had higher strength than CC-L girder at transfer resulting in the increase of the stiffness (MOE).

Table 8.25. Initial Camber Δ_i of the Girders.

Girder ID	Δ_i @ Midspan, in. (mm)	Δ_i @ Quarter span (1/4 span, 3/4 span length), in. (mm)
CC-R	0.60 (15.2)	-
SCC-R	0.60 (15.2)	-
CC-L	0.45 (11.4)	0.40, 0.35 (10.2, 8.9)
SCC-L	0.40 (10.1)	0.30, 0.30 (7.6, 7.6)

Camber can be estimated by the strain profile at the midspan. To estimate the early camber growth, the curvature was measured using embedded concrete strain gages in the girder, located at the center of gravity of the bottom strands, web mid-height, and the center of gravity of top strands. Camber growth prior to placement of the deck was observed in the CC-L and SCC-L girders. The measured initial camber is compared to the predicted values, as shown in Table 8.26. The predicted values fall within ±20 percent error of measured values, indicating fairly good agreement between the measured and the predicted values for both girders.

Table 8.26. Comparison between Measured Camber and Predicted Camber.

Girder ID	Measured Camber, Δ_{im}, in. (mm)	Predicted Camber, $\Delta_{ip} = \Delta_{fpi} - \Delta_{Girder}$, in. (mm)	$\frac{\Delta_{im}}{\Delta_{ip}}$
CC-R	0.60 (15.24) ↑	0.51 (12.95) ↑	1.18
SCC-R	0.60 (15.24) ↑	0.50 (12.70) ↑	1.20
CC-L	0.45 (11.43) ↑	0.54 (13.72) ↑	0.83
SCC-L	0.40 (10.16) ↑	0.49 (12.45) ↑	0.82

The final cambers at different times are presented in Table 8.27. Based on the change in curvature, the CC girders had slightly higher camber than the SCC girders. During earlier ages the amount of camber growth of the CC-L and SCC-L girders was larger than for the CC-R and SCC-R girders. This is attributed to the lower stiffness (MOE) of the limestone mixtures. After approximately 7 days, the rate of camber growth stabilized. The CC-L girder had 35 percent higher camber than the SCC-L girder, and the CC-R girder had 7 percent higher camber than the

SCC-R girder at about 28 days. Among all girders, the CC-L girder had the largest amount camber indicating larger creep effects. According to the measured prestress losses, the CC-L girder has the largest amount of prestress losses at the midspan among all the girders before casting the deck.

Table 8.27. Camber Growths at 7 and 28 Days after Transfer.

Girder ID	Δ_7 in. (mm)	Δ_{28} in. (mm)	$\Delta_{28} - \Delta_7$ in. (mm)
CC-R	0.64 ↑ (16.26)	0.75 ↑ (19.05)	0.11 ↑ (2.79)
SCC-R	0.68 ↑ (17.27)	0.70 ↑ (17.78)	0.02 ↑ (0.51)
CC-L	0.79 ↑ (20.07)	0.84 ↑ (21.34)	0.05 ↑ (1.27)
SCC-L	0.60 ↑ (15.24)	0.62 ↑ (15.75)	0.02 ↑ (0.51)

Figure 8.50 shows the history of camber and deflection of the girder and composite deck system. The deflection of all girders was measured with string pots and strain gages in the field and at HBSML for about 130 days. The camber growth of the CC girders was higher than that of the SCC girders. This can be attributed to a higher strength gain rate of SCC mixtures. This minimizes the adverse effect on MOE due to low coarse aggregate contents of SCC mixtures. The final deflection values of the CC and SCC girders were within 0.25 in. (6 mm) at 130 days, indicating that long-term deflection may be similar for CC and SCC girders. The final difference of deflection history generally came from the difference of the initial camber growth. The increased paste content of the SCC mixture would indicate that the creep and deflection would be higher for SCC mixtures; however, the higher strength likely compensated for this resulting in similar stiffness (MOE) at the final stage.

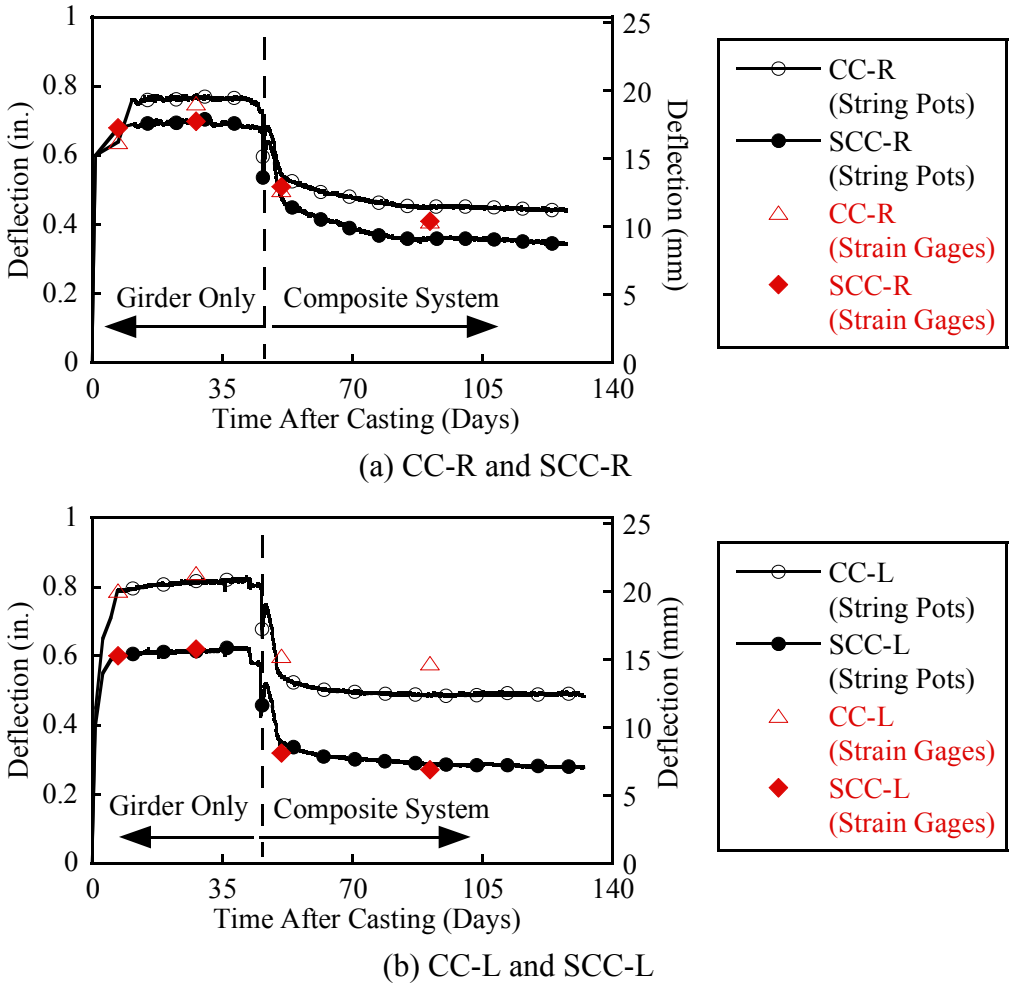

Figure 8.50. History of Camber and Deflection of Girder and Composite Girder-Deck Systems.

As shown in Figure 8.51, the transition phase of all the composite girder-deck system is quite similar. After casting the CIP deck, the downward deflection, Δ_{FD}, increased. Before the CIP concrete hydrated, the girder had to sustain the weight of the CIP deck and acted as a noncomposite girder. After the CIP deck hardened, the girder and the CIP deck became the composite deck system, resulting in increased stiffness (I) and upward deflection of the composite system, Δ_C. During the hydration process of the CIP deck, it is difficult to define the initiation of composite deck action. For this study, the peak of the curve was assumed as the time of initiation of the composite action.

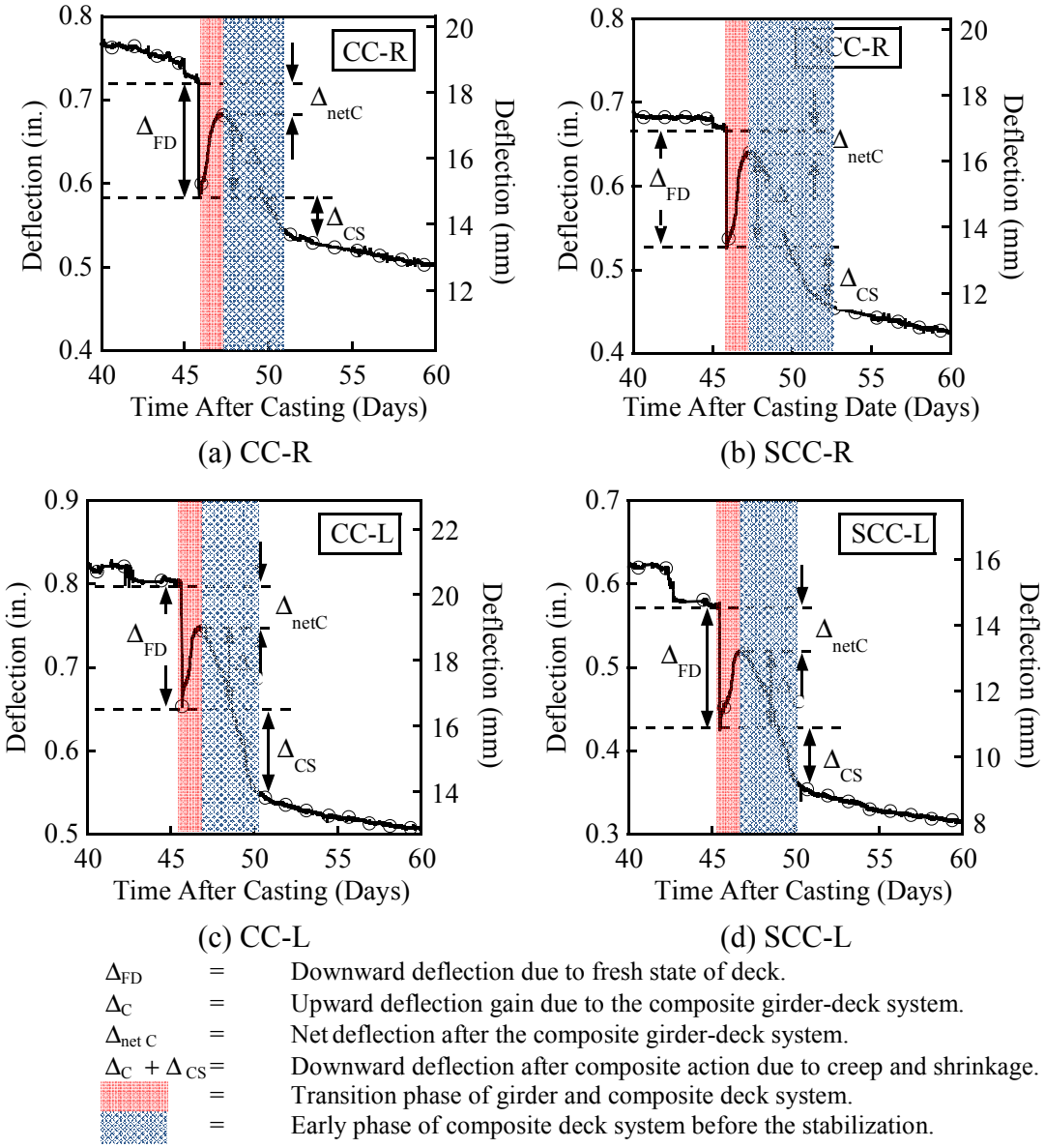

Figure 8.51. Transition Phase of the Girder to the Composite Deck System.

Table 8.28 compares the measured deflection and the estimated deflection for the transition from the girder to the composite deck system. All girders had approximately a 0.04 in. (1.0 mm) downward net deflection measurement after composite action. Even though the composite deck system gains increased stiffness, the creep due to the increased total weight and shrinkage of the CIP deck causes a small net downward deflection.

Table 8.28. Estimated and Measured Deflection Corresponding to Composite Action.

Girder ID	Estimated Value			Measured Value
	Δ_{FD}, in. (mm)	Δ_C, in. (mm)	Δ_{netC}, in. (mm)	Δ_{netC}, in. (mm)
CC-R	0.180 ↓ (4.57)	0.034 ↑ (0.86)	0.146 ↓ (3.71)	0.04 ↓ (1.20)
SCC-R	0.182 ↓ (4.62)	0.049 ↑ (1.24)	0.133 ↓ (3.38)	0.03 ↓ (0.76)
CC-L	0.207 ↓ (5.26)	0.044 ↑ (1.12)	0.163 ↓ (4.14)	0.05 ↓ (1.27)
SCC-L	0.204 ↓ (5.18)	0.034 ↑ (0.86)	0.170 ↓ (4.32)	0.05 ↓ (1.27)

Approximately 5 days after deck placement, deflection stabilized for all composite girder-deck systems. Therefore, the transition and early phases are significant for the history of overall deflection. When the shrinkage of the deck is similar due to the same deck concrete for all systems, the relative difference of deflection is due to creep effect. Figure 8.51 shows that additional downward deflection, $\Delta_C + \Delta_{CS}$, occurs after composite action due to creep and shrinkage of composite girder-deck system. After the early phase of the composite deck system, prestress losses due to creep and shrinkage of deck and girder and relaxation of the strands continuously influence the camber and deflection, $\Delta_C + \Delta_{CS}$. The CC-L girder had approximately 25 percent larger deflection ($\Delta_C + \Delta_{CS}$) than other girders.

8.8 SUMMARY

Based on the experimental results for the four full-scale Type A girders, the following conclusions were drawn:

1) High workability, stability, and passing ability and reduction of casting time and labor were achieved when casting the Type A SCC girders at the precast plant. The surface finish conditions were considered to be very good.
2) The SCC and CC mixtures have similar compressive strengths at 16 hours with each aggregate type and strength level. At later ages, the strength development of the SCC-R and SCC-L mixtures was significantly higher than for the CC-R and CC-L mixtures.

3) The cracking moment of the SCC girders was slightly lower than that of the CC girders. However, the flexural capacities of the SCC girders were similar to that of the CC girders. The initial flexural stiffness and elastic response of the CC and SCC girders were similar.
4) Overall cracking trends (i.e., first cracking in the deck, first web-shear cracking) were similar with the CC and SCC girders for the flexural and development length tests. It was observed that slightly more cracks and higher maximum crack widths developed in the SCC girders. This reduced stiffness and resulted in 15 percent larger deflections in SCC-L girder, compared to CC-L girder. However, the effect on the flexural capacity is minimal.
5) The SCC-R girder had similar or shorter initial and final transfer lengths than the CC-R girder. The SCC-L girder had shorter initial and final transfer lengths compared to the CC-L girder. Normalized transfer lengths with compressive strength show that compressive strength does not significantly lead to smaller transfer length of the SCC girders compared to the CC girders. The initial and longer-term transfer lengths of all the girders were shorter than 60 d_b, which is the value used by the AASHTO LRFD Specifications (2006).
6) The 2004 and 2006 AASHTO LRFD development length equations provided a conservative estimate of the development length for both the CC and SCC girders. The 2004 AASHTO LRFD alternative development length equation (2006 AASHTO LRFD Equation 5.11.4.2-1) provides a closer estimate of the development length for both the CC and SCC girders. The development length expression in the 2006 AASHTO LRFD is reasonable for design.
7) Elastic shortening and gains were reasonably estimated using the expression in the AASHTO LRFD (2004 and 2006 AASHTO LRFD Article 5.9.5.1). However, the AASHTO LRFD Specifications (2004 and 2006) overestimated the long-term losses at approximately 140 days. However, it should be noted that the girders were tested at a relatively short time after casting and typical design calculations call for long-term loss estimates at later ages.
8) The increase in stiffness resulting from the higher strengths influences the camber growth. In general, the CC girders had higher camber growth than the SCC girders

due to different and lower rates of strength development. After stabilization of the strength development and casting of the deck, the CC and SCC girder-deck systems exhibited similar composite stiffness values resulting in comparable net deflection histories after deck casting.

CHAPTER 9
SUMMARY, CONCLUSIONS AND RECOMMENDATIONS

9.1 SUMMARY

The objective of this research was to investigate the hardened properties of SCC for precast, prestressed structural applications. A comprehensive study was performed to provide potential users with specific information on the performance and design of SCC precast, prestressed girders. The experiments and analyses provide extensive data and a better understanding of SCC hardened characteristics. This research included investigations on the following:

- fresh characteristics,
- mechanical properties,
- shear characteristics,
- bond characteristics,
- creep,
- durability, and
- full-scale testing and validation.

Different SCC mixture constituents and proportions were evaluated for mechanical properties, shear characteristics, bond characteristics, creep, and durability. Variables evaluated included mixture type (CC or SCC), coarse aggregate type (river gravel or limestone), and coarse aggregate volume. To correlate these results with full-scale samples and investigate structural behavior related to strand bond properties, four full-scale girder-deck systems, 40 ft (12 m) long, with CC and SCC pretensioned girders were fabricated and tested. The research team used the data from this research to determine if the AASHTO LRFD Specifications are appropriate for the design of precast structural members containing SCC mixtures. It should be noted that only Texas Type A girders were evaluated. The conclusions and recommendations are based on these results and serves to identify potentially influencing variables for other girders types or sizes or other applications.

9.2 CONCLUSIONS

9.2.1 Fresh Characteristics

1) The fresh characteristics of all laboratory SCC mixtures had adequate workability and excellent stability.
2) The fresh characteristics of the plant SCC mixtures had adequate workability and stability. Some segregation was observed when the SCC was transported from the mixer to the cast area.

9.2.2 Mechanical Properties

1) The SCC exhibited higher early strengths, workability, and later age strengths.
2) The volume of coarse aggregate was found to be negatively correlated to the compressive strength in the 5 and 7 ksi (34 and 48 MPa) 16-hour release strength river gravel and limestone mixtures. The 7 ksi (48 MPa) 16-hour release strength limestone mixtures exhibited a positive correlation. This may be attributed to the weaker limestone aggregate strength. The aggregate volume had a minimal influence, from an engineering perspective, on the compressive strengths.
3) The high stiffness of the river gravel resulted in significantly higher values of elastic modulus in these mixtures compared to the limestone mixtures. The CC tends to have higher elastic modulus values than the SCC. The effect of the volume of the coarse aggregate is more pronounced for the 7 ksi (48 MPa) 16-hour release strength mixtures with both aggregate types.
4) The 2006 AASHTO equation (2006 AASHTO LRFD Equation 5.4.2.4-1) was appropriate to predict the MOE of the SCC when assuming K_1 is 1.0 and the unit weight was 149 lb/ft^3 (2385 kg/m^3). For the river gravel mixtures, K_1 and the unit weight were 1.05 and 150 lb/ft^3 (2400 kg/m^3), respectively. For the limestone mixtures, K_1 and unit weight were 0.95 and 148 lb/ft^3 (2370 kg/m^3), respectively. The 2006 AASHTO LRFD equation provides a reasonable prediction of the MOE for the river gravel and limestone SCC mixtures with ranges of f'_c from approximately 6 to 12 ksi (41 to 83 MPa). The equations developed in this research were appropriate for estimating the MOE of the river gravel and limestone SCC mixtures with f'_c values ranging from 5 to 17 ksi (34 to 120 MPa).

5) The MOR of SCC mixtures containing river gravel was higher than that of the limestone SCC mixtures. The SCC mixtures exhibit lower MOR values when compared with the CC mixtures.
6) The 2006 AASHTO LRFD lower bound equation for MOR (2006 AASHTO LRFD Article 5.4.2.6) is appropriate for estimating the MOR of the SCC mixtures evaluated in this study with f'_c values ranging from 5 to 10 ksi (34 to 69 MPa). The 2006 AASHTO LRFD upper bound equation for MOR (2006 AASHTO LRFD Article 5.4.2.6) is appropriate for estimating the MOR of the SCC mixtures evaluated in this study with f'_c values less than 13 ksi (90 MPa).
7) The STS of the SCC mixtures containing river gravel is significantly higher than that of the SCC limestone mixtures. The low strength of limestone aggregate likely leads to lower STS values.
8) Contrary to the MOR results, the SCC mixtures tended to have higher STS values than the CC mixtures.
9) The 2006 AASHTO LRFD Equation for predicting STS (2006 AASHTO LRFD Article 5.4.2.7) estimated the STS of the SCC mixtures evaluated in this study with f'_c from 5 to 16 ksi (34 to 110 MPa) fairly well.
10) Models for the MOE, MOR, and STS have been developed for estimating the mechanical properties of the SCC evaluated in this study.
11) The volume of the coarse aggregate was not a statistically significant variable for predicting MOR and STS of the CC and SCC mixtures.

9.2.3 Shear Characteristics

1) The plot of τ/σ versus w provides a quantifiable comparative assessment of the aggregate interlock for the CC and SCC mixtures having different paste strengths and a different level of initial fracture of the aggregate. As the crack width increases, the decreasing value of the normalized shear stress indicates a decrease in aggregate interlock.
2) The *E*-value, a measure of the absorbed energy of the aggregate interlock, provides a quantifiable comparative assessment up to a selected crack slip limit. The 5 ksi (34 MPa) river gravel SCC and CC specimens exhibited higher *E*-values than the other

mixtures [7 ksi (48 MPa) river gravel CC and SCC, 5 and 7 ksi (34 and 48 MPa) limestone CC and SCC specimens]. This indicates that high-strength concrete [28-day compressive strength greater than 10 ksi (70 MPa)] can still exhibit aggregate interlock. In addition, the SCC mixture containing river gravel exhibits a higher potential to increase the contribution of aggregate interlock to shear.

3) The effects of coarse aggregate type and volume on the *E*-value were determined with statistical assessment (mixed procedure). The batch of concrete is regarded as the random effect in the mixed procedure statistical approach. The contrast was used to assess the effect of type and volume of coarse aggregate on the aggregate interlock.
4) Aggregate type is a critical factor influencing aggregate interlock. For both the SCC and CC specimens, concrete mixtures containing river gravel exhibited more aggregate interlock compared to those containing limestone aggregate. Statistically, the effect of aggregate type is clearly identified at all slip ranges.
5) The volume of aggregate influences the contribution of aggregate interlock to the shear capacity for the SCC and CC mixtures tested. The effect of volume is observed on both river gravel and limestone mixtures based on statistical analysis (the contrasts) with a *p*-value of 0.05.
6) Lower strength concrete tends to have less coarse aggregate fractures resulting in more aggregate interlock, leading to a large amount of energy absorption. Therefore, the strength of concrete is highly related to the amount of fracture of aggregate interlock at small crack widths when crack slip initiates.
7) The friction coefficients and fracture reduction factors were determined based on the statistical analysis (mixed procedure). The fracture reduction factors, *c*, were 0.43 and 0.62 for the SCC and CC mixtures tested, respectively. The friction coefficients, μ, were 0.32 and 0.30 for the SCC and CC mixtures tested, respectively.
8) The SCC exhibited lower maximum shear stresses compared with the CC.
9) An upper limit of the β value is proposed for both CC and SCC and combined CC and SCC data based on this study. The shear friction factor in this study, (approximately 0.10) is lower than the previously proposed value of 0.18 reported in the MCFT.

10) When the SCC and CC mixtures have the same concrete strength and this strength is higher than 10 ksi (70 MPa), the CC mixtures exhibit a higher concrete shear strength than the SCC mixtures when both are evaluated without shear reinforcement.
11) Finally, the proposed equation for β to compute the concrete shear strength using the MCFT approach (Equation 6.38) is necessary to estimate the appropriate shear capacity of high-strength CC and SCC girders, rather than with the AASHTO and MCFT (a_g = 0) expressions. The AASHTO and the MCFT expressions overestimate the shear capacity when low shear reinforcement ratios and small shear crack angles are assumed.

9.2.4 Bond Characteristics

1) All 39 pull-out samples for evaluating the top bar effect for mild steel reinforcement had maximum stresses that exceeded the yield strength.
2) Most reinforcing bars failed by creating a splitting cone shaped failure surface initiated by concrete cone failure.
3) Most top bars exhibited lower bond strengths than the bottom bars for both the SCC and CC mixtures, indicating the existence of the top bar effect.
4) The relatively high bond strength of the SCC-R mixture may be attributed to the higher concrete compressive strength. However, the higher concrete compressive strength for the SCC-L mixture does not provide the same benefit of increased pull-out strength. The SCC-L mixture had slightly lower bond stress values than the CC-L mixtures.
5) The bond can be assessed using a bond ratio based on the ratio of the average bond stress of the bottom bar to the average bond stress of the companion top bar. The SCC-R mixture had the lowest bond ratio indicating the least top bar effect. The SCC-L mixture has highest bond ratio indicating the higher reduction of bond due to the top bar effect.
6) The measured fresh properties of the SCC and CC are not correlated with the bond ratio indicating the top bar effect in this study.
7) Based on a statistical analysis, the mixture type, aggregate type, and combination of aggregate and mixture types are not significant factors influencing the bond ratio.

8) All bond ratios are less than the top bar multiplier factor, 1.4, recommended in the AASHTO LRFD Specifications (2004 and 2006) for determining the tension development length of mild reinforcement. Therefore, the current AASHTO top bar factor of 1.4 is appropriate for the CC and SCC mixtures evaluated in this study.

9.2.5 Creep

1) The river gravel SCC mixtures show similar creep to the river gravel CC mixtures with the same 16-hour target compressive strengths. Although the 16-hour compressive strengths of the SCC and CC mixtures were almost the same, the creep of the limestone CC was higher than that of the limestone SCC. In addition, CC samples with lower compressive strengths exhibited higher creep. The effect of the 16-hour compressive strength was found to not be a significant factor affecting creep.
2) Because the stiffness of the river gravel is higher than that of limestone, river gravel mixtures had lower creep compared to the limestone mixtures, as expected. The MOE provides an indication of the stiffness of aggregate. According to the mechanical property testing, the MOE of concrete with the limestone coarse aggregate is lower than the MOE for concrete with the river gravel. The effect of coarse aggregate type was clearly observed in the CC mixtures. However, the effect of the coarse aggregate types was not significant for the SCC mixtures.
3) The perceived impact of high paste volume and low coarse aggregate volume on the creep of SCC seems to be unfounded for the mixtures evaluated in this research. However, the SCC mixtures exhibited higher strengths than the CC mixtures, which could account for the similar or lower creep values.
4) The 2006 AASHTO LRFD Specifications allows prediction models to have ±50 percent error in creep prediction. The 2004 and 2006 AASHTO LRFD models, the ACI 209 model, and the CEB-FIP model provide fairly good predictions for the creep of both CC and SCC mixtures. Because the 2006 AASHTO LRFD model was calibrated for high-strength concrete with low *w/c*, the prediction model seems to better predict CC and SCC mixtures evaluated in this study.
5) Prediction models are available that consider the compressive strength, MOE of aggregate, and mixture proportions. The BP, B3, and GL 2000 prediction models are

based on data from normal strength CC and overestimated the creep for the SCC and CC mixtures evaluated in this research by more than 50 percent.

9.2.6 Durability

1) The 5 ksi (34 MPa) 16-hour release strength SCC mixtures exhibit low resistance to freezing and thawing. This could be a result of high paste volume, higher *w/cm*, or poor void distribution.
2) The 7 ksi (48 MPa) 16-hour release strength SCC mixtures exhibited good freezing and thawing resistance.
3) All SCC mixtures exhibited very low permeability compared to the CC mixtures at later ages indicating a potential for high resistance to chloride ion penetration.
4) After 140 days of ponding, the 5 ksi (34 MPa) and 7 ksi (48 MPa) 16-hour release strength SCC mixtures have low diffusion coefficients. These values are typical of CC mixtures with similar *w/c*.

9.2.7 Full-scale Testing and Validation

9.2.7.1 Fresh Characteristics

1) High workability, stability, and passing ability and reduction of casting time and labor were achieved when casting the Type A SCC girders at the precast plant. The surface finish conditions were considered to be very good.

9.2.7.2 Material Mechanical Properties

1) The SCC and CC mixtures have similar compressive strengths at 16 hours with each aggregate type and strength level. At later ages, the strength development of the SCC-R and SCC-L mixtures was significantly higher than for the CC-R and CC-L mixtures.

9.2.7.3 Flexural Behavior

1) The cracking moment of the SCC girders was slightly lower than that of the CC girders. However, the flexural capacities of the SCC girders were similar to that of the CC girders. The initial flexural stiffness and elastic response of the CC and SCC girders were similar.

2) Overall cracking trends (i.e., first cracking in the deck, first web-shear cracking) were similar with the CC and SCC girders for the flexural and development length tests. It was observed that slightly more cracks and higher maximum crack widths developed in the SCC girders. This reduced stiffness and resulted in 15 percent larger deflections in SCC-L girder, compared to CC-L girder. However, the effect on the flexural capacity is minimal.

9.2.7.4 Transfer Length

1) The SCC-R girder had similar or shorter initial and final transfer lengths than the CC-R girder. The SCC-L girder had shorter initial and final transfer lengths compared to the CC-L girder. Normalized transfer lengths with compressive strength show that compressive strength does not significantly lead to smaller transfer length of the SCC girders compared to the CC girders. The initial and longer-term transfer lengths of all the girders were shorter than 60 d_b, which is the value used by the AASHTO LRFD Specifications (2006).

9.2.7.5 Development Length

1) The 2004 and 2006 AASHTO LRFD development length equations provided a conservative estimate of the development length for both the CC and SCC girders. The 2004 AASHTO LRFD alternative development length equation (2006 AASHTO LRFD Equation 5.11.4.2-1) provides a closer estimate of the development length for both the CC and SCC girders. The development length expression in the 2006 AASHTO LRFD is reasonable for design.

9.2.7.6 Prestress Losses

1) Elastic shortening and gains were reasonably estimated using the expression in the AASHTO LRFD (2004 and 2006 AASHTO LRFD Article 5.9.5.1). However, the AASHTO LRFD Specifications (2004 and 2006) overestimated the long-term losses at approximately 140 days. However, it should be noted that the girders were tested at a relatively short time after casting and typical design calculations call for long-term loss estimates at later ages.

9.2.7.7 Camber and Deflection

1) The increase in stiffness resulting from the higher strengths influences the camber growth. In general, the CC girders had higher camber growth than the SCC girders due to different and lower rates of strength development. After stabilization of the strength development and casting of the deck, the CC and SCC girder-deck systems exhibited similar composite stiffness values resulting in comparable net deflection histories after deck casting.

9.3 RECOMMENDATIONS

The following recommendations and future works recommended based on the findings from this study.

1) The research findings indicate that SCC can be implemented for use in precast plants in Texas, specifically those plants producing precast, prestressed girders similar to those evaluated in this study. However, the research found that SCC could be sensitive to environmental and transport conditions. Precast plants should have a good quality control program in place and careful monitoring of the aggregate moisture is necessary. Some segregation of the SCC was observed by the researchers when fabricating the full-scale girders – producers should be aware of this potential segregation issue.
2) TxDOT should use the AASHTO LRFD (2006) or the proposed prediction equations developed herein for estimating the MOE, MOR, and STS for typical prestressed girder designs in Texas when f'_c ranges 5 to 10 ksi (34 to 70 MPa).
3) TxDOT should use the proposed prediction equations developed herein for predicting the MOE, MOR, and STS for SCC mixtures with f'_c values ranging from 10 to 16 ksi (70 to 110 MPa).
4) TxDOT should use the proposed equation (Equation 6.38) for estimating the concrete shear strength of high-strength CC and SCC girders with concrete compressive strengths greater than 10 ksi (70 MPa).
5) TxDOT should use the AASHTO LRFD (2006) multiplier of 1.4 for computing the development length of top bars in SCC structural members.

6) TxDOT should use the AASHTO LRFD (2006) prediction equation for estimating the creep of SCC.
7) For environments exhibiting freeze-thaw cycles, TxDOT should not use SCC mixtures with 16-hour release strength less than 7 ksi (48 MPa).
8) TxDOT should use the AASHTO LRFD (2006) equations for computing the cracking moment, nominal moment, transfer length, development length, and prestress losses for SCC girder-deck systems similar to those tested in this study.
9) Lastly, as with most research, not all combinations of materials, mixtures, or girders were evaluated and reasonable care should be taken when extending the findings of this research to other applications.

REFERENCES

AASHTO (1994). *Bridge design specifications and commentary*, American Association of Highway and Transportation Officials (AASHTO), Washington, D.C.

AASHTO (1996). *Bridge design specifications and commentary*, American Association of Highway and Transportation Officials (AASHTO), Washington, D.C.

AASHTO (2002). *Standard specifications for highway bridges*, 17th Edition. American Association of Highway and Transportation Officials (AASHTO), Washington, D.C.

AASHTO (2004). *Bridge design specifications and commentary*, American Association of Highway and Transportation Officials (AASHTO), Washington, D.C.

AASHTO (2006). *Interim bridge design specifications and commentary*, American Association of Highway and Transportation Officials (AASHTO), Washington, D.C.

AASHTO T22 (2004). "Standard method of test for compressive strength of cylindrical concrete specimens." Standard Specifications for Transportation Materials and Methods of Sampling and Testing, Washington, D.C.

AASHTO T23 (2004). "Standard method of test for making and curing concrete test specimens in the field." Standard Specifications for Transportation Materials and Methods of Sampling and Testing, Washington, D.C.

AASHTO T97 (2004). "Standard method of test for flexural strength of concrete (using simple beam with third-point loading)." Standard Specifications for Transportation Materials and Methods of Sampling and Testing, Washington, D.C.

AASHTO T121 (2004). "Standard method of test for mass per cubic meter (cubic foot), yield, and air content (gravimetric) of concrete." Standard Specifications for Transportation Materials and Methods of Sampling and Testing, Washington, D.C.

AASHTO T126 (2004). "Standard method of test for making and curing concrete test specimens in the lab." Standard Specifications for Transportation Materials and Methods of Sampling and Testing, Washington, D.C.

AASHTO T152 (2004). "Standard method of test for air content of freshly mixed concrete by the pressure meter." Standard Specifications for Transportation Materials and Methods of Sampling and Testing, Washington, D.C.

AASHTO T161 (2004). "Standard method of test for resistance of concrete to rapid freezing and thawing." Standard Specifications for Transportation Materials and Methods of Sampling and Testing, Washington, D.C.

AASHTO T198 (2004). "Standard method of test for splitting tensile strength of cylindrical concrete specimens." Standard Specifications for Transportation Materials and Methods of Sampling and Testing, Washington, D.C.

ACI Committee 209 (1992). "Prediction of creep, shrinkage, and temperature effects in concrete structures." *ACI 209R-92*, American Concrete Institute, Farmington Hills, Michigan.

ACI Committee 209 (2008). "Guide for modeling and calculating shrinkage and creep in hardened concrete." *ACI 209.2R-08*, American Concrete Institute, Farmington Hills, Michigan.

ACI Committee 237 (2007). "Self-consolidating concrete." *ACI 237R-07*, American Concrete Institute, Farmington Hills, Michigan.

ACI Committee 318-05 (2005). "Building code requirements for structural concrete (ACI 318-05) and commentary (318R-05)." *ACI 318-05/318R-05*, American Concrete Institute, Farmington Hills, Michigan.

ACI Committee 363 (1992). "State of the art report on high-strength concrete" *ACI363-R*, American Concrete Institute, Farmington Hills, Michigan.

ACI Committee 408 (2003). "Bond and development of straight reinforcing bars in tension." *ACI 408R-03*, American Concrete Institute, Farmington Hills, Michigan.

Ahmad, S. H., and Shah, S. P. (1985). "Structural properties of high-strength concrete and its implications for precast prestressed concrete." *PCI J.*, 30(6), 92–119.

Aitcin, P. C., and Mehta, P. K. (1990). "Effect of coarse aggregate characteristics on mechanical properties of high-strength concrete." *ACI Mater. J.*, 87(2), 103–107.

Al-Manaseer, A., and Lam, J. P. (2005). "Statistical evaluation of shrinkage and creep models." *ACI Mater. J.*, 102(3), 170–176.

Al-Omaishi, N. (2001). "Prestress losses in high strength pretensioned concrete bridge girder." Doctoral Dissertation, University of Nebraska-Lincoln, Lincoln, Nebraska.

ASCE-ACI Committee 445 (1998). "Recent approaches to shear design of structural concrete." *J. of Struct. Engrg.*, ASCE, 124(12), 1375–1417.

Assie, S., Escadeillas, G., Waller, V., Marcheses, G., and Vachon, M. (2005). "Self-compacting and vibrated concrete compared by their physico-chemical durability properties." *Proc. of the Second North American Conf. on the Des. and Use of Self Consolidating Concr. and the Fourth Int. RILEM Symp. on Self-Consolidating Concr.*, Center for Advanced Cement-Based Materials (ACBM), Chicago, 373–379.

ASTM A416 (2006). "Standard Specification for Steel Strand, Uncoated Seven-Wire for Prestressed Concrete" *Annual book of ASTM standards*, The American Society for Testing and Materials, West Conshohocken, Pennsylvania.

ASTM A615 (2008). "Standard specification for deformed and plain carbon-steel bars for concrete reinforcement." *Annual book of ASTM standards*, The American Society for Testing and Materials, West Conshohocken, Pennsylvania.

ASTM C33 (2007). "Standard specification for concrete aggregates." *Annual book of ASTM standards*, The American Society for Testing and Materials, West Conshohocken, Pennsylvania.

ASTM C143 (2005). "Standard test method for slump of hydraulic cement concrete." *Annual book of ASTM standards*, The American Society for Testing and Materials, West Conshohocken, Pennsylvania.

ASTM C469 (2005). "Standard test method for static modulus of elasticity and poisson's ratio of concrete in compression." *Annual book of ASTM standards*, The American Society for Testing and Materials, West Conshohocken, Pennsylvania.

ASTM C512 (2002). "Standard test method for creep of concrete in compression." *Annual book of ASTM standards*, The American Society for Testing and Materials, West Conshohocken, Pennsylvania.

ASTM C618 (2008). "Standard specification for coal fly ash and raw or calcined natural pozzolan for use in concrete." *Annual book of ASTM standards*, The American Society for Testing and Materials, West Conshohocken, Pennsylvania.

ASTM C1202 (1997). "Standard test method for concrete's ability to resist chloride ion penetration." *Annual book of ASTM standards*, The American Society for Testing and Materials, West Conshohocken, Pennsylvania.

ASTM C1556 (2003). "Standard test method for determining the apparent chloride diffusion coefficient of cementitious mixtures by bulk diffusion." *Annual book of ASTM standards*, The American Society for Testing and Materials, West Conshohocken, Pennsylvania.

ASTM C1610/C (2006). "Test method for static segregation of self-consolidating concrete using column technique." *Annual book of ASTM standards*, The American Society for Testing and Materials, West Conshohocken, Pennsylvania.

ASTM C1611 (2005). "Test method for slump flow of self-consolidating concrete." *Annual book of ASTM standards*, The American Society for Testing and Materials, West Conshohocken, Pennsylvania.

ASTM C1621 (2006). "Test method for passing ability of self-consolidating concrete by j-ring." *Annual book of ASTM standards*, The American Society for Testing and Materials, West Conshohocken, Pennsylvania.

Aulia, T. B., and Deutschmann, K. (1999). "Effect of mechanical properties of aggregate on the ductility of high performance concrete." University of Leipzig, Germany.

Baalbaki (1992). "Influence of coarse aggregate on elastic properties of high-performance concrete." *ACI Mater. J.*, 88(5), 499–503.

Barnes, R. W. (2000). "Development length of 0.6-inch prestressing strand in standard i-shaped pretensioned concrete beams." ***Rep. No. 1388-1***, Center for Transportation Research, University of Texas, Austin.

Barnes, R. W., Grove, J. W., and Burns, N. H. (2003). "Experimental assessment of factors affecting transfer length." ***ACI Struct. J.***, 100(6), 740–748.

Barragan, B., Gettu, R., Agullo, L., and Zerbino, R. (2006). "Shear failure of steel fiber-reinforced concrete based on push-off tests." ***ACI Mater. J.***, 103(4), 251–257.

Bazant, Z., and Baweja, S. (1995). "Justification and refinements of model B3 for concrete creep and shrinkage 1. Statistics and sensitivity." ***Mater. Struct.***, 28(9), 415–430.

Bazant, Z., and Baweja, S. (2000). "Creep and shrinkage prediction model for analysis and design of concrete structures." The Adam Neville Symposium: Creep and Shrinkage-Structural Design Effects, ***SP-194***, American Concrete Institute, 1–100.

Bazant, Z., and Gambarova, P. (1980). "Rough cracks in reinforced concrete." ***J. of Struct. Engrg.***, ASCE, 106(ST4), 819–841.

Bazant, Z., and Li, Z. (1995). "Modulus of rupture: size effect due to fracture initiation in boundary layer." ***J. of Struct. Engrg.***, ASCE, 121(4), 739–746.

Bazant, Z., and Panula, L. (1978a). "Practical prediction of time-dependent deformations of concrete part I: Shrinkage." ***Mater. Struct.***, 11(65), 307–316.

Bazant, Z., and Panula, L. (1978b). "Practical prediction of time-dependent deformations of concrete part II: Basic creep." ***Mater. Struct.***, 11(65), 317–328.

Bazant, Z., and Panula, L. (1978c). "Practical prediction of time-dependent deformations of concrete part III: Drying creep." ***Mater. Struct.***, 11(66), 415–423.

Bazant, Z., and Panula, L. (1978d). "Practical prediction of time-dependent deformations of concrete part IV: Temperature effect on basic creep." ***Mater. Struct.***, 11(66), 423–434.

Bazant, Z., and Panula, L. (1979). "Practical prediction of time-dependent deformations of concrete part V: Temperature effect on drying creep." ***Mater. Struct.***, 12(69), 169–183.

Bazant, Z., and Panula, L. (1980). "Creep and shrinkage characterization for prestressed concrete structures." ***PCI J.***, 25(3), 86–122.

Bazant, Z., and Panula, L. (1984). "Practical prediction of creep and shrinkage of high strength concrete." ***Mater. Struct.***, 17(101), 375–378.

Bentz, E. C. (2000). "Sectional analysis of reinforced concrete members." Doctoral Dissertation, University of Toronto.

Bentz, E. C., Vecchio, F. J., and Collins, M. P. (2006). "Simplified modified compression field theory for calculating shear of reinforced concrete elements." *ACI Struct. J.*, 103(4), 614–624.

Bonen, D., and Shah, S. P. (2004). "The effects of formulation on the properties of self-consolidating concrete." Concrete Science and Engineering: A Tribute to Arnon Bentur, *Proc. of the Int. RILEM Symp.*, RILEM Publications, Bagneux, France, 43–56.

Boresi, A. P., and Schmidt, R. J. (2002). *Advanced mechanics of materials*, Wiley, New York.

Branson, D. E., and Christianson, M. L. (1971). "Time-dependent concrete properties related to design-strength and elastic properties, creep, and shrinkage." Designing for Effects of Creep, Shrinkage, and Temperature in Concrete Structures, *SP-27*, American Concrete Institute, 257–277.

Brooks, M. D., Gerstle, K. H., and Logan, D. R. (1988). "Effect of initial strand slip on the strength of hollow core slabs." *PCI J.*, 33(1), 90–111.

Buckner, C. D. (1995). "A review of strand development length for pretensioned concrete members." *PCI J.*, 40(2), 84–105.

Burgueño, R., and Bendert, D. A. (2005). "Effect of self-consolidating concrete mix design on the shear behavior of RC beams." *Proc. of the Second North American Conf. on the Des. and Use of Self Consolidating Concr. and the Fourth Int. RILEM Symp. on Self-Consolidating Concr.*, Center for Advanced Cement-Based Materials (ACBM), Chicago, 1265–1270.

Burgueño, R., and Bendert, D. A. (2007). "Structural behavior and field-monitoring of scc prestressed box beams for demonstration bridge." Self-Consolidating Concrete for Precast Prestressed Applications, *SP-247*, American Concrete Institute, Fajardo, Puerto Rico, 67–76.

Burgueño, R., and Haq, M. (2007). "Effect of SCC mixture proportioning on transfer and development length of prestressing strand." Self-Consolidating Concrete for Precast Prestressed Applications, *SP-247*, American Concrete Institute, Fajardo, Puerto Rico, 105–116.

Carrasquillo, R. L., Nilson, A. H., and Slate, F. O. (1981). "Properties of high strength concrete subject to short-term loads." *ACI J., Proc.*, 78(3), 171–178.

Catrodale, R. W., Kreger, M. E., and Burns, N. H. (1988). "A study of pretensioned high strength concrete girders in composite highway bridge-laboratory tests." *Rep. No. 318-3*, Center for Transportation Research, The University of Texas, Austin.

CEB-FIP (1990). *High-strength concrete state of the art report*, Thomas Telford, London.

CEB-FIP (1993). *CEB-FIP model code 1990*, Thomas Telford, London.

Cetin, A., and Carrasquillo, R. L. (1998). "High-performance concrete: influence of coarse aggregates on mechanical properties." *ACI Mater. J.*, 95(3), 252–261.

Choulli, Y., Mari, A. R., and Cladera, A. (2005). "Shear behaviour of full-scale prestressed I-beams made with self-compacting concrete." *Proc. of the Second North American Conf. on the Des. and Use of Self Consolidating Concr. and the Fourth Int. RILEM Symp. on Self-Consolidating Concr.*, Center for Advanced Cement-Based Materials (ACBM), Chicago, 851–856.

Christensen, B. J., and Ong, F. S. (2005). "The resistance of self-consolidating concrete (scc) to freezing and thawing cycles." *Proc. of the Second North American Conf. on the Des. and Use of Self Consolidating Concr. and the Fourth Int. RILEM Symp. on Self-Consolidating Concr.*, Center for Advanced Cement-Based Materials (ACBM), Chicago, 347–353.

Collins, M. P., and Mitchell, D. (1980). "Shear and torsion design of prestressed and nonprestressed concrete beams." *PCI J.*, 25(5), 32–100.

Collins, M. P., and Mitchell, D. (1991). *Prestressed concrete structures*, Prentice-Hall, Englewood Cliffs, New Jersey.

CSA A23.3-04 (1994). "Design of concrete structures." Canadian Standards Association, Ottawa, Ontario.

D'Ambrosia, M. D., Lange, D. A., and Brinks, A. J. (2005). "Restrained shrinkage and creep of self-consolidating concrete." *Proc. of the Second North American Conf. on the Des. and Use of Self Consolidating Concr. and the Fourth Int. RILEM Symp. on Self-Consolidating Concr.*, Center for Advanced Cement-Based Materials (ACBM), Chicago, 921–928.

Daczko, J. A., Kurtz, M. A., Bury, M., and Attiogbe, E. (2003). ""Zero energy" system for precast concrete production." *Concr. Int.*, 25(4), 103–107.

Dehn, F., Holschemacher, K., and Weiße, D. (2000). "Self-compacting concrete (SCC) time development of the material properties and the bond behavior." University of Leipzig, Germany.

Domone, P. L. (2006). "Self-compacting concrete: an analysis of 11 years of case studies." *Cem. and Concr. Compos.*, 28, 197–208.

Duthinh, D. (1999). "Sensitivity of shear strength of reinforced concrete and prestressed concrete beams to shear friction and concrete softening according to modified compression field theory." *ACI Struct. J.*, 96(4), 495–508.

EFNARC (2001). "European guidelines for self-compacting concrete." www.efnarc.org (Dec. 5. 2003).

EFNARC (2005). "European guidelines for self-compacting concrete." www.efnarc.org (Aug. 5. 2008).

Erkmen, B., Shield, C. K., and French, C. E. (2007). "Time-dependent behavior of full-scale self-consolidating concrete precast prestressed girders." Self-Consolidating Concrete for

Precast Prestressed Applications, *SP-247*, American Concrete Institute, Fajardo, Puerto Rico, 139–154.

Felekoglu, B., Turkel, S., and Baradan, B. (2007). "Effect of water/cement ratio on the fresh and hardened properties of self-compacting concrete." *Build. and Environ.*, 42(4), 1795-1802.

Fenwick, R. C., and Paulay, T. (1968). "Mechanism of shear resistance of concrete beams." *J. of Struct. Engrg.*, ASCE, 94(10), 2325–2350.

FHWA and NCBC (2005). "Q&A: What is the status on the use of self-consolidating concrete in bridges?" *HPC bridge views*, the Federal Highway Administration and the National Concr. Bridge Counc., Skokie, Illinois, 1–4.

Gardner, N. J., and Lockman, M. J. (2001). "Design provisions for drying shrinkage and creep of normal-strength concrete." *ACI Mater. J.*, 98(2), 159–167.

Gardner, N. J., and Zhao, J. W. (1993). "Creep and shrinkage revisited." *ACI Mater. J.*, 90(3), 236–246.

Ghezal, A., and Khayat, K. H. (2002). "Optimizing self-consolidating concrete with limestone filler by using statistical factorial design methods." *ACI Mater. J.*, 99(3), 264–272.

Girgis, A. F., and Tuan, C. Y. (2004). "Bond strength of self-consolidating concrete for prestress concrete applications." *Rep. No. SPR-P1(04) P571*, University of Nebraska, Lincoln.

Gross, S. P., Yost, J. R., and Gaynor, E. (2007). "Experimental study of prestress land and camber in high-strength SCC beams." Self-Consolidating Concrete for Precast Prestressed Applications, *SP-247*, American Concrete Institute, Fajardo, Puerto Rico, 77–92.

Guyon, Y. (1953). *Prestressed concrete*, John Wiley and Sons, New York.

Hamilton, H. R., and Labonte, T. (2005). "Self-consolidating concrete (SCC) structural investigation." *Rep. No. 455404712*, Department of Civil and Coastal Engineering, University of Florida, Gainesville.

Hanson, N. W., and Kaar, P. H. (1959). "Flexural bond tests of pretensioned prestressed beams." *ACI J., Proc.*, 55(1), 783–802.

Hawkins, N. M., Kuchma, D. A., Mast, R. F., Marsh, M. L., and Reineck, K. H. (2005). "Simplified shear design of structural concrete members." *NCHRP Report 549*, Transportation Research Board, Washington D.C.

Hegger, J., Will, N., and Bülte, S. (2007). "Bond strength and shear capacity of prestressed beams made of SCC." Self-Consolidating Concrete for Precast Prestressed Applications, *SP-247*, American Concrete Institute, Fajardo, Puerto Rico, 123–138.

Houde, J., and Mirza, M. S. (1972). "Investigation of shear transfer across cracks by aggregate interlock." *Rep. No. 72-06*, Ecole Polytechnique de Montreal, Department of Genie Civil, Division de Structures Montreal, Quebec.

Hoyer, E., and Friedrich, E. (1939). "Beitrag zur frage der haftspannung in eisenbetonbauteilen ("contribution to the question of bond stress in reinforced concrete elements")." *Beton und Eisen*, 38, 107-110.

Hueste, M. D., Chompreda, P., Trejo, D., Cline, D. B. H., and Keating, P. B. (2003). "Mechanical properties of high strength concrete produced for prestressed bridge girders." *Rep. No. 0-2101-2*, Texas Transportation Institute, Texas A&M University, College Station.

Hueste, M. D., Chompreda, P., Trejo, D., Cline, D. B. H., and Keating, P. B. (2004). "Mechanical properties of high-strength concrete for prestressed members." *ACI Struct. J.*, 101(4), 457–466.

Huo, X. S., Al-Omaishi, N., and Tadros, M. K. (2001). "Creep, shrinkage, and modulus of elasticity of high performance concrete." *ACI Mater. J.*, 98(6), 440–449.

Issa, M., Alhassan, M., Shabila, H., and Krozel, J. (2005). "Laboratory performance evaluation of self-consolidating concrete." *Proc. of the Second North American Conf. on the Des. and Use of Self Consolidating Concr. and the Fourth Int. RILEM Symp. on Self-Consolidating Concr.*, Center for Advanced Cement-Based Materials (ACBM), Chicago, 857–862.

Janney, J. R. (1954). "Nature of bond in pre-tensioned prestressed concrete." *ACI J., Proc.*, 50(5), 717–736.

Jeanty, P. R., Mitchell, D., and Mirza, M. S. (1988). "Investigation of "top bar" effects in beams." *ACI Struct. J.*, 85(3), 251–257.

Kaar, P. H., LaFraugh, R. W., and Mass, M. A. (1963). "Influence of concrete strength on strand transfer length." *PCI J.*, 8(5), 47–67.

Khayat, K. H. (1996). "Effects of antiwashout admixtures on properties of hardened concrete." *ACI Mater. J.*, 93(2), 134–146.

Khayat, K. H. (1998). "Viscosity enhancing admixtures for cement-based materials: overview." *Cem. Concr. Compos.*, 20, 171–188.

Khayat, K. H., and Assaad, J. (2002). "Air-void stability in self-consolidating concrete." *ACI Mater. J.*, 99(4), 408–416.

Khayat, K. H., Attiogbe, E. K., and See, H. T. (2007). "Effect of admixture combination on top-bar effect of highly flowable and self-consolidating concrete mixtures." Self-Consolidating Concrete for Precast Prestressed Applications, *SP-247*, American Concrete Institute, Fajardo, Puerto Rico, 33–44.

Khayat, K. H., and Guizani, Z. (1997). "Use of viscosity-modifying admixture to enhance stability of highly fluid concrete." *ACI Mater. J.*, 94(4), 332–340.

Koehler, E. P., and Fowler, D. W. (2008). "Self-consolidating concrete for precast structural applications: mixture proportioning, workability, and early-age hardened properties." *Rep. No. 0-5134-1*, Center for Transportation Research, University of Texas, Austin.

Laible, J. P., White, R. N., and Gergely, P. (1977). "Experimental investigation of shear transfer across cracks in concrete nuclear containment vessels." *SP-53*, American Concrete Institute, 203–226.

Lane, S. N. (1990). "Development length of prestressing strand." *Public Loads*, 54(2), 200–205.

Lane, S. N. (1998). "A new development length equation for pretensioned strands in bridge beams and piles." *Final Rep. No. FHWA-RD-98-116*, Federal Highway Administration, Washington, D.C.

Larson, K. H., Peterman, R. J., and Esmaeily, A. (2005). "Determining the time-dependent and bond characteristics of a scc mix for kansas prestressed concrete bridge girders." *Proc. of the Second North American Conf. on the Des. and Use of Self Consolidating Concr. and the Fourth Int. RILEM Symp. on Self-Consolidating Concr.*, Center for Advanced Cement-Based Materials (ACBM), Chicago, 845–850.

Logan, D. R. (1997). "Acceptance criteria for bond quality of strand for pretensioned prestressed concrete applications." *PCI J.*, 42(2), 52–90.

Ma, J., and Dietz, J. (2002). "Ultra high performance self compacting concrete." University of Leipzig, Germany.

MacDonanld, K. A., and Lukkarila, M. R. (2002). "Impact of production and proportioning on microstructure and properties of self-consolidating concrete." *Proc. of the First North American Conf. on the Des. and Use of Self Consolidating Concr.*, Center for Advanced Cement Based Materials (ACBM), Chicago, 9–14.

Maekawa, K., Streissler, E. W., and Pimanmas, A. (2003). *Nonlinear mechanics of reinforced concrete*, Spon Press, New York.

Mattock, A. H. (1979). "Flexural strength of prestressed concrete sections by programmable calculator." *PCI J.*, 24(1), 32–54.

Mehta, P. K., and Monterio, P. J. M. (2005). *Concrete: microstructure, properties, and materials*, McGraw-Hill, New York.

Menzel, C. A. (1952). "Effect of settlement of concrete on results of pullout tests." *Res. Dept. Bull. 41*, Research and Development Laboratories of the Portland Cement Association, Skokie, Illinois.

Mitchell, D., Cook, W. D., Kahn, A. A., and Tham, T. (1993). "Influence of high strength concrete on transfer and development length of pretensioning strand." *PCI J.*, 38(3), 52–66.

Naaman, A. E. (2004). *Prestressed concrete analysis and design: fundamentals*, Techno Press, Ann Arbor, Michigan.

Naito, C. J., Parent, G., and Brunn, G. (2006). "Performance of bulb-tee girders made with self-consolidating concrete." *PCI J.*, 51(6), 72–85.

Neville, M. A. (1995). "Aggregate bond and modulus of elasticity of concrete." *ACI Mater. J.*, 94(1), 71–74.

Norwegian Council for Strandardization (1992). *Concrete structures—design rules*, *NS 3473*, *norges standardiseringsforbund*, Oslo, Norway.

Okamura, H., and Ouchi, M. (1999). "Self-compacting concrete. development, present use and future." First International Symposium on SCC, *RILEM publications PRO 7*, Stockholm, Sweden, 3–14.

Okamura, H., and Ozawa, K. (1994). "Self-compactable high performance concrete in japan." international workshop on high performance concrete, *SP-169*, American Concrete Institute, Detroit, 31–44.

Ozyildrim, C. (2007). "Bulb T-beams with self-consolidating concrete on route 33 in Virginia." *Transportation Research Record*, 2020, 76–82.

Patel, R., Hossain, K. M. A., Shehata, M., Bouzoubaa, N., and Lachemi, M. (2004). "Development of statistical models for mixture design of high-volume fly ash self-consolidating concrete." *ACI Mater. J.*, 101(4), 294–302.

Paulay, T., and Loeber, P. J. (1974). "Shear transfer by aggregate interlock." Shear in Reinforced Concrete, *SP-42*, American Concrete Institute, Detroit, 1–15.

PCI (2003). "Interim guidelines for the use of self-consolidating concrete in precast/prestressed concrete institute member plants." *TR-6-03*, Precast/Prestressed Concrete Institute, Chicago.

PCI Committee on Prestress Losses (1975). "Recommendations for estimating prestressed losses." *PCI J.*, 20(4), 45–75.

PCI design handbook (2004). Precast/Prestressed Concrete Institute, Chicago.

Pineaud, A., Cabrillac, R., Remond, S., Pimienta, P., and Rivillon, P. (2005). "Mechanical properties of self-compacting concrete - influence of composition parameters." *Proc. of the Second North American Conf. on the Des. and Use of Self Consolidating Concr. and the Fourth Int. RILEM Symp. on Self-Consolidating Concr.*, Center for Advanced Cement-Based Materials (ACBM), Chicago, 863–868.

RILEM Technical Committee TC 107 (1995). "Guidelines for characterizing concrete creep and shrinkage in structural design codes or recommendations." ***Mater. Struct.***, 28, 52−55.

Ruiz, E. D., Staton, B. W., DO, N. H., and Hale, W. M. (2007). "Prestress losses in beams cast with self-consolidating concrete." Self-Consolidating Concrete for Precast Prestressed Applications, ***SP-247***, American Concrete Institute, Fajardo, Puerto Rico, 93−104.

Russell, B. W., and Burns, N. H. (1993). "Design guidelines for transfer, development and debonding of large diameter seven wire strands in pretensioned concrete girders." ***Rep. No. 1210-5F***, Center For Transportation Research, The University of Texas, Austin.

SAS Institute (2006). ***Base SAS 9.1.3 procedures guide, second edition, volumes 1, 2, 3, and 4***, SAS Institute Inc., Cary, North Carolina.

Schindler, A. K., Barnes, R. W., Kavanaugh, B., Roberts, J., and Kelly, L. (2007a). "Creep and shrinkage of self-consolidating concrete." ACI 2007 Convention Session Notes, April 23, Atlanta, Georgia.

Schindler, A. K., Barnes, R. W., Roberts, J. B., and Rodriguez, S. (2007b). "Properties of self-consolidating concrete for prestressed members." ***ACI Mater. J.***, 104(1), 53−61.

Sengul, O., Tasdemir, C., and A., T. M. (2002). "Influence of aggregate type on mechanical behavior of normal and high-strength concretes." ***ACI Mater. J.***, 99(6), 528−533.

Shahawy, M. (2001). "A Critical evaluation of the AASHTO provisions for strand development length of prestressed concrete member." ***PCI J.***, 46(4), 94−117.

Shiba, D., Kitagawa, K., Shimoda, M., and Izumi, T. (1998). "Study on qualities of high flow concrete using new high-range water-reducing agent polyether type." ***4th CANMET/ACI/JCI Int. Conf. on Recent Advances in Concr. Technology***, Supplementary Papers, ***SP-179***, American Concrete Institute, 71−85.

Sonebi, M. (2004). "Applications of statistical models in proportioning medium-strength self-consolidating concrete." ***ACI Mater. J.***, 101(5), 339−346.

Stoker, M. F., and Sozen, M. A. (1970). "Investigation of prestressed concrete for highway bridges-part v: bond characteristics of prestressing strand." ***Bull. 503***, Engineering Experiment Station, University of Illinois, Urbana.

Suksawang, N., Nassif, H. H., and Najim, H. S. (2006). "Evaluation of mechanical properties for self-consolidating, normal, and high-performance concrete." ***Transportation Research Record***, 1979, 36−45.

Tadros, M. K., Al-Omaishi, N., Seguirant, S. J., and Gallt, J. G. (2003). "Prestress losses in pretensioned high-strength concrete bridge girders." ***NCHRP Report 496***, ***Transportation Research Board***, Washington, D.C.

Thomas, M. (2007). "Optimizing the use of fly ash in concrete", *IS548*, Portland Cement Association, Skokie, Illinois.

Thomas, M. D. A., and Bamforth, P. B. (1999). "Modeling chloride diffusion in concrete effect of fly ash and slag." *Cem. Concr. Compos.*, 29, 487–495.

Thomas, M. D. A., and Bentz, E. C. (2000). "Life-365 manual." released with program by Master Builders and www.Masterbuilders.com, 55 (Aug. 5. 2008).

Trent, J. D. (2007). "Transfer length, development length, flexural strength, and prestress loss evaluation in pretensioned self-consolidating concrete members." M.S. Thesis, The Virginia Polytechnic Institute and State University, Blacksburg.

TxDOT (2001). *Bridge design manual*, Texas Department of Transportation, Austin.

TxDOT (2004). "Standard specifications for construction and maintenance of highways, streets, and bridges." Texas Department of Transportation, Austin.

TxDOT (2006). "Section 7 DMS-7300, precast concrete fabrication plants." Texas Department of Transportation, Austin.

Vecchio, F. J., and Collins, M. P. (1986). "The modified compression field theory for reinforced concrete elements subjected to shear." *ACI Struct. J.*, 83(2), 219–231.

Walraven, J. (2005). "Self-compacting concrete: challenge for designer and researcher." *Combining the 2nd North American Conf. on the Des. and Use of Self-Consolidating Concr. and the 4th Int. RILEM Symp. on Self-Compacting Concr.*, Center for Advanced Cement-Based Materials (ACBM), Chicago, 431–446.

Walraven, J. C. (1981). "Fundamental analysis of aggregate interlock." *J. Struct. Div.*, ASCE, 107(11), 2245–2270.

Walraven, J. C., and Reinhardt, H. W. (1981). "Theory and experiments on mechanical behavior of cracks in plain and reinforced concrete subjected to shear loading." *Heron*, 26(1A), 68.

Walraven, J. C., and Stroband, J. (1994). "Shear friction in high-strength concrete." *SP-149*, American Concrete Institute, Singapore, 311–330.

Xu, G., and Beaudoin, J. J. (2000). "Effect of polycarboxylate superplasticizer on contribution of interfacial transition zone to electrical conductivity of portland cement mortars." *ACI Mater. J.*, 97(4), 418–424.

Yoshikawa, H., Wu, Z., and Tanabe, T. A. (1989). "Analytical model for shear slip of cracked concrete." *J. of Struct. Engrg.*, ASCE, 115(4), 771–788.

Zhu, W., and Bartos, P. J. M. (2003). "Permeation properties of self-compacting concrete." *Cem. Concr. Res.*, 33(6), 921–926.

Zia, P., Nuñez, R. A., Mata, L. A., and Dwairi, H. M. (2005). “Implementation of self consolidating concrete for prestressed concrete girders.” Seventh International Symposium on the Utilization of High-Strength/High-Performance Concrete, *SP-228*, American Concrete Institute, 297−316.

APPENDIX A
PREDICTION EQUATIONS FOR CREEP

A.1 AASHTO LRFD Specifications (2004)

Based on the philosophy of design and practice, the AASHTO LRFD equations are simple and have robustness for the mixture proportions. The 2004 AASHTO LRFD equations are based on the recommendation of the ACI Committee 209 and Collins and Mitchell (1991). The 2004 AASHTO LRFD doesn't apparently consider the concrete strength at prestress transfer which is a more realistic value for precasters. In general, the equation from the AASHTO LRFD Specifications (2004) regards the ambient relative humidity, geometric configuration such as volume to surface ratio, and the compressive strength as the main factors in predicting both creep and shrinkage of concrete. The AASHTO LRFD Specifications (2004) recommend the following equation to determine the creep coefficient:

$$\psi(t,t_i) = 3.5 \;\; k_c \; k_f \left(1.58 - \frac{H}{120}\right) t_j^{-0.118} \; \frac{(t-t_i)^{0.6}}{10.0 + (t-t_i)^{0.6}} \qquad \text{(A.1)}$$

Where $\psi(t, t_i)$ is the creep coefficient, H is relative humidity in percent, t is the age of concrete in days, and t_i is the age of concrete when the load is initially applied in days. The parameter k_c is a factor for the effect of the volume-to-surface ratio (V/S) of the component and is determined from the following equation:

$$k_c = \left[\frac{t}{\frac{26\, e^{0.36\,(V/S)} + t}{t}}\right]\left[\frac{1.80 + 1.77\, e^{-0.54\,(V/S)}}{2.587}\right] \qquad \text{(A.2)}$$

The maximum volume to surface ratio is 6.0 in. for use of this equation.

The parameter k_f is a factor for the effect of concrete strength, and is determined from the following equation:

$$k_f = \frac{1}{0.67 + \left(\frac{f'_c}{9}\right)} \tag{A.3}$$

where f'_c is the specified compressive strength at 28 days (ksi).

The AASHTO LRFD Specifications (2004) provide the following equation for shrinkage,

$$\varepsilon_{sh} = -k_s k_h \left(\frac{t}{35.0 + t}\right)\left(0.51 \times 10^3\right) \tag{A.4}$$

where t is drying time in days and k_h is a humidity factor that is specified as follows,

$$\text{For } H < 80\%,\ k_h = \frac{140 - H}{70} \tag{A.5}$$

$$\text{For } H \geq 80\%,\ k_h = \frac{3(100 - H)}{70} \tag{A.6}$$

where H is the average ambient relative humidity in percent, and k_s is a factor for the volume-to-surface ratio that is specified,

$$k_s = \left[\frac{\frac{t}{26\, e^{0.36(V/S)} + T}}{\frac{t}{45 + t}}\right]\left[\frac{1064 - 94\,(V/S)}{923}\right] \tag{A.7}$$

The maximum volume to surface ratio for use of this equation is 6.0 in.

A.2 AASHTO LRFD Specifications (2006)

The 2006 AASHTO LRFD equation is the latest prediction equation for the better prediction of the modern concrete structures. The 2006 AASHTO LRFD considers the modern characteristics of high-strength concrete for prestressed, precast concrete mixtures which have relatively low water-cement ratios and high-range water reducing admixtures. According to work by Tadros ***et al.*** (2003), creep and shrinkage have similar time-development patterns and rapidly increase during the several weeks after casting concrete. After initial periods the development slows down. Even though the mixture proportions were not explicitly considered in the equations of the creep and shrinkage, the strength and the development strength are highly correlated to creep and shrinkage of the mixture proportions. The CEB-FIP model and ACI 209 model can be alternatively used to predict creep and shrinkage according to the AASHTO LRFD general guidelines. According to the AASHTO LRFD Specifications, it should be noted that the large concrete members have less shrinkage than small specimens measured by laboratory testing.

The AASHTO LRFD equations for creep and shrinkage were modified and updated based on the ACI Committee 209 recommendation (ACI Committee 209 1992) with recently found data (AASHTO 2006, Al-Omaishi 2001, Huo ***et al.*** 2001, Tadros ***et al.*** 2003).

According to the 2006 AASHTO LRFD Specifications (Article 5.4.2.3.2-1), the creep coefficient may be taken as:

$$\psi(t,t_i) = 1.9\, k_{vs}\, k_{hc}\, k_f\, k_{td}\, t_i^{-0.118} \tag{A.8}$$

Where,

$\psi(t,t_i)$ = Creep coefficient

$$k_{vs} = 1.45 - 0.13\,(V/S) \geq 0.0 \tag{A.9}$$

$$k_{hc} = 1.56 - 0.008\,H \tag{A.10}$$

$$k_f = \frac{5}{1 + f'_{ci}} \tag{A.11}$$

$$k_{td} = \frac{t}{61 - 4\, f'_{ci} + t} \tag{A.12}$$

where H is relative humidity (%), k_{vs} is the factor actor for the effect of the volume-to-surface ratio of the component, k_f is the factor for the effect of concrete strength, k_{hc} is humidity factor for creep, k_{td} is time development factor, t is maturity of concrete (days), defined as age of concrete between time of loading for creep calculations, and time being considered for analysis of creep or shrinkage effects, t_i is age of concrete when load is initially applied (days), V/S is volume-to-surface ratio (in.). f'_{ci} is specified compressive strength of concrete at time of prestressing for pretensioned members. If concrete age at time of initial loading is unknown at design time, f'_{ci} may be taken as 0.80 f'_c (ksi).

The strain due to shrinkage, ε_{sh}, at time, t, may be taken as

$$\varepsilon_{sh} = -k_{vs}\ k_{hs}\ k_f\ k_{td}\ 0.48 \times 10^{-3} \tag{A.13}$$

in which:

$$k_{hs} = 2.00 - 0.014H \tag{A.14}$$

where k_{vs}, k_f, and k_{td} were defined previously and k_{hs} is humidity factor for shrinkage.

A.3 ACI Committee 209 (1992)

The ACI 209 model is the empirical approach with data prior to 1968 (Al-Manaseer and Lam 2005). It provides a prediction model for creep and shrinkage based on the age adjusted effective method and empirical approach. This model is based on the research of the Branson and Christianson (Branson and Christianson 1971). ACI Committee 209 (1992) considers many factors to predict creep and shrinkage. In this equation, the ratio of fine aggregate from the mixture proportions and variable characteristics of concrete are considered as factors that can predict and determine creep and shrinkage with detailed formulas. The creep coefficient for a loading age of 7 days for moist cured concrete and for 1-3 days steam cured concrete is given by following equation:

$$v_t = \frac{t^{0.60}}{10 + t^{0.60}} v_u \tag{A.15}$$

$$v_u = 2.35\,\gamma_c \text{ and } \gamma_c = \gamma_{la}\ \gamma_\lambda\ \gamma_h\ \gamma_{vs}\ \gamma_s\ \gamma_\psi\ \gamma_a \tag{A.16}$$

where γ_{la} is a loading age in days for cured or steamed cured concrete, γ_λ is ambient relative humidity in percent, γ_h is the average thickness in inches of the part of the member under consideration, γ_{vs} is the volume to surface ratio, γ_s is the observed slump in inches, γ_ψ is the ratio of the fine aggregate to total aggregate by weight in percent, and γ_a is the air content in percent (ACI Committee 209 1992).

The equation for shrinkage from ACI Committee 209 (1992) is separated by ages,

Shrinkage after 1-3 days for moist cured concrete:

$$(\varepsilon_{sh})_t = \frac{t}{55 + t}(\varepsilon_{sh})_u \tag{A.17}$$

$$(\varepsilon_{sh})_u = 780\,\gamma_{sh} \times 10^{-6} \tag{A.18}$$

$$\gamma_{sh} = \gamma_\lambda\ \gamma_h\ \gamma_{vs}\ \gamma_s\ \gamma_\psi\ \gamma_c\ \gamma_a \tag{A.19}$$

Shrinkage after 7 days for moist cured concrete:

$$(\varepsilon_{sh})_t = \frac{t}{35 + t}(\varepsilon_{sh})_u \tag{A.20}$$

where γ_c is the cement content in pounds per cubic yard. The other equation variables are consistent with those for creep.

A.4 CEB-FIP (1993)

These equations from CEB-FIP (1993) predict with MOE of 28 days and time dependent parameters for creep and shrinkage. CEB-FIP (1993) recommended an equation to estimate creep as follows:

$$\varepsilon_{cc}(t,t_0) = \frac{\partial_c(t_0)}{E_{ci}} \phi(t,t_0) \tag{A.21}$$

where E_{ci} is the MOE at the age of 28 days and $\phi(t, t_0)$ is the creep coefficient. The creep coefficient may be calculated from:

$$\phi(t,t_0) = \phi_0 \, \beta_c(t-t_0) \tag{A.22}$$

where ϕ_0 is the notional creep coefficient, β_c is the coefficient to describe the development of creep with time after loading, t is the age of concrete (days) at the moment considered, and t_0 is the age of concrete at loading (days).

The notional creep coefficient may be estimated from:

$$\phi_0 = \phi_{RH} \, \beta(f_{cm}) \, \beta(t_0) \tag{A.23}$$

Where,

$$\phi_{RH} = 1 + \frac{1 - \dfrac{RH}{RH_0}}{0.46\left(\dfrac{h}{h_0}\right)^{1/3}} \tag{A.24}$$

$$\beta(f_{cm}) = \frac{5.3}{(f_{cm}/f_{cmo})^{0.5}} \tag{A.25}$$

$$\beta(t_0) = \frac{1}{0.1 + (t_0 / t_1)^{0.2}} \tag{A.26}$$

where f_{cm} is the mean compressive strength of concrete at the age of 28 days (MPa), f_{cmo} is 10 MPa, RH is the relative humidity of the ambient environment in percent, RH_0 is 100 percent, h is the notional size of member (mm), h_0 is 100 mm, and t_1 is 1 day.

The development of creep with time is given by:

$$\beta_c(t - t_0) = \left[\frac{(t - t_0)/t_1}{\beta_H + (t - t_0)/t_1} \right]^{0.3} \tag{A.27}$$

Where,

$$\beta_H = 150 \left\{ 1 + \left(1.2 \frac{RH}{RH_0} \right)^{18} \right\} \frac{h}{h_0} + 250 \leq 1500 \tag{A.28}$$

where t_1 is 1 day, RH_0 is 100 percent, and h_0 is 100 mm.

The shrinkage equation from CEB-FIP (1993) is:

$$\varepsilon_{cs}(t, t_s) = \varepsilon_{cso}\, \beta_s(t, t_s) \tag{A.29}$$

where ε_{cso} is the notional shrinkage coefficient, β_s is a coefficient to describe the development of shrinkage with time, t is the age of concrete (days), and t_s is the age of concrete at the beginning of shrinkage (days).

A.5 *BP Models (1984)*

The BP model was originally proposed by Bazant and Panula (1978, 1979). The formula to estimate drying creep was updated to a prediction equation extended to high-strength concrete which is higher than 10 ksi (69 MPa) (Bazant and Panula 1984).

The strain related to the creep and applied load can be calculated from the following equation:

$$\varepsilon = J(t,t')\,\sigma = \left(\frac{1}{E_0} + C_0(t,t') + C_d(t,t',t_0) - C_P(t,t',t_0)\right)\sigma \tag{A.30}$$

$$\text{Basic creep} = \frac{1}{E_0} + C_0(t,t') + C_d(t,t',t_0) \tag{A.31}$$

where E_0 is an asymptotic modulus of concrete which is an age independent value, $C_d(t, t', t_0)$ is an increase of creep (creep during drying), and $C_p(t, t', t_0)$ is a decrease of creep (creep after drying).

The shrinkage equation from Bazant and Panula (1980) is,

$$\varepsilon_{sh} = \varepsilon_{sh\infty}\, k_h\, S\left(\hat{t}/\tau_{sh}\right) \tag{A.32}$$

$$\varepsilon_{sh\infty} = \varepsilon_{s\infty}\frac{E(7+600)}{E(t_0+\tau_{sh})} \tag{A.33}$$

where $\varepsilon_{sh\infty}$ is the ultimate shrinkage strain, E is Young's modulus, τ_{sh} is shrinkage square root half time which can consider the size dependency which is the function of cross-section shape and effective cross-section thickness, $\hat{t}$ is the duration of drying, k_h is a function of ambient humidity, which can be obtained from $1 - h^3$ for $h \le 0.98$, and -0.2 for ($h = 1$ [swelling in water]), and linear interpolation for $0.98 \le h \le 1$. h is the relative humidity in decimal number ($0 \le h \le 1$), and $S\left(\hat{t}/\tau_{sh}\right)$ is the time function for shrinkage.

A.6 B3 Model (1996)

The B3 model is the equation simplified based on the BP and BP-KX models proposed by Bazant and Baweja (1995). The B3 model is a more rational and theoretical formulation based on extensive data points. The B3 model is justified and refined based on the data set of the RILEM Data Bank (Bazant and Baweja 1995). The B3 model was proposed by Bazant and Baweja (2000). When a constant stress, σ, is applied at time, *t'*, the creep is linearly dependent on the stress. The fundamental equation for the long-term concrete strain can be expressed as follows:

$$\varepsilon(t) = J(t,t')\,\sigma + \varepsilon_{sh}(t) + \alpha\,\Delta T(t) \tag{A.34}$$

where σ is the uniaxial stress, ε is the strain, $\varepsilon_{sh}(t)$ is the shrinkage strain at time, t, $\Delta T(t)$ is the temperature change from reference temperature at time, t, and α is the thermal expansion coefficient. The compliance function, $J(t, t')$, which represents the creep function (elastic and creep strain) due to unit axial constant stress applied at time t' can be decomposed as the following equation:

$$J(t,t') = q_1 + C_0(t,t') + C_d(t,t',t_0) \tag{F.35}$$

where q_1 is the instantaneous elastic strain per unit stress, $C_0(t, t')$ is the basic creep strain per unit stress, and $C_d(t, t', t_0)$ is the drying creep strain per unit stress detailed in Bazant and Baweja (2000). This model was also developed based on the following limitations for the compressive strength and cement paste. The compressive strength should be between 2.5 and 10 ksi (10 and 69 MPa) and cement content ranges between 270 and 1215 lb/yd^3 (160 and 720 kg/m^3).

The shrinkage strain can be calculated from the following expression:

$$\varepsilon_{sh} = -\varepsilon_{sh\infty}\,k_h\,S(\hat{t}) \tag{A.36}$$

where $\varepsilon_{sh\infty}$ is the ultimate shrinkage strain (Equation A.33), $\hat{t}$ is the duration of drying (days), k_h is function of ambient humidity, and $S(\hat{t})$ is the time function for shrinkage.

A.7 GL 2000 Model (2001)

The GL 2000 model was the updated version based on previous GZ model proposed by Gardner and Zhao (1993). The GL 2000 model was influenced by the CEB-FIP model. This model was developed for normal strength concrete which has a 28-day compressive strength less than 12 ksi (82 MPa) and a *w/c* between 0.4 and 0.6 (Gardner and Lockman 2001).

The creep coefficient, $\phi(t)$ can be calculated as following equation:

$$\phi(t)=\phi(t_c)\left[\begin{array}{l} 2\left(\dfrac{(t-t_0)^{0.3}}{(t-t_0)^{0.3}+14}\right)+\left(\dfrac{7}{t_0}\right)^{0.5}\left(\dfrac{t-t_0}{t-t_0+7}\right)^{0.5} \\ +2.5\left(1-1.086h^2\right)\left(\dfrac{t-t_0}{t-t_0+0.15(V/S)^2}\right)^{0.5} \end{array}\right] \tag{A.37}$$

If $t_0=t_c$, $\phi(t_c)=1$ when $t_0>t_c$

$$\phi(t_c)=\left[1-\left(\frac{t_0-t_c}{t_0-t_c+0.15\,(V/S)^2}\right)^{0.5}\right]^{0.5} \tag{A.38}$$

where t_0 is the age of concrete at loading (days), t_c is the age of concrete after drying (days), $\phi(t_c)$ is the function to account drying before loading, and *V/S* is the volume-to-surface ratio (in.).

The shrinkage strain, ε_{sh} can be calculated with following equation:

$$\varepsilon_{sh}=\varepsilon_{shu}\,\beta(h)\,\beta(t) \tag{A.39}$$

$$\varepsilon_{shu}=1000\,K\left(\frac{4350}{f_c'}\right)^{0.5}10^{-6} \tag{A.40}$$

$$\beta(t) = \left(\frac{t - t_c}{t - t_c + 97\,(V/S)^2} \right)^{0.5} \tag{A.41}$$

$$\beta(h) = 1 - 1.18\,h^4 \tag{A.42}$$

where ε_{shu} is the nominal ultimate shrinkage strain, $\beta(h)$ is the term to consider the humidity, $\beta(t)$ is the term to consider the effect of time, t_c is the age drying commenced (days), and f'_c is the compressive strength at 28 days (ksi). K is the coefficient for type of cement. K is 1.0 for Type I cement, 0.7 for Type II cement, and 1.15 for Type III cement. h is the relative humidity in decimal.

APPENDIX B
THEORETICAL A_X AND A_Y FOR AGGREGATE INTERLOCK

The equations to estimate the contact areas on the crack plane are presented in this section. In this study, these equations were solved by using the Program Maple (Version 11).

Walraven's theoretical formula is as follows:

$$\sigma = \sigma_{pu}\,(\bar{A}_x - \mu\bar{A}_y) \tag{B.1}$$

$$\tau = \sigma_{pu}\,(\bar{A}_x + \mu\bar{A}_y) \tag{B.2}$$

where A_x and A_y depend on the crack width, w, the crack slip, Δ, the maximum aggregate size, D_{max}, and total aggregate volume per unit volume of concrete, p_x, σ_{pu} is the matrix yielding strength; $\sigma_{pu} = 6.39\, f_{cc}^{'0.56}$ (ksi) from Walraven. A_x and A_y are projected contact area between spherical aggregate and paste matrix. This values change with different geometrical conditions such as crack slip, crack width, and the maximum aggregate size, D_{max}. The derivations of A_x and A_y are presented in Walraven's reports. The derivations are briefly presented as follows:

Case A : $\Delta < w$ (B.3)

$$A_y = \int_{\Delta}^{\frac{D_{\max}}{w^2+\Delta^2}} p_k \frac{4}{\pi} F\left(\frac{D}{D_{\max}}\right) G_1(\Delta, w, D)\, dD$$

$$A_x = \int_{\Delta}^{\frac{D_{\max}}{w^2+\Delta^2}} p_k \frac{4}{\pi} F\left(\frac{D}{D_{\max}}\right) G_2(\Delta, w, D)\, dD$$

Case B : $\Delta > w$ (B.4)

$$A_y = \int_{2w}^{\frac{w^2+\Delta^2}{w}} p_k \frac{4}{\pi} F\left(\frac{D}{D_{\max}}\right) G_3(\Delta, w, D)\, dD + \int_{\frac{w^2+\Delta^2}{w}}^{\frac{D_{\max}}{w}} p_k \frac{4}{\pi} F\left(\frac{D}{D_{\max}}\right) G_1(\Delta, w, D)\, dD$$

$$A_x = \int_{2w}^{\frac{w^2+\Delta^2}{w}} p_k \frac{4}{\pi} F\left(\frac{D}{D_{\max}}\right) G_4(\Delta, w, D)\, dD + \int_{\frac{w^2+\Delta^2}{w}}^{\frac{D_{\max}}{w}} p_k \frac{4}{\pi} F\left(\frac{D}{D_{\max}}\right) G_1(\Delta, w, D)\, dD$$

with

$$G_1(\Delta, w, D) = D^{-3}\left(\sqrt{D^2-(w^2+\Delta^2)}\,\frac{\Delta}{\sqrt{w^2+\Delta^2}}\,u_{\max} - w\,u_{\max} - u_{\max}^2\right)$$

$$G_2(\Delta, w, D) = D^{-3}\left(\begin{array}{l}\Delta - \sqrt{D^2-(w^2+\Delta^2)}\,\dfrac{w}{\sqrt{w^2+\Delta^2}}\,u_{\max} + (u_{\max}+w)\sqrt{\dfrac{1}{4}D^2-(w+u_{\max})^2} \\ -w\sqrt{\dfrac{1}{4}D^2-w^2} + \dfrac{1}{4}D^2\arcsin\dfrac{w+u_{\max}}{\frac{1}{2}D} - \dfrac{D^2}{4}\arcsin\dfrac{2w}{D}\end{array}\right)$$

$$G_3(\Delta, w, D) = D^{-3}\left(\frac{1}{2}D - w\right)^2$$

$$G_4(\Delta, w, D) = D^{-3}\left(\frac{\pi}{8}D^2 - w\sqrt{\frac{1}{4}D^2 - w^2} - \frac{D^2}{4}\arcsin\frac{2w}{D}\right)$$

APPENDIX C
E-VALUES FOR EVALUATING AGGREGATE INTERLOCK

This section presents the summary of E-values for estimating absorbed energy. Tables C.1 and C.2 show the summary of E-values for river gravel and limestone mixtures, respectively. The information is the data set for the statistical analysis to analyze the effects of key parameters for evaluating aggregate interlock.

Table C.1. River Gravel SCC and CC Mixtures.

ID	Mixture	Vol.CA	Batch #	Sam. #	δ 1 (slip, mm)	δ 2 (slip, mm)	δ 3 (slip, mm)	δ 4 (slip, mm)	δ 5 (slip, mm)	δ 6 (slip, mm)	E1 (Energy)	E2 (Energy)	E3 (Energy)	E4 (Energy)	E5 (Energy)	E6 (Energy)	f'_c (psi)	f_t (psi)	Pre (kip)
PA3a_1RA	SR5/31.5	31.5	1	1	0.5	0.7	1.0	2.0	4.0	5.5	4.07	3.30	2.67	1.86	1.42	1.28	12414	915	46.0
PA3a_1RB	SR5/31.5	31.5	1	2	0.5	0.7	1.0	2.0	4.0	5.5	3.17	2.67	2.24	1.62	1.28	1.16	12414	915	41.0
PA3a_2RB	SR5/31.5	31.5	2	3	0.5	0.7	1.0	2.0	4.0	5.5	2.74	2.44	2.15	1.64	1.28	1.17	12130	905	39.6
PA3b_1RA	SR5/34.6	34.6	3	4	0.5	0.7	1.0	2.0	4.0	5.5	3.91	3.16	2.56	1.81	1.40	1.28	12393	966	26.9
PA3b_1RB	SR5/34.6	34.6	3	5	0.5	0.7	1.0	2.0	4.0	5.5	3.43	2.85	2.39	1.71	1.34	1.22	12393	966	40.8
PA3b_2RB	SR5/34.6	34.6	4	6	0.5	0.7	1.0	2.0	4.0	5.5	3.35	2.80	2.31	1.71	1.32	1.19	11632	804	36.3
PA3c_1RA	SR5/37.8	37.8	5	7	0.5	0.7	1.0	2.0	4.0	5.5	4.09	3.22	2.52	1.77	1.37	1.25	12186	947	38.5
PA3c_1RB	SR5/37.8	37.8	5	8	0.5	0.7	1.0	2.0	4.0	5.5	2.99	2.60	2.24	1.66	1.30	1.19	12186	947	45.4
PA3c_2RA	SR5/37.8	37.8	6	9	0.5	0.7	1.0	2.0	4.0	5.5	3.95	3.26	2.67	1.84	1.40	1.28	11462	974	38.6
PA4_1RA	SR7/32.3	32.3	7	10	0.5	0.7	1.0	2.0	4.0	5.5	2.58	2.22	1.89	1.44	1.14	1.05	14690	1089	45.6
PA4_1RB	SR7/32.3	32.3	7	11	0.5	0.7	1.0	2.0	4.0	5.5	2.96	2.52	2.14	1.60	1.23	1.10	14690	1089	43.8
PA4_2RB	SR7/32.3	32.3	8	12	0.5	0.7	1.0	2.0	4.0	5.5	2.62	2.24	1.90	1.46	1.16	1.06	14860	1227	43.1
PA5_1A	SR7/35	35	9	13	0.5	0.7	1.0	2.0	4.0	5.5	3.17	2.65	2.18	1.56	1.20	1.16	15167	1088	36.7
PA5_1B	SR7/35	35	9	14	0.5	0.7	1.0	2.0	4.0	5.5	3.54	3.17	2.65	1.83	1.34	1.19	15167	1088	41.4
PA5_2B	SR7/35	35	10	15	0.5	0.7	1.0	2.0	4.0	5.5	2.79	2.47	2.12	1.56	1.25	1.15	15539	1046	43.6
PA6_1A	SR7/37.6	37.6	11	16	0.5	0.7	1.0	2.0	4.0	5.5	4.71	3.53	2.65	1.73	1.28	1.16	16008	970	39.8
PA6_1B	SR7/37.6	37.6	11	17	0.5	0.7	1.0	2.0	4.0	5.5	2.65	2.40	2.13	1.63	1.27	1.17	16008	970	38.3
PA6_2B	SR7/37.6	37.6	12	18	0.5	0.7	1.0	2.0	4.0	5.5	2.59	2.35	2.07	1.48	1.16	1.08	16072	967	47.0
CG1_1A	CR5/44.3	44.3	13	19	0.5	0.7	1.0	2.0	4.0	5.5	3.44	3.00	2.55	1.77	1.27	1.14	10353	961	39.5
CG1_1B	CR5/44.3	44.3	13	20	0.5	0.7	1.0	2.0	4.0	5.5	3.98	3.42	2.91	2.00	1.38	1.20	10353	961	44.4
CG1_2A	CR5/44.3	44.3	14	21	0.5	0.7	1.0	2.0	4.0	5.5	5.75	4.36	3.42	2.12	1.49	1.32	10449	973	41.6
CG2_1A	CR7/44.3	44.3	15	22	0.5	0.7	1.0	2.0	4.0	5.5	3.18	2.81	2.44	1.87	1.32	0.95	12552	1004	45.2
CG2_1B	CR7/44.3	44.3	15	23	0.5	0.7	1.0	2.0	4.0	5.5	3.76	3.04	2.54	1.81	1.34	1.18	12552	1004	52.7
CG2_2B	CR7/44.3	44.3	16	24	0.5	0.7	1.0	2.0	4.0	5.5	2.42	2.21	1.97	1.55	1.24	1.14	11345	1020	53.9

Note: Pre = Precracking load.

Table C.2. Limestone SCC and CC Mixtures.

ID	Mixture	Vol.CA	Batch #	Sam. #	δ 1 (slip, mm)	δ 2 (slip, mm)	δ 3 (slip, mm)	δ 4 (slip, mm)	δ 5 (slip, mm)	δ 6 (slip, mm)	E1 (Energy)	E2 (Energy)	E3 (Energy)	E4 (Energy)	E5 (Energy)	E6 (Energy)	f'_c (psi)	f_t (psi)	Pre (kip)
PB3a_1B	SL5/29.0	29	17	25	0.5	0.7	1.0	2.0	4.0	5.5	2.07	1.80	1.59	1.30	1.10	1.04	14274	958	31.8
PB3a_1A	SL5/29.0	29	18	26	0.5	0.7	1.0	2.0	4.0	5.5	2.24	2.01	1.81	1.50	1.27	1.20	14274	958	27.6
PB3a_2B	SL5/29.0	29	17	27	0.5	0.7	1.0	2.0	4.0	5.5	1.76	1.62	1.48	1.26	1.08	1.01	14207	879	31.5
PB3b_1A	SL5/31.9	31.9	19	28	0.5	0.7	1.0	2.0	4.0	5.5	1.47	1.42	1.34	1.17	1.04	0.99	13441	831	34.8
PB3b_1B	SL5/31.9	31.9	19	29	0.5	0.7	1.0	2.0	4.0	5.5	2.03	1.79	1.57	1.28	1.08	1.02	13441	831	32.6
PB3b_2A	SL5/31.9	31.9	20	30	0.5	0.7	1.0	2.0	4.0	5.5	1.71	1.59	1.47	1.28	1.11	1.06	13345	973	32.6
PB3c_1B	SL5/34.8	34.8	21	31	0.5	0.7	1.0	2.0	4.0	5.5	2.24	1.90	1.61	1.25	1.04	0.98	13297	885	32.4
PB3c_2A	SL5/34.8	34.8	22	32	0.5	0.7	1.0	2.0	4.0	5.5	2.10	1.80	1.58	1.25	1.04	1.00	12910	810	34.4
PB3c_1A	SL5/34.8	34.8	21	33	0.5	0.7	1.0	2.0	4.0	5.5	2.38	2.00	1.70	1.35	1.12	1.05	13297	885	31.9
PB4_1A	SL7/31.9	31.9	23	34	0.5	0.7	1.0	2.0	4.0	5.5	2.05	1.80	1.59	1.28	1.07	1.01	15711	1244	36.7
PB4_1B	SL7/31.9	31.9	23	35	0.5	0.7	1.0	2.0	4.0	5.5	1.97	1.73	1.53	1.27	1.11	1.05	15711	1244	28.8
PB4_2B	SL7/31.9	31.9	24	36	0.5	0.7	1.0	2.0	4.0	5.5	1.92	1.85	1.56	1.20	1.02	0.97	15014	988	36.7
PB5_1A	SL7/34.5	34.5	25	37	0.5	0.7	1.0	2.0	4.0	5.5	1.72	1.62	1.51	1.28	1.06	1.00	15817	975	38.4
PB5_2B	SL7/34.5	34.5	26	38	0.5	0.7	1.0	2.0	4.0	5.5	1.62	1.50	1.39	1.20	1.04	0.98	16311	1134	34.9
PB5_1A	SL7/34.5	34.5	25	39	0.5	0.7	1.0	2.0	4.0	5.5	2.01	1.82	1.63	1.30	1.09	1.02	15817	975	32.6
PB6_1A	SL7/37	37	27	40	0.5	0.7	1.0	2.0	4.0	5.5	1.90	1.72	1.54	1.27	1.07	1.00	15221	878	35.6
PB6_1B	SL7/37	37	27	41	0.5	0.7	1.0	2.0	4.0	5.5	2.03	1.80	1.57	1.26	1.06	1.01	15221	878	35.2
PB6_2B	SL7/37	37	28	42	0.5	0.7	1.0	2.0	4.0	5.5	1.98	1.77	1.59	1.32	1.13	1.06	15412	880	33.4
CL1_2A	CL5/40.1	40.1	29	43	0.5	0.7	1.0	2.0	4.0	5.5	3.29	2.70	2.19	1.54	1.21	1.11	10316	764	31.6
CL1_2B	CL5/40.1	40.1	29	44	0.5	0.7	1.0	2.0	4.0	5.5	2.42	2.12	1.84	1.43	1.19	1.10	10316	764	33.8
CL1_1A	CL5/40.1	40.1	30	45	0.5	0.7	1.0	2.0	4.0	5.5	2.76	2.36	2.01	1.56	1.27	1.16	8143	820	30.8
CL2_1B	CL7/40.1	40.1	31	46	0.5	0.7	1.0	2.0	4.0	5.5	3.25	2.46	1.90	1.29	0.96	0.87	13345	1001	34.4
CL2_1A	CL7/40.1	40.1	31	47	0.5	0.7	1.0	2.0	4.0	5.5	5.16	3.68	2.66	1.69	1.25	1.12	13345	1001	38.0
CL2_2B	CL7/40.1	40.1	32	48	0.5	0.7	1.0	2.0	4.0	5.5	3.38	2.70	2.11	1.45	1.15	1.06	13510	979	28.6

Note: Pre = Precracking load.

APPENDIX D
STATISTICAL ANALYSIS FOR SHEAR CHARACTERISTICS

This section show the source file to analyze the data to evaluate the effect of key parameters.

D. 1 Statistical Analysis for Effect of Volume of Coarse Aggregate at Individual Crack Slip

```
* proc mixed procedure;

* separate analyses for each delta;

* set up for HTML ouput;
ods html; ods graphics on;


*  each mix has two batches, one with 2 samples and the other with 1;
* samples are measured repeatedly (6 times here), once for each value of delta;

data SHEAR1; array w w1-w3; array d d1-d3; array n n1-n3; array s s1-s3; array x x1-x3; array y y1-y3; array z z1-z3; array w w1-w3;
array c c1-c3; array m m1-m3;
input mix $ agg $ vol batch $ sample $ w1-w3 d1-d3 n1-n3 s1-s3 x1-x3 y1-y3 paste z1-z3 w1-w3 comp c1-c3 m1-m3;
* agg=aggregate type com=avg. compressive strength, split=avg. splitting tensile strength, pre=precracking load;
do over e; energy=e; delta=d; output; end;
drop d1-d6 e1-e6;
cards;


;;;

proc print;

proc sort; by delta;
proc mixed method=reml cl covtest; by delta;
class mix batch sample delta;
model energy = mix;
random batch(mix);
lsmeans mix/adjust=tukey;

estimate 'agg R' intercept 1 mix .125 .125 .125 .125 .125 .125 .125 .125 0 0 0 0 0 0 0 0;
estimate 'agg L' intercept 1 mix  0 0 0 0 0 0 0 0 .125 .125 .125 .125 .125 .125 .125 .125;
estimate 'agg R - agg L' intercept 0 mix  .125 .125 .125 .125 .125 .125 .125 .125 -.125 -.125 -.125 -.125 -.125 -.125 -.125 -.125;
```

```
estimate 'agg R5SCC at vol 31.5' intercept 1 mix 1 0 0 0 0 0 0 0 0 0 0 0 0 0 0;
estimate 'agg R5SCC at vol 34.6' intercept 1 mix 0 1 0 0 0 0 0 0 0 0 0 0 0 0 0;
estimate 'agg R5SCC at vol 37.8' intercept 1 mix 0 0 1 0 0 0 0 0 0 0 0 0 0 0 0;
estimate 'agg R7SCC at vol 32.3' intercept 1 mix 0 0 0 1 0 0 0 0 0 0 0 0 0 0 0;
estimate 'agg R7SCC at vol 35' intercept 1 mix    0 0 0 0 1 0 0 0 0 0 0 0 0 0 0;
estimate 'agg R7SCC at vol 37.6' intercept 1 mix 0 0 0 0 0 1 0 0 0 0 0 0 0 0 0;
estimate 'agg R5CC at vol 44.3' intercept 1 mix 0 0 0 0 0 0 1 0 0 0 0 0 0 0 0;
estimate 'agg R7CC at vol 44.3' intercept 1 mix 0 0 0 0 0 0 0 1 0 0 0 0 0 0 0;
estimate 'agg L5SCC at vol 29' intercept 1 mix    0 0 0 0 0 0 0 0 1 0 0 0 0 0 0;
estimate 'agg L5SCC at vol 31.9' intercept 1 mix 0 0 0 0 0 0 0 0 0 1 0 0 0 0 0;
estimate 'agg L5SCC at vol 34.8' intercept 1 mix 0 0 0 0 0 0 0 0 0 0 1 0 0 0 0;
estimate 'agg L7SCC at vol 31.9' intercept 1 mix 0 0 0 0 0 0 0 0 0 0 0 1 0 0 0;
estimate 'agg L7SCC at vol 34.5' intercept 1 mix 0 0 0 0 0 0 0 0 0 0 0 0 1 0 0;
estimate 'agg L7SCC at vol 37' intercept 1 mix 0 0 0 0 0 0 0 0 0 0 0 0 0 1 0;
estimate 'agg L5CC at vol 40.1' intercept 1 mix 0 0 0 0 0 0 0 0 0 0 0 0 0 0 1;
estimate 'agg L7CC at vol 40.1' intercept 1 mix 0 0 0 0 0 0 0 0 0 0 0 0 0 0 1;
estimate 'vol slope for agg R5 (SCC 31.5(5ar) SCC 34.6 (5br) SCC 37.8 (5cr))' mix -.70334 -.00748 0.710818 0 0 0 0 0 0 0 0 0 0 0 0;
estimate 'vol slope for agg R7 (SCC 32.3(7ar) SCC 35 (7br) SCC 37.6 (7cr))' mix 0 0 0 -.71151 0.008894 0.702618 0 0 0 0 0 0 0 0 0;
estimate 'vol slope for agg L5 (SCC 29(5ar) SCC 31.9 (5br) SCC 34.8 (5cr))' mix 0 0 0 0 0 0 0 0 -.70711 0 0.707107 0 0 0 0;
estimate 'vol slope for agg L7 (SCC 31.9(7ar) SCC 34.5 (7br) SCC 37 (7cr))' mix 0 0 0 0 0 0 0 0 0 0 -.71168 0.009243 0.70244 0 0;
estimate ' vol slope for SG' mix -0.03349 -0.01520 0.00369 -0.02877 -0.01284 0.00251 0.04205 0.04205 0 0 0 0 0 0 0 0;
estimate 'vol slope for LG' mix  0 0 0 0 0 0 0 0 -0.05304 -0.02703 -0.00101 -0.02703 -0.00370 0.01873 0.04654 0.04654;
estimate 'vol*agg with 5abcr, 7abcr, 5abcl, and 5abcl' mix -0.03349 -0.01520 0.00369 -0.02877 -0.01284 0.00251 0.04205 0.04205 0.05304
0.02703 0.00101 0.02703 0.00370 -0.01873 -0.04654 -0.04654;
run;

* close HTML output;
ods graphics off; ods html close;

proc plot;

plot split*comp='+';
plot split*pre='x';
plot comp*pre='*';

run;
* close HTML output;
ods graphics off; ods html close;
```

D. 2 Statistical Analysis for Effect of Volume of Coarse Aggregate Across Crack Slip

```
* repeated measured analyses for each delta;

* set up for HTML ouput;
ods html; ods graphics on;


* each mix has two batches, one with 2 samples and the other with 1;
* the first batch thus has 2 reps at each time, the second only 1;
* samples are measured repeatedly (6 times here), once for each value of delta;


data SHEAR4; array e e1-e6; array d d1-d6;
input mix $ agg $ vol batch $ sample $ d1-d6 e1-e6 comp split pre;
* agg=aggregate type com=avg. compressive strength, split=avg. splitting tensle strength, pre=precracking load;
do over e; energy=e; delta=d; output; end;
drop d1-d6 e1-e6;
cards;
;;;

proc print;
run;

* compare mixes across delta, with interaction;
proc mixed method=reml cl covtest;
class mix batch sample delta;   * order variables consistently with the model;
model energy = mix|delta;
random batch(mix);
repeated delta/subject=sample type=unr r=1;  * subjects must all be labeled differently;

lsmeans mix/adjust=tukey;

estimate 'agg R' intercept 1 mix .125 .125 .125 .125 .125 .125 .125 .125 0 0 0 0 0 0 0 0;
estimate 'agg L' intercept 1 mix  0 0 0 0 0 0 0 0 .125 .125 .125 .125 .125 .125 .125 .125;
estimate 'agg R - agg L' intercept 0 mix  .125 .125 .125 .125 .125 .125 .125 .125 -.125 -.125 -.125 -.125 -.125 -.125 -.125 -.125;
estimate 'agg R5SCC at vol 31.5' intercept 1 mix 1 0 0 0 0 0 0 0 0 0 0 0 0 0 0 0;
estimate 'agg R5SCC at vol 34.6' intercept 1 mix 0 1 0 0 0 0 0 0 0 0 0 0 0 0 0 0;
estimate 'agg R5SCC at vol 37.8' intercept 1 mix 0 0 1 0 0 0 0 0 0 0 0 0 0 0 0 0;
estimate 'agg R7SCC at vol 32.3' intercept 1 mix 0 0 0 1 0 0 0 0 0 0 0 0 0 0 0 0;
estimate 'agg R7SCC at vol 35' intercept 1 mix    0 0 0 0 1 0 0 0 0 0 0 0 0 0 0 0;
estimate 'agg R7SCC at vol 37.6' intercept 1 mix 0 0 0 0 0 1 0 0 0 0 0 0 0 0 0 0;
estimate 'agg R5CC at vol 44.3' intercept 1 mix 0 0 0 0 0 0 1 0 0 0 0 0 0 0 0 0;
estimate 'agg R7CC at vol 44.3' intercept 1 mix 0 0 0 0 0 0 0 1 0 0 0 0 0 0 0 0;
estimate 'agg L5SCC at vol 29' intercept 1 mix    0 0 0 0 0 0 0 0 1 0 0 0 0 0 0 0;
estimate 'agg L5SCC at vol 31.9' intercept 1 mix 0 0 0 0 0 0 0 0 0 1 0 0 0 0 0 0;
estimate 'agg L5SCC at vol 34.8' intercept 1 mix 0 0 0 0 0 0 0 0 0 0 1 0 0 0 0 0;
```

```
estimate 'agg L7SCC at vol 31.9' intercept 1 mix 0 0 0 0 0 0 0 0 0 0 1 0 0 0 0;
estimate 'agg L7SCC at vol 34.5' intercept 1 mix 0 0 0 0 0 0 0 0 0 0 0 1 0 0 0;
estimate 'agg L7SCC at vol 37' intercept 1 mix 0 0 0 0 0 0 0 0 0 0 0 0 1 0 0;
estimate 'agg L5CC at vol 40.1' intercept 1 mix 0 0 0 0 0 0 0 0 0 0 0 0 0 1 0;
estimate 'agg L7CC at vol 40.1' intercept 1 mix 0 0 0 0 0 0 0 0 0 0 0 0 0 0 1;
estimate 'vol slope for agg R5 (SCC 31.5(5ar) SCC 34.6 (5br) SCC 37.8 (5cr))' mix -.70334 -.00748 0.710818 0 0 0 0 0 0 0 0 0 0 0 0;
estimate 'vol slope for agg R7 (SCC 32.3(7ar) SCC 35 (7br) SCC 37.6 (7cr))' mix 0 0 0 -.71151 0.008894 0.702618 0 0 0 0 0 0 0 0 0;
estimate 'vol slope for agg L5 (SCC 29(5ar) SCC 31.9 (5br) SCC 34.8 (5cr))' mix 0 0 0 0 0 0 0 0 -.70711 0 0.707107 0 0 0 0;
estimate 'vol slope for agg L7 (SCC 31.9(7ar) SCC 34.5 (7br) SCC 37 (7cr))' mix 0 0 0 0 0 0 0 0 0 0 0 -.71168 0.009243 0.70244 0 0;
estimate ' vol slope for SG' mix -0.03349 -0.01520 0.00369 -0.02877 -0.01284 0.00251 0.04205 0.04205 0 0 0 0 0 0 0 0;
estimate 'vol slope for LG' mix  0 0 0 0 0 0 0 0 -0.05304 -0.02703 -0.00101 -0.02703 -0.00370 0.01873 0.04654 0.04654;
estimate 'vol*agg with 5abcr, 7abcr, 5abcl, and 5abcl' mix -0.03349 -0.01520 0.00369 -0.02877 -0.01284 0.00251 0.04205 0.04205 0.05304
0.02703 0.00101 0.02703 0.00370 -0.01873 -0.04654 -0.04654;

run;
* repeat above but assume toeplitz correlation structure (although this probably is
     not appropriate for unequally spaced deltas);
proc mixed method=reml cl covtest;
class mix batch sample delta;   * order variables consistently with the model;
model energy = mix|delta;
random batch(mix);
repeated delta/subject=sample type=toeph r=1;  * subjects must all be labeled differently;

run;


* close HTML output;
ods graphics off; ods html close;
```

D. 3 Statistical Analysis Friction Factor and Fracture Reduction Factor

```
* separate analyses for each width;

* set up for HTML ouput;
ods html; ods graphics on;


* each mix has two batches, one with 2 samples and the other with 1;
* samples are measured repeatedly (3 times here), once for each value of width;

data SHEAR1; array w w1-w3; array d d1-d3; array n n1-n3; array s s1-s3; array x x1-x3; array y y1-y3; array z z1-z3; array a a1-a3;
array c c1-c3; array m m1-m3;
input mix $ agg $ vol batch $ sample $ w1-w3 d1-d3 n1-n3 s1-s3 x1-x3 y1-y3 paste z1-z3 a1-a3 comp c1-c3 cm1-cm3 m1-m3;
* agg=aggregate type com=avg. compressive strength,n=normal stress, s=shear stress, x=Ax, y=Ay, paste=paste strength, z=c*paste,
a=c*m*paste, c=fracture factor, m=firction factor;
If sample =20 then delete;If sample =22 then delete;
do over c; fracture =c; friction=m; width=w; output; end;
drop w1-w3 d1-d3 n1-n3 s1-s3 x1-x3 y1-y3 z1-z3 a1-a3 c1-c3 cm1-cm3 m1-m3;
cards;

;;;

proc print;

proc sort; by width;
proc mixed method=reml cl covtest; by width;
class mix batch sample width;
model fracture = mix;
*model friction = mix;
random batch(mix);
lsmeans mix/adjust=tukey;

estimate 'All' intercept 1 mix .0625 .0625 .0625 .0625 .0625 .0625 .0625 .0625 .0625 .0625 .0625 .0625 .0625 .0625 .0625 .0625;
estimate 'agg R' intercept 1 mix .125 .125 .125 .125 .125 .125 .125 .125 0 0 0 0 0 0 0 0;
estimate 'agg L' intercept 1 mix  0 0 0 0 0 0 0 0 .125 .125 .125 .125 .125 .125 .125 .125;
estimate 'agg R - agg L' intercept 0 mix  .125 .125 .125 .125 .125 .125 .125 .125 -.125 -.125 -.125 -.125 -.125 -.125 -.125 -.125;
estimate 'agg SR' intercept 1 mix .166667 .166667 .166667 .166667 .166667 .166667 0 0 0 0 0 0 0 0 0 0;
estimate 'agg SL' intercept 1 mix  0 0 0 0 0 0 0 0 .166667 .166667 .166667 .166667 .166667 .166667 0 0;
estimate 'agg CR' intercept 1 mix 0 0 0 0 0 0 0.5 0.5 0 0 0 0 0 0 0 0;
estimate 'agg CL' intercept 1 mix 0 0 0 0 0 0 0 0 0 0 0 0 0 0 0.5 0.5;
estimate ' SCC' intercept 1 mix .083333 .083333 .083333 .083333 .083333 .083333 0 0  .083333 .083333 .083333 .083333 .083333 .083333 0
0;
estimate 'CC' intercept 1 mix 0 0 0 0 0 0 .25 .25 0 0 0 0 0 0 .25 .25;
estimate 'SCC-CC' intercept 1 mix .083333 .083333 .083333 .083333 .083333 .083333 -.25 -.25 .083333 .083333 .083333 .083333 .083333
.083333 -.25 -.25;
*estimate 'agg R5SCC at vol 31.5' intercept 1 mix 1 0 0 0 0 0 0 0 0 0 0 0 0 0 0 0;
```

```
*estimate ‘agg R5SCC at vol 34.6’ intercept 1 mix 0 1 0 0 0 0 0 0 0 0 0 0 0 0 0 0;
*estimate ‘agg R5SCC at vol 37.8’ intercept 1 mix 0 0 1 0 0 0 0 0 0 0 0 0 0 0 0 0;
*estimate ‘agg R7SCC at vol 32.3’ intercept 1 mix 0 0 0 1 0 0 0 0 0 0 0 0 0 0 0 0;
*estimate ‘agg R7SCC at vol 35’ intercept 1 mix    0 0 0 0 1 0 0 0 0 0 0 0 0 0 0 0;
*estimate ‘agg R7SCC at vol 37.6’ intercept 1 mix 0 0 0 0 0 1 0 0 0 0 0 0 0 0 0 0;
*estimate ‘agg R5CC at vol 44.3’ intercept 1 mix 0 0 0 0 0 0 1 0 0 0 0 0 0 0 0 0;
*estimate ‘agg R7CC at vol 44.3’ intercept 1 mix 0 0 0 0 0 0 0 1 0 0 0 0 0 0 0 0;
*estimate ‘agg L5SCC at vol 29’ intercept 1 mix    0 0 0 0 0 0 0 0 1 0 0 0 0 0 0 0;
*estimate ‘agg L5SCC at vol 31.9’ intercept 1 mix 0 0 0 0 0 0 0 0 0 1 0 0 0 0 0 0;
*estimate ‘agg L5SCC at vol 34.8’ intercept 1 mix 0 0 0 0 0 0 0 0 0 0 1 0 0 0 0 0;
*estimate ‘agg L7SCC at vol 31.9’ intercept 1 mix 0 0 0 0 0 0 0 0 0 0 0 1 0 0 0 0;
*estimate ‘agg L7SCC at vol 34.5’ intercept 1 mix 0 0 0 0 0 0 0 0 0 0 0 0 1 0 0 0;
*estimate ‘agg L7SCC at vol 37’ intercept 1 mix 0 0 0 0 0 0 0 0 0 0 0 0 0 1 0 0;
*estimate ‘agg L5CC at vol 40.1’ intercept 1 mix 0 0 0 0 0 0 0 0 0 0 0 0 0 0 1 0;
*estimate ‘agg L7CC at vol 40.1’ intercept 1 mix 0 0 0 0 0 0 0 0 0 0 0 0 0 0 0 1;
*estimate ‘vol slope for agg R5 (SCC 31.5(5ar) SCC 34.6 (5br) SCC 37.8 (5cr))’ mix -.70334 -.00748 0.710818 0 0 0 0 0 0 0 0 0 0 0 0 0;
*estimate ‘vol slope for agg R7 (SCC 32.3(7ar) SCC 35 (7br) SCC 37.6 (7cr))’ mix 0 0 0 -.71151 0.008894 0.702618 0 0 0 0 0 0 0 0 0 0;
*estimate ‘vol slope for agg L5 (SCC 29(5ar) SCC 31.9 (5br) SCC 34.8 (5cr))’ mix 0 0 0 0 0 0 0 0 -.70711 0 0.707107 0 0 0 0 0;
*estimate ‘vol slope for agg L7 (SCC 31.9(7ar) SCC 34.5 (7br) SCC 37 (7cr))’ mix 0 0 0 0 0 0 0 0 0 0 0 -.71168 0.009243 0.70244 0 0;
estimate ‘ vol slope for SG’ mix -0.03349 -0.01520 0.00369 -0.02877 -0.01284 0.00251 0.04205 0.04205 0 0 0 0 0 0 0 0;
estimate ‘vol slope for LG’ mix  0 0 0 0 0 0 0 0 -0.05304 -0.02703 -0.00101 -0.02703 -0.00370 0.01873 0.04654 0.04654;
estimate ‘vol*agg with 5abcr, 7abcr, 5abcl, and 5abcl’ mix -0.03349 -0.01520 0.00369 -0.02877 -0.01284 0.00251 0.04205 0.04205 0.05304
0.02703 0.00101 0.02703 0.00370 -0.01873 -0.04654 -0.04654;
run;

* close HTML output;
ods graphics off; ods html close;

proc plot;

plot fracture*comp=‘+’;
plot friction*comp=‘x’;
*plot comp*pre=‘*’;

run;
* close HTML output;
ods graphics off; ods html close;
```

APPENDIX E
STRAINS OF CHANNELS FOR CREEP

This section provides the data of each channel. These data were used to evaluate the creep of SCC and CC in this study. Figures E.1 – E.8 show the creep and shrinkage data of each mixture.

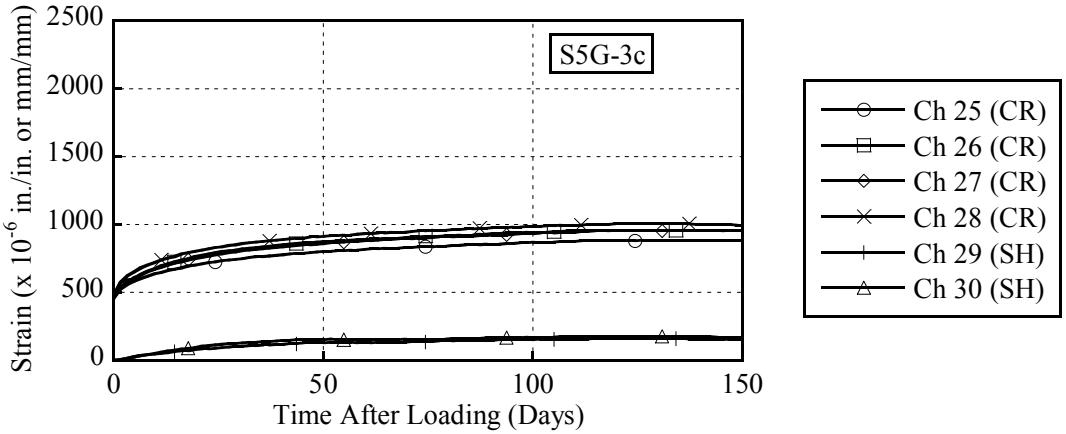

Figure E.1. Creep and Shrinkage for Batches S5G-3c.

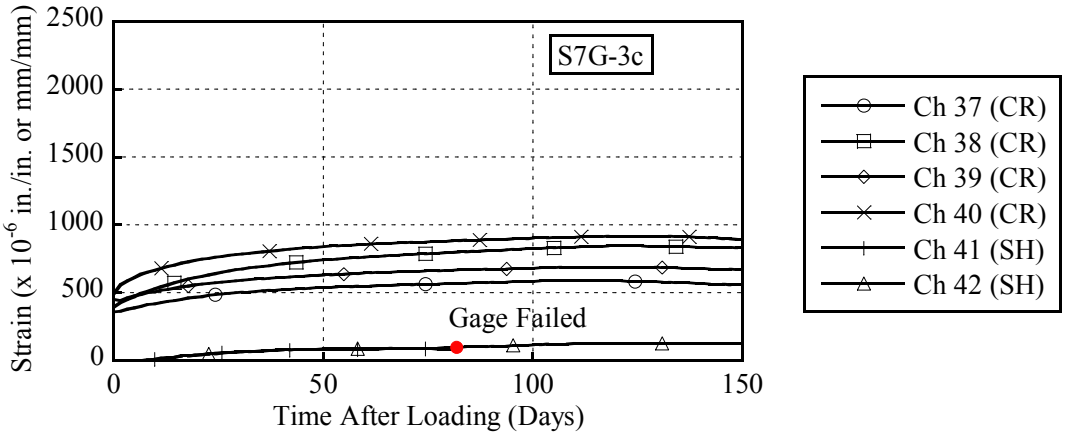

Figure E.2. Creep and Shrinkage for Batches S7G-3c.

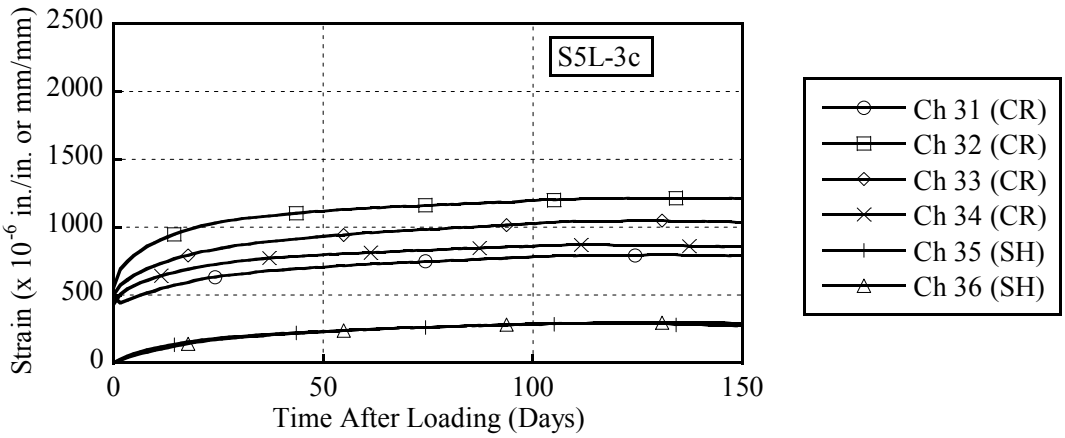

Figure E.3. Creep and Shrinkage for Batches S5L-3c.

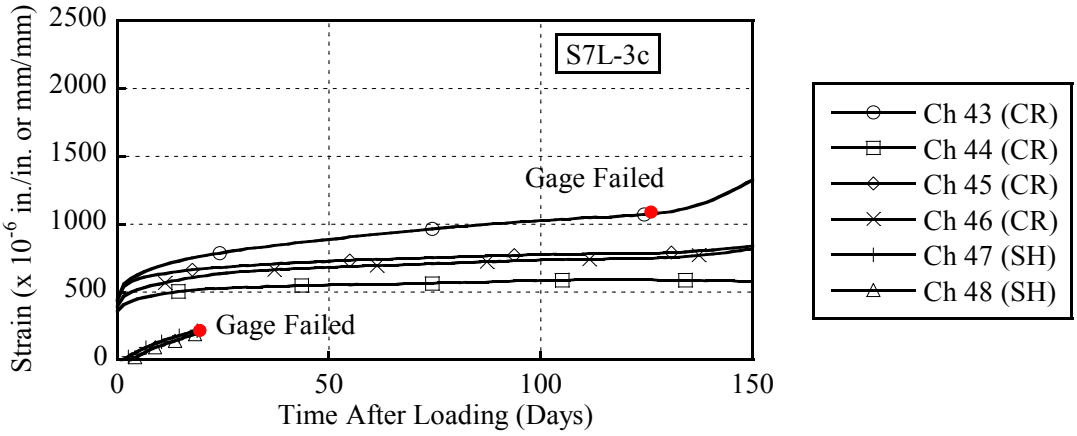

Figure E.4. Creep and Shrinkage for Batches S7L-3c.

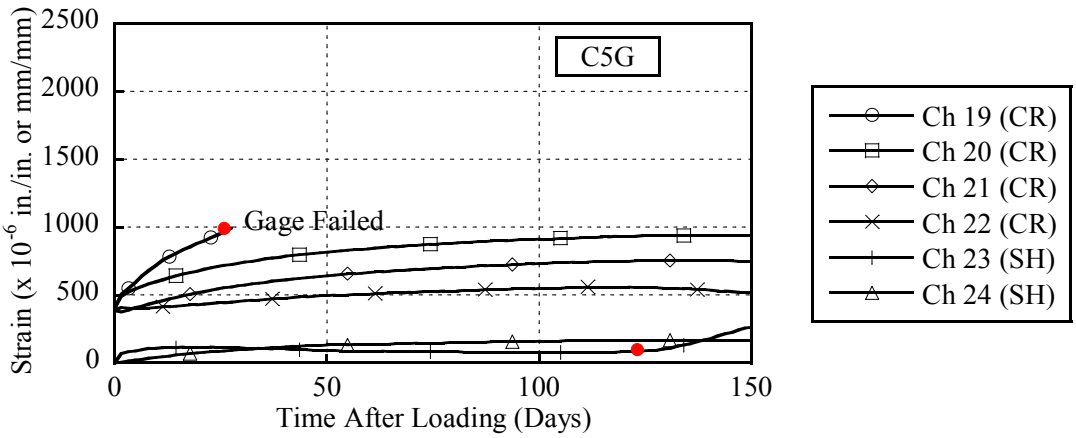

Figure E.5. Creep and Shrinkage for Batches C5G.

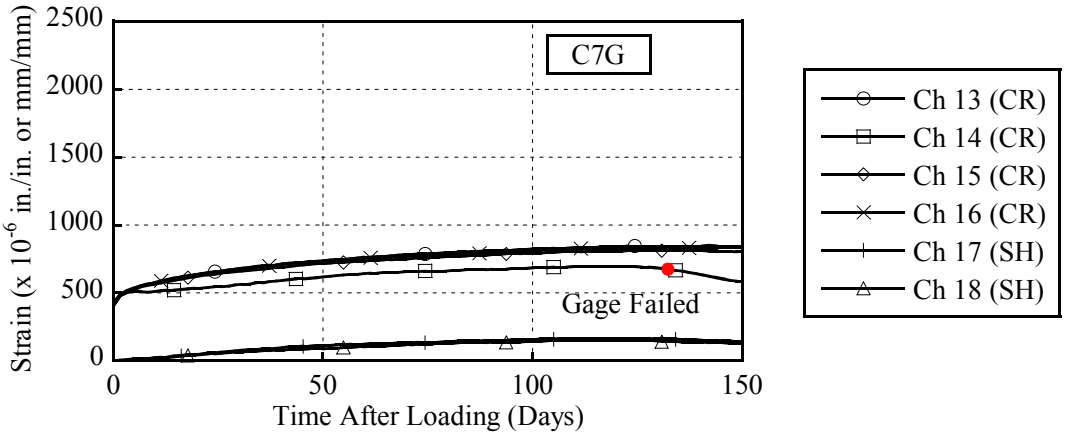

Figure E.6. Creep and Shrinkage for Batches C7G.

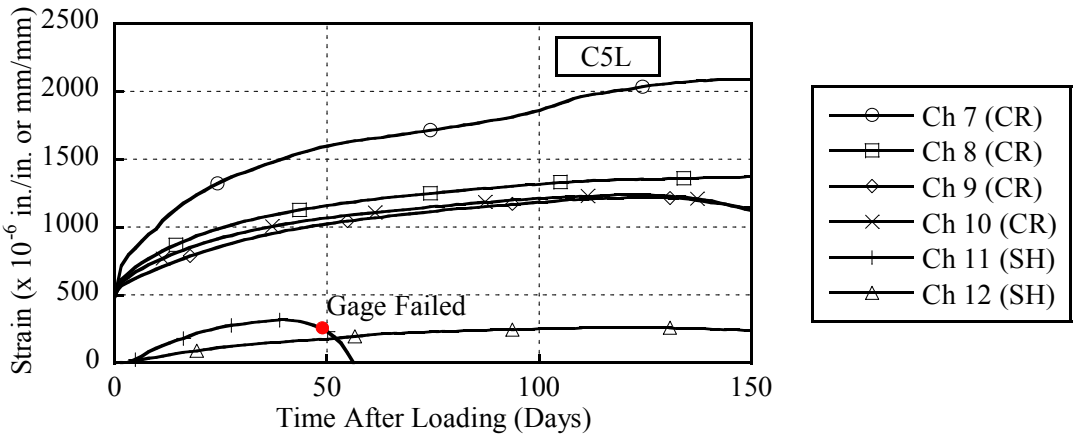

Figure E.7 Creep and Shrinkage for Batches C5L.

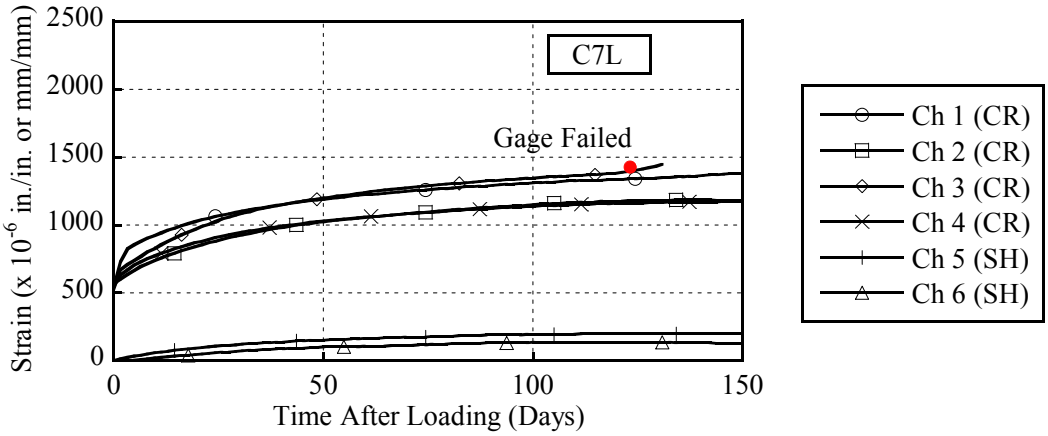

Figure E.8. Creep and Shrinkage for Batches C7L.

APPENDIX F
COMPARISONS OF CREEP

This section provides the comparisons between two mixtures to compare the effect of key parameters. Figure F.1 shows the comparisons between creep of different mixtures having different target strength at 16 hours.

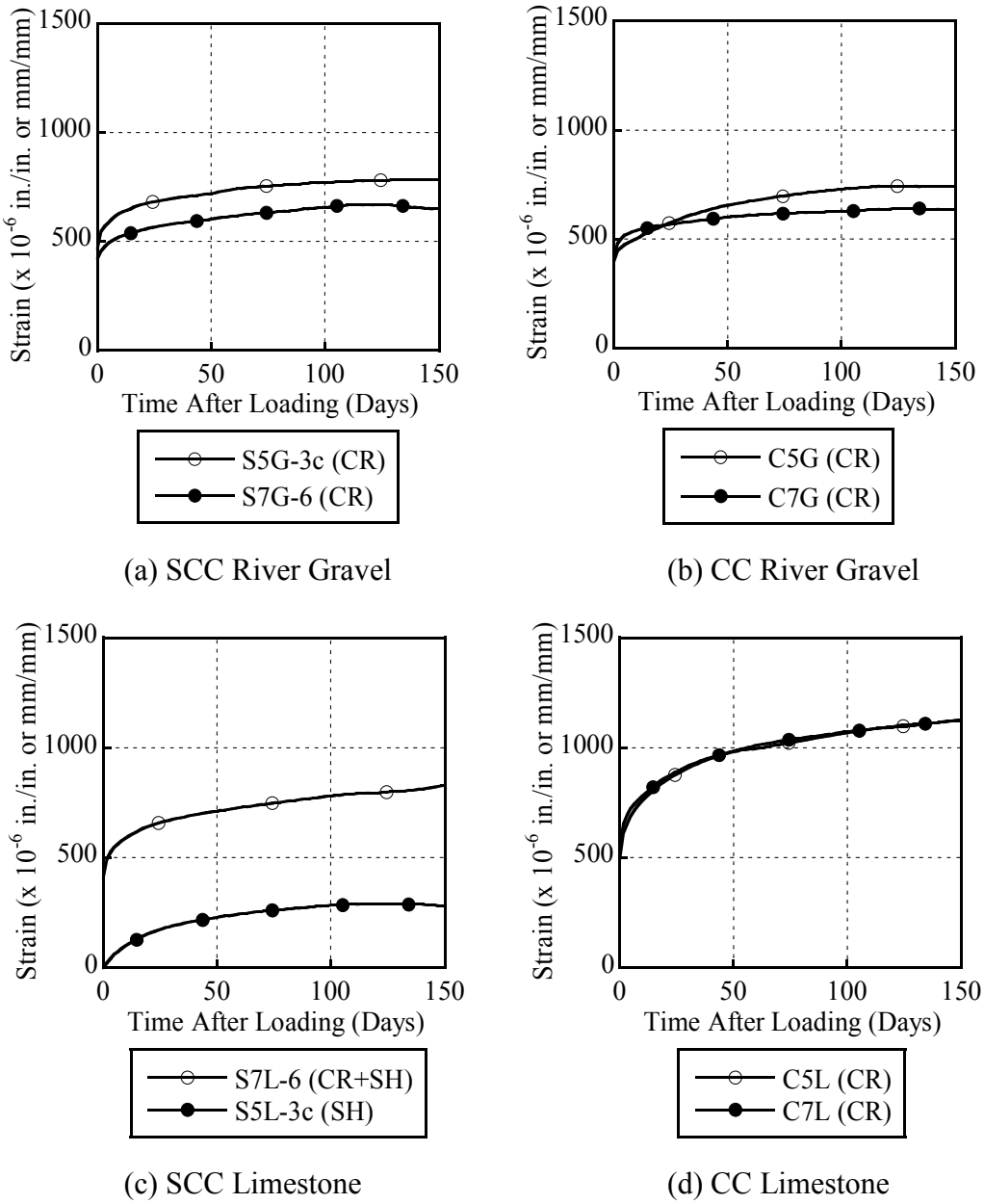

Figure F.1. Creep of Compressive Strength (5 ksi [34 MPa] versus 7 ksi [48 MPa]).

Figure F.2 shows the comparisons between creep of different mixtures having different type of aggregate.

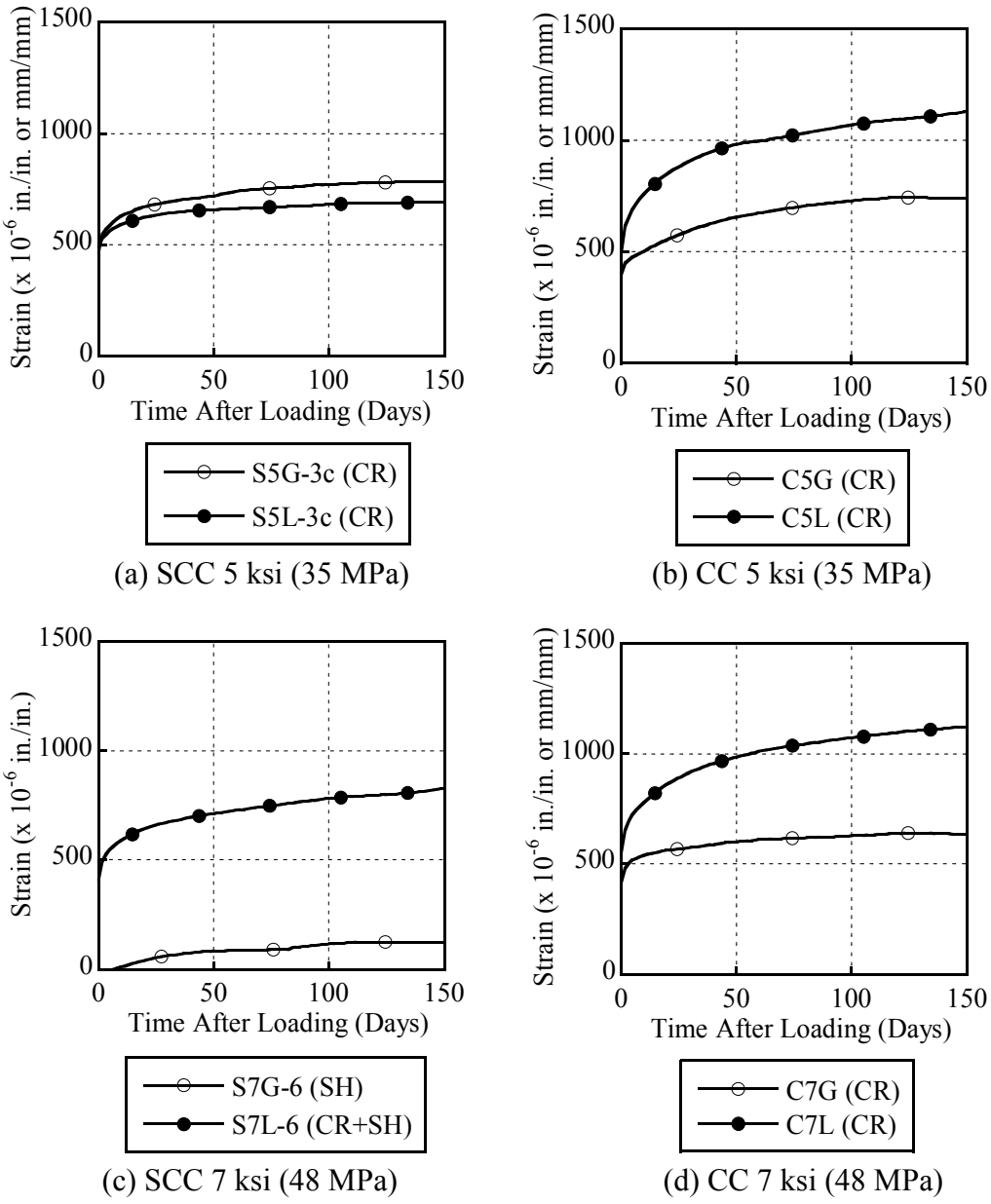

Figure F.2. Creep of Aggregate Type.

APPENDIX G
PREDICTION AND MEASURED VALUE FOR CREEP

Figures G.1 – G.8 shows the creep and shrinkage of each mixture with prediction curves.

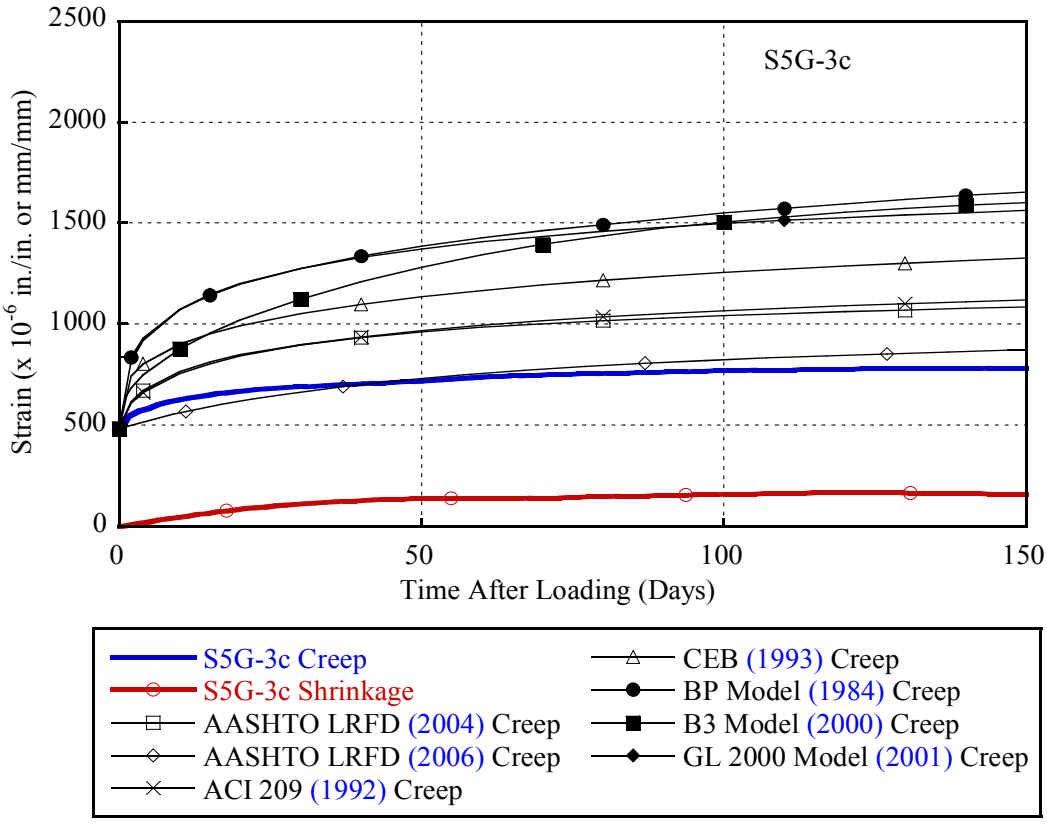

Figure G.1. Creep and Shrinkage versus Predictions for S5G-3c.

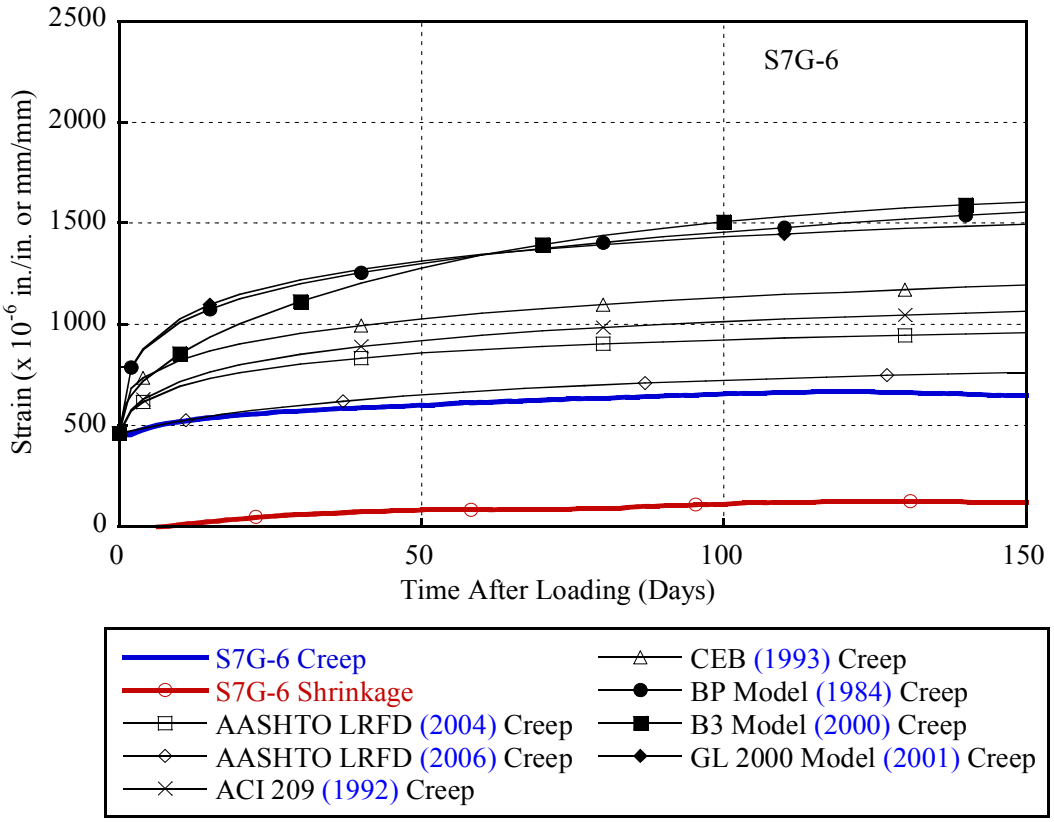

Figure G.2. Creep and Shrinkage versus Predictions for S7G-6.

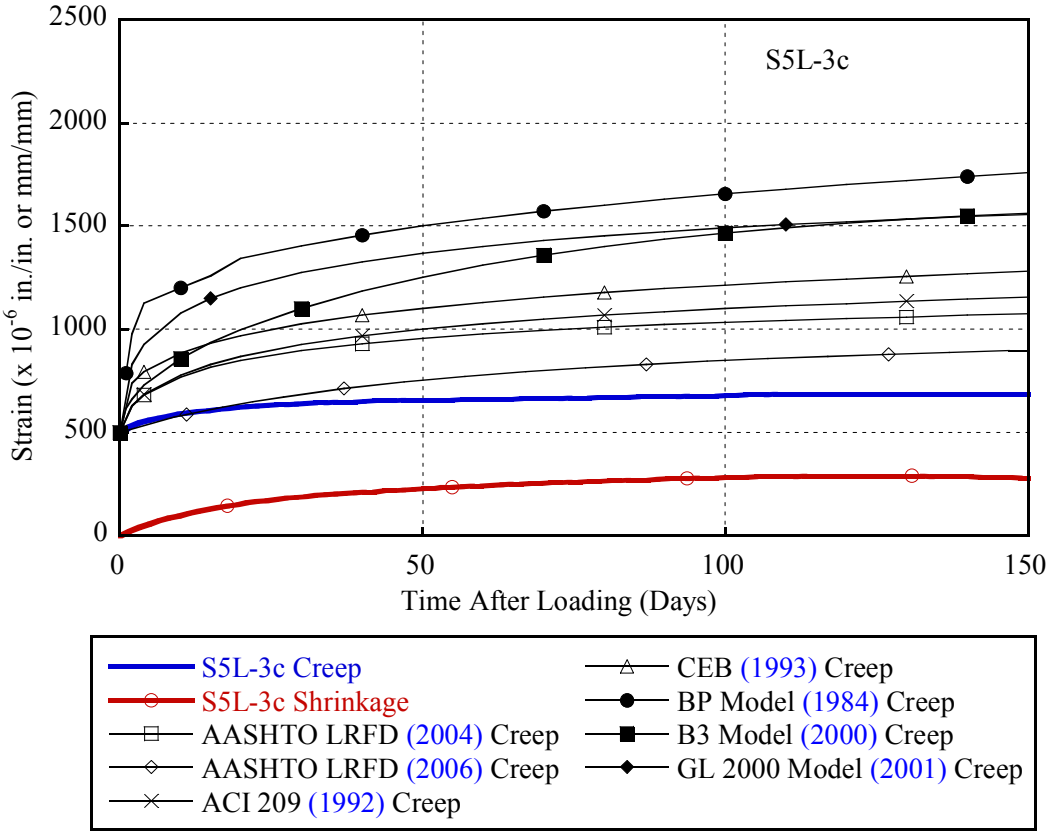

Figure G.3. Creep and Shrinkage versus Predictions for S5L-3c.

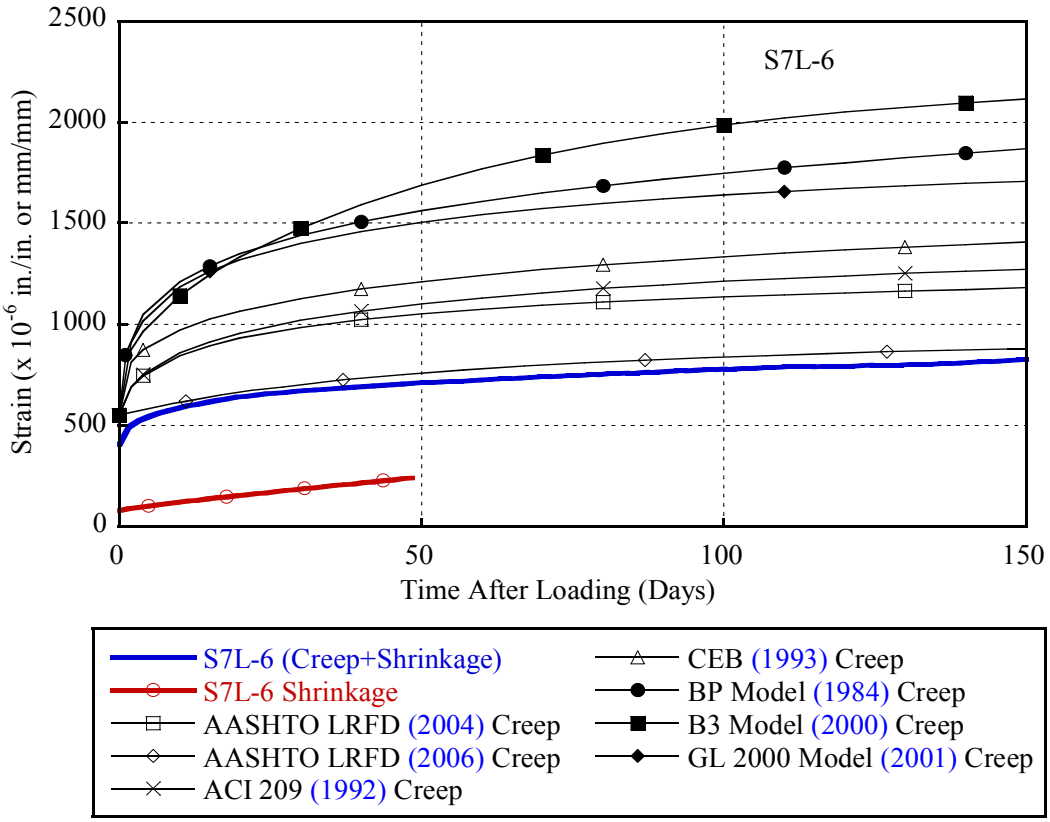

Figure G.4. Creep and Shrinkage versus Predictions for S7L-6.

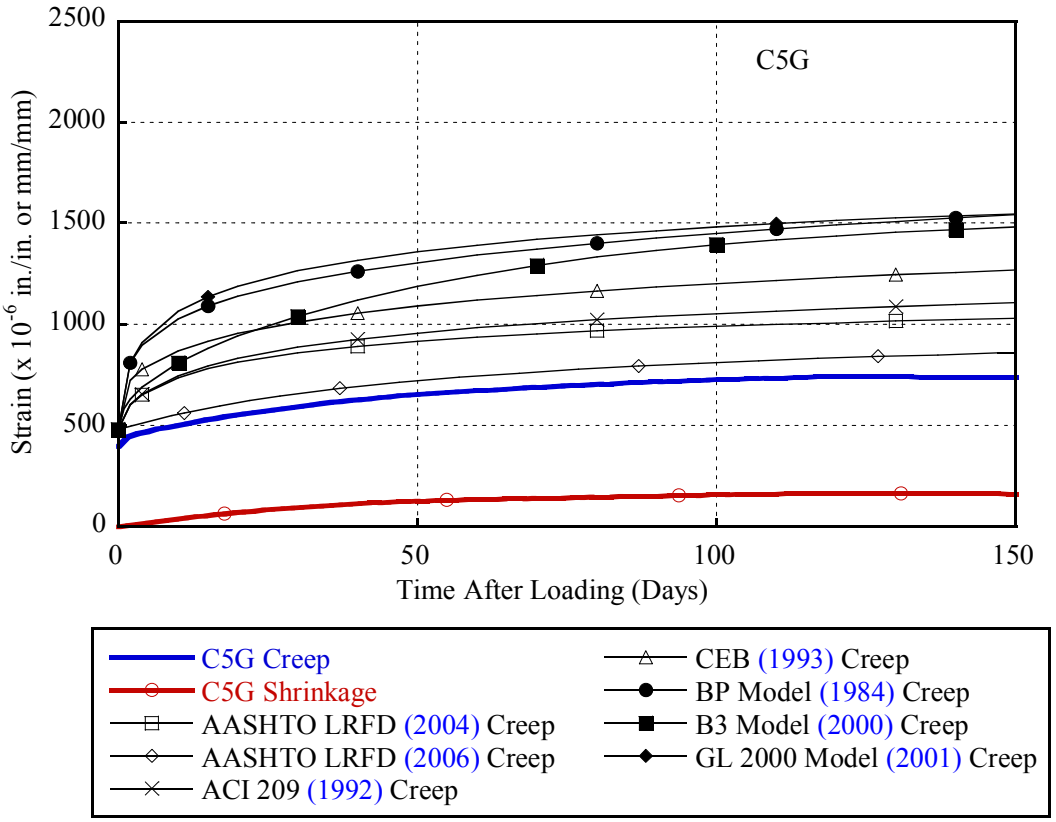

Figure G.5. Creep and Shrinkage versus Predictions for C5G.

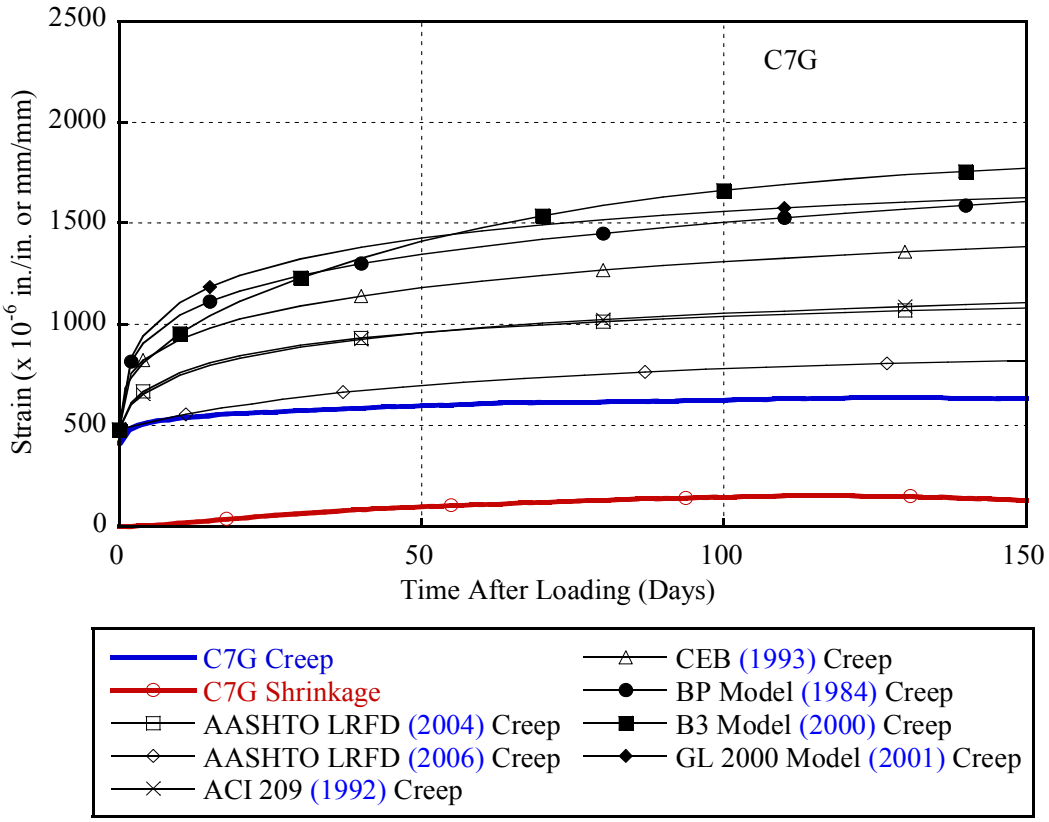

Figure G.6. Creep and Shrinkage versus Predictions for C7G.

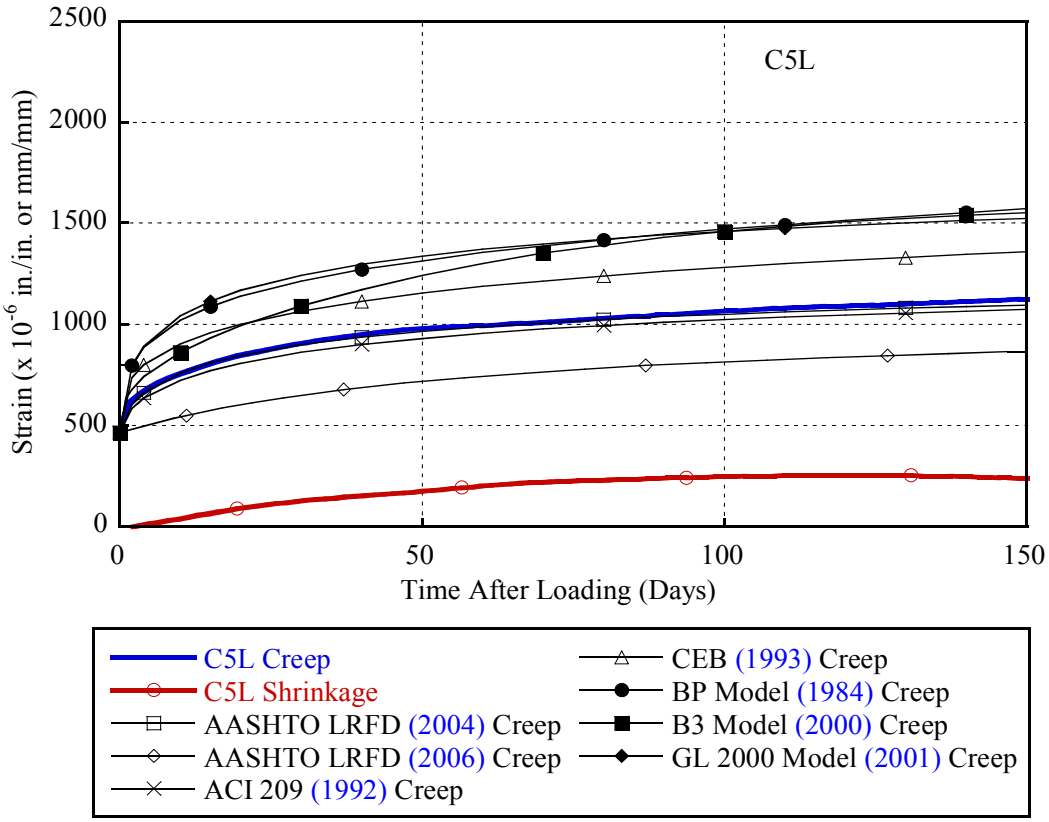

Figure G.7. Creep and Shrinkage versus Predictions for C5L.

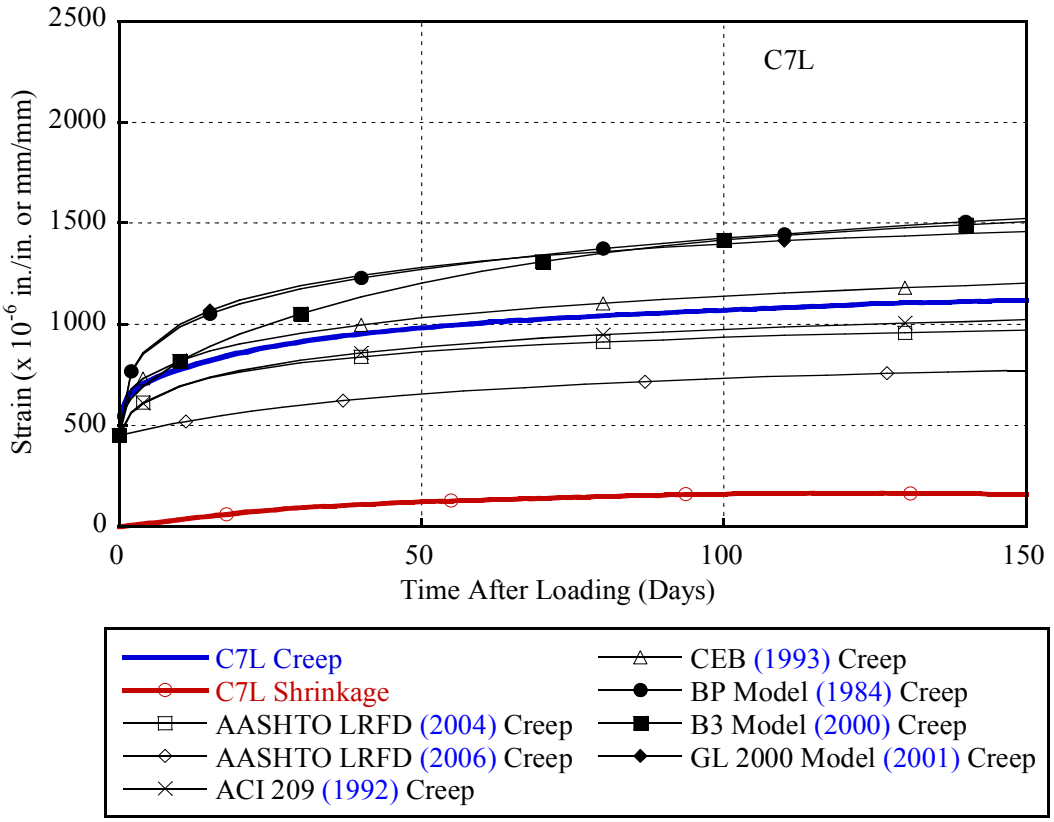

Figure G.8. Creep and Shrinkage versus Predictions for C7L.